Transactions of the ASME®

Transactions of the ASME, Journal of Engineering for Gas Turbines and Power (ISSN 0022-0825) is published quarterly (Jan., Apr., July, Oct.) for $120 per year by The American Society of Mechanical Engineers, 345 East 47th Street, New York, NY 10017. Second class postage paid at New York, NY and additional mailing offices. POSTMASTER: Send address change to The Journal of Engineering for Gas Turbines and Power, c/o The AMERICAN SOCIETY OF MECHANICAL ENGINEERS, 22 Law Drive, Box 2300, Fairfield, NJ 07007-2300.
CHANGES OF ADDRESS must be received at Society headquarters seven weeks before they are to be effective. Please send old label and new address.
PRICES: To members, $29.00, annually; to nonmembers, $120.00.
Add $12.00 for postage to countries outside the United States and Canada.
STATEMENT from By-Laws. The Society shall not be responsible for statements or opinions advanced in papers or ... printed in its publications (B 7.1, para. 3).

INDEXED by Applied Mechanics Reviews and Engineering Information, Inc.

Journal of Engineering for Gas Turbines and Power

Published Quarterly by The American Society of Mechanical Engineers
VOLUME 111 • NUMBER 2 • APRIL 1989

TECHNICAL PAPERS

TECHNICAL BRIEFS

ANNOUNCEMENTS

F100-PW-229 Higher Thrust in Same Frame Size

B. L. Koff
Senior Vice President,
Government Engine Business,
Pratt & Whitney,
West Palm Beach, FL 33410-9600

The F100-PW-229 fighter aircraft engine is a higher thrust derivative of the F100-PW-220 and in the same frame size. The engine was developed from the F100 Engine Model Derivative (EMD) Program and parallel IR&D efforts. The increased thrust was achieved by increasing the flow and pressure ratio of the two-spool compression system accompanied by an increase in turbine temperature. The increased length compression system was offset by an innovative design intermediate case and a reduced length combustor to maintain overall engine axial length. The −229 engine has a thrust-to-weight ratio of 8.0 with a 20–30 percent performance increase over the −220 model across the flight map. Significant improvements in maintainability have been incorporated while retaining the proven durability and operability features of the −220 engine. The Government–industry partnership is working well, continually providing increased performance engines for our first-line fighters.

Background

The F100-PW-220 engine shown in Fig. 1 was qualified at a thrust level of 24,000 lb (sea level static) in 1985 featuring numerous significant improvements over the earlier models. These included an increased life core (ILC) with extensive compressor modifications, a low-smoke rolled ring combustor, a new turbine utilizing advanced materials, a gear-type fuel pump with substantially increased tolerance to foreign object damage, an engine diagnostic unit (EDU) to improve maintainability, and a digital electronic engine control (DEEC) capable of "threading the needle" throughout the flight envelope.

During the qualification Accelerated Mission Test (AMT), the −220 engine ran 4000 Total Accumulated Cycles (TACs). Maximum power thrust was held at 102 percent with no unscheduled engine removals (UERs), no in-flight shutdowns (IFSDs) and only eight maintenance events (15 allowed). These same core engine components were reassembled and operated *another* 4000 cycles! Figure 2 shows some highlights of both these historic durability test demonstrations. As in the previous 4000 cycle AMT, engine peak thrust was automatically held above 100 percent by the DEEC, which "tells" the fuel control to put more fuel in the combustor as the turbomachinery deteriorates. For the components whose lives are driven by cyclic or hot time usage, the 8000 cycle Accelerated Mission Test approximates 18 years of Air Force operation. Figures 3 and 4 show a first turbine vane and blade comparison between the −220 model at 8000 TAC cycles and the previous −100/−200 model at 1350 TACs. At a cost increase of 50 percent to the airfoils, the −220 turbine provides an *order of magnitude* improvement in life capability over the previous turbine. The level of durability achieved with the −220 core has been credited in a cost savings to the Air Force of $490 million over the next 18 years.

Contributed by the International Gas Turbine Institute and presented at the 33rd International Gas Turbine and Aeroengine Congress and Exhibition, Amsterdam, the Netherlands, June 5–9, 1988. Manuscript received by the International Gas Turbine Institute October 1, 1987. Paper No. 88-GT-312.

F100-PW-229 Configuration Evolution

The demonstrated durability level of the −220 core formed the basis for a 20–30 percent thrust level growth within the same frame size. This effort was considered an acceptable risk as a result of the ongoing Engine Model Derivative (EMD) Program coupled with Independent Research and Development (IR&D) and U.S. Government Exploratory and Advanced Development Technology Programs. This evolu-

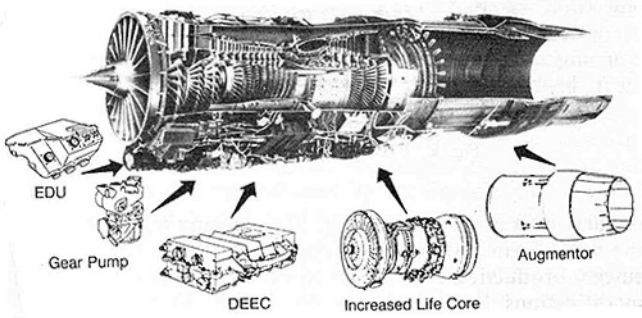

Fig. 1 F100-PW-220 configuration

	4,000cy/9yrs	8,000cy/18yrs
Total cycles	4,083	8,191
Hot (combat) test hours	362	729
Air combat missions	650	1,465
Air-to-ground missions	786	1,434
Engine accelerations	34,551	76,738
Augmentor lightoffs	8,254	19,308

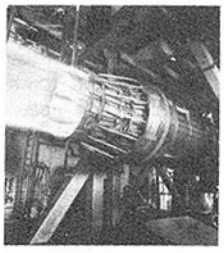

Fig .2 F100-PW-220 Accelerated Mission Test (AMT)

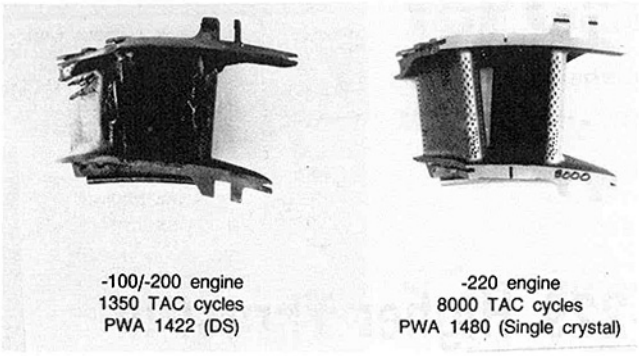

Fig. 3 First turbine vane comparison

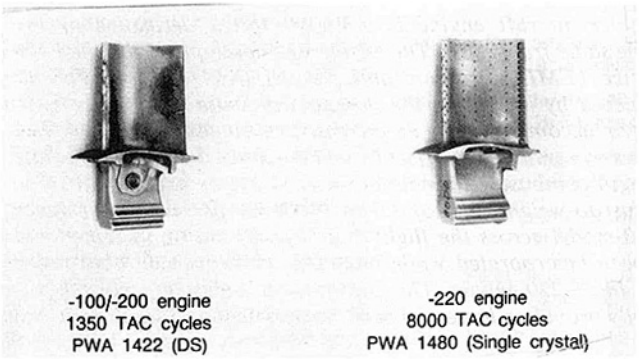

Fig. 4 First turbine blade comparison

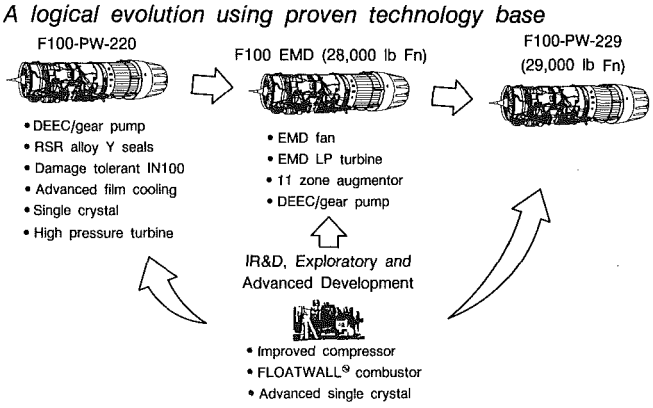

Fig. 5 F100-PW-229 configuration

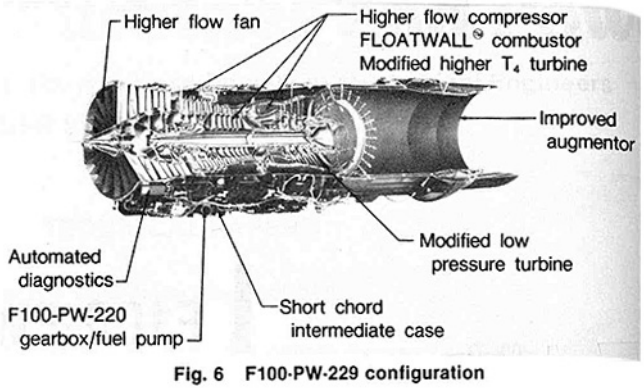

Fig. 6 F100-PW-229 configuration

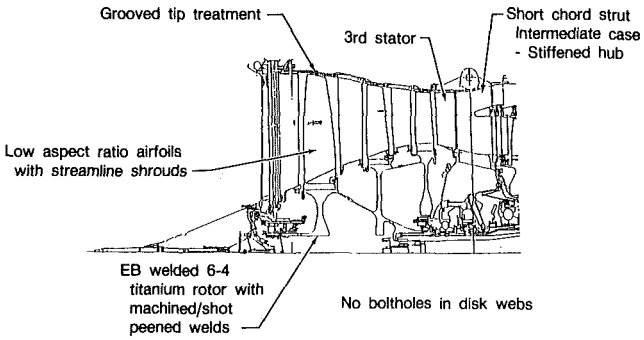

Fig. 7 F100-PW-229 fan

tionary process is shown in Fig. 5. Achieving higher thrust in the same frame size permits upgrading the performance of current production F-15 and F-16 aircraft without installation modifications.

Engine thrust is determined by three parameters as measured at the engine nozzle: airflow, pressure, and temperature. At maximum power, further increases in exhaust temperature are not available since all but the nozzle cooling air is already burned in the afterburner. This means that the thrust increase must be provided by a modest increase in fan flow—still within the same frame size to fit current installations—combined with an increase in overall cycle pressure ratio. In order to maintain the frame size (and engine diameter) it was necessary to increase the fan pressure ratio while increasing the fan flow. This kept the Mach number in the bypass duct at an acceptable level to avoid increased pressure loss.

Both to meet the increased power requirements of the fan and to provide growth margin, an increased flow size engine compressor operating at higher pressure ratio was provided. The combination of additional fan supercharging and a larger flow size compressor resulted in meeting the objective of only a modest increase in turbine temperature over the proven −220 model. Both the fan, with three rotors and three stators, and the larger compressor introduced increased axial length over the −220 model. In order to accommodate the increases, a new reduced length Floatwall combustor was adapted and the intermediate case was redesigned to incorporate short cord struts. These changes resulted in an F100-PW-229 engine that retained the same mount locations of the current F100 engine and could fit within current F-15 and F-16 aircraft envelopes. Figure 6 shows the −229 engine cross section illustrating the overall arrangement, major engine features, and key components.

Designing the Components

Fan. The fan shown in Fig. 7 was developed during the EMD Program and has completed two successive 4000 TAC Cycle Accelerated Mission Tests. The design incorporates a three rotor, three stator configuration behind an integral anti-iced vane frame with struts and variable inlet guide vanes. The first two rotor stages have midspan shrouds. A similar configuration on the F100-PW-100/−200 model has demonstrated outstanding ability to "chew up and digest" parts in air combat.

The rotor spool is electron beam welded 6A1-4V Titanium. The welds are machined and shot peened all over to provide infinite life. The intermediate case struts were axially shortened to accommodate the addition of a third stator, which was added to unload the intermediate case and eliminate strut-induced blade vibration. Maintaining axial rigidity of the 30 percent shorter intermediate case (frame) proved to be a substantial design challenge. Shaped stiffening rings at the inner flowpath struts provided the required rigidity to accommodate the higher thrust load of the larger flow and higher pressure ratio compressor. Achieving high axial rigidity of the intermediate case using short chord struts was a key barrier problem that was overcome to allow the configuration to fit current airframe mounts.

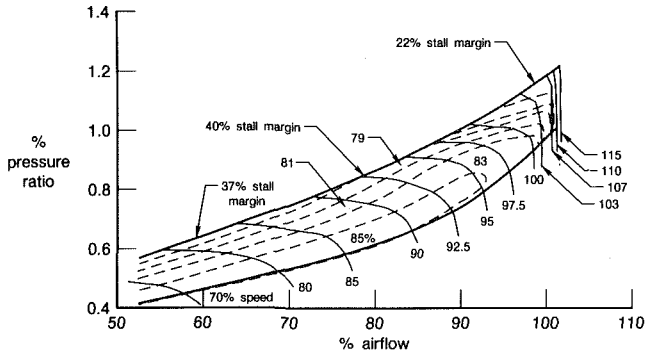

Fig. 8 F100-PW-229 fan map

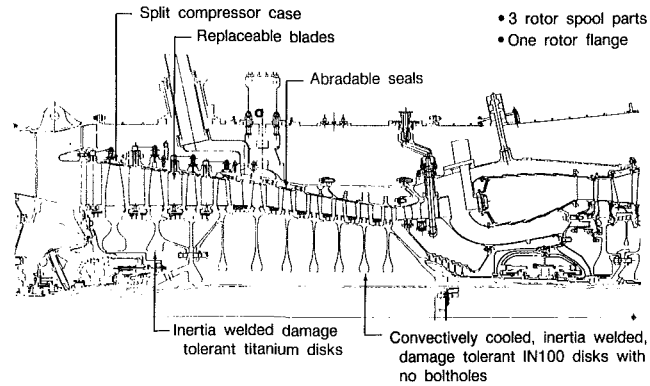

Fig. 9 F100-PW-229 compressor

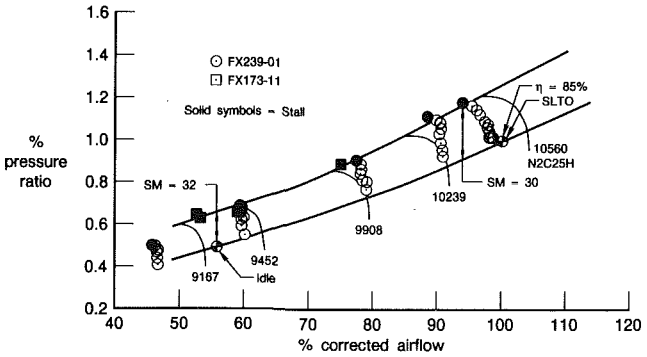

Fig. 10 F100-PW-229 compressor map

The fan map shown in Fig. 8 illustrates a high specific flow configuration exhibiting high stall margin across a wide speed range necessary to accommodate the wide variety of transients encountered in fighter engine applications.

Compressor. The compressor was originally designed with nine stages in the F100 flow size using combined IR&D and U.S. Air Force contract funding. For the −229 engine application, the first four stages were replaced with fives stages to increase flow and pressure ratio. This ten-stage configuration is shown in Fig. 9 and incorporates numerous features to enhance both performance and maintainability. All the blades are replaceable by using a split stator case that also maintains a high degree of roundness during a "cold iron" throttle burst to maximum rotor speed. During development testing one engine was intentionally stalled 100 times with no airfoil distress. Features such as the variable stator system, damage-tolerant titanium and superalloy disk materials, coated knife edge seals, honeycomb shrouds, and RSR blade tip abradable

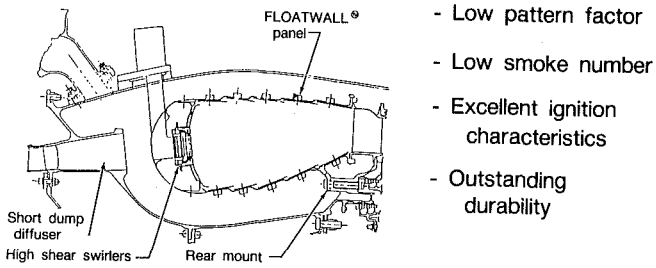

Fig. 11 F100-PW-229 reduced length floatwall combustor

seals were retained from the proven −220 design, having successfully passed a 4000, and then 8000 TAC cycle AMT.

The compressor rotor is internally convectively cooled with third-stage compressor air, which is vented aft to cool the low-pressure turbine rotor also. The compressor rotor spool has only *one* flange and *three* structural parts consisting of two inertia-welded damage-tolerant titanium stages, a third-stage disk and hub (subshaft) and a seven-stage inertia-welded drum section with an integral aft shaft. Inertia welding the substantially tougher IN100 damage tolerant material in a decreasing diameter or cone presented a manufacturing challenge that was overcome with development, tooling, and attention to detail.

The performance of the first ten-stage compressor was evaluated in a core engine and is shown in Fig. 10. The stall line is essentially as predicted with demonstrated stall margins of 30–32 percent from idle to full power. This stall line was measured with clearance conditions representative of an engine after full break-in due to snap throttle transients. Also shown are several stall points from the first full engine configuration, including the low spool. These stall points substantiate the stall line from the core engine, indicating that there are no degrading effects due to interactions between the high and low pressure spools. Efficiency levels of 85 percent were demonstrated that fully meet the initial engine goals.

Combustor. The −220 combustor that was successfully qualified to 4000 TAC cycles and then run another 4000 cycles used F100 aerodynamics, advanced technology cowl and swirlers, and a rolled ring liner configuration derived from the PW2037 commercial turbofan. The F100-PW-229 engine uses a new "Floatwall™" combustor concept derived from technology programs using first IR&D funding followed by Government technology funding. The design and development program of this more advanced, higher temperature and shorter combustor was initiated by the Government–industry partnership in anticipation of future needs for turbine engines.

The axially shorter Floatwall™ combustor shown in Fig. 11 is aft mounted to improve the load path and improve sealing at the first stage nozzle diaphragm. The flow splitter on previous F100 model aft of the diffuser and forward of the dome has been eliminated by incorporating advanced diffuser technology. Even though it is shorter than the F100-PW-220 combustor, the performance of the new F100-PW-229 combustor matches the outstanding −220 results in pattern factor (measure of hot streaks), profile, smoke, and altitude relight characteristics. The Floatwall™ combustor has significant temperature margin over previous configurations and is the wave of the future combustion design.

High-Pressure Turbine. Except for "lessons learned" modifications to retain temperature margin, durability and to accommodate temperature growth, the −229 high-pressure turbine shown in Fig. 12 utilizes the successful −220 configuration and experience. The rotor spool has minimum stress concentrations and no bolt or cooling holes in the disk webs. As in the compressor, damage-tolerant IN100 material

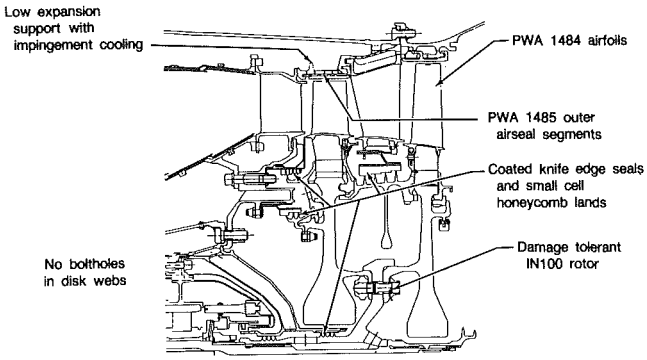

Fig. 12 F100-PW-229 high-pressure turbine

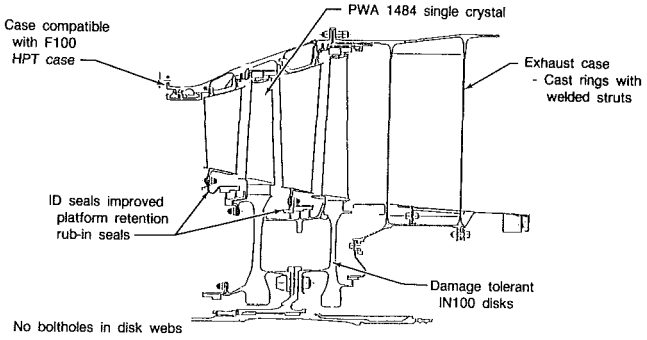

Fig. 13 F100-PW-229 low-pressure turbine

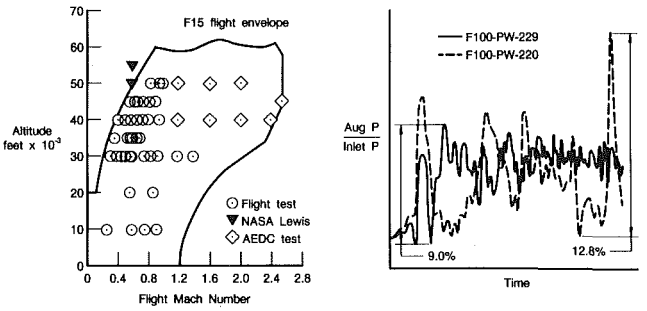

Fig. 14 F100-PW-229 augmentor

is used so that defects within the high stressed rotating parts will not propagate to critical crack length between scheduled inspection periods. The turbine airfoils were upgraded from PWA 1480 to the next generation single-crystal material PWA 1484 to retain durability margin and accommodate growth. The turbine blade outer air seals were also upgraded to PWA 1485 material to minimize cooling air and resist erosion at higher temperatures. Once again, the new key features incorporated were developed in the Government–industry partnership technology program and "lead the commitment" to reduce risk during full-scale development.

Low-Pressure Turbine. The −229 low-pressure turbine shown in Fig. 13 was developed in the Engine Model Derivative (EMD) Program to match the increased fan power requirement. Features include larger flow area, a second-generation single-crystal PWA 1484 first-stage uncooled blade for increased life, damage tolerant IN100 disks, and improved seals and shrouds.

The F100 low-pressure turbine has two uncooled stages that are relatively lightly loaded aerodynamically. The original F100 divided the work equally between the two stages. To accommodate the higher gas temperature of the −229 and retain

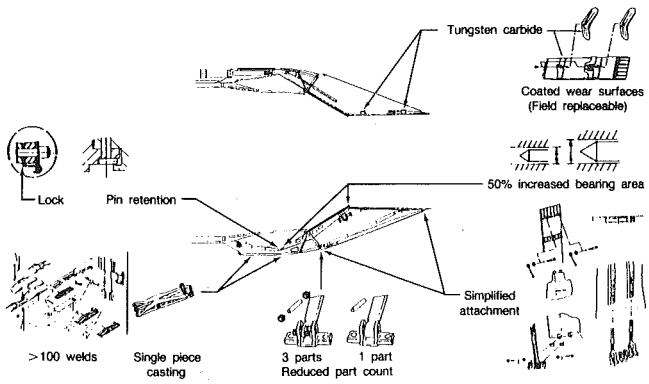

Fig. 15 F100-PW-229 nozzle module

an uncooled first blade, the work was shifted primarily to the first stage of the LPT to extract more energy. This was possible without performance penalty because of advanced computational fluid dynamics (CFD) three-dimensional analytical tools and techniques employed in the aerodynamic redesign to maintain performance and increase flow capacity. With a 70/30 percent split between the two stages, more work (and therefore temperature) is extracted in the first stage, so that the increased gas temperature is felt only by the inlet vane. The remaining three airfoil rows run in the −229 at the same (or lower) temperature as in the base −220. With the revised stage work split and the upgrade of materials, the LPT airfoil inspection requirements have been extended to equal those of the high-pressure turbine.

Augmentor/Nozzle. At the request of the Air Force and after an extensive design review, an Advanced Fuel Management (AFM) system concept was incorporated in the EMD Program in early 1981. The primary purpose of this improved fuel distribution system is to reduce the pressure pulse of the augmentor transient during an engine acceleration from military to maximum power. This pressure pulse can cause a fan stall during a combination of adverse conditions encountered in the "upper left-hand" (low speed/high altitude) region of the flight envelope. This AFM system also required using a Digital Electronic Engine Control (DEEC), which was qualified in the −220 model. The success of the AFM and DEEC system resulted in a 30 percent reduction in the bypass duct pressure pulse as seen by the fan. The design approach used in the AFM utilizes small volume spray rings for faster fill and response in combination with eleven fuel segment zones versus five on the −220 for a smoother light-off.

The AFM development experience has been excellent as shown in Fig. 14, with 5800 hours accumulated in the F100 EMD, Highly Integrated Digital Electronic Control (HIDEC) and −229 development programs, including flight tests. This system has demonstrated the ability to accelerate from idle to maximum thrust in less than 4 seconds. Also recent −229 altitude tests have proven that the system has unlimited transient capability.

The −229 augmentor/nozzle operates at 20 percent higher internal pressure and also higher temperatures relative to the −220. This required a general strengthening of the structural parts with an opportunity to improve the wearout modes identified on the earlier F100 model. The nozzle module is shown in Fig. 15 and features reduced tooling requirements, reduced assembly time, a 20 percent parts reduction, castings to eliminate hundreds of welds, and coatings to reduce wear in critical areas. The new −229 nozzle also fits all F100 engines and results in improved durability, maintainability, and minimum weight impact due to the application of improvements in design and materials. Durability testing of the first augmentor/nozzle module completed 2000 AMT TACs without replacement of a single part for cause.

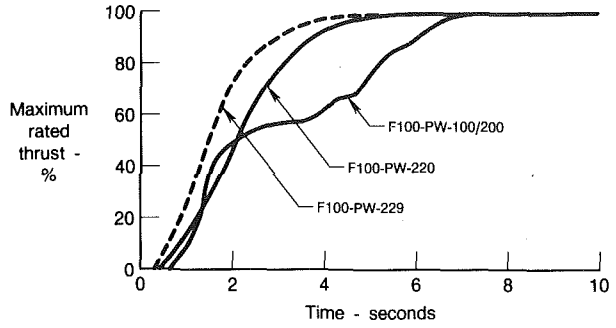

Fig. 16 F100-PW-229 controls

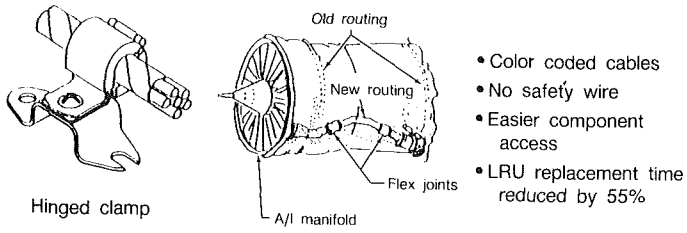

Fig. 17 F100-PW-229 externals

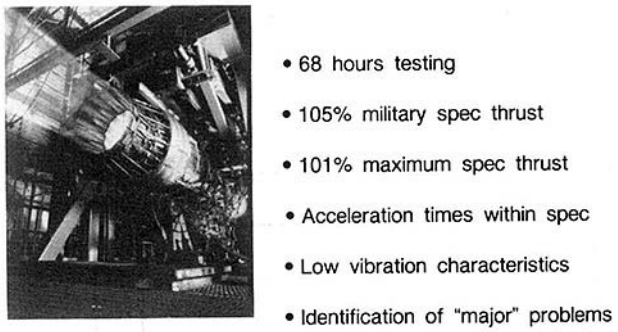

Fig. 18 Performance demonstrated on first engine to test

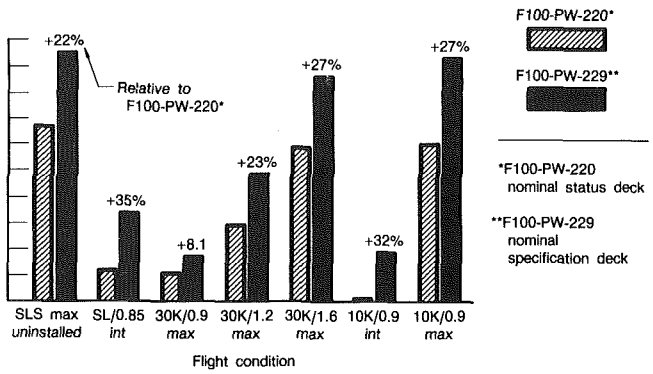

Fig. 19 F100-PW-229 versus F100-PW-220 performance

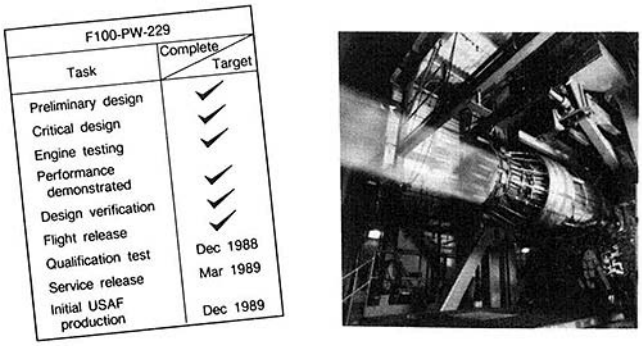

Fig. 20 F100-PW-229 status

Controls/Accessories. The −229 controls are based on the −220 DEEC system, which has met all performance goals and exceeded reliability predictions. The rugged gear-type main fuel pump, and most of the actuators and sensors, are either common with the −220 components, or have been tailored slightly for the −229 application. Improvements have been made to the electronic control to enhance memory, processor speed, and aircraft data bus communication. The augmentor control system distributes fuel quickly and accurately upon request from the DEEC to each of the eleven fuel segment zones. Improvements have also been made in several areas to enhance field maintenance and depot repair further, including color-coded electrical cables and a modularly repairable augmentor light-off detector.

Figure 16 shows an acceleration time to reach maximum thrust comparison between the −100/200, the −220, and −229 models. As shown, the −220 model achieves maximum thrust a full 2 seconds faster than the −100/200 model during a throttle burst from idle speed. F-15 pilots at Eglin Air Force base have reported significant improvements in aircraft acceleration with the −220 engines. As shown, the −229 model accelerates even faster than the −220 model from idle to maximum power.

Externals. Based on Air Force Reliability and Maintainability (R&M) input, the external features of the −229 were designed to improve reliability and reduce the maintenance-man-hours (MMH) required in operational use. Figure 17 illustrates some of the external improvements achieved by the industry/government R&M team. Features included color-coded wiring harnesses, clamping to "ground," quick release clamps, 70 percent fewer loose parts, single-feed anti-ice, double cone tubing ferrules to eliminate lock wire, and flex hoses to reduce plumbing. As a result, the average time to replace any one of the 27 external components in the Line Replaceable Unit (LRU) category has been reduced by 55 percent.

Engine. The integration of new components into a complex and total engine system, while simultaneously dealing with "show stopper" problems, is a measure of the maturity level achieved by our combined jet engine manufacturer and vendor industrial base. Figure 18 summarizes what the team achieved on the first −229 engine sent to test. The fact that the first engine on its first trip to test demonstrated key requirements was happily noted! Additionally, the early identification of major problems such as compressor aero/clearance matching and low-pressure turbine area match was particularly helpful in order to take early corrective action. Two engines and one core were instrumented with a total of over 3000 pressure taps, thermocouples, and strain gages to evaluate and verify the technology level selected, the analytical model, and design intent.

Figure 19 shows a performance comparison between the −220 and −229 engines at seven rating points. Except for 30K/Mach 0.9, the −229 achieves in excess of 20 percent thrust increase across the flight regime while fitting current F100 installations.

The status of the −229 engine development in Fig. 20 shows that excellent progress is being made toward meeting the qualification schedule goals. Extensive durability testing has been conducted as a part of the flight verification. The very

first – 229 AMT engine successfully completed a 2000 TAC cycle endurance demonstration and the same development engine is being built to run another 2000 TACs! It wasn't long ago that it took more than ten years of development and a billion dollars to approach this durability level.

The joint Government–industry team and IR&D efforts provided the technologies needed for dramatically improving engine reliability, durability, and maintainability. This makes a good case for the argument that America's continuing technology will provide competitive superiority tomorrow. So far, the "formula" consisting of the Government–industry effort, the IR&D program, and corporate capital investment seems to be working well. America's aerospace industry, and jet engines in particular, are out in front as evidenced by an overwhelming favorable balance of trade.

Don't be surprised if further substantial performance increases are developed for the F100-PW-229 engine from the on-going technology program. The last time our fighter aircraft engaged the Soviet MiG's in the 1983 Israeli–Syrian conflict in Lebanon, the outcome left no doubt with an 85 to zero kill ratio in favor of American equipment. The Soviet engine manufacturers Tumansky and Lyulka have not taken this lightly and have developed new powerful engines for the MiG 29 and Sukhoi 27 fighters. The F100-PW-229 fighter engine, its derivatives, and other new engines developed from the ongoing technology program will keep us out in front. We can't afford to be second here.

XG40—Advanced Combat Engine Technology Demonstrator Program

A. F. Jarvis
Rolls-Royce plc,
Bristol, United Kingdom

Commenced in 1982, the XG40 program is central to the demonstration of Rolls-Royce technology appropriate to the requirements of the advanced combat engine for mid-1990s operation. At the same time, the technology in scaled form is viewed as having wider application than for the advanced combat engine alone. This program is jointly funded by UK MoD and Rolls-Royce. In the paper the concepts and scope of the program are described. Associations with previous research programs and other advanced technology demonstrator programs of Rolls-Royce are stated. To meet the multirole capabilities of the advanced fighter and taking the European requirements in particular, the combat engine must be designed to give enhanced dry thrust, retain good dry specific fuel consumption, and reduce reheated fuel consumption compared with current fighter engines. A thrust/weight ratio of 10:1 is targeted and at the same time, requirements for operating cost, reliability, and durability are stringent. As a demonstrator, XG40 has been designed to meet the foregoing performance requirements. At the same time, advanced materials, manufacturing technology, and design of structures have been incorporated to enable the required levels of reliability, durability, component cost, and weight to be demonstrated. Although a demonstrator, XG40 was designed at a scale judged to be appropriate to the likely next generation European fighter requirement. Thus, the engine is in the 90/95 kN nominal Sea Level Static Combat thrust class. Configuration and design are discussed. XG40 is a total technology demonstration program. Principal modules each have a full-scale aerothermal rig program and appropriate structure rig programs. Apart from rigs, the program, including durability testing, utilizes a number of cores and engines plus spares. Achievements and progress toward milestones are reviewed.

Introduction

XG40 was initiated in 1982 and evolved to form a major Military Demonstrator Program aimed primarily at the requirements of the Advanced Combat Engine for 1990s operation. The program is jointly funded by Rolls-Royce and the United Kingdom Ministry of Defence.

Origins

While XG40 was initiated as a Component Technology Demonstration Program, it was conceived at the time that it would evolve to include demonstration of the integrated components in engine demonstrators. Thus, cycle, engine configuration, and size were extensively studied and selected with this in mind as well as appropriate levels of technology. To provide the necessary framework to this process of study and selection, two military applications of the technology were used, namely:

- Advanced Combat Engine requirements, including EFA, later to become EJ200
- Future re-engine of Tornado

Other applications of the same advanced technology were foreseen for possible requirements of Advanced STOVL, Advanced Strike Trainer, and Light Combat Aircraft. Eventual exploitation of the technology in Civil Engine Developments was foreseen, but these applications were not instrumental in the specification and design of XG40. Although the origins of XG40 were closely associated with RB199 growth proposals emerging in the early 1980s (the designation makes reference to 40 percent higher thrust, SLS combat, than the RB199 MK101), XG40 is a completely new configuration of advanced technology and is not derived from the RB199.

Influential in the origins of the XG40 were the preceding research and other component demonstration programs, providing a sound basis for the technology levels selected in XG40 and, in the case of the fan, actually providing the initial turbomachinery components.

Program Scope and Timing

The total program (see Fig. 1) comprises three subprograms:

- Component Technology Demonstration Program
- Engine Demonstration Program
- Life Assessment Demonstration Program

Contributed by the International Gas Turbine Institute and presented at the 33rd International Gas Turbine and Aeroengine Congress and Exhibition, Amsterdam, The Netherlands, June 5-9, 1988. Manuscript received by the International Gas Turbine Institute September 21, 1987. Paper No. 88-GT-300.

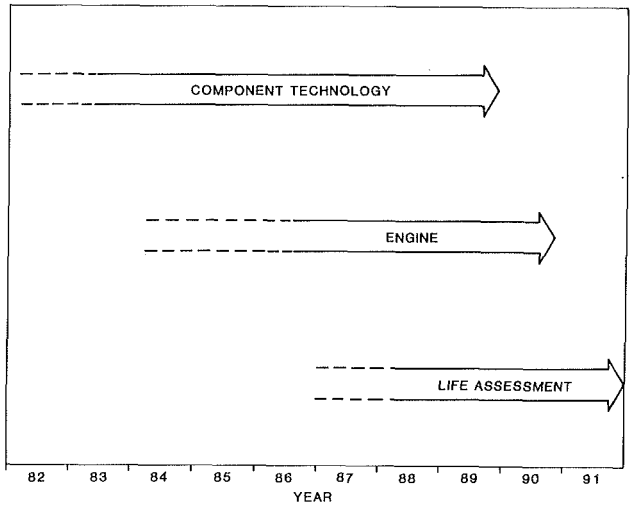

Fig. 1 XG40 demonstration programs

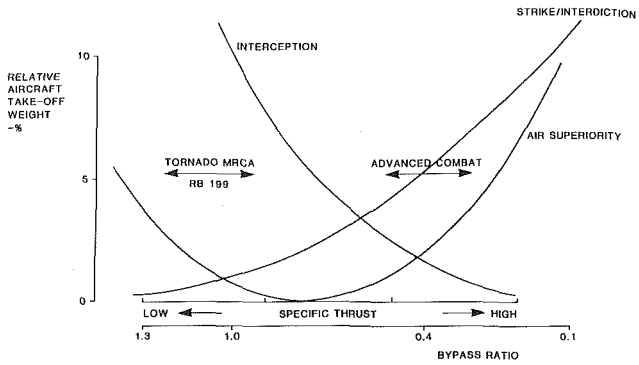

Fig. 2 Cycle options for combat aircraft

Table 1 XG40 leading particulars

THRUST/WEIGHT CLASS	10:1
FAN PRESSURE RATIO	3.9
OVERALL PRESSURE RATIO	26.0
REHEATED THRUST	90 Kn PLUS
DRY THRUST	50 Kn PLUS
MAXIMUM SOT	1800 K PLUS

The first of the above three – the Component Technology Demonstration Program – is aimed at conceptual studies, aerothermal rig programs, systems, and structures rig programs and includes a high-pressure single-spool (core) engine program. The program allows for a further degree of component investigation when the need arises from the Engine Demonstration Program, and thus overlaps in timing the latter program.

The second program – the Engine Demonstration Program – has as its objective demonstration of the combined HP spool and LP spool in an engine environment including both dry and reheat operation. Performance, system performance, structures, and engine control are all planned to be demonstrated. Comprehensive instrumentation is specified plus advanced testing techniques including, for example, extensive use of X rays. Sea level and altitude test facilities are used.

The Life Assessment Program has as its primary purpose the demonstration of the potential of the "hot end" to meet the component design lives when operating in conditions as close as possible to the real environment. Thus, the program is based on high-pressure spool and fully integrated demonstrator engine cyclic endurance testing. Sea level and altitude test facilities are used. Accelerated Service Endurance Test (ASET) schedules are included. Also, selected aspects of Flight Clearance Testing are included to broaden the scope of testing to verify the design capability in areas not covered by cyclic endurance and ASET type schedules.

The phases of the overall program are carefully timed, with sequenced and dependent activities to ensure that excessive commitment to a later stage of demonstration without an adequate demonstration of earlier technical elements is avoided. XG40 is also interactive with ongoing research and other demonstration programs and again program event timing reflects these dependencies.

Technical behavior, both aerothermal and structural, is modeled for individual components, assemblies, and of course, the high-pressure single spools and engines. Achievement against the modeling forms part of the "gating" control to allow the program to proceed to the next planned step or reschedule.

Challenging, but realistic, technical targets have been set for the XG40 program. It is recognized that some refinement of the design may be required to meet the technical targets. Thus, for example, on major aerodynamic rig programs, allowance is made for the initial design to be tested plus a further partial redesign of gas path components. Exceptionally, a third design refinement will be allowed, provided the funding can be found from within the overall program without increasing the total spending.

Apart from rigs, the program, including durability testing, utilizes a number of cores and engines, plus adequate spares.

Technical Concept

The technical concept of XG40 has been to ensure that for the technology selected:

- Targets are set to competitive levels.
- It is possible to demonstrate the technology in a time frame consistent with emerging Advanced Fighter Engine requirements and in particular, with those of EJ200.
- Designs are based on previous research and demonstrator programs.

Cycle and engine size selections were approached initially from the above considerations plus parallel objectives that the XG40 engine without scaling should be interchangeably installable in Tornado.

The cycle was neither optimized for the mid-1990s Advanced Fighter requirement generally nor the emerging EJ200 requirement in particular but core size was carefully selected and a range of fan pressure ratios is included in the program. Figure 2 shows the effect of aircraft role on cycle selection. Table 1 gives leading particulars of XG40.

Central to the technical concept of XG40 has been to design components generally to productionized forms. In this way the scope of XG40 has been broadened beyond the more traditional aerothermal and performance objectives of demonstrator programs to include additionally:

- Demonstration of productionized parts cost model
- Demonstration of realistic mass model
- Demonstration of design for modularity
- Demonstration of whole engine dynamics
- Demonstration of structures behavior on representative designs

•Demonstration of advanced manufacturing techniques/processes on representative designs
•Demonstration of advanced materials in representative geometries.

High thrust/weight ratio and high specific thrust demanded by the advanced combat engine require high values of fan pressure ratio and turbine inlet temperature. Reheat fuel usage is particularly important for many of the Advanced Combat Aircraft missions and again low fuel usage is best met with high turbine inlet temperature and high fan pressure ratio. With high fan pressure ratio a single spool core is appropriate for the core pressure ratio required to meet the overall engine pressure ratio.

Component design lives have been set at levels consistent with achieving competitive maintenance material costs. The lives are achievable with the benefit of improved design analysis methods, materials, cooling, and coatings technology within prescribed weight and cost targets.

In the configuration and design of XG40, reliability and maintainability objectives that are appropriate to a new 1990s Advanced Combat engine have been taken into account. XG40 has been designed to encompass full modularity and is capable of accommodating engine health and performance monitoring systems. During the demonstration programs, relevant data are being collected and analyzed.

Design to cost aims have been set consistent with achieving the required levels of maintenance material costs. Stringent first cost targets have been set and components have been designed to be producible using advanced manufacturing techniques and processes, thus enabling credible production cost estimates to be modeled.

XG40 is a key vehicle for the demonstration of advanced manufacturing techniques and processes and examples of these are given later.

With respect to initial material selection, the philosophy has been to use advanced materials at various stages of their development and characterization. However, beyond the datum design, advancements are specified to be demonstrated within the program, including high-temperature composites.

Complementary programs for advanced control systems and accessories are underway. Hydromechanicals representative of production are specified for XG40; the digital controllers are test bed mounted in the XG40 program.

The configuration of XG40 is shown in Fig. 3.

Aspects of Component Design

Fan. With the wide bypass ratio variation between extreme operating points, e.g., low/medium altitude loiter and high altitude minimum Mach number, variable geometry should offer aerodynamics advantages, although conflicting with cost and weight and reliability objectives. Demonstrations of both variable inlet guide vanes (VIGV) and variable outlet guide vanes (VOGV) are included in XG40 as "back-to-back" experiments with no VIGV (the basic design) and with a fixed single row OGV.

The fan is designed with rig type bolted-in stator vanes to permit investigative restagger. This compromise of the stator away from a lightweight productionized standard structure is accepted in the interest of the aerodynamics demonstration since technology on this type of productionized structure already exists. The rotor assembly has bolted disks to facilitate aerodynamic change. All stages of blades are unsnubbered with advantages to performance and bird and foreign object ingestion resistance and are designed to latest flutter-free criteria. The bladed disks are representative of production structures and the demonstration of vibration and flutter-free characteristics is included in the program.

The fan is overhung with the advantages over straddle mounting of avoidance of vulnerability of structures to bird ingestion FOD and unbalance, simplified bearing arrangements, and no IGV structure blockage effects. These advantages outweigh the possibly easier LP spool dynamics with straddle mounting.

Intercasing Between Fan and HPC. This casing is an integral cast titanium structural component that presents a challenge to manufacturing technology to keep sections thin, hence weight down.

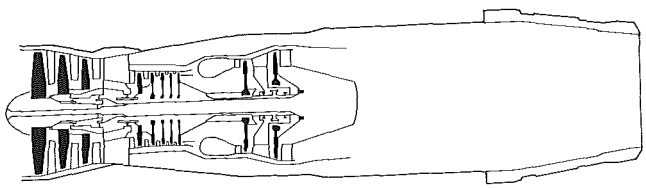

Fig. 3 XG40 configuration

HP Compressor

The design pressure ratio of the HP compressor is 6.5. Two series of existing Research Compressors were studied to evolve the XG40 HP compressor as a five-stage machine with low aspect ratio blades. Studies of both higher and lower numbers of stages were undertaken at the start of the program. The five-stage machine was within demonstrated loadings, had lower blade and disk stresses and lower exit Mach number than the four-stage, offered acceptably low blade count to meet cost targets, and was thus selected as the appropriate technology level of XG40 (see Fig. 4). For investigatory reasons, variable IGV's and variable first-stage stators are incorporated, but it is intended that the latter would be fixed in any production compressor based on XG40. Since specifying the initial HP compressor, the emerging requirements for advanced combat aircraft for power off-take for active control evolved and surge margin targets for XG40 were revised. Improved blading was specified.

The HP compressor rotor comprises a first-stage disk, a second to fourth-stage drum, and a fifth-stage disk integral with the compressor drive shaft. Titanium is used for stages 1 to 4, including high-temperature titanium for the drum. The fifth-stage disk and drive shaft is in nickel-based superalloy. Circumferential root fixing is used in stages 2 to 5.

Good rotor and stator tip clearance control is achieved by matching thermal response rates of the gas path casings with the rotors. The HP compressor gas path casings, made in low expansion steel, are isolated from the main structural engine casing made in titanium and have carefully designed thermal capacity and a controlled environment.

Stators are cantilevered to alleviate recirculation and temperature pickup associated with shrouded inner support. Heat generation at the rotor rim in the event of abnormal running is reduced too.

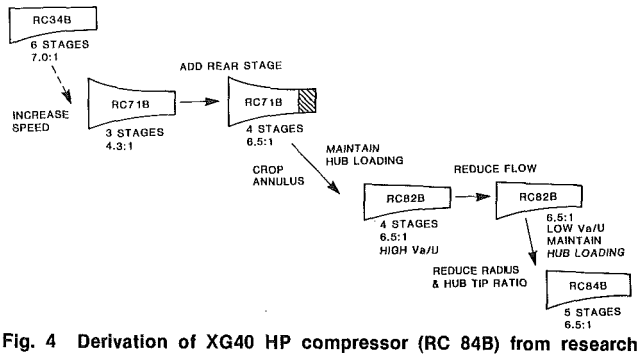

Fig. 4 Derivation of XG40 HP compressor (RC 84B) from research compressors

Combustion Chamber

High combustion chamber temperature rise and operating fuel/air ratio require a relatively high proportion of the combustor air stream to be fed to the primary zone to ensure low smoke levels are met; the resultant air available for combustor wall cooling and dilution is reduced.

Confidence in this balance of the thermodynamic design has been drawn from earlier and continuing Advanced Military Combustor programs within the Advanced Core Engine Technology (ACET) and Advanced Core Military Engine (ACME) UK demonstrators (see Fig. 5).

Sizing of the combustor for relight has taken into account RB199 experience. The chamber is canted but otherwise has a conventional dump diffuser upstream. Vaporizer fuel injection has been selected to attain the shortest, lightest (and lowest cost) design; temperature traverse achievements are at least comparable with alternative injection systems.

Nickel-based superalloys are used for the combustor. The vaporizers are nutted and removable to ease demonstration of alternative materials and coatings. Wall cooling is by fine hole Z rings plus external convection improved by minimizing annulus areas and including external turbulation on the combustor walls. Thermal barrier coating are specified too.

HP Turbine. To achieve high thrust/weight ratio and meet cost requirements, a single-stage shroudless HP turbine has been designed, based on data from RB199 and RB211 turbine designs, together with data from UK research and demonstration programs, namely, Research Turbine, Advanced Core Engine Technology (ACET), and High Temperature Demonstrator Unit (HTDU). See Fig. 6. The mechanical features are derived from an ACET design (ACET IIA), which is a previously established but continuing advanced military shroudless turbine technology demonstrator. Rotor blade cooling, which is multipass with films, is high pressure fed via low radius preswirl with fully sealed coverplate. Blade damping is provided for. A Rolls-Royce in-house low-density single-crystal nickel-based superalloy has been specified, but the rotor design can accept higher density alloys.

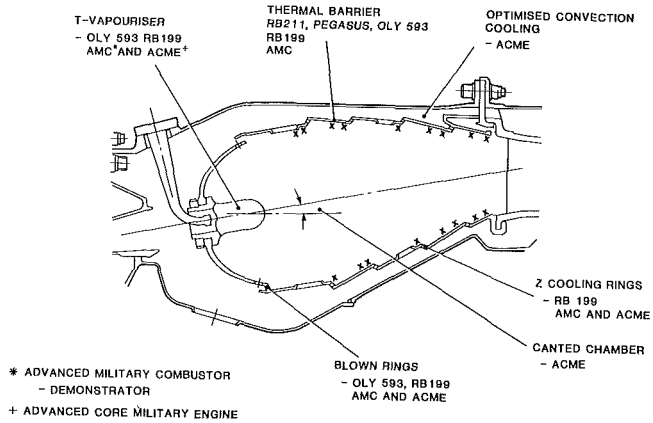

Fig. 5 XG40 combustor derivation

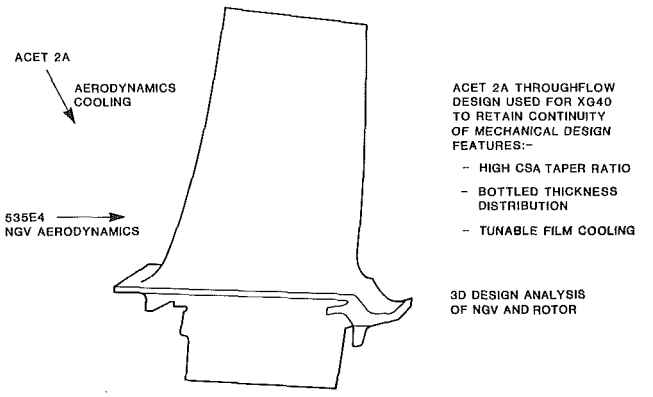

Fig. 6 XG40 HP turbine blade derivation

XG40 is making an important contribution to the demonstration of single-crystal turbine blade manufacturing technology. Significant demonstrations of aerofoil thermal barrier coatings and advanced blade tip treatments to resist oxidation and abrasion are designed in. Initially the HP turbine has passive tip clearance control, but demonstration of active control systems is planned.

HP turbine disk and coverplate have been designed in nickel-based powder superalloys.

The nozzle guide vane (NGV) technology in XG40 is built on RB199 experience, plus data from both HTDU and ACET. Vanes have inserts with multiple impingement surface films and trailing edge exhaust. The leading edge has shower head cooling. Platforms have impingement cooling. Thermal barrier coatings on aerofoils and platforms are to be demonstrated.

LP Turbine and Exhaust. The single-stage LP turbine has a structural NGV and a shrouded rotor. The HP and LP contra-rotate, with a low deflection LP NGV. Structural requirements determined the thickness of the NGV, but with the low camber NGV adopted the aerodynamics have been little compromised. A multiblade narrow chord exit guide vane assembly enables the gas to be deswirled before main diffusion. Figure 7 refers.

The rotor blade is cast in the same single crystal material as the HP turbine and has been designed with a cooling system offering maximum lightness to assist disk stressing.

The engine rear bearing support structure has been positioned through the LP NGV with benefits to HP turbine tip clearance control. The NGV and turbine rotor blade are cooled by stage 3 HP compressor bleed.

An important manufacturing technology demonstration has been the integral cast exhaust diffuser, which includes the narrow chord hollow section exit guide vanes. Initially uncooled, potential for uprating with cooling is provided.

Oil/Air System. Separated bearing chambers have been designed, thus avoiding hot, weak-mixture, intershaft spaces with the accompanying risk of oil fire and carbon formation. Heat to oil is reduced also by the design of low-pressure bearing chambers sealed with brush seals and by the use of external bearing track cooling in main thrust bearings. Bearing chamber pressurization is by fan delivery air, from total head scoops, which have adequate pressure, but minimized temperature.

Conventional oil pumping and scavenging systems have been designed, but XG40 has alternative advanced designs for

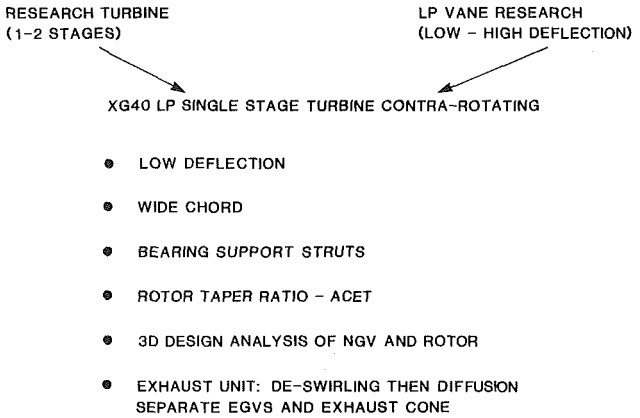

Fig. 7 XG40 LP turbine derivation

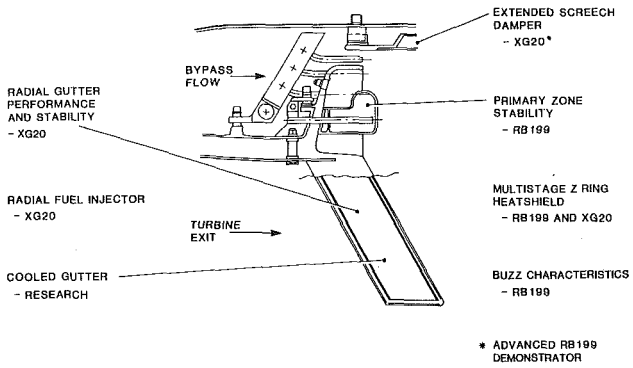

Fig. 8 XG40 afterburner derivation

pumping and scavenging utilizing the centrifugal fields in the bearing chambers.

Air System. The new features incorporated in XG40 include extensive use of brush seals and LP pressurization from total head air system scoops in the intercasing. The HP turbine rotor blade cooling system follows established RB199 practice. An alternative high radius rim seal, with cooling air temperature advantages, was considered and rejected for XG40 pending further demonstration of a seal running under such arduous environmental conditions.

Reheat System. High turbine exit temperatures of the advanced combat engine set new challenges, particularly to turbine stream fuel injection and flameholder systems.

Cooled metal fuel injectors have been designed and, for the baseline design of XG40, cooled metal structures are used for flameholder systems. Uncooled hot composites for selected flameholder systems have also been studied, however, and demonstrations commenced. Swirl burners present a further possible alternative allowing in principle the elimination of hot stream flameholders.

The extra vitiation of the turbine stream reduces its boost potential, but increases its proneness to buzz; thus XG40 is designed with special reference to reducing buzz. Cooling air flow for the jet pipe and nozzle has been designed to be minimized in order to increase the boost potential of the bypass stream. Multistaged operation of the reheat has been designed in conjunction with advancements in fuel metering. Derivation of the technology base for the XG40 reheat system is shown in Fig. 8.

Engine Control. Dry engine control is designed to demonstrate variable geometry features, including fully variable dry nozzle control. Also derivation of the optimum turbine blade temperature control by selection from three alternative pyrometers is a design objective.

Reheated engine control is designed to permit closed loop control from alternative inputs, including fan duct Mach number. Reheat staging is designed for fully transient operation.

Program Status

There follows a statement of progress and achievements at the time of going to press.

Fan. Full-scale aero rig programs of both a 3.4 pressure ratio fan and a 3.9 pressure ratio fan have been successfully completed. The fan aero rig program is now concentrated on the latter fan for which some reblading of the first version has been identified. The aim is to demonstrate a further version optimized more for the advanced combat aircraft requirements. A complete demonstration of intake swirl and distortion at levels to be met by the advanced combat aircraft is planned for this version too.

Blade and vane vibration has been fully measured during rig testing and monitored during engine demonstration testing. Flutter on the third stage of the 3.4 pressure ratio fan was readily fixed with snubbers. Improved design methods used for the 3.9 pressure ratio fan have been successful in achieving flutter-free operation over the required operating range without snubbers and this fan has also been shown to be satisfactory under severely distorted inlet flow.

Intermediate Casing. The challenge to manufacturing was to achieve an integral casing in titanium with complex coring and fine wall sections. RR worked closely with the casting supplier and successful castings for both the early fan version and the more complex version introduced at the same time as the 3.9 pressure ratio fan have been produced.

HP Compressor. Both the initial design and the revised aerodynamic design referred to earlier have been aero rig tested. Improvements in surge pressure ratio have been attained, and also gains in efficiency up to 90 percent design speed. A revised first-stage rotor to improve top end matching and a single row outlet guide vane (OGV) substituted for the existing double row OGV to reduce losses will be demonstrated.

Forward rows of blades and vanes have been vibration monitored with strain gages. Latter rows are scheduled to be measured for vibration during testing on a HP single-spool engine.

During manufacture and building of the HP compressor, producibility of certain novel design features has been demonstrated. Two instances have been the barrelled dovetail blade roots and the low stiffness thermally compensated stator rings. The point is made here to exemplify the benefits of designing demonstrators to productionized geometries to enable design refinement of mechanical details to be in place before subsequent full-scale development of the particular design feature.

Combustion. A comprehensive aero rig program has been completed and the aerothermodynamic targets set for the combustor met, including tight temperature traverse quality. One minor redesign of forward cooling rings has been required to achieve design flame tube wall temperatures.

Smoke results taken from the HP single-spool engine testing to date confirm the design objectives; engine smoke measurements are planned too.

In view of the good progress on the aerothermal demonstrations, the forward program of demonstration for the combustor is thus more centered on life assessment and durability aspects.

HP Turbine. The shroudless rotor blade is the key component of the HP turbine around which both manufacturing and major engineering demonstration test programs have been built.

Casting the blade advanced further aspects of single-crystal casting core manufacturing technology and casting technology. However, XG40 gained from prior single-crystal casting experience, in particular the ACET IIA turbine blade, to which the XG40 blade is very similar.

Economical use of cooling air has placed demands on fine hole machining techniques; XG40 has played a strong part in providing the incentives to derive the required machining techniques, which not only yield a small number of components for the demonstration program needs, but have good process capability for production. Other important areas of manufacturing technology advance are being demonstrated, based on the XG40 turbine, including thermal barrier coatings on nozzle guide vanes, blades, and liners; rotor blade and liner tip treatments; directionally solidified and single-crystal material nozzle guide vanes in monolithic and multipiece designs.

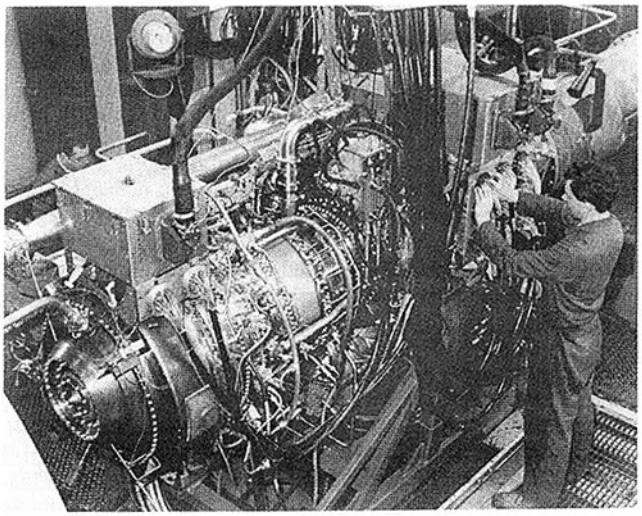

Fig. 9 XG40 high-pressure single-spool engine installation in high altitude test plant

Turbine aerodynamics have been demonstrated to date in full-scale plastic cold flow rig testing. Design efficiency has been attained on the initial design and no aerodynamic change is required. An aerodynamic rig enabling "engine standard" metal parts to be tested is planned, but priority has been given to testing on the HP single-spool engine (see Fig. 9) and the full engine; turbine performance has met design point expectations. Further detailed exploration of performance is planned for the HP single-spool engine, including demonstration of tip clearance effects; a thermally driven variable turbine shroud ring arrangement is incorporated for the latter testing.

For turbine blade cooling programs, resin models of blades have been made for measurement of internal pressure loss and heat transfer coefficients. Direct assessment of vane and blade cooling and core hot end temperature assessment in general has been made initially in dedicated thermal paint tests on the HP single-spool engine. In general, a level of overcooling has been seen on the initial design, which was deliberately cautious. Refinements to cooling readily achieved by alterations to film cooling will be demonstrated. Transient temperature surveys on the turbine disk and blades are planned.

Central to the demonstration of the HP turbine is the HP single-spool engine in its role as a realistic hot turbine rig. Although the HP single-spool engine is, of course, much more than this, having the full engine standard HP compressor and combustor, the timing of the HP single-spool engine in the XG40 program was largely determined by the HP turbine test requirements. In particular, the demonstration and evolution of satisfactory rotor blade structural dynamics is carried out on the HP single-spool engine as well of course as performance and cooling demonstration.

The HP single-spool is run on an altitude test facility to get correct engine conditions. Supporting fatigue rigs and both static and dynamic damping rigs are used in the rotor blade dynamics program. The ACET shroudless turbine blade demonstration program has run and continues closely associated with the XG40 program, which has benefited greatly from the ACET program, important aspects of which have been running in advance of the XG40 program.

To date, a full datum strain gage test program with the blade undamped has been carried out over the full running range. A damped version is planned. Structural improvements to increase high cycle fatigue strength have also been identified. Cyclic testing of the rotor blade is a major element of the XG40 Life Assessment Program. A second HP single-spool engine is being built for cyclic testing and an engine will follow.

LP Turbine and Exhaust. Casting of this rotor blade, which has a relatively high aspect ratio and is shrouded, required considerable casting expertise to achieve the dimensional control required. The task has been invaluable in advancing the single-crystal casting capability.

To meet an accelerated program requirement for LP turbine NGV's of increased throat capacity, a successful casting manufacturing trial of a major resetting of finished waxes was carried out to obviate making new wax dies.

The turbine aerodynamics have been demonstrated initially with plastic blades and vanes on a cold flow rig at 0.87 scale to permit the use of an existing research rig. Design efficiency was achieved and no aerodynamic redesign is required. A full-scale rig with engine standard vanes and blades in metal will be tested. In-engine performance of the LP turbine is satisfactory too.

From the testing completed to date on the engine, limited evidence from thermal paint suggests the nozzle guide vane is overcooled.

Structurally the LP turbine rotor blade conforms with established shrouded blade practice, and while the blade is planned to be strain gaged to assess vibration characteristics, the test is not prioritized to the early point of the program.

Detailed modeling of the NGV support suggested the running deflections would be only marginally acceptable. Therefore, early in the demonstration of the LP turbine, X rays of this section were included in the initial engine testing and showed the structure operated satisfactorily.

Casting the exhaust diffuser with its integral cascade of vanes proved a major challenge to the supplier but was successfully completed closely to requirements. There is not a requirement for a large number of such a component in a demonstration program so evolving the casting process capability is a greater challenge. The first unit has been run on the initial engine test. Durability will be demonstrated later in the Life Assessment Program.

Reheat System. Rig demonstration of the reheat system is based on two-dimensional work at Bristol and full-scale engine standard rig testing, generally on the High Altitude Test Facility (HATF) at RAE (Pyestock) with some testing at the Rolls-Royce HATF at Derby. The so-called phase 1 design has been demonstrated and a lighter weight phase 2 design, which differs in having unshrouded colanders, is on test at the time of going to press.

Pressure loss, performance, stability, buzz, and screech targets have been met. The screech shroud requires cooling development, which has commenced. Initial temperature surveys of the cooled metal flameholders and fuel injectors are encouraging. XG40 has radial turbine stream gutters; alternative sections and cooling designs are included in the program. Burning length variation will be demonstrated in the reheat program to provide data for weight versus performance tradeoff.

Nozzle. XG40 base line demonstration program is not planned to demonstrate advanced nozzles. An existing slave component nozzle actuated with an advanced version of the RB199 air actuation system is operating satisfactorily on the engine.

Controls. *Engine starting and initial control in the dry* mode, sea level static, has been demonstrated satisfactorily on the first engine test. Figure 10 shows the engine installed in the sea level test bed. Initial operation of one of the rows of variable vanes in the HP compressor has been unsatisfactory with hunting, so modifications have been introduced.

Engine Performance

Overall performance demonstrated to date in the dry mode

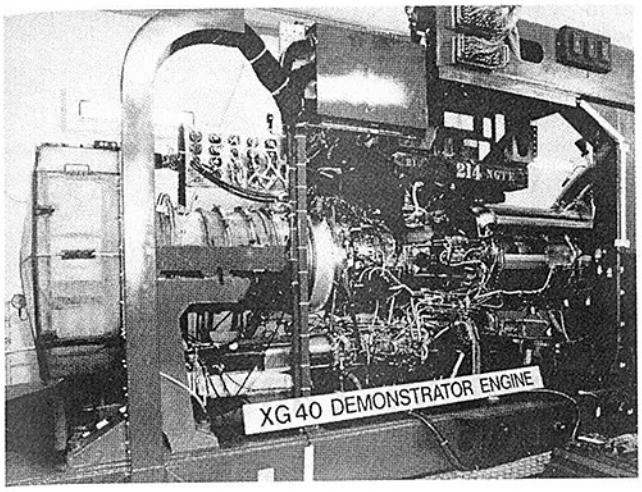

Fig. 10 XG40 engine installed in test plant

closely met the predictions synthesized from rig component performance.

HP Single Spool

The following testing has been completed to date:

- HP turbine rotor blade dynamics survey
- Component performance assessment
- Starting characteristics
- Smoke measurement
- Low-speed windmilling characteristics
- Turbine X ray of various steady-state conditions
- HP compressor variable vanes rescheduling
- Air/oil system trimming
- Hot end temperature paint test

The future program includes HP turbine rotor blade dynamics, detail performance, and component transient temperatures.

Engine

The following testing has been completed to date:

- Auto starting
- Full dry performance
- Oil/air systems
- Oil consumption
- Whole engine dynamics
- X-ray LP spool
- Hot end temperature paints
- Controls – dry mode
- Test cell installation performance effects
- Advanced data acquisition system demonstration

The next test on the engine, which is being rebuilt with the 3.9 pressure ratio fan, will include full dry and reheated demonstration.

Acknowledgments

This work has been carried out with the support of the Procurement Executive, Ministry of Defence.

World's First Full STIG™ LM5000 Installed at Simpson Paper Company

D. A. Kolp
Manager of Engineering
Energy Services Inc.,
Farmington, CT 06032
Mem. ASME

D. J. Moeller
Vice President—Engineering,
Simpson Paper Co.,
Anderson, CA 96002

In early 1988, Simpson Paper Company installed the world's first GE LM5000 cogeneration plant with full high and low pressure steam injection. The full STIG LM5000 achieves a dramatic power increase (from 32.5 MW to 49.5 MW) and remarkable improvements in efficiency from 36 to 43 percent, while reducing NO_x emissions from 225 to less than 25 ppmv before further reduction with SCR. The plant, installed at Ripon, CA, features: (1) 130,000 lb/hr (59,000 kg/h) of steam injection at three locations on the gas turbine; (2) the first-time use of SCR with the STIG LM5000 resulting in an ultimate NO_x emission rate of 6–13 ppmv; (3) a unique feedwater heat exchanger arrangement to reduce boiler stack temperature to 250°F (121°C); and (4) an innovative submicron inlet air filtration system to minimize the need for compressor washing. The details of cycle selection, design, installation, performance, and economic benefits of this first full STIG installation provide a useful insight into the potential of a flexible new technology.

History

Located 90 miles east of San Francisco, Simpson Paper Company's Ripon Mill annually produces 22,000 tons of high-quality printing paper. This paper is used for annual reports, books, manuals, greeting cards, menus,and wine labels. Ripon was chosen for the 200-acre mill site because of its proximity to the major west coast markets of San Francisco and Los Angeles. The mill has an electrical demand of 4000 kW and a steam demand of 45,000 lb/hr when operating at full steady-state capacity.

In May of 1983, Simpson Paper Company completed a 33,000 kW/220,000 lb/hr (100,000 kg/h) steam cogeneration plant at its Shasta Mill in northern California. The prime mover for this plant is an IM5000 gas turbine consisting of a GE LM5000 gas generator and an IHI ITA 1203 power turbine. Between initial operation in 1983 and Dec. 1, 1987, this cogeneration plant had logged over 36,000 hours. In January of 1986, Simpson Paper Company completed a second IM5000 cogeneration plant at its San Gabriel Mill in Pomona, CA. This plant is also rated at 33,000 kW and produces up to 200,000 lb/hr (90,900 kg/h) of steam for use in the paper mill. The San Gabriel cogeneration plant had logged over 16,000 hours of operation by Dec. 1, 1987.

In July of 1985, Simpson Paper Company with Pacific Gas & Electric Company, Ishikawajima-Harima Heavy Industries (IHI), General Electric Company, and Energy Services Incorporated adapted Simpson's Shasta Mill cogeneration facility for partial steam injection. Because the Shasta Mill could not utilize all its waste-heat-generated steam during the summer months, Simpson Paper Company opted to inject this excess steam back into the fuel nozzles and compressor discharge ports (CDP's) of the gas generator to increase power and improve heat rate. The results were dramatic. Under ISO conditions, power increased from 33 MW to 42 MW, and the thermal efficiency improved from 36 to 42 percent.

During the ensuing months, the effect of steam injection upon plant availability and reliability was closely scrutinized. The data taken during this period indicate that plant availability was 95.6 percent with steam injection versus 96.0 percent with water injection for NO_x reduction. Reliability was 99.5 percent with steam injection and 98.5 percent with water injection. In addition, hot section distress was significantly reduced with steam injection. The conclusion was that massive steam injection has no deleterious effect on either gas turbine availability or reliability and in fact improves hot section component life. Thus, a decision to implement STIG may be based purely on net incremental operating benefits versus the additional equipment cost compared to a non-STIG gas turbine.

In 1986 GE offered its LM5000 gas generator with full steam injection, which incorporates injection into the low-pressure turbine as well as into the fuel nozzles and high compressor discharge ports. Based on its experience at Shasta, Simpson Paper Company elected to install a full steam-injected IHI IM5000 gas turbine at its paper mill in Ripon, CA. Papermaking at the Ripon Mill requires only 45,000 lb/hr (20,400 kg/h) of 150 psig (1030 kPa) steam compared to the LM5000 unfired, waste-heat-steam-generating capability of 140,000 lb/hr (63,000 kg/h). Simpson Paper Company planned to inject all excess steam into the LM5000. Although Simpson and ESI investigated the use of a smaller gas turbine that more nearly

Contributed by the International Gas Turbine Institute and presented at the 33rd International Gas Turbine and Aeroengine Congress and Exhibition, Amsterdam, The Netherlands, June 5–9, 1988. Manuscript received by the International Gas Turbine Institute December 22, 1987. Paper No. 88-GT-198.

matched the thermal load of the Ripon Mill, the ability of the LM5000 to utilize excess steam in the STIG cycle proved more attractive economically than installing a smaller turbine.

Description

Plant Layout. Figure 1 shows the arrangement of the major components of the full STIG system. Notice that the space required to site this 49.5 MW plant is less than one acre (4000 m^2) as compared with three to ten times this area to site a comparably efficient combined cycle or coal burning power-generating plant.

Major Equipment. The IM5000 installed at Ripon is nearly identical to the IM5000s that Simpson is running at its Shasta Mill and San Gabriel Mill except that it is fitted with steam injection manifolds and nozzles, which facilitate the injection of high-pressure, superheated [750 psig (5170 kPa), 600°F (315°C)] steam into the fuel nozzles and compressor discharge ports and injection of low-pressure [300 psig (2070 kPa)/450°F (232°C)] steam upstream of the gas generator low-pressure turbine. Also, the annulus area in the high-pressure turbine section is increased to reduce the high-pressure compressor speed and to keep the compressor discharge pressure within the design limits of the high pressure compressor casing. The photo in Fig. 2 shows the LM5000 gas generator that has been installed at Ripon.

The electric generator selected for this site is a 49,500 kW, 58,235 kva, 13.8 kV, 0.85 pf turbogenerator supplied by Electric Machinery Company. The rotor and stator windings are totally enclosed water/air cooled (TEWAC). Although the gen-

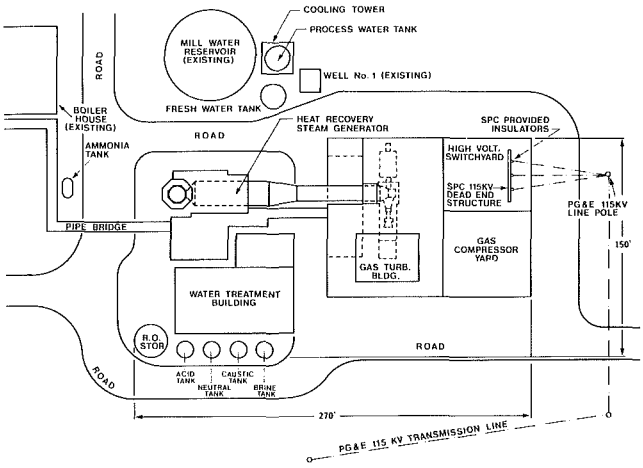

Fig. 1 Ripon Mill cogeneration plant layout

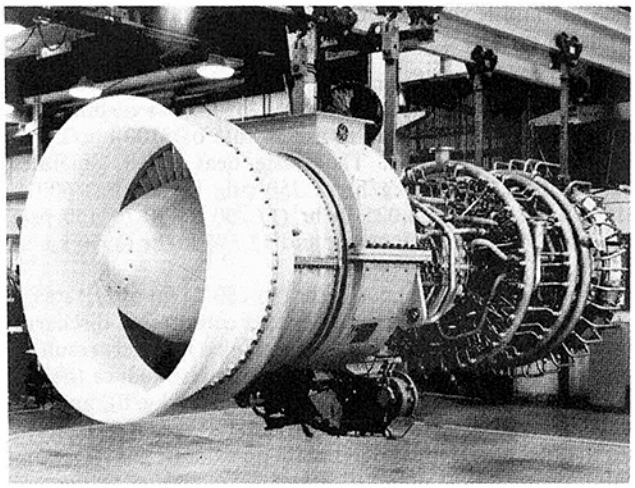

Fig. 2 Full STIG LM5000 gas generator

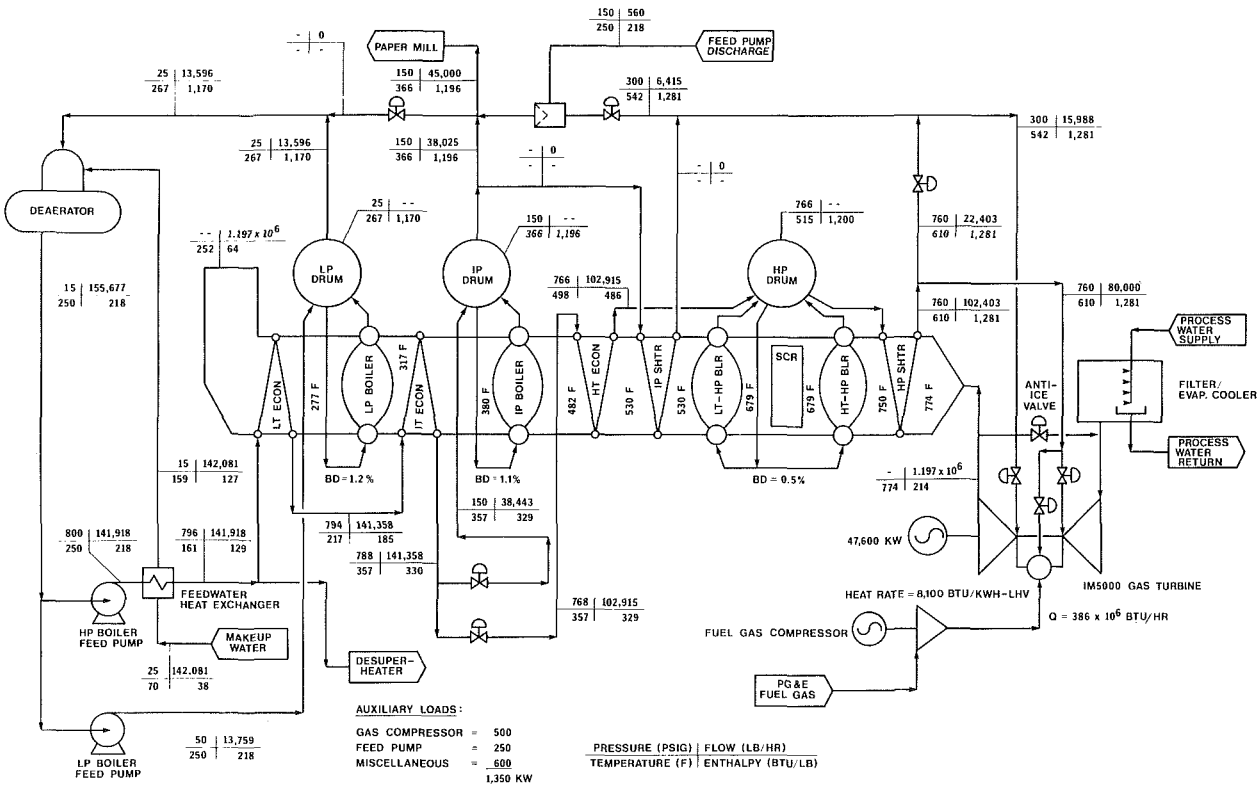

Fig. 3 Heat balance for Ripon Mill cogeneration plant with mill operating

erator is designed for outdoor installation, Simpson chose to install it indoors to minimize site noise, improve maintenance and maintainability, and enhance the overall appearance of the plant. The generator is equipped with brushless excitation and an optical rotor field ground detection and alarm system. A grounding brush rig is used in conjunction with an insulated coupling arrangement to ensure that no circulating currents can cause bearing damage.

A Deltak waste heat steam generator is installed at the Ripon site. The boiler consists of high-pressure [750 psig (5,170 kPa)], intermediate pressure [150 psig (1,035 kPa)], and low-pressure [25 psig (172 kPa)] evaporators, an HP and IP superheater, and three separate economizers. The IP evaporator is capable of operating at the LP STIG pressure of 300 psig (2070 kPa) when the mill is shut down, or at 150 psig (1035 kPa) when supplying process steam to the mill.

Cycle. At site conditions with steam supplied to both the gas turbine and the paper mill, the LM5000 gas turbine produces 47,600 kW of power at a heat rate of 8100 btu/kWh-lhv (8,545 kJ/kWh-lhv). The waste heat boiler generates 102,403 lb/hr (46,400 kg/h) of 750 psig (5170 kPa)/600°F (315°C) HP steam, 38,025 lb/hr (17,250 kg/h) of 150 psig (1030 kPa)/saturated IP steam and 13,596 lb/hr (5960 kg/h) of 25 psig (172 kPa) LP steam.

As Fig. 3 indicates, 80,000 lb/hr (36,280 kg/h) of HP steam is introduced into the fuel nozzles and compressor discharge ports (CDPs). Any higher ratio of steam to fuel may result in decreased combustion efficiency and may also reduce the engine stall margin. Of the 80,000 lb/hr (36,280 kg/h), approximately 40,000 lb/hr (18,140 kg/h) of HP steam is injected into the fuel nozzle area to maintain an exhaust gas NO_x concentration of 25–30 ppmv (dry and corrected to 15 percent O_2); the remaining 40,000 lb/hr (18,140 kg/h) is injected into the compressor discharge ports (CDPs). HP steam injected into the CDPs has a negligible effect on NO_x emissions. Pound for pound, HP steam injection into either the fuel nozzle area or the CDPs results in the same gas turbine power output and heat rate improvement.

The 16,000 lb/hr (7250 kg/h) of LP steam injection also increases engine power and improves the heat rate, but the benefits are not as pronounced as in the case of HP steam injection. The boiler was designed to maximize HP steam production for this reason, and in the event that future engine modifications might enable the LM5000 to accept more HP steam, effect further performance improvements. As the heat balance indicates, 22,400 lb/hr (10,160 kg/h) of HP steam is throttled to 300 psig (2070 kPa) and combined with the output of the IP boiler for use in LP STIG or further throttled for mill process steam. Notice that in the illustrated example the boiler exhaust stack temperature is 252°F (122°C). This low stack temperature is achieved by cooling the deaerated feedwater to 161°F (72°C) using makeup water, and by operating the IP drum at 150 psig (1,035 kPa), rather than at the 300 psig (2,070 kPa) necessary for LP STIG. Operating the IP drum at the lower pressure, with a correspondingly lower saturation temperature, enables the IP boiler to produce more steam at a lower stack temperature. The overall cycle efficiency with the paper mill operating and excess steam injected into the turbine is 55.6 percent.

The heat balance for the full STIG LM5000, i.e., with no steam flow to the mills, is only slightly different from that in Fig. 3. The HP boiler produces 101,000 lb/hr (45,800 kg/h) of HP steam; the IP boiler operating at 300 psig (2070 kPa) produces only 26,000 lb/hr (11,800 kg/h) of IP steam, compared to 38,000 lb/hr (17,200 kg/h) in Fig. 3. The gas turbine generates 49,500 kW of power at a heat rate of just under 8000 btu/kWh-lhv (8440 kJ/kWh-lhv).

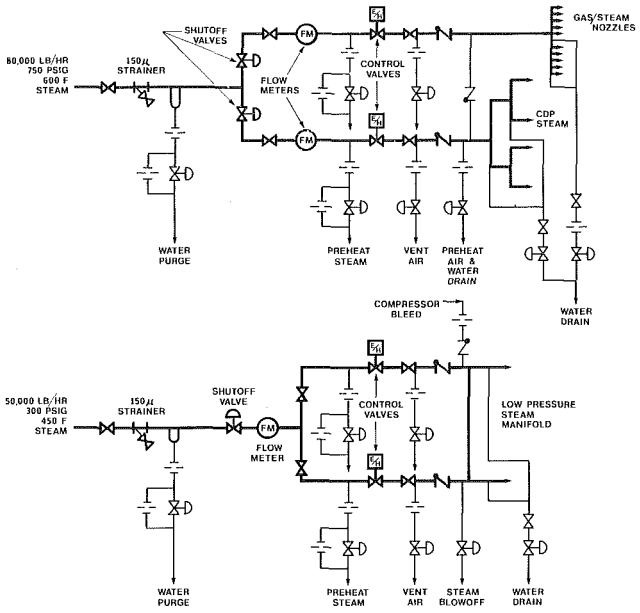

Fig. 4 Full-steam injection schematic

The higher IP evaporator pressure in the full STIG case reduces heat transfer across this element. As a result, the exhaust gas passing thorugh the LP evaporator is at a higher temperature than that shown in Fig. 3. Therefore, enough LP steam is produced to heat the 70°F (21°C) makeup entering the deaerator to the saturation temperature of 250°F (121°C) without the use of the low-temperature (LT) economizer. Since the LT economizer is not utilized, the stack temperature in the full STIG case is 274°F (134°C), versus 252°F (122°C), in the partial STIG case depicted in Fig. 3. The full STIG cycle efficiency with the paper mill shut down is approximately 43 percent and the plant's entire output is in the form of electrical power.

STIG gas turbine performance and waste heat boiler performance are interdependent. That is, the boiler's steam production is a function of the gas turbine exhaust mass flow, specific heat, and temperature, and the turbine exhaust gas flow, specific heat, and temperature are a function of the amount of steam injected into the turbine. The challenge at Ripon was to select a boiler design that would maximize steam production using the exhaust gas generated by the gas turbine when that amount of steam was injected into the gas turbine. IHI provided ESI with performance data at the site design condition, 59°F (15°C), for the maximum allowable HP steam injection, 80,000 lb/hr (36,280 kg/h), and varying amounts of LP steam injection. ESI, in turn, input the exhaust gas mass flow, temperature, and specific heat into a computer model of the Ripon boiler, which calculated the amount of steam that would be produced under each exhaust gas condition provided by IHI. By interpolation, the computer program identified the operating point where boiler steam production matched steam injection. This operating point was subsequently given to Deltak as the design point for the Ripon heat recovery steam generator.

Steam Injection System. As noted in the cycle description, a maximum of some 130,000 lb/hr (59,000 kg/h) of total waste-heat-generated HP and IP steam is available in the full STIG LM5000 plant. Figure 4 illustrates that this may be divided into 80,000 lb/hr (36,280 kg/h) of HP steam and 50,000 lb/hr (22,680 kg/h) for LP STIG.

The HP steam passes through a 150-micron, last-chance strainer, which protects the control valves and nozzles from any large particles that may have been dislodged in the piping; however, a good steam blow prior to initial operation and first-

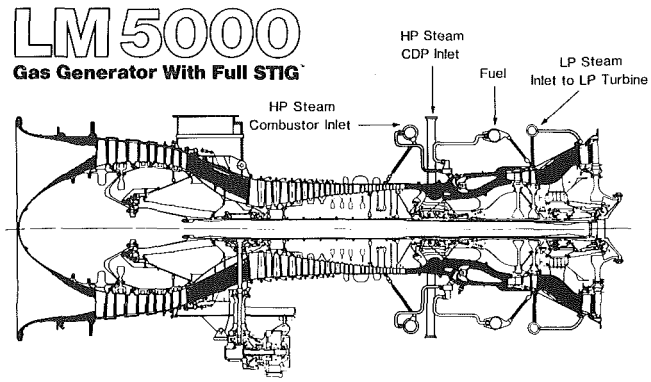

Fig. 5 Cross section of LM5000 with full STIG hardware

rate moisture removal at the steam drums is the best defense against exceeding the 20-micron particle size specified in G.E.'s steam contamination limits. Downstream of the strainer, a water purge drip leg removes condensate during warm-up of the STIG piping. The HP steam line splits after the drip leg, one branch supplying steam to the fuel/steam nozzles and the other supplying steam to the compressor discharge ports. The shutoff valves downstream of the drip leg remain closed until the early stages of warm-up are completed. Once opened, the shutoff valves permit the HP steam to pass through the preheat steam valves, thereby warming up the steam piping leading to the electrohydraulic steam metering valve. At the same time, 1000°F (538°C) compressor discharge air is flowing in the reverse direction into the engine-mounted CDP steam manifold, through the check valve in the crossover line and out of the gas/steam nozzles. The STIG injection piping is thus warmed with steam to the upstream side of the closed metering (control) valves and with compressor discharge air to the check valves downstream of the metering valves. Once the metering valves open, the vent air valves release any air or condensate in the short segment of pipe between the metering valves and the check valves. HP steam flowing to both the fuel nozzles and the CDPs is measured by flow meters located upstream of the metering valves. Water drain valves remove any condensate that may have collected in the fuel nozzle and CDP manifolds prior to start-up.

The LP STIG system operates much the same as the HP system. The LP steam is introduced between the high and low turbine rotors. In addition, to prevent gas path gases from circulating through the LP steam manifold and fouling the steam nozzles, eighth-stage compressor bleed air purges the manifold whenever the turbine is operating without LP STIG steam injection.

Turbine Auxiliaries

Inlet Air Filtration. The very high simple-cycle efficiency of the LM5000 gas generator is significantly reduced if the compressor blades become fouled. To minimize fouling, high-efficiency inlet air filters are installed at each of the Simpson Paper Company sites. At Shasta Mill, a single-stage Farr Co. 30/30 prefilter is followed by a single-stage of Farr Co. HP-200 high-efficiency deep pleated filters. As Fig. 6 illustrates, the single-stage high-efficiency filter removes 97.5 percent of all 1.0-micron particles in the turbine inlet air. When power degradation reaches 2000 kW, Simpson Paper Company water washes the compressor sections of the engine to remove fouling deposits and then rinses the turbine section through the fuel nozzles to remove any salts that may have migrated from the compressor during the wash. At Shasta, the interval between these water washes is approximately three to four weeks.

At the second Simpson cogeneration site at San Gabriel Mill in Pomona, CA, a Farr Co. pulse-type deep-pleated canister filter, followed by an HP-200 final stage were used instead of

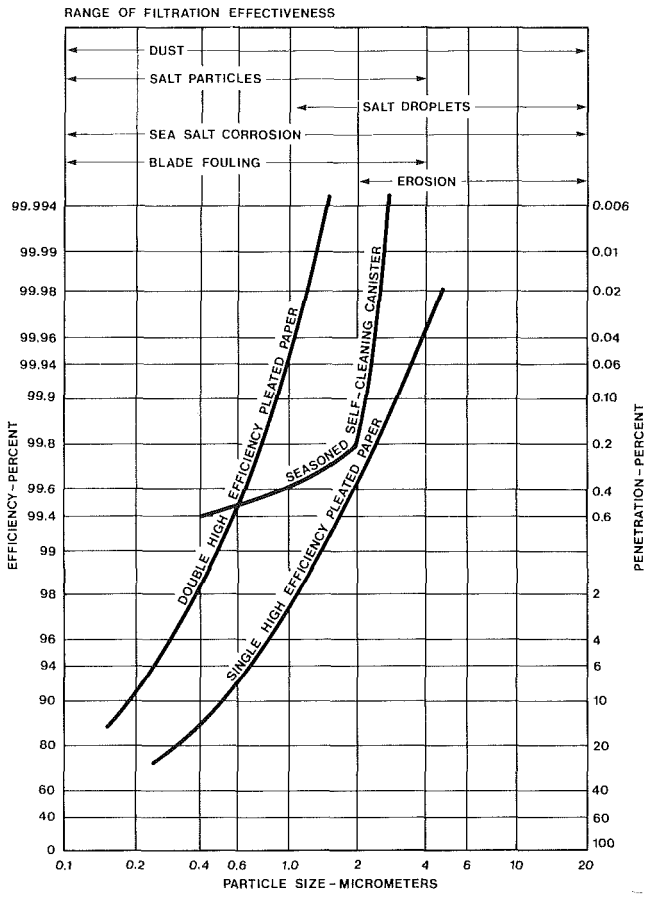

Fig. 6 Comparison of inlet air filtration efficiency

the Shasta Mill arrangement. As Fig. 6 depicts, once seasoned with an initial charge of dust, these canister-type units remove 99.6 percent of all 1.0-micron particles. It should be noted however that the very low inlet air velocity required for proper operation of this type of filter results in a massive filter house and evaporative cooler that is nearly twice as costly as the Shasta Mill arrangement. Offsetting this increased initial cost however, the interval between compressor water washes at the San Gabriel site has been increased to eight to twelve weeks.

At the Ripon Mill, Simpson Paper Company has installed a filter system, which consists of two sets of the deep-pleated filters in series. Figure 6 shows that 99.95 percent of all 1.0-micron particles are removed. It is expected that this design will further reduce the frequency of water washing required to maintain peak compressor efficiency. Although the initial cost of the Ripon filter system is considerably less than the self-cleaning, canister-type enclosure installed at the San Gabriel site, the major reason for the change was Energy Services' concern that the San Gabriel system would not operate properly at Ripon. The tule fog that persists for months during the winter season may cause water accumulation in the canisters equal in head to the pressure drop across the canisters, and permit captured salts to leach through the paper, reaching the filter barrier. The Ripon system uses a dry extension of the evaporative cooler media as a free-water moisture barrier.

Evaporative Cooler. A 98 percent-efficient evaporative cooler is installed at the Ripon site, which reduces inlet air temperature to essentially wet bulb temperature. During the five warmest months of the year there is a 10°F (5.5°C) difference between the dry bulb and wet bulb temperautres at the Ripon site. Over the course of a year, this translates into approximately 8550 MWh of added generation capacity. Simple payback on the approximately $100,000 added cost of the

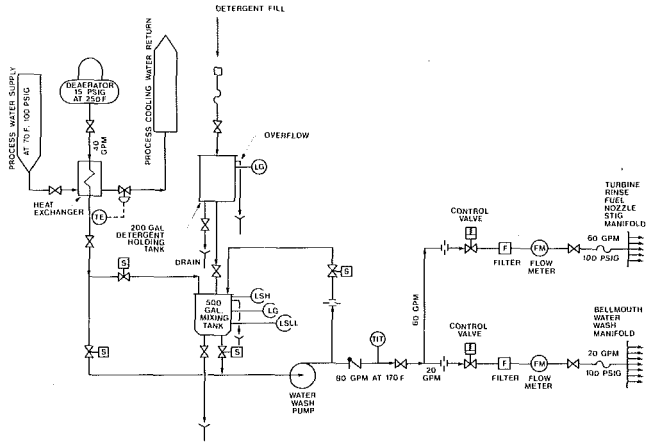

Fig. 7 Schematic of Ripon cogeneration water wash system

evaporative cooler and pumps, and the premium for stainless steel inlet, silencer, and plenum, is a matter of months.

Fuel System. The compression ratio of the STIG LM5000 with full steam injection is higher than the standard LM5000 without steam injection. Also, the fuel nozzle flow path is reduced to accommodate the concentric steam flow path. These considerations, plus the fact that the increased power capability requires high fuel flow, with corresponding higher pressure drop in the fuel delivery system, mean the pressure of the gas fuel supplied to the metering valve must be significantly higher than for the standard non-STIG LM5000.

One of two 100 percent 700 hp (520 kW) Dresser-Worthington low-speed reciprocating gas compressors supplies up to 22,000 lb/hr (10,000 kg/h) of natural gas from a design suction pressure of 250 psig (1725 kPa) to 700 psig (4830 kPa). The corresponding pressure required for a standard non-STIG LM5000 is 600 psig (4140 kPa).

Process Water. One of two 100 percent 100 hp (75 kW) centrifugal pumps circulates 1200 gpm (272 m/h) of 80°F (27°C) water through the heat exchangers of the various cogeneration plant auxiliaries. The majority of this water is used to cool the air circulating inside the TEWAC electric generator and to cool the gas turbine and generator lube oil. The remaining cooling water is needed primarily for the gas compressor heat exchangers, feed water pump heat exchangers, boiler water, and steam sample coolers and heat pumps. In the process of removing heat from these auxiliary systems, the water temperature rises to approximately 90°F (32°C). The heated water is cooled to 80°F (27°C) using a two-cell cooling tower. Each cell is equipped with a two-speed fan. Ordinarily, both fans on both towers operate at low speed; on exceptionally cold days, only one slow-speed fan of the two is required; on a few of the hottest days, it is necessary to run both fans at high speed to maintain the 80°F (F27°C) cooling water supply temperature.

Anti-Icing System. Ambient air temperatures range from 20°F (−7°C) to 100°F (38°C) at the Ripon site. While the evaporative cooler serves to cool inlet air and maximize power output during the summer months, water flow to the evaporative cooler is shut off when ambient temperatures fall below 45°F (7°C) because of the risk of ice formation in the plenum and engine bellmouth area.

Since the air is accelerated and reduced in pressure as it passes from the inlet air plenum to the engine bellmouth, the temperature at the bellmouth is depressed as much as 10°F (5°C) below the plenum temperatures, providing an opportunity for ice formation. For this reason, and to prevent excessive compressor discharge pressure at low ambient temperatures without relying solely on the high-pressure fuel control override, an anti-icing system is provided to ensure that the inlet plenum temperature will not fall below 42°F (5°C). As the inlet air temperature approaches 42°F (5°C), a control valve (refer to Fig. 3) in the anti-icing duct leading from the power turbine exhaust elbow to the plenum opens, introducing up to 3 percent of the turbine exhaust gas into the inlet air stream through perforations in the leading edge of each inlet silencer baffle. A temperature probe senses the resultant inlet air temperature and positions the control valve to maintain 42°F (5°C).

Water Wash. The gas turbine compressor water wash system is supplied with deaerator water cooled from 250°F (121°C) to 150°F (65°C). Figure 7 illustrates how a temperature control valve governs the flow of process cooling water through a shell-and-tube heat exchanger to cool water from the deaerator storage tank to the compressor water washing and compressor and turbine rinsing system. A predetermined amount of detergent is transferred from a holding tank into a mixing tank. The remainder of the mixing tank is then filled with cooled 150°F (65°C) water from the deaerator. The detergent solution is sprayed over the compressor blades from nozzles in the engine bellmouth while motoring the gas generator with the pneumatic starter. After the detergent solution soaks into the dirt film on the compressor blades, water is drawn directly from the deaerator, cooled, and sprayed first through the bellmouth nozzles and then through the fuel nozzle manifold until all accumulated contaminants and detergent solution are rinsed from the engine, completing the water wash.

Boiler Auxiliaries

Selective Catalytic Reactor (SCR). Simpson Paper Company had demonstrated at its Shasta Mill that steam injection could be used to maintain LM5000 NO_x levels below 14 ppm (dry/volumetric and corrected to 15 percent O_2). However, the San Joaquin County Health Department, which has jurisdiction over the emissions of the Ripon Mill, had already established a precedent requiring a nearby gas turbine site to meet NO_x limits of 6–13 ppmv. Since these new NO_x standards could not be met with steam injection alone and since high steam injection into the combustor increases CO emissions, a selective catalytic reactor (SCR) was employed in conjunction with steam injection to control NO_x. Using steam injection to reduce NO_x to 25 ppmv on the LM5000 results in CO emissions of approximately 60 lb/hr (27.2 kg/h) or 250 tons/year, a Federal EPA benchmark. Although Simpson was not required to meet the 250-ton standard, they felt a corporate obligation to achieve the highest possible air quality standards. Therefore, at Ripon NO_x is controlled with steam injection to 25 ppmv, and additional reduction to the county requirement of 6–13 PPMV is accomplished by means of an SCR. CO emissions will not exceed 250 tons/year.

The SCR used at Ripon was supplied by Mitsubishi and utilizes a titanium dioxide (TiO_2) catalyst. The catalyst induces the following reactions between NO_x in the exhaust gas and the ammonia, which is injected into the exhaust gas upstream of the SCR:

$$4NO + 4NH_3 + O_2 = 4N_2 + 6H_2O$$

$$6NO_2 + 8NH_3 = 7N_2 + 12H_2O$$

A schematic of the ammonia injection system is shown in Fig. 8.

200 psig (1380 kPa) liquid ammonia is introduced into an electrically heated (10 kW) evaporator at ambient temperature and at a typical flow rate of 23 lb/hr (10 kg/h). After vaporization, the gaseous ammonia is expanded across two pressure regulating valves, which reduce the pressure to 2.5 psig (17 kPa) before it passes into a 44 gal (0.17 m^3) accumulator. On initial start-up, once the ammonia is vaporized, the shutoff

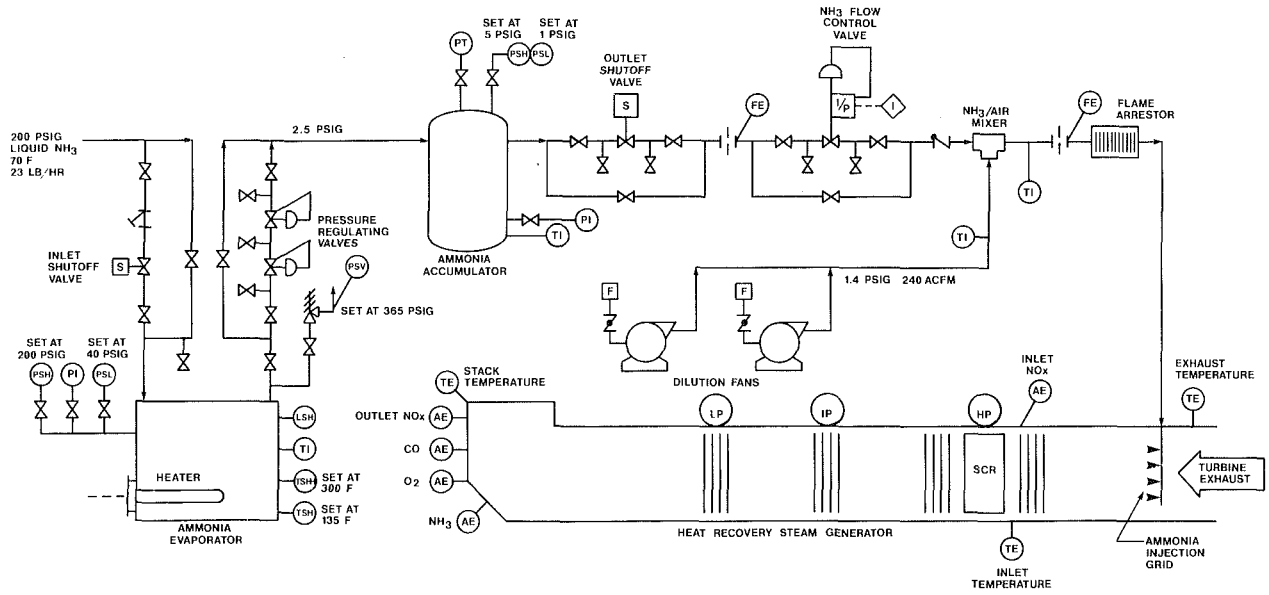

Fig. 8 SCR ammonia injection system for NO_x control

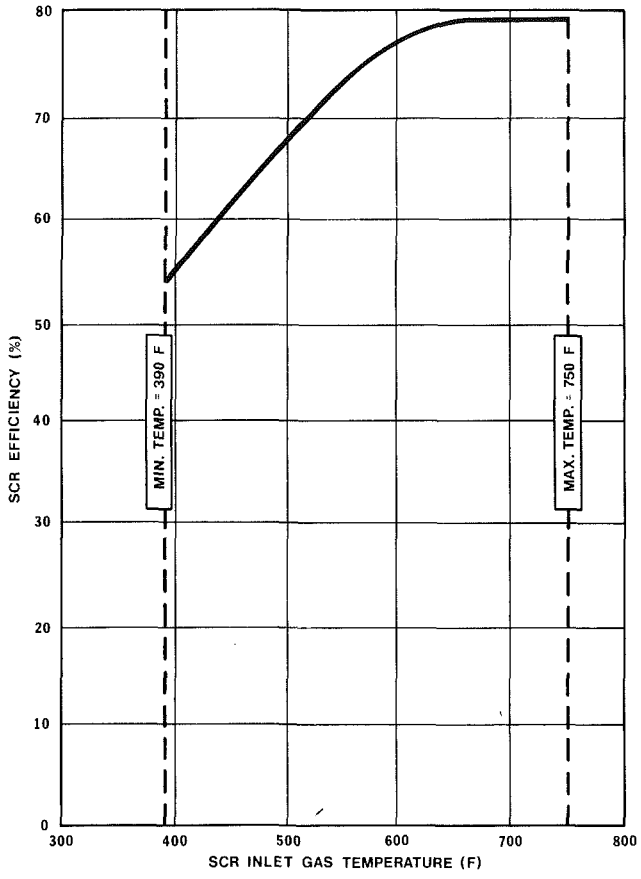

Fig. 9 Effects of exhaust gas temperature on SCR efficiency

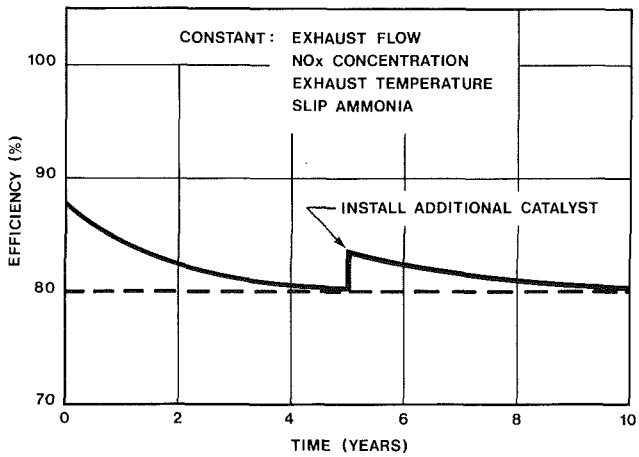

Fig. 10 Life expectancy of selective catalytic NO_x reactor

valve is opened and the ammonia vapor passes through the flow control valve where it is metered according to demand and mixed with 240 cfm (6.8 cmm) of dilution air supplied by axial fans mounted near the injection skid. Ammonia demand is established by monitoring the NO_x concentration and exhaust gas mass flow into the SCR. The NH_3 flow control valve automatically controls the flow of ammonia to meet the demand.

Catalyst efficiency is a function of the temperature of the exhaust gas in which the ammonia and NO_x react. The Deltak HP evaporator tube banks are split into two sections; one HT (high temperature) section, and one LT (low temperature) section. The HT–HP evaporator and superheater are upstream of the SCR and maintain an exhaust gas temperature in the range of 650°F (342°C) to 690°F (366°C) throughout the gas turbine's normal operating regime. As Fig. 9 indicates, operation in this range optimizes SCR efficiency.

The SCR should not be operated in exhaust gases above 750°F (399°C) because the catalyst deteriorates, nor should ammonia be injected below 390°F (199°C) because an explosive gas, ammonium nitrate, forms in the ductwork. In the case of a liquid-fueled gas turbine, a coating of ammonium bisulfate fouls the catalyst, causing a sharp reduction in reactor efficiency below 390°F (199°C). The ammonium bisulfate deposited in colder sections of the boiler does not evaporate. Removal of this coating is an arduous task. To preclude problems, ammonia is not injected into the exhaust gas stream below 500°F (260°C).

Figure 10 shows how a typical SCR can retain its guaranteed operating efficiency for a period of five years. Adding catalyst (not replacing the entire old catalyst) can increase the life of the SCR an additional five years for a gas turbine fueled with natural gas.

Makeup/Feedwater Heat Exchanger. In 1987, ESI patented a makeup/feedwater heat transfer concept to improve cogeneration cycle efficiency. This heat transfer system was first

installed at the Ripon site. The heart of this energy-saving idea is an ordinary shell-and-tube heat exchanger (see Fig. 3), which utilizes 250°F (121°C) deaerator feedwater to heat ambient-temperature, deionized makeup water. The heated makeup water continues on into the deaerator where low-pressure steam adds the additional energy necessary to raise it to the saturation temperature of the deaerator and release any noncondensibles, thereby completing the deaeration process. The cooled feedwater leaving the shell-and-tube heat exchanger passes through a low-temperature (LT) economizer located downstream of the low-pressure (LP) evaporator section of the boiler.

The LT economizer is the key to optimizing the cycle. Since the feedwater enters the LT economizer at a lower temperature (161°F in Fig. 3) than the 267°F (130°C) water in the LP evaporator, which is situated ahead of it in the gas stream, there is enough mean temperature difference to remove additional energy from the gas stream and thus lower the boiler exhaust stack temperature from 277°F (136°C) to 252°F (122°C) as shown in Fig. 3. This system not only reduces the boiler stack temperature by introducing cooled water into the back end of the boiler, but by means of the heat exchanger, accomplishes this task with deaerated feedwater, thus protecting the boiler from the internal corrosion that would occur if the cold, nondeaerated makeup water were introduced directly into the economizer. It should be noted that this system is most practical when relatively large quantities of makeup are required, such as with the STIG cycle.

Water Treatment System. The Ripon cogeneration plant design posed some extremely severe water treatment conditions. The raw well water used in the plant has total dissolved solids (TDS) of between 500 and 800 ppm (parts per million). The General Electric specification calls for no more than 30 ppb (parts per billion) of sodium, potassium, vanadium, or lithium in the STIG injection steam. To meet such a stringent steam purity standard with reasonable boiler blowdown, makeup water supplied to the deaerator is deionized to less than 1 ppm TDS, and highly efficient moisture separating equipment is installed in the steam drums.

To make the leap from 800 ppm to 1 ppm TDS as economically as possible, Simpson chose to use a reverse osmosis (R.O.) unit in their water treatment system. The water treatment plant is designed to handle 350 gpm (80 m/h) and has 50 percent redundancy on all equipment except the R.O. unit, which consists of two 50 percent capacity banks. The treatment process begins with a train of triplex activated-carbon filters to remove organics from the well water, followed by a triplex zeolite softener, which removes calcium carbonate, magnesium silicate, and calcium sulfate, which can foul the R.O. membranes. Downstream of the softeners are three 5-micron cartridge filters that remove any remaining traces of particulate matter before the water is pumped at 285 psig (1970 kPa) through two stages of R.O. membranes. The R.O. product, which has a TDS of 40 ppm, is stored in an R.O. storage tank. The storage tank acts as a buffer, which permits the R.O. system to operate at design flows for long periods of time regardless of the fluctuations in plant water demand. Water is pumped from the R.O. storage tank through a triplex mixed bed demineralizer, which reduces the TDS to less than 1 ppm before it enters the deaerator as makeup. Using this system, Simpson expects their deionized water costs to be less than $400,000/year.

Steam Modulation. Unlike its sister cogeneration plants at Shasta and San Gabriel, the Ripon cogeneration plant has no bypass stack to modulate the flow of turbine exhaust gas to the heat recovery boiler. There are several reasons for this design change. All the steam that this unfired waste heat boiler can produce may be injected into the gas turbine; thus, under steady-state conditions, none of the exhaust gas need be bypassed, regardless of the process steam requirements of the

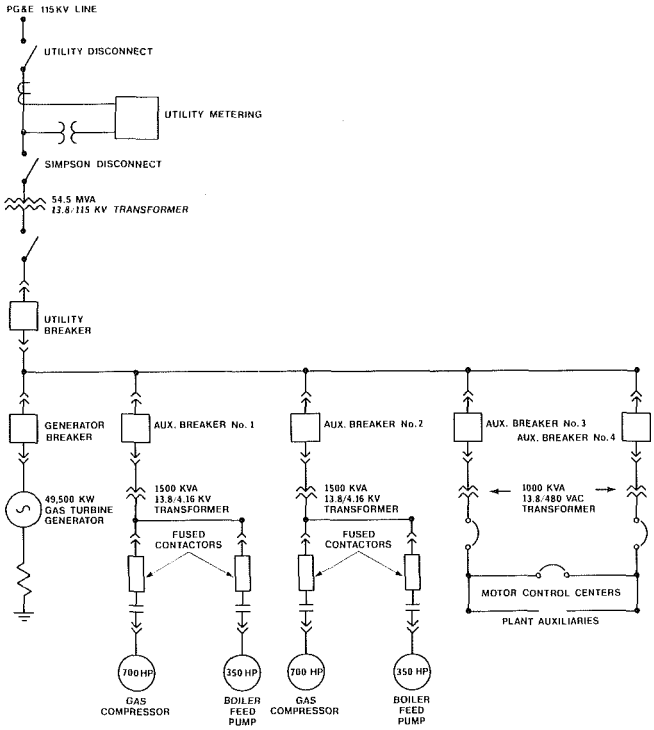

Fig. 11 Elementary Ripon plant one line diagram

paper mill. Also, a bypass stack, which would have permitted easier start-up of the cogeneration plant, would allow exhaust to bypass the SCR during plant start-up and would increase the total annual NO_x emissions. Even temporarily bypassing the SCR might have complicated the emissions permitting process. Other reasons for eliminating the bypass are that on a unit of this size a bypass stack can add up to $250,000 to the cost of the installation, and some lost energy through leakage, although slight, is inevitable. Finally, the San Gabriel Mill has fresh air firing capability and requires a bypass damper to isolate the boiler from the gas turbine when the boiler is operating on forced draft fans (fresh air firing). There are no plans to add fresh air firing to Ripon.

Occasionally, due to temporary upset conditions, all the steam produced in the waste heat boiler cannot be injected into the gas turbine or used in the papermaking process. Under these circumstances, a pressure control valve on the HP superheater relieves excess steam to atmosphere and maintains 750 psig (5170 kPa) in the header to satisfy whatever HP steam demand remains. Excess steam is vented through a diffuser and a silencer. The diffuser/silencer is designed for continuous operation at full HP steam production and maintains sound emissions under 85 dBA at a distance of one meter and 55 dBA at 100 meters.

As in its sister plants, the steam from both Ripon's IP and LP drums may be throttled, or even bottled, if the demand for intermediate and low-pressure steam is reduced below their respective generating capacities. As the pressure increases and saturation temperature rises, heat transfer and steam production are reduced until the drum is completely bottled. Both the IP and LP drums are designed to be completely bottled without relieving their respective safety valves, provided that HP steam production is being utilized in the gas turbine.

Electrical

All of the power generated at the Ripon Mill is exported to the local utility, Pacific Gas & Electric Company; the 4000 kW consumed in the paper mill is purchased from PG&E. As Fig. 11 indicates, the cogeneration unit generates 49,500 kW at 13.8 kV. The power is transformed to 115 kV and carried

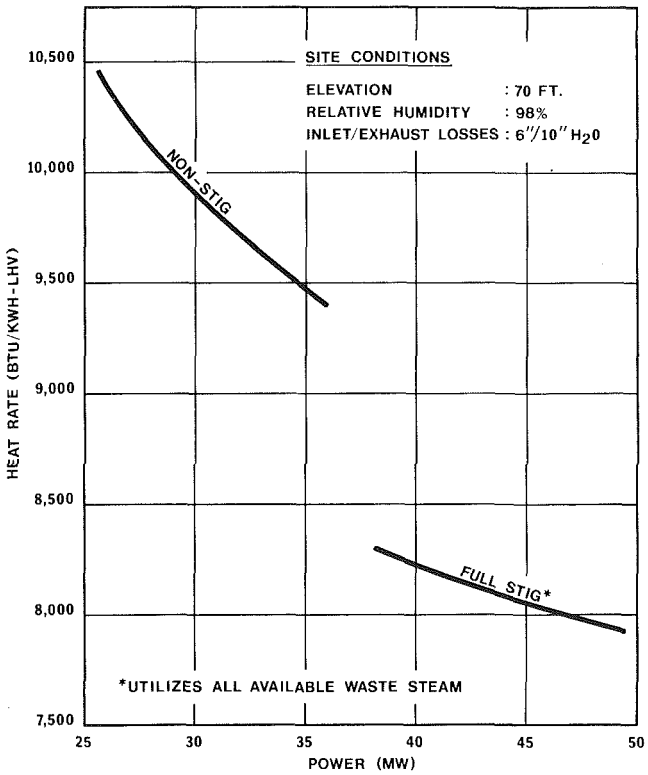

Fig. 12 Comparison of full STIG and non-STIG LM5000 performance

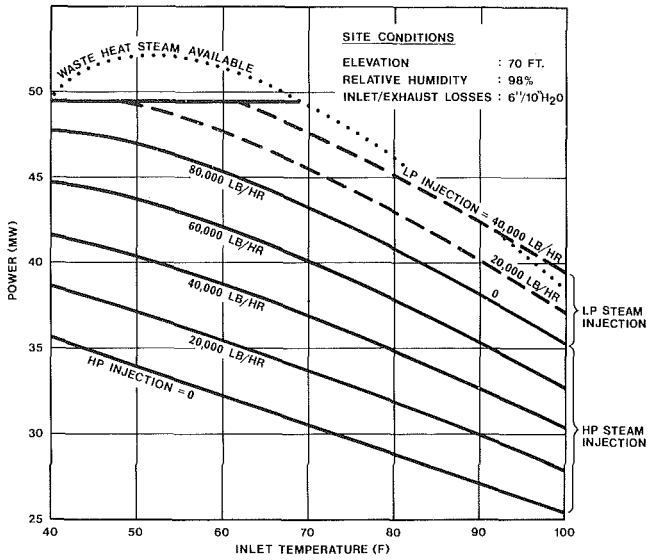

Fig. 13 Effect of high-pressure and low-pressure steam injection on LM5000 power output

over a new transmission line that Simpson and three other new cogenerators have installed between their sites and PG&E's 115 kV distribution grid.

The cogeneration plant auxiliary load is approximately 1350 kW, which powers primarily the gas compressors and the 350 hp (260 kW) boiler feed pumps. These relatively large auxiliary loads are served by 4160 VAC power; the smaller auxiliaries are 480 VAC.

Performance

Gas Turbine. As Fig. 12 indicates, the performance benefits of STIG are twofold. STIG reduces heat rate approximately 19 percent and increases power approximately 52 percent using waste heat steam.

The dramatic influence of steam injection is apparent in Fig. 13. Note that the HP steam (Fuel Nozzle and CDP Injection) is more effective than the LP steam (LP Turbine Injection) in increasing engine power output. On average 1000 lb/hr (450 kg/h) of HP steam increases power approximately 150 kW whereas 1000 lb/hr (450 kg/h) of LP steam raises power only 110 kW. This is primarily due to the fact that the cooling effect of the high-pressure steam permits additional fuel to be burned without increasing the engine's firing temperature. At 49,500 kW, the LM5000 runs into a high compressor casing pressure limitation of 430 psig (2970 kPa). Steam that is available above this pressure limit may be injected to replace fuel while the power remains at 49,500 kW (dome-shaped area above 49,500 kW line). Increasing injection at constant power reduces the turbine heat rate.

The data depicted in Fig. 13 reflect LM5000 performance utilizing the steam that can be generated from the turbine's own waste heat exhaust stream. The manufacturer's limit on HP steam injection is 80,000 lb/hr (36,300 kg/h) or 7 percent of the engine's inlet air flow (whichever is less); the LP steam injection limit is 72,000 lb/hr (32,700 kg/h). Although the energy in the LM5000 exhaust stream at Ripon is insufficient to generate 152,000 lb/hr (69,000 kg/h) of combined HP and LP steam, an installation with a duct burner could be used to

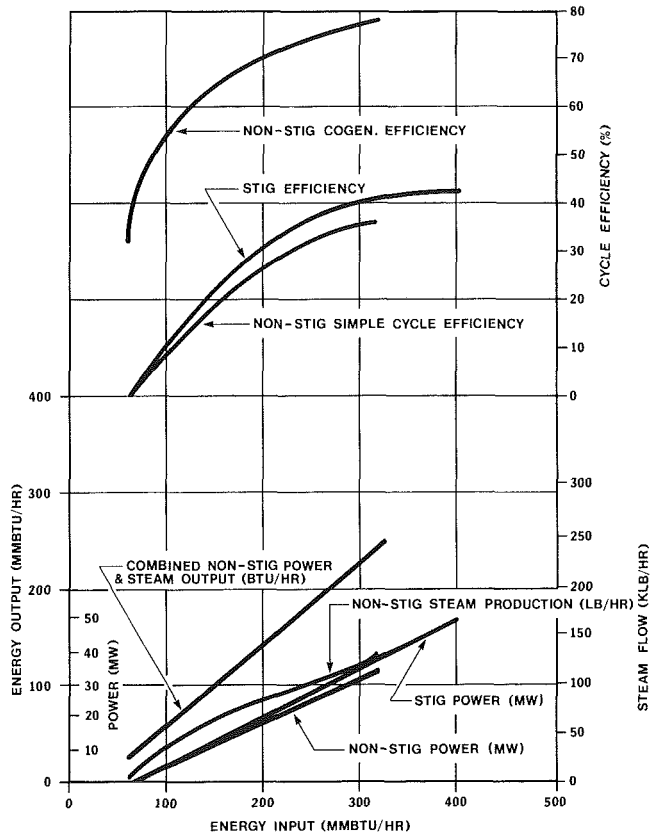

Fig. 14 LM5000 energy input versus energy output

reach these steam production levels, thus maximizing power, as long as turbine operating limits such as firing temperature, rotor speeds, and engine case pressures are not exceeded.

A thumbnail sketch that further compares the LM5000 in a pure cogeneration mode (power and steam production) to a full STIG LM5000 is given in Fig. 14.

At first glance, it appears that the pure cogeneration mode with a cycle efficiency approaching 80 percent versus the full STIG efficiency of 43 percent would be the preferred choice; and this may be so when steam is needed to support a process such as papermaking. However, as the curves at the bottom of Fig. 14 indicate, approximately half of the useful energy

Table 1 Heat recovery boiler operating at 59°F (15°C) turbine inlet air temperature

OPERATING CONDITIONS		PARTIAL STIG	FULL STIG
Exhaust Gas Flow,	MMLB/HR	1.197	1.227
	MMKG/HR	0.543	0.556
Exhaust Gas Temperature,	F.	774	758
	C.	412	403
HP Steam Flow,	LB/HR	102,403	101,169
	KG/HR	46,441	45,882
HP Steam Pressure,	PSIG	760	750
	kPa	5,244	5,175
HP Steam Temperature,	F.	610	600
	C.	321	315
IP Steam Flow,	LB/HR	38,025	26,353
	KG/HR	17,244	11,951
IP Steam Pressure,	PSIG	150	300
	kPa	1,035	2,070
IP Steam Temperature,	F.	366	456
	C.	185	235
LP Steam Flow,	LB/HR	13,596	33,036
	KG/HR	6,166	14,982
LP Steam Pressure,	PSIG	25	25
	kPa	172	172
LP Steam Temperature,	F.	267	267
	C.	130	130
Exhaust Stack Temperature,	F.	252	274
	C.	122	134

produced in the non-STIG (pure cogeneration) mode is in the form of steam, the other half being electricity. On the other hand, all of the energy produced by the full STIG is electricity. Simpson Paper Company values electric power at $60.00/MWh, which is equivalent to $17.60/10^6 btu ($16.70/10^6 kJ) while steam is valued at $3.12/10^6 btu ($2.94/10^6 kJ). Thus, electric energy production is nearly six times as valuable as steam production, although the steam can be produced more efficiently.

Heat Recovery Boiler. The Ripon boiler is relatively complex in its construction. In addition, this boiler must operate in both the full STIG and partial-STIG modes. Table 1 shows how both the exhaust gas conditions and the steam output vary when operating in each of these modes.

Emissions. Full load carbon monoxide (CO) emissions of the full STIG LM5000 are directly influenced by two factors, the fuel nozzle steam injection rate and the turbine inlet air temperature. Increased nozzle steam injection rates decrease NO_x emissions but increase CO in the turbine exhaust stream. Figure 15 shows how increasing inlet air temperature can sharply reduce CO emissions. For example, increasing inlet air temperature from 40°F (4°C) to 100°F (38°C) reduces CO emissions 30-fold from 150 lb/hr (68 kg/h) to 5 lb/hr (2.2 kg/h).

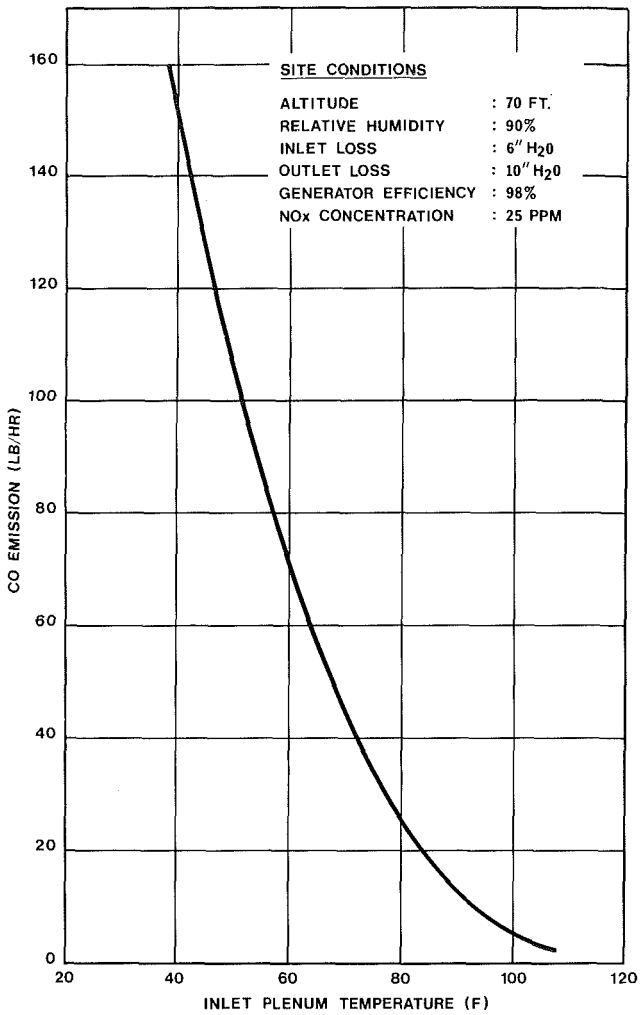

Fig. 15 CO emissions as a function of inlet air temperature for full STIG LM5000

The interrelation between NO_x controlled by fuel nozzle steam injection, CO, and inlet air temperature is more completely illustrated in Fig. 16.

To meet the EPA CO limit of 250 tons/year, an LM5000 operating 95 percent of the time may produce only 60 lb/hr (27 kg/h) of CO. According to Fig. 16, at an inlet temperature of 59°F (15°C), the LM5000 NO_x emissions cannot be reduced below 26 ppmv without exceeding the 60 lb/hr (27 kg/h) CO limit. As noted earlier, Simpson installed an 80 percent efficient SCR to reduce NO_x emissions from 26 ppmv to the county's target of 6 ppmv. The effect of steam injection and the SCR on NO_x emissions over the entire operating range of the LM5000 is shown graphically in Fig. 17.

The top two curves in Fig. 17 depict LM5000 operation on liquid fuel and natural gas fuel with no steam injection for NO_x control. NO_x emissions on liquid fuel are more than double those on gas fuel at corresponding power outputs. Since the Ripon site operates exclusively on gas fuel, the remaining curves are based on gas fuel operation only. The "Minimum Injection" curve refers to the fact that before any steam may be injected into the compressor discharge ports (CDPs), or into the LP turbine (LPT), a minimum of 8000 lb/hr (3600 kg/h) of HP steam must first be injected into the fuel nozzle area. Further NO_x reduction to 25 ppmv is achieved by increasing "Nozzle Injection" up to 45,000 lb/hr (20,400 kg/h). As the lowest curve, "Injection and SCR," indicates, com-

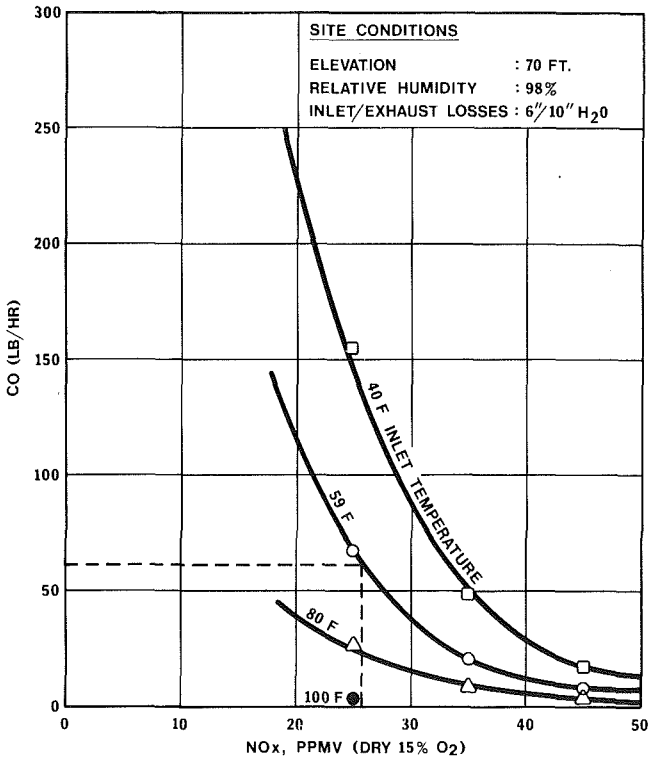

Fig. 16 NO_x (ppmv) versus CO (lb/hr) at full power

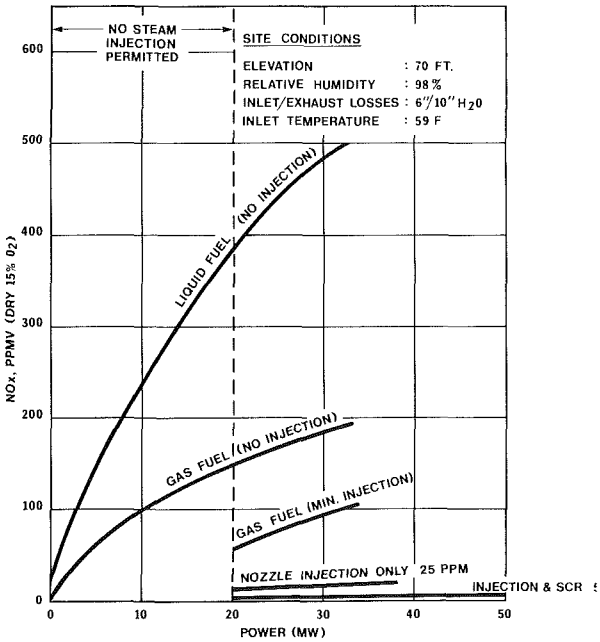

Fig. 17 NO_x control with steam injection and SCR

bining nozzle steam injection with an 80 percent efficient SCR results in NO_x concentrations of approximately 5 ppmv, which are less than the county regulation of 6–13 ppmv. To avoid flame instability, no steam is injected at any of the three injection locations below power levels of 20,000 kW.

Economics

Based on Energy Services' experience, a typical LM5000 STIG cogeneration plant may be installed for $30 million. A standard offer California utility contract for such a plant values

Table 2

Description	LM5000 Partial STIG	LM5000 Partial Combined Cycle
Est. Incremental Capital Cost ($)	2,000,000	3,750,000
Incremental Net Power Production (KW)	14,750	5,720
Incremental Fuel Consumption (BTU/KWH-LHV)	5,162	0
Steam to Process (LB/HR)	45,000	45,000
Excess Steam Available for Power Production (LB/HR)	65,000**	65,000
Incremental Annual Operating Benefits:*		
Power @ $60.00/MWH	$7,080,000	$2,745,600
*Incremental Annual Operating Costs:**		
Fuel @ $2.50/MMBTU	$1,692,000	$0
Steam @ 3.125/MMBTU	$1,625,000	$1,625,000
Net Incremental Annual Benefit *	$3,763,000	$1,120,000
Simple Payback (Investment increment beyond cost of traditional cogeneration)	0.5 years	3.3 years

* Assumes 8,000 hours of operation per year.

** Steam production augmentation raises 65,000 LB/HR to 90,000 LB/HR.

electric power generation at $60.00/MWh including both capacity and energy credit. Assuming values of $3.12/mmbtu and $2.50/mmbtu for steam and fuel, respectively, and typical costs for operation, maintenance, insurance, taxes, and cost of capital, the LM5000 STIG cogeneration plant may be installed well within most corporations' requirement for return on investment.

In order to demonstrate the inherent value of STIG operation, it is useful to compare such a cycle with a more conventional combined cycle equipment configuration based on the LM5000. Using average site conditions as a basis, the following table presents the base assumptions used to analyze the incremental operating benefits versus the incremental capital cost for STIG and combined cycle operation when compared with the traditional cogeneration mode of operation.

Description	Cogen	STIG	Combined cycle
Power output, kW	32,500	47,600	38,720
Auxiliary power, kW	1000	1350	1500
Net power, kW	31,500	46,250	37,220
Heat rate, btu/kWh-lhv	9550	8120	8015
Steam to process, lb/hr	110,000	45,000	45,000
Capital cost, $	28,000,000	30,000,000	31,750,000

As can be seen above, the traditional cogeneration mode of operation assumes that all steam produced in the heat recovery boiler will be utilized in an industrial process. If the industrial process were not capable of utilizing 100 percent of steam production, the alternatives rest with partial STIG or combined cycle. The figures depicted above for STIG and combined cycle assume the industrial process will require 45,000 lb/hr of steam, thus leaving an excess of 65,000 lb/hr. In the case of STIG, steam will be injected into the gas turbine for power augmentation, heat rate enhancement, and subsequent steam produc-

Table 3

Description	LM5000 Full STIG	LM5000 Full Combined Cycle
Power Output (KW)	49,500	41,440
Aux. Power (KW)	1,350	1,500
Net Power Output (KW)	48,150	39,940
Heat Rate (BTU/KWH-LHV)	7,960	7,490
Capital Cost	$30,000,000	$33,000,000
Annual Power Credit to STIG *	$3,940,800	Base
Annual Fuel Cost Penalty to STIG **	$1,858,540	Base
Net Present Value: ***		
Plant Capital Cost	$30,000,000	$33,000,000
STIG Power Credit	($37,150,000)	
STIG Fuel Penalty	$17,520,000	
Evaluated Net Present Value	$10,370,000	$33,000,000

* Power Credit = (48,150 KW-39,940 KW)(8,000 HR/YR)($0.06/KWH)

** Fuel Penalty = ((49,500 KW-41,440 KW)(8,000 HR/YR)(7,960 BTU/KWH-LHV)(1.11LHV/HHV)($2.50/MMBTU)) + ((41,440)(8,000 HR/YR)(7,960BTU/KWH-LHV - 7,490BTU/KWH-LHV)(1.11LHV/HHV) ($2.50/MMBTU))

*** Assumes a 30 year life cycle analysis discounted at 10%. The Annual Power Credit and Fuel Penalty values are multiplied by a net present value factor of 9.427.

tion augmentation. In combined cycle, the excess steam will drive an extraction-condensing steam turbine generator. Table 2 outlines the incremental capital and operating costs as well as the incremental benefits of STIG and combined cycle using traditional cogeneration as a basis.

Neglecting any increases in the cost associated with operation, maintenance, insurance and property taxes and excluding federal and state taxes and cost of capital, an incremental investment in STIG will provide a simple payback of approximately 6 months. An incremental investment in combined cycle will require a simple payback period of over 3 years. Comparing these two payback periods demonstrates that due to the low incremental capital requirement for STIG and the minimal effect on system efficiency (compared with combined cycle), when faced with a site condition where steam produced in the LM5000 cogeneration plant cannot be utilized in the site's industrial process, it is far more economical to use such excess steam for STIG operation as opposed to driving a steam turbine generator.

As mentioned previously, the LM5000 is also capable of operating in a mode referred to as full STIG, whereby 100 percent of steam generation is injected into the gas turbine. This configuration is well suited for utility applications where steam is not required for an industrial process, or, like Ripon, the process is shut down for significant periods of time during the year. Table 3 provides a net present value evaluation which compares the costs of an LM5000 full STIG and LM5000 full combined cycle operating 8,000 hours per year.

Based on the above evaluation and assuming that all costs associated with operation, maintenance, insurance, taxes, and cost of capital are equivalent, it can be concluded that over the life-cycle analysis period, the LM5000 full STIG cycle capital and operating costs are approximately 30 percent of the equivalent costs of an LM5000 combined cycle plant.

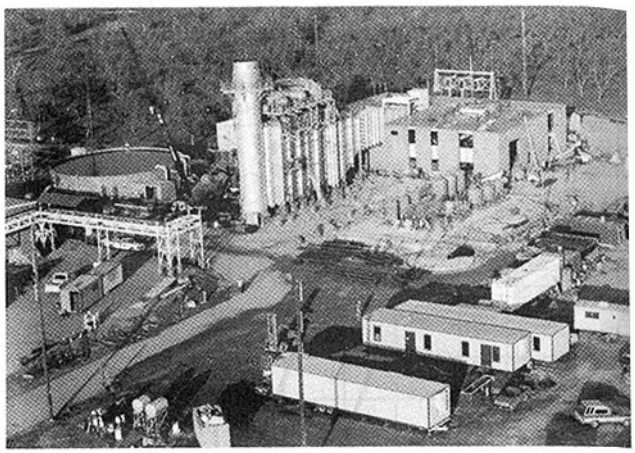

Fig. 18 Ripon cogeneration plant under construction

It should be pointed out however that these very substantial differences are due in large measure to the relatively low present cost of fuel compared to the current value of electric power.

Conclusions

A 49,500 kW LM5000 STIG/cogeneration plant at Simpson Paper Company's Ripon Mill went into commercial operation in the spring of 1988. This first full STIG installation has demonstrated that steam injection increases efficiency from 36 to 43 percent compared to the simple-cycle LM5000. More significantly, the power is increased from a simple-cycle output of 32,500 kW, to a full STIG output of 49,500 kW, an increase of over 50 percent. Both the increased efficiency and power are achieved at an initial equipment cost of no more than $2,000,000 over that of the ordinary cogeneration plants Simpson has installed at other sites.

The full STIG LM5000 plant has the capability of generating power only, or producing a combination of power and steam for use in the paper mill's processes. Simpson has determined that the unit produces essentially identical revenues in either mode. Total capital and operating costs of a full STIG LM5000 are approximately 30 percent of the equivalent costs of a comparable LM5000 combined cycle plant.

Utilizing a combination of fuel nozzle steam injection and an SCR, the plant meets the most stringent NO_x emissions requirements in existence in the United States, i.e., 6–13 ppm (volumetric/dry, corrected to 15 percent O_2). At the same time the unit satisfies the EPA power plant guideline of 250 tons/year for CO emissions.

References

Burnham, J. B., Giuliani, M. H., and Moeller, D. J., 1987, "Development, Installation, and Operating Results of a Steam Injection System (STIG) in a General Electric LM5000 Gas Generator," ASME JOURNAL OF ENGINEERING FOR GAS TURBINES AND POWER, Vol. 109, pp. 257–262.

Cerri, G., and Arsuffi, G., 1987, "Steam Injected Gas Generators in Power Plants," ASME *Cogen-Turbo*, Sept. 2–4, pp. 45–54.

Moeller, D. J., and Kolp, D. A., 1984, "Simpson Paper Co.: First 35 MW IM5000 in Cogeneration Plant," ASME Paper No. 84-GT-55.

Soroka, G., and Kamali, K., 1987, "Modular Remotely-Operated, Fully Steam-Injected Plant for Utility Application," ASME *Cogen-Turbo*, Sept. 2–4, pp. 55–60.

Williams, R. H., and Larson, E. D., 1986, "Steam-Injected Gas Turbines and Electric Utility Planning," *IEEE Technology and Society Magazine*, Mar., pp. 28–38.

A. J. Scalzo
Technical Director.

L. D. McLaurin
Manager, Engine Design and Development.

G. S. Howard
Manager, Aerodynamics and Performance.

Combustion Turbine Operations,
Westinghouse Electric Corporation,
Generation Technology Systems Division,
Orlando, FL

Y. Mori
Deputy General Manager,
Turbine Engineering Department,
Power Systems Engineering Division,
Power Systems Headquarters.

H. Hiura
Deputy Manager, Engineering Department,
Takasago Machinery Works.

T. Sato
Manager, Turbo-Machinery Laboratory,
Takasago Research and Development Center.

Mitsubishi Heavy Industries, Ltd.,
Tokyo and Takasago, Japan

A New 150-MW High-Efficiency Heavy-Duty Combustion Turbine

The 501F 60-Hz Combustion Turbine has been developed jointly by Westinghouse Electric Corporation and Mitsubishi Heavy Industries, Ltd. It continues a long line of large heavy-duty single-shaft combustion turbines by combining the proven efficient and reliable concepts of the W501D5 with the low NO_x technology of the MW701D, together with the experience of the advanced cooled MF111. The new engine is described along with the improved evolutionary changes made from previous engines. Planned design and performance verification programs including model, full-scale component testing, and full-load engine tests are described. Mature output and efficiency in simple cycle mode will be 145 MW and 34 percent, respectively, with expected combined cycle efficiencies in excess of 50 percent.

Introduction

The 501F is a 3600 rpm heavy-duty combustion turbine designed to serve the 60-Hz power generation needs for utility and industrial service in the 1990s. This engine represents the latest in the evolutionary cycle that continues a long line of large single-shaft heavy-duty combustion turbines. Jointly developed by Westinghouse Electric Corporation and Mitsubishi Heavy Industries, Ltd., the 501F combines the efficient, reliable design concepts of the W501D5 [4] with the low NO_x combustion technology of the MW701 D [2] and the state-of-the-art cooling utilized in the advanced, high-temperature MF111 [9]. The result is an advanced design, high-temperature, efficient, low NO_x, more powerful combustion turbine based on time proven reliable design concepts that will satisfy the large combustion turbine power generation needs for the next decade. Designed for both simple and combined cycle applications, it will operate on all conventional combustion turbine fuels as well as with coal-derived low-Btu gas produced in an integrated gasification combined cycle power plant (IGCC) [3]. Currently being planned for 1990 operation, it will have an initial simple cycle ISO rating of 135 MW with a heat rate of 10,150 Btu/kWh (LHV) at a turbine inlet temperature of 1210°C (2210°F) on natural gas fuel. The mature rating shown in Table 1 is at a turbine inlet temperature of 1260°C (2300°F) and will be achieved after obtaining sufficient field experience. In combined cycle applications the thermal efficiency of the mature plant can exceed 50 percent (LHV) in power blocks of 200 MW nominal power rating.

Table 1 501F plant performance

	INITIAL	MATURE
POWER, NET KW	135,000	145,000
HEAT RATE, KJ/KW-HR	10,706	10,548
BTU/KW-HR	10,150	10,000
AIR FLOW, KG/SEC	413.6	413.6
LBS./SEC	912	912
PRESSURE RATIO	14:1	14.2:1
EXHAUST TEMPERATURE, °C	545	571
EXHAUST TEMPERATURE, °F	1013	1061

Contributed by the International Gas Turbine Institute and presented at the 33rd International Gas Turbine and Aeroengine Congress and Exhibition, Amsterdam, The Netherlands, June 5-9, 1988. Manuscript received by the International Gas Turbine Institute July 21, 1987. Paper No. 88-GT-162.

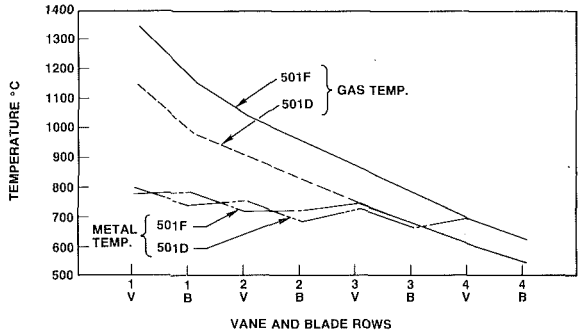

Fig. 1 501F metal and gas temperatures

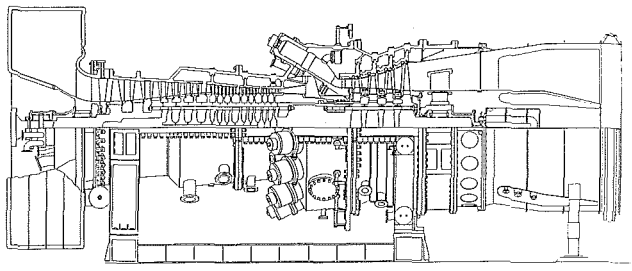

Fig. 2 501F longitudinal section

Since the late 1940s, with the growth of the aviation gas turbine, combustion turbine technologies have experienced a continuous evolution. This has, in general, been reflected in the technology of the heavy-duty combustion turbines used for power generation and mechanical drive applications. During the past ten years, heavy-duty combustion turbines have operated at a turbine inlet temperature in the vicinity of 1093°C (2000°F). In the past, increases in firing temperatures have been driven by competitive market pressures; however, a ten-year hiatus from increases in firing temperature, due primarily to a lack of these pressures, has provided sufficient time for advancements in manufacturing, material processing, and quality control to allow for the state-of-the-art cooling technology, used successfully by the aviation industry for many years, to be utilized in the larger units. The first heavy-duty combustion turbine to incorporate these advanced-cooling technologies was the MF111, with initial commercial operation in August of 1986 at a turbine inlet temperature of 1160°C (2120°F). In addition, stringent emission regulations in Japan provided increased pressure on Mitsubishi Heavy Industries, Ltd. to develop the low NO_x Hybrid Combustion system that has operated successfully at Higashi-Niigata Tohoku Electric Power Company Plant since 1984. Across the board advances in computer technology in the past decade have also enabled manufacturers to improve analytical procedures in all aspects of design including stress analysis, heat transfer, aerodynamics, fluid mechanics, and structural dynamics. For some critical components, the computer proram completely integrates all the governing engineering disciplines into a single iterative routine for quick, accurate optimization. Benefits of this technological advance are shown in Fig. 1 where optimal cooling system design allows metal temperatures in the 501F to be kept within W501D5/MW701D experience.

Supplementing these advances in analytical techniques is a comprehensive testing program consisting of airfoil cascades, turbine model tests, full-scale verification of combustor designs and rotor blade vibratory dynamics followed by an instrumented shop test at load, and finally by an instrumented field test.

This paper describes the features of this latest in a long line of heavy-duty combustion turbines of the 501 model series. Aerodynamic, cooling, and mechanical design improvements are discussed along with the evolutionary changes based on time proven design concepts. Technological advances as well as planned verification test programs are discussed including cascade and model turbine aerodynamic tests, combustor tests, rotating blade vibration tests, and shop test at load.

General Description

Figure 2 illustrates the general configuration of the 501F heavy-duty combustion turbine. Several basic long established design concepts and philosophies are evident, such as the two-bearing single-shaft construction, cold-end power drive, and axial exhaust. These fundamental time proven concepts used by the authors' companies for over 25 years have now become industry standards. The axial exhaust concept introduced on the W501AA in 1970 has been retained because of its improved performance and plant arrangement advantages in combined cycle power plants.

As in all past W501/MW701 designs, the single rotor is made up of the compressor and turbine components supported by two tilting pad bearings. The 501F rotor is of bolted construction supported by two 17-in.-dia, two-element tilting-pad bearings for load carrying and an upper half fixed bearing. This provides inherent stability of the tilting pad with the reliability of the plain bearing, thus eliminating the top pad fluttering problem that has led to local babbitt failures ("spragging"). The thrust bearing is a 22.5-in. double-acting Kingsbury thrust bearing that uses the LEG (Leading Edge Groove) Lubrication System.

The compressor rotor is comprised of a number of elements, spigotted and bolted together by 12 through bolts. The turbine rotor section is made up of disks bolted together by 12 through bolts and using CURVIC[1] clutches, which consist of toothed connection arms that extend from adjacent disks and interlock providing precise alignment and torque carrying features. This turbine rotor design has amassed over 10 million hours of reliable service in all sizes of combustion turbines.

The air inlet system, which contains a silencer, delivers air to the compressor via a plenum-bell mouth and houses the inlet, main journal, and thrust bearings. The compressor is a 16-stage axial flow design of 14:1 pressure ratio that is based on the highly successful W501/MW701 compressor. A four-stage turbine was selected to maintain moderate aerodynamic loadings even at the increased firing temperature.

The combustion system consists of 16 can-annular combustors with the same diameter and length as the W501D5/MW701D. This low NO_x hybrid design is an improvement on the current highly successful design that has been in commercial operation for over three years in the MW701D on liquified natural gas fuel [2]. The presence or absence of flame and the uniformity of distribution of fuel flow between combustors are monitored by thermocouples located downstream of the last stage turbine blades. These can also detect combustor malfunctions when at load while U/V detectors are used to sense ignition during the early starting phase.

All engine casings are split horizontally to facilitate maintenance with the rotor in place. Inlet and compressor casings are of nodular cast iron and cast steel, respectively, while combustor, turbine, and exhaust casings are alloy steel. The inlet bearing housing is supported by eight radial struts, and the aft end bearing housing is supported by six tangential struts. Airfoil-shaped covers protect the tangential struts from the blade path gases and support the inner and outer diffuser cones. Tangential struts respond slowly during transients and

[1]Trademark of Gleason Works.

maintain alignment of the bearing housing by rotating it as required to accommodate thermal expansion. Individual inner casings (blade rings) are used for each turbine stationary stage and can be readily removed and replaced or serviced with the rotor in place. Similar blade rings have been added in the compressor for stages seven through sixteen. Another feature of these blade rings is that they have a high thermal response independent of the outer casing and can be aligned concentric to the rotor to prevent blade rubs, minimize clearance, and maximize performance.

Cooling circuits for the turbine section displayed in Fig. 3 are similar to those used on the W501D5 [4]. They consist of a rotor cooling circuit and four stationary cooling circuits. Rotor cooling air is provided by compressor discharge air extracted from the combustor shell. This air is externally cooled and filtered before returning to the torque tube casing for seal air supply and for cooling of the turbine disks as well as the first, second, and third-stage turbine rotor blades. This cooled, filtered air provides a blanket of protection from hot blade path gases and eliminates excessive contaminants that could block critical intricate cooling passages of the rotor blades.

Direct compressor discharge air is used to cool the row 1 vane while compressor bleed air from stages 13, 10, and 6 is used to provide cooling air to turbine blade ring cavities at stages 2, 3, and 4, respectively. This supply of bleed air also cools the stage 2, 3, and 4 vane segments and ring segments and provides cooling air for the turbine interstage disk cavities. This precludes the ingestion of hot blade path gases by providing cooling air for the interstage seal flow and the fore and aft disk faces.

The stationary vanes and rotating blades for the first two turbine stages are coated for corrosion protection. Compressor diaphragms are also coated to improve aerodynamic performance and corrosion protection. For some environments, compressor rotor blades may be coated for corrosion protection.

Cycle Parameter Selections

The 501F engine, like all recently designed combustion turbines of the authors' companies, is specifically designed for both simple and combined cycle service. The operating firing temperature level is selected to be commensurate with state-of-the-art materials and combined convection/impingement/film/pin fin cooling required for utility and industrial service life. The value selected is 1260°C (2300°F) at the inlet to the first turbine rotor blade.

After the turbine inlet temperature has been selected, the cycle pressure ratio can be chosen to maximize simple cycle power output and combined cycle efficiency. Figures 4 and 5, which are plots of simple and combined cycle efficiencies as a function of specific power with parameters of cycle pressure ratio and turbine inlet temperature, are used to select a pressure ratio of 14 to 1. The selection of 14:1 results in a cycle that has near maximum simple cycle output with a potential combined cycle efficiency greater than 50 percent, as shown by Fig. 5.

The last parameter to be selected is the cycle air flow, whose quantity is determined by the turbine exit annular flow area. It can be shown that the last stage blade stress level is directly proportional to the exit annular area. Since the long highly twisted last stage blade is uncooled, the blade material capability and last stage gas temperature then determine the flow capacity of the engine. A flow of 912 lb/sec has been selected, which will result in a conservatively stressed blade and still yield an engine efficiency in simple cycle of over 34 percent.

Compressor Design

The compressor is a newly designed, highly efficient, 16-stage axial flow compressor patterned after the proven compressor of the W501D5. Flow and pressure coefficients of the 501F compressor have been kept similar to the D5 compressor by increasing the mean diameter of the stages to accommodate the 15 percent increase in flow. In addition, the rear stages of the new compressor have larger diameters to help balance spindle thrust. Interstage bleeds for starting and

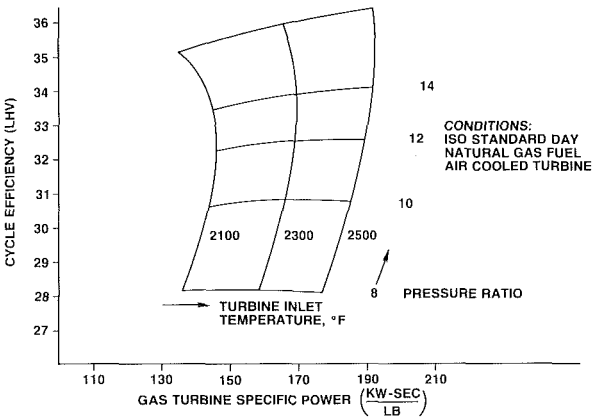

Fig. 4 Simple cycle performance

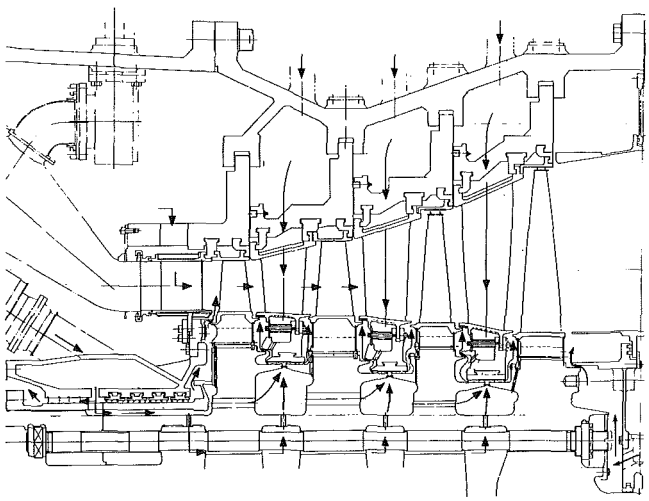

Fig. 3 501F cooling circuits

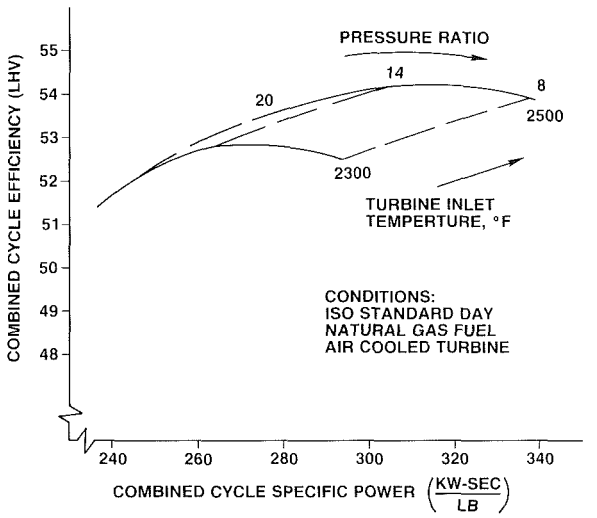

Fig. 5 Combined cycle performance

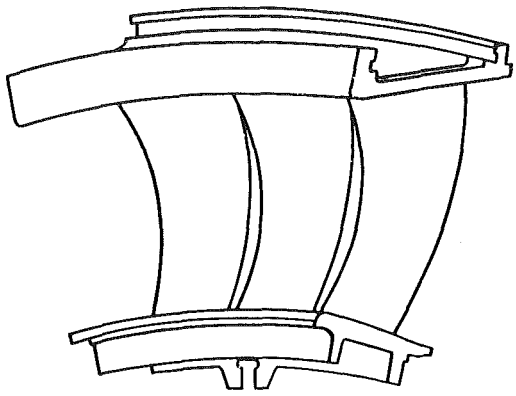

Fig. 6 Isometric of three-dimensional designed row 3 vane segment

cooling flows are in the sixth, tenth, and thirteenth stages, with the thirteenth stage used only for supplying cooling air to the second-stage turbine stationary blading and interstage cooling system. The compressor is also equipped with variable inlet guide vanes, which improve the compressor low-speed surge characteristic and are used in combined cycle applications for improved part-load performance and steam cycle heat-up.

The blade path was designed utilizing a three-dimensional streamline curvature flow field analysis computer program. Rotor blades are double circular arc designs in the first four stages. The stators and all other rotor blades are conventional W-65 airfoil sections. All rotor blades incorporate an improved root design that has flat contact faces (as in turbine blade roots) for ease of manufacturing and inspection and a new locking system, which is inspectable and still allows the blades to be removed in the field with the rotor in place. In most cases, a conservative design approach allows for the continued use of the standard strength grade of AISI 403, while in the first two stages, 17-4PH (17 percent Cr precipitation hardened stainless steel) was introduced to maintain acceptable factors of safety.

Stationary blading is fabricated into two 180 deg diaphragms per stage for easy removal and will maintain the highly efficient inner shroud sealing system currently used on the W501/MW701. These seals will be supported by machined lips on the inner shroud and can be removed to facilitate inspection and maintenace of shrouds and seals. Two exit guide vanes are used, instead of one, to straighten the flow leaving the compressor. Stationary blading and shrouds are standard strength AISI 403 throughout.

Turbine Design

The design of the 501F has maintained moderate aerodynamic loadings in spite of the increased inlet temperature by choosing a four-stage turbine with higher peripheral speed compared to the W501D5/MW701D. Furthermore, improvements in aerodynamic air foil shapes have been made possible by utilization of a fully three-dimensional flow analysis computer code. Understanding the flow phenomena within the cascade makes a low loss blading design possible. Figure 6 is a view of the third-stage turbine vane, which has been designed using this state-of-the-art computer code. Note the vane cross-sectional rotation dictated by the end wall effects. This sophisticated airfoil design approach was employed to assure that the turbine has the highest practical aerodynamic efficiency.

The first and second-stage rotors contain 72 and 66 blades, respectively, and are the free-standing type, while the third and fourth-stage rotors contain 112 and 100 blades, respectively, and utilize integral "Z" tip shrouds. The use of a shrouded system is a departure from past design practice on the 501 series, but has been in use on the CW352 and MW252 turbines. This approach considers increases in power and mass flow that introduce the potential for flow-induced nonsynchronous vibration caused by the aeroelastic interaction between blade structure and flow [5]. This potential can reach critical values in the back end blading where frequencies are below the sixth harmonic. Options are to increase the blade natural frequency, or to provide for increased structural damping, or both. The required increases in blade chords as dictated by the aeroelastic criterion for the free-standing option made the integral "Z" shroud option more attractive because of the added potential for future turbine upgrading and the reduction in bearing span afforded by the smaller chord widths. The analysis of the shrouded blade strength was accomplished using a state-of-the-art three-dimensional Finite Element Model (FEM) cyclic symmetry procedure to define blade group vibratory modes, as well as stresses due to centrifugal force and gas loading. The configuration was optimized using an integrated computer aided engineering (CAE) system for rotating blade design that provides for continuous iteration procedures including thermal performance, aerodynamics, vibratory, heat transfer, and mechanical requirements. This Turbine Interactive Design System (TDSYS) [6] assures that all aspects of the design are considered including complex trade-off analyses in order to develop an optimal design in which all requirements are met.

The first turbine stationary row consists of 32 precision-cast, single-vane segments of ECY768, a Westinghouse-developed cobalt base alloy. As in past W501/MW701 designs, the row 1 single vanes are removable, without any cover lift, through access manways. Inner shrouds are supported from the torque tube casing to limit flexural stresses and distortion, thus maintaining control of critical row 1 vane angles. There are 24 precision-cast, two-vane segments of ECY768 material in the second turbine stationary row. The third and fourth turbine stationary rows are precision-cast X45 vane segments with 16 three-vane and 14 four-vane segments, respectively.

Each row of vane segments is supported in a separate inner casing (blade ring) that is keyed and supported to permit radial and axial thermal response independent of possible external cylinder distortions. Blade ring distortion in the 501F turbine is further minimized by use of segmented isolation rings that support the vane segments and also ring segments over the rotor blades to form a thermal barrier between the flow path and the blade ring. As in all past W501/MW701 designs, the interstage seal housings are uniquely supported from the inner shrouds of rows 2, 3, and 4 vane segments by radial keys that permit the thermal response of the seal housings to be independent of the more rapid thermal response of the vane segments.

The Row 1 vane cooling design is shown in Fig. 7. This highly effective configuration, which evolved directly from the W501D5 design [7] utilizes state-of-the-art concepts with three impingements inserts in combination with an array of film cooling exits and a trailing edge pin fin system. The first two cavities take direct compressor discharge air to maximize the available pressure head while the aft cavity utilizes spent shroud cooling air for its lower pressure needs. Film cooling is used at the leading edge as well as at selected pressure and suction side locations. This limits vane wall thermal gradients and external surface temperatures, while providing an efficient reentry for spent cooling air. Pin fins, used successfully for the first time on the W501D5 row 1 vane, are employed to increase turbulence and surface area, thereby optimizing the overall trailing edge cooling effectiveness. The design of the row 1 vane is such that the low cycle fatigue (LCF) design criterion is satisfied by control of wall gradients [8]. The row 2 vane cooling is a less complex version of row 1 vane cooling. It utilizes twin impingement inserts with film cooling exits and a trailing

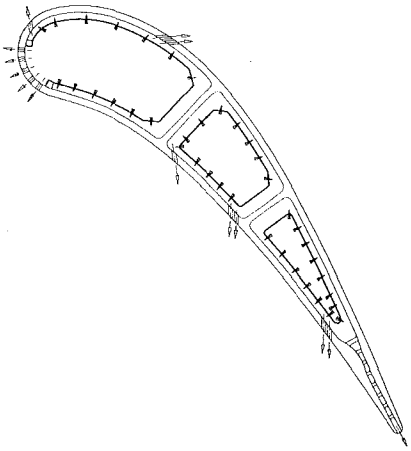

Fig. 7 Cross section of row 1 vane showing cooling flows

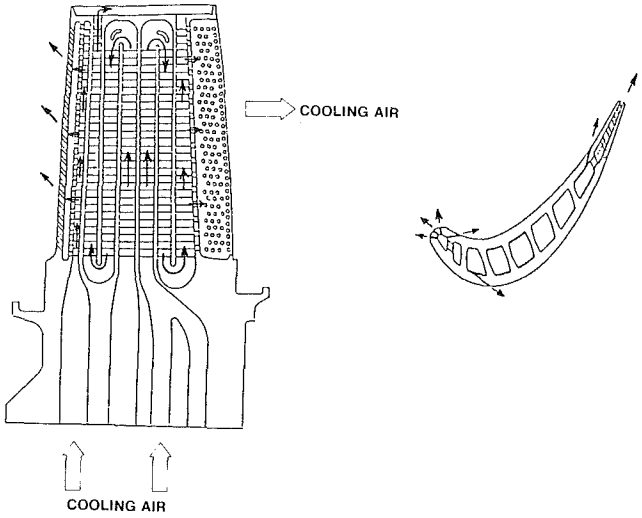

Fig. 8 First-stage blade cooling

edge pin fin exit system. For this row, 13th-stage compressor bleed air is ducted directly to the twin insert system. Film cooling is only required at one location on the suction side and at the exit of the aft insert on the pressure side.

Compressor bleed air from the 10th stage is used to supply cooling air to the third-stage blade ring cavity. Cooling air is directed to the inlet cavity of a three-cavity multipass convective cooled vane airfoil. Leading edge cavity flow also supplies the interstage seal and cooling system while the third pass cavity exits at pressure side "gill holes" on the vane surface. The fourth-stage vane is uncooled but does transport sixth-stage compressor bleed air for the fourth-row interstage seal and cooling system.

The rotating blades are precision cast of INCONEL 738 for the first three rows. Forged Udimet 520 is used for the last row. All rows utilize long blade root extensions or transitions in order to minimize the three-dimensional stress concentration factor that results when load is transferred between cross sections of different size and shape. The blade roots are the same geometric multiple serration type used on past W501/MW701 designs with four serrations used on the first two rows and five serrations used on the rear two stages.

The first stage blade is cooled by a combination of convection techniques via multipass serpentine passages and pin fin cooling in the trailing edge exit slots. The cooling circuitry is shown in Fig. 8. Air supply for blade cooling is high-pressure compressor discharge air that has been cooled and filtered and returned to the turbine rotor via four supply pipes in the combustor shell. Cooling air flows outward through four slots in the root and conveyed radially through the blade shank as shown. Impingment and shower head film cooling are selected for the leading edge region. Basic empirical relationships of the convective heat transfer phenomenon using serpentine passages and turbulence promoters have been verified at the Takasago Research and Development Center utilizing fundamental heat transfer test rigs. In addition, this design has been verified by the row 1 blade experience of MF 111 [9]. Pin fin cooling in the trailing edge combined with the film cooling on the pressure side has also been verified for rotating blades by a suitable rig test at the Takasago R&D Center. By using this verified state-of-the-art technology, the design creep rupture and low cycle fatigue (LCF) life are satisfied by maintaining low temperature and thermal gradients. The row 2 rotor blade is also precision cast and is cooled by a combination of convection techniques via serpentine passage and pin fin cooling in the trailing edge exit slots. Row 3 blade is precision cast with single pass convective cooling holes. The single pass design has been extensively verified by laboratory testing and field experience.

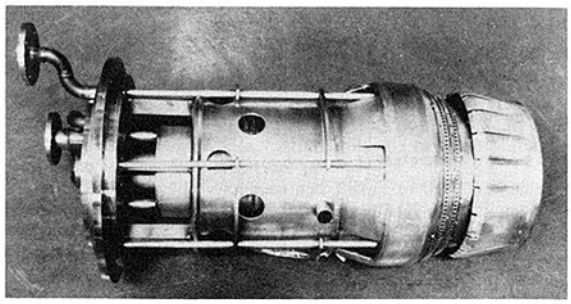

Fig. 9 Improved low NO_x combustor

The cooling system shown in Fig. 3 maintains the NiCrMoV turbine disks below 400°C (752°F), which keeps the disk below the creep range and assures that life is only limited by corrosion and/or wear. Fleet leaders with this disk design are the W501A turbines with up to 150,000 operating hours.

Low NO_x Combustion System

The 501F gas turbine has 16 cannular combustors with the same diameter and length as the MW501D and MW701D. A new premix lean-burn hybrid combustor shown in Fig. 9 is to be applied to meet the existing and new NO_x emissions limitations around the world while having dual fuel capability. The hybrid concept, proposed in 1977 [1], was first developed for engine use in the MW701D[2] and has been in commercial operation since Dec. 1984 at Tohuko Electric Power Company Hagashi Nigata combined cycle plant where NO_x emissions have been reduced to 60 ppmv on natural gas fuel without water or steam injection at a turbine inlet temperature of 1085°C (1985°F).

The hybrid combustor features a two-stage burner assembly and a bypass valve, which directs a portion of the compressor delivery air directly into the transition piece to enhance flame stability during starting and to maintain desired fuel/air ratio during loading. This unique valving system then is modulated to full closed at full load. The new hybrid combustor differs from the present one by having the ratio of pilot to main fuel trimmed considerably to reduce pilot burner NO_x generation and, thereby, overall NO_x emission. The combustion liners and transition pieces are provided with a Mitsubishi Heavy Industries Ltd. developed configuration named MTFIN, shown in Fig. 10 and already proven in service in the MF111. This twin layer composite structure has inherently more efficient cooling, thus providing more air for the low-NO_x system.

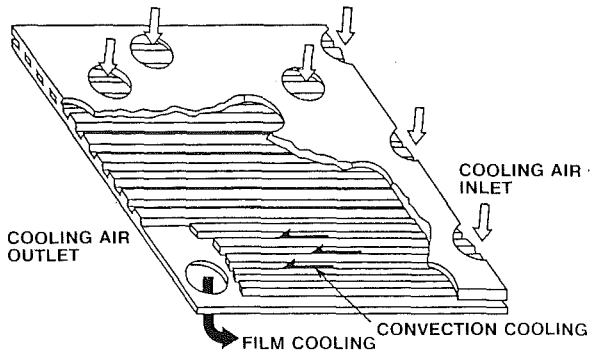

Fig. 10 Schematic of MTFIN

Table 2 Verification test schedule

	1987	1988	1989
TURBINE AERODYNAMIC TESTS			
CASCADE TEST			
MODEL TURBINE TESTS			
COMBUSTOR TESTS			
COMPONET TESTS			
HIGHT PRESSURE TESTS			
ROTATING BLADE VIBRATION TEST			
SHOP TEST			

COMPLETED
SCHEDULED

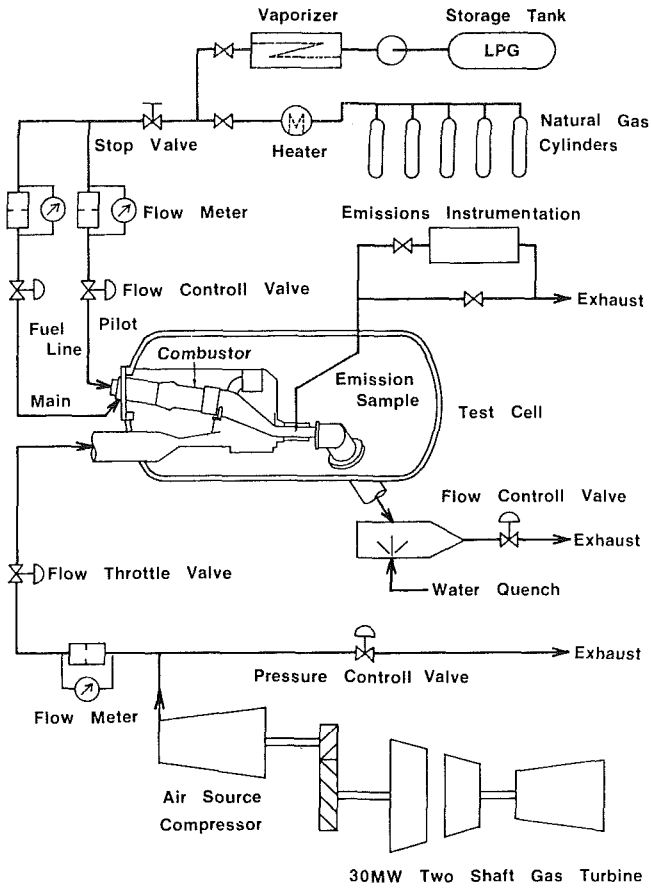

Fig. 11 Schematic of combustion test facility

Verification Testing

All new advanced technology parts applied in the 501F engine are qualified for engine use by verification tests, including: (*a*) rotating blade vibration, (*b*) turbine aerodynamic, and (*c*) combustion tests. Overall engine performance and durability will be verified by engine shop tests. The verification test schedule is shown in Table 2.

(a) Rotating Blade Vibration Test for the Blades of the Compressor and Turbine. The rotating blade vibration test will be performed to verify the vibration characteristics for selected rotating blades of the compressor and turbine. The first and second-stage blades of the compressor and of all four stages of turbine will be tested to verify natural frequencies. Damping characteristics will also be measured for the shrouded blades of the third and fourth stages of the turbine. These damping characteristics will be used to obtain turbine blade dynamic responses via a cyclic symmetry computer routine.

(b) Turbine Aerodynamic Test. In order to verify the turbine performance, several aerodynamic tests were performed. These included cascade tests and model turbine tests. Two-dimensional performance of the typical sections was verified by using a high speed cascade tunnel. To assure the cycle match with the compressor, the flow capacity of the first nozzle was also verified in an annular cascade test rig. Results of the cascade tests were all satisfactory. A model turbine test rig of the fourth stage was constructed to confirm the benefit of the newly incorporated three-dimensional aerodynamic design techniques. Measured performance of the fourth stage clearly showed the usefulness of the three-dimensional design techniques. In addition, a model turbine test of the first two stages will be run in early 1988 to provide final verification of the critical stage matching and three-dimensional aerodynamic design techniques.

(c) Combustion Test. A newly designed hybrid combustor with improved performance is being tested in component test rigs for verification of the exhaust emissions (NO_x, UHC, and CO), pressure drop, pattern factor, wall cooling, and vibrational performance characteristics. Dynamic pressure oscillations in the combustion chambers are also being investigated. A combustion test consists of a cold flow test, a flame propagation test, shaker test, an atmospheric test, and a high-pressure test. Figure 11 shows a schematic of the high-pressure test facility. The test rig is capable of operation at 501F rated engine conditions. In the test cell, a full-scale hybrid combustor, transition piece, and bypass valve are installed. The exit instrumentation consists of seven thermocouple rakes and four emission probes. Combustion liner temperatures are monitored by embedded thermocouples. Vibratory stresses on the combustion liners, transition pieces, supports, and fuel nozzles are measured by strain gages. Pressure transducers are also attached to provide information on the dynamic pressure oscillation within the combustion chamber.

(d) Engine Shop Test. In order to verify the correct operation for the 501F engine, a shop test including full load condition will be carried out in Mar. 1989. During the shop test, the generator will be coupled with the gas turbine and the electrical output produced by the generator will be absorbed by the water rheostat in the test facility.

The shop test is the important final stage for the confirmation of the following:

1 Compressor inlet air flow over the entire IGV range
2 Compressor surge margin
3 Engine starting and acceleration characteristics
4 Mechanical operation of the engine from starting to overspeed including rotor vibration characteristics

5 Mechanical and thermal performance of the engine over its entire operating range on oil fuel

6 Reliability of the engine by measurement of gas and metal temperatures, pressure, vibratory stresses, etc.

7 Emission characteristics of the engine and the effects of water/steam injection upon emissions and thermal performance on oil fuel.

To provide these data, the engine will be extensively instrumented to measure thermodynamic values, metal temperatures, static and vibratory strains, vibration characteristics, displacements, and other parameters. Dynamic strain gages are installed on the turbine blades to verify dynamic responses. The signals from the rotating sensors are transmitted by a telemetry system. Clearance measurement systems using proximity probes allow stator-to-rotor radial displacement measurements during transients. Through the use of an infrared pyrometer, it will be possible to obtain the temperature distribution on each turbine blade of the first stage under operating conditions. Data acquisition equipment is installed to record the special engineering test data. This equipment includes tape recorders, spectrum analyzers, plotters, and chart recorders.

Summary

The 501F, jointly developed by Westinghouse and Mitsubishi Heavy Industries, has been described together with the latest state-of-the-art technology and verification programs utilized to assure its efficiency and reliability. Time proven design and maintenance features of past W501/MW701 engines have been retained. Improvements in material processing, manufacturing, and quality control have enabled the use of advances pioneered by the aviation industry in high-temperature blades and vanes and introduced for the first time in heavy-duty combustion turbines by the MF111. This advanced high-temperature 150-MW class combustion turbine will have a mature rating in simple cycle mode of 145 MW and 34 percent efficiency with combined cycle ratings exceeding 200 MW and 50 percent efficiency.

References

1 Mumford, S. E., Hung, W. S. Y., and Singh, P. P., "A Potential Low NO_x Emission Combustor for Gas Turbines Using the Concept of Hybrid Combustion," ASME JOURNAL OF ENGINEERING FOR POWER, Vol. 99, No. 4, 1977.

2 Aoyama, K., and Mandai, S., "Development of a Dry Low NO_x Combustor for a 120-MW Gas Turbine," ASME JOURNAL OF ENGINEERING FOR GAS TURBINES AND POWER, Vol. 106, 1984, pp. 795–800.

3 Hendry, R. L., and Pillsbury, P. W., "Commercial Demonstration of the Dow Gasification Process in an Integrated Combined Cycle Cogeneration Application," *Proceedings American Power Conf.*, 1987.

4 Scalzo, A. J., Holden, P. C., and Howard, G. S., "The Westinghouse 501D Combustion Turbine Engine," ASME Paper No. 81-GT-32.

5 Scalzo, A. J., Allen, J. M., and Antos, R. J., "Analysis and Solution of a Nonsynchronous Vibration Problem in the Last Row Turbine Blade of a Large Industrial Turbine," ASME JOURNAL OF ENGINEERING FOR GAS TURBINES AND POWER, Vol. 108, Oct. 1986.

6 Sato, T., Aoki, S., and Mori, H., "A Gas Turbine Interactive Design System – TDSYS – for Advanced Gas Turbine," ASME Paper No. 85-JPGC-GT-11.

7 Tobery, E. W., and Bunce, R. H., "Cascade Heat Transfer Tests of the Air Cooled W501D First Stage Vane," ASME Paper No. 84-GT-114.

8 Sato, T., Takeishi, K., and Sakon, T., "Thermal Fatigue Life Prediction of Air-Cooled Gas Turbine Vanes," ASME JOURNAL OF ENGINEERING FOR GAS TURBINES AND POWER, Vol. 108, 1986, pp. 414–420.

9 Akita, E., et al., "Development and Testing of the 13MW Class Heavy Duty Gas Turbine MF-111," ASME Paper No. 87-GT-37.

Design for the 145-MW Blast Furnace Gas Firing Gas Turbine Combined Cycle Plant

H. Takano
Manager, Energy Technology Section,
Chiba Works,
Kawasaki Steel Corporation

Y. Kitauchi
Engineer, Gas Turbine Designing Section,
Takasago Machinery Works,
Mitsubishi Heavy Industries, Ltd.

H. Hiura
Deputy Manager, Engineering Department,
Takasago Machinery Works,
Mitsubishi Heavy Industries, Ltd.

A 145-MW blast furnace gas firing gas turbine combined cycle plant was designed and installed in a steel works in Japan as a repowering unit. A 124-MW large-scale gas turbine with turbine inlet temperature 1150°C (1423 K) was adopted as a core engine for the combined cycle plant. The fuel of this gas turbine is blast furnace gas mixed with coke oven gas. These are byproducts of steel works, and the calorific value of the mixed gas is controlled to be about 1000 kcal/Nm³ (4187 kJ/Nm³). A specially designed multicannular type combustor was developed to burn such a low Btu fuel. The gas turbine, generator, steam turbine, and fuel gas compressor are connected to make a single-shaft configuration. As a result of introducing the gas turbine combined cycle plant, the plant thermal efficiency was above 45 percent (at NET) and the total electricity generation in the works has increased from 243 MW to 317 MW. This paper describes the design features of this combined cycle plant.

Introduction

Recently the movement for the improvement of plant thermal efficiency has become increasingly important in the steel industries. Many efforts have been made to improve the plant total thermal efficiency.

Figure 1 illustrates the energy flow schematic diagram in the Chiba Works of Kawasaki Steel Corporation. Most of the energy consumed in the Chiba Works is derived from coal supplied from sources external to the Works.

There are three kinds of byproduct gases generated in the steel manufacturing processes: coke oven gas from the coke oven, blast furnace gas from the blast furnace, and LD gas from the converter. It is a key design point how to convert the potential heat energy efficiently and economically from coal-derived byproduct gas to electric power.

To provide this increased efficiency, a 145-MW blast furnace gas firing gas turbine combined cycle plant was planned and introduced to the Chiba Works to rejuvenate the existing power plant.

This newly introduced plant has the following basic design concepts:

(*i*) Multicannular combustor with variable geometry bypass valve for low-Btu gas firing, which can burn the byproduct gas (calorific value from 900 kcal/Nm³ (3768 kJ/Nm³) to 1100 kcal/Nm³ (4605 kJ/Nm³)).

(*ii*) Single shaft combined cycle arrangement to enable the compact design gas turbine, generator, steam turbine, and byproduct fuel compressor connected together. The steam turbine also acts as the starter during the startup cycle.

(*iii*) Digital computer control and CRT operation.

(*iv*) Capacity of a gas turbine should be matched with the available amount of byproduct gas, 270,000 Nm³/h.

(*v*) Fuel byproduct gas should not be vented outside the system for safety reasons.

Basic Economic Merit Analysis for Rejuvenation

To rejuvenate the existing power plant in the Chiba Works, the following design target was selected: Electricity conversion

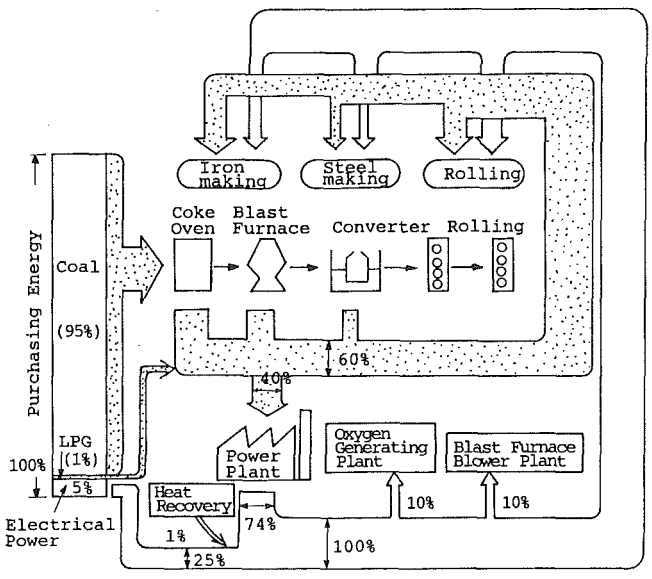

Fig. 1 Energy flow schematic diagram

Contributed by the International Gas Turbine Institute and presented at the 33rd International Gas Turbine and Aeroengine Congress and Exhibition, Amsterdam, The Netherlands, June 5–9, 1988. Manuscript received by the International Gas Turbine Institute December 21, 1987. Paper No. 88-GT-97.

efficiency from the byproduct gas will exceed 45 percent; this will result in 90 percent of the electric power consumed in the Works being generated by the Works.

Feasibility studies showed that the gas turbine combined cycle plant had the most potential and the 100–130-MW class large gas turbine with 1150°C (1423 K) firng temperature could be applicable as a core engine for the combined cycle plant.

Advantages of rejuvenation by introducing the gas turbine combined cycle plant are summarized in Fig. 2.

- Electricity generation is increased from 243 MW to 285 MW at the same fuel consumption due to the thermal efficiency improvement.
- By improvement of the electricity conversion ratio, the operation of the blast furnace with increased coke ratio (485 kg/ton pig iron to 510 kg/ton pig iron) can result and there can be more byproduct blast gas available than can be applicable for electricity generation.
- Total electricity generation is increased about 74 MW, which provides the improved economic advantage.

The heat balance based on the standard design condition is illustrated in Fig. 3.

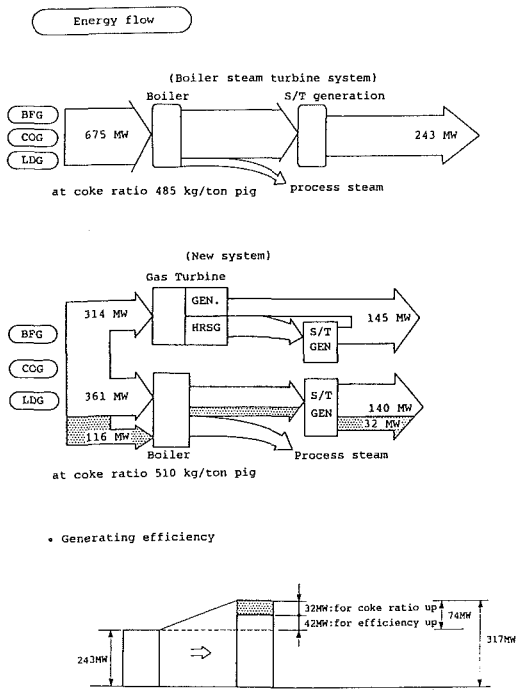

Fig. 2 Merit of the rejuvenation

Joint Research for Combustor Development

Blast furnace gas, coke oven gas, and LD gas from the converter are the byproduct gases in the steel works, and it has long been a challenge to utilize them more efficiently and economically.

Applications as a fuel for the gas turbine have been utilized in European, USA, and Japanese steel industries by utilizing first-generation gas turbine engines, which had relatively lower turbine inlet gas temperatures (approximately 800°C (1073 K)). There was only one application of the blast furnace gas firing gas turbine with 1000°C (1273 K) turbine inlet gas temperature. All of these had large external combustors in order to maintain a stable combustion.

In this new plant application, study for the selection of the large 50-Hz gas turbine, which has a turbine inlet gas temperature of 1150°C (1423 K), was carried out.

The combustor design with new concept was focused on the following points: A large amount of air must be supplied for combustion because of its substantial lower calorific value; this is a disadvantage for controlling the fuel-to-air ratio. Stable and highly efficient combustion is required within the turn-down ratio 2.5 in the gas turbine combustors. Less air is available for cooling, so combustor basket cooling is disadvantageous.

To solve the above, a multicannular combustor design was selected because of the smaller combustor basket surface area available, compared with the large single can type combustor design.

A specially designed variable geometry bypass valve was applied to compensate the air flow supplied to the combustion area. This valve has great potential to improve the combustion characteristics during gas turbine part-load operation.

The combustor configuration is illustrated in Fig. 4. The variable geometry bypass valve is attached to the transition piece and air flow supplied to the combustion area can be regulated by adjusting the valve openings.

Prior to the combustor detail design, joint combustion development rig tests were carried out by firing the actual blast

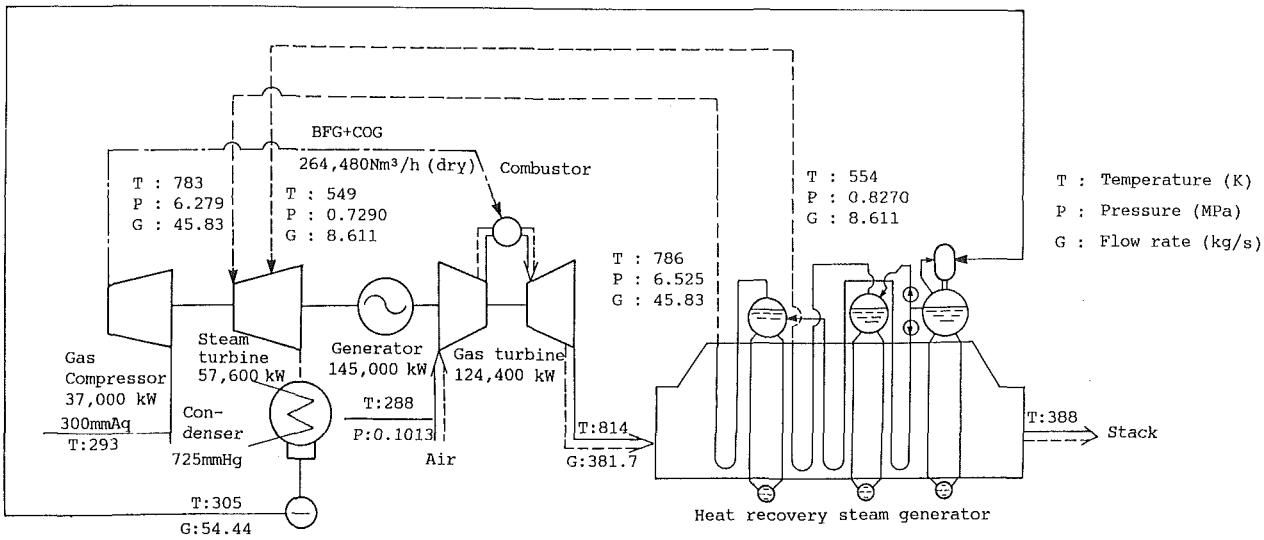

Fig. 3 Heat balance diagram

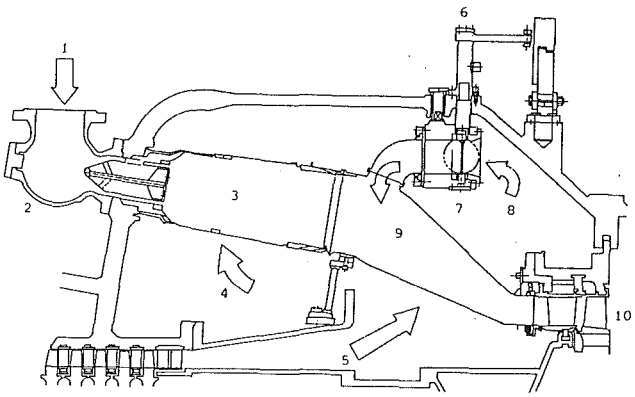

1.BFG+COG fuel gas
2.Spherical elbow
3.Combustor
4.Air for combustion
5.Compressor discharge air
6.Variable ring
7.Bypass valve
8.Bypass air
9.Transition piece
10.Turbine

Fig. 4 Combustor configuration

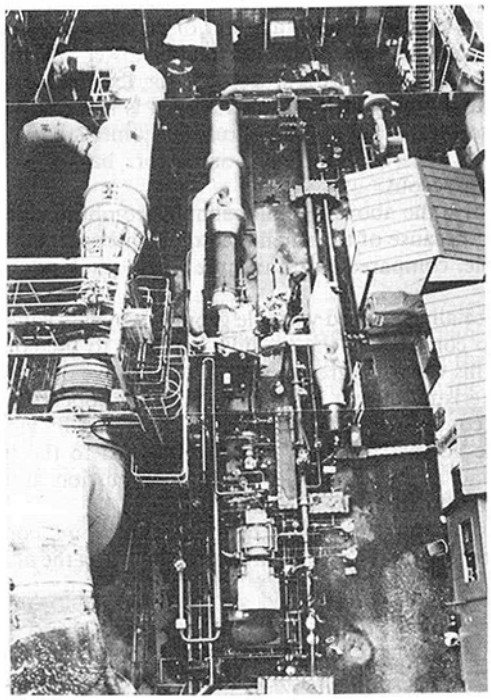

Fig. 5 Combustor test rig

furnace/coke oven gas in the Chiba Works of Kawasaki Steel Corporation (Fig. 5).

Rig test results are summarized as follows:

(*i*) Direct ignition by the spark type ignitor with Btu values higher than 900 kcal/Nm^3 (3768 kJ/Nm^3) can be achieved and the critical fuel-to-air ratio for the ignition was obtained as shown in Fig. 6.

(*ii*) Stable and highly efficient combustion can be obtained under the expected operating fuel-to-air ratio, including no-load condition and the full-load condition. Under the part-load condition, the variable geometry bypass valve improved the combustion efficiency as shown in Fig. 7.

(*iii*) NO_x emission level was confirmed under 10 ppm (without any correction for oxygen, humidity, or heat rate). Because of the substantial advantage of the low Btu fuel firing, the theoretical maximum flame temperature is lower than fuels with the higher heating value.

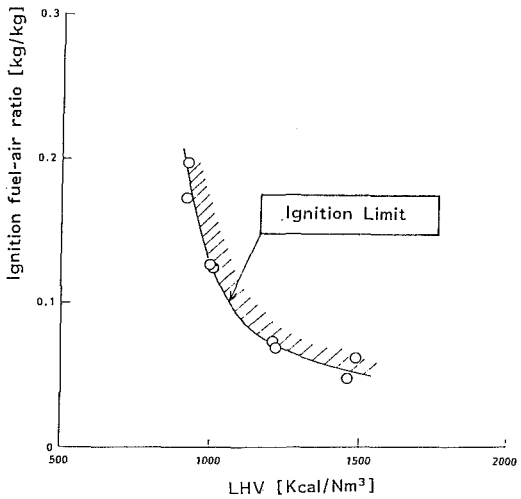

Fig. 6 Critical fuel-to-air ratio for ignition

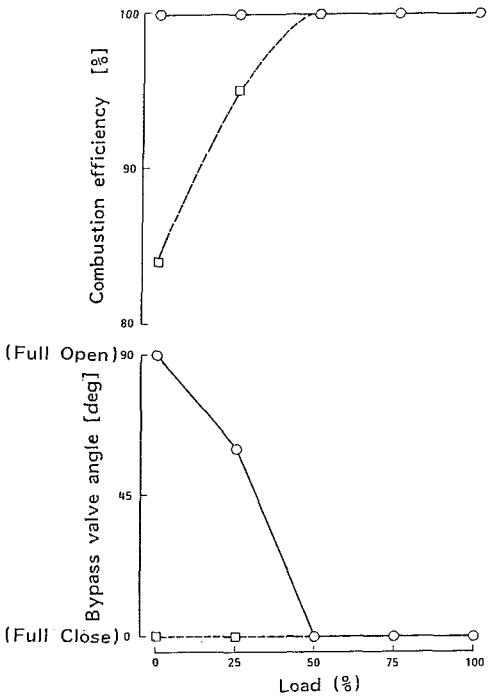

Fig. 7 Combustion efficiency improvement using bypass valve

Plant Design Specifications and Basic Design Concept

The plant design specifications are summarized in Table 1.

MW701D gas turbine produces 124.4 MW of power, and a steam turbine produces 57.6 MW by using the steam from the heat recovery steam generator, which is arranged downstream of the MW701D gas turbine.

37 MW of power is used to drive the fuel gas compressor and 145 MW of electric power is produced from the generator.

Basic Capacity Consideration

As a core engine, the MW701D of Mitsubishi Heavy Industries, Ltd. was selected and modified to match the air flow to burn lower calorific value fuels.

Typical contents of the byproduct gases: blast furnace gas, coke oven gas, and LD gas, are summarized in Table 2.

These gas contents are expected to vary depending on the steel manufacturing process operational conditions.

Table 1 Specifications of main components

Gas Turbine	
Type	Single shaft, open cycle type
Gas turbine output	124,400 kW
Fuel gas compressor input	37,000 kW
Turbine inlet pressure	1.297 MPa
Turbine inlet temperature	1,154°C (1427K)
Turbine	4 stages axial
Compressor	19 stages axial
Combustor	18 cannular type
Fuel gas compressor	17 stages axial (Shaft driven)
Speed of gas turbine	3,000 rpm
Speed of fuel gas compressor	6,310 rpm

Steam Turbine	
Type	Single cylinder, single flow, dual pressure, condensing type
Output	57,600 kW
Inlet pressure	
(High pressure)	6.279 MPa
(Low pressure)	0.7290 MPa
Inlet temperature	
(High pressure)	510°C (783K)
(Low pressure)	276°C (549K)
Speed	3,000 rpm

Heat recovery steam generator	
Type	Exhaust heat recovery, dual pressure type
Evaporation	
(High pressure)	45.83 kg/s
(Low pressure)	8.611 kg/s
Outlet pressure	
(High pressure)	6.525 MPa
(Low pressure)	0.8270 MPa
Outlet temperature	
(High pressure)	513 °C (786K)
(Low pressure)	281°C (554K)

Table 2 Typical content of byproduct gases

Gas Condition			BFG	COG	LDG	BFG+COG
Composition	CO	Vol %	21.97	7.00	68.20	20.88
	CO_2	Vol %	21.10	2.86	17.40	19.78
	H_2	Vol %	2.18	55.52	1.00	6.05
	N_2	Vol %	54.75	3.40	13.40	51.02
	CH_4	Vol %	-	27.82	-	2.02
	C_2H_4	Vol %	-	3.29	-	0.24
	O_2	Vol %	-	0.11	-	0.01
Contained sulphur		ppm	50	100	50	54
Contained moisture			Saturated			
*Net calorific value		kcal/Nm³ (kJ/Nm³)	726 (3040)	4500 (18840)	2080 (8709)	1000 (4187)
Gas temperature		°C	Ambient temp. +5°C			
Gas pressure		mmAq	300			
Dust			≤ 5mg/Nm³			

*Based on dry composition

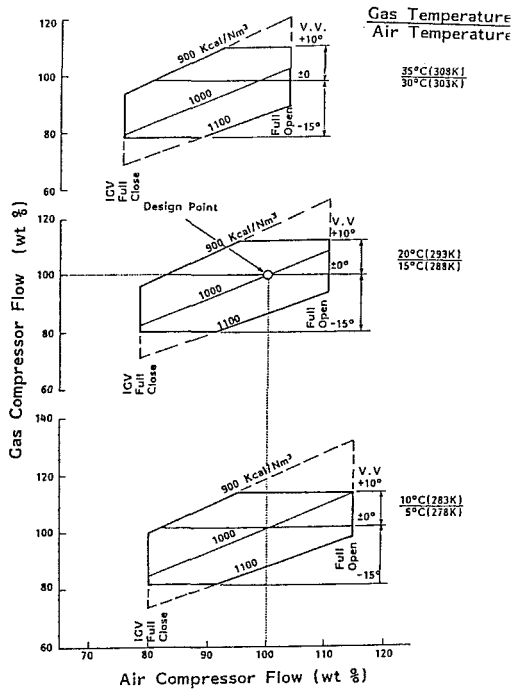

Fig. 8 Selection of the capacity of the gas turbine compressor and the fuel gas compressor

The gas turbine capacity and fuel gas compressor capacity should be carefully selected to have the flexibility to meet with the expected variable conditions due to the variation of the steel manufacturing processes:

- Calorific value is expected to vary from 900 kcal/Nm³ (3768 kJ/Nm³) to 1100 kcal/Nm³ (4605 kJ/Nm³). 1000 kcal/Nm³ (4187 kJ/Nm³) is selected as a design point. Under normal operating conditions, blast furnace gas mixed with LD gas is supplied and coke oven gas is added to compensate the calorific value variations.
- The temperature of the byproduct gas is also expected to vary from 5°C (278 K) to 35°C (308 K). In the specific case the fuel gas compressor can operate up to a temperature of 70°C (343 K). The temperature variation causes a large change in the water content of the gas because the available byproduct gases are substantially at 100 percent humidity. This also reduces the apparent calorific value when the gas temperature increases.

Considering the above, the air flow of the MW701D gas turbine and the capacity of the fuel gas compressor were selected to have the flexibility illustrated in Fig. 8.

Figure 8 also shows the possible operation range to have the maximum rated turbine inlet gas temperature.

Air flow of the MW701D is regulated by modulating the variable pitched inlet guide vanes, and fuel flow of the fuel gas compressor is regulated by modulating the variable pitched stator vanes.

Special Considerations for Plant Design

Some special considerations were paid to designing the systems, especially for the shaft design and the fuel system design.

Single Shaft Arrangement. The gas turbine, generator, steam turbine, and fuel gas compressor are connected to make a single shaft configuration as illustrated in Fig. 9.

- Gas turbine, steam turbine, and fuel gas compressor have their own thrust bearings, and the axial expansion of the shaft is absorbed by two diaphragm-type couplings, which are arranged at the ends of the steam turbine.
- The steam turbine is specially designed to act as a starting device during the plant starting period. The steam required is

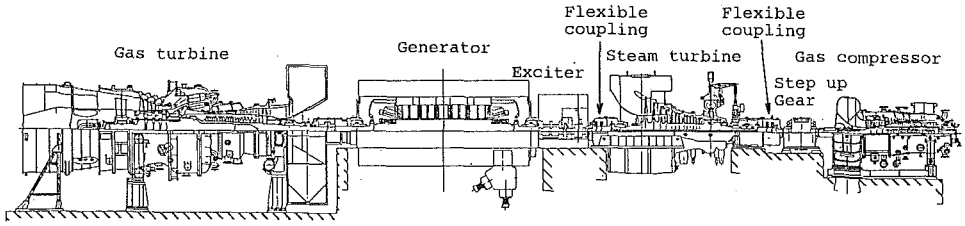

Fig. 9 Single shaft arrangement

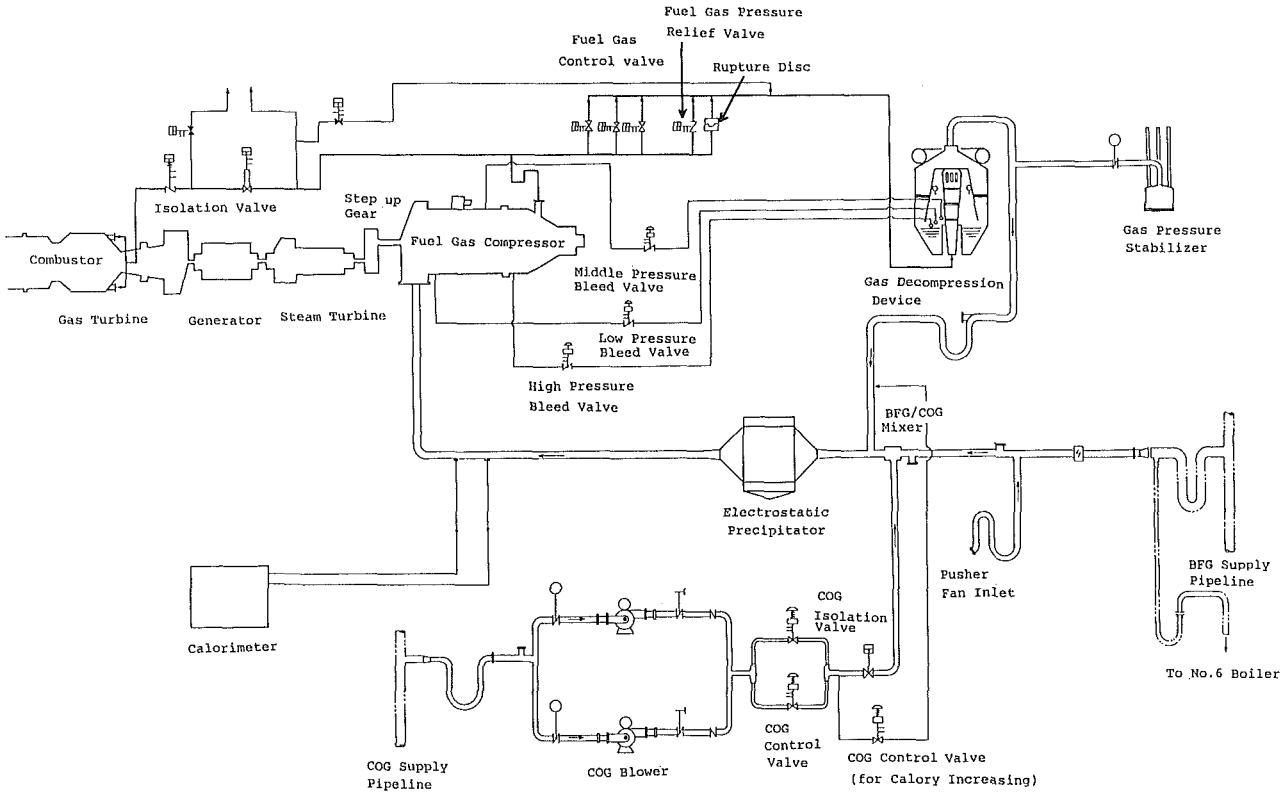

Fig. 10 Fuel flow schematic diagram

supplied to the steam turbine from the external sources until the steam becomes available from the heat recovery steam generator.

- The lubrication oil system is a common design of the whole shaft system; required lubrication oil is supplied to each bearing from the shaft-driven lubrication oil pump, which is mounted on the step-up gear box.
- ISO VG32 lubrication oil is applied.
- Barring of the shaft is available through the turning device also mounted on the step-up gear box.

This arrangement provides compact plant layout and economic advantage.

Calorific Value Control. To maintain stable combustion and efficient plant operation, calorific value control is required.

The fuel flow schematic diagram is illustrated in Fig. 10.

Blast furnace gas and LD gas are normally mixed together and controlled to maintain the lower heating value as constant as possible (between 680 kcal/Nm^3 (2847 kJ/Nm^3) and 780 kcal/Nm^3 (3266 kJ/Nm^3)).

Such mixed gas is branched from the existing gas pipeline and supplied to the new plant. At the inlet interface of the plant, coke oven gas is added to increase the calorific value up to 1000 kcal/Nm^3 (4187 kJ/Nm^3).

The amount of the additional coke oven gas is regulated by the controller to compensate the consumed coke oven gas as a function of the total fuel consumption.

Fuel Throttling. Applied mixed gas as a fuel has a low Btu and approximately 300 mm H_2O low pressure.

A large amount of the gas must be compressed and the amount of the fuel must be throttled to minimize the gas fuel compressor driving power, which has a great effect on the performance.

From the above consideration, the following concepts are adopted:

- Fuel throttling is basically carried out by modulating the variable pitched front four stages of stator vanes under the higher load operation over 70 percent of full load.
- Bypass fuel throttling by the bypass flow control valves is added to control the required fuel amount at the load lower than 70 percent of the load to compensate the variable pitched vanes.

Fuel Gas Decompression Device and Gas Pressure Stabilizer. Fuel byproduct gas is designed basically not to be vented to the outside of the system because of the CO content of the gas.

During part-load operation, load rejection, and gas turbine

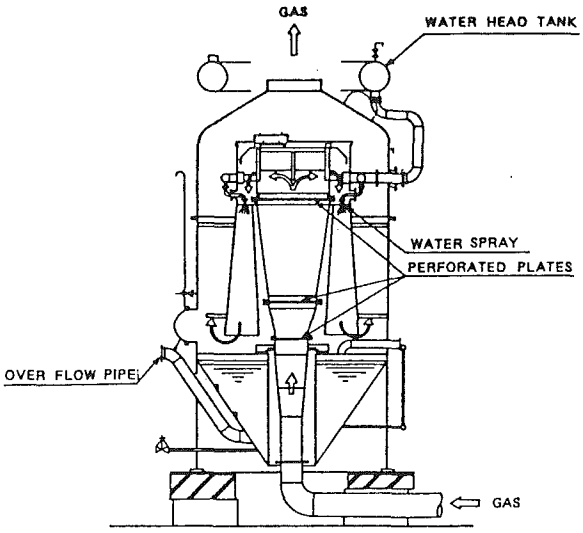

Fig. 11 Gas decompression device

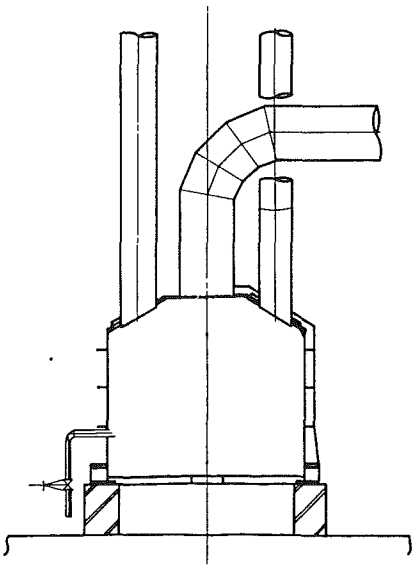

Fig. 12 Gas pressure stabilizer

trip case, the compressed discharged fuel gas from the fuel gas compressor is decreased in pressure and temperature through the patented gas decompression device and it is safely recirculated in the gas pipeline (Fig. 11).

In the emergency trip condition from full-load operation, it is possible to increase the gas pressure in the pipeline up to 600 1000 mm H_2O. This has the possibility to disturb the calorific control in the other processes where the same source gas is used.

To prevent such a disturbance of the pressure during the gas turbine trip, a specially designed gas pressure stabilizer is installed (Fig. 12).

Normally, gas pressure in the gas pipeline is regulated at 300 to 350 mm H_2O pressure fluctuation by the gas holder level control.

In the specially designed newly patented gas pressure stabilizer, the gas sealing water level is set at the level of 400 mm H_2O. When the gas pressure exceeds this level during the gas turbine coasting down period after a trip, the gas can be exhausted to the atmosphere at a safely isolated place.

The water will quickly become resealed when the gas pressure decreases to the level of lower than 400 mm H_2O. Approximately 40 s is required to maintain the gas pressure within the acceptable pressure fluctuation levels during the gas turbine trip.

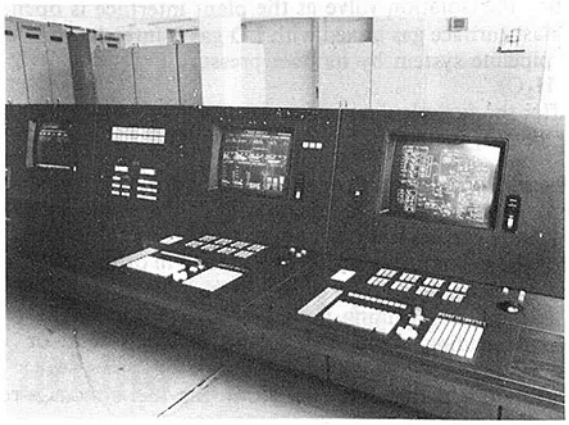

Fig. 13 Operator control console

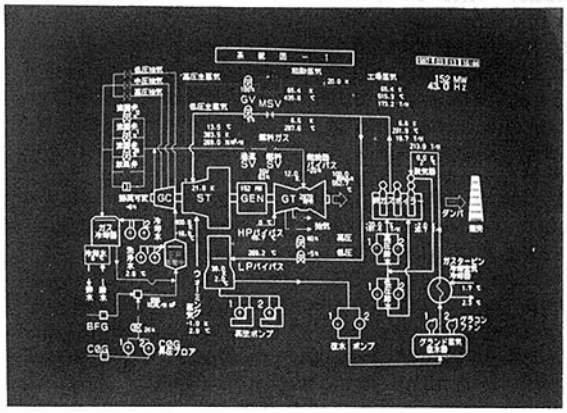

Fig. 14 Typical intelligible schematics

Dust Removal in the Byproduct Gas and Fuel Gas Compressor Cleaning Method. In the applied byproduct gas, there is dust at the level of 5 mg/Nm^3; this kind of dust will form depositions on the blade and vanes of the fuel gas compressor after long periods of operation.

To prevent this fouling, the dust should be removed in the precipitator to the level of 1 mg/Nm^3.

An on-line nutshell cleaning device is mounted at the fuel gas compressor inlet for cleaning of the vanes and blades.

Digital Computer Controlled Fuel Governing System With CRT Operation. In this plant, the gas turbine, generator, steam turbine, fuel gas compressor, and their auxiliaries are combined together and make a sophisticated system.

The operator must know the many operational situations to maintain safe operation.

The many operational informations are summarized as intelligible schematics on the CRT to help the operator monitor the operational conditions. Any operations, including corrective actions, are also available from the CRT board.

The operational console is illustrated in Fig. 13 and typical intelligible schematics are shown in Fig. 14.

By introducing the above CRT operational system, this plant can be designed to be operable basically by one operator in spite of the sophisticated system.

Plant Starting-Up Procedure

Before plant start-up, the air in the pipelines of the fuel system should be completely purged by nitrogen.

Then the isolation valve at the plant interface is open and the blast furnace gas mixed with LD gas is introduced into the fuel pipeline system by its own pressure (approximately 300 mm H_2O).

After the fuel pipeline system is completely filled with blast furnace gas, the machine becomes available for start-up.

Warm-Up Operation for the Steam Turbine. By utilizing external steam, warm-up operation for the steam turbine at 800 rpm is carried out until an acceptable metal temperature rise of the steam turbine rotor is obtained in order to allow the rapid acceleration.

The required warming period is determined by the preset timer depending upon the steam turbine's hot or cold condition.

During this period, the fuel gas in the fuel system is recirculated through the fuel gas compressor.

Operation for Increasing the Calorific Value in the Fuel Pipeline. After completion of the warm-up operation for the steam turbine, the operation for increasing the calorific value up to 1000 kcal/Nm^3 (4187 kJ/Nm^3) by adding coke oven gas into the recirculated blast furnace gas proceeds.

The calorific value in the recirculated gas is monitored by the calorific meter, which is mounted downstream of the electric precipitator.

Ignition. After completion of the calorific value adjustment, the speed of the shaft is decreased to 600 rpm and the ignition operation is started.

Retractable-type spark plugs are mounted on two of the 18 cannular-type combustors and utilized for ignition.

The established flame in the two combustors propagates to the adjacent combustors and eventually stable flames are established in all of the combustors. This is monitored by ultraviolet flame detectors in two of the opposite combustors.

Acceleration. After establishing the flame in the combustors, the supply of the steam for the steam turbine is increased as a function of the speed. The amount of fuel injected to the combustor is governed by the controller to maintain a prescheduled acceleration rate. During this period, the amount of the fuel is controlled by regulating the fuel bypass throttling valves.

Steam also starts to be generated in the heat recovery steam generator depending upon the heat input to it from the gas turbine exhaust.

All the generated steam is recirculated through the steam turbine bypass line and completely isolated from the steam utilized for the steam turbine.

Operation at Rated Speed of 3000 rpm. Twenty minutes after ignition, the gas turbine reaches its rated speed of 3000 rpm and the turbine maintains the same condition for some time until the steam pressure in the heat recovery steam generator reaches 3.533 MPa. Then, changeover of the steam utilized in the steam turbine from the external source to the steam generated in the heat recovery steam generator becomes available and changeover is carried out.

Synchronization and Loading Operation. After completion of the steam changeover, generator synchronization with the grid becomes available. After synchronization, electrical power is increased up to any load set by the operator.

While loading up, steam pressure in the heat recovery steam generator is increased up to 6.525 MPa by a preprogrammed time schedule. After establishing the 6.525 MPa steam pressure, steam pressure is maintained at this pressure.

During load operation, load is governed by the amount of fuel injection; at the higher load of 70 percent, the amount of fuel is governed by the variable pitched stator vanes of the fuel gas compressor, which enables efficient operation to match the fuel gas compressor breathing capacity with the amount of fuel consumed.

Conclusion

One method of efficient usage of byproduct gases with lower calorific value in the steel industries was introduced.

This plant will be scheduled to commence commercial operation in Dec. 1987.

We believe this kind of design consideration can provide an encouraging guide for rejuvenating existing power plants that use byproduct fuels in the steel industries.

References

Muyama, A., Hiura, H., and Morimoto, K., 1984, "Repowering in Steel Works by Introducing Blast Furnace Gas Firing Gas Turbine," ASME JOURNAL OF ENGINEERING FOR GAS TURBINES AND POWER, Vol. 106, No. 4, pp. 806-811.

Development of a 30PS Class Small Gas Turbine and Its Power-Up Version

A. Hoshino
Senior Manager.

T. Sugimoto
Assistant Manager.

T. Tatsumi
Assistant Manager.

Y. Nakagawa
Engineer.

Industrial Gas Turbine Engineering Dept.,
Jet Engine Division,
Kawasaki Heavy Industries Ltd.,
Akashi, Japan

Due to the recent popularity of small and medium-sized industrial gas turbines in many fields, gas turbines below 100 SHP have been employed as prime movers, a power range traditionally reserved for diesel and gasoline engines. Generally speaking, however, small gas turbines have many design difficulties in thermal efficiency, high rotational speed, compact auxiliary equipment, etc., derived from limitations of their dimensions. Small gas turbines S5A-01 and S5B-01, which have 32 PS output power at standard conditions, have been developed and are being produced. Presently, a 30 percent growth rated power producer for S5A-02 and S5B-02 gas turbines is under development. These engines' configurations are as follows: single-stage centrifugal compressor; single-stage radial turbine; single can combustor; hybrid fuel nozzle with pressure atomizer and airblast atomizer; fuel control valve with pulse width modulation system; electric motor drive fuel pump. In this paper, the authors describe the design features and development history of the base engine and the experimental results with the growth rated version.

1 Outline of S5A/B-01 Engines

There are two types of S5 basic engine with different output shaft speeds, designated S5A-01 and S5B-01. The principal characteristics are shown in Table 1. General views are shown in Figs. 1 and 2. Performance curves are shown in Fig. 3. The compressor, turbine, and combustor are all single-stage configurations to simplify the construction.

The engine system consists of a power section, reduction gear box, fuel system, and electric system. Figure 2 shows the unit layout.

2 Power Section

1 Construction. The power section consists of the compressor, the turbine, shaft and bearings, housings and supporting members. The layout of the power section is shown in Fig. 4.

2 Determination of the Thermal Cycle Parameters. Attainable component efficiencies can be assessed by defining the type of components. Figure 5 shows the specific power and fuel consumption at different turbine inlet temperatures and cycle pressure ratios based on the assumed component efficiencies. Better turbine efficiency could be obtained by higher turbine inlet temperature and higher pressure ratio, assuming that the efficiencies of the individual components were constant. Actually, the component efficiencies vary with the turbine inlet temperature and the pressure ratio.

Improvement of the thermal cyclic efficiency as well as reduction of component efficiencies resulting from higher turbine inlet temperature and higher pressure ratio must be considered when determining the cycle parameters. Figure 6 shows the results of the cycle calculations considering component efficiency variation. These results indicate the necessity to choose the cycle parameters carefully, especially the pressure ratio. A pressure ratio of approximately 4.0 was chosen for the reasons mentioned above.

3 Compressor Section. The single-stage backward bladed centrifugal impeller is made from precipitation hardening stainless steel 17-4PH. This impeller has nine full blades and nine splitter blades, and is designed under the following considerations:

1 The leading edge is made as sharp as possible, to avoid excessive shock loss in the region of high Mach numbers.
2 A long inducer was employed to reduce the aerodynamic loading.
3 Half of the blades were made as splitters to reduce inlet blockage.
4 Backward angles of 40 deg were employed to reduce outlet Mach number and to get high reduction.
5 The diffuser channels were designed to expand in both width and depth directions to get high static pressure recovery.
6 The reasons for the choice of 17-4PH are its high strength and good erosion resistance.

An exterior view of compressor impeller is shown in Fig 7. Compressor performance is shown in Fig. 8 based on measured results.

4 Combustor and Fuel Nozzle. The combustor is a can-type with a combination pressure atomizer and air-blast

Contributed by the International Gas Turbine Institute and presented at the 33rd International Gas Turbine and Aeroengine Congress and Exhibition, Amsterdam, The Netherlands, June 5-9, 1988. Manuscript received by the International Gas Turbine Institute September 12, 1987. Paper No. 88-GT-2.

Table 1 Principal characteristics for Type S5A-01 and S5B-01 gas turbines

Type	S5A-01	S5B-01
Rated power	32PS (15 °C, at standard atmospheric condition)	
Specific fuel consumption	465 g/PS.hr	
Pressure ratio	3.8	
Compressor	1 stage radial	
Combustor	Single can	
Turbine	1 stage radial	
Turbine rotor speed	96,000 rpm	
Output speed	3,600 rpm	12,000 rpm
Reduction gear	1 stage epicyclic + 1stage parallel	1 stage epicyclic
Governor	Electric	
Fuel type	Kerosine, Diesel, JP-4, JP-5	
Lubricating oil	MIL-L-23699 or equivalent, 2 L	
Starter type	0.8 KW - 12V DC, 1 set	
Dimension	390L×320W×390H	510L×330W×255H
Weight	32 Kg	34 Kg

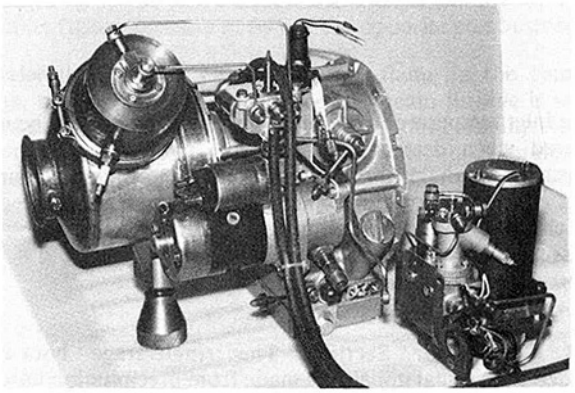

Fig. 1 General view of Type S5A-01 gas turbine

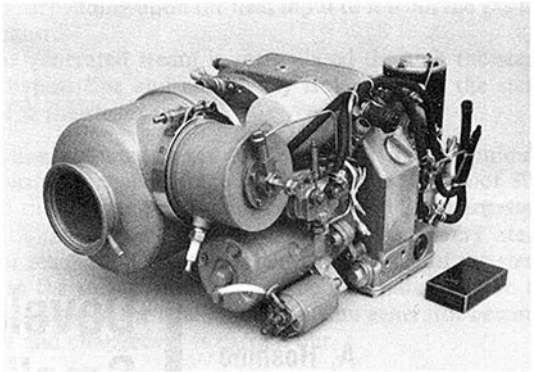

Fig. 2 General view and unit layout of Type S5B-01 gas turbine

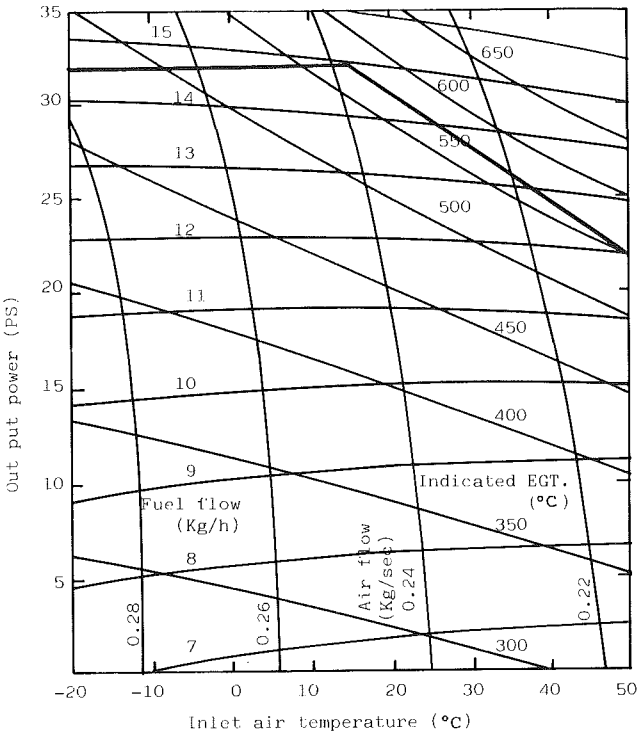

Fig. 3 Performance curves for Type S5A/B-01 gas turbines

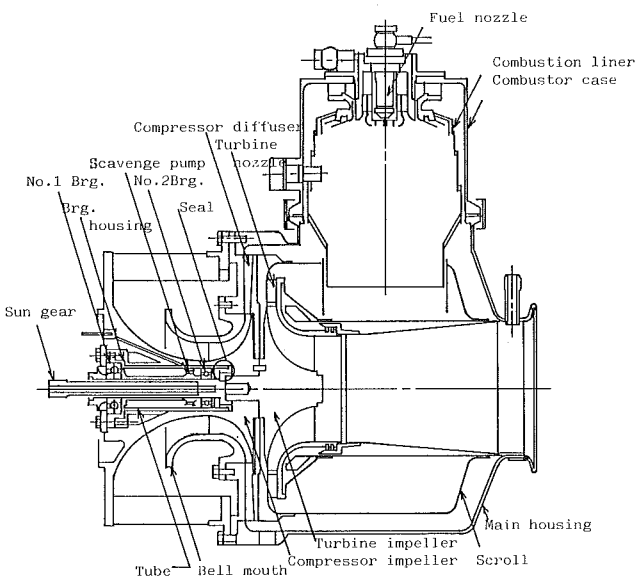

Fig. 4 Layout of the power section

atomizer nozzle. A schematic configuration of the combustor and the fuel nozzle is shown in Fig. 9. The combustor liner consists of the dome, the middle section, the transition piece, and the end piece. These parts are assembled by welding, and the principal material is a nickel-base heat-resistant alloy: HASTELLOY-X.

Many difficulties were caused by the restriction on the combustor size. The combustor system has been developed and improved step by step. The combustor development was started with a simple vortex pressure atomizer nozzle. This type of fuel nozzle was unstable during engine startup, because of pressure limitations on the motor-driven fuel pump. It also caused compressor surging by choking the turbine nozzle with carbon deposit.

A duplex-type pressure atomizer was considered, but the machining was very difficult because of the very small dimensions. So, a rotating cup atomizer and air assist nozzle were investigated. Finally an air-blast nozzle, which requires

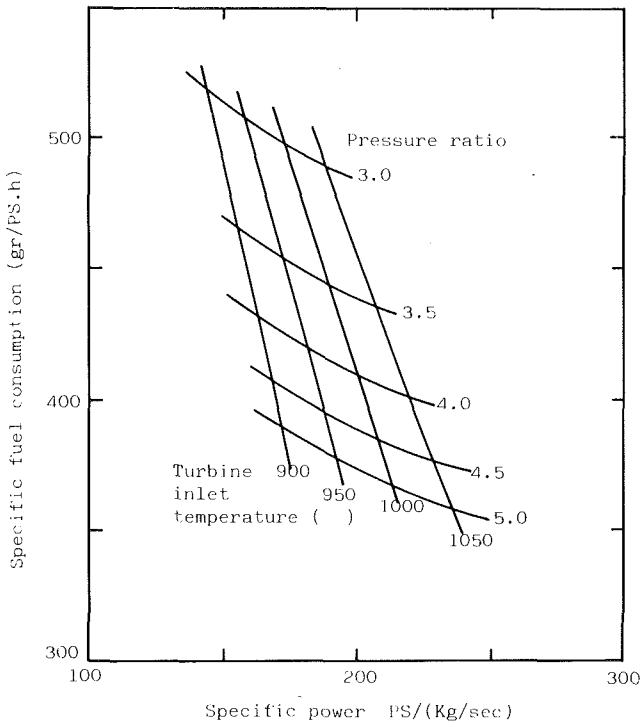

Fig. 5 Results of thermal cycle calculation, assuming constant component efficiencies

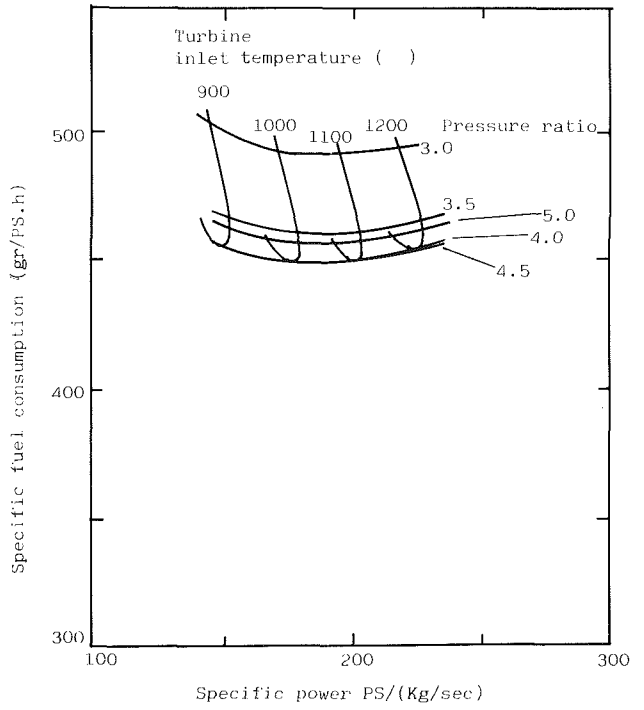

Fig. 6 Results of thermal cyclic calculation with adjusted component efficiencies

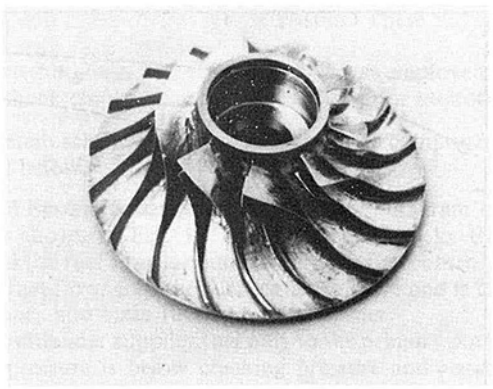

Fig. 7 Exterior view of compressor impeller

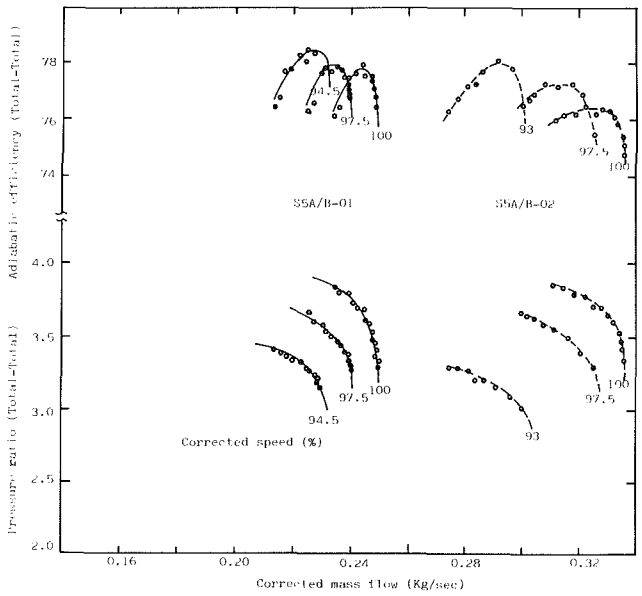

Fig. 8 Measured results of compressor performance

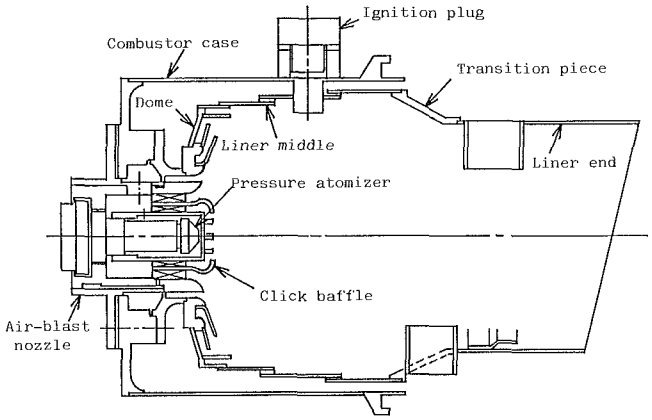

Fig. 9 Schematic configuration of the combustor and the fuel nozzle

no extra equipment, was chosen and was combined with a pressure atomizer.

The final configuration of the fuel nozzle is shown in Fig. 9. This fuel nozzle has the following features:

1 A "click baffle," which is a cover for the primary fuel nozzle tip shaped like a crown, was employed to avoid pileup of the carbon deposit on the nozzle tip.

2 A separator was employed to divide the air flow into sweeping air and blasting air.

3 A swirler was built into the fuel nozzle to stabilize the flame.

An example of the measured combustor efficiency is shown in Fig. 10.

5 Turbine Section. The single-stage radial inflow turbine was made from the nickel-base heat-resistant alloy INCONEL

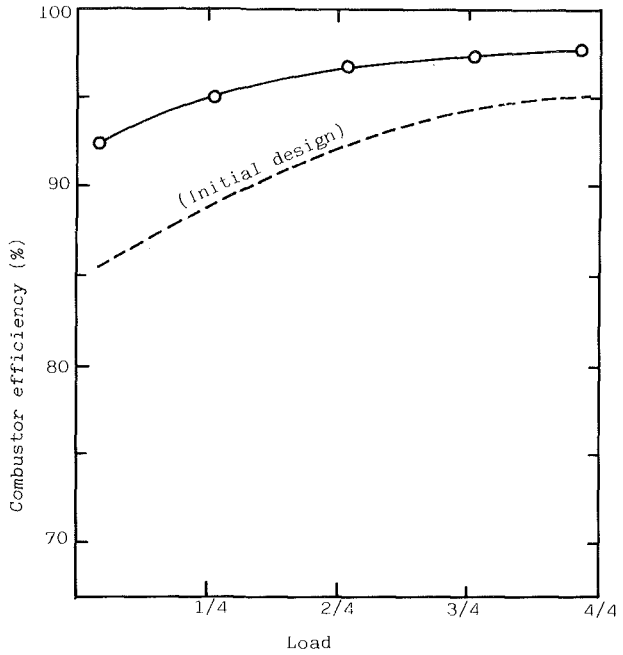

Fig. 10 Example of measured combustor efficiency

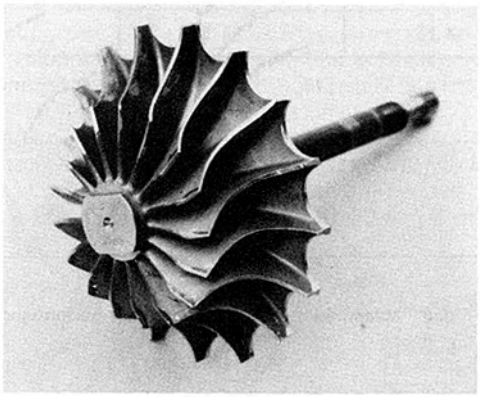

Fig. 11 Exterior view of turbine impeller

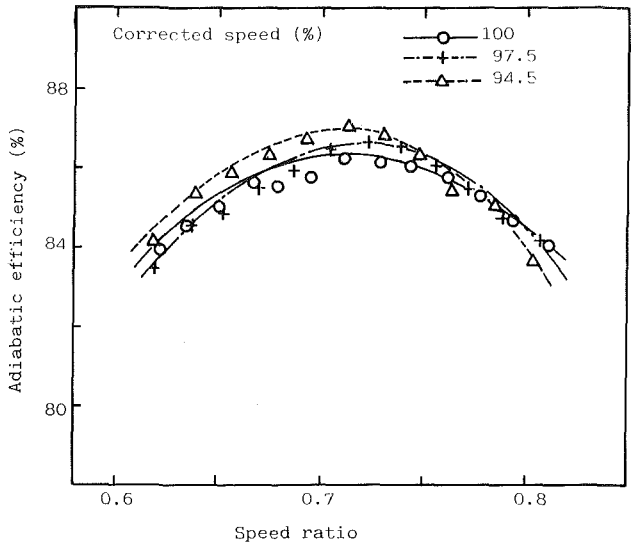

Fig. 12 Example of measured turbine performance

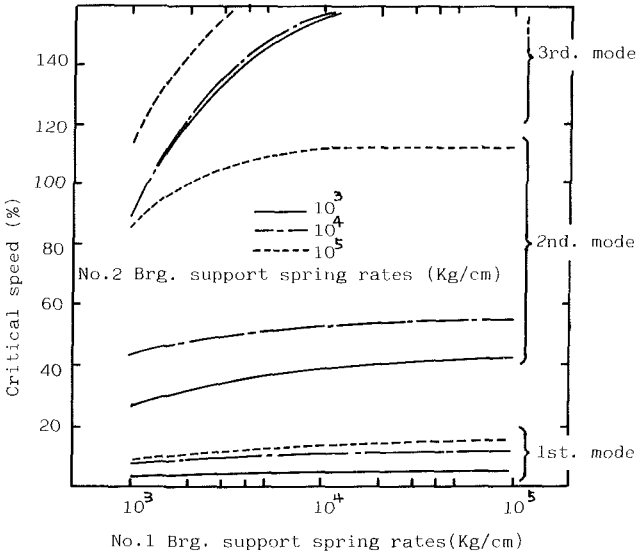

Fig. 13 Results of the critical speed calculation

713LC. The chromium-molybdenum alloy steel shaft was welded to the turbine disk by friction.

The turbine was designed by considering the following items:

1 The tip speed was set rather high so as to keep an optimum region of velocity ratio ν = rotor tip speed/adiabatic expansion velocity = 0.65 ~ 0.75.

2 A scalloped disk was employed to reduce the centrifugal and thermal stress.

3 The turbine nozzle vanes were designed to have a large radius at both leading and trailing edges, to match the inlet flow angle deviation and to resist erosion caused by small particles.

An exterior view of the turbine impeller is shown in Fig. 11. The measured turbine performance is shown in Fig. 12.

6 Shaft and Bearings. Of the many choices for the arrangement of the rotors and bearings, the overhung layout was adopted for the following reasons:

1 The bearings can be placed in the region of low temperature.

2 The oil supply and the scavenge system can be simplified.

3 The heat rejection to the lubricating oil can be reduced.

4 Hot section inspection is easy.

Bearing span, overhung length, and support stiffness of the bearings were investigated to satisfy the requirements with respect to critical speed and rotor tip clearance. The No. 2 bearing was designed to be installed inside the bore of the compressor impeller to reduce the length of the overhang and also to be elastically supported, while the No. 1 bearing was rigidly supported. To obtain the required stiffness and good support accuracy, the bearing housing is made of one piece and machined like a squirrel cage. The outer surface of the bearing housing constitutes a squeeze film damper. The results of the critical speed calculation are shown in Fig. 13.

Because of the high rotational speed, it is necessary to reduce the residual imbalance of the assembled rotor. So, each wheel is balanced individually, and the rotor is rebalanced in the final assembled condition. This method has a disadvantage due to lack of rotor exchangeability. However, it provides an advantage of very small residual imbalance.

Centrifugal oil supply and axial scavenge pump were mounted on the shaft to provide lubrication for the No. 2

bearing, because the space for this bearing is very small. The shroud of the scavenge pump is made of fluorine resin. It contains the lubricating oil passage for the No. 1 bearing and is designed not to disturb the flexibility of the bearing housing.

7 Seals. Compressor air leakage severely deteriorates the engine performance. Various types of air seals are adopted corresponding to the local condition. Labyrinth seals for rotating parts, piston ring seals for exhaust diffuser connection, and graphite laminated stainless steel sheet gaskets for the turbine nozzle flange are employed.

3 Fuel Control System

1 Design Objectives. We had designed the fuel system for this gas turbine under the following considerations:

1 An electric motor-driven fuel pump was adopted as the main fuel pump to obtain high fuel pressure instantaneously with engine start.

2 A combined pressure atomizer and air blast atomizer was adopted to cover the wide operating fuel flow range while keeping good atomization characteristics. These nozzles are equipped with flow dividers.

3 A switching-type fuel metering valve was employed to obtain antishock characteristics and flexibility for mounting.

The system schematic and functions of the components are described below.

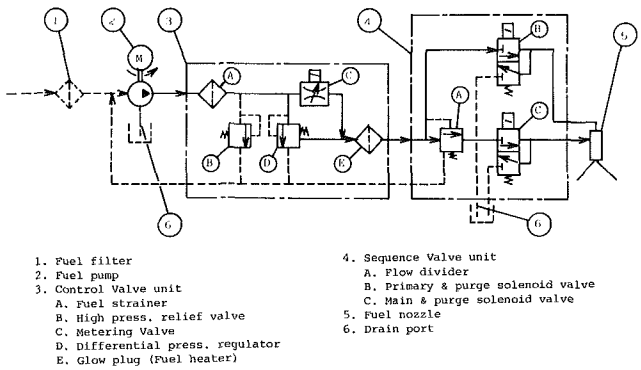

Fig. 14 Schematic diagram of fuel system

2 Fuel System Schematic. A schematic diagram of fuel system is shown in Fig. 14. Fuel is pressurized by the fuel pump and the fuel flow is controlled by the fuel control valve. Metered fuel flows into the fuel sequence valve and is divided into primary and main fuel by a flow divider.

The flow divider supplies fuel only to the primary port when the fuel pressure is below cracking pressure and supplies to both the primary and main ports above the cracking pressure.

The cracking pressure is approximately 20 kg/cm^2. By adoption of the flow divider, the following advantages are obtained:

1 Even at the time when the fuel flow is very small during engine starts, the pressure is instantly raised up to get good ignition reliability.

2 At the time when the fuel flow is very large at full-load condition, excessive fuel pressure can be avoided.

3 Fuel Controller. The fuel control system consists of speed sensors, governor module, Fuel-Injection (F-I) module, and metering valve. A functional diagram of this system is shown in Fig. 15. The functions of each unit are described as follows.

I Governor Module. Basically, this module detects engine speed and generates an electric signal corresponding to the speed. During engine startup, the governor module generates a voltage corresponding to the scheduled function. On the other hand, at steady state, this signal is proportionally controlled against speed fluctuation caused by load variation.

The output signal is modified according to signals from the

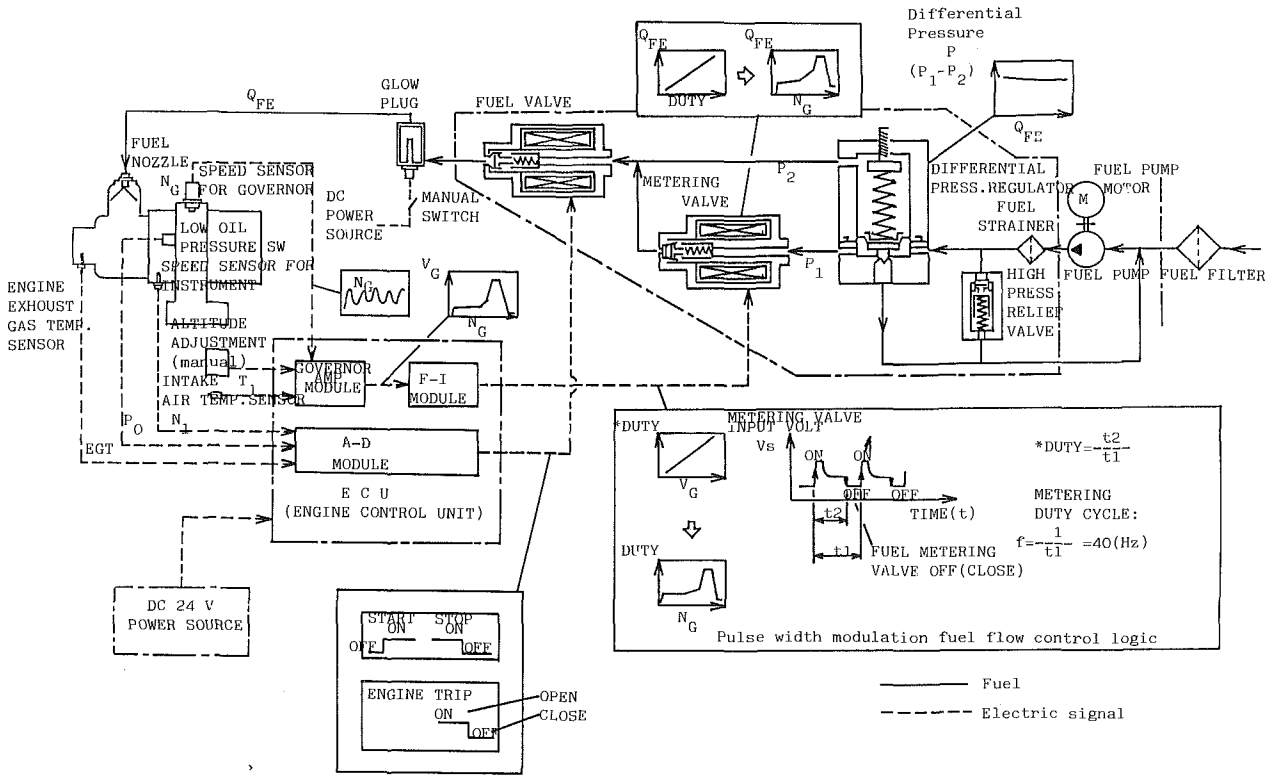

Fig. 15 Functional diagram of the fuel controller

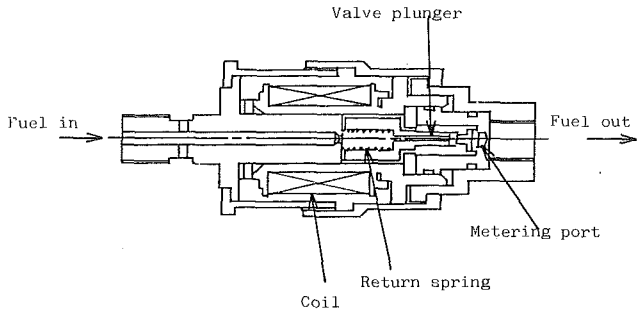

Fig. 16 Schematic configuration of the fuel metering valve

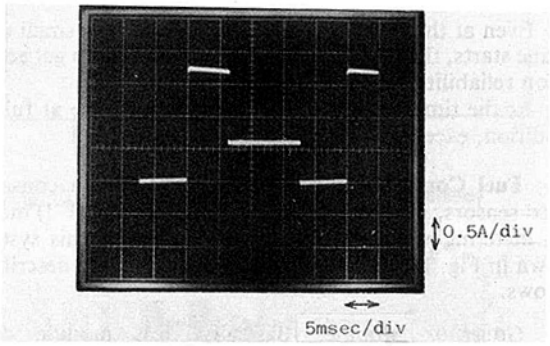

Fig. 17 Output pulse of F-I module

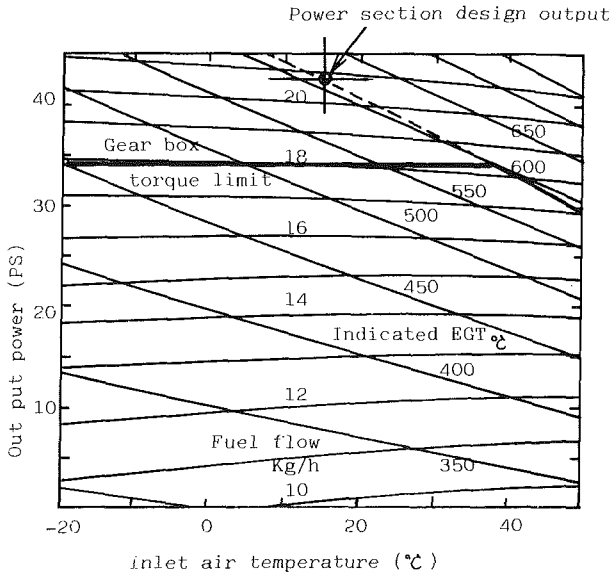

Fig. 18 Typical engine performance curves of S5A/B-02 gas turbine

inlet temperature sensor and the altitude selector (manual setting) and also the fuel enrichment switch.

II F-I Module and Metering Valve. At the beginning of the development, a moving-coil direct drive metering valve supported by a beam spring was employed. This type of valve had disadvantages that flow rate deviated with changing mounting direction or under shock and vibration. So, a switching valve, which was designed under the following considerations, was employed:

1 The stability of combustion was not disturbed by using intermittent flow control.

2 A governor output signal was used as input signal for the pulse width modulator to keep compatibility with the former controller.

3 The drive current of the switching coil was reduced as much as possible to minimize the size of the amplifier and to prevent coil overheating.

4 High-speed switching was obtained by optimum design for output pulse and coil inductance.

Figure 16 shows the configuration of the fuel metering valve. Values of 4.5 ms for ON switching and 1.5 ms for OFF switching under the condition of 0.1 mm valve lift was achieved.

The F-I module receives the voltage signal from governor module and generates a pulse proportional to it. For the switching frequency, 40 Hz was chosen to avoid unstable combustion and degradation of dynamic response. The output pulse of F-I module is shown in Fig. 17. The step pulse as shown was adapted to get high-speed switching and to increase effective pulse duty. This method also brings the advantage of low power loss.

Table 2 Comparison of design point performance

	Unit	S5A/B-01	S5A/B-02
Output power (ISO condition)	PS	32.0	42.5
Pressure ratio	——	3.8	3.8
Air flow	Kg/s	0.235	0.310
Specific fuel consumption	g/PS•hr	465	484
Rotational speed of power producer	RPM	96,000	96,000

4 Growth Rated Version

1 Design Features. The growth rated power producer for S5A-02 and S5B-02 offers 42.5 PS rated output power by means of increasing the air flow rate by 30 percent, as shown in Table 2.

The major aerodynamic components, i.e., compressor impeller with enlarged inducer diameter, high flow rate compressor diffuser, turbine nozzle, and turbine wheel with enlarged exducer diameter, have been redesigned. The tip speeds of both impellers are almost the same as those of the S5A/B-01.

The power-producer casing, combustor, gear box, and other accessories are identical with those of S5A/B-01.

2 Experimental Results. Experimental results of the compressor are shown in Fig. 8. More than a 30 percent increase in air flow rate is obtained at design speed without serious efficiency decrement.

Typical engine performance curves of S5A-02 and S5B-02 are shown in Fig. 18.

5 Summary

The 30PS class small gas turbine S5A/B-01 has been developed and used as a prime mover, mainly for transportable gen-sets that feature compactness and light weight. Growth rated power producer is under development for wider application.

Acknowledgments

The authors would like to thank the many people who cooperated with us in manufacturing and testing.

References

Hoshino, A., 1985, "Development of Small Gas Turbine Combustor With Airblast Atomizer," ASME Paper No. 85-IGT-10.

Gas Turbine Reliability: How? How Much? Where?

H. D. Lenz
Cooper Industries,
EN-Tronic Controls,
Mount Vernon, OH 43050

H. W. Hill, Jr.
Ohio University,
Electrical and Computer Engineering,
Athens, OH 45701

Methods to establish component reliability have been in existence for nearly forty years. However, these methods have not been applied to gas turbine systems, because of a lack of consistent definitions and methodology. This paper describes a systematic procedure for calculating control-system reliability, which also can be extended to calculations for mechanical equipment. This is accomplished by a computerized model. Using the results of this model, practical methods and configurations are described to improve gas turbine reliability, such as: redundancy of essential components; quality of components; environmental factors; sensing devices and actuators; and circuits and logic design. The paper also compares these methods and the resulting reliability improvements in system cost and complexity.

Introduction

Reliability of gas turbine units is important because it directly and significantly affects their overall operating cost. Figure 1 shows quantitatively the effect of different downtime costs on the operating cost for gas turbine installations. In the typical example highlighted in the figure, downtime costs of $100,000/hour result in a $2,000,000 revenue loss for a 20-h downtime due to control failure. The concept of *availability* is used to measure the likelihood of unit downtime. Availability is computed by

$$\text{Availability} = (\text{MTBF} - \text{MTTR}) \div \text{MTBF} \quad (1)$$

In equation (1), MTBF is the Mean Time Between Failures, measured in hours, and is computed from the *failure rates* of the individual components and modules of the system that could cause a turbine to trip. MTTR is the Mean Time To Repair the system after failures (also measured in hours), and depends on the complexity of a system and the time required to troubleshoot and repair a particular component within the system. If the system is very reliable, and also easy to repair, then the availability will be close to one and the downtime will be very small. On the other hand, if the system is unreliable, and difficult to repair, then the availability will be close to zero and the downtime will be large.

In systems without redundancy, failure of any component will cause system failure. For such systems, the MTBF is computed as the sum of the reciprocals of the *failure rates* (λ) for all components:

$$\text{MTBF} = 1/(\lambda_1 + \lambda_2 + \lambda_3 + \lambda_4 + \ldots) \quad (2)$$

Failure rates are very small for practical components, so they are usually calculated in terms of failures/million hours. System complexity is an important issue because failure rate increases with parts count. Generally, complexity decreases reliability and repairability, and increases cost. *It is very difficult to "add on" more reliability to an existing design; any component added will have some negative effect on system reliability.*

Description of System

The block diagram in Fig. 1 shows the subsystems and functions of a gas turbine control system that affect reliability. For this consideration, the system has been subdivided into two parts: safety and utilization. Other parts of a gas turbine control system, such as operator displays, maintenance information, and optimization functions are not discussed here because they do not contribute to tripping of the unit (Lenz, 1984).

The distinction between the safety and utilization parts of the system is important because while many of the considerations for the systems are the same, there is one important difference: The safety system should be designed for optimum

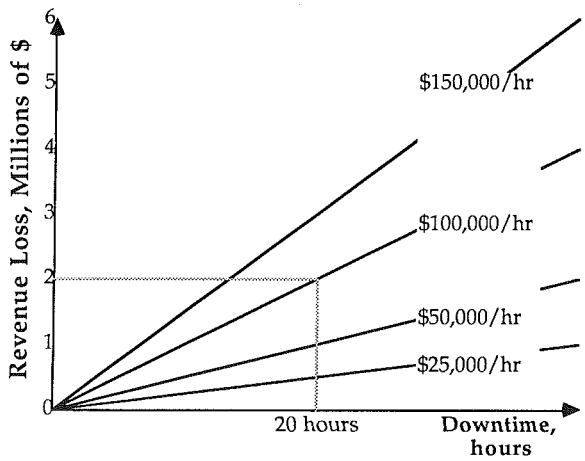

Fig. 1 Revenue loss versus downtime for 15-MW gas turbine

Contributed by the International Gas Turbine Institute and presented at the 33rd International Gas Turbine and Aeroengine Congress and Exhibition, Amsterdam, The Netherlands, June 5-9, 1988. Manuscript received by the International Gas Turbine Institute September 15, 1987. Paper No. 88-GT-315.

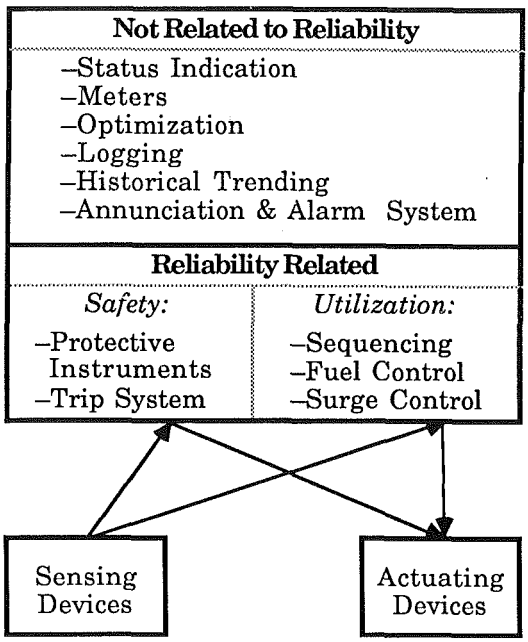

Fig. 2 Control system reliability relationships

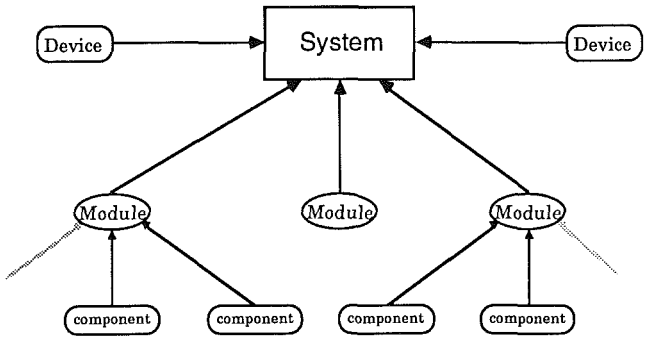

Fig. 3 Hierarchy of control-system reliability model

fail-safety to protect equipment and personnel while the utilization part should be designed for maximum up time. This is also the reason for maintaining maximum separation between the utilization system and the safety system since the safety system is to protect the unit from any failures and malfunctions in the utilization part. The considerations to maintain reliability and fail-safety in the safety system are further discussed in a later part of this paper.

Reliability Model

Determining the Mean Time Between Failures (MTBF) of a complex system is considerably simplified if a *series reliability model* is used. The series reliability model is based on the assumption that failure of any part of a system causes failure of the complete system. This is a worst-case and therefore severe assumption. In practice, parts whose failures do not affect system performance (depending on the definition of system failure) are omitted from the model, and true redundancy (where multiple part failures must happen for system failure) is approximated by using *redundancy factors*.

Redundancy factors come from the expression of the MTBF for a parallel system

$$\text{MTBF} = n/\lambda - n(n-1)/4\lambda + n(n-1)(n-2)/18\lambda - \ldots \quad (3)$$

Here λ is the failure rate of any one of the n identical components. For $n=2$ (often referred to as simple redundancy), the MTBF is $3/2\lambda$. Because the MTBF is calculated as the reciprocal of the total failure rate, this is the same figure as would be achieved if a single component with an equivalent failure rate of $2\lambda/3$ were used. In other words, the system failure rate has been reduced to 2/3 of the failure rate for a single component. This multiplying factor is called the *redundancy factor*. For three components in parallel ("triple" redundancy), the redundancy factor is 6/11.

In the series reliability model, failure rates are determined for every component part of the system. These failure rates are simply added to determine the system failure rate. Finally, the system MTBF is computed as the reciprocal of the system failure rate. The major advantage of using this series model is that because the failure rates of all component parts are added, the components can be grouped for the sake of convenience (such as by mechanical assembly). When a more

P R I N T E D - C I R C U I T B O A R D R E L I A B I L I T Y C A L C U L A T I O N

Component Name: FIELD CARD DIGITAL INPUT Part Number: ZE544-001A-100 Date: 4/20/87

Assumed Environment (per MIL-Hdbk-217D): Ground, Fixed:

PI-E = 2.50
PI-L = 1.00 Ambient Temp. = 27.0

DIODES:

Part Number:	Qty.:	Description:	PI-E	PI-Q	PI-R	PI-A	PI-S2	PI-C	LAMBDA-B	LAMBDA	N*LAMBDA
2-82E-042-001	4	DIODE 1N4454	3.90	7.50	1.00	0.60	0.75	1.00	4.90E-04	6.45E-03	0.02580

LED DIODES:

Part Number:	Qty.:	Description:	PI-E	PI-Q	PI-T	LAMBDA-B	LAMBDA	N*LAMBDA	T
2-82E-049-015	4	DIODE-LED	2.40	0.50	100.0	0.00E+00	0.00E+00	0.0000	NA

RESISTORS:

Part Number:	Qty.:	Description:	PI-R	PI-Q	PI-E	S	LAMBDA-B	LAMBDA	N*LAMBDA	T
2-84E-021-046	2	78 RESISTOR	1.0	5.0	2.9	0.05	1.98E-04	2.87E-03	0.00575	30.0
2-84E-021-046	4	150 RESISTOR	1.0	5.0	2.9	0.05	1.98E-04	2.87E-03	0.01150	30.0
2-84E-021-046	4	150 RESISTOR	1.0	5.0	2.9	0.10	2.17E-04	3.15E-03	0.01261	30.0
2-84E-021-046	4	22K,1/2W RESISTOR	1.0	5.0	2.9	0.05	1.98E-04	2.87E-03	0.01150	30.0

CAPACITORS:

Part Number:	Qty.:	Description:	PI-E	PI-CV	S	PI-Q	LAMBDA-B	LAMBDA	N*LAMBDA	T
2-83E-016-018	4	0.1uF/50V CAPACITOR	1.6	0.68	0.1	10	7.25E-04	7.89E-03	0.03156	30.0

PRINTED-CIRCUIT BOARD: Quality Level: NON-MIL-SPEC PI-Q = 2

Part Number:	Qty.:	Description:	N1	N2	PI-C	PI-S	PI-E	LAMBDA-B	LAMBDA	N*LAMBDA
ZE544E-001C-100	1		50	1	1.0	0.2	2.3	4.10E-05	1.21E-02	0.01207

For Component Name: FIELD CARD DIGITAL INPUT Part Number: ZE544-001A-100 Total Failure Rate = 1.11E-01
MBTF = 9.03E+06

Least reliable part: ZE544E-001C-100 Description: failure rate of component = 1.21E-02
Least reliable set: 2-83E-016-018 Description: 0.1uF/50V CAPACITOR failure rate of set = 0.03156

Fig. 4 Sample module spreadsheet for reliability evaluation

complicated model is used, all components for a particular function must be considered together, regardless of physical location.

A series reliability model was implemented for the gas turbine control system. Figure 3 shows the hierarchy of the model. At the lowest level are the *components*. These correspond to the smallest pieces for which reliability data are tabulated, and ordinarily correspond to items on the most detailed parts lists. Components are grouped according to the mechanical assembly on which they reside (e.g., mounting plate or printed-circuit board). These groups of components are referred to as *modules* and together form the *system*. The blocks labeled *device* on the diagram are assemblies that a control-system manufacturer would purchase intact (such as a power supply) or additional items that would be included to form the system (such as actuating or sensing devices).

Typically an initial calculation of the system MTBF yields a value that is lower than required. Examination of the module failure rates can quickly isolate the module with the largest contribution to the high system failure rate (and low MTBF) (Fig. 4). As detailed in the description of the computerized model, below, in the tabulation of module failure rates, the worst module is automatically highlighted in the system summary sheet. Likewise, on the module sheets, components (and groups of components) with the highest failure rates are flagged.

In a large system such as a gas turbine, more than one module of a given type may be used, just as a component may be used more than once within the modules. Consequently, the module that has the highest failure rate may not have the most negative effect on system reliability, if a slightly more reliable but also more numerous module exists. Likewise, on the module level, the component that is most unreliable may not have the greatest impact on reducing the module reliability if the component is used in small numbers. It is important, therefore, to identify the most unreliable *group* of components, and also the most unreliable *group* of modules, to highlight areas where improvement would have the greatest impact on improving system reliability.

Studies of MTBF for practical systems invariably involve a large number of repetitive calculations. For example, computation of the failure rate for a single component part typically requires multiplication of five factors to account for the part quality, the ambient temperature, the environment, and the part stresses. Particularly because many of these factors have the same values for parts of given type (e.g., microprocessors or switches), some form of computer data processing seemed invaluable.

An early problem was hardware compatibility: The software was to be written at a university, and later run at a manufacturer's facility. Because both entities owned personal computers, it was decided to use these machines.

Once the hardware question was resolved, the software issue was quickly decided. The goal of the reliability analysis was to produce a *tool* for computing MTBFs of many different systems, rather than just for a one-time study. Also, it was highly desirable that changes to the model be easily incorporated. Use of one of the popular "spreadsheet" environments seemed very advantageous. The work was initially done as a template for Lotus 123™, then converted to Paradox™ format by Cooper Industries.

Figure 4 shows the layout of the *Module Spreadsheet*. This form is the first level of the study. One of these forms is filled out for every module of the system. This is a one-time effort when the modules are designed. For maximum accuracy in filling out the forms, and also to speed up the work, assembly parts lists are used, with one line per item in the parts list. The first column contains the manufacturer's part number, and the second column the quantity of the particular part. The next several columns vary with part type, but follow the guidelines set down in MIL-Hdbk-217E (U.S. Department of Defense, 1987) for MTBF calculations. The entries here adjust the basic part failure rate for different quality levels, temperature, environment, and for stresses peculiar to a given part. The penultimate column is the part failure rate, and the last column is the part failure rate multiplied by the quantity. Occasionally some parts will be shown with zero failure rate: This occurs either if the part is considered to be extremely reliable, or if failure of the part is judged not to affect system performance. A database was built into the program so that when a component was used in more than one module, all failure-rate data for that part were automatically entered.

One of the principal reasons for using MIL-Hdbk-217E is the handbook's encyclopedic listing of failure rates. However, even with these extensive tables, the numbers are still somewhat generic: Components purchased from a particular manufacturer may have far lower failure rates than those listed in the handbook. During the reliability study, if a component had a high failure rate from the handbook data, an attempt was made to obtain manufacturers' reliability information. Often this resulted in an order-of-magnitude improvement in failure rate. Using the spreadsheet made it particularly easy to change to the more realistic numbers.

At the bottom of the spreadsheet, the least reliable part (the one with the highest failure rate) is flagged, as well as the least reliable *set* (the group of identical components with the highest failure rate). As discussed above, this aids reliability-improvement projects by indicating where an improvement in reliability can most easily be accomplished.

Figure 5 shows the *Summary Spreadsheet*, which is similar to the Module Spreadsheet in many ways. Here the line items are the modules of the system, as well as the *devices* (modules bought complete from another vendor). As with the module spreadsheets, the module with the highest failure rate is flagged, as well as the sets of modules (where more than one identical module is used) with highest failure rate.

Discussion of Reliability Summary Model Results

Figure 5 represents the results of the summary reliability model for a gas turbine unit driving two (2) centrifugal compressors through a gear. This particular model includes the gas turbine control panel only but the sensing devices or mechanical equipment could easily be added to the model. A brief explanation of some of the columns in the model is of benefit. The failure rate in the individual module is given per million hours. Two factors are used to calculate the total failure rate for a particular item. One is the *Redundancy Factor*, which is 0.66 for simple redundancy and 0.55 for triple redundancy. Redundancy factors are also used for coincident logic, for which the value is 0.66. The *Use Factor* allows for correction for the part of the module or the component which is not affecting a trip of the unit. The items themselves are grouped into input modules, interface modules, processor modules, and certain control functions such as temperature, vibration, and speed with a failure rate total for each group. This format allows easy distinction for the items whose improvement in reliability would have the greatest benefit on system reliability.

Possibilities for Improvement and Comparisons

The model indicates which areas offer the highest potential for improvement. Vibration and temperature monitoring contribute more than 50 percent of the system failure rate.

The following techniques can be applied to achieve specific improvements (see Fig. 6).

System Redundancy. Complete system redundancy improves the reliability of the total system by 50 percent, triple redundancy by 83 percent. However, complete system redun-

6	BA544-002A-100	DIGITAL INPUT BUS CARD	2.084	1.000	.400	5.002
2	BA544-002A-200	DIG.OUTPUT INTERF.CARD	1.175	1.000	1.000	2.350
6	BA544-002A-220	32-DIGITAL OUTPUT INTERFACE	2.250	1.000	.300	4.050
1	BA544-002A-450	12 ANALOG IN 4 ANALOG OUT	5.250	1.000	.200	1.050
2	BA544-002A-500	ANALOG INPUT INTERFACE	1.110	1.000	.800	1.776
1	BA544-002A-800	A/D CONVERTER INTERFACE	1.180	1.000	1.000	1.180
2	BA544-002A-900#1	CONTROLLER PROCESSOR	4.753	1.000	1.000	9.506
1	BA544-002A-900#2	COMMUNICATIONS PROCESSOR	5.040	1.000	0.000	0.000
2	BA544-002A-910	DUAL PORT RAM ASSY.	2.460	1.000	1.000	4.920
					GROUP TOTAL	29.83
1	CA544-004A-150	INCOMING POWER SYSTEM (EST).	1.000	1.000	1.000	1.000
1	CA544-004A-200	IF RACK POWER SUPPLY (EST).	3.000	1.000	1.000	3.000
1	CA544-004A-202	BUS VOLTAGE MONITOR BOARD.	1.580	1.000	.500	.790
					GROUP TOTAL	4.79
3	DA544-002A-830	DIGITAL DISPLAY INTERFACE.	.770	1.000	0.000	0.000
1	DA544-005A-220#1	LED DISPLAY BOARD.	1.150	1.000	0.000	0.000
					GROUP TOTAL	0.00

SYSTEM FAILURE RATE PER 10-6 HRS 125 MEAN TIME BETWEEN FAILURES 8000 HRS

LEAST RELIABLE MODULE: BA544-002A-900#1 DESCRIPTION: CONTROLLER PROCESSOR MODULE FAILURE RATE: 4.753
LEAST RELIABLE MODULE SET: AV544-001A-550 DESCRIPTION: 1-ANALOG INPUT TRIP VIBR SET FAILURE RATE: 32.130

Fig. 5 Summary spreadsheet

Feature	Approx. Effect on System Reliability	Change in System Cost & Complexity	Effect on Quantity of Actuating & Sensing Devices
System (Double) Redundancy	+ 50%	Large Increase	Double
System Triple Redundancy	+ 83%	Very Large Increase	Triple
Vibration & Temperature Redundancy	+ 28%	Moderate Increase	Vibration & Temperature Device Double
Vibration & Temperature Coincidence Logic	+ 28%	Small Increase	No Change
Discrete Instruments	Significant Decrease	Large Increase	No Change
Temperature Scanning	+ 36%	Decrease	No Change

Fig. 6 Effects of different control-system configurations

dancy causes a significant increase in cost and complexity, not only of the panel but also in sensing and actuating devices.

Essential Redundancy. With essential redundancy only functions that are high contributors to the failure rate are duplicated. For the example in Fig. 5, vibration and temperature monitoring would benefit significantly from redundancy. Simple or triple redundancy would improve the reliability for these functions by 50 or 83 percent, respectively.

Coincidence Logic. For some vibration and temperature monitoring functions, coincidence logic (a form of redundancy) can be applied. As an example, for a bearing-temperature sensing point, the alarm setpoint of an adjacent point would be used to verify the trip set point. Coincidence logic has the advantage of not requiring duplication of the sensing devices.

Other Reliability Considerations

In addition to the points made previously there are other considerations and possibilities for improving the reliability. One of these possibilities is to reduce the number of trip points to the absolute minimum required for safe operation, and for the type of the operation. Traditionally, the number of trip points has grown over time. Cooper Industries, ESC, and Rolls Royce have made a joint effort to reduce the number of trip points required for the gas turbine and driven equipment with respect to the absolutely essential equipment requirements and to the type of operation. All trip functions that were backed up by another trip function were eliminated. A separate list of trip functions for attended and unattended operation was developed. In an attended operation, the number of trips can be reduced because it can be assumed that the operator can take corrective action when pre-alarm levels are exceeded.

Other simple circuit considerations, such as maximizing time delays on trip functions to avoid nuisance trips during transient conditions or contact bounce, should be made.

Another effective means of increasing reliability and decreasing cost is to reduce the number of sensing devices per sensing point. The reduction of sensing devices affects the reliability of the unit considerably since these constitute the majority of the failures in a gas turbine control system. Figure 7 shows a conventional control circuit associated with a particular function; in contrast, Fig. 8 suggests several improvements by replacing the conventional control circuits (consisting of multiple switches and transmitters for alarm, shutdown, and control) by one or two transmitters and doing the setpoint logic in the control panel.

Integral System Versus Discrete Instrumentation

The failure-rate calculation in Fig. 5 is made for an integral system, meaning that components are reduced to a minimum by the use of common power supplies, common circuit components, and a processor-based control system. It can be shown that a control system designed with discrete instrumentation components more than doubles the failure rate of the control panel, as compared to an integral system.

Conclusion and Future Work

This paper describes methodical procedures to establish failure rates for gas turbine control systems and suggests that a common approach should be used in the industry. It discusses a number of improvements that can be used to increase the reliability of gas turbines and gas turbine control systems.

The evaluation of gas turbine reliability should not be undertaken without consideration of other factors such as

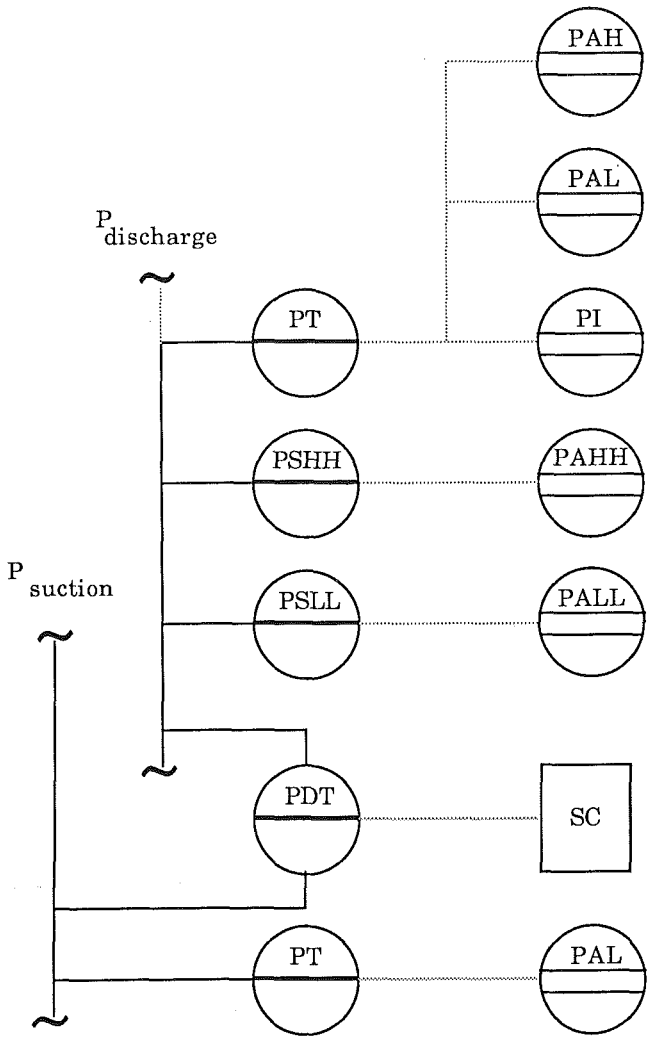

Fig. 7 Conventional control circuit

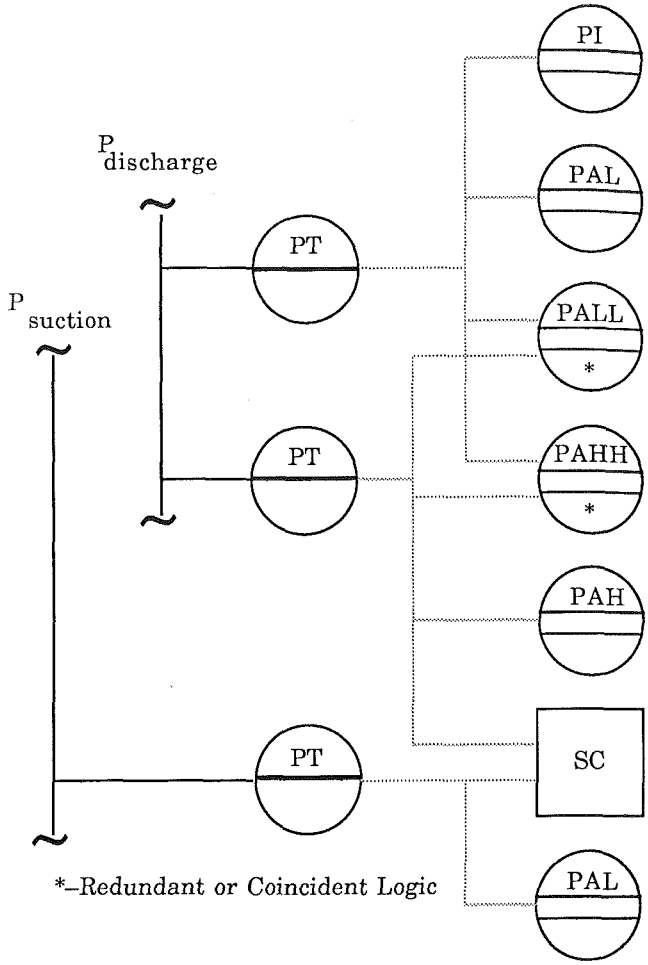

Fig. 8 Alternate control circuit for improved reliability

preventive maintenance information and maintenance predictions that can be used to improve the availability of gas turbine units further.

As a part of this reliability study the reliability of software was investigated. However, no practical methods were found to evaluate software reliability. Also, no significant failures seem to have occurred because of inadequate software reliability.

References

Lenz, H. D., 1984, "Design Objectives and Experience With Processor-Based Gas Turbine Controls," ASME Paper No. 84-GT-80.

U.S. Department of Defense, 1987, *Military Handbook of Reliability Prediction of Electronic Equipment*, MIL-Hdbk-217E.

Fault Diagnosis of Gas Turbine Engines From Transient Data

G. L. Merrington
Aeronautical Research Laboratory,
Defence Science and Technology
Organisation,
Melbourne, Australia

The desirability of being able to extract relevant fault diagnostic information from transient gas turbine data records is discussed. A method is outlined for estimating the effects of unmeasured fault parameters from input/output measurements. The resultant sensitivity of the technique depends on the sampling rate and the measurement noise.

Introduction

In a military environment, some combat aircraft can operate for up to 70 percent of the total mission time with their engines in a non-steady-state condition. This means there is a high probability that engine faults will occur during transient engine operation, and if the aircraft is equipped with an Engine Monitoring System (EMS) capable of recording such events, a time history of some of the important engine parameters will be available for postflight analysis. There is a need then to develop fault diagnostic procedures to extract the relevant informaiton from the EMS pre-and postevent records.

The requirement poses problems in that most of the fault diagnostic techniques currently available are based on steady-state information and are therefore basically unsuitable. Furthermore, some classes of engine faults, such as altitude/aircraft-maneuver-related engine stalls cannot be easily reproduced under sea level static (SLS) test conditions. It would be advantageous then, from a maintenance point of view, to be able to derive some of the required diagnostic information from the available flight data.

In this paper a method is outlined for analyzing transient engine data records with the view to correlating changes in the engine dynamic characteristics with particular engine faults. By so doing, changes in unmeasured parameters, such as misscheduled variable geometry, can be inferred from observed input/output measurements (engine fuel flow, spool speeds) during normal engine running. When combined with other correlative data techniques, this forms an important component of a larger, more comprehensive engine fault diagnostic research program.

Engine Faults and Transient Performance

Some engine faults impact upon the steady-state performance of an engine and the symptoms can usually be reproduced under SLS test conditions. Other faults, such as those leading to reduced surge margins in the compression system, may not necessarily be reflected in a loss of steady-state performance but could seriously degrade the operability of the engine especially at altitude, during aircraft maneuvers and following missile release. For instance, misscheduled variable geometry within the engine or corrupted sensor signals can be cause for concern.

In the past maintenance personnel have tended to rely on manufacturer supplied information, in the form of procedures laid down in Technical Manuals combined with experience, to diagnose common engine faults. In certain cases this may involve the use of trial and error methods and/or component substitution to eradicate the problem. However, with the adoption of on-condition maintenance, improved diagnostic tools are continually being sought in order to achieve reliable fault isolation at the component and/or module level.

The advent of relatively inexpensive computer-based data acquisition systems fitted to many current generation aircraft has provided the means for capturing transient engine data both in flight and during ground tests. As alluded to previously, some EMS enable important engine/aircraft parameters to be automatically captured any time a measured parameter exceedance is detected in an on-board computer. Thus, to utilize this information fully and thereby increase the current level of engine diagnostic capability, there is a need to implement new analysis procedures in ground-based computing facilities. The following procedure represents one such approach.

Analysis Procedure for Extracting Dynamic Characteristics

Parameter estimation and identification procedures are continually finding new applications in the field of fault detection and isolation, including gas turbines (Isermann, 1981; Baskiotis et al., 1979; Merrill, 1984). The primary aim of the present exercise is to develop techniques for application to in-flight recorded data to aid fault diagnosis within the constraints imposed by existing EMS.

The transient response of a gas turbine can be identified in terms of well-defined dynamic characteristics, namely time constants and steady-state gains. These in turn are governed by aerothermodynamic states within the gas path in combination with mechanical considerations such as spool inertias. To simplify the problem for discussion, the present analysis is confined to the single input/single output (SISO) fuel/spool speed response. However, as matrix methods are employed in the analysis, additional inputs/outputs can be added when and if necessary.

Contributed by the International Gas Turbine Institute and presented at the 33rd International Gas Turbine and Aeroengine Congress and Exhibition, Amsterdam, The Netherlands, June 5-9, 1988. Manuscript received by the International Gas Turbine Institute September 24, 1987. Paper No. 88-GT-209.

In a gas turbine, the spool speed/fuel flow response over the normal operating speed range is characterized by a nonlinear relationship of the form

$$N = f(WF, t_N, K_N, P, T) \tag{1}$$

In the vicinity of a steady-state set point, the response is closely approximated by a simple lag

$$\Delta N = \frac{K_N}{1 + t_N S} \Delta WF \tag{2}$$

which in terms of the overfueling becomes

$$N = \frac{K_N}{t_N S} WFE$$

or alternatively in discrete time

$$N_t = AN_{t-1} + BWFE_{t-1} \tag{3}$$

where $A \simeq 1$ and $B = K_N \Delta t / t_N$.

Some engine faults will modify the steady-state behavior and can therefore be expected to appear as changes in K_N. Similarly, other faults will influence the transient performance characterized by changes in the effective t_N or a combination of K_N nd t_N. Thus it follows that the embedded fault information will be associated with the fault parameter B. The basic problem reduces to estimating the parameters A and B in equation (3) from noisy transient measurements and correlating these with known fault conditions ultimately to form a fault library. A parameter estimation scheme was used to extract this information.

Parameter Estimation Procedure

Equation (3) is linear in the parameters, and is in a form suitable for regression analysis (Goodwin and Payne, 1977), that is

$$N_t = \theta^T \psi(t) + \epsilon(t)$$

where

$$\psi_{(t)} = (-N_{t-1}, \ldots, -N_{t-n}, WFE_{t-1}, \ldots, WFE_{t-m})$$
$$\theta^T = (A_1, \ldots, A_n, B_1, \ldots, B_m)$$

The simplest estimator is the Least-Squares Estimator (LSE) where the estimate for $\theta = (A, B)^T$ in equation (3) is given by

$$\hat{\theta} = \begin{bmatrix} \hat{A} \\ \hat{B} \end{bmatrix} = \begin{bmatrix} \frac{1}{n} \sum_{t=1}^{n} N_{t-1}^2 & \frac{1}{n} \sum_{t=1}^{n} WFE_{t-1} N_{t-1} \\ \frac{1}{n} \sum_{t=1}^{n} N_{t-1} WFE_{t-1} & \frac{1}{n} \sum_{t=1}^{n} WFE_{t-1}^2 \end{bmatrix}^{-1} \begin{bmatrix} \frac{1}{n} \sum_{t=1}^{n} N_t N_{t-1} \\ \frac{1}{n} \sum_{t=1}^{n} N_t \, WFE_{t-1} \end{bmatrix}$$

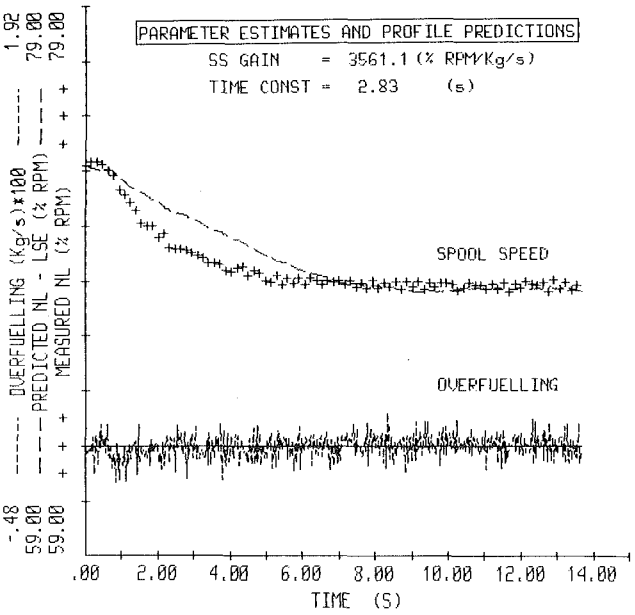

Fig. 1 LSE prediction: noisy measured turbojet data

The LSE is known to produce asymptotically biased estimates in the presence of measurement noise even for very large data samples (Goodwin and Payne, 1977). The degree of bias depends on the signal to noise (S/N) ratio of the individual signals and for some applications small levels of residual bias can be tolerated. The present problem falls into this category in that relative differences between the fault/no-fault estimates of the parameter assume much greater importance than the absolute values of the individual estimates, provided the level of bias error is consistent.

Simulated turbofan data, derived from a modified version of a generic thermodynamic simulation given by Sellers and Daniele (1975), superimposed with white measurement noise, was used in the analysis, together with SLS test cell data from a small turbojet. The LSE was found to yield satisfactory results for small levels of measurement noise. However, the bias and the associated uncertainty of the parameter estimates deteriorated markedly in the presence of typical noise levels experienced in the test cell. This is illustrated in Fig. 1, where the predicted spool speed for a small turbojet based on the measured fuel flow and the estimated model parameter is compared with the actual measured data. It is immediately apparent that the correlation is poor for these noisy experimental data.

To overcome this problem, a modified estimator was proposed (Merrington, 1988) where improved estimates are obtained by using well-known hill-climbing techniques to obtain a new minimum variance fit of the predicted/measured speed

Nomenclature

A = parameter, equation (3)
$A8$ = final nozzle area
B = parameter, equation (3)
CPR = compressor pressure ratio
EGT = exhaust gas temperature
f_s = sampling frequency
FPR = fan pressure ratio
K_N = spool steady-state gain
LSE = least-squares estimator
N = spool speed
NL = fan speed
NH = compressor speed
P = pressure
S = Laplace operator
SISO = single input, single output
SLS = sea level static
S/N = single-to-noise ratio
t = time
t_N = spool time constant
T = temperature
WF = engine fuel flow
WFE = engine overfueling $= WF - WFSS$
$WFSS$ = steady-state fuel flow
ΔN = $N_t - N_{t-1}$
Δt = sample time
$\epsilon(t)$ = equation error
θ = parameter vector
σ = standard deviation of the measurement noise
ψ = vector of observations

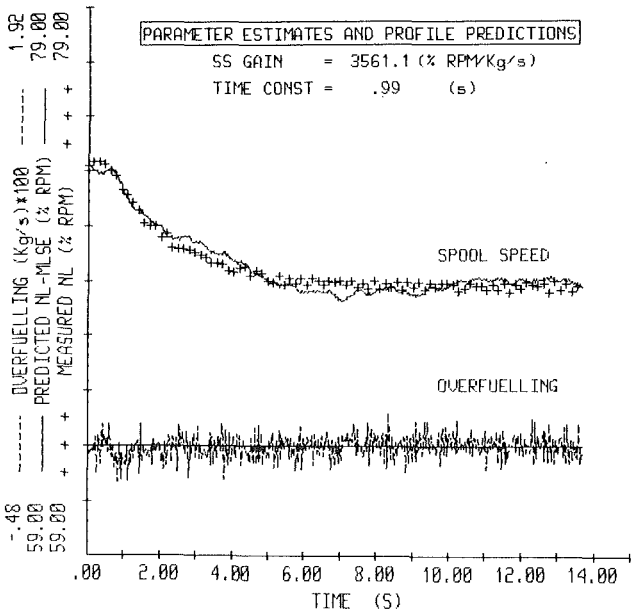

Fig. 2 Prediction using modified estimator

profiles (Fig. 2). This method uses the LSE as a first estimate, from which improved estimates are subsequently obtained using the prefiltering characteristics of the model. In essence, this technique resembles the Instrumental Variable (IV) method (Isermann, 1984; Ljung and Soderstrom, 1983; Yound, 1984) but with the important difference that conceptually at least, it is more easily understood by performance engineers. Monte-Carlo testing, using simulated turbo-fan test data superimposed with white measurement noise, indicated that the resultant bias errors were insignificant (<0.1 percent) for levels of measurement noise normally experienced in the field. As a further test of the method, the linearized model equation (3) was configured with variable coefficients to predict the full nonlinear idle/max power and max/idle power speed transients using the measured fuel as input (Fig. 3). The coefficients were estimated at a number of steady-state set points across the speed range from small accelerations/decelerations. The good agreement with the measured test data is justification for the use of the estimator as a tool for extracting the spool dynamic characteristics from noisy engine data. It therefore remains to evaluate the use of the estimator to diagnose faults from transient data records.

The Estimator as a Fault Diagnostic Tool

Two simple faults are chosen to illustrate the important features of the estimator as a fault diagnostic tool. The first is a biased exhaust gas temperature (EGT) sensor error in an engine controlled to an EGT schedule, which can introduce significant transient and steady-state performance effects. The second is a changed final nozzle schedule during an acceleration, which does not impact upon the steady-state performance but can influence the transient performance. The method is applied to results obtained from a generic military turbofan simulation referred to previously, because it enables effects of measurement noise and data sampling rate to be investigated in a carefully controlled environment with the aid of Monte-Carlo testing techniques.

Exhaust Gas Temperature Sensor Bias Error. Exhaust gas temperature limiting in gas turbines is effective in reducing hot-section over-temperatures. In military turbofans, closed-loop control of the final nozzle is commonly employed to achieve this using an error signal derived from EGT sensor outputs and the desired schedule value. Thus an EGT sensor

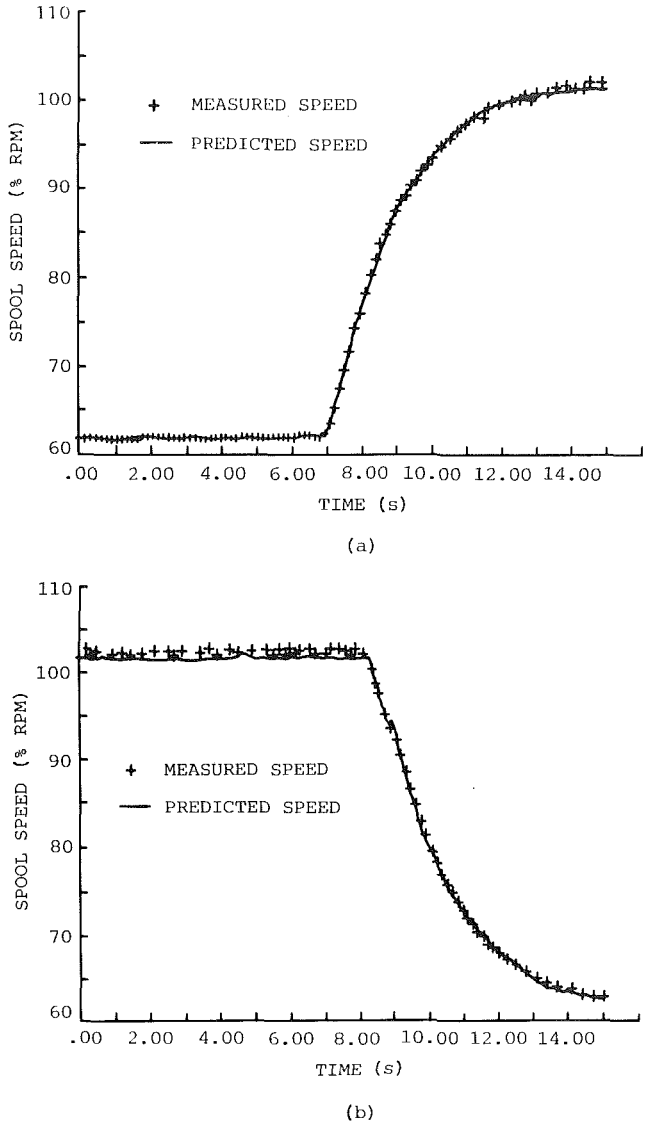

Fig. 3 Full turbojet transients

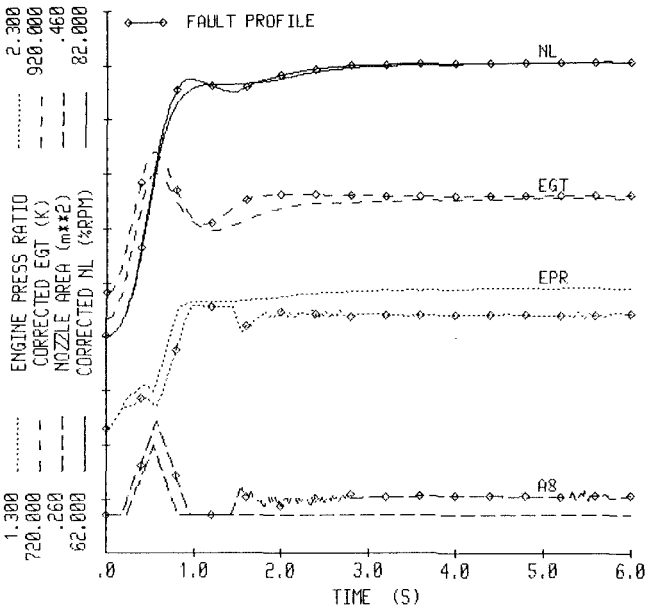

Fig. 4 Turbofan with EGT sensor bias

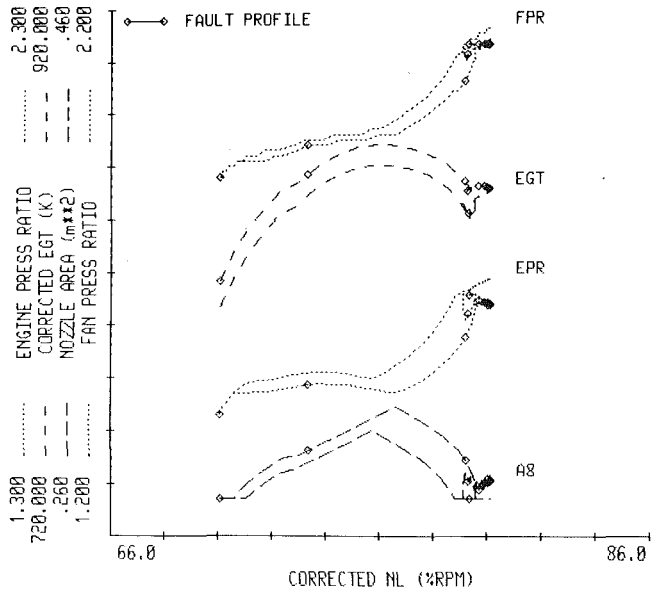

Fig. 5 EGT sensor bias data versus NL

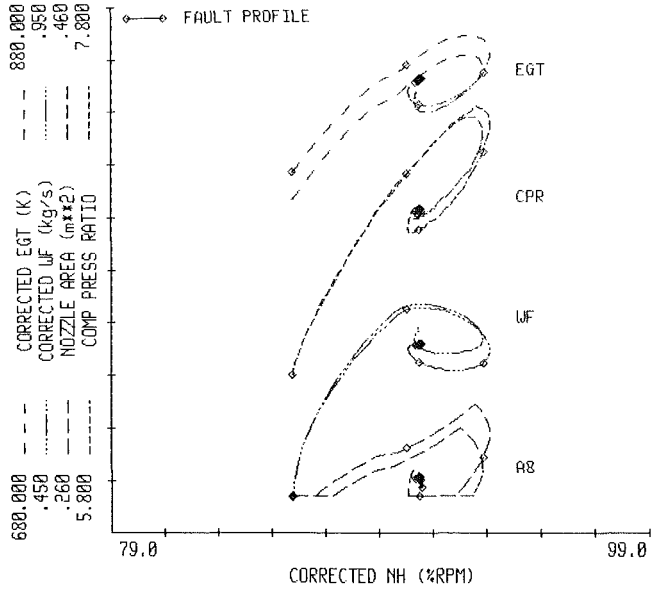

Fig. 6 EGT sensor bias data versus NH

bias error immediately impacts upon the transient/steady-state engine performance when the limiter loop becomes active.

Simulated turbofan results for an acceleration under closed-loop fan speed control combined with an active EGT limiter are given in Fig. 4. The positive sensor bias culminates in a steady-state performance decrement (reduced engine pressure ratio and therefore thrust) as a result of an increase in final nozzle area and reduced fueling. Moreover, transient profile trajectory changes indicating increased surge margin in the fan, as shown by the curve of fan pressure ratio (Fig. 5), and a corresponding marginal reduction in the compressor over part of the transient as shown by the curve of compressor pressure ratio (Fig. 6), accompany the bias.

Normally, EGT forms an integral part of EMS output and therefore bias effects can quickly be identified from temporal and crossplot data. However, parameter estimation techniques that can extract the fault information from input/output measurements in isolation without the need for

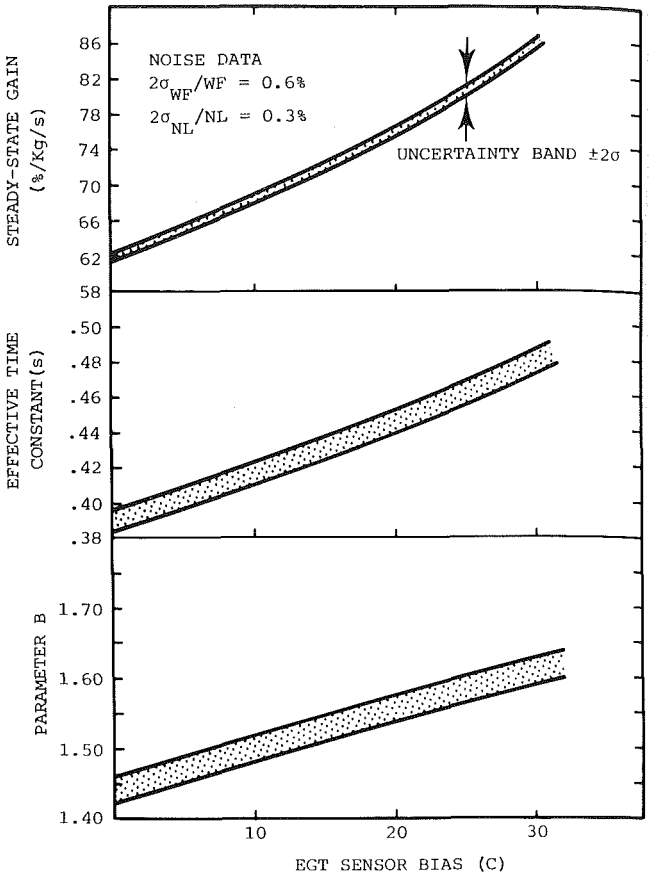

Fig. 7 Parameter fault signatures: EGT sensor bias

measurements of the actual fault parameter can provide an important additional degree of redundancy for fault diagnosis purposes.

Estimator results for the turbofan acceleration as a function of sensor bias are given in Fig. 7. The resultant trends in the LP spool dynamic characteristics constitute a useful fault signature and the uncertainty limits correspond to representative levels of measurement noise, namely $NL = 0.3$ percent, $WF = 0.6$ percent for a 50-Hz sampling frequency. More particularly, the trend in K_N confirms the effect of the bias error on the steady-state performance and similarly, trends in t_N and B correlate with transient performance changes.

In the above, the estimator has been applied to large accelerations ($\Delta NL > 5$ percent) producing estimates of the effective spool dynamic characteristics for the particular transient. While the resultant estimates do not have the same physical meaning as those obtained for a small linearized response about a steady-state set point, they do provide a convenient way of monitoring changes in the fault/no-fault transient profiles. It is this attribute that is appealing in the fault diagnosis application in that simple linear model structures can still provide useful diagnostic information even in the nonlinear domain.

Misscheduled Final Nozzle. Misscheduling of gas turbine variable geometry can be instrumental in promoting compression system instabilities by reducing available surge margins. Therefore, misscheduling resulting from actuator wear, incorrect adjustment, and/or corrupted sensor input may not necessarily be apparent from steady-state results. Furthermore, if variable geometry position is not included in the normal EMS output, then it will be necessary to infer changes from the available transient engine data. A misscheduled final nozzle is selected to demonstrate this.

In some military turbofans, the nozzle is scheduled open at

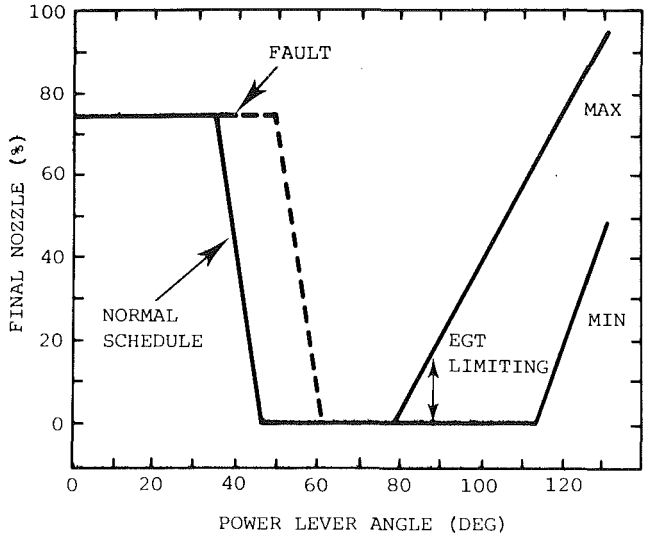

Fig. 8 Typical nozzle schedule for a military turbofan

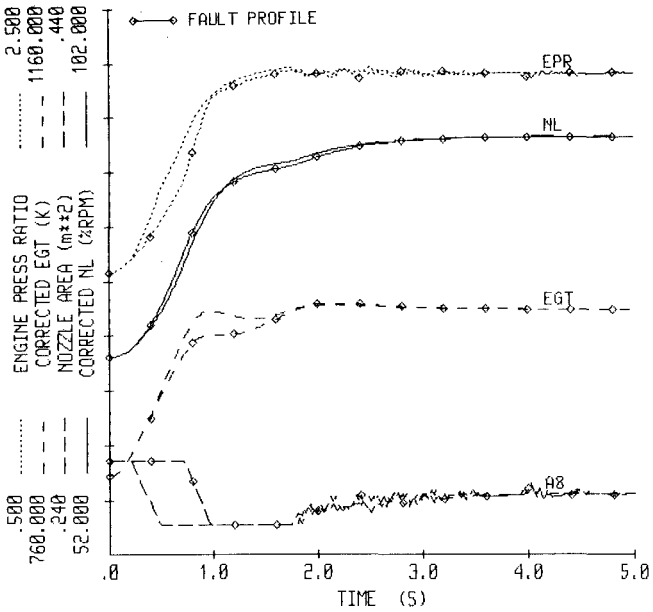

Fig. 9 Turbofan with misscheduled final nozzle

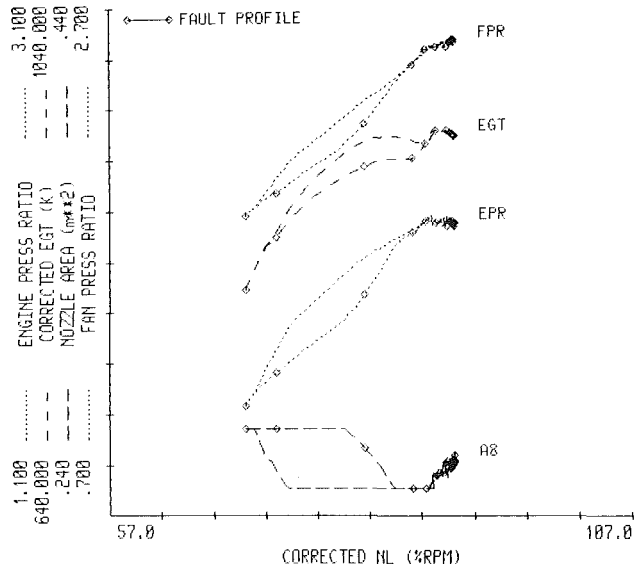

Fig. 10 Misscheduled final nozzle versus NL

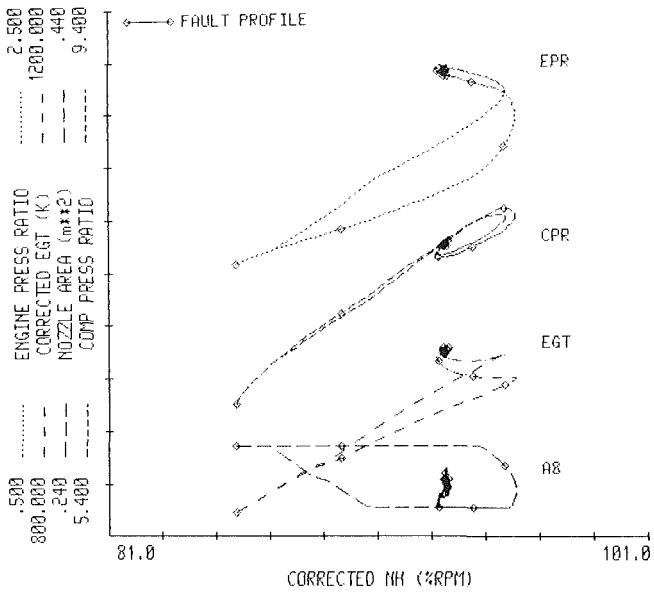

Fig. 11 Misscheduled final nozzle data versus NH

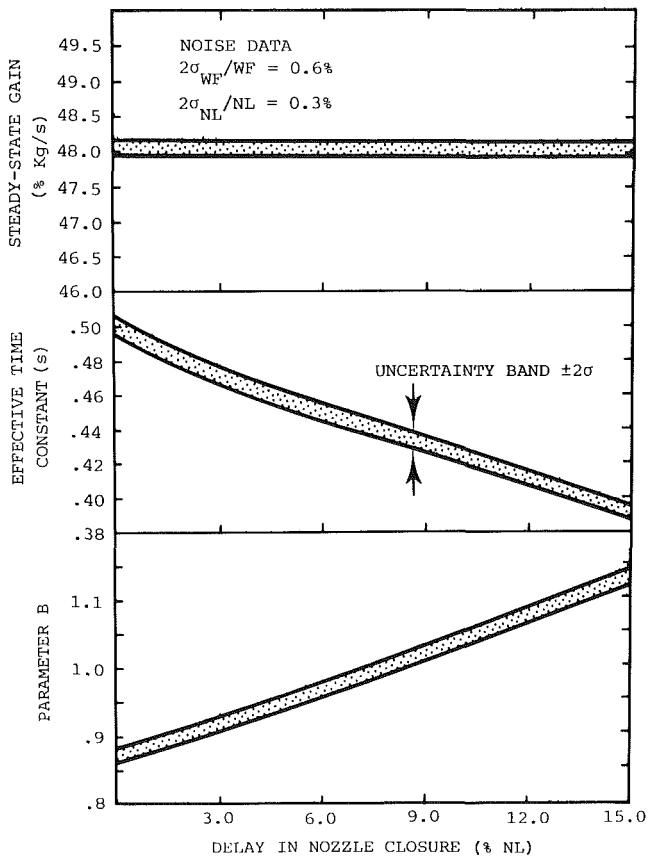

Fig. 12 Parameter fault signatures; misscheduled final nozzle

low power then ramped to the floor during accelerations until the EGT limiter loop becomes active (Fig. 8). For convenience, the nozzle closure trigger point for the simulated turbofan is chosen as a fixed percentage of NL and the fault is characterized in terms of a retardation in this (ΔNL percent). Typical fault/no fault profiles are displayed in Fig. 9, indicating no changes to the resultant steady-state performance. However, surge margins in the fan/compressor are increased/decreased respectively over at least part of the transient (Figs. 10 and 11).

Estimator results (Fig. 12) exhibit a clear correlation with

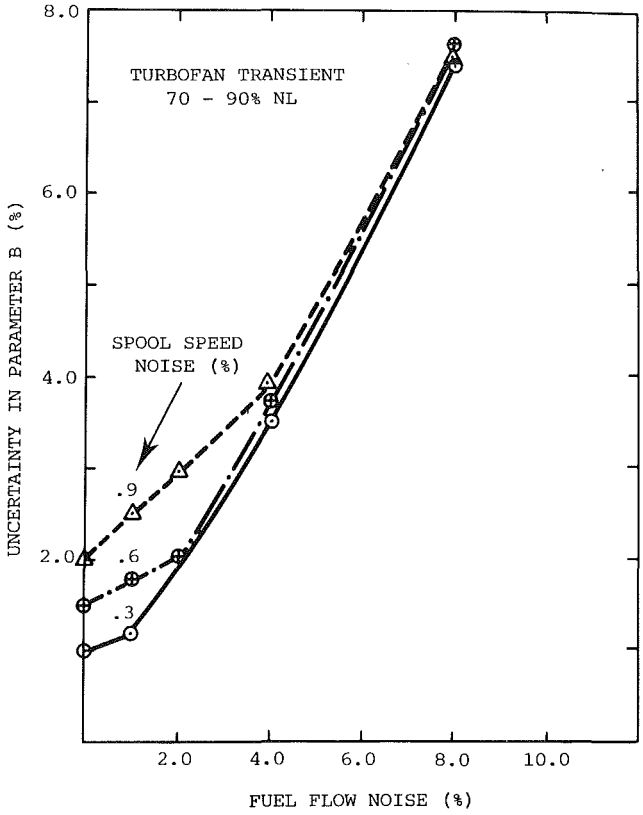

Fig. 13 Effect of measurement noise on estimator performance

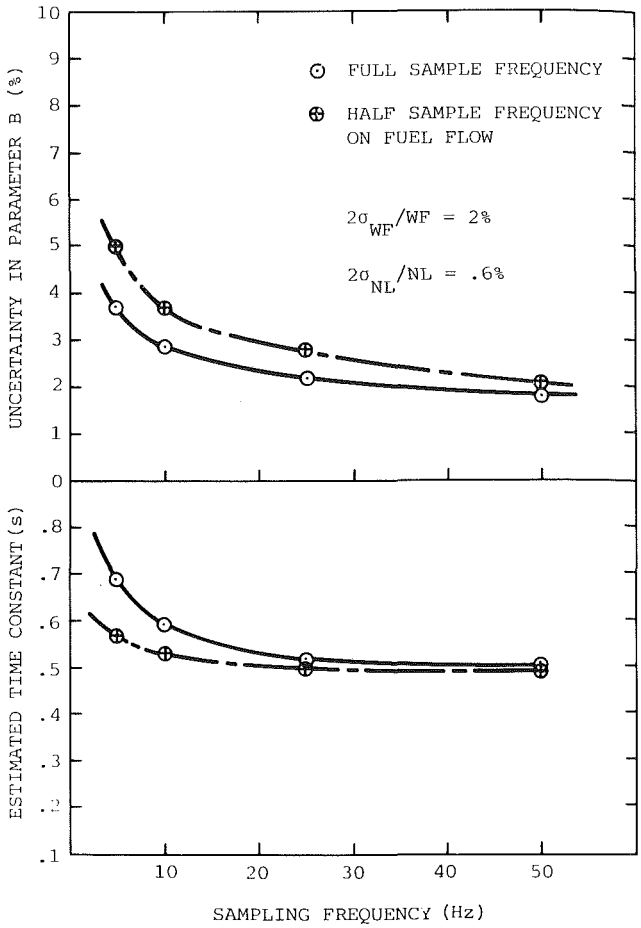

Fig. 14 Effect of sampling rate on estimator performance

trigger point delay except for K_n, which is invariant as expected. In addition, the fault signatures, namely curves of K_N, t_N, and B, differ significantly from the EGT bias results (Fig. 7). The estimator technique clearly discriminates between the two faults but many more fault signatures need to be compiled before definitive statements can be made as to the uniqueness or otherwise of the individual signatures.

The important point that emerges from the above analysis is that the estimator technique provides a convenient tool for extracting information on unmeasured fault parameters from available input/output transient data. Moreover, it will be shown that the sensitivity of the fault estimator technique is critically dependent on (*a*) level of measurement noise, and (*b*) data sampling rate.

Effect of Measurement Noise. The performance of the fault estimator deteriorates in the presence of measurement noise due principally to increased uncertainty in the estimates as distinct from bias effects. The uncertainties in the estimated parameters, which are specified by the $\pm 2\,\sigma$ bands about the means (Figs. 7 and 12), in turn determine the minimum variations in the actual unmeasured fault parameters that can be detected by the fault estimator. Therefore, the magnitude of the uncertainties ultimately establishes the sensitivity of the method and as a consequence, is more important than the effects of residual bias errors because the latter can reasonably be expected to be of similar magnitude in the fault/no-fault cases. Furthermore, the present results indicate that the noise on the input fuel signal can seriously degrade the overall performance of the estimator (Fig. 13). The reason for this is that the peak overfueling becomes a more suitable choice of reference signal than the mean fueling level. To summarize, performance constraints imposed by the measuring system set minimum obtainable estimator sensitivity levels and therefore the full potential of the method may only be realized if the measuring system is correctly designed in the first place.

Effect of Sampling Rate. Typical characteristic frequencies of interest in gas turbines, based on the spool time constants, are less than 5 Hz. Results presented so far correspond to acquisition rates of 25–50 Hz. In some aircraft EMS, lower sampling frequencies of 1–10 Hz are employed and therefore it is essential to examine briefly the effects of reduced sampling rates on the uncertainty of the fault estimator. Uncertainty estimates, derived from Monte-Carlo tests using white measurement noise (constant σ), are given in Fig. 14 for the no-fault acceleration results discussed previously. The following observations can be made:

1 Uncertainty increases as sampling rate decreases.

2 If reduced sampling rate is employed on the input fuel signal, as in some operational EMS, the uncertainty increases at an even higher rate. This stems from the resultant smoothing of the input signal, which in turn provides improved estimates of the time constant at the lower frequencies.

3 Sampling rates below 10 Hz are to be avoided.

Near-optimum results are obtained using 25–50 Hz full rate sampling on each signal. However, if reduced rate sampling must be tolerated on the input signal then the uncertainty that prevails corresponds approximately to the level of uncertainty for the full sampling rate on both signals but at the lower frequency (Fig. 14). The performance differences become insignificant as $f_s \geq 50$ Hz.

Conclusions

A method is outlined for extracting fault diagnostic information from gas turbine engine transient data records. It has the potential to provide information pertaining to unmeasured

parameters, such as variable geometry misscheduling by cross-correlating the estimates with previously compiled fault signatures. Moreover it can provide such diagnostic information from data gathered during normal engine running.

The performance of the fault estimator is critically dependent on the capabilities of the measuring system, namely sampling rates and measurement noise. Optimum performance is obtained at $f_s \geq 50$ Hz but tolerable estimator sensitivities prevail down to $f_s = 10$ Hz. Reduced sampling rate on the input signal yields a similar uncertainty to that obtained with a full sampling rate system but operating at the lower frequency.

Measurement noise, especially on the input signal, is cause for concern. The most suitable measure of this is the (S/N) ratio based on the peak overfuelling. Therefore the problem is accentuated with small engine transients because for the same noise statistics, the (S/N) ratio decreases in line with the reduced peak overfueling. Noise levels encountered in many EMS, namely $NL \simeq 0.3$ percent, $WF \simeq 0.6$ percent as used in the examples, provide adequate estimator sensitivity.

The technique described here is not intended as a stand-alone procedure but is to be used in conjunction with corrected data cross-plotting procedures to provide information on unmeasured parameters. In addition, the method is applicable to in-flight recorded data analysis in situations where it is difficult to reproduce the fault under SLS tests. Finally, information on new faults can be readily added to the existing fault library to improve and extend its capability.

References

Baskiotis, C., Raymond, J., and Rault, A., 1979, "Parameter Identification and Discriminant Analysis for Jet Engine Mechanical State Diagnosis," *Proceedings, IEEE Conference on Decision and Control*, Fort Lauderdale, FL, pp. 648–652.

Goodwin, G. C., and Payne, R. L., 1977, *Dynamic System Identification: Experiment Design and Data Analysis*, Academic Press, New York.

Isermann, R., 1984, "Process Fault Detection Based on Modelling and Estimation Methods—A Survey," *Automatica*, Vol. 20, pp. 387–404.

Ljung, L., and Soderstrom, T., 1983, *Theory and Practice of Recursive Identification*, MIT Press, Cambridge, MA.

Merrill, W., 1984, "Identification of Multivariable High Performance Turbofan Engine Dynamics From Closed-Loop Data," *Journal of Guidance*, Vol. 7, No. 6, pp. 677–683.

Merrington, G. L., 1988, "A Modified Least Squares Estimator for Gas Turbine Identification," ARL Aero Prop T. M. 445.

Sellers, J. F., and Daniele, C. J., 1975, "DYNGEN—A Program for Calculating Steady-State and Transient Performance of Turbojet and Turbofan Engines," NASA TN D-7901.

Young, P., 1984, *Recursive Estimation and Time Series Analysis*, Springer Verlag.

Health Monitoring of Variable Geometry Gas Turbines for the Canadian Navy

D. E. Muir
GasTOPS Ltd.,
Ottawa, Canada

H. I. H. Saravanamuttoo
Carleton University/GasTOPS Ltd.,
Ottawa, Canada

D. J. Marshall
Canadian Forces,
Ottawa, Canada

The Canadian Department of National Defence has identified a need for improved Engine Health Monitoring procedures for the new Canadian Patrol Frigate (CPF). The CPF propulsion system includes two General Electric LM2500 gas turbines, a high-pressure-ratio engine with multiple stages of compressor variable geometry. A general method for predicting the thermodynamic performance of variable geometry axial compressors has been developed. The new modeling technique is based on a meanline stage-stacking analysis and relies only on the limited performance data typically made available by engine manufacturers. The method has been applied to the LM2500-30 marine gas turbine and the variations in engine performance that can result from a malfunction of the variable geometry system in service have been estimated.

Introduction

The Canadian Forces have operated DDH-280 gas turbine powered destroyers since the mid-1970s. These ships use Pratt & Whitney FT12 and FT4 engines in a COGOG arrangement and have been very successful. The FT12 and FT4 are first-generation engines and do not include the variable compressor geometry that is often found in higher performance second-generation engines of substantially higher pressure ratio on a single spool.

The new Canadian Patrol Frigate (CPF) employs a CODOG arrangement with General Electric LM2500 engines used for boost power. In addition, the DDH-280 class are being significantly modified under the TRibal class Update and Modification Program (TRUMP) including the substitution of Allison 570K engines for the FT12 cruise engines (Mack and Hurl, 1987). Both the LM2500 and 570K incorporate several stages of variable stators in their compressors, required to give a high pressure ratio and adequate surge margin on a single spool.

Engine Health Monitoring (EHM) systems developed for the earlier fixed-geometry engines (MacGillivray et al., 1984) did not have to consider the possibility of maladjustment of the variable stators. For example, the Olympus and Tyne engines of the Royal Navy are fixed geometry and it has been shown that changes in the relationship between the compressor speeds are a good indicator of developing problems (Matthee and Saravanamuttoo, 1982). The use of variable geometry engines, however, has rendered such simple assessments of machinery condition either inadequate or completely misleading. For each geometry setting, a different relationship between the engine performance parameters exists; thus, some means of predicting the influence of the variable geometry on engine performance is required.

The overall performance of a gas turbine engine is governed by the performance characteristics of its constituent components and by the laws of compatibility of mass flow, work and rotational speed, which determine the interaction or "matching" between these components. Hence, engine performance simulations based on component matching procedures provide a systematic means of investigating engine performance (Saravanamuttoo and MacIsaac, 1983). If suitable component performance representations can be acquired or estimated, engine performance over a wide range of operating conditions can be predicted. Furthermore, having established a component-based engine model, the influence of specific modes of component degradation on overall engine performance can be investigated by appropriately modifying the individual component performance maps.

A major impediment to the development of component-based engine models is the lack of available component data. These data are usually proprietary to the engine manufacturer and with the scant information normally provided, the estimation of suitable component performance maps remains, at best, a difficult task. The most troublesome component in this regard is the compressor, because of the strong dependency of its performance on rotational speed. Relatively simple methods of estimating compressor performance, such as the scaling techniques described by Saravanamuttoo and MacIsaac (1983), have been used successfully to model certain fixed-geometry compressors; however, because of the assumption of geometric similarity that underlies these methods, they are unsuitable for estimating the performance of compressors that incorporate variable stator geometry.

The remainder of this paper describes the development and application of a more fundamental approach to multistage component performance modeling; specifically, multistage ax-

Contributed by the International Gas Turbine Institute and presented at the 33rd International Gas Turbine and Aeroengine Congress and Exhibition, Amsterdam, The Netherlands, June 5-9, 1988. Manuscript received by the International Gas Turbine Institute October 1987. Paper No. 88-GT-77.

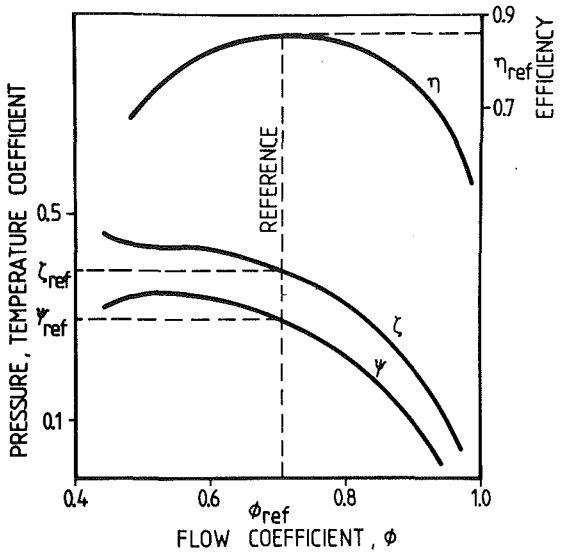

Fig. 1 Axial compressor stage characteristics

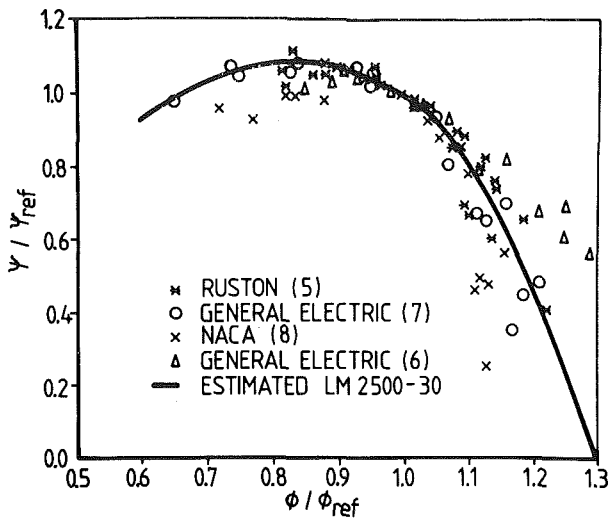

Fig. 2 Generalized stage pressure coefficient curve

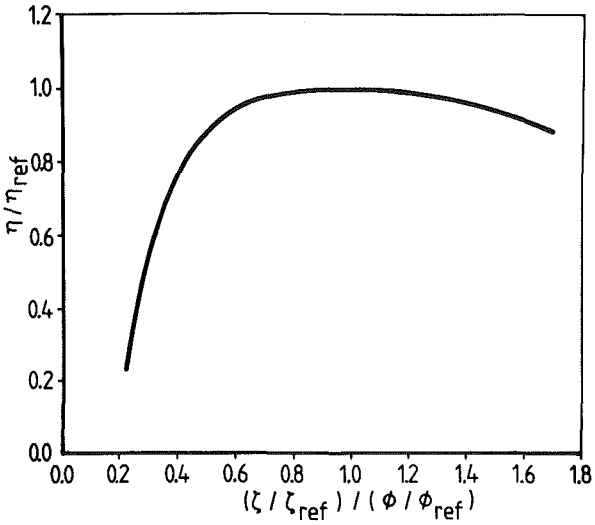

Fig. 3 Generalized stage efficiency curve (Howell and Bonham, 1950)

ial compressors. The new modeling technique utilizes individual stage performance characteristics to synthesize overall compressor performance. As such, the performance of variable-geometry axial compressors can be estimated accurately.

Notably, the new compressor modeling technique relies only on the limited performance data typically made available by the engine manufacturer.

Compressor Model Development

The overall performance of a multistage axial compressor depends on the performance of its constituent stages. The performance of a single axial compressor stage is, in turn, often presented in terms of nondimensional coefficients for:

Flow

$$\phi = C_a/U$$

Pressure Ratio

$$\psi = \frac{C_p T_{os}(PR_s^{\gamma-1/\gamma} - 1)}{U^2}$$

Temperature Rise

$$\zeta = \frac{C_p \Delta T_{os}}{U^2}$$

Efficiency

$$\eta = \frac{T_{os}(PR_s^{\gamma-1/\gamma} - 1)}{\Delta T_{os}} = \psi/\zeta$$

where

C_a = stage inlet axial velocity
U = tangential blade speed
PR_s = stage pressure ratio
T_{os} = stage inlet total air temperature
ΔT_{os} = stage total temperature rise
C_p = specific heat
γ = ratio of specific heats

Figure 1 illustrates typical variations of pressure, temperature, and efficiency coefficient with flow coefficient for an axial compressor stage. These relationships are commonly referred to as stage characteristics.

For modeling purposes, it is useful to develop generalized relationships between ζ/ζ_{ref}, ψ/ψ_{ref}, ϕ/ϕ_{ref}, and η/η_{ref}. The values of ζ_{ref}, ψ_{ref}, and ϕ_{ref} are arbitrarily chosen as those corresponding to the maximum stage efficiency η_{ref}, as indicated in Fig. 1. The importance of the generalized stage characteristics representation is that, if the maximum efficiency point of a stage (ϕ_{ref}, ζ_{ref}, ψ_{ref}, η_{ref}) is known or assumed, the complete ψ, η, and ζ stage characteristics can be deduced readily.

Figure 2 shows a plot of ψ/ψ_{ref} versus ϕ/ϕ_{ref} assembled using stage pressure rise data from a number of sources (Carchedi and Wood, 1975; Balsa and Mellor, 1974; Milner and Wenzel, 1975; Budinger and Kaufman, 1955). The bold line on the figure represents the curve that best models the LM2500-30 compressor stage pressure rise characteristics, as determined by the stage characteristic estimation procedures described below. A generalized efficiency relation developed by Howell and Bonham (1950) and shown in Fig. 3 was found adequately to model the off-design variation in compressor stage efficiency for the LM2500-30.

If the individual performance characteristics of each axial compressor stage are known, overall compressor performance over a range of rotational speeds and mass flows can be estimated by a "stage-stacking" procedure. The stage-stacking method is a simple one-dimensional or meanline

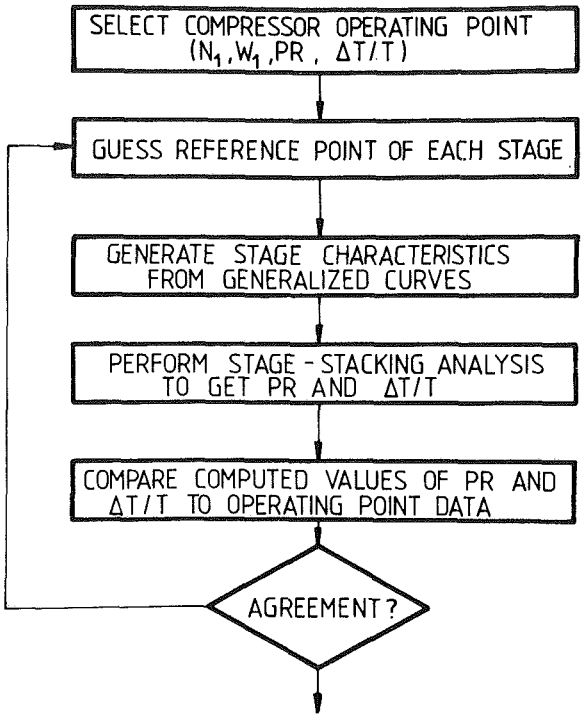

Fig. 4 Stage characteristic development

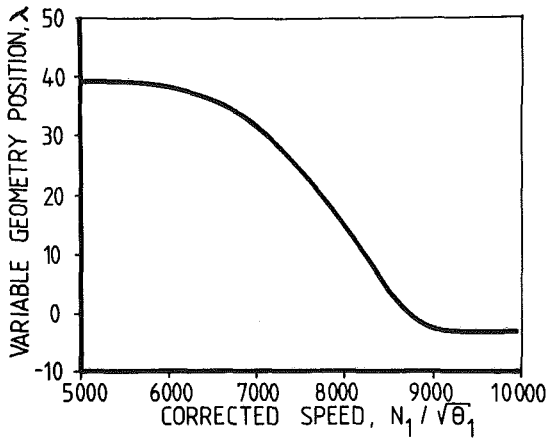

Fig. 5 Estimated LM2500-30 variable geometry schedule

calculation that makes use of the dimensionless stage characteristics, along with certain other gas path geometry data, to evaluate the overall compressor pressure ratio and temperature rise. Details of the stage-stacking procedure can be found in the works of Robbins and Dugan (1965), Stone (1958), and Doyle and Dixon (1962).

The stage characteristics of the LM2500-30 compressor have been estimated using a numerical search procedure, which makes use of the stage-stacking analysis to match overall compressor performance to a known running line. The basic method is summarized in Fig. 4. At a given compressor speed and mass flow (established by the operating line data points) the numerical search procedure begins by assuming specific values for the reference point (η_{ref}, ϕ_{ref}, and ψ_{ref}) of each stage. The generalized stage characteristic representations are then used to obtain the performance maps for each stage and the stages are "stacked" to get the overall compressor pressure ratio PR, and temperature rise ratio $\Delta T/T$. If the calculated PR and $\Delta T/T$ values do not agree with the

Table 1 LM2500-30 compressor operating line data (General Electric, 1981)

$N_1/\sqrt{\theta_1}$	P_2/P_1	$W_1\sqrt{\theta_1}/\delta_1$	$\Delta T_{12}/T_1$
9450	18.06	147.5	1.530
9160	17.21	144.0	1.439
8971	16.25	137.8	1.389
8813	15.30	131.6	1.343
8660	14.37	125.5	1.307
8508	13.44	119.2	1.262
8364	12.45	112.2	1.220
8105	10.35	96.7	1.112
7772	7.88	76.6	0.983

Table 2 Estimated LM2500-30 compressor gas path geometry

Stage	Inlet mean radius, in.	Effective inlet annulus area, in.^{2}
1	11.00	553
2	11.16	513
3	11.31	471
4	11.47	428
5	11.63	383
6	11.78	338
7	11.94	291
8	12.09	242
9	12.25	213
10	12.29	188
11	12.32	164
12	12.36	144
13	12.39	127
14	12.43	112
15	12.46	101
16	12.50	90

operating line data, then the assumed values of η_{ref}, ϕ_{ref}, and ψ_{ref} for each stage are modified.

In order to implement the above search procedure at various points along the LM2500-30 compressor operating line, certain data are required and a number of simplifying assumptions must be made. These data requirements and assumptions are as follows:

(a) Compressor Operating Line Data. General Electric (1981) provides tabulated LM2500-30 performance data over a wide range of inlet temperatures (−65°F to 130°F) and power turbine speeds (1200 to 3600 rpm) at an inlet pressure of 14.7 psia. Included in these data are the compressor rotational speed N_1, inlet air mass flow rate W_1, exit pressure P_2, and exit temperature T_2, from which the corrected compressor operating characteristics can be derived. Table 1 presents the LM2500-30 compressor operating line data taken from General Electric (1981).

(b) Gas Path Dimensions. The stage-stacking analysis requires that the mean radius and effective annulus area at the inlet to each stage be known. These parameters were estimated from a cross-sectional layout of the LM2500 presented in a General Electric product brochure (General Electric, 1980) and subsequently refined in the course of the stage characteristic development work to include the estimated effects of blockage due to endwall boundary layer growth. Table 2 summarizes the estimated LM2500-30 compressor gas path geometry.

(c) Flow Angles. The stage-stacking analysis also requires that the absolute air flow angle at the inlet to each stage be known. For a variable geometry compressor, the variation in these angles with different variable geometry positions must also be known or assumed.

Figure 5 presents an estimated LM2500 variable geometry schedule obtained from field measurements on a pipeline gas compression unit. The stagger angles of the inlet guide vanes (IGVs) and first six rows of stator vanes are varied by seven rings under the control of a single actuating lever. As shown in

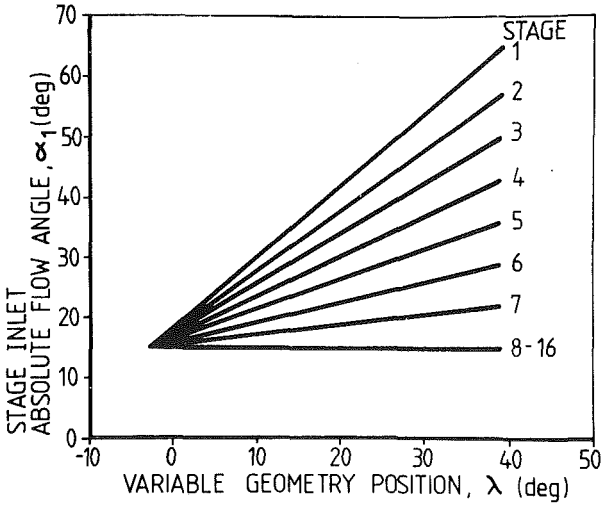

Fig. 6 Estimated LM2500-30 compressor stage inlet flow angles

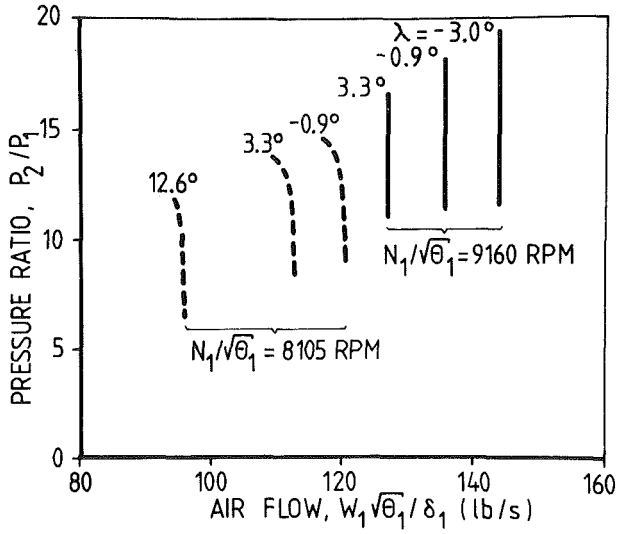

Fig. 8 Estimated LM2500-30 compressor performance

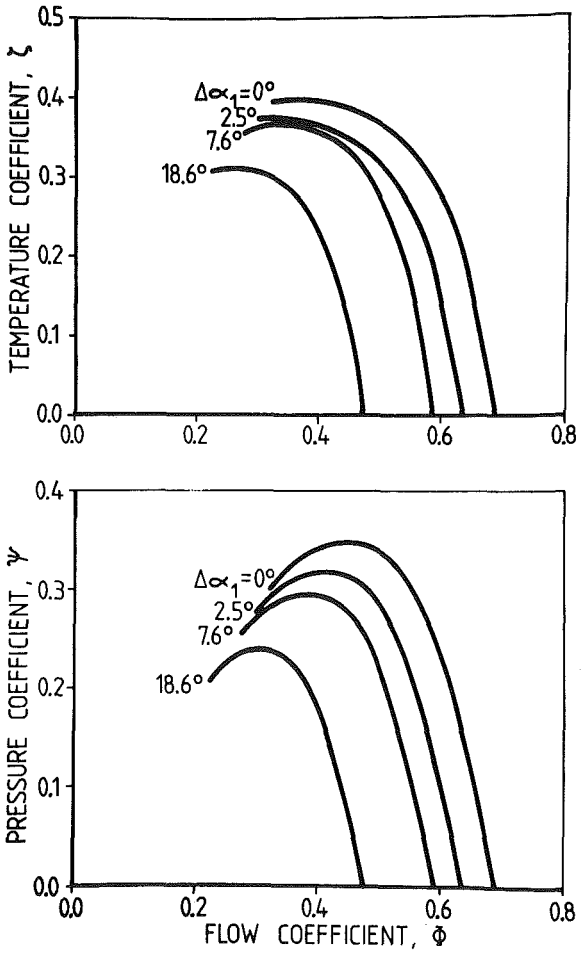

Fig. 7 Estimated LM2500-30 compressor stage characteristics

the figure, the angular position of the actuating lever is scheduled as a function of corrected compressor speed, $N_1/\sqrt{\theta_1}$. As compressor speed is reduced, the stagger of the variable vanes is increased to limit the amount of air flow and thus avoid unstable operating conditions.

Since details of the compressor blading and the variable geometry actuating mechanism are proprietary to the engine manufacturer, a number of assumptions were made concerning the stage inlet absolute flow angles. Firstly, it was assumed that at the fully open actuator position ($\lambda = -3$ deg) the flow angle at the inlet to each stage is 15 deg. This value is typical of axial compressor designs for gas turbine applications. Secondly, it was assumed that the IGVs are rotated such that the relative flow angle at the compressor inlet is kept reasonably constant from which a total IGV travel of 50 deg can be estimated. Finally, it was assumed that the total travel of the variable stator vanes decreased linearly as follows:

Total IGV travel:	50 deg
Total Stage 1 Stator travel:	42 deg
Total Stage 2 Stator travel:	35 deg
Total Stage 3 Stator travel:	28 deg
Total Stage 4 Stator travel:	21 deg
Total Stage 5 Stator travel:	14 deg
Total Stage 6 Stator travel:	7 deg

Based on the above assumptions, the stage inlet absolute flow angles can be related to the variable geometry position as shown in Fig. 6.

(d) Stage Characteristics. As previously described, the LM2500-30 compressor stage characteristics were developed by a trial-and-error procedure whereby the stage characteristics for each stage were guessed, a stage-stacking analysis was then performed and finally, the computed overall compressor performance was compared to known operating data. Since the LM2500-30 compressor is comprised of 16 stages, 16 different sets of stage characteristics are possible. In order to make the stage characteristic development process more manageable, three simplifying assumptions were made:

1 The shape of each stage characteristic was defined by the generalized pressure coefficient and efficiency curves given in Figs. 2 and 3.

2 At a corrected speed referred to as the "match" speed, it was assumed that the performance of all stages could be modeled by a single set of stage-averaged characteristics. This speed was determined by trial and error to be $N_1/\sqrt{\theta_1} = 9160$ rpm.

3 At each speed other than the match speed, the fixed geometry stages were modeled by their match speed characteristics and the variable geometry stages were modeled by a series of stage characteristics, each representing a different change in rotor inlet absolute flow angle relative to the match speed angle.

Figure 7 presents the LM2500-30 stage characteristics that were derived from the procedures described above and Fig. 8 gives the overall compressor pressure ratio versus flow map,

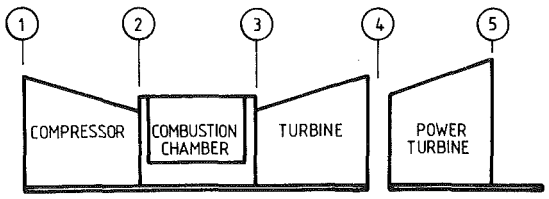

Fig. 9 LM2500-30 engine configuration

which result from stacking the stages together at two specific speeds. These compressor characteristics show good agreement with the only published data known to the authors (Spector and Miller, 1983) and demonstrate the dramatic influence that the variable geometry has on overall compressor performance.

Engine Performance Simulation

The General Electric LM2500-30 is a single spool, free turbine engine as depicted in Fig. 9. From a thermodynamic viewpoint, the engine is comprised of four major components: the compressor, the combustor, the gas generator turbine, and the power turbine. If suitable thermodynamic descriptions for these components can be obtained, the steady-state performance of the engine can be predicted by determining the operating points that satisfy the following compatibility conditions:

1 compatibility of flow between the compressor and the gas generator turbine

2 compatibility of flow between the gas generator turbine and power turbine

3 balance of work between the compressor and its driving turbine

4 balance of work between the power turbine and the propeller load

These operating points are found by a trial-and-error procedure using data obtained from the nondimensional component characteristics.

The development of LM2500-30 compressor characteristics was described above. The gas generator turbine and power turbine nondimensional flow and temperature drop maps were derived from the tabulated data presented by General Electric (1981). These data, along with reasonable assumptions concerning the secondary engine cycle parameters (combustor pressure loss, bleed flow fraction, fluid properties, etc.) can be used to evaluate each of the major thermodynamic cycle parameters, including the turbine performance characteristics, over a wide range of engine operating conditions. The combustor performance is described by a simple energy balance relationship, which determines the quantity of fuel required to raise the compressor delivery air temperature to gas generator turbine inlet conditions.

The simulated LM2500-30 engine performance curves are compared to the data published by General Electric (1981) in Fig. 10. A power turbine speed of 3600 rpm was used for this comparison. As indicated in the figure, the simulated performance predictions show remarkably good agreement with the published data. It is emphasized that ability to estimate the variation in LM2500 performance over a wide range of operating conditions is predicated on the existence of an engine model that accurately predicts the off-design performance of each of the major engine components.

The influence of compressor variable geometry setting on overall engine performance is illustrated in Fig. 11. Superimposed on the nominal engine performance curves predicted by the engine model are the simulated engine running lines for various fixed variable geometry positions λ. The simulated results indicate that significant changes in engine performance can be expected if the variable geometry system is not tracking

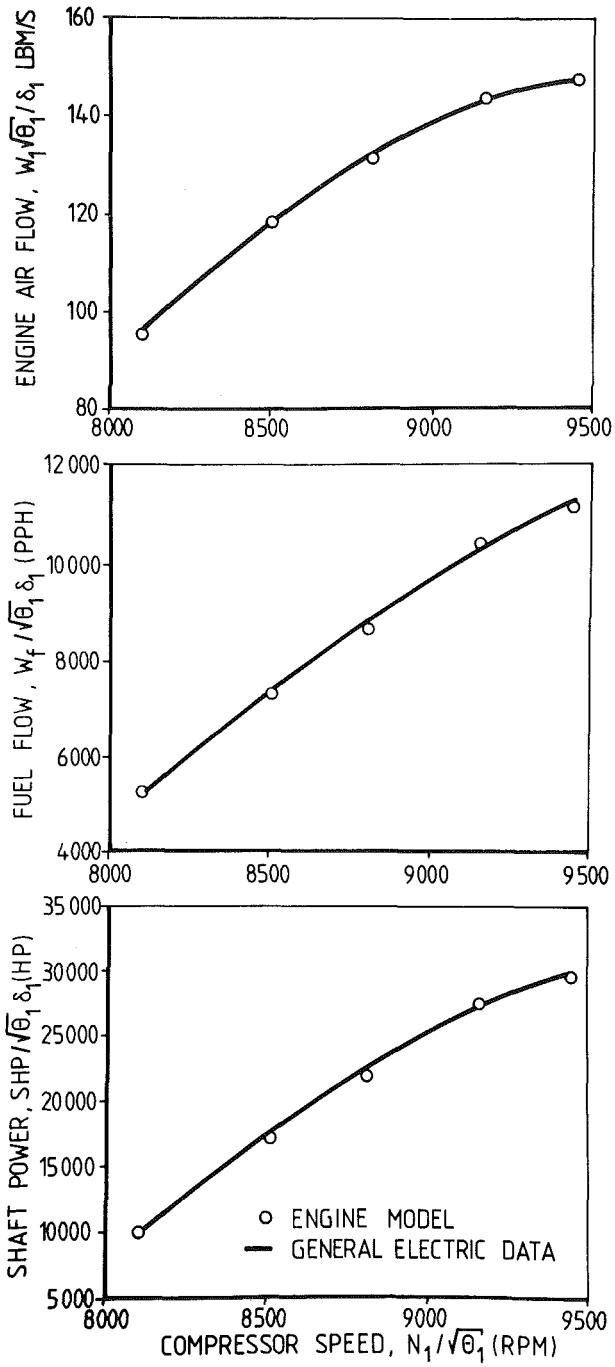

Fig. 10 Comparison of engine simulation with published data (General Electric, 1981) at $N_2 = 3600$ rpm

properly. An increase in the variable geometry position at a given speed is equivalent to closing the variable stator vanes, thus reducing the engine airflow. This in turn causes the engine control system to reduce fuel flow and power. For example, at the rated speed of 9160 rpm, the engine model predicts that a 1 deg increase in the variable geometry position from $\lambda = -3$ deg to $\lambda = -2$ deg will result in a 3 percent reduction in airflow, a 4 percent decrease in fuel flow, and a power loss of 5 percent. Opening the variable stator vanes at a given speed has the opposite effect.

Proposed Use

The proposed use of the engine simulation in a naval EHM system is depicted in Fig. 12. Within a specific data capture

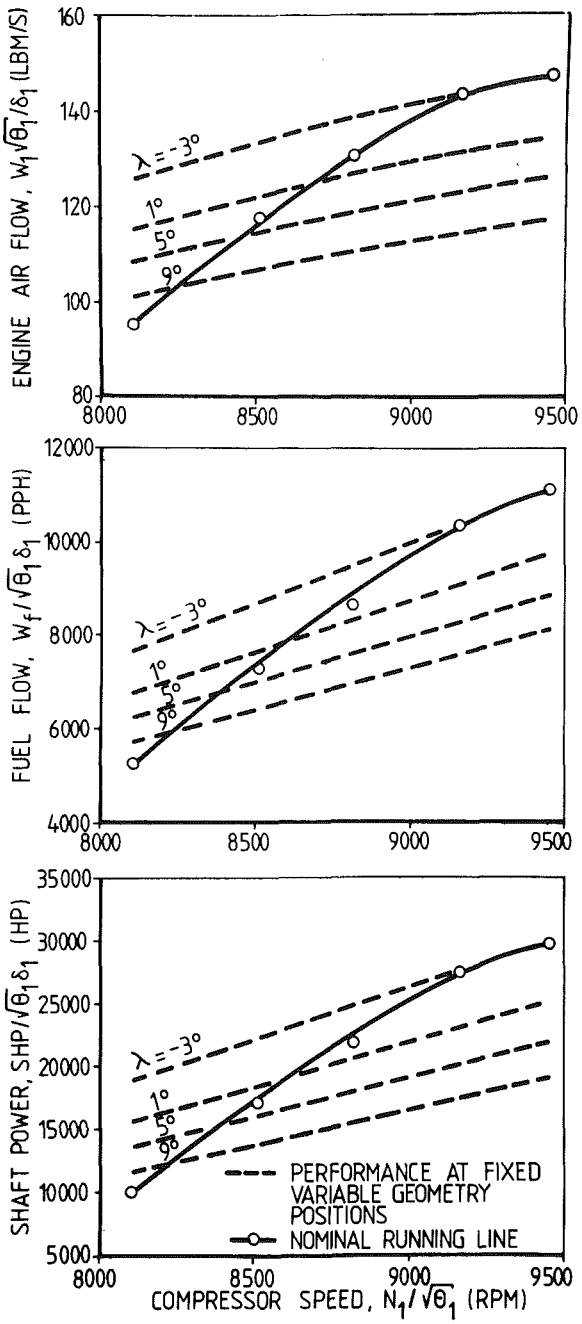

Fig. 11 Influence of compressor variable geometry setting on LM2500-30 engine performance (N_2 = 3600 rpm)

window, an automatic data acquisition system will acquire raw engine performance data from existing engine sensors. As a minimum, the processing of these data will include data smoothing and data validity checks, correction for nonstandard engine inlet conditions, comparison of measured performance parameters to baseline values, and evaluation of performance deviations (Engine Fault Signature). Performance-related fault diagnosis is to be accomplished by an algorithm that compares the Engine Fault Signature to a "library" of known or simulated fault signatures and produces a list of most probable faults.

Around the time of writing this paper, the propulsion system of the Canadian Patrol Frigate is due to be installed in the first ship of the class. It is significant that a comprehensive mathematical model of the gas turbines has been developed already, demonstrating excellent agreement with the manufacturer's performance predictions. The judicious use of this model in parallel with machinery trials can result in early detection of performance degradation or improper adjustment of variable geometry and its availability prior to actual engine running should be very valuable to a new operator of the engine.

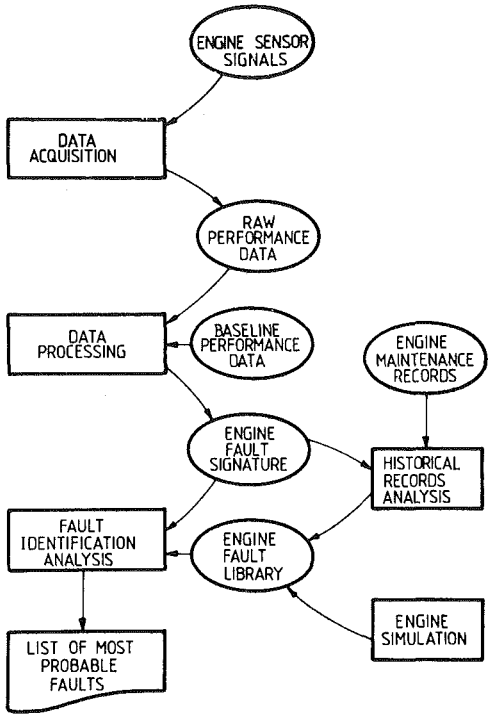

Fig. 12 Proposed use of engine simulation

The simulation of the compressor characteristics by stage stacking is a significant advance in modeling for EHM applications and is particularly valuable for engines with several stages of variable compressor stators. Additionally, the individual stage modeling approach enables compressor fault models to be developed on a more fundamental basis. For example, a compressor model based on stage-stacking procedures has been used to investigate the quantitative effects of compressor fouling on pipeline gas turbines, yielding a considerable insight into the behavior of an engine with a fouled compressor (Aker and Saravanamuttoo, 1988). An axial compressor tip clearance fault model is also under development using a similar approach (Muir and Kirkhope, 1985).

Conclusion

The use of variable compressor geometry in high-performance gas turbines introduces new problems in determining the health of the unit. The Canadian Forces will be introducing two engines of this type into service in the next few years, the GE LM2500 and the Allison 570K. A stage-stacking method, using generalized stage characteristics, has been used to create a realistic compressor model, which can estimate variable geometry effects at the stage level. The resulting compressor performance prediction scheme has been used to produce a comprehensive mathematical model of the GE LM2500 steady-state performance. It is particularly noteworthy that this model is available to the user before the first engines have been installed in a ship.

References

Aker, G. F., and Saravanamuttoo, H. I. H., 1988, "Predicting Gas Turbine Performance Degradation Due to Compressor Fouling Using Computer Simula-

tion Techniques," ASME JOURNAL OF ENGINEERING FOR GAS TURBINES AND POWER, in press.

Balsa, T. F., and Mellor, G. L., 1974, "The Simulation of Axial Compressor Performance Using an Annulus Wall Boundary Layer Theory," ASME Paper No. 74-GT-56.

Budinger, R. E., and Kaufman, H. R., 1955, "Investigation of the Performance of a Turbojet Engine With Variable-Position Compressor Inlet Guide Vanes," NACA RM E54L23a.

Carchedi, F., and Wood, G. R., 1975, "Design and Development of a 12:1 Pressure Ratio Compressor for the Ruston 6-MW Gas Turbine," ASME JOURNAL OF ENGINEERING FOR GAS TURBINES AND POWER, Vol. 97, pp. 549–560.

Doyle, M. D., and Dixon, S. L., 1962, "The Stacking of Compressor Stage Characteristics to Give an Overall Compressor Performance Map," *Aeronautical Quarterly*, Nov.

General Electric, 1981, "Marine and Industrial Engine Division LM2500-30 Marine Gas Turbine Performance Data," MID-TD-2500-8.

General Electric, 1980, "General Electric LM2500 Industrial Gas Turbine System," GEA-10523C 4/80 (5M).

Howell, A. R., and Bonham, R. P., 1950, "Overall and Stage Characteristics of Axial Flow Compressors," *Proc. IMechE*, Vol. 163.

Mack, I. D., and Hurl, D. J., 1987, "The Replacement Cruise Engine for the DDH 280 Tribal Class Destroyer," ASME Paper No. 87-GT-243.

MacGillivray, P. J., MacIsaac, B. D., and Saravanamuttoo, H. I. H., 1984, "Development of Diagnostic Model for Marine Gas Turbines," ASME Paper No. 84-GT-221.

Matthee, F. A. H., and Saravanamuttoo, H. I. H., 1982, "Development of a Low Cost Performance Monitoring System for Use on Board Naval Vessels," ASME Paper No. 82-GT-297.

Milner, E. J., and Wenzel, L. M., 1975, "Performance of a J85-13 Compressor With Clean and Distorted Inlet Flow," NASA TMX-3304.

Muir, D. E., and Kirkhope, K. J., 1985, "Test Plan for T56 Compressor Fault Studies," GasTOPS Ltd. Report GTL-19-22.2-TR.1, National Research Council of Canada contract report.

Robbins, W. H., and Dugan, J. F., 1965, "Prediction of Off-Design Performance of Multi-stage Compressors," NASA SP-36.

Saravanamuttoo, H. I. H., and MacIsaac, B. D., 1983, "Thermodynamic Models for Pipeline Gas Turbine Diagnostics," ASME JOURNAL OF ENGINEERING FOR POWER, Vol. 105, pp. 875–884.

Spector, R. B., and Miller, A. A., 1983, "GE LM2500 Aircraft Derivative Gas Turbine System," General Electric Company Report GER-3431.

Stone, A., 1958, "Effects of Stage Characteristics and Matching on Axial Flow Compressor Performance," *Trans. ASME*, Vol. 80, p. 1273.

R. G. Harker
President.

J. L. Sandy
ROMIS-PM Specialist.

Bently Nevada Corporation,
Minden, NV 89423

Rolling Element Bearing Monitoring and Diagnostics Techniques

Rolling element bearings require distinctly different techniques for monitoring and diagnostics from those used for fluid-film type bearings. A description of these techniques and the instrumentation used to acquire the necessary data is provided for comparison. Also included are some case studies to illustrate how these techniques are applied.

Introduction

In today's industrial community, rolling element bearings are being utilized in a vast quantity of different machinery designs and applications. Therefore, it becomes imperative for the Maintenance Engineer to understand the techniques and instrumentation used to monitor and diagnose problems associated with rolling element bearing machinery.

In order to clarify further the differences between the techniques used to monitor/diagnose fluid-film bearing problems versus those techniques used to monitor/diagnose rolling element bearing problems, Table 1 shows a comparison of the characteristics for the two types of bearings. As indicated in the table, a rolling element bearing has some different characteristics from those of a fluid-film bearing. Due to the fact that a rolling element bearing restricts rotor motion, forces generated by the rotor are transferred through the rolling elements to the bearing's outer ring, which contains the outer race, and ultimately to the bearing housing. Because of this transmission, a direct measurement at the bearing outer ring or a casing (housing) measurement are the primary accepted methods for monitoring machines with rolling element bearings (Sandy, 1987). Since a fluid-film bearing can experience relative motion within the bearing clearance resulting in poor transmission of rotor-related vibration to the casing, the industry-accepted measurement for fluid-film bearing machinery is a shaft-relative measurement (e.g., proximity probe).

Another characteristic that is unique and normal to rolling element bearings is the generation of vibrations at specific "bearing-related" frequencies. It was shown by Foiles (1987) that these frequencies are generated by the bearing based on the bearing's geometry, number of rolling elements, and the speed at which the shaft is rotating. How to use these bearing-related vibration signals for monitoring and diagnosing rolling element bearing-related malfunctions will be presented in a later section of this paper.

Contributed by the International Gas Turbine Institute and presented at the 33rd International Gas Turbine and Aeroengine Congress and Exhibition, Amsterdam, The Netherlands, June 5–9, 1988. Manuscript received by the International Gas Turbine Institute May 22, 1987. Paper No. 88-GT-212.

Rolling Element Bearing Vibration Signal Regions

Rolling element bearing machinery produces vibrations in three different frequency regions (Fig. 1) (Bently Nevada Applications Note, 1987).

1 **Rotor Vibration Region.** Rotor-related vibrations nor-

Table 1 Comparison of rolling element bearing characteristics versus fluid-film bearing characteristics

Fluid-Film Bearing	Rolling Element Bearing (Excludes Damper-Backed Bearings)
1. Fluid-Film supports rotor.	1. Rolling elements and raceways supports rotor.
2. Allows rotor motion (within the bearing clearance) relative to bearing.	2. Restricts rotor motion relative to bearing.
3. Virtually unlimited life if properly maintained and operated.	3. Finite life due to fatigue even if properly maintained and operated.
4. Good damping and shock absorbing qualities.	4. Poor damping and shock absorbing qualities.
5. Poor transmission of rotor-related vibration to casing.	5. Good transmission of rotor-related vibration to outer ring/casing.
	6. Generates vibrations at bearing-related frequencies based on on bearing geometry, speed, and number of elements.

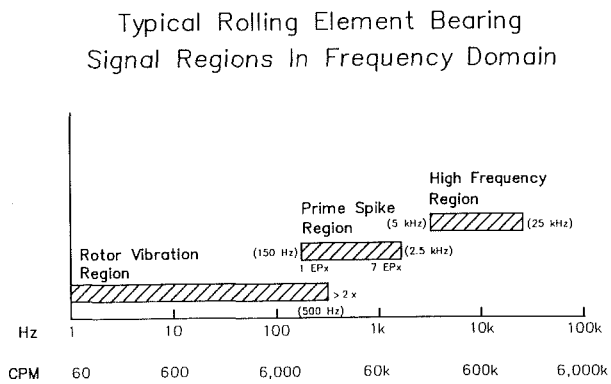

Fig. 1 Frequency

mally occur in the range of 1/4 to 3 times shaft rotative speed (1/4X-3X) and are best measured in terms of velocity or displacement. Since most general purpose machines operate within the speed range from 1200 to 3600 rpm, these rotor-related vibration signals tend to fall within the frequency range from 10 to 500 Hz (600 cpm to 30 kcpm). Many rolling element bearing failures are the direct result of a rotor-related malfunction (e.g., imbalance, misalignment, or rotor instability), which must be corrected to eliminate bearing overload and subsequent failure. If vibration data are not monitored in this frequency region, the rotor-related malfunction will remain undetected and the rolling element bearing will chronically fail and need replacement.

2 Prime Spike Region. The second vibration frequency region to monitor for machines with rolling element bearings is the prime spike (element passage) region. As previously mentioned, a rolling element bearing generates vibrations with characteristic frequencies based on its geometry, number of rolling elements, and speed. Prime spike is a term used by Bently Nevada Corporation to describe a vibration frequency range that includes those bearing frequencies that are generated by the rolling elements traversing either an inner or outer race flaw. This frequency range normally includes from 1 to 7 times the element passage rate (1-7 EPx) and can be measured effectively in terms of displacement, velocity, or acceleration. Element passage rate (EPx) is defined as the rate at which the rolling elements pass a point on either the inner or outer bearing race. Field studies indicate that approximately 90 percent of all rolling element bearing failures are related to either an inner or outer race flaw. The other 10 percent are related to either a rolling element flaw or a cage flaw, both of which generate vibrations with frequencies in the rotor vibration region. By establishing the prime spike region and filtering out the rotor-related vibration components, it is possible to gain improved monitoring of rolling element bearing condition.

3 High-Frequency Region. The third vibration frequency region to monitor for machines with rolling element bearings is the high-frequency region. When a flaw develops in a rolling element bearing, the vibration signals generated are in the form of short, sharp impulses. Since it is a lightly damped device, an accelerometer will react to this type of input (short, sharp impulse) by "ringing" at its resonance frequency. Utilizing the accelerometer's mounting resonance and measuring its amplitude in units of acceleration, it is possible to monitor rolling element bearing conditions in the high-frequency region. However, due to noise susceptibility problems and the possibility of "self-peening" of the bearing flaws, which can result in decreasing readings as the bearing failure progresses, high-frequency measurements for bearing failure detection should only be used as a *supplement* to measurements made in the rotor vibration and prime spike regions. High-frequency measurements are primarily used for the following:

1 To provide *possible* indication at early stages of rolling element bearing failure. However, due to the reasons mentioned above, caution must be used in interpreting the results.

2 To help detect certain other machine malfunctions (e.g., cavitation, rubs, steam or gas leaks, valve problems, blade passage, or gear mesh problems).

Based on observation of many rolling element bearings in the field by Bently Nevada Corporation, and many of their customers, most of the information on the condition of rolling element bearings and warning of their failure occurs in the prime spike region (1-7 EPx). Information about *rotor behavior* generally occurs in the region between 1/4 and 3 times rotating speed (1/4X-3X). Information at very high frequencies (8 EPx and higher to the megahertz region) may contain very early warning bearing failure information, as well as other data concerning machinery condition (e.g., rubs, gear noise, cavitation, valve noise, etc.). As explained in the Bently Nevada Applications Note, "Predictive Maintenance Through the Monitoring and Diagnostics of Rolling Element Bearings," 1987, the *principal* and *vital* data are contained in the prime spike region (1-7 EPx).

Causes of Premature Failure in Rolling Element Bearings

As mentioned in Table 1, a rolling element bearing has a finite life. The bearing *will fail* due to fatigue, caused by the high cyclic stresses between the rolling elements and raceways, even if operated under ideal design conditions. Design life calculations can be performed to ascertain the minimum number of hours of operation that the bearing should achieve when properly installed and operated within its design limits.

A *major* assumption when calculating minimum rolling element bearing life is that the bearing is properly installed and maintained. However, most rolling element bearing manufacturers state that this is not so and approximately 95 percent of the rolling element bearings installed in the field fail prematurely. Most premature bearing failures can be attributed to one or more of the following causes:

1 Excessive loading
   (*a*) Steady-state (e.g., misalignment or static load)
   (*b*) Dynamic (e.g., imbalance or rotor system in stability)
2 Improper lubrication (insufficient or excessive)
3 External contamination
4 Improper installation
5 Incorrect sizing (e.g., wrong design or wrong load rating)
6 Exposure to vibration while not rotating (false brinelling)
7 Passage of electric current through the bearing

When analyzing rolling element bearing failures (normal or premature), it is important not only to determine that the bearing is failing, but also to determine the underlying cause of that failure. Most rolling element bearing manufacturers state that in order to determine the cause of bearing failure, the bearing must be analyzed (e.g., microscopic, metallurgy) in an early stage of failure. If the bearing is allowed to operate to a stage of total failure, it is impossible to be able to determine the cause of that failure. To ensure success, two important goals must be achieved when monitoring/diagnosing rolling element bearing problems:

1 Elimination of premature rolling element bearing failures.

2 The "monitoring system" must be able to ascertain that a bearing problem exists in an early enough failure stage to allow a complete analysis of the bearing to determine the cause of failure.

Since a primary goal of any monitoring/diagnostic program is to be able to analyze a bearing to determine cause of failure, some discussion of rolling element bearing failure stages is necessary.

Rolling Element Bearing Failure Stages

A rolling element bearing progresses through three failure stages, each of which exhibits unique vibration characteristics and requires specific monitoring/diagnostic techniques (Bently Nevada Applications Note, 1987). The three failure stages in order of occurrence are:

1 Prefailure.
2 Failure.
3 Near catastrophic/catastrophic.

Prefailure Stage. In the prefailure stage, the bearing has entered the earliest stages of failure. The bearing develops hairline cracks or microscopic spalls that are normally not visible to the human eye, but are clearly evident in microscopic or metallurgical tests. From a vibration standpoint, there may be an increase in the high-frequency (>7 EPx) vibration produced by the bearing. Temperature and prime spike vibration

measurements will show no significant changes. From an analyst's viewpoint, it is important to know the bearing has entered this failure stage. However, from an economic viewpoint this is not the stage to replace the bearing because it usually has a significant amount of safe operating life remaining.

Failure Stage. In the failure stage, the bearing develops flaws that are visible to the human eye. At this stage, the bearing usually produces audible sound and the bearing temperature will rise. Vibration amplitudes in the "bearing related" range (prime spike) reach easily detectable levels. Once the failure stage is reached, it is necessary either to change the bearing or increase the frequency of monitoring to estimate how long the bearing will safely operate before causing a catastrophic machine failure. From an economical standpoint, this stage is considered the time to replace the bearing. Another point to consider is if the bearing is allowed to operate into the next failure stage, it will be *impossible* to determine the cause of the bearing failure. This action will eliminate the possibility of diagnosing and correcting the primary malfunction, which ultimately results in a similar failure at a later date.

Near Catastrophic/Catastrophic Stage. When the bearing enters this stage, rapid failure of the bearing is *imminent*. Audible noise produced by the bearing significantly increases and the bearing temperature increases until the bearing overheats. Rapid wear causes the bearing clearance to increase, which then allows significant shaft motion relative to the bearing. Since a rolling element bearing is designed to *restrict* shaft motion, it can be very dangerous to allow the bearing to reach this stage due to the probability of creating a rub within the machine. From a vibration standpoint, the bearing-related (prime spike) vibration amplitude levels will show significant increases. High-frequency vibration data (>7 EPx) may be unreliable and caution should be used in its interpretation. Due to "self-peening" of the bearing flaws, high-frequency amplitude levels often *decrease* during this stage and it can *appear* the bearing is in an earlier stage of failure. The occurrence of this "self-peening" phenomenon is especially true for low-speed machines (Bently, 1983).

Transducers and Instrumentation for Vibration Measurement and Monitoring of Rolling Element Bearings

The instrumentation used for vibration monitoring/diagnostics of rolling element bearings can be classified into two categories, primary or secondary (Sandy, 1987).

1 Primary Measurement Instrumentation.

(*a*) *REBAM® Instrumentation System.* REBAM is an acronym for Rolling Element Bearing Activity Monitor. The REBAM system uses a high-gain, low-noise eddy current proximity transducer that is installed in the bearing housing observing the bearing's outer ring, which contains the outer race (Fig. 2).

The REBAM transducer measures the very small (microinch/micrometer) deflection of the outer ring as the rolling elements pass the area observed by the transducer. These deflections are measured in terms of displacement. Through the use of electronic filters, the REBAM vibration signal is separated into the rotor vibration and prime spike regions for monitoring/diagnostics. The REBAM system is a direct and very sensitive method of rolling element bearing measurement, which provides a very high signal-to-noise ratio, as compared to casing-mounted acceleration or velocity measurements.

(*b*) *Casing Vibration Instrumentation Systems.* Rolling element bearing machinery casing vibration measurements are taken using either a velocity transducer or an accelerometer-based system.

When using a velocity transducer-based system, the vibration signal is measured in terms of velocity or displacement. When using an accelerometer-based system, the vibration signal is measured in terms of acceleration or velocity. Again, through the use of electronic filters, the vibration signal is separated into the rotor vibration and prime spike regions for rolling element bearing monitoring/diagnostics.

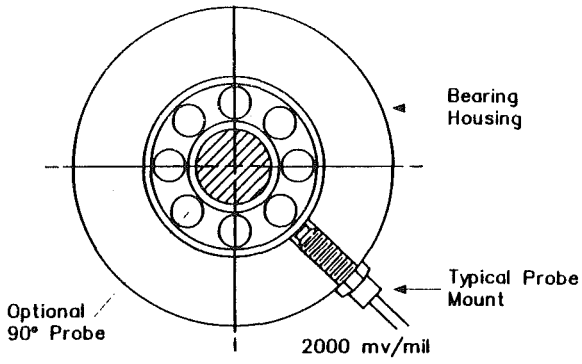

Fig. 2 Typical REBAM (Rolling Element Bearing Activity Monitor) probe mount

If an accelerometer-based system is used, high-frequency measurements are available. However, due to the problems previously mentioned, high-frequency measurements are used as a *supplement* to measurements made in the rotor vibration and prime spike regions.

2 Secondary Measurement Instrumentation.

(*a*) *Shaft Relative Instrumentation System.* Shaft relative measurements are taken using an eddy current proximity transducer and have been accepted industry-wide as the primary measurement for vibration monitoring/diagnostics of fluid-film bearing machines. However, a proximity probe-based system can also be used effectively to monitor rolling element bearing performance, and it also provides rotor-related vibration information for the machine. As is the case with the REBAM transducer, the shaft relative vibration signal from the proximity probe can be separated into the rotor vibration and prime spike regions for monitoring/diagnostics of rolling element bearing machinery.

Rolling Element Bearing Case Histories

Three distinctly different case histories are presented to show how vibration signal regions can be utilized to analyze either rolling element bearing condition or rotor-related vibration problems. The vibration trends used in each case history were taken utilizing an accelerometer-based instrumentation system. It should also be noted that data presented in each case history were taken during the initial implementation stage of a predictive maintenance program at the Bently Nevada production facilities.

Case History No. 1. Data were taken on a 1 HP, 1725 rpm induction motor that belt drives a set of internal brushes in a PAR deburring machine (Sandy, 1987). The PAR deburring machine is used to polish and debur copper sheets used in the manufacture of printed circuit boards.

The three sets of graphs (Figs. 3–5) represent overall-value vibration trends taken at three different measurement points on the motor (i.e., motor drive-end vertical, motor nondrive end vertical, and motor nondrive end axial). These graphs were computer generated and depict a chronological trend for the overall velocity and prime spike values for each location.

The top graph of overall velocity values provides a means for determining the general mechanical condition of rolling element bearing machinery. The frequency range for this measurement extends from 10 Hz to 2.5 kHz (600 cpm to 150 kcpm),

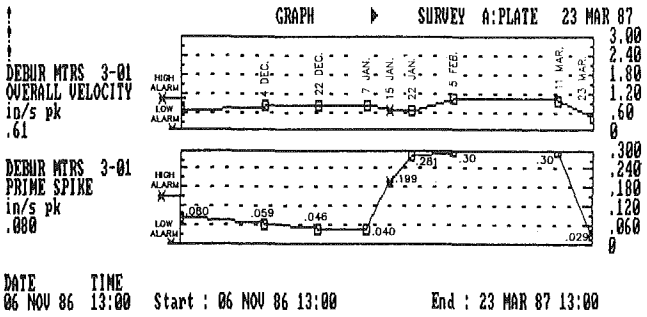

Fig. 3 Motor drive end—vertical

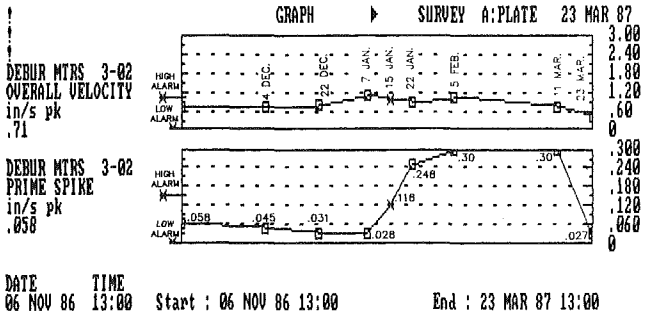

Fig. 4 Motor nondrive end—vertical

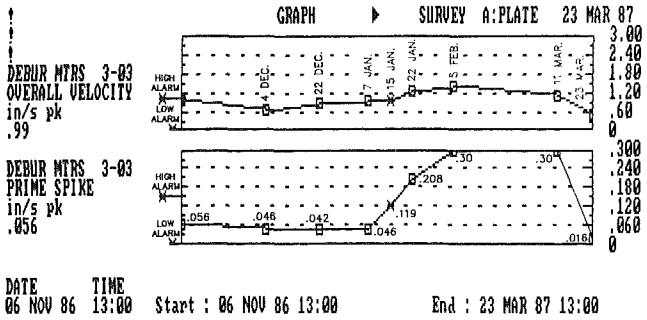

Fig. 5 Motor nondrive end—axial

which includes the rotor vibration region and overlaps the prime spike region. This range gives very good indication of rotor-related malfunctions and it is also somewhat sensitive to bearing-related problems.

The bottom graph of prime spike values provides a means for determining rolling element bearing condition. The frequency range for this measurement extends from 150 Hz to 2.5 kHz (9 kcpm to 150 kcpm) and includes the bearing's fundamental element passage frequency (EPx) and harmonics up to 7 EPx.

As stated previously, the high-frequency measurement is a supplementary measurement to the measurements made in the rotor vibration and prime spike regions. Since no additional information was obtained from the high-frequency region in this case history, it has been excluded from the data shown.

As the data show, during the time frame from 7 Jan. to 11 Mar., the prime spike region shows a significant upward vibration trend with very little activity shown in the overall velocity region. This suggests the upward vibration trend is *not* caused by a rotor-related malfunction (i.e., imbalance, misalignment, etc.) and is most likely related to a rolling element bearing problem. Another point that should be highlighted is that even though all three measurement points show this upward vibration trend, the values obtained at the motor

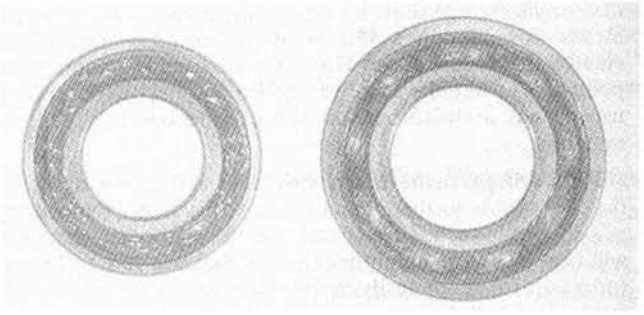

Photo 1 Comparison view of nondrive-end bearing (left) to drive-end bearing (right). Note contamination and lack of lubricant in drive-end bearing.

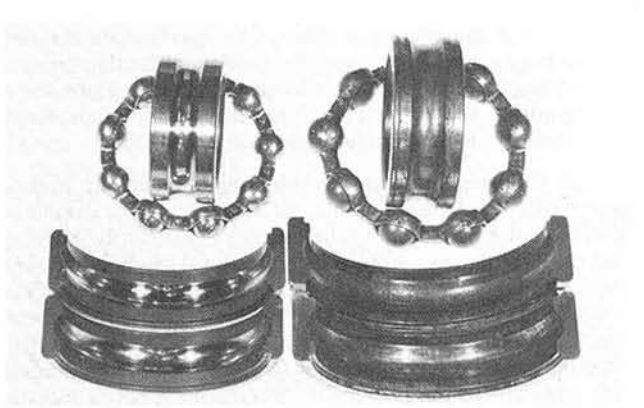

Photo 2 Cutaway comparison on nondrive-end bearing (left) to drive-end bearing (right). Note damage to drive-end bearing races, rolling elements, and cage.

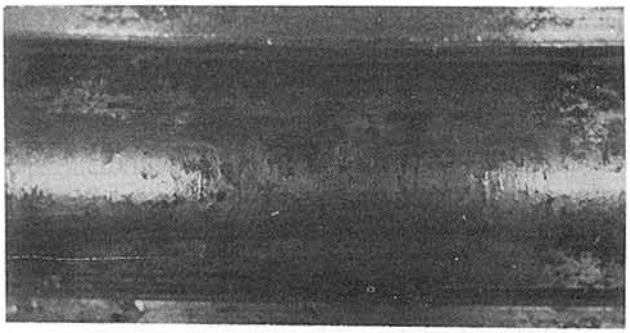

Photo 3 Close-up view of drive-end bearing outer race. Clear evidence of bearing damage.

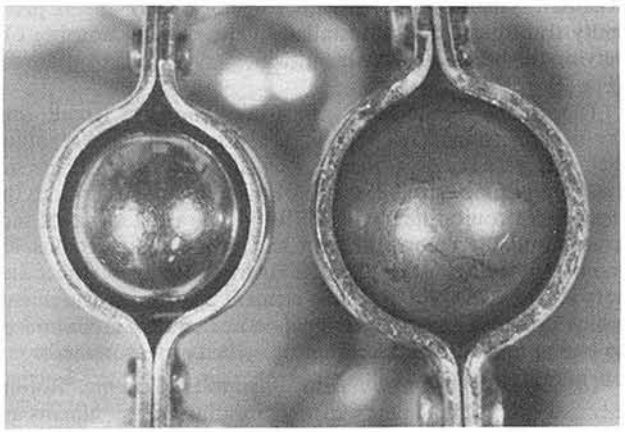

Photo 4 Closeup comparison view of nondrive-end bearing (left) rolling elements and cage to drive-end bearing (right) rolling elements and cage. Note damage on drive-end bearing rolling elements and cage.

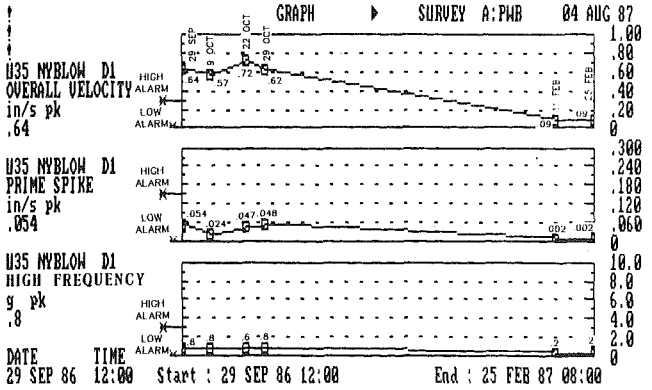

Fig. 6 Motor drive end—vertical

drive-end vertical position appear to rise more quickly and indicate the problem is most likely in that end of the motor.

On 11 Mar., the motor was shut down and disassembled for inspection. As Photos 1–4 show, significant damage had occurred in the rolling element bearing that was installed in the drive-end of the motor.

It was later ascertained that an acidic water solution was being drawn into the drive-end bearing during operation due to a faulty seal. This in turn caused the grease lubricant to solidify and also corroded the bearing rolling element/raceway surfaces.

The motor was reinstalled with new seals and rolling element bearings. As shown in the 23 Mar. vibration readings, the vibration levels were significantly reduced, which indicated the motor was operating satisfactorily and required no further mechanical corrections.

Case History No. 2. Data were taken on a 2.5 hp, 3540 rpm induction motor that drives a New York centrifugal blower. The blower provides circulation air for an area that contains open-air tanks filled with acid solutions. Due to access problems, vibration readings can only be taken at the motor drive-end vertical position. Once again an accelerometer-based system was used to capture the vibration data (Fig. 6).

As the data show, during the time frame from 29 Sept. to 29 Oct., the overall velocity values are high for a unit of this type, while the vibration values in the prime spike and high-frequency regions are very low. This suggests the high vibration trend is *not* caused by a rolling element bearing problem and is most likely caused by a rotor-related malfunction (i.e., imbalance, misalignment, etc.).

It was decided to perform a more complete analysis to determine the cause of the malfunction. During the course of setting up the analysis instrumentation two things were visually observed. First, one support foot of the motor had a visible gap between it and the metal support base (Photos 5 and 6); this is commonly called "soft foot," which usually generates vibration characteristics that appear in the rotor vibration region. Second, the concrete foundation that supports the fan/motor had cracks that appeared to propagate from under the motor/fan support structure (Photo 7).

Further discussions with the maintenance personnel revealed the fact that the motor had been dropped prior to installation and because another was not available, it was installed. This motor/fan had operated in this damaged state for approximately one year and is considered to be the cause of the cracks in the concrete foundation.

A new motor was installed and the vibration levels obtained after 11 Feb. were significantly reduced. This indicated no further mechanical corrections were required.

Case History No. 3. Data were taken on a 1.5 hp, overhung,

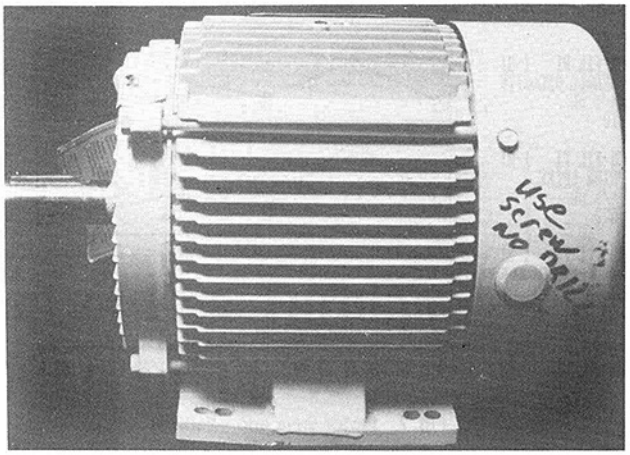

Photo 5 Side view of original motor used to drive New York blower. Note gap between support surface and motor drive-end support foot.

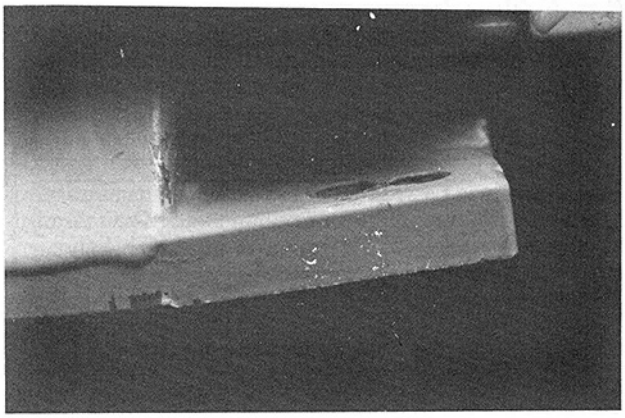

Photo 6 Close-up view of damaged motor drive-end support foot. Approximately 1/4 in. gap between support foot and support surface.

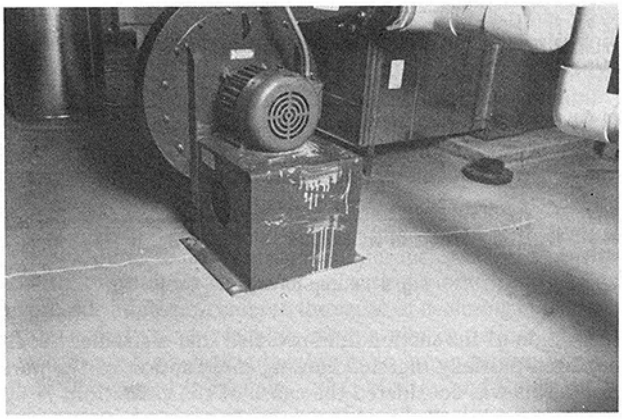

Photo 7 End view of New York blower and its support base. Note propagation of cracks in concrete floor from under the blower's support base.

single-stage centrifugal pump that is driven by an induction motor at a speed of 3450 rpm. The pump circulates an acid solution that is used in the manufacture of printed circuit boards. The pump is considered to be a critical piece of equipment for this process.

As the data show (Figs. 7–9), on 22 Dec. the pump experienced high vibration in all three frequency regions and was emitting "noises" that are typically associated with cavitation. The pump was shut down in order to inspect its suction inlet.

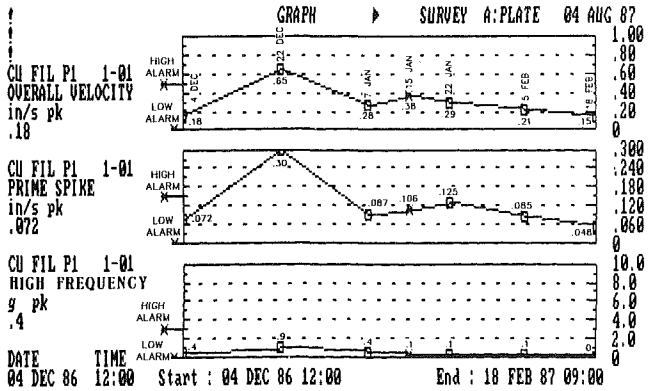

Fig. 7 Motor drive end—vertical

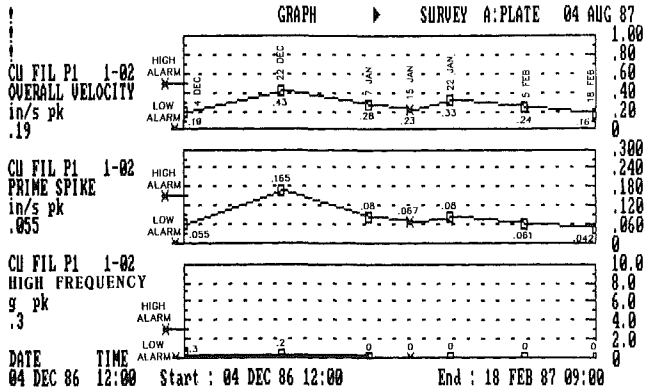

Fig. 8 Motor nondrive end—vertical

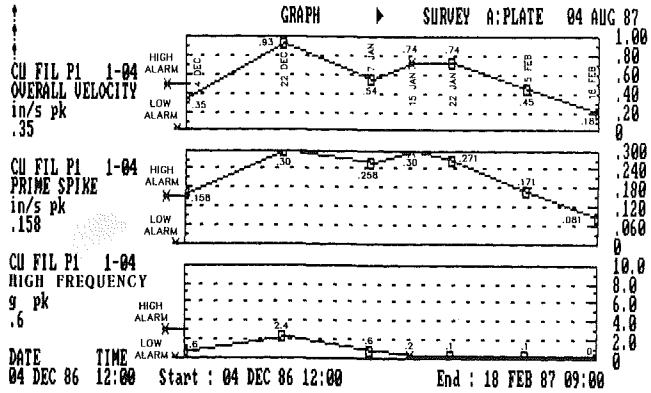

Fig. 9 Pump drive end—vertical

Inspection of the suction inlet revealed that a strainer "sock" has been partially ingested causing interruption of the pump flow. This was considered the cause of the cavitation. A new strainer was installed and the pump was restarted. However, the pump vibration levels in the prime spike and overall velocity regions remained high. Due to production requirements, the pump was left in service with the stipulation to monitor its vibration levels frequently. On 5 Feb., the vibration levels decreased, but a pump seal leak occurred that forced a shutdown for repair. When the pump was opened for inspection, extensive damage to the impeller (see Photos 8 and 9) was observed. Due to the solution being pumped, the impeller is made of a PVC-type of material. As the photos show, extensive material had been removed from the vanes and it is assumed this action occurred during the cavitation process. The impeller

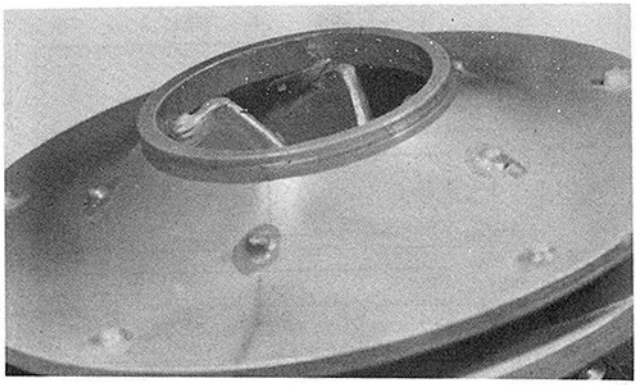

Photo 8 Closeup view of pump impeller that shows cracks between the vanes and shroud. Also note radial crack that extends from the impeller eye to the outside edge of the shroud.

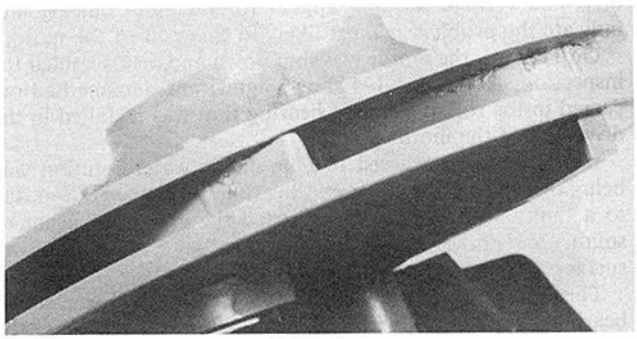

Photo 9 Closeup view of pump impeller that shows crack that runs the length of the joint between the vane and shroud. Also note the locations where material was removed from the vane by cavitation.

is a closed type and, as the photos show, there are cracks that run the length of each vane along the joint between the vane and shroud. There is also a radial crack on the shroud that extends from the impeller eye to the outside edge of the shroud. It is assumed this damage also occurred during pump cavitation.

A new pump impeller was installed and the unit was restarted. As the data show, the vibration levels were significantly reduced, which indicated no further mechanical corrections were required.

Summary

It has been the purpose of this paper to outline the instrumentation and the techniques used to apply it when monitoring or analyzing machines with rolling element bearings. Hopefully, some insight into how the techniques can be utilized has been gained.

Acknowledgments

The authors wish to thank the personnel of the Bently Nevada facilities maintenance department for their assistance in gathering of data and inspection of damaged machine parts.

References

Applications Note, 1987, "Predictive Maintenance Through the Monitoring and Diagnostics of Rolling Element Bearings," Bently Nevada Corporation.

Bently, D. E., 1983, "Definition of the Prime Spike Detection Scheme for Rolling Element Bearings," Technical Report for Bently Nevada Corporation.

Foiles, B., 1987, "Rolling Element Bearing Frequencies," Technical Report edited by Bently Nevada Corporation.

Sandy, J. L., 1987, "Early Detection of Rolling Element Bearing Failure," *Proceedings, Sensors Expo*, Helmers Publishing, Inc., pp. 141–146.

Assessment of Gas Turbine Vibration Monitoring

A. Lifson
Southwest Research Institute,
San Antonio, TX 78250

G. H. Quentin
Electric Power Research Institute,
Palo Alto, CA 95129

A. J. Smalley
Southwest Research Institute,
San Antonio, TX 78250

C. L. Knauf
Consultant,
Port Jefferson, NY 11777

This paper presents a basis for selecting and justifying vibration monitoring equipment for power-generating gas turbines. Users of industrial gas turbines from utility and petrochemical companies are surveyed; a utility forced outage data base is analyzed; typical vibration limits are presented; and the current capabilities of commercial monitoring systems and vibration transducers are summarized. The industry survey by site visits and questionnaire develops common trends; it itemizes malfunctions that can be successfully identified with appropriate vibration monitoring; it summarizes current practices, benefits, limitations, and operating experience with various transducer types, as applied to harsh gas turbine environments. Vibration limits, trending, and sources of vibration are addressed. Operational factors are considered in planning and cost justifying vibration monitoring systems for a basic trip protection, periodic measurements, and on-line computerized continuous protection. Seventeen case histories and examples illustrate and support these findings. Analysis of the utility-generated data base complements the industry survey; it isolates the contribution of different vibration-related outages for base loaded and peaking units; graphic results break down these outages into duration, man-hours to repair, and frequency of occurrence.

Introduction

The assessment of vibration monitoring becomes especially important as the pronounced trend in the utility industry continues toward an increase in orders for large gas turbine units and development of plans to add additional capacities to their installations. A recent survey (Waldman, 1986) indicates that the domestic and foreign market for large gas turbine units has strengthened; the number of new orders for gas turbines in the range of 60 MW and above has almost tripled in 1986 compared to 1985. To meet this stronger demand, several major domestic and foreign manufacturers have recently introduced new gas turbines sized in the 130 to 150 MW range (Brandt, 1987; Chellini, 1986).

With the improvement in thermal efficiency promised by this new generation of large gas turbines and by combined cycle or cogeneration application, the likelihood of base loading as opposed to peaking services increases (Catina et al., 1987). The role of gas turbines in integrated gasification combined cycle plants also means more continuing operation and an increased need for high availability (Shepard, 1986); during the 1960s and 1970s, it was observed that large steam turbine units suffered a decrease in availability with increasing size and it is important to use all available resources whose effectiveness has been demonstrated to avoid the same trend for large gas turbines. To emphasize the potential problem with gas turbines, data compiled by one European insurance company indicate one serious failure occurs per 26 large industrial gas turbines per year (Bloch and Geitner, 1985) and as observed by Edison Electric Institute (Grenstad et al., 1982) the gas turbines operating in peaking service fail about three times more often than steam turbines, and when the auxiliary equipment is included, the gas turbine systems fail ten times more often than the steam turbine system.

Data from an EPRI survey (Benett et al., 1980) of approximately 50 utilities reiterate the need for improved reliability and maintenance of gas turbines. Survey data further showed that many reliability and maintenance problems were associated with the vibration monitoring system, including deterioration of cables from the hot environment in gas turbine compartments, and resultant false vibration trips.

On the other hand, there are numerous case histories that show that appropriately set up vibration monitoring systems can provide important clues to the cause of declining machinery health, orderly back tracking after a trip or failure, and in some instances, an early indication of an impending equipment failure (Ricca and Bradshaw, 1984; Murray and Reid, 1986). Recognizing these potential benefits of machine protection against possible malfunction, the vibration monitoring of plant machinery has grown exponentially in the last ten years.

Despite rapid expansion, there is limited documentation of the benefits of investing in vibration monitoring systems for gas turbines. Most engineers agree on the qualitative benefits, and that the cost of an extensive multiparameter monitoring system generally represents only a small fraction of the total plant losses associated with equipment failure (Myrick, 1982; Simmons and Lifson, 1985). However, the investment is still significant and quantitative support that relates the amount spent on purchasing and maintaining the monitoring system to the resultant increase in machine availability is hard to find. This paper is an initial effort to meet this need for guidance

Contributed by the International Gas Turbine Institute and presented at the 33rd International Gas Turbine and Aeroengine Congress and Exhibition, Amsterdam, The Netherlands, June 5-9, 1988. Manuscript received by the International Gas Turbine Institute December 3, 1987. Paper No. 88-GT-204.

and documentation in selecting and assessing vibration monitoring for industrial gas turbines. To accomplish our goal, an industry survey has been performed (by site visits, mailed questionnaires, and telephone contacts) to bring together the practices and experience of industrial users of gas turbines and vendors of vibration monitoring equipment. To provide a statistical backup to information obtained from the industry survey, the ERAS (EPRI Reliability Assessment System) data base compiled by ARINC Research (Brown and Young, 1984) from the information provided by several utilities has been evaluated to extract pertinent information on vibration-related gas turbine outages.

Transducer Selection

Some form of vibration measurement device is found on almost all industrial gas turbines. To detect and diagnose vibration-related problems, it is necessary to select a transducer type that will measure the vibration (machine housing or shaft) most likely to reveal the expected failure characteristics. Shaft measurements, which are performed by eddy current noncontact displacement probes, are selected for detection of rotor-related malfunctions, which include: imbalance, misalignment, shaft bow, and fluid film bearing instability problems. Velocity pick-ups or accelerometers, installed on machine casings or bearing housings, are selected to detect bearing housing and high-frequency rotor-related malfunctions, which include: ball bearing failure, support looseness, casing or foundation resonances, loose parts, and gear or blade problems.

Gas turbines generate a vast number of spectral components and have been known to experience most of the above-mentioned vibration problems. Therefore, no single transducer type can be relied upon to meet all the application requirements. The power generation and petrochemical industry survey indicates that, depending on initial installation time and company philosophy, large industrial gas turbines with fluid film bearings can be monitored with eddy current probes, velocity pick-ups, accelerometers, dual probes, and sometimes by a combination of several transducer types.

For rigidly mounted machine bearing housings, more information about shaft dynamic behavior can be obtained from a noncontact displacement sensor than a velocity pick-up or accelerometer; a number of large industrial gas turbine users are improving their vibration monitoring capability by adding such shaft displacement sensors. However, vibration transducers installed on the flexibly mounted machine bearing housings have proved to be useful in indicating problems associated with the damaged bearing supports.

The aircraft derivative gas turbines typically have rolling element type bearings and have traditionally been monitored with velocity pick-ups installed on the machine casing. However, recently developed high-temperature accelerometers can better indicate gas turbine vibration malfunction in a higher frequency spectrum range; several gas turbine users have already upgraded their installations with the accelerometer, claiming that they have better longevity than velocity pick-ups.

High temperatures of gas turbine compartments impose additional requirements on selection of a vibration transducer and its attached cable and connector (McHugh, 1983). The high-temperature vibration sensing instruments are significantly more expensive than the lower temperature rated counterparts. However, as indicated by vibration monitoring equipment vendors and gas turbine users, a wrong transducer selection often leads to nuisance shutdowns due to the malfunctioning vibration equipment. The vibration transducer, cables, and connectors should be rated up to the highest temperature expected, which is often reached shortly after the gas turbine shutdown.

To monitor shaft vibration, ideally, two eddy current probes are installed 90 deg apart on each gas turbine bearing. The two probes together can provide valuable information, such as orbital display, which is not possible to obtain with seismic transducers. Commonly used eddy current probes are rated up to 350°F (180°C); for higher temperatures, specific probe environmental limits should be reviewed. By adding redundant probes at locations that are difficult to access and operate in a harsh environment, the reliability of the monitoring system can be improved; a limited number of users are already doing this. To prevent the eddy current probe cables from being exposed to the high gas turbine temperatures, they may be kept cool by running them through an oil drain line. A knowledge of a phase angle reference is an important parameter for vibration diagnostic and trending process. Therefore, often, an additional eddy current transducer is used to observe a once per revolution event, commonly a notch on the rotating shaft. For temporary installations, a simple piece of tape attached to the shaft surface can be sufficient for a phase angle measurement. Of course, the permanently machined notch offers better reliability and consistency than the tape.

Seismic vibration transducers, such as velocity pick-ups and accelerometers, can be installed on the machine casing (aircraft derivative gas turbines), or bearing housing (large industrial gas turbines). Velocity pick-ups are usually rated up to 600–750°F (315–400°C), which is generally adequate for most gas turbine installations. An accelerometer with a built-in amplifier can generally withstand temperatures only up to 260°F (125°C); therefore a remote charge amplifier is required for high-temperature accelerometers rated up to 1020–1380°F (550–750°C).

There are also some large industrial gas turbine installations that utilize a dual probe consisting of a combination of an eddy current probe and a seismic transducer (usually a velocity pick-up). Two such probes on each bearing 90 deg apart are again desirable, although the use of a single vertical dual probe is quite common. Some companies rely on the measurements of absolute shaft vibration, i.e., vibration readings from the eddy current probe added to the vibration reading from the seismic probe, while others use the relative shaft displacement data for detecting a vibration problem and utilize the vibration information from seismic probes to assist in identifying the root cause of the problem. Absolute measurements of shaft vibration performed by the dual probe usually provide better indication of such problems as imbalance, but they are subject to errors introduced by the sensitivity of the bearing housing vibration to the transmission path, and also are less suitable than relative shaft vibration measurements for establishing the bearing vibration with respect to the bearing clearance.

A summary of advantages, disadvantages, and application of the various transducer types used for gas turbine vibration monitoring is presented in Table 1.

Vibration Limits and Trending

Due to large variation of possible vibration-related malfunctions in gas turbines, vibration limits are based on statistical or consensus evaluations of vibration levels and particular plant experience. As such, there are no absolute limits that will assure successful long-term operation or firm upper limits that will cause failure for any specific gas turbine. The best we can hope for is to increase our probability of successful long-term operation and minimize unscheduled outages due to equipment failure. Using statistical criteria, there will always be unexpected failures and amazing vibration endurance of some machines. In general, high vibrations are bad, low vibrations are good, and the line separating the two is somewhat uncertain. Thus, lowering the vibration to reasonably obtainable levels should be encouraged.

An important factor to recognize in applying vibration limits is growth of vibration amplitudes with time. All machines, regardless of their health, exhibit some form of vibration;

Table 1 Comparison of vibration transducers

TRANSDUCER TYPE	ADVANTAGES	DISADVANTAGES	INSTALLATION
EDDY CURRENT NONCONTACT DISPLACEMENT PROBES	•Can measure static and dynamic shaft motion. •Accurate low frequency response. •No wear. •Small size. •Measures directly in displacement units. •Easy to calibrate.	•Mechanical or electrical runout noise. •Limited high frequency sensitivity. •Calibration sensitive to shaft materials. •Difficult to install or replace. •Requires external power source. •Possibility of probe length and bracket (if installed) resonance.	Popular on machines with fluid film bearings. Usually one pair of X-Y probes 90° apart per bearing. Often added as addition to other probes. Sometimes extra redundant pair on difficult to access bearing(s) exposed to hot temperature environment. Extra X-Y pair is installed either on opposite side of the bearing (better arrangement for static shaft measurements) or approximately 10-15° apart from the first pair (better arrangement for vibration reading comparison).
VELOCITY PICK-UPS	•Simple to install with space available. •No external power source. •Strong response in the mid frequency range. •*Can be installed on temporary basis.*	•Transducer resonance noise and phase shift. •Cross-axis signal noise. •Can be affected by magnetic fields. •*Can be difficult to install due to space* limitations. •Performance degradation due to component wear. •Difficult to calibrate. •Does not measure shaft dynamic motion.	Typical on older machines. Mounted on machine casing on aircraft derivative gas turbines with usually 1 to 3 probes per *machine, often installed in horizontal plane.* Mounted on bearing housing on large industrial gas turbines.
ACCELEROMETERS	•Simple to install. •Good high frequency response. •Some models suitable for high temperature environment. •Small size. •Relatively good reliability.	•A remote charge amplifier required for high temperature environment (approximately above 260°F (125°C)). •Possibility of low frequency noise due to: integration to displacement, solid state electronics in a charge amplifier, loose connections. •Requires external power source. •Temporary installations may be subject to noise. •Does not measure shaft dynamic motion.	Typical on aircraft derivative gas turbines, where mounted on machine casing, usually in horizontal plane. Sometimes added to or replaced older velocity pick-ups on aircraft derivative gas turbines. Occasionally added to existing vibration probes on large industrial gas turbines mainly for improved diagnostics.
DUAL PROBES	•Combined advantages of eddy current probes, and velocity pick-up or accelerometer. •Measures shaft and housing vibration separately, and can measure absolute shaft displacement.	•Combined disadvantages of eddy current probes, and velocity pick-ups or accelerometers.	Common on some large industrial gas turbines. Usually one probe per bearing, installed in vertical direction. Sometimes two probes 90° apart per bearing.

Table 2 Gas turbine vibration levels

	LARGE INDUSTRIAL GAS TURBINES WITH FLUID FILM BEARING		AIRCRAFT DERIVATIVE WITH ROLLING ELEMENT BEARINGS
	Shaft Measurement	Bearing Housing Measurement	Casing Measurement
Normal Vibration	0.5 - 3 mils	0.1 - 0.3 in/s	1 - 3 mils
Alarm Level	3 - 5 mils	0.5 - 1.0 in/s	2 - 5 mils
Shutdown Limit	6 - 10 mils	0.8 - 1.0 in/s	3 - 10 mils
Limit Multiplier for Unit Acceleration/Deceleration	1 - 3	1	2

NOTES:
•Larger vibrations are usually seen on industrial gas turbines with larger shaft-bearing clearances.
•Gas turbines with sharp critical speeds usually have higher limit multiplier for unit acceleration/deceleration.
•The highest vibration on the aircraft derivative gas turbine is usually seen on the gas generator, the lowest on the free turbine.

however, on machines where a mechanical defect has deteriorated to an unacceptable level, rapid growth in vibration and consequent failure can be expected.

Large industrial gas turbines are usually monitored on a continuous basis with vibration alarm and shutdown limits based on overall vibration level. To decrease the possibility of a catastrophic failure, an automatic machine shutdown is advisable, if the vibration shutdown limit is exceeded. However, some utilities, especially the ones that experience high rates of vibration control related problems, leave a final decision to plant personnel to decide on the exact course of action if the vibration level is above the shutdown limit. A summary of typical vibration levels for normal operation, and alarm and shutdown limits, as well as an additional correction factor (multiplier) for unit acceleration/deceleration, are given in Table 2. As indicated in the table, the industry practice of using mils or in/s (based on shaft rotating speed) varies, depending on the gas turbine type and measurement location.

To investigate the root cause of a vibration problem, a knowledge of overall vibration level alone is usually not adequate for determining the source of the vibration. In this case, the use of additional vibration monitoring equipment and vibration monitoring techniques is made; for example, the vibration frequency spectrum is checked to identify predominant frequency components and orders. Also, the shaft orbit is investigated to detect any irregularities (such as flattening or looping of the orbit), and shaft eccentricity may be checked to determine the rotor position in the bearing. In assessing changes in d-c output from eddy probes, it is important to note that temperature increase can contribute to a reduction in output voltage from eddy probe systems. Calibration curves at different temperatures should be reviewed when quantifying changes in shaft position.

Several utilities and the majority of petrochemical users have adopted some type of vibration monitoring program where gas turbine vibration data are recorded at regular intervals and vibration trends are established to watch for the rate of increase in vibration such that the corrective action can be planned in advance. Immediate action might be required if a sudden significant step change in vibration has occurred. Some companies also rely on sophisticated predictive maintenance programs in which vibration spectra are compared for trends and against a baseline spectrum, which is established when the machine is in good condition.

Cost of Vibration Monitoring

To justify a vibration predictive maintenance program on gas turbines, it is necessary to demonstrate the return on investment, i.e., show that the potential savings of the program offset the cost of the program.

The costs associated with the program include: purchase price and installation of the vibration monitoring equipment; labor and material cost for the vibration system maintenance and data handling; lost production due to nuisance gas turbine shutdowns attributable to vibration monitoring equipment malfunctions.

The potential savings of the vibration monitoring program

include: prevention of a catastrophic failure; reduced maintenance and downtime cost due to early identification; severity assessment of a vibration-related problem; orderly backtracking after a trip or failure; and reduced insurance costs.

The industry-wide survey of gas turbine users indicates that the plant personnel who are responsible for gas turbine equipment maintenance view vibration monitoring as an essential part of an overall machinery protection system. A general feeling among the gas turbine users is that at least a basic vibration monitoring system for trip protection should be installed on a gas turbine unit. Often the installation of an additional periodic vibration monitoring system or computerized continuous vibration monitoring system can be justified for base loaded or cogeneration units.

There are many instances when an appropriately set up vibration monitoring system and program provided an early indication of incipient machine failure or resulted in improved maintenance and allowed for an orderly machine shutdown. There are, of course, some instances when even the most sophisticated machinery vibration monitoring system failed to indicate a deteriorating machine condition or even a catastrophic failure (usually as a result of a blade loss).

Table 3 presents some typical costs of vibration monitoring systems, broken into three categories: basic vibration monitoring for trip protection, periodic vibration monitoring, and on-line computerized continuous vibration monitoring.

Table 3 Typical costs of gas turbine vibration monitoring systems

TYPE OF MONITORING SYSTEM	COST	COMMENTS
Basic Vibration Monitoring for Trip Protection	$600 to $900 per channel	Continuous analog protection, based on overall vibration level. Sensor cost not included.
Periodic Vibration Monitoring	$20,000 to $25,000 for a single data collector and a PC based data management system	Vibration spectrum data recorded at regular intervals-typically monthly comparison with baseline trends of data.
On-Line Computerized Continuous Vibration Monitoring	40 channel system: $1500 to $2000 per channel 500 channel system: $300 to $700 per channel	Regular storage of spectral information and trending; variety of displays including orbits, Nyquist, Bode, Waterfall. Cost does not include trip protection, monitor, and sensors.

The costs represent recent estimates and are presented as guidelines; accurate costs can only be developed when quotations are obtained from a supplier for a specific application. A basic vibration monitoring system for trip protection can shut down a turbine almost immediately the moment an excessive vibration is sensed. The other two types of vibration monitoring system will not respond immediately to a sudden change in vibration since they record vibration at some preset intervals, ranging from a few seconds to days. Periodic and computerized continuous vibration monitoring systems are mainly used as predictive maintenance tools for long-term trending of vibration and vibration problem diagnostics, supplementing the basic vibration monitoring system for trip protection.

Data Base Analysis

This section of the paper presents an analysis of relevant data from the ERAS data base compiled for five years, from Jan. 1982 to Dec. 1986. The ERAS data base consists of approximately 4500 gas turbine related outage records obtained from 13 plants with a total number of 28 turbines operating in combined cycles and 31 operating as peaking units. The importance of quantitative information on unavailability of a particular type of equipment and man-hours spent to repair a damaged component is well understood throughout the utility industry. Such information, if properly extracted and classified according to various mechanisms of gas turbine vibration-related outages, can serve as a valuable tool for identifying critical areas of vibration monitoring.

All the vibration-related outages were represented in the form of a hierarchical tree, as shown in Fig. 1, where vibration-related outages on gas turbines, generators, and auxiliaries were divided into the following categories:

1 Vibration controls consisting of a vibration probe (transducer, connector, cable) and a monitoring device.
2 Real vibration, caused by a machine malfunction.
3 Vibrations with cause undetermined.

Then, for each block and block group type in this tree, the

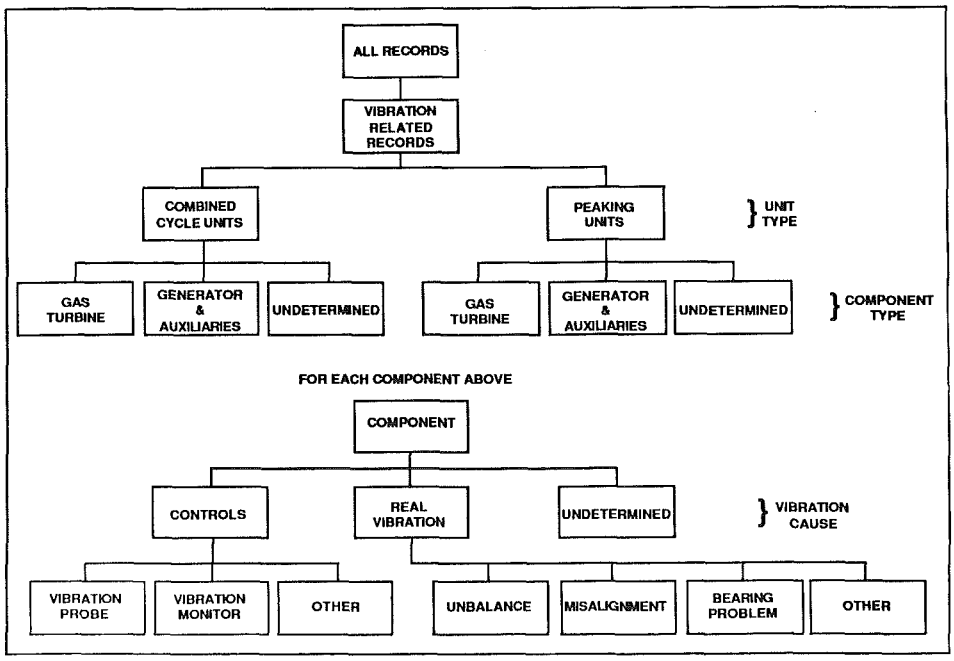

Fig. 1 Classification of ERAS data base outage record

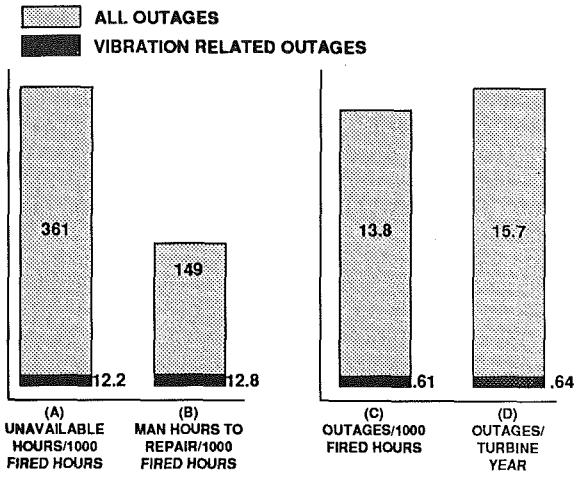

Fig. 2 Vibration-related outages versus all outages, computed from ERAS data base, 1982–1986

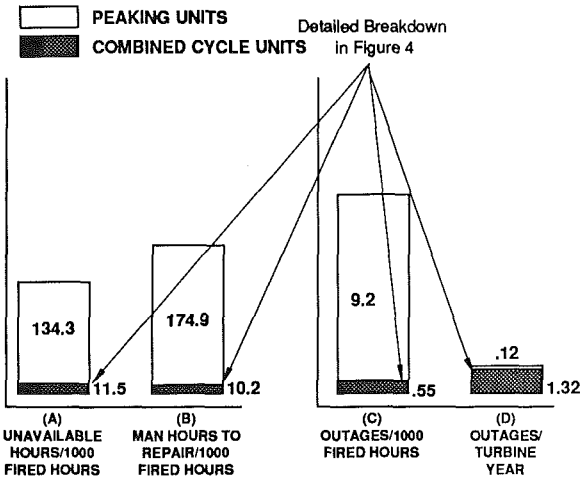

Fig. 3 Combined cycle unit outages versus peaking unit outages, computed from ERAS data base, 1982–1986

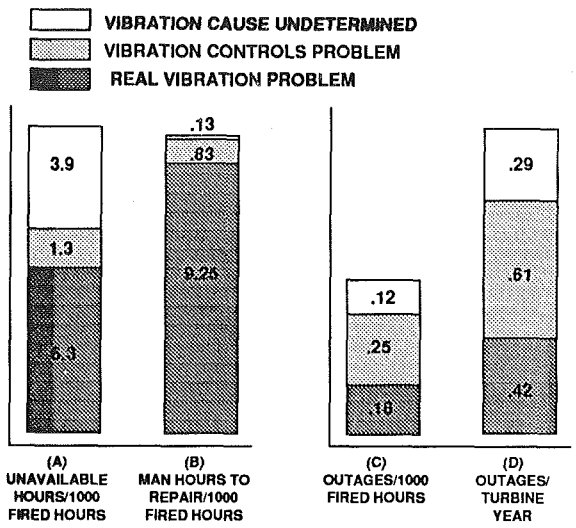

Fig. 4 Comparison of vibration-related outages for combined cycle units, computed from ERAS data base, 1982–1986

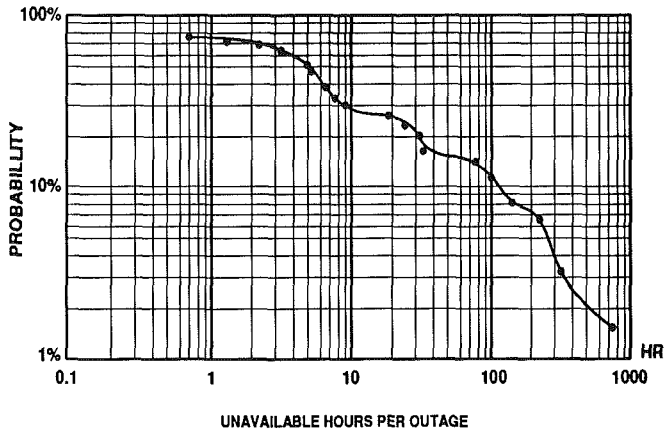

Fig. 5 Probability that unavailable hours per outage will be larger than curve value: real vibration

outage-related information was calculated including number of outages, man-hours to repair, and unavailable hours per turbine year, per 1000 fired hours, and per outage.

Figures 2, 3, and 4 present examples of the results of these calculations for complete gas turbine trains (gas turbine, its generator, and auxiliary equipment). They indicate:

- Vibration-related outages are responsible for approximately 3.3 percent of all unavailable hours (Fig. 2*a*) and 4.2 percent of all outages on gas turbines surveyed (Figs. 2*c* and 2*d*).
- In the survey, peaking units have significantly higher unavailability than combined cycle units (based on fired hours (Fig. 3*a*)).
- In the survey, the cause of vibration-related outages for combined cycle units remains undetermined in 22 percent of all cases (Figs. 4*c* and 4*d*), thus suggesting that the development of effective vibration diagnostic techniques would be beneficial.
- For combined cycle units, malfunctioning vibration controls (vibration probe, connector, cable, and monitor) are responsible for 45 percent of the vibration-related outages surveyed (Figs. 4*c* and 4*d*). However, it appears that this is mostly a nuisance-type problem since the number of unavailable hours per 1000 fired hours due to malfunctioning controls is quite small, 1.3, compared to unavailable hours due to "real" vibration problems, 6.3 (Fig. 4*a*). Also, it requires approximately 11 times more manpower to repair real vibration problems than to repair malfunctioning vibration controls (Fig. 4*b*).

Another way to judge the significance of a given outage is with respect to its duration. Figure 5 shows the cumulative distribution of unavailable hours per gas turbine outage as it relates to real vibration problems. At each point on this graph, a percentage of the outages (vertical axis), which is higher than a certain outage duration (horizontal axis) has been computed. For example, this cumulation distribution graph shows that approximately 10 percent of these outages had a duration of more than 100 hours.

Among real vibrations, imbalance has been found to be the most prevalent problem, but results include instances of misalignment, bearing failure, seal damage, etc.

It should be noted that the data presented here reflect experience from only 13 power plants and, as such, should be treated cautiously when applied to other installations. It is felt that information presented here is of conservative nature: The full outage duration and its severity might not be fully known at the time of reporting; sometimes vibration-related outages are not properly identified in the field due to lack of comprehensive vibration diagnostic equipment, and thus would fall into the other than vibration category when reported.

Examples of Vibration Monitoring Successes

A difficult task in justifying the gas turbine vibration pro-

grams is to obtain supporting case history data. The question is often asked by gas turbine users: *Can the vibration monitoring system prevent a catastrophic gas turbine failure?* Usually, the cost of a vibration monitoring system can be easily justified if only one catastrophic failure per gas turbine lifetime can be detected. For example, a catastrophic failure resulting in destruction of four turbine blade stages on an aero-derivative gas turbine could cost approximately $300,000 and the destruction of a single first-stage blade row on a large industrial gas turbine could cost $500,000. One of the ways to help answer this and related questions is to provide the user with examples of cases where a vibration monitoring system provided a beneficial protection.

(A) Prevention or Indication of Major Failures

1 An industrial gas turbine (approximately 50 MW) with two bearings exhibited increasingly high vibration measured by displacement probes during startup. Initially it would alarm regularly and trip occasionally. The situation worsened to where it tripped consistently on startup. On coastdown, rubbing was sometimes audible. On the basis of these vibration levels during startup the unit was opened up. It was found that a significant number of compressor blades had moved axially in the third stage and were rubbing against the adjacent diaphragm. The blades were still salvageable and, when they were locked back in place, the vibration problem during startup was eliminated; no rebalancing was necessary. Progressive development of this problem undetected would have led to fracture of a blade and a catastrophic failure, based on industry experience with similar problems.

2 The machine housing mounted gas turbine vibration monitoring system on an industrial gas turbine indicated high vibration at subsynchronous, synchronous, and twice synchronous (gas turbine) operating speed. Upon immediate machine shutdown and inspection, the problem was identified as a rub between the gas turbine rotor and the bearing inner surface. The rub was caused by carburization of the oil in the bearing due to a damaged seal that was leaking excessively.

3 A sudden excessive increase in overall vibration was noticed on an aero-derivative gas turbine. The cause of vibration was traced to an oil tube rubbing against the rotating gas turbine shaft. If this problem had gone unnoticed, the oil tube would most probably have ruptured, causing extensive bearing damage due to loss of oil supply to the bearing and/or possible fire.

4 An aircraft derivative gas turbine unit was vibrating excessively during startup, with the highest vibration level present at the rotor synchronous speed. Inspection showed extensive blade damage, which would probably have gotten progressively worse, leading eventually to blade failure.

5 After overhaul, an industrial gas turbine tripped on high vibration. After taking the machine apart, it was determined that the antirotation bearing pin had been left off the compressor end bearing. The bearing rotated and blocked off the supply of oil, which caused the bearing to fail. The rotor had dropped as a result and caused minor damage to the blades, but they were still usable. After the bearing was replaced, the unit started satisfactorily.

6 During a startup of an aero-derivative gas turbine, high vibration, well above the baseline vibration level commonly seen on this type of unit, was recorded. The unit was shut down immediately and upon disassembly it was found that some of the blade tips were damaged by rubbing. The blade rubs were attributed to creep of the blade material. Based on previous experience with this type of turbine, this rub, if undetected, would have led to a catastrophic failure of the high-speed turbine.

7 An eddy current, noncontact vibration transducer installed on a gas turbine generator outboard bearing indicated high vibration, suggesting a rotor-bearing clearance increase. Upon inspection, the babbitt was found to be wiped out. Subsequent investigation revealed that the gas turbine and the generator had been misaligned.

8 During a startup, a large industrial gas turbine tripped on high vibration, detected by noncontact vibration transducers; the vibration sensed by a seismic probe remained below alarm levels. Later investigation revealed that a large portion of a metal plate had been inadvertently left in the gas turbine coupling. Apparently, the machine shutdown was initiated quickly enough not to cause any significant damage; upon removal of the plate, the machine was successfully brought on-line.

9 On a large industrial gas turbine, a significant step change in vibration was indicated by a dual vibration probe. To reduce the vibration, the unit was balanced but no thorough investigation of the problem was performed. Six months later, four compressor blades were lost. Plant maintenance personnel strongly believe that this failure could have been prevented if the appropriate corrective actions had been taken after the step change in vibration occurred.

10 A large industrial gas turbine experienced a large step change in vibration; the unit tripped at 8 mils at 2900 rpm before reaching running speed. After the vibration trip was raised, the unit was vibrating at 12 mils at running speed. The vibration was brought down to 2 mils by balancing but the unit was neither disassembled nor checked by borescope. After the incident, the gas turbine was run for three years until another step change in vibration occurred, which was attributed to flexing of the marriage coupling between the compressor and the turbine. Upon disassembly of the unit, it was discovered that the first and second-stage gas turbine blades were damaged. It is believed that foreign objects damaged these blades three years ago when the problem was first discovered.

11 On over ten different occasions, the exhaust bearing on large industrial gas turbines in combined cycle service was wiped out by overload caused by misalignment. Velocity probes only were installed on these machines and did not indicate a problem. If noncontact proximity probes had been installed in an X–Y arrangement it would have significantly increased chances for identifying these misalignment problems from the highly elliptical bearing vibration orbit for this bearing.

(B) Improved Maintenance and Availability

1 Several cases of deteriorating bearing conditions due to wear and increased clearances were identified by velocity pickups installed on a medium-sized industrial gas turbine in utility service (approximately 25 MW). Such successful identification of the bearing-related problems is attributed to an orderly vibration monitoring program, which provided for a trend comparison of vibration spectrum on a six-month interval basis.

2 Eddy current noncontact displacement probes installed on a large industrial gas turbine indicated that the bearing orbit was more flattened than normal; vibration also substantially increased at twice running speed frequency. Upon investigation, it was determined that the cooling water had not been turned on for the gas turbine water-cooled legs. After the water was turned on, the orbits became less flattened and vibration at twice running speed frequency decreased.

3 An aircraft derivative gas turbine tripped on high vibration. The reason for the trip was that the gas turbine sliding mounts locked up due to hardening of grease in the joint. When the sliding mounts were refilled with new grease, the vibration symptoms went away. In this case, vibration monitoring indicated a need for maintenance, which would otherwise have overloaded the bearings and probably shortened their life. A similar incident, with increase in vibration due to lock-up of the sliding mounts, and similar corrective action, was reported by another utility.

4 Eddy current noncontact displacement probes installed

on an in-board bearing of a large gas turbine generator indicated an excessive 7 to 8 mil vibration. Since the gas turbine could not be conveniently shut down, the decision was made to operate the machine at reduced load to bring vibration to an acceptable level. This was a steadily deteriorating situation, and after several months, the minimum acceptable load was reached. At this time the unit was overhauled and it was determined that the bearing had been steadily destroying itself by breaking out pieces of babbitt. Replacement of the bearing eliminated the problem.

5 A step change in vibration from 3 mils to 6 mils was indicated by an eddy current probe installed on the exhaust bearing of a large industrial gas turbine. Gas turbine blade damage was suspected, but the unit was critical to the chemical plant performance, and therefore the decision was made to keep the unit on line and watch closely for any other changes in vibration signals. No other changes in vibration were noticed and the machine was in service for the next three months before undergoing a scheduled maintenance shutdown. Upon unit disassembly, it was determined that the vibration problem was a result of partial blade loss at the last turbine stage.

6 Several utilities and petrochemical companies reported that there are numerous cases when gas turbine and generator unbalance problems were successfully identified through the use of gas turbine vibration monitoring. In several instances, misalignment between a gas turbine and generator was successfully identified from changes in the orbits of in-board end bearings of the generator and turbine, and the changes in the rotor static position with respect to bearing clearances.

Summary and Discussion

The industry-wide survey of gas turbine users indicates that vibration monitoring is an essential part of an overall machinery protection system. The survey further shows that at least a basic vibration monitoring system should be installed on a gas turbine unit. There are many instances when an appropriately set up vibration monitoring system and program provided an early indication of incipient machine failure or resulted in improved maintenance and allowed for an orderly machine shutdown.

High temperatures of gas turbine compartments impose additional requirements on selection of a vibration transducer and its attached cable and connector; inappropriate transducer application can often lead to nuisance shutdowns due to malfunctioning vibration equipment.

Statistical data on typical vibration levels and limits have been provided in the paper. However, there are no absolute limits that will assure successful long-term operation nor firm upper limit that will cause failure for any specific gas turbine. An important factor to recognize in applying vibration limits is growth of vibration amplitudes with time. On machines where a mechanical defect has deteriorated to an unacceptable level, rapid growth in vibration and consequent failure can be expected.

Analysis of the ERAS data base indicates that vibration-related outages significantly affect gas turbine units availability; peaking units have a higher unavailability rate than combined cycle units; control problems are responsible for almost half of the vibration-related gas turbine outages, but represent just a small fraction of the overall unavailable hours.

As Fig. 5 shows, 10 percent of vibration problems can cause over 100 hours unavailability, and a few vibration problems cause 300 hours or more. If a vibration monitoring system can be designed to anticipate and manage these problems effectively, then it becomes a valuable component of a predictive maintenance program.

Acknowledgments

This paper is based on results of a recent project sponsored by the Electric Power Research Institute (EPRI).

The authors are also indebted to many representatives of electric utility and petrochemical industries, as well as gas turbine and vibration equipment suppliers, who devoted time to contribute to our survey both in written responses and verbal discussions.

References

Benett, R. R., Riedel, H. J., and Kruck, J. E., 1980, "Application Survey/Evaluation of Gas Turbine Needs," EPRI AF-911, Project 990-1.

Bloch, H. R., and Geitner, F. K., 1985, *Major Process Equipment Maintenance and Repair*, Gulf Publishing Company, Book Division.

Brandt, D. E., 1987, "The Design and Development of Advanced Heavy Duty Gas Turbine," ASME Paper No. 87-GT-14.

Brown, M., and Young, R., 1984, "Development of an EPRI Reliability Assessment System (ERAS), for Combined Cycle Power Plants," EPRI AP-3420, Project 990-7, Mar.

Catina, J. L., and Fortune, H. J., 1987, "Repowering Chesterfield 1 and 2 With Combined Cycle," ASME Paper No. 87-GT-2.

Chellini, R., 1986, "Repowering a Steam Power Plant With a Gas Turbine," *Diesel & Gas Turbine Worldwide*, Oct.

Grenstad, P. E., Smith, M. J., and Duncan, R. L., 1982, "A Baseload Gas Turbine to Meet Utility Requirements for Reliability and Availability," ASME JOURNAL OF ENGINEERING FOR POWER, Vol. 104, Apr.

McHugh, 1983, "Vibration Measurements—Principles and Practice as Applied to General Electric Heavy Duty Gas Turbines," *Proceedings of Vibration Institute*, Vibration Monitoring and Analysis.

Murray, B. G., and Reid, A., 1986, "Vibration Based Condition Monitoring in the Ninian Field," *International Conference on Condition Monitoring*, Brighton, United Kingdom.

Myrick, S. T., 1982, "Survey Results on Condition Monitoring in the Petrochemical Industry," *Proceedings of Vibration Monitoring and Analysis Meeting*.

Ricca, P. M., and Bradshaw, P. M., 1984, "How Trans-Alaska Pipeline System's Rotating Machinery Maintenance Program Evolved," *Oil and Gas Journal*, Aug.

Shepard, M., 1986, "Evolution in Combustion Gas Turbines," *International Turbomachinery*, Nov./Dec.

Simmons, H. R., and Lifson, A., 1985, "Vibration Measurements for Determining Plant Component Reliability," *Proceedings of American Power Conference*, Chicago, IL, Apr. 23–25.

Waldman, B., 1986, "Power Generation Survey," *Diesel & Gas Turbine Worldwide*, Oct.

A. B. Palazzolo
Assistant Professor.

R. R. Lin
Research Assistant.

Texas A&M University,
Department of Mechanical Engineering,
College Station, TX 77843

A. F. Kascak
NASA Lewis Research Center,
Cleveland, OH 44135

R. M. Alexander
Associate Professor,
Texas A&M University,
Department of Mechanical Engineering,
College Station, TX 77843

Active Control of Transient Rotordynamic Vibration by Optimal Control Methods

Although considerable effort has been put into the study of steady-state vibration control, there are few methods applicable to transient vibration control of rotor-bearing systems. In this paper optimal control theory has been adopted to minimize rotor vibration due to sudden imbalance, e.g., blade loss. The system gain matrix is obtained by choosing the weighting matrices and solving the Riccati equation. Control forces are applied to the system via a feedback loop. A seven mass rotor system is simulated for illustration. A relationshp between the number of sensors and the number of modes used in the optimal control model is investigated. Comparisons of responses are made for various configurations of modes, sensors, and actuators. Furthermore, spillover effect is examined by comparing results from collocated and noncollocated sensor configurations. Results show that shaft vibration is significantly attenuated in the closed-loop system.

Introduction

Rotating machinery may experience dangerously high dynamic loading due to the sudden mass imbalance associated with blade loss. For example, the recent destruction of a 300-MW turbine generator set in Texas was blamed on excessive bearing loads due to loss of a blade from the final rows of the LP turbine. The objective of this research is to investigate the capability of optimal control method to suppress rotor vibrations caused by sudden mass imbalance.

Pilkey (1976) described an optimal design technique for rotating shafts based on limiting performance. This would provide optimal active stiffness and damper values for an active control loop. This method, however, requires a priori knowledge of the forcing function. Heinzmann (1980) developed an active vibration control rig for steady-state vibration. No specific control algorithm was presented, i.e., active damping and stiffness (derivative and proportional feedback) were manually tuned in by an operator. Allaire (1981, 1983) developed an analytical model of an actively controlled Jeffcott rotor on rigid supports. The active dampers and stiffness were assumed to be manually tuned to control steady-state vibration. He extended this work to include a flexibly mounted Jeffcott rotor.

Stanway (1984) utilized state variable feedback eigenstructure assignment to control a six degree-of-freedom Jeffcott type rotor model. The responses at all degrees of freedom must be measured. Nonami (1985) utilized state feedback, optimal control, and modal space velocity feedback to suppress steady-state (synchronous) rotor vibrations. Reinig and Desrochers (1986) developed an approach to identify and counteract the imbalance force in a Jeffcott rotor with rigid bearings. The controlled vibrations were steady state, and transient due to acceleration through a critical speed. Feng (1986) developed an active vibration control scheme with actuator forces from varying bearing oil pressure.

Salm and Schweitzer (1984) examined modal space-output feedback-optimal control. Spillover effects in the reduced order model were presented. The authors show how stability of the closed-loop system is assured if the sensors and actuators are collocated (i.e., every actuator occurs at a sensor location) and if the stiffness and damping feedback gain matrices are positive definite. The control strategy is addition of modal damping and stiffness values, and the examples presented treat steady-state response. The method presented in the paper is similar to Salm and Schweitzer but is applied to transient rotor vibration.

Effort are now being undertaken to design and test an active vibration control system to suppress vibrations that would occur following blade loss in an aircraft gas turbine engine. The laboratory tests utilize noncontacting eddy current probes for sensing displacement and velocities (differentiated displacements), and piezoelectric pushers to apply forces through the squirrel cage bearing supports. Work is also planned to develop advanced pushers to operate effectively in the high-temperature environment of the gas turbine. Results of this research will be presented in future papers.

Theory

Optimal Control. The matrix differential equation for a rotor bearing system including control forces can be expressed as

Contributed by the International Gas Turbine Institute and presented at the 33rd International Gas Turbine and Aeroengine Congress and Exhibition, Amsterdam, The Netherlands, June 5-9, 1988. Manuscript received by the International Gas Turbine Institute January 1, 1988. Paper No. 88-GT-73.

$$[M]_{(N\times N)}\{\ddot{Z}\}_{(N\times 1)} + [C_D]_{(N\times N)}\{\dot{Z}\}_{(N\times 1)} + [K]_{(N\times N)}\{Z\} = \{F_D(t)\}_{(N\times 1)} + [\tilde{B}]_{(N\times M)}\{U\}_{(M\times 1)} \quad (1)$$

where N and M are the number of degrees of freedom and the number of actuators, respectively. The $[M]$, $[C_D]$, and $[K]$ matrices are the rotor-bearing system mass, damping, and stiffness matrices as defined by Palazzolo (1983). We substitute the modal transformation

$$\{Z\}_{(N\times 1)} = [\Phi]_{(N\times t)}\{\xi\}_{(t\times 1)} \quad (2)$$

where t is the number of modes used in modal space control. Utilize orthogonality conditions assuming a proportionately damping system to obtain

$$\{\ddot{\xi}\} + [\mathrm{diag}(2\zeta_i\Omega_i)]\{\dot{\xi}\} + [\mathrm{diag}(\Omega_i^2)]\{\xi\} = [\Phi]^T[\tilde{B}]\{U\} + [\Phi]^T\{F_D\} \quad (3)$$

where the mode shapes have been orthonormalized

$$[\Phi]^T[M][\Phi] = [I]_{(t\times t)} \quad (4)$$

Equation (3) can be written as a first-order (state space) form by adding an identity equation as follows:

$$\begin{bmatrix} [I_t] & \vdots & [0] \\ \cdots & \cdots & \cdots \\ [0] & \vdots & [\mathrm{diag}(-\Omega_i^2)] \end{bmatrix} \begin{Bmatrix} \{\ddot{\xi}\} \\ \cdots \\ \{\dot{\xi}\} \end{Bmatrix} + \begin{bmatrix} [\mathrm{diag}(2\zeta_i\Omega_i)] & \vdots & [\mathrm{diag}(\Omega_i^2)] \\ \cdots & \cdots & \cdots \\ [\mathrm{diag}(\Omega_i^2)] & \vdots & [0] \end{bmatrix} \begin{Bmatrix} \{\dot{\xi}\} \\ \cdots \\ \{\xi\} \end{Bmatrix} = \begin{Bmatrix} [\Phi]^T[\tilde{B}]\{U\} \\ \cdots \\ [0] \end{Bmatrix} + \begin{Bmatrix} [\Phi]^T\{F_D\} \\ \cdots \\ [0] \end{Bmatrix} \quad (5)$$

By multiplying equation (5) by the inverse matrix of the leading coefficient matrix and writing in abbreviated notation, it becomes

$$\{\dot{X}\}_{(2t\times 1)} = [A]_{(2t\times 2t)}\{X\}_{(2t\times 1)} + [B_F]_{(2t\times N)}\{F_D\}_{(N\times 1)} + [B_U]_{(2t\times M)}\{U\}_{(M\times 1)} \quad (6)$$

where

$$[A]_{(2t\times 2t)} = \begin{bmatrix} [\mathrm{diag}(-2\zeta_i)] & \vdots & (\mathrm{diag}(-\omega_i^2)] \\ \cdots & \cdots & \cdots \\ [I_t] & \vdots & [0] \end{bmatrix} \quad (7)$$

$$[B_F]_{(2t\times N)} = \begin{bmatrix} [\Phi]^T \\ \cdots \\ [0] \end{bmatrix}, \qquad [B_U]_{(2t\times M)} = \begin{bmatrix} [\Phi]^T[\tilde{B}] \\ \cdots \\ [0] \end{bmatrix},$$

$$\{X\}_{(2t\times 1)} = \begin{Bmatrix} \{\dot{\xi}\} \\ \cdots \\ \xi \end{Bmatrix} \quad (8)$$

Since it is not practical to measure the displacement and velocity at all the system degrees of freedom (dof), an observer system may be constructed to estimate the state vector from a smaller number of measurements. This approach, however, may not be feasible for a rotordynamic system, which involves high frequencies that prohibit real time state estimation. Another approach to control is output feedback, i.e., limit the measurements to those defined in the output vector $\{Y\}$, which can be expressed as

$$\{Y\}_{(r\times 1)} = [C_S]_{(r\times 2N)} \begin{Bmatrix} \{\dot{Z}\} \\ \cdots \\ \{Z\} \end{Bmatrix}_{(2N\times 1)} \quad (9)$$

The output feedback control force is defined by

$$\{U\}_{(M\times 1)} = -[G']_{(M\times r)}\{Y\}_{(r\times 1)} \quad (10)$$

Substituting equation (9) into equation (10) and converting this equation to modal space with equation (2) yields

$$\{U\}_{(M\times 1)} = -[G'][C_S] \begin{bmatrix} [\Phi] & \vdots & (0) \\ \cdots & \cdots & \cdots \\ [0] & \vdots & [\Phi] \end{bmatrix} \begin{Bmatrix} \{\dot{\xi}\} \\ \cdots \\ \{\xi\} \end{Bmatrix} \quad (11)$$

or in abbreviated notation

$$\{U\}_{(M\times 1)} = -[\tilde{G}]_{(M\times 2t)}\{X\}_{(2t\times 1)} \quad (12)$$

where

$$[\tilde{G}]_{(M\times 2t)} = [G'][C_S] \begin{bmatrix} [\Phi] & \vdots & [0] \\ \cdots & \cdots & \cdots \\ [0] & \vdots & [\Phi] \end{bmatrix} \quad (13)$$

The objective of output feedback control in modal space can now be identified as obtaining the gain matrix $[G']$ in equation (10) that reduces the modal coordinates ξ_i in equation (2).

Nomenclature

$[\tilde{B}]$ = coefficient matrix of control force matrix
$[A]$ = coefficient matrix associated with $\{X\}$
$[B_F]$ = coefficient matrix associated with $\{F_D\}$
$[B_U]$ = coefficient matrix associated with $\{U\}$
$[C_D]$ = proportional damping matrix
$[C_F]$ = feedback damping matrix
$[C_S]$ = matrix associated with sensor locations
e_1 = eccentricity
F_i = imbalance forces due to mass imbalance
$\{F_D(t)\}$ = external forces (disturbance)
$[G']$ = system gain matrix
$[I]$ = identity (unity) matrix
I_P = polar moment of inertia
I_T = moment of inertia
$\min J$ = minimize the performance index J
$[K]$ = stiffness matrix
$[K_F]$ = feedback stiffness matrix
M = number of actuators
$[M]$ = mass matrix
N = number of degrees of freedom
$[P]$ = matrix solution from Riccati equation
$[Q]$ = weighting matrix associated with state vector
r = number of observer's output
$[R]$ = weighting matrix associated with control vector
t = number of modes used
$\{U\}$ = control force matrix
$\{X\}$ = state vector
$\{Y\}$ = output vector
$\{Z\}$ = space coordinates
ζ_i = ith modal damping
$\{\xi\}$ = modal coordinates
$[\Phi]$ = mode shape matrix
$[\Phi]^T$ = transpose of mode shape matrix
$[\Omega_i]$ = ith natural frequency
$[\mathrm{diag}(\ )]$ = diagonal matrix

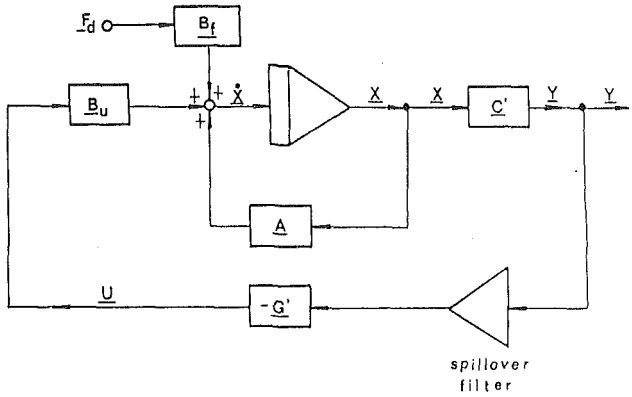

Fig. 1 Output feedback diagram

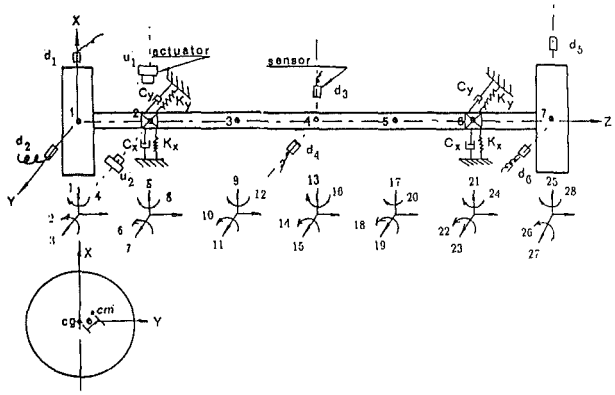

Fig. 2 Schematic diagram for the seven mass rotor model

The linear quadratic regulator problem goes one step further and also seeks simultaneously to reduce the required control forces $\{U_i\}$. The performance index to be minimized is defined as

$$\min J = \min \int_0^\infty (\{X\}^T [Q] \{X\} + \{U\}^T [R] \{U\}) dt \tag{14}$$

where $[Q]$ and $[R]$ are symmetric, positive-definite weighting matrices that govern the relative importance of minimizing the modal coordinates ξ_i and the actuator force U_K. As will be shown in the results section, diminishing $[R]$ will result in larger actuator forces but smaller vibrations (governed by the ξ_i). Optimal control theory produces the solution for equation (14) in the form of equation (12). The gain matrix $[\tilde{G}]$ is computed from

$$[\tilde{G}]_{(M\times 2t)} = [R]^{-1}_{(M\times M)} [B_U]^T_{(M\times 2t)} [P]_{(2t\times 2t)} \tag{15}$$

and the matrix $[P]$ is obtained as the solution matrix to the algebraic (steady-state) Riccati equations (10) and (11). The steady-state (algebraic) Ricatti equation is

$$[P][A] + [A]^T[P] - [P][B_U][R]^{-1}[B_U]^T[P] + [Q] = [0]_{(2t\times 2t)} \tag{16}$$

where the matrices $[P]$, $[A]$, and $[Q]$ are $2t$ by $2t$, the matrix $[B_U]$ is $2t$ by M, and the matrix $[R]$ is M by M.

In order to solve equation (13) exactly for $[G']$, the number of measured outputs (i.e., r is the sum of velocities and displacements) must be equal to twice the number of modes t used for the modal space. We define the matrix $[\beta]$ as

$$[\beta]_{(r\times 2t)} = [C_S]_{(r\times 2N)} \begin{bmatrix} [\Phi] & \vdots & [0] \\ \cdots & \cdots & \cdots \\ [0] & \vdots & [\Phi] \end{bmatrix}_{(2N\times 2t)} \tag{17}$$

Assuming that $r = 2t$ and $[\beta]$ is nonsingular, the gain matrix $[G']$ can be derived from equations (13) and (15) as

Table 1 Numerical values of seven mass rotor model

Nodes	Weight (N)	I_T^1 $(N\times m^2)$	I_P^2 $(N\times m^2)$	Z^3 (m)
1	14.3	0.01476	0.02571	0.0
2	11.74	0.0034	0.0	0.067
3	4.67	0.0057	0.0	0.186
4	4.67	0.0057	0.0	0.306
5	4.67	0.0057	0.0	0.426
6	11.74	0.0034	0.0	0.545
7	14.3	0.01476	0.02571	0.612

I_T^1 : Moment of inertia (note weight has been used)
I_P^2 : Polar moment of inertia
Z^3 : Node location in Z-axis

Table 2 Connectivity between elements of seven mass rotor model

Element	Length (m)	Weight (N)	Connect	Diameter (m)
1	0.067	2.61	1-2	0.0254
2	0.119	4.67	2-3	0.0254
3	0.119	4.67	3-4	0.0254
4	0.119	4.67	4-5	0.0254
5	0.119	4.67	5-6	0.0254
6	0.067	2.61	6-7	0.0254

E : $20\times 10^{10} N/m^2$
K_x : $830,000 N/m$
K_y : $875,500 N/m$
C_B : $C_x = C_y = 0 N sec/m$
ρ : $0.07685 N/cm^3$
Mass : 1.458 K_g
e : 1.168×10^{-4} m
me : $1.703\times 10^{-4} K_g$ m

$$[G'] = [R]^{-1}[B_U]^T[P][\beta]^{-1} \tag{18}$$

The actuator forces can then be obtained from equation (10). Combining equations (1), (9), and (10), the closed-loop matrix differential equation is

$$[M]_{(N\times N)}\{\ddot{Z}\}_{(N\times 1)} + [[C_D] - [C_F]]_{(N\times N)}\{\dot{Z}\}_{(N\times 1)} + [[K] - [K_F]]_{(N\times N)}\{Z\}_{(N\times 1)} = \{F_D(t)\} \tag{19}$$

where

$$\left[[C_F]_{(N\times N)} \vdots [K_F]_{(N\times N)}\right] = -[\tilde{B}][G'][C_S] \tag{20}$$

Equation (19) was numerically integrated with the Newmark-Beta algorithm to obtain the exact response of the controlled system, and was also integrated in a reduced modal space utilizing the closed-loop system left and right eigenvectors. The latter method was utilized to simulate the control system as shown in Fig. 1, with the ideal spillover filter included. Spillover represents the response that occurs in the modes that are not included in the modal space defined in equation (2). These modes may have unstable eigenvalues, hence the filter is used to exclude higher mode contribution from the feedback loop.

Results

A seven mass rotor with two bearings was used for illustration. Figure 2 shows the rotor system including 6 elements and 7 nodes (stations), with 28 degrees of freedom (dof). The rotor

Table 3 Open loop eigenvalues

No.	Real part	Imag. part
1	-0.194665E-14	-0.465082E+03
2	-0.194665E-14	0.465082E+03
3	-0.206636E-15	-0.493915E+03
4	-0.206636E-15	0.493915E+03
5	-0.308827E-13	-0.477361E+03
6	-0.308827E-13	0.477361E+03
7	0.139397E-13	-0.507092E+03
8	0.139397E-13	0.507092E+03
9	-0.142756E-13	-0.102633E+04
10	-0.142756E-13	0.102633E+04
11	0.000000E+00	-0.102643E+04
12	0.000000E+00	0.102643E+04
13	0.932140E-13	-0.280367E+04
14	0.932140E-13	0.280367E+04
15	0.213304E-12	-0.280527E+04
16	0.213304E-12	0.280527E+04
17	0.620382E-12	-0.478415E+04
18	0.620382E-12	0.478415E+04
19	0.620680E-12	-0.478530E+04
20	0.620680E-12	0.478530E+04

Table 4 Closed-loop eigenvalues of noncollocated configuration

No.	Real part	Imag. part
1	-0.159297E+02	-0.491694E+03
2	-0.159297E+02	0.491694E+03
3	-0.779224E+02	-0.485348E+03
4	-0.779224E+02	0.485348E+03
5	-0.153775E+02	-0.478988E+03
6	-0.153775E+02	0.478988E+03
7	-0.782901E+02	-0.472411E+03
8	-0.782901E+02	0.472411E+03
9	-0.735068E+01	-0.102632E+04
10	-0.735068E+01	0.102632E+04
11	-0.723941E+01	-0.102622E+04
12	-0.723941E+01	0.102622E+04
13	0.185242E+02	-0.280946E+04
14	0.185242E+02	0.280946E+04
15	0.185190E+02	-0.280780E+04
16	0.185190E+02	0.280780E+04
17	0.637900E+02	-0.478278E+04
18	0.637900E+02	0.478278E+04
19	0.636873E+02	-0.478169E+04
20	0.636873E+02	0.478169E+04

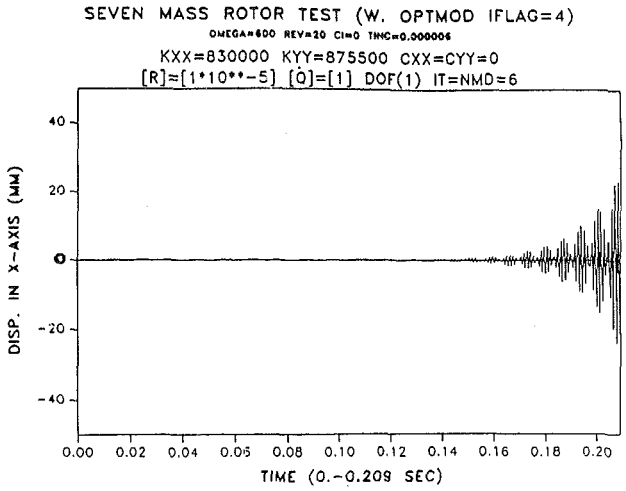

Fig. 3 Response history at dof 1 with direct integration method

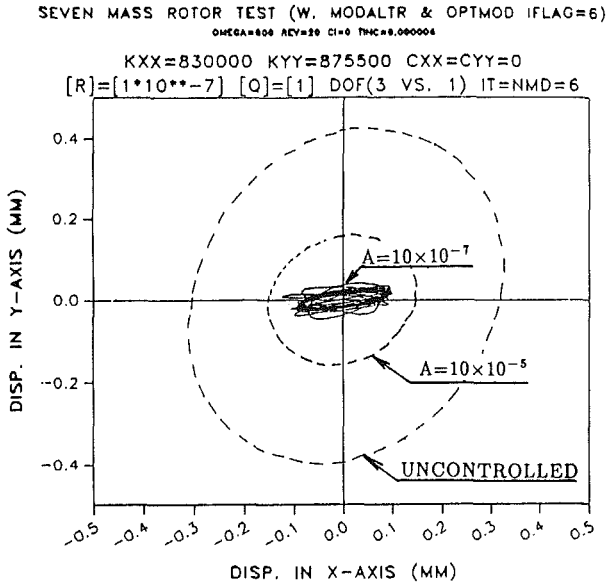

Fig. 4 Orbit at node 1 (dof 3 versus dof 1) with noncollocated case

geometric and material properties are listed in Table 1 and Table 2.

The eccentricity at station 1 is used to simulate the mass imbalance incurred due to a sudden blade loss. The resulting external forces at dof 1 and 3 are

$$F_1(t) = \begin{cases} 0. & t<0 \\ m_1 e_1 \omega^2 \cos(\omega t) & t \geq 0 \end{cases}$$

$$F_3(t) = \begin{cases} 0. & t<0 \\ m_1 e_1 \omega^2 \cos(\omega t - 90 \text{ deg}) & t \geq 0 \end{cases}$$

$$F_j(t) = 0 \text{ for } j \neq 1 \text{ or } 3 \qquad (21)$$

where

$$m_1 e_1 = 1.458\text{kg} \times 1.168 \times 10^{-4}\text{m} = 1.703 \times 10^{-4}\text{kgm}$$

The rotor model includes rotary inertia but not shaft gyroscopics, which were insignificant in this case.

Uncontrolled Case. The rotor is simulated to run at two different speeds: 5730 rpm (600 rad/sec) and 12,500 rpm (1309 rad/sec). The transient response was performed by direct integration and by modal superposition, utilizing the 12 lowest eigensolutions shown in Table 3. The direct integration was performed with Newmark-Beta parameters of $\alpha = 0.25$ and $\delta = 0.5$. The integration time step is 0.000006 s (1/1745 and 1/800 revolution, respectively). The response results of direct integration were nearly identical to those yielded by the modal superposition. These results are compared with the controlled cases as described below.

Optimal Control (Modal Space) Output Feedback

Noncollocated Case. The optimal control approach discussed above was applied to several test cases. Six sensors are located at dofs 1, 3, 13, 15, 25, and 27, and two actuators are placed at dofs 5 and 7, as shown in Fig. 2. Since no sensor is placed at the actuator locations, this is a noncollocated test case.

Each sensor measures velocity and displacement; thus there are 12 independent outputs (i.e., $r = 12$ as in equation (9)). This implies that the dimension of the modal subspace must be

Table 5 Closed-loop eigenvalues of optimal control with collocated sensors

No.	Real part	Imag. part
1	-0.213979E+03	0.000000E+00
2	-0.229033E+03	0.000000E+00
3	-0.145775E+02	-0.478939E+03
4	-0.145775E+02	0.478939E+03
5	-0.150392E+02	-0.491641E+03
6	-0.150392E+02	0.491641E+03
7	-0.330121E+02	-0.103083E+04
8	-0.330121E+02	0.103083E+04
9	-0.149928E+04	0.000000E+00
10	-0.331793E+02	-0.103086E+04
11	-0.331793E+02	0.103086E+04
12	-0.147189E+04	0.000000E+00
13	-0.642707E+03	-0.287230E+04
14	-0.642707E+03	0.287230E+04
15	-0.641128E+03	-0.287890E+04
16	-0.641128E+03	0.287890E+04
17	-0.578606E+03	-0.448046E+04
18	-0.578606E+03	0.448046E+04
19	-0.578854E+03	-0.448510E+04
20	-0.578854E+03	0.448510E+04

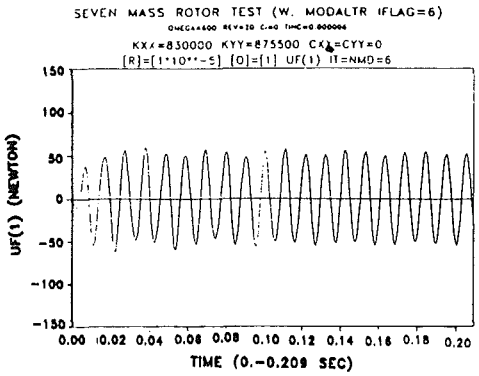

(a) $A=10^{-5}$

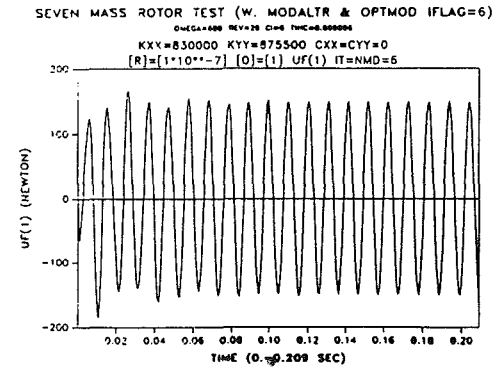

(b) $A=10^{-7}$

Fig. 5 Force history of actuator 1 with noncollocated case

equal to 6, by condition on $[\beta]$ in equation (18). The performance index weighting matrices $[Q]$ and $[R]$ were

$$[Q] = [I]_{12\times 12} \quad [R] = A \times [I]_{2\times 2} \tag{22}$$

where the constant A has been arbitrarily assigned to be 10^{-3}, 10^{-5}, and 10^{-7}.

The equations of motion were solved by direct integration and some of the results are shown in Fig. 3, which shows the

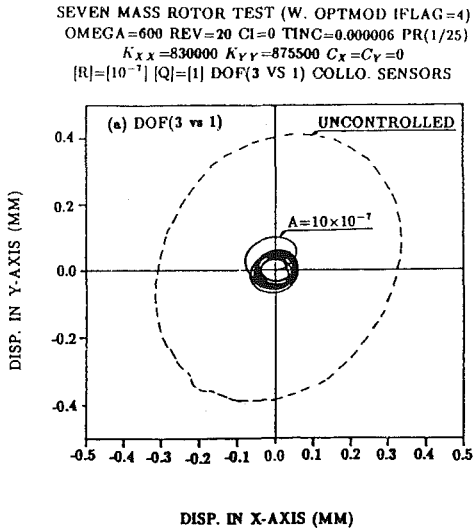

Fig. 6 Orbit at node 1 (dof 3 versus dof 1) with collocated case

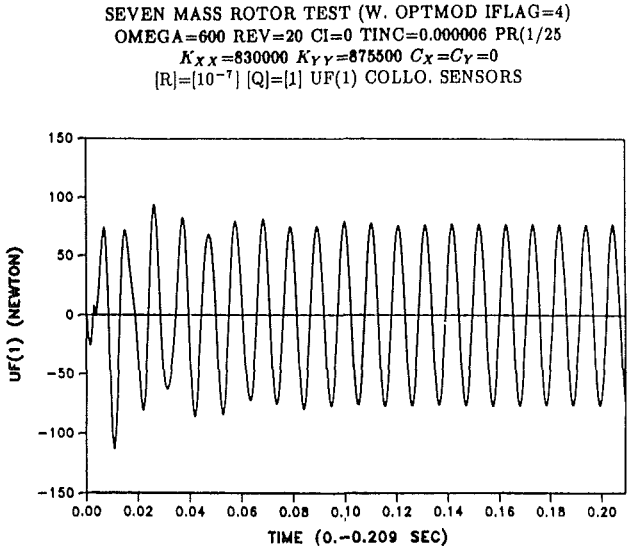

Fig. 7 Force history of actuator 1 with collocated case

response at dof 1. The motion is unstable, as can be verified by inspecting the closed-loop eigenvalues as shown in Table 4.

The modal superposition method was employed to simulate the closed-loop system, including an ideal low pass filter to eliminate response contributed from the higher modes. This filter is labeled as a spillover filter in Fig. 1. The results are shown in Fig. 4, which contains the response at dof 1 and 3. It shows that the shaft vibration is significantly reduced with optimal control. Note as A decreases from 10^{-5} to 10^{-7} so does the maximum vibration. Figure 5 shows that the actuator forces increases as A decrease. The actuator forces are less than 150 N and the vibration orbit at node 1 has been reduced from 0.45 mm to 0.15 mm.

Collocated Case. Although the shaft vibration has been successfully attenuated by filtering in the noncollocated test cases, the system is unstable without filtering as verified by the closed-loop eigenvalues. Following suggestions made in Salm and Schweitzer (1984) the closed-loop system was stabilized by collocating one pair of sensors with the actuators. This was accomplished by relocating the sensors to dofs 1, 3, 5, 7, 25, and 27 while keeping the actuators at dofs 5 and 7. The closed-loop system becomes stable so direct integration was employed,

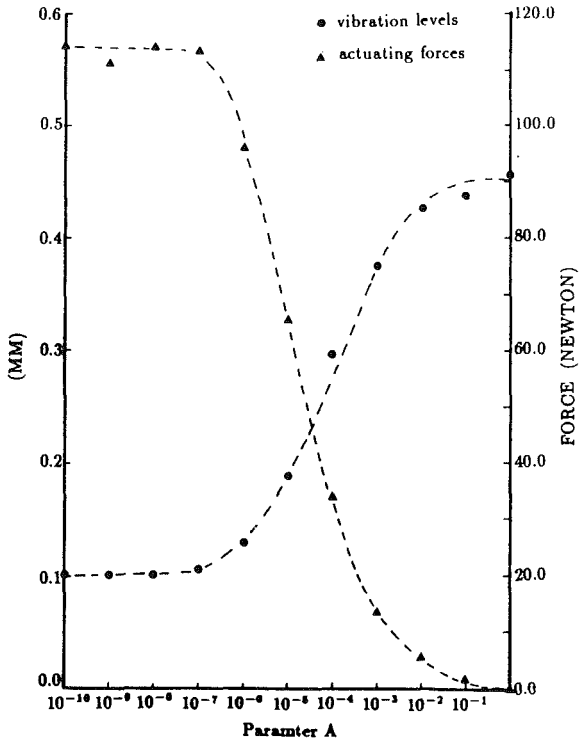

Fig. 8 Relationships among the weighting parameter matrix *A*, vibration levels, and the required actuating forces at mode 1

permitting the low pass spillover filter in Fig. 1 to be removed. This point is affirmed by the closed-loop eigenvalues (see Table 5).

Results of the collocated case are shown in Fig. 6. The vibration levels are significantly reduced from the uncontrolled case, and are even smaller than the corresponding noncollocated case. The vibration orbit at node 1 and node 2 have been reduced from 0.45 mm to 0.10 mm and 0.20 mm to 0.05 mm, respectively. The maximum actuator forces (as shown in Fig. 7) are only 100 N, which is smaller than those in the noncollocated case. Again, the vibration level could be reduced further by decreasing the value of the weighting matrix parameter A in equation (22). Figure 8 shows that the vibration orbits at node 1 decrease with the decrease of the weighting matrix parameter A, while the actuator forces increase.

Conclusion

Application of modal space optimal control with output feedback to rotor-dynamic transient vibrations from blade loss has been investigated. The transient vibration level of the rotor-dynamic system can be significantly reduced by the optimal control method. The vibration level and the actuator forces in the collocated case are smaller than those in the noncollocated case, and the motion of the closed-loop system is stable.

The vibration level is significantly affected by the chosen value of weighting matrix parameter A. As A decreases, the maximum vibration level decreases; however the required actuactor force levels increase. The assumption of proportional damping restricts the application of the theory presented to lightly damped rotors such as those supported by rolling element bearings. In order to construct a physical control system to implement the theory developed here one may use eddy current displacement probes for sensors and magnetic bearings, electromagnetic shakers, or piezoelectric pushers for actuators.

Testing is currently underway at NASA to determine the effectiveness of applying active vibration control to gas turbine aircraft engine. Results of that research will be published in the future literature.

Acknowledgments

The authors wish to express their gratitude to the Army Office at NASA Lewis Research Center (NAG-3-763), the Texas A&M Engineering Excellence Fund, and the Texas A&M Turbomachinery Research Consortium (TRC) for sponsoring this research. Our appreciation is also extended to Professor G. Schweitzer for his discussion of stability while visiting Texas A&M.

References

Allaire, P., Lewis, D., and Jain, V., 1981, "Feedback Control of a Single Mass Rotor on Rigid Supports," *Journal of Franklin Institute*, Vol. 313, No. 7, pp. 1–11.

Allaire, P., Lewis, D., and Knight, J., 1983, "Active Vibration Control of a Single Mass Rotor on Flexible Supports," *Journal of Franklin Institute*, Vol. 315, No. 3.

Fath, A. F., 1969, "Computational Aspects of the Linear Optimal Regulator Problem," *IEEE Transactions on Auto. Control*, Oct., pp. 547–549.

Feng, G., and Xin, N., 1986, "Automatic Control of the Vibration of the Flexible Rotor With Microcomputer," *Int. Conf. on Rotordynamics, IFTOMM and JSME*, Tokyo, Sept.

Heinzmann, J. D., Flack, R., and Lewis, D., 1980, "The Implementation of Automatic Vibration Control in High Speed Rotating Test Facilty," University of Virginia Report UVA/464761/MAE80/160.

Laub, A., 1979, "A Schur Method for Solving Algebraic Ricatti Equations," *IEEE Transactions on Automatic Control*, Vol. AC-24, No. 6, pp. 913–921.

Nonami, K., 1985, "Vibration Control of Rotor Shaft Systems by Active Control Bearings," ASME Paper No. 85-DET-126.

Palazzolo, A. B., Wang, B. P,, and Pilkey, W. D., 1983, "Eigensolution Reanalysis of Rotor Dynamic Systems by the Generalized Receptance Method," ASME JOURNAL OF ENGINEERING FOR POWER, Vol. 105, pp. 543–550.

Pilkey, W. D., Wang, B. P., and Vannoy, D., 1976, "Efficient Optimal Design of Suspension Systems for Rotating Shafts," *ASME Journal of Engineering for Industry*, Vol. 98, pp. 1026–1029.

Reinig, K. D., and Desrochers, A. A., 1986, "Disturbance Accommodating Controllers for Rotating Mechanical Systems," *ASME Journal of Dynamic Systems, Measurement, and Control*, Vol. 108, pp. 24–31.

Salm, J., and Schweitzer, G., 1984, "Modeling and Control of a Flexible Rotor With Magnetic Bearings," *IMechE Conf. on Rotordynamics*, Paper C277/84, pp. 553–561.

Stanway, R., and O'Reilly, C., 1984, "State Variable Feedback Control of Rotor Bearing Suspension Systems," *IMechE Rotordynamics Conference*, C274/84, pp. 515–524.

Wiberg, D., 1971, *State Space and Linear Systems*, McGraw-Hill-Schaums Outlines.

APPENDIX

Ricatti Equation Solution Procedure

The method presented here for solving the steady-state (algebraic) Ricatti equation is outlined by Fath (1969) and Wiberg (1971). Although there exist more efficient and accurate means for accomplishing this task (Laub, 1979) this method was both simple and accurate.

The steady-state (algebraic) Ricatti equation is

$$[P][A] + [A]^T[P] - [P][B_U][R]^{-1}$$
$$[B_U]^T[P] + [Q] = [0]_{(2t\times 2t)} \tag{23}$$

where the matrices $[P]$, $[A]$, and $[Q]$ are $2t$ by $2t$, the matrix $[B_U]$ is $2t$ by M, and the matrix $[R]$ is M by M. The matrices are defined by the plant equation

$$\{\dot{X}\}_{(2t\times 1)} = [A]\{X\} + [B_F]\{F_D\} + [B_U]\{U\} \tag{24}$$

the performance index equation

$$J = \int_0^\infty (\{X\}^T[Q]\{X\} + \{U\}^T[R]\{U\})dt \tag{25}$$

and the feedback gain matrix equation

$$\{U\} = -[R]^{-1}[B_U]^T[P]\{X\} \tag{26}$$

Equation (23) is a coupled, nonlinear algebraic equations for the elements of $[P]$. This system of nonlinear equations is solved by converting it into an eigenvalue problem as follows.

Consider the $4t$ by $4t$ matrix eigenvalue problem;

$$\Upsilon_i\{\Theta\} = \begin{bmatrix} [A] & \vdots & -[B_U][R]^{-1}[B_U]^T \\ \cdots & \cdots & \cdots \\ -[Q] & \vdots & -[A]^T \end{bmatrix}_{(4t\times 4t)} \{\Theta\}_i \tag{27}$$

Suppose that this equation has been solved and its eigenvectors partitioned according to

$$\{\Theta\}_{i(4t\times 1)} = \begin{Bmatrix} \{\Theta\}_{U_i} \\ \{\theta\}_{L_i} \end{Bmatrix} \tag{28}$$

It can be shown (Wiberg, 1971) that the eigenvalues γ_i are placed symmetrically about the imaginary axis. This implies $2t$ eigenvalues have real parts less than zero and the remaining $2t$ eigenvalues are identical to the first $2t$ but have positive real parts, i.e.,

$$\lambda_{2t+i} = -\bar{\lambda}_i \tag{29}$$

We arrange the $2t$ eigenvalues with negative real parts and their corresponding eigenvectors in the following matrices:

$$[\Lambda]_{(2t\times 2t)} = \begin{bmatrix} \lambda_1 & 0 & \cdots & 0 \\ 0 & \lambda_2 & \cdots & 0 \\ \vdots & \vdots & \ddots & \vdots \\ 0 & 0 & \cdots & \lambda_{2t} \end{bmatrix} \tag{30}$$

$$\begin{bmatrix} [F] \\ [G] \end{bmatrix}_{(4t\times 2t)} = \begin{bmatrix} \{\Theta\}_{U_1} & \vdots & \cdots & \vdots & \{\Theta\}_{U_{2t}} \\ \cdots & \cdots & \cdots & \cdots & \cdots \\ \{\Theta\}_{L_1} & \vdots & \cdots & \vdots & \{\Theta\}_{L_{2t}} \end{bmatrix}_{(4t\times 2t)} \tag{31}$$

Combining equations (25) and (31) shows

$$\begin{bmatrix} [F] \\ \cdots \\ [G] \end{bmatrix} [\Lambda] = \begin{bmatrix} [A] & \vdots & -[B_U][R]^{-1}[B_U]^T \\ \cdots & \cdots & \cdots \\ -[Q] & \vdots & -[A]^T \end{bmatrix} \begin{bmatrix} [F] \\ [G] \end{bmatrix} \tag{32}$$

Writing out the partitioned equations yields

$$[F][\Lambda] = [A][F] - [B_U][R]^{-1}[B_U]^T[G] \tag{33}$$

and

$$[G][\Lambda] = -[Q][F] - [A]^T[G] \tag{34}$$

Substituting equation (33) into equation (34) yields

$$[\Lambda] = [F]^{-1}[A][F] - [F]^{-1}[B_U][R]^{-1}[B_U]^T[G] \tag{35}$$

$$[G][F]^{-1}[A][F] - [G][F]^{-1}[B_U][R]^{-1}[B_U]^T[G] = -[Q][F] - [A]^T[G] \tag{36}$$

We postmultiply this equation by $[F]^{-1}$

$$[G][F]^{-1}[A] + [A]^T[G][F]^{-1} - [G][F]^{-1}[B_U][R]^{-1}[B_U]^T[G][F]^{-1} + [Q] = [0] \tag{37}$$

and define

$$[P]_{(2t\times 2t)} = [G]_{(2t\times 2t)}[F]^{-1}_{(2t\times 2t)} \tag{38}$$

Then, equation (37) becomes

$$[P][A] + [A]^T[P] - [P][B_U][R]^{-1}[B_U]^T[P] + [Q] = [0]_{(2t\times 2t)} \tag{39}$$

which is the algebraic Ricatti equation (23).

Structural Analysis Applications

R. L. McKnight
General Electric AEBG,
Cincinnati, OH 45030

The programs in the structural analysis area of the HOST program emphasized the generation of computer codes for performing three-dimensional inelastic analysis with more accuracy and less manpower. This paper presents the application of that technology to Aircraft Gas Turbine Engine (AGTE) components: combustors, turbine blades, and vanes. Previous limitations will be reviewed and the breakthrough technology highlighted. The synergism and spillover of the program will be demonstrated by reviewing applications to thermal barrier coatings analysis and the SSME HPFTP turbine blade. These applications show that this technology has increased the ability of the AGTE designer to be more innovative, productive, and accurate.

Introduction

The activities of the NASA Turbine Engine Hot Section Technology Project were directed toward functionality and durability needs of AGTE hot section components: the combustor, turbine vanes, and turbine blades. The overall approach of this program was to assess the existing analysis methods for strengths and deficiencies, and then to conduct supporting analytical and experimental research to rectify those deficiencies and, at the same time, incorporate state-of-the-art improvements into the analysis methods.

Structural analysis has two major objectives in the design of AGTEs. The first major objective is to generate and verify a functional design. The second major objective is to quantify the durability/reliability of these designs. The first objective can be accomplished by analyzing candidate designs for a simplified mission cycle, the maximum envelope of the technical requirements. Evaluations are made by comparing the code outputs—displacements, stresses, and strains—against technical requirements and design practices. The second objective requires that the entire mission cycle be analyzed and the code output be combined with durability/reliability technology in a postprocessing operation.

For both these types of analysis, some portion of the airframe-engine system is mathematically simulated and a history of the operating environment and interaction effects of the remainder of the system imposed as loads and boundary conditions. For functionality the simpler-maximum history can be imposed on a larger portion of the overall system. Since durability/reliability is a point function, smaller portions of the system must be run through the total complex history of loading. For both of these analyses, the loading, environment, and interactions are provided to the analyst from other "expert" groups.

A deficiency common to both types of analysis is that of economy/productivity as measured by the total period of time, number of man-hours, and the computer resources required to complete a design analysis. For functional analyses, the second major deficiency was due to the combination of the formulation models (Finite-Element Model, Finite Difference Model, Boundary Element Model) and the numerical accuracy of the computer. These limitations affected the ability to simulate large systems accurately with their complex interactions without exceptionally fine modeling. For durability/reliability analyses, the second mjaor deficiency was the inability of the combination of the formulation models, constitutive models, and the numerical accuracy of the computer to simulate the local inelastic material behavior accurately. This deficiency was particularly evident in the hot section components exposed to the severe thermal and mechanical operating environments of the AGTE. The local, durability limiting areas of these structures are exposed to time varying temperature distribution, which affects both the material properties and the thermal and mechanical stresses in a complex three-dimensional manner.

The HOST program successfully accomplished its goals by attacking the above deficiencies. This was done through a series of programs in which were developed constitutive models, three-dimensional inelastic structural analysis codes, a three-dimensional thermal transfer code, and a component specific modeling system. The application of these advanced tools was almost simultaneous with their development. The remainder of this paper will present selective applications of these technologies.

Combustor Design and Analysis

The combustor is one of the most challenging and complex components of the AGTE. Its design involves many "expert" groups: controls, fuel nozzles, chemical combustion kinetics, heat transfer, and structures. It presents one of the major productivity drains in AGTE designs, both for initial design and for subsequent tuning for mission variations. HOST attacked all aspects of this problem, economy/productivity as well as accuracy, in the component specific modeling effort. In this program the many diverse disciplines that impact on a combustor liner design were integrated into a component specific system utilizing the HOST technologies.

The COSMO computer system consists of a Thermodynamic Engine Model (TDEM), a Thermomechanical

Contributed by the International Gas Turbine Institute and presented at the 33rd International Gas Turbine and Aeroengine Congress and Exhibition, Amsterdam, The Netherlands, June 5–9, 1988. Manuscript received by the International Gas Turbine Institute November 17, 1987.

Load Model (TDLM), and Combustor Structural Model. The TDEM generates the engine internal flow variables for any point in the operating mission by the specification of three variables, altitude (h), Mach number (M), and power level (PL) for the allowed flight map of an engine, as shown in Fig. 1. Additional control variables are ambient temperature deviations from the standard atmosphere, air frame bleed air requirements, and engine deterioration. For each input condition, specified by h, M, and PL, the TDEM calculates gas weight flow (w), temperature (t), and pressure (p) for the combustor.

The TDEM technique is shown in Figs. 2 to 4. The engine to be analyzed must have its aerodynamic stations (Fig. 2) defined thermodynamically by an engine cycle deck (computer program), which can be run to generate the internal flow variables at chosen aerodynamic stations (Fig. 3). In COSMO the complete engine operating map (Fig. 1) is encompassed by selecting 148 operating points for which w, t, p, as well as N_1 and N_2, the fan and core speeds, are calculated for the stations pertinent to the COSMO components.

From these station data an Engine Performance Cycle Map is constructed. This is essentially a set of three-dimensional data arrays that map the station data (w, t, p, n_1, and N_2) onto the engine operating map (Fig. 1). Given an arbitrary operating point defined by h, M, and PL it is then, in principle, possible to interpolate on the engine performance cycle map to determine station data. These station parameters are nonlinear functions of the input parameters and much effort went into the development of these multidimensional interpolation techniques.

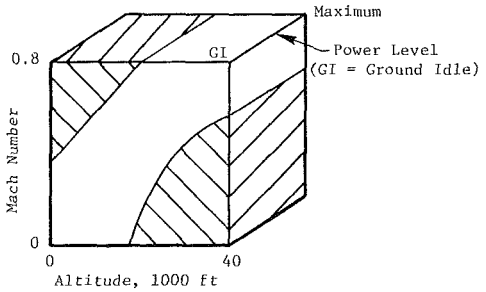

Fig. 1 Engine operating map

The functioning of the TDEM is shown in Fig. 4. Given an engine mission, as shown schematically in Fig. 5, it can be defined by values of the input variables h, M, and PL at selected times through the mission. Using these input variables and the Engine Performance Cycle Map the interpolation program calculates engine station parameters throughout the mission (Fig. 4). These are then used to define the station mission profiles of w, t, p, N_1, and N_2 as functions of time at each aerodynamic station. These station mission profiles then become the input to the TDLM.

The TDLM is the computer program that works with the output of the TDEM to produce the mission cycle loading on the individual hot section components, in this case the combustor. This software translates the major engine performance parameter profiles from the TDEM into profiles of the component thermodynamic loads (pressures, temperatures, rpm). The formulas that perform this mapping in the TDLM models were developed for the specific engine components of the CF6-50C engine. Adaptation of these models to a different engine would require the evaluation of these formulas for their simulation capability and reformulating where necessary.

The heart of the component specific structural modeling is geometric modeling and mesh generation using the recipe concept. A generic geometry pattern is determined for each component. A recipe is developed for this basic geometry in terms

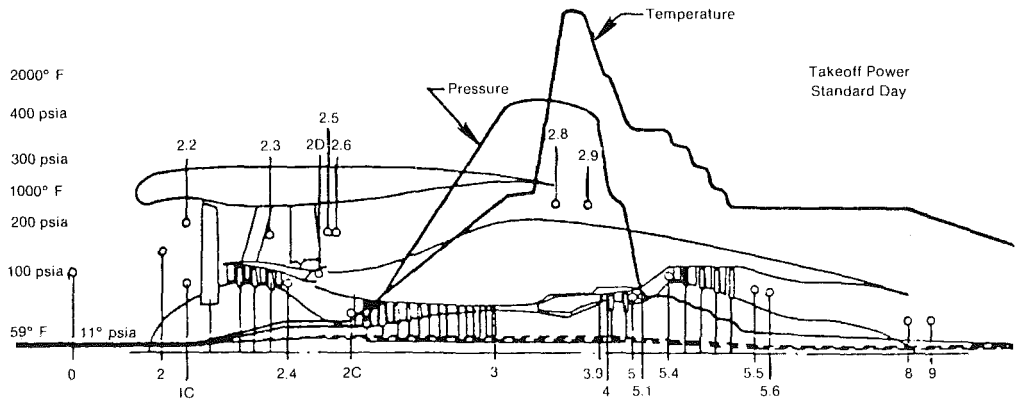

Legend

0	Ambient	2C	HP Compressor Inlet
2	Engine Inlet	3	HP Compressor Discharge
2.2	Fan Tip (Bypass) Stream Inlet	3.9	HP Turbine First-Stage Nozzle Inlet (Without Cooling Flow)
1C	Fan Hub (LP Compressor) Stream Inlet	4	HP Turbine Rotor Inlet (With Cooling Flow)
2.3	Fan Discharge	5	HP Turbine Discharge (Without Cooling Flow)
2.4	LP Compressor Discharge	5.1	HP Turbine Discharge (With Cooling Flow)
2.5	Bypass Stream Mixing Plane	5.4	LP Turbine Inlet (With Cooling Flow)
2.6	Bypass Duct Inlet (After Mixing)	5.5	LP Turbine Discharge (Without Cooling Flow)
2.8	Bypass Duct Jet Nozzle Throat	5.6	LP Turbine Discharge (With Cooling Flow)
2.9	Bypass Duct Nozzle Exit (Complete Expansion)	8	Primary Jet Nozzle Throat
		9	Primary Jet Nozzle Exit (Complete Expansion)

Temperature Fan – – – – –
Core ———
Pressure Fan — — — —
Core ———

Fig. 2 Aerodynamic stations

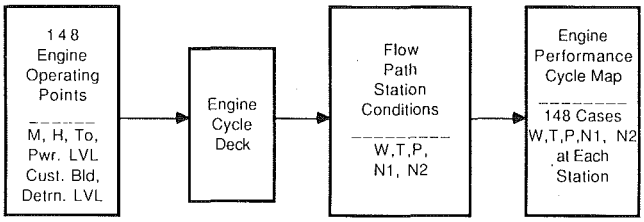

Fig. 3 Thermodynamic engine model cycle map generation

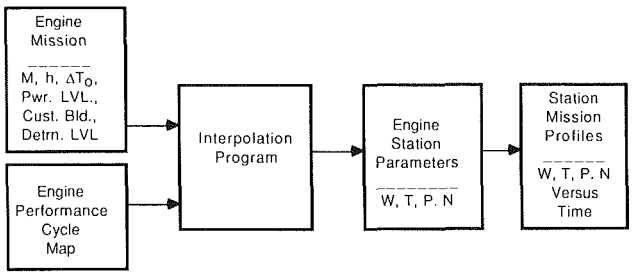

Fig. 4 Thermodynamic engine model

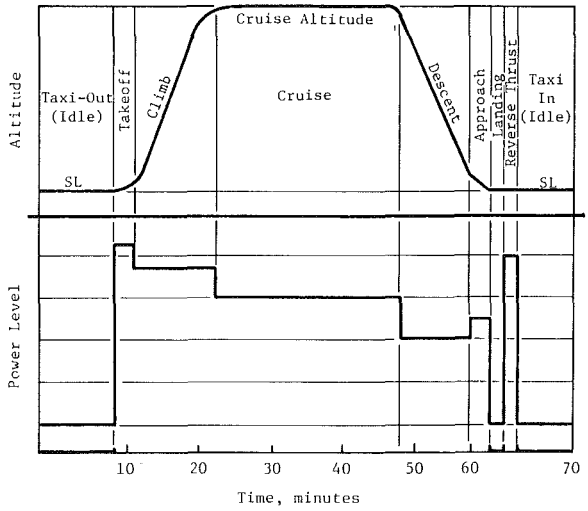

Fig. 5 Typical flight cycle

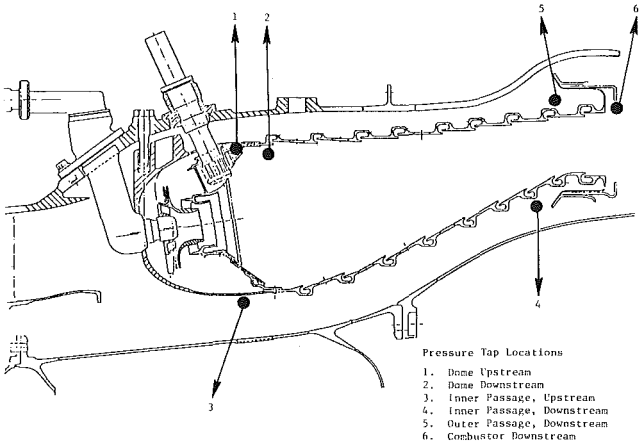

Fig. 6 Rolled ring combustor

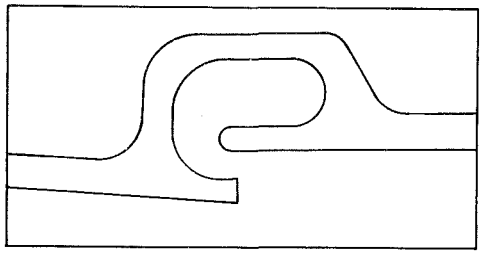

Typical Nugget

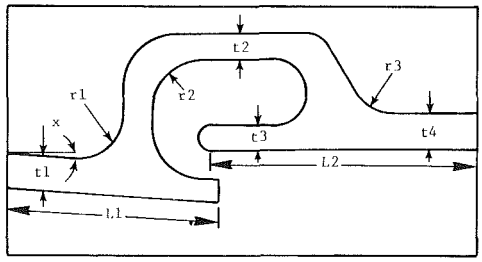

Physical Input Parameters

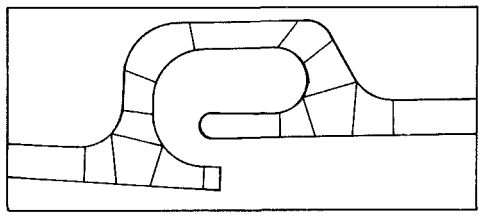

Master Region Definition

Fig. 7 Combustor recipe process

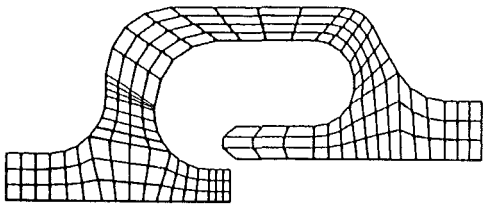

2D Model

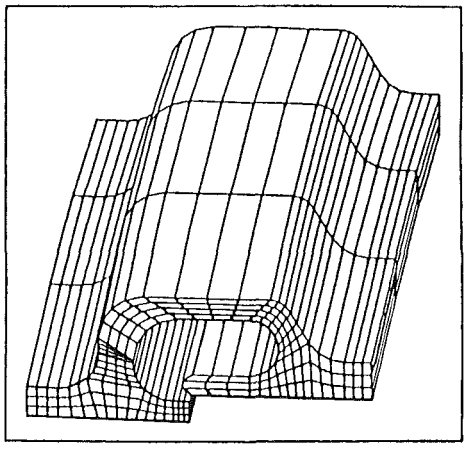

3D Model

Fig. 8 Combustor nugget finite element models

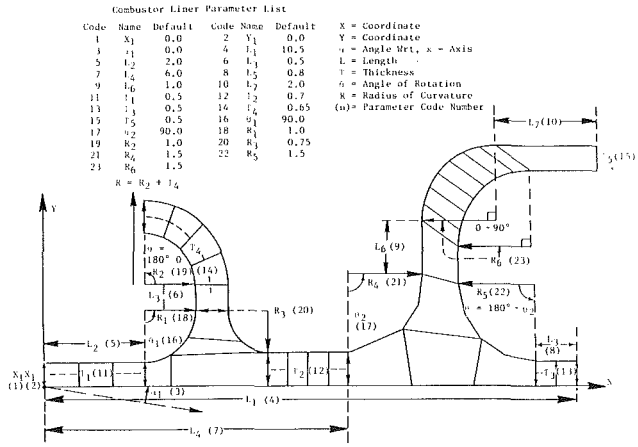

Fig. 9 Combustor liner parameters

of point coordinates, lengths, thicknesses, angles, and radii. Figures 6 to 8 show this process for a rolled ring combustor. These recipe parameters are encoded in computer software as variable input parameters with a set of default numerical values defined. Figure 9 defines the recipe that generates the combustor structural model.

A snapshot of a typical run of the combustor model is shown in Fig. 10. As indicated, the model contains a default set of recipe parameters; only changes to this list need be given. After the recipe parameters have been set, only five parameters need be specified to generate a three-dimensional sector model of a combustor to perform a hot streak analysis. The first parameter (shown as the number of exhaust nozzles) is required to divide the 360 deg combustor into the proper number of sectors. The next parameter (shown as the number of circumferential elements) is used by the analyst to split up the circumferential sector into a number of slices, *NS*, for the three-dimensional elements and bias these slices by specifying *NS*-1 percentages.

For the particular case involved three exhaust nozzles are specified with four circumferential elements. These circumferential elements are then biased, starting at the hot streak, as 5, 15, and 30 percent. This leaves the final slice to be 50 percent. This is all the information required to generate a three-dimensional finite-element model consisting of 20-noded isoparametric finite elements. In this case the model consists of 648 elements, 3192 nodes, and has 768 element faces with pressure loading. Figures 11 and 12 are graphic depictions of this three-dimensional model. The temperatures and pressures from the TDLM are mapped onto this model and the necessary data files are generated for a nonlinear structural analysis.

The subsystem that performs the three-dimensional nonlinear finite-element analysis of the combustor model was developed in the HOST program "Three-dimensional Inelastic Analysis Methods for Hot Section Structures." This software performs incremental nonlinear finite-element analysis of complex three-dimensional structures under cyclic thermomechanical loading with temperature-dependent material properties and material response behavior. The nonlinear analysis considers both time-independent and time-dependent material behavior. Among the constitutive models available are a simplified model, a classical model, and a unified model. A major advance in the ability to perform time-dependent analyses is the dynamic time incrementing strategy incorporated in this software.

The COSMO system consists of an executive module, which controls the TDEM, TDLM, the geometric modeler, the structural analysis code, the file structure/data base, and certain ancillary modules. These ancillary modules consist of a bandwidth optimizer module, a deck generation module, a remeshing/mesh refinement module, and a postprocessing module. The executive directs the running of each module, controls the flow of data among modules, and contains the self-adaptive control logic. Figure 13 is a flow chart of the COSMO system showing the data flow and the action positions of the adaptive controls. The modular design of the system allows each subsystem to be viewed as a plug-in module, which can be replaced with alternates.

The ideas, techniques, and computer software contained in COSMO have proven to be extremely valuable in advancing the productivity and design analysis capability of combustors. This software, in conjunction with modern supercomputers, is able to reduce a design task that previously required man-months of effort over a time period of months to a one-man, less than a day effort. Along with this time compression comes increased accuracy from the advanced modeling and analysis techniques. As a result of this, more analytical design studies can be performed, reducing the chances for field surprises and the amount of combustor testing required.

Turbine Blade Analysis

The analysis of turbine blades is an excellent barometer of the improvements brought about by the HOST program. There was a pre-HOST program called "Turbine Blade Tip Durability Analysis," which established the state of the art prior to HOST. A commercial air-cooled turbine blade with a well-documented history of cracking in the squealer tip region was subjected to cyclic nonlinear analysis by a commercially available computer program ANSYS. This three-dimensional problem had previously been analyzed, elastically, by an in-house computer program. At the end of the HOST program, this problem was once again used to establish the changes brought about by HOST.

The problem involved was the significant creep fatigue encountered in a Stage 1 high-pressure turbine blade. These blades are hollow, air-cooled, and paired together on a single three-tang dovetail. Figure 14 shows one such blade and indicates the region of analysis. The three-dimensional finite-element model of the component blade tip above the 75-percent span was constructed of 580 eight-noded isoparametric brick elements with 1119 nodes. A detailed, exploded view of this model depicting the squealer tip, tip cap, and spar as discrete three-dimensional components is shown in Fig. 15.

This ANSYS model was exercised on the CDC-7600 computer. This model had previously been run on the TAMP-MASS computer program and the Honeywell 6000 computer. In 1986, this model was converted to 580, 20-noded isoparametric finite elements and run on one of the codes developed under "Three-Dimensional Inelastic Analysis Methods for Hot Section Structures." Table 1 shows the times and costs experienced under the various conditions. The impact of the advancements in technology and computer hardware is apparent from this table.

Thermal Barrier Coating Analysis

Another technological area in the HOST program was that of "Surface Protection." Programs were developed under this area to produce an understanding and to generate theories and computer tools for the design, analysis, and life prediction of Thermal Barrier Coatings (TBC). Figure 16 shows one type of test specimen involved in this effort. Figure 17 shows the axisymmetric finite-element model used to simulate these test specimens. Figure 18 is a furnace thermal test cycle that these specimens were cycled through. Figures 19 and 20 are representative analytical results for the critical life locations.

Without the developments in the structural analysis area of

```
$FRN /GN/NUGPRO

      NUGGET RECIPE    VERS.II 8/29/85

DO YOU HAVE A PARAMETER FILE 21? (0/1)
*
            CODE       VALUE                    CODE       VALUE
              1         0.                       2         0.
              3         0.                       4         1.16700
              5         0.19200                  6         0.04500
              7         0.81000                  8         0.06800
              9         0.10000                 10         0.20400
             11         0.06000                 12         0.08000
             13         0.06000                 14         0.06800
             15         0.06800                 16       110.00000
             17        90.00000                 18         0.06000
             19         0.06700                 20         0.12000
             21         0.12500                 22         0.08300
             23         0.09500

  ENTER PARAMETER CHANGES (ENTRY CODE, NEW VALUE)
      WHEN DONE ENTER     0 0

*0 0
            CODE       VALUE                    CODE       VALUE
              1         0.                       2         0.
              3         0.                       4         1.16700
              5         0.19200                  6         0.04500
              7         0.81000                  8         0.06800
              9         0.10000                 10         0.20000
             11         0.06000                 12         0.08000
             13         0.06000                 14         0.06800
             15         0.06800                 16       110.00000
             17        90.00000                 18         0.06000
             19         0.06300                 20         0.12000
             21         0.12500                 22         0.08300
             23         0.09500

 DO YOU WANT TO CHANGE PARAMETERS? (0/1)
*
READING FILE NUGCON
READING DONE
              27 ELEMENTS READ

ENTER ENGINE TEMPERATURE AND PRESSURE FILE NAME
*/GN/NUGINF
READING FILE /GN/NUGINF                ,
READING DONE
              36 CENTROIDS READ


ENTER THE NUMBER OF EXHAUST NOZZLES
  AND THE NO. OF CIRCUMFIRENTIAL ELEMENTS
  BETWEEN T-AVE AND T-HOT (MAX NO.=10)
*3 4

ENTER THE  3 CIRCUMFIRENTIAL BIASING PARAMETERS
 -- ENTER AS PERCENTS, THE SUM BEING LESS THAN 100% --
*5 15 30

********  3192 NODES IN 3-D MODEL     ********
********   648 ELEMENTS IN 3-D MODEL  ********
********   768 FACES WITH PRESSURES   ********

 ### 2-D NODE  FILE IS TEMP FILE 20 ###
 ### PARAMETER FILE IS TEMP FILE 21 ###
 ### 3-D  UIF  FILE IS TEMP FILE 26 ###
```

Fig. 10 Typical program run

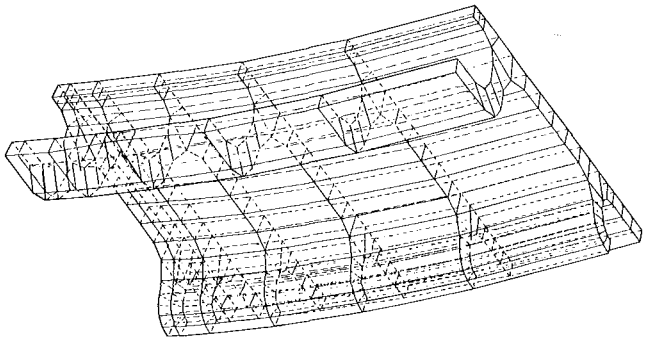

Fig. 11 Three-dimensional model layout

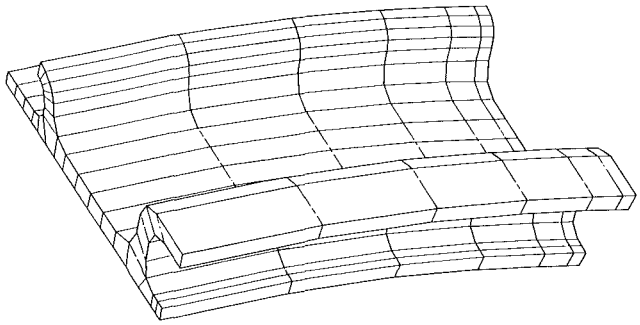

Fig. 12 Hidden line plot of three-dimensional model

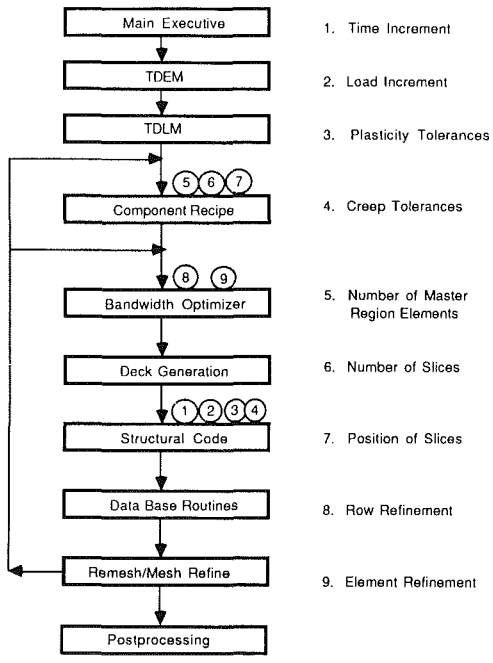

Fig. 13 System flowchart showing adaptive control positions

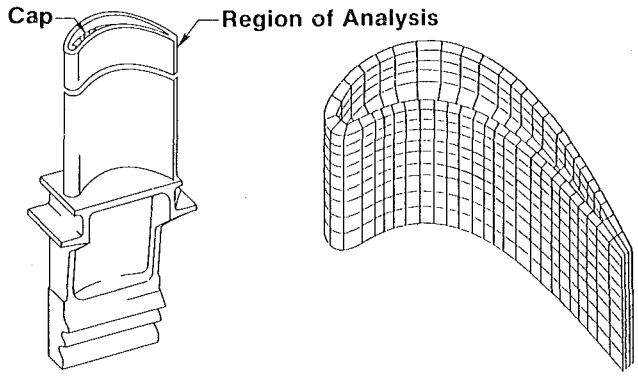

Fig. 14 Stage 1 high-pressure turbine blade and finite element model

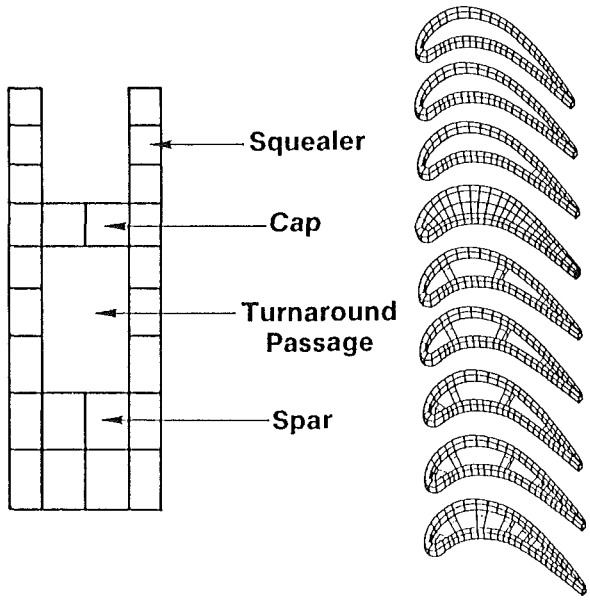

Fig. 15 Finite element model of blade tip

Table 1 Turbine blade tip model history

Year	Computer program	Finite element	Computer	Wall time	Computer time
1975	TAMP-MASS	8-noded isoparametric	Honeywell 6000	60 hr	20 hr
1981	ANSYS	8-noded isoparametric	CDC-7600	24 hr	3 hr
1986	HOST three-dimensional inelastic	20-noded isoparametric	CRAY-1	115 sec	114 sec

HOST this test simulation would not have been attempted because of the excessive amounts of computer time that would have been required. This problem is highly time dependent and numerically sensitive. The material properties and the creep properties differ greatly among the three constituents of this material system. An added nonlinearity occurs due to the growth of an oxide scale between the bond coat and the top coat. The dynamic time incrementing algorithm developed under the three-dimensional inelastic HOST program made the analysis of this nonlinear system possible.

SSME HPFTP Turbine Blade

One final example of the application of HOST technology is the NASA program with the acronym SADCALM. This stands for "Structural Analysis Demonstration of Constitutive and Life Models." Under this program, coated single-crystal turbine blades such as the one indicated in Fig. 21 will be analyzed by the most advanced technology developed under HOST. This includes the 20-noded isoparametric finite element and the constitutive models developed in the three-dimensional inelastic programs. The single-crystal-crystallographic constitutive model developed under the anisotropic constitutive modeling programs, and three HOST life theories, "Cyclic Damage Accumulation," "Total Strain-Strain Range Partitioning," and "Hysteretic Energy," will be used. This program involves testing, analysis,

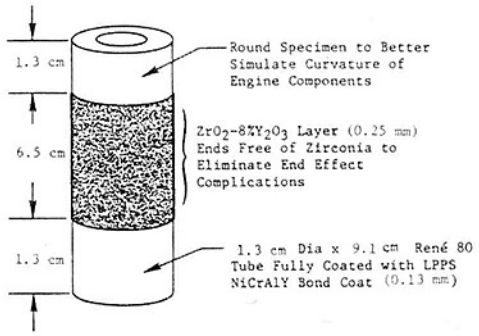

(a) Test Specimen Configuration

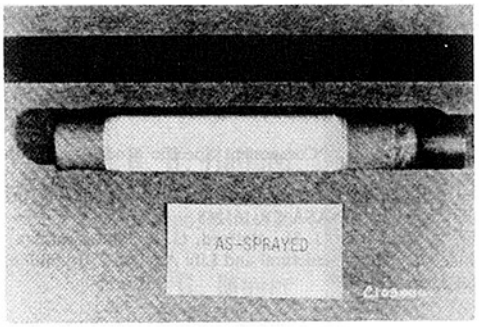

(b) As-Sprayed Specimen

Fig. 16 Thermal barrier coated tubular specimen

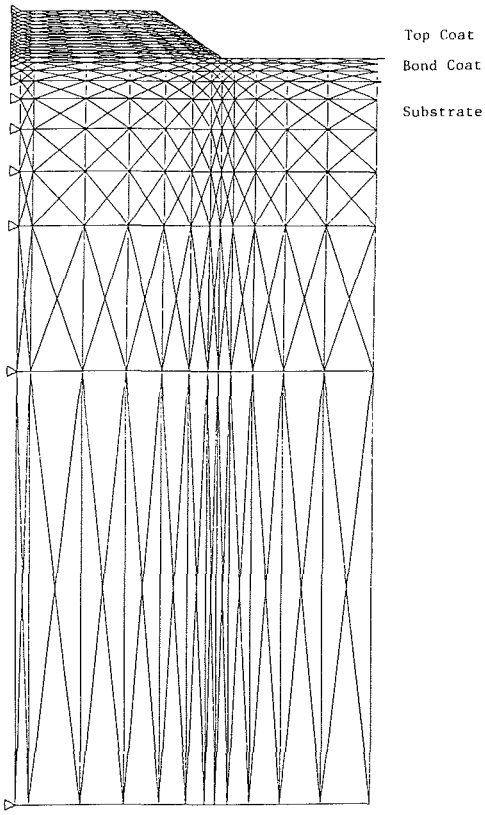

Fig. 17 Finite element mesh for thermal barrier coated tubular specimens

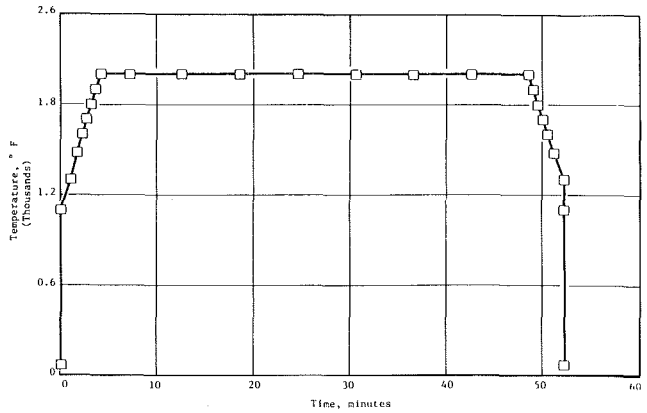

Fig. 18 Thermal loading cycle

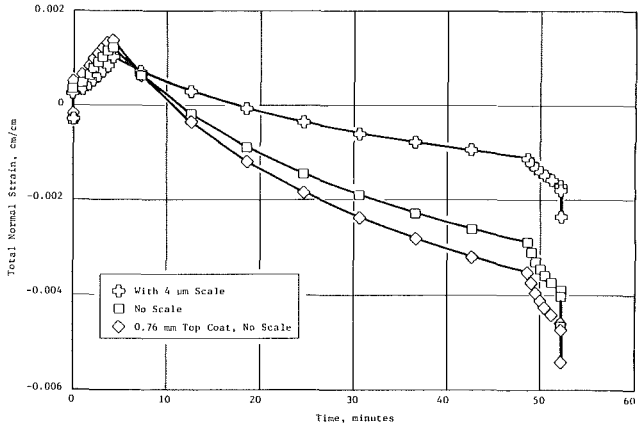

Fig. 19 Calculated total normal strain in top coat at top coat/bond coat interface of thermal barrier coated tubular specimen during thermal cycle. Bond coat thickness 0.13 mm; top coat thickness 0.254 mm unless indicated otherwise.

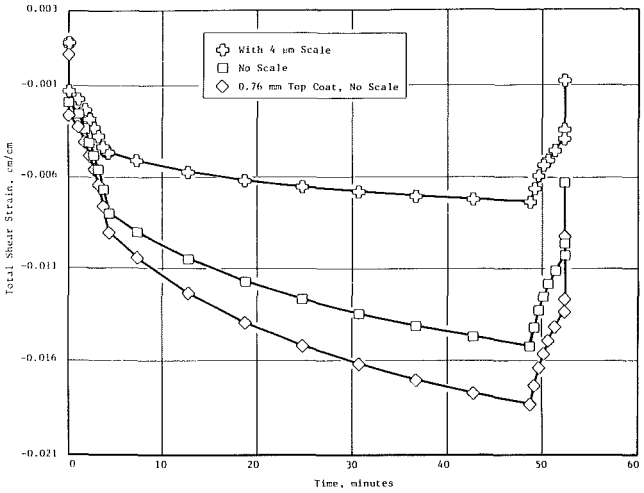

Fig. 20 Calculated total shear strain in top coat at top coat/bond coat interface of thermal barrier coated tubular specimen during thermal cycle. Bond coat thickness 0.13 mm; top coat thickness 0.254 mm unless indicated otherwise.

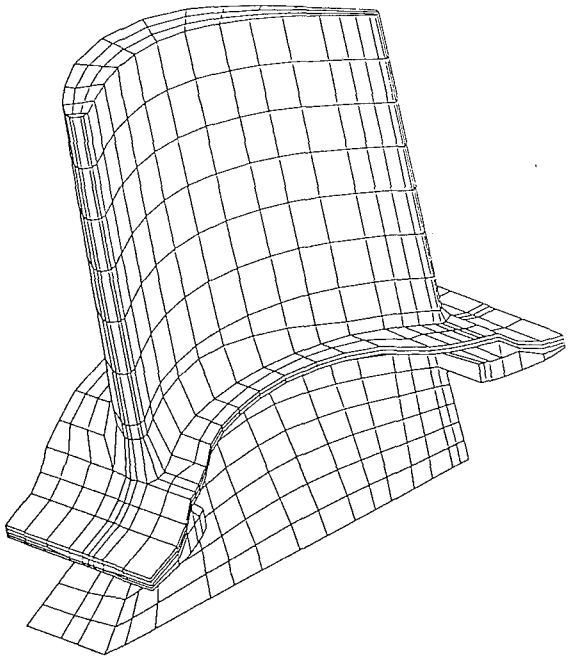

Fig. 21 SIESTA plot of converted NASA blade model

and correlation and will provide an excellent opportunity to demonstrate the benefits of the HOST program.

Conclusions

The ideas, techniques, and computer software developed under the NASA HOST program have proven to be extremely valuable in advancing the productivity and design analysis capability for hot section structures of AGTEs. This software in conjunction with modern supercomputers is able to reduce a design task significantly. These ideas are amenable to further generalization/specialization and extension to all areas of the engine structure. These techniques will have their major payoff in the next generation of aerospace propulsion systems with their increasingly large number of parametric variations.

References

Maffeo, R., 1985, "Burner Liner Thermal/Structural Load Modeling, TRANCITS Program User's Manual," NASA CR-174891.

McKnight, R. L., 1983, "Component Specific Modeling; First Annual Status Report," NASA CR-174765.

McKnight, R. L., 1985, "Component Specific Modeling; Second Annual Status Report," NASA CR-174925.

McKnight, R. L., Laflen, J. H., and Spamer, G. T., 1981, "Turbine Blade Tip Durability Analysis," NASA CR-165268.

McKnight, R. L., Laflen, J. H., Halford, G. R., and Kaufman, A., 1983, "Turbine Blade Nonlinear Structural and Life Analysis," *Journal of Aircraft*, Vol. 20, No. 5, pp. 475–480.

Fatigue Life Prediction Modeling for Turbine Hot Section Materials

G. R. Halford
NASA Lewis Reseach Center
Cleveland, OH 44135

T. G. Meyer

R. S. Nelson

D. M. Nissley

G. A. Swanson

United Technologies,
Pratt and Whitney,
East Hartford, CT 06108

This paper presents a summary of the life prediction methods developed under the NASA Lewis Research Center's Hot Section Technology (HOST) program. A major objective of the fatigue and fracture efforts under the HOST program was to significantly improve the analytic life prediction tools used by the aeronautical gas turbine engine industry. This has been achieved in the areas of high-temperature thermal and mechanical fatigue of bare and coated high-temperature superalloys. Such technical improvements will eventually reduce life cycle costs. The cyclic crack initiation and propagation resistance of nominally isotropic polycrystalline alloys and highly anisotropic single crystal alloys have been addressed. A sizeable data base has been generated for three alloys [cast PWA 1455 (B−1900+Hf), wrought Inconel 718, and cast single-crystal PWA 1480] in bare and coated conditions. Two coating systems, diffusion aluminide (PWA 273) and plasma-sprayed MCrAlY overlay (PWA 286), were employed. Life prediction modeling efforts were devoted to creep-fatigue interaction, oxidation, coatings interactions, multiaxially of stress-strain states, mean stress effects, cumulative damage, and thermomechanical fatigue. The fatigue crack initiation life models developed to date include the Cyclic Damage Accumulation (CDA) Model of Pratt & Whitney and the Total Strain Version of Strainrange Partitioning (TS-SRP) of NASA Lewis for nominally isotropic materials, and the Tensile Hysteretic Energy Model of Pratt & Whitney for anisotropic superalloys. The fatigue model being developed by the General Electric Company is based upon the concepts of Path-Independent Integrals (PII) for describing cyclic crack growth under complex non-linear response at the crack tip due to thermomechanical loading conditions. A micromechanistic oxidation crack extension model has been derived by researchers at Syracuse University. The models are described and discussed in the paper. Only limited verification has been achieved to date as several of the technical programs are still in progress and the verification tasks are scheduled, quite naturally, near the conclusion of the program. To date, efforts have concentrated on developement of independent models for cyclic constitutive behavior, cyclic crack initiation, and cyclic crack propagation. The transition between crack initiation and crack propagation has not been thoroughly researched as yet, and the integration of these models into a unified life prediction method has not been addressed.

Introduction

Background. Life cycle costs ranging from initial design costs to field replacement costs of limited durability component parts are the driving elements for improved analytic life prediction capability. Since life cycle costs are the highest for hot section gas turbine engine components, our efforts have concentrated on the problems in this area. Accurate calculation of expected service lifetimes is crucial to the final judgement to proceed with a particular design. Inaccurate life calculations result in overly expensive designs, either from an underutilization of potential or a lack of adequate life. The fatigue and fracture portion of the HOST program was initiated to reduce life cycle costs through improved accuracy of analytic life predictive models. The specific areas of primary concern are very high-temperature cyclic crack initiation and propagation in both isotropic and anisotropic superalloys used in hot section turbine engine components.

HOST Life Prediction Program. Table 1 lists the specific programs that have supported the fatigue and fracture life prediction efforts. Each will be discussed and the most significant of the numerous accomplishments will be pointed out. Space does not permit elaboration of the numerous methods nor of the experimental details. The reader is referred to the more thoroughly documented original references.

In addition to the Industrial Contracts and University Grants supported by the HOST program, some funding was set aside to rejuvenate aging test facilities in the area of fatigue and fracture. The advanced, high-temperature fatigue and structures research laboratory at Lewis (McGaw and Bar-

Contributed by the International Gas Turbine Institute and presented at the 33rd International Gas Turbine and Aeroengine Congress and Exhibition, Amsterdam, The Netherlands, June 5-9, 1988. Manuscript received by the International Gas Turbine Institute November 16, 1987.

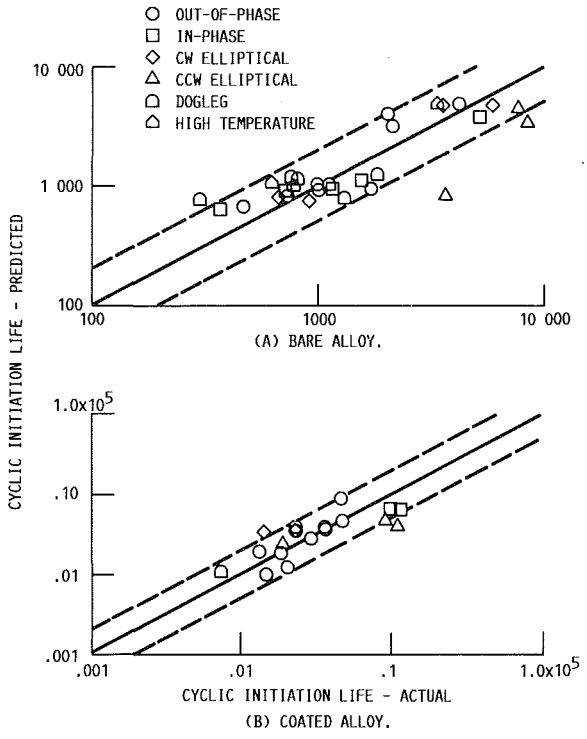

Fig. 1 Application of preliminary CDA model to TMF Life prediction for the cast nickel-base alloy, PWA 1455 (B1900 + H_F), after Moreno (1986).

tollatta, 1987) is now operational, and in fact has grown to the point of requiring further expansion. The facility is equipped with the very latest closed-loop, servo-controlled machinery, and most importantly boasts a unique computerized nerve center for programmed test control; data taking, storage, and retrieval; and data reduction and plotting.

Isotropic Material and Modeling

Cyclic Crack Initiation. The majority of usable cyclic lifetime of turbine engine hot section components is usually spent in what is called the "cyclic crack initiation" portion of the fatigue life. Strictly speaking, crack initiation does indeed contain a considerable amount of cyclic crack growth, although the physical size of the cracks is quite small. From an engineering point of view, any crack growth below a crack size of approximately 0.8 mm (1/32 in.) typically is included in the "initiation" portion of the life. Justification for this definition is based upon: (*a*) the inability to detect cracks of smaller size reliably, and (*b*) the inability of cyclic crack growth laws to model cyclic extension of cracks smaller than this size adequately. Such a definition of cyclic crack initiation is used in the development of the Pratt & Whitney Cyclic Damage Accumulation Model addressed in the next section.

Pratt & Whitney Cyclic Damage Accumulation (CDA) Model. The interaction of creep with fatigue at high temperatures is being studied in detail under NASA/HOST Contract NAS3-23288, "Creep-Fatigue Life Prediction for Engine Hot Section Materials (Isotropic)" (Moreno, 1983; Moreno et al., 1986; Nelson et al., 1986). This effort has investigated fundamental approaches to high-temperature crack initiation life prediction using a cast nickel-base alloy, PWA 1455 (B1900+Hf), as the base material. During the program, over 157 specimen tests were completed under loading conditions that consisted of monotonic tensile and creep tests as well as continuously cycled fatigue tests. A review of existing fatigue models was conducted, and desirable features of each of these were identified. A new method of high-temperature

Table 1 HOST fatigue and fracture programs

- NAS3-23288, Pratt & Whitney (R.S. Nelson)
  Creep-Fatigue Crack Initiation--Isotropic
- NAS3-23940, General Electric (J.J. Laflen)
  Elevated Temperature Crack Growth--Isotropic
- NAS3-23939, Pratt & Whitney (G.A. Swanson)
  Life Prediction/Constitutive Modeling--Anisotropic
- NAG3-348, Syracuse University (H.W. Liu)
  Crack Growth Mechanisms--Isotropic
- Lewis (M.A. McGaw)
  High-Temperature Fatigue and Structures Laboratory

fatigue life prediction called Cyclic Damage Accumulation (CDA) was subsequently developed that incorporates many of these features.

Complex loadings were introduced during the latter stages of the program to study the effects of thermomechanical fatigue, multiaxial loading, cumulative damage, environment, mean stress, and coatings. An additional 160 strain-controlled fatigue tests have been conducted as a part of these tasks. Three different surface treatments were utilized for the TMF tests: bare (no coating), overlay NiCoCrAlY coated, and diffusion aluminide coated. Several refinements have been incorporated into the CDA life prediction model based on the results of these complex tests. The current form of the model for accumulated transgranular damage is given by

$$1 = \int_0^{N_i} \left(\frac{1}{\bar{\epsilon}_p}\right)\left(\frac{1}{G_{NL}}\right)\left(\frac{dD}{dN}\right)_R \left[\left(\frac{\Delta\sigma}{\Delta\sigma_R}\right)\left(\frac{\sigma_T}{\sigma_{TR}}\right) + D_{TD}\left(\frac{F_{ox}}{f_{ox_R}}\right)\right] dN \quad (1)$$

where

N_i = initiation life, transgranular mode
$\bar{\epsilon}_p$ = primary creep ductility
G_{NL} = nonlinear damage accumulation function
$\left(\frac{dD}{dN}\right)_R$ = reference cyclic damage rate
σ_T = maximum tensile stress in current cycle
σ_{TR} = reference maximum tensile stress
$\Delta\sigma$ = stress range of current cycle
$\Delta\sigma_R$ = reference stress range
D_{TD} = time-dependent damage rate modifier
f_{ox} = cyclic oxidation rate for current fatigue cycle
f_{ox_p} = reference fatigue/cyclic oxidation rate

The basis for equation (1) is explained by Moreno (1983), Moreno et al. (1984), and Nelson (1986). A goal of the program to develop the CDA model was to limit the complexity of the experiments to determine the material behavior constants. For example, only monotonic creep tests and continuous cycling fatigue experiments are required to evaluate the constants in the first term of the CDA expression. The second term requires that cyclic oxidation measurements be made during fatigue testing.

Nonlinear damage accumulation calculations are now possible for both cycle-dependent and time-dependent cases. Modular terms that capture the effects of multiaxiality, coatings, and intergranular cracking are currently under development. The ability of the model to correlate thermomechanical fatigue data is shown in Fig. 1 for bare and coated material. Complete details of test conditions employed are given by Nelson (1986). Most of the thermomechanical fatigue (TMF) tests were performed at temperatures between

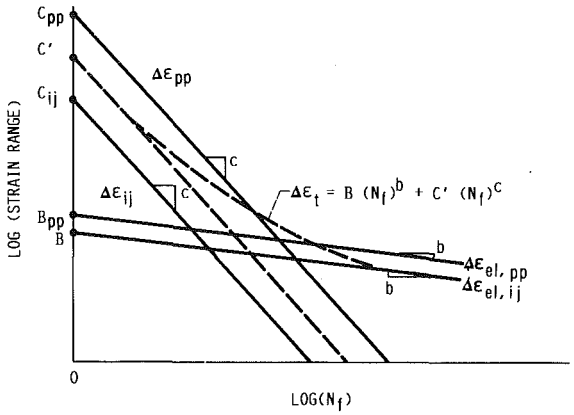

Fig. 2 Schematic representation of total strain strainrange partitioning (TS-SRP)

538 and 871°C at one CPM with total mechanical strain ranges between 0.4 and 0.5 percent. The dogleg experiments utilized 54 s hold periods in either tension or compression. Work continues on a refined version of the model, which will attempt to capture all the important life trends seen during the latter stages of the contract.

The final task under the program is to perform a similar series of tests on an alternate alloy, wrought Inconel 718. A total of 55 of these specimen tests have now been completed, including isothermal, thermomechanical fatigue, and multiaxial strain-controlled tests. It is expected that the final form of the CDA model may include additional refinements required to predict properly the life trends for forged alloys.

Lewis Research Center Total Strain Version of Strainrange Partitioning. The Strainrange Partitioning (SRP) method for characterizing and predicting creep-fatigue behavior of alloys has long been associated with using inelastic strains to relate to cyclic life. Recent advances by Halford and Saltsman (1983) and Saltsman and Halford (1985) now permit the approach to be expressed in terms of total strain range versus cyclic life. These developments make the SRP method more attractive for application to life prediction of aeronautical gas turbine hot section components.

Here, materials and loading conditions result in strain levels that, while they are severe and produce low-cycle fatigue cracking, involve only small amounts of inelastic deformation within nominally elastic strain fields. The limited inelasticity produced locally may exert a significant influence on life. The type of inelastic strains present (time-dependent creep and time-independent plasticity) and the direction of the strains (tension or compression) can be quite important in governing the resultant cyclic crack initiation life. The total strain based SRP approach (TS-SRP) has been developed to deal explicitly with the above conditions. A brief description is given below to show how the procedures are employed.

The total strain range, $\Delta\epsilon_t$, is the sum of two terms, the elastic, $\Delta\epsilon_{el}$, and the inelastic, $\Delta\epsilon_{in}$, strain ranges. Each strain range is related to cyclic life by a power law relation as shown in equation (2) and Fig. 2.

$$\Delta\epsilon_t = \Delta\epsilon_{el} + \Delta\epsilon_{in} = B(N_f)^b + C'(N_f)^c \tag{2}$$

Application of equation (2) at high temperatures requires the evaluation of the coefficients, B and C', and the exponents, b and c. It is assumed, initially, that b and c are constants for all conditions at a given temperature, i.e., they are time and waveshape independent, and that B and C' are time and cycle waveshape dependent.

To determine C', as many of the four basic SRP inelastic strain range versus life relations, *PP*, *CC*, *PC*. and *CP*, as are required for the cycle of interest must be known. How the inelastic strains are partitioned within the cycle must also be known, i.e., how much of each type of *PP*, *CC*, *PC*, or *CP* strain range is present in the hysteresis loop. Experimental procedures for establishing the four inelastic SRP life relations, techniques for approximating them, and experimental partitioning procedures are given by Hirschberg and Halford (1976), Halford et al. (1977), and Manson et al. (1975), respectively.

In principle , the partitioning and thus the determination of C' could be accomplished analytically using advanced cyclic constitutive equations such as those developed under the NASA/HOST Program by Lindholm (1984) and Ramaswamy et al. (1985). Advanced cyclic constitutive models are capable of computing the exact details of a stress-strain hysteresis loop, knowing only the imposed temperature, total mechanical strains, and how they vary with time for a representative cycle. Details of the inelastic straining rates are also computable, and hence creep strains (time-dependent) and plastic strains (time-independent) can be separated, i.e., partitioned. If a constitutive model is not available, the empirical approach presented by Saltsman and Halford (1988) can be used to determine C' and B. The required equations are summarized below:

$$C' = \left[\sum F_{ij}(C_{ij})^{1/c}\right]^c \tag{3}$$

$$B = K_{ij}(C')^n \tag{4}$$

$$F_{ij}/(\Delta\epsilon_t)^\alpha = A(t)^m \tag{5}$$

$$K_{ij} = A_i(t)^{m_i} \tag{6}$$

where $ij = pp$, cc, pc, or cp.

The cyclic strain hardening exponent n in equation (4) is obtained from completely reversed rapid strain-cycling *PP* results

$$\Delta\epsilon_{el,pp} = K_{pp}(\Delta\epsilon_{pp})^n \tag{7}$$

For cycles involving creep

$$\Delta\epsilon_{el,ij} = K_{ij}(\Delta\epsilon_{ij})^n \tag{8}$$

A complete nomenclature for TS-SRP is given by Saltsman and Halford (1988).

To apply the TS-SRP approach, the specific mission cycles of interest are identified and the cyclic stress-strain-temperature-time history is determined at the critical location in the structural component. Then, the appropriate elastic and inelastic strain range versus life relations are calculated and added together to obtain the desired total strain range versus cyclic life diagram. Entering the diagram with the known total strain range, the cyclic life is determined directly without having to calculate the magnitude of the inelastic strain range. Example life prediction calculations by the TS-SRP approach have been reported by Halford and Saltsman (1983), Moreno et al. (1985), and Saltsman and Halford (1988). The degree of success of the method is shown in Fig. 3. Here, the TS-SRP method was applied by Moreno et al. (1985) to a series of five different types of complex verification experiments performed on the nickel-base superalloy B1900+Hf. A direct comparison of the TS-SRP approach with the CDA model was also made by Moreno et al. (1985), wherein the principal features of each method were emphasized. The TS-SRP model and the Pratt & Whitney CDA model were both designed for application to strain-driven fatigue loading conditions in the nominally elastic regime. Both methods are currently being adapted for application to TMF problems.

Cycle Crack Propagation. Cyclic growth of cracks and defects in turbine engine hot section components is of con-

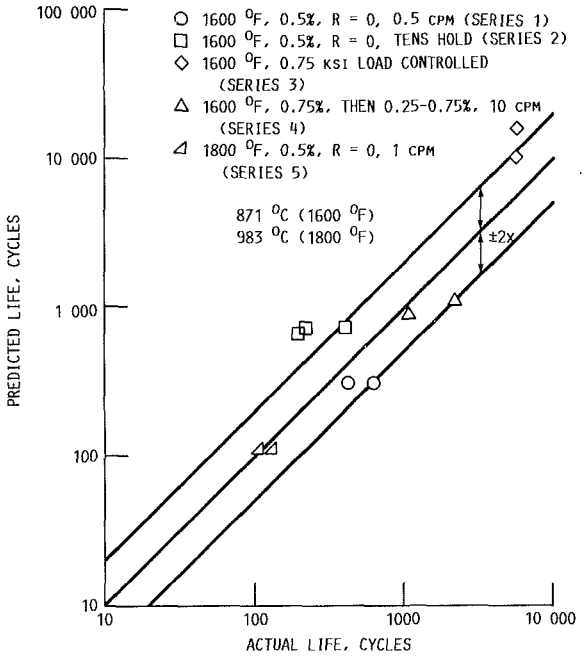

Fig. 3 Prediction of complex verification experiments using TS-SRP, after Moreno (1985)

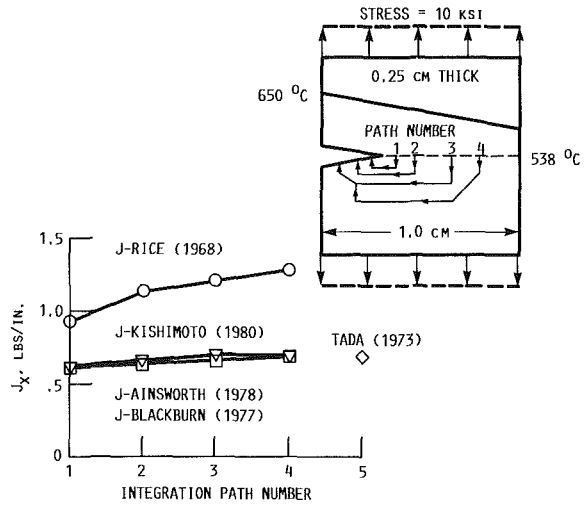

Fig. 4 Evaluation of path-independent integrals under linear temperature gradient in single-edge notch specimens of Inconel 718, after Kim and Orange (1988).

siderable concern because of the lack of structural redundancy in the construction of these components. As such, crack growth to a critical fracture size must be avoided to prevent catastrophic fast fracture and subsequent loss of engine function. Typically, concern for fast fracture is associated more with rotating components than with static structures. For combustor liners, guide vanes, stationary spacers, and other nonrotating components, concern for cyclic crack growth is more economic in nature than safety related. In the HOST fatigue and fracture program, two approaches to crack growth were taken. An engineering methodology was applied in an attempt to develop directly useful design tools, and a scientific approach examined the micromechanisms of crack extension at the crystallographic level and the interaction with oxidation phenomena.

General Electric Path-Independent Integral Model. A major goal of the contract program with the General Electric

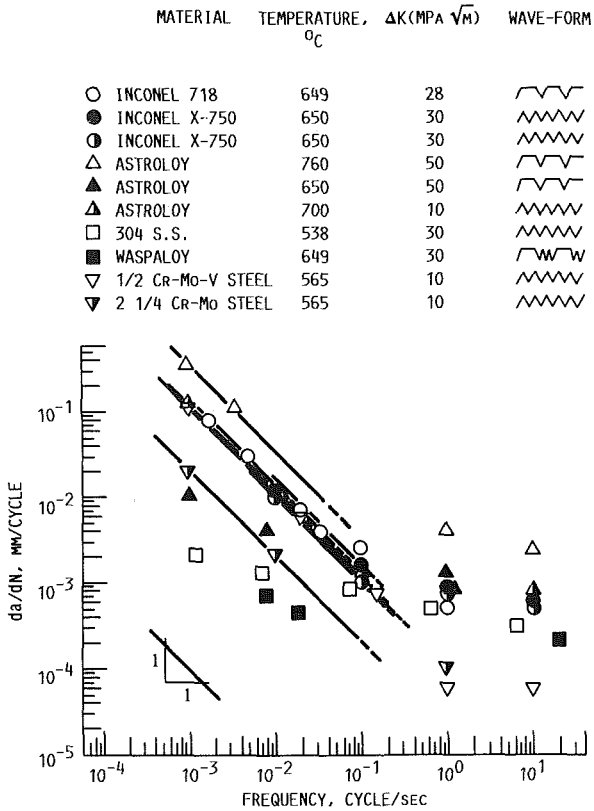

Fig. 5 Evaluation of the micromechanistic oxidation crack extension model of Liu and Oshida (1986)

Company is to develop reliable and accurate engineering life prediction capabilities to deal with cyclic crack growth at elevated temperatures. Several of the Path-Independent Integrals, *Jx*, that have been proposed over the past few years have been shown to be applicable to fracture mechanics calculations of cyclic crack growth under uniform and nonuniform thermal gradients and thermomechanical loadings. Specifically, the various *Jx* integrals proposed by Tada et al. (1973), Ainsworth et al. (1978), Blackburn et al. (1977), Kishimoto et al. (1980), and Atluri (1982) have been found suitable for analysis of crack stress fields involving nonlinear and time-dependent thermomechanical response (Kim and Orange, 1988). The traditional Rice *J*-integral (Rice, 1968), however, becomes path dependent and loses its physical significance for thermomechanical loadings. Figure 5 compares the results of a series of calculations applied to an instrumented single edge notch specimen of Inconel 718 with a linear thermal gradient. The current program with the General Electric Company will continue into 1989, during which time one of the path-independent integrals will be selected for further verification under realistic thermomechanical loading conditions found in the hot section of gas turbine engines.

Syracuse University Oxidation Crack Extension Model. Liu and Oshida (1986) and Oshida and Liu (1988) have taken a micromechanistic approach to dealing with crack propagation in superalloys. A model of intermittent microrupture of grain boundary oxide has been proposed for high-temperature fatigue crack extension. The model is outlined briefly below for the case of a trapezoidal waveform.

Oxygen arriving at a grain boundary crack tip must diffuse into the region ahead of the crack in order to form oxide along the grain boundary. When the crack tip grain boundary oxide, at a given stress level, reaches a critical size δa, the oxide will rupture and the crack will grow by the amount δa. The critical size δa depends on the stress intensity level during the holding

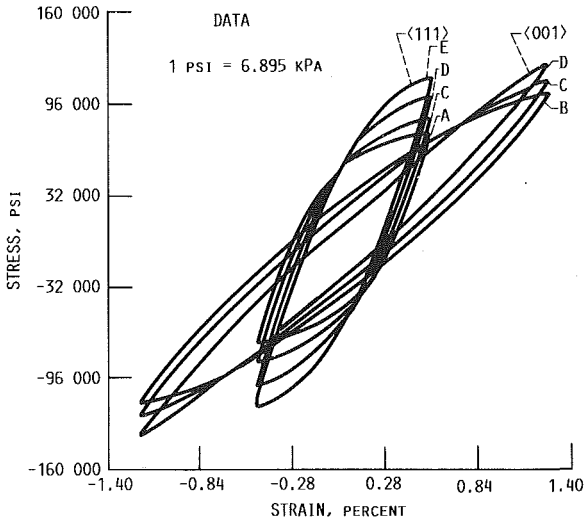

Fig. 6 Experimental loops in ⟨001⟩ and ⟨111⟩ directions at 871°C (1600°F) at strain rates of: (A) 0.001 percent per second, (B) 0.0025 percent per second, (C) 0.01 percent per second, (D) 0.1 percent per second and (E) 0.5 percent per second

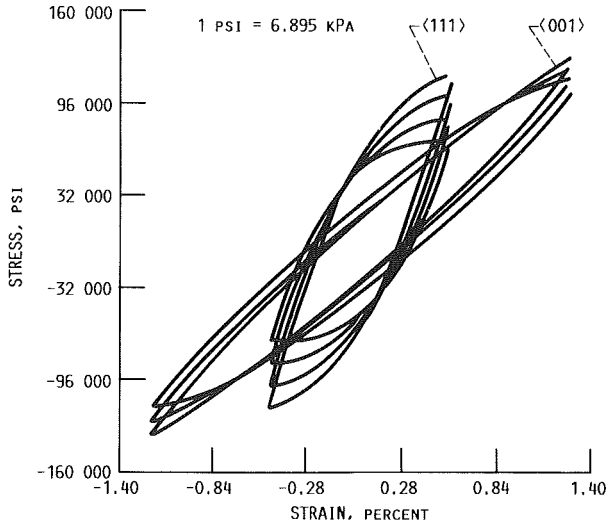

Fig. 7 Micro-model with both octahedral and cube slip terms correlated to ⟨111⟩ and ⟨001⟩ data

period. Once the crack tip has advanced to its new position, the process of grain boundary diffusion, grain boundary oxidation, and microrupture of a crack tip grain boundary can recur intermittently during a fatigue cycle, and in fact, many microruptures can take place. After each microrupture, the penetration of grain boundary oxide must start all over again from a "time" zero. The time interval δt necessary to reach the critical size δa is given by

$$\delta t = (B/D_{gb})\,(\delta a/\beta B)^{1/n} \tag{9}$$

where

B = magnitude of the diffusion jumping vector or interatomic spacing
D_{gb} = grain boundary diffusion coefficient
β, β' = proportionality constants
n = positive exponent (less than unity)

The number of microruptures during the holding period Δt_H is

$$m = \Delta t_H/\delta t = (\Delta t_H D_{gb}/B)\,(\beta B/\delta a)^{1/n} \tag{10}$$

m is linearly proportional to the holding period and is inversely proportional to the frequency.

Fatigue crack growth per cycle is the sum of the microruptures during the holding period

$$da/dN = m\delta a \tag{11}$$

From equations (9) to (11) we obtain

$$da/dN = \beta' \Delta t_H D_{gb}\,(B/\delta a)^{1-n/n} = \beta'(D_{gb}/f)\,(B/\delta a)^{1-n/n} \tag{12}$$

Note that da/dN is inversely proportional to frequency f. Figure 5 taken from Liu and Oshida (1986) illustrates the success the approach has had in correlating crack growth under high-temperature environments. The experimental results shown in the figure were obtained from the open literature.

Anisotropic Material Modeling

Pratt & Whitney Single Crystal Constitutive Model. Because of the exceptionally strong link between the cyclic deformation mechanisms in single-crystal alloys and the fatigue crack initiation process, it was deemed advisable to develop both the cyclic constitutive and cyclic crack initiation life prediction models within a single program. Furthermore, since single-crystal alloys invariably require a protective coating for successful high-temperature applications, it was also necessary to develop a cyclic constitutive and life model for the coating systems. The constitutive models will be discussed in the following section.

A unified constitutive model has been formulated for PWA 1480 single crystal material and is currently in the final stages of development. The model uses the unified approach for computing all inelastic strain rather than the conventional approach of treating creep and plasticity separately. The model assumes that all inelastic behavior results from shear strains on each of the twelve octahedral and six cube slip systems and that the global inelastic strains are simply the sum of these slip systems strains. Slip system inelastic shear strain rates are governed by a set of viscoplastic equations that involve the slip system stresses and two evolutionary state variables. The general form of the equation governing inelastic shear strain on the rth slip system as given by Swanson (1987) is

$$\dot{\gamma}_r = \frac{(\pi_r - \omega_r)\,|\pi_r - \omega_r|^{P-1}}{K^P} \tag{13}$$

where

$\dot{\gamma}_r$ = inelastic shear strain rate on the slip system
π_r = effective stress acting on the slip system
ω_r = back stress acting on the slip system
K = drag stress acting on the slip system

The model has been formulated to include several effects that have been reported to influence deformation. These include contributions from slip system stresses other than the Schmid shear stress, latent hardening due to simultaneous straining on all slip systems, and cross-slip from the octahedral to the cube slip systems.

A large body of isothermal constitutive data has been obtained at temperatures ranging from 427 to 1149°C using uniaxial specimens oriented in the ⟨001⟩, ⟨011⟩, ⟨111⟩, ⟨123⟩ crystal orientations. The constitutive model constants have been determined from these isothermal tests. Figures 6 and 7 show the measured stress strain behavior and the calculated constitutive model behavior at 871°C. The model is currently being evaluated against the stress-strain response of thermomechanical fatigue (TMF) tests that were conducted for life modeling. The single-crystal constitutive model as well as the coating constitutive model reported below are compatible with a commercially available finite element computer code.

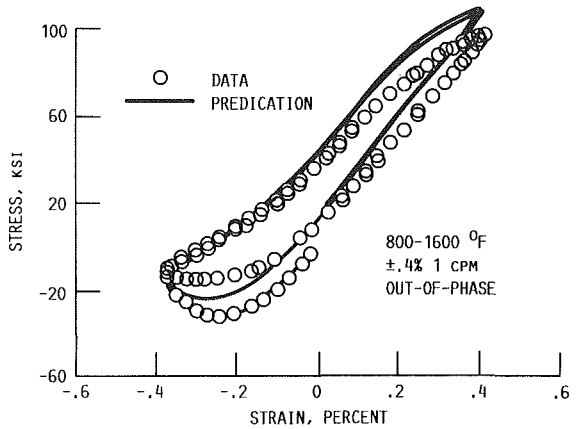

Fig. 8 Overlay coating constitutive model prediction of thermal mechanical cycle and comparison with data

Pratt & Whitney Coating Constitutive Model. Thermomechanical fatigue (TMF) cracks in turbine airfoils of PWA 1480 material generally originate from a coating crack. Thus, for airfoil life prediction, it is important to model the coating mechanical behavior as well as that of the PWA 1480. In this program, viscoplastic constitutive models are being developed for two fundamentally different coating types that are commonly used in gas turbines to provide oxidation protection: (1) a plasma-sprayed NiCoCrAlY overlay coating, and (2) a pack-cementation-applied NiAl diffusion coating.

The isotropic formulation of Walker (1981) was chosen as the overlay coating constitutive model, based on its ability to reproduce isothermal and thermomechanical hysteresis loop data reported by Swanson et al. (1987). The predicted overlay coating response of an out-of-phase thermomechanical cycle is compared to data in Fig. 8. For these purposes, solid cylindrical specimens of coating material were cut from a billet prepared by hot isostatic pressing of material powder. The aluminide diffusion coating constitutive model is currently under development, and will be more difficult to determine owing to the fact that it will be impossible to make solid specimens of stand-alone coating material.

Cyclic Crack Initiation. Directionally cast, anisotropic, nickel-base superalloys (particularly single crystals) exhibit greater creep-fatigue resistance than their conventionally cast polycrystalline counterparts. To take full advantage of these improved material properties, however, requires the development of accurate cyclic constitutive and life prediction models for these highly directional alloys. Direct modification of polycrystalline behavior models is inadequate, and a new approach that recognizes the micromechanisms of crystal response is necessary. Unfortunately, the program was able to address only the crack initiation aspects of single crystal superalloys. Cyclic crack growth life prediction modeling must await future efforts.

Pratt & Whitney Coating and Single Crystal Life Prediction Model. Generally, all coated PWA 1480 orientations (i.e., ⟨001⟩, ⟨011⟩, ⟨111⟩, and ⟨123⟩) that were tested in thermomechanical fatigue initiated cracks in the metal at sites where coating cracking had occurred. Isothermal tests of coated ⟨001⟩ PWA 1480 also typically initiated cracks first in the coating layers. However, many coated non- ⟨001⟩ isothermal fatigue tests initiated cracks underneath the specimen outer surface in either the PWA 1480 or the coating/PWA 1480 interfacial region. Initiation occurred predominately at porosity sites.

The following life prediction approach was developed to account for the observed specimen cracking modes:

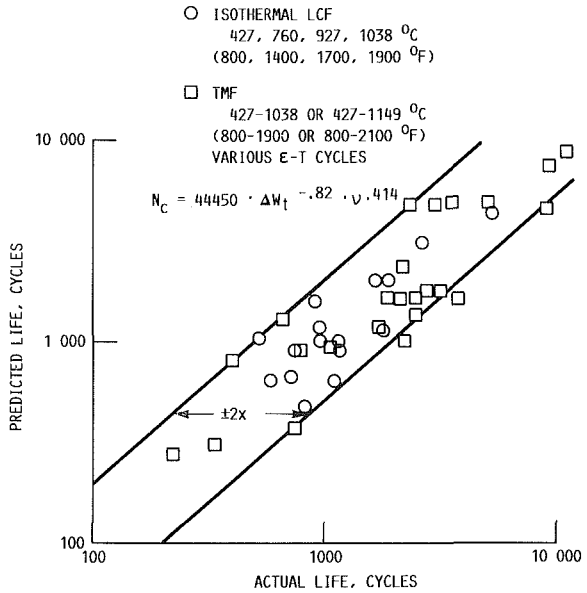

Fig. 9 Overlay coating life model correlation of isothermal life data and prediction of thermal mechanical fatigue life data

$$N_f = N_c + N_{sc} + N_{sp}$$

or (14)

$$N_f = N_{si} + N_{sp}$$

whichever is smaller, where

N_c = cycles to initiate a crack through the coating
N_{sc} = cycles for coating initiated crack to penetrate a small distance into the substrate
N_{si} = cycles to initiate a substrate crack due to macroscopic slip, oxidation effects, or defects
N_{sp} = cycles to propagate substrate crack to failure
N_f = total cycles to fail specimen or component

The following modified tensile hysteretic energy model was developed for the overlay coating:

$$N_c = C(\Delta W_t)^{-b}\nu^m \tag{15}$$

where

$$\nu = \frac{1}{\sum_{\text{cycle}} \frac{r(T_i)}{r(T_o)} t_i - D_o}; \nu \le 1.0 \tag{16}$$

$r(T)$ = $r_o \exp(-Q/T)$ = temperature- and time-dependent damage rate
ΔW_t = tensile hysteretic energy, N − m/m^3 (in-lbf/in.^{3})
T_i = individual temperature levels in the cycle, K(R)
t_i = time (min) at T_i, including 100 percent of tensile hold and 30 percent of compressive hold times in the cycle, if any
T_o = threshold temperature for temperature dependent damage, assumed to be 1088 K (1960 R)
D_o = "incubation damage"
Q = effective activation energy for temperature-and time-dependent damage.

The term ν is an extension of the Ostergren (1976) time-dependent damage frequency term. As used herein, it includes both temperature- and time-dependent damage functions to model thermally activated processes.

Model constants were determined from isothermal tests

conducted at 427, 760, 927, and 1038°C (800, 1400, 1700, and 1900 °F). Coating hysteresis loops were predicted using the PWA 286 constitutive model incorporated into a one-dimensional model. This model determines the stress-strain of the substrate and coating by imposing an equivalent displacement history. Differences in coefficients of thermal expansion are included in the model.

The model unifies isothermal and TMF predicted lives within a factor of about 2.5, as seen in Fig. 9. Generally, the worst predicted test lives were limited to 1149°C (2100°F) maximum temperature TMF tests.

Prediction of these test results should improve when 1149°C (2100°F) isothermal tests are included in the data set used to determine model constants.

Additional model modification will be necessary to include the effect of biaxial coating loads introduced by the thermal growth mismatch between the coating and the substrate during uniaxial TMF tests and engine transients.

PWA 273 aluminide coating and PWA 1480 crack initiation model development for calculating N_{sc}, N_{sp}, and N_{si} is currently in process. At present, based on isothermal fatigue correlations, the most promising candidate models for these materials are also derived from an approach based on hysteretic energy.

Concluding Remarks

In conclusion, we would like to emphasize that significant accomplishments have been achieved in the fatigue and fracture arena through the atmosphere created by the HOST Project. We are now much better able to deal with durability enhancement in the aeronautical propulsion industry through theoretical, analytical, and experimental approaches. Given the ability to complete the tasks we have started, we expect to reap even greater rewards in the near future.

The major accomplishments to date are summarized below:

1. An advanced high-temperature fatigue and structures research laboratory has been implemented at NASA Lewis.
2. Two new crack initiation life prediction methods have been developed for application to complex-fatigue loading of nominally isotropic superalloys at high temperatures.
3. Cyclic constitutive models for oxidation protective coatings and for highly anisotropic single-crystal turbine blade alloys have been developed and verified.
4. A preliminary cyclic crack initiation life prediction model for coated single-crystal superalloys has been proposed and is undergoing continued evaluation. The model utilizes tensile hysteretic energy and frequency as primary variables.
5. Two high-temperature cyclic crack growth life prediction models have been proposed; micromechanistic and phenomenological engineering approaches have been taken. The micromechanistic approach is based upon oxidation interactions with mechanical deformation at the crack tip, while the engineering approach has its origins in the use of Path-Independent Integrals to describe the necessary fracture mechanics parameters.

References

Ainsworth, R. A., Neale, B. K., and Price, R. H., 1978, "Fracture Behavior in the Presence of Thermal Strains," *Tolerance of Flaws in Pressurized Components*, IMechE, London, United Kingdom, pp. 171–178.

Atluri, S. N., 1982, "Path-Independent Integrals in Finite Elasticity and Inelasticity, With Body Forces, Inertia, and Arbitrary Crack-Face Conditions," *Engineering Fracture Mechanics*, Vol. 16, No. 3, pp. 341–363.

Blackburn, W. S., Jackson, A. D., and Hellen, T. K., 1977, "An Integral Associated With the State of a Crack Tip in a Nonelastic Material," *International Journal of Fracture*, Vol. 13, No. 2, pp. 183–200.

Halford, G. R., Saltsman, J. F., and Hirschberg, M. H., 1977, "Ductility Normalized-Strainrange Partitioning Life Relations for Creep-Fatigue Life Prediction," in: *Environmental Degradation of Engineering Materials*, M. R. Louthan and R. P. McNitt, eds., Virginia Tech. Printing Dept., V.P.I. and State University, Blacksburg, VA, pp. 599–612 (NASA TM-73737).

Halford G. R., and Saltsman, J. F., 1983, "Strainrange Partitioning—A Total Strainrange Version," in: *Advances in Life Prediction Methods*, D. A. Woodford and J. R. Whitehead, eds., ASME, New York, pp. 17–26.

Hirschberg, M. H., and Halford, G. R. 1976, "Use of Strain-range Partitioning to Predict High-Temperature Low-Cycle Fatigue Life," NASA TN D-8072

Kim, K. S., and Orange, T. W., 1988, "A Review of Path-Independent Integrals in Elastic-Plastic Fracture Mechanics," *Fracture Mechanics: 18th National Symposium*, ASTM STP-945, ASTM, Philadelphia, PA, pp. 713–729 (see also NASA CR-174956).

Kishimoto, K., Aoki, S., and Sakata, M., 1980, "On the Path Independent Integral—J," *Engineering Fracture Mechanics*, Vol. 13, No. 4, pp. 841–850.

Lindholm, U. S., Chan, K. S., Bodner, S. R., Weber, R. M., Walker, K. P., and Cassenti, B. N., 1984, "Constitutive Modeling for Isotropic Materials (HOST)," NASA CR-174718.

Liu, H. W., and Oshida, Y., 1986, "Grain Boundary Oxidation and Fatigue Crack Growth at Elevated Temperatures," *Theoretical and Applied Fracture Mechanics*, Vol. 6, No. 2, pp. 85–94.

Manson, S. S., Halford, G. R., and Nachtigall, A. J., 1975, "Separation of the Strain Components for Use in Strainrange Partitioning," in: *Advances in Design for Elevated Temperature Environment*, S. Y. Zamrik and R. I. Jetter, eds., ASME, New York, pp. 17–28.

McGaw, M. A., and Bartolotta, P. A., 1987, "A High Temperature Fatigue and Structures Testing Facility," *4th Annual Hostile Environments and High Temperature Measurements Conference Proceedings*, Society for Experimental Mechanics, Bethel, CT, pp. 12–29 (see also NASA TM-100151).

Moreno, V., 1983, "Creep Fatigue Life Prediction for Engine Hot Section Materials (Isotropic)," NASA CR-168228.

Moreno, V., Nissley, D. M., and Liu, L. S., 1985, "Creep Fatigue Life Prediction for Engine Hot Section Materials (Isotropic)," NASA CR-174844.

Moreno, V., Nissley, D. M., Halford, G. R., and Saltsman, J. F., 1985, "Application of Two Creep-Fatigue Life Models for the Prediction of Elevated Temperature Crack Initiation of a Nickel-Base Alloy," AIAA Paper 85-1420.

Nelson, R. S., Schoendorf, J. F., and Lin, L. S., 1986, "Creep Fatigue Life Prediction for Engine Hot Section Materials (Isotropic)," NASA CR-179550.

Oshida, Y., and Liu, H. W., 1988, "Grain Boundary Oxidation and An Analysis of the Effects of Oxidation on Fatigue Crack Nucleation Life," *Low Cycle Fatigue—Directions for the Future*, ASTM STP-942, ASTM, Philadelphia, PA, pp. 1199–1217.

Ostergren, W. J., 1976, "A Damage Function and Associated Failure Equations for Predicting Hold Time and Frequency Effects in Elevated-Temperature, Low-Cycle Fatigue," *Journal of Testing and Evaluation*, Vol. 4, No. 5, pp. 327–339.

Ramaswamy, V. G., Van Stone, R. H., Dame, L. T., and Laflen, J. H., 1985, "Constitutive Modeling for Isotropic Materials," NASA CR-175004.

Saltsman, J. F., and Halford, G. R., 1988, "An Update of the Total Strain Version of SRP," *Low Cycle Fatigue—Directions for the Future*, ASTM STP-942, ASTM, Philadelphia, PA, pp. 329–341.

Swanson, G. A., Linask I., Nissley, D. M., Norris, P. P., Meyer, T. G., and Walker, K. P., 1987, "Life Prediction and Constitutive Models for Engine Hot Section Anisotropic Materials," NASA CR-179594.

Tada, H., Paris, P. C., and Irwin, G. R., 1973, *The Stress Analysis of Cracks Handbook*, Del Research Corporation, Hellertown, PA.

Walker, K. P., 1981, "Research and Development Programs for Nonlinear Structural Modeling With Advanced Time-Temperature Dependent Constitutive Relationships," NASA CR-165533.

Structural Analysis Method Development for Turbine Hot Section Components

R. L. Thompson
NASA Lewis Research Center
Cleveland, OH 44135

This paper summarizes the structural analysis technologies and activities of the NASA Lewis Research Center's gas turbine engine Hot Section Technology (HOST) program. The technologies synergistically developed and validated include: time-varying thermal/mechanical load models; component-specific automated geometric modeling and solution strategy capabilities; advanced inelastic analysis methods; inelastic constitutive models; high-temperature experimental techniques and experiments; and nonlinear structural analysis codes. Features of the program that incorporate the new technologies and their application to hot section component analysis and design are described. Improved and, in some cases, first-time three-dimensional nonlinear structural analyses of hot section components of isotropic and anisotropic nickel-base superalloys are presented.

Introduction

Hot section components of aircraft gas turbine engines are subjected to severe thermal-structural loading conditions during the engine mission cycle. The most severe and damaging stresses and strains are those induced by the steep thermal gradients that occur during the startup and shutdown transients. The transient, as well as steady-state, stresses and strains are difficult to predict, in part, because the temperature gradients and distributions are not well known or readily predictable and, in part, because the cyclic elastic-viscoplastic behaviors of the materials at these extremes of temperature and strain are not well known or readily predictable.

A broad spectrum of structures-related technology programs has been underway at the NASA Lewis to address these deficiencies at the basic as well as the applied levels, with participation by industry and universities. One of these programs was the structures element of the turbine Hot Section Technology (HOST) program. The structures element focused on three key technology areas: inelastic constitutive model development, three-dimensional nonlinear structural methods and code development, and experimentation to calibrate and validate the models and codes. These technology areas were selected not only because today's hot section component designs are materially and structurally difficult to analyze with existing analytical tools, but because even greater demands will be placed on the analysis of advanced designs. It is the need for improved engine performance (higher temperatures, lower cooling flows), lower engine weight, and improved engine reliability and durability that will spur development of advanced analytical tools and expanded experimental capabilities.

Because materials used in today's turbine engine hot section components are operating at elevated temperature, time-independent (plastic) and time-dependent (creep and stress relaxation) material behavioral phenomena occur simultaneously, and these phenomena will be exacerbated in future component designs. Classical elastic-plastic theories, where creep and plasticity are uncoupled, do not adequately characterize these interactive phenomena. These interactions are captured with inelastic (viscoplastic or unified) constitutive models. Under HOST, several viscoplastic models were developed for high-temperature isotropic and anisotropic nickel-base superalloys used in hot section components. These models were incorporated in several nonlinear three-dimensional structural analysis codes.

The analysis demands placed on hot section component designs result not only from the use of advanced materials and their characterization, but also from the use of new and innovative structural design concepts. There is an obvious need to develop advanced computational methods and codes, with the focus on improved accuracy and efficiency, to predict nonlinear structural response of advanced component designs. Under HOST, improved time-varying thermal-mechanical load models for the entire engine mission cycle from startup to shutdown were developed. The thermal model refinements are consistent with those required by the structural codes, including considerations of mesh-point density, strain concentrations, and thermal gradients. An automated component-specific geometric modeling capability that will produce three-dimensional finite element models of the hot section components was also developed. Self-adaptive solution strategies were developed and included to facilitate the selection of appropriate elements, mesh sizes, etc. New and improved nonlinear three-dimensional structural analysis codes, including temporal elements with time-dependent properties to account for creep effects in the materials and components, were developed. A data transfer module was developed to

Contributed by the International Gas Turbine Institute and presented at the 33rd International Gas Turbine and Aeroengine Congress and Exhibition, Amsterdam, The Netherlands, June 5-9, 1988. Manuscript received by the International Gas Turbine Institute January 11, 1988.

Table 1 HOST structural analysis programs

NAS3-23925, Southwest Research Institute (U.S. Lindholm), Constitutive Modeling for Isotropic Materials.

NAS3-23927, General Electric (V.G. Ramaswamy), Constitutive Modeling for Isotropic Materials.

NAS3-379, University of Akron (D.N. Robinson), Multiaxial Theories of Viscoplastic for Isotropic and Anisotropic Materials.

NAG3-512, University of Connecticut (E.H. Jordan), Constitutive Modeling of Single Crystal and Directionally Solidified Superalloys.

NAG3-511, University of Cincinnati (D.C. Stouffer), Anisotropic Constitutive Modeling for Nickel-Base Single Crystal Superalloy René N4.

NAS3-23272, General Electric (R. Maffeo), Burner Liner Thermal/Structural Load Modeling.

NAS3-23687, General Electric (R.L. McKnight), Component-Specific Modeling.

NAS3-23698, General Electric (R.L. McKnight), Three-Dimensional Inelastic Analysis Methods for Hot Section Components I.

NAS3-23697, Pratt and Whitney Aircraft (E.S. Todd), Three-Dimensional Inelastic Analysis Methods for Hot Section Components II.

IAN 40-1447-84 and DE-AC05-840R 21400, Oak Ridge National Laboratory (J.R. Corum), Determination of Surface of Constant Inelastic Strain Rate at Elevated Temperature.

NASA Lewis Research Center (J.R. Ellis and P.E. Moorhead), High-Temperature Fatigue and Structures Laboratory/Structural Component Response Facility.

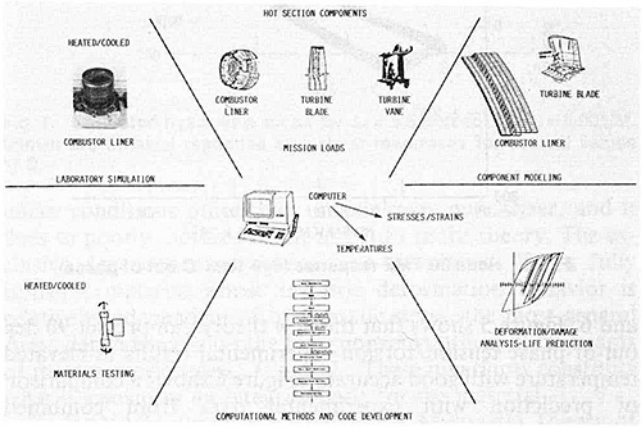

Fig. 1 Nonlinear structural analysis technologies and activities under HOST

transfer temperatures automatically from finite difference and finite element thermal analysis codes to finite element structural analysis codes.

Essential for the confident use of these models and structural analysis codes in the analysis and design of hot section components is their calibration and validation. Under HOST, experimental facilities were upgraded and experiments conducted to calibrate and validate the models and codes develped. Unique uniaxial and multiaxial high-temperature thermomechanical tests were conducted. In addition, unique thermomechanical tests on sections of conventional and advanced combustor liners were conducted in the Structural Component Response rig at NASA Lewis. Extensive, quality databases were generated. Advanced strain and temperature instrumentation was also evaluated.

Table 1 is a summary of the contracts and grants that were an integral part of the structures element under HOST. Research efforts under grants and contracts, as well as in-house efforts, are described in the paper, along with the most significant of the many accomplishments for each. Figure 1 summarizes the nonlinear structural analysis technologies and activities under HOST.

Isotropic Material Modeling

Southwest Research Institute Contract. Unified constitutive models were developed for structural analysis of turbine engine hot section components under NASA/HOST con-

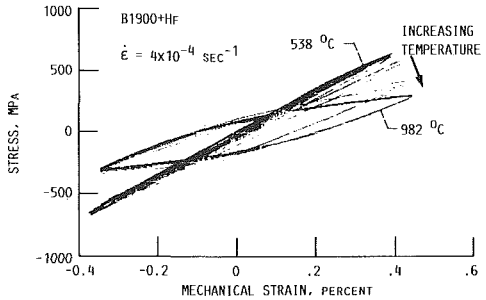

Fig. 2 Controlled strain cycling with temperature change from 538°C to 982°C

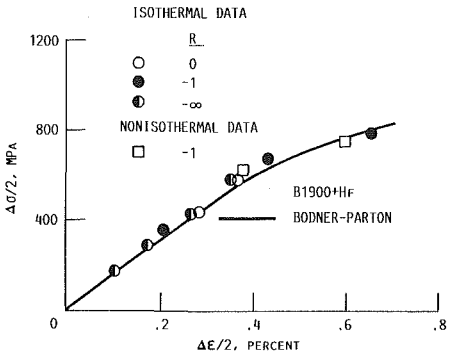

Fig. 3 Comparison of isothermal and nonisothermal cyclic data of B1900 + HF at 760°C

tract NAS3-23925, "Constitutive Modeling for Isotropic Materials" (Chan et al., 1986). During this project, two existing models of the unified type were developed for application to isotropic, cast, nickel-base alloys used for air-cooled turbine blades and vanes. The two models are those of Walker (1981) and Bodner and Partom (1975). Both models were demonstrated to yield good correlation with experimental results for two alloys: PWA alloy B1900+Hf and MAR-M247. The experimental correlations were made with testing under uniaxial and biaxial tensile, creep, relaxation, cyclic, and thermomechanical loading conditions over a range in strain rates and temperatures up to 1100°C. Also, both models were implemented in the MARC nonlinear finite element computer code with test cases run for a notched round tensile specimen and an airfoil portion of a typical cooled turbine blade.

Typical results of thermomechanical strain cycling of B1900+Hf material are shown in Figs. 2 and 3. In Fig. 2, we show a single specimen cycled to saturation at 538°C, a temperature increase to 982°C with saturated loops achieved at that temperature, and a return to 538°C, all under constant strain range control. Two observations evidence absence of thermal history effect. The high-temperature excursion resulted in no change in the hysteresis loop at 538°C, and the cyclic stress range associated with a given cyclic strain was the same under this type of nonisothermal history as under strictly isothermal cycling, as shown in Fig. 3. Both types of cycling agree with the Bodner-Partom model prediction, which is based on isothermal data only.

A second example is the analysis of an airfoil of a typical cooled turbine blade. Simulations were run in which a classical creep-plasticity model was compared with the Walker and Bodner-Partom models for B1900+Hf material. The airfoil was exercised through three full flight spectra of taxi, take off, climb, cruise, descent, taxi, and shutdown. Computational efficiency with the unified models was as good or better than with a more classical elastic-plastic approach. The effective stress versus strain response at the airfoil critical location is compared in Fig. 4 for all three constitutive models. The

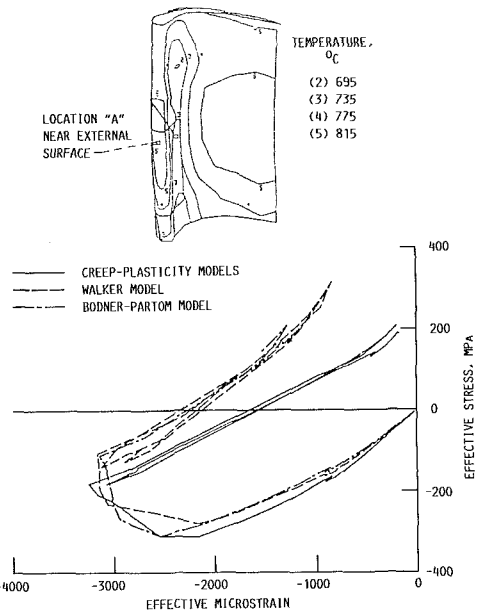

Fig. 4 *Airfoil calculations at location "A" using the MARC finite element analysis code*

unified models yield very similar results but substantially different from the classical creep-plasticity model. Unfortunately, no experimental results are available or easily obtainable for this complex problem.

In summary, the program has demonstrated that for the cast nickel-base alloys studied, B1900+Hf and MAR-M247, both isothermal and nonisothermal complex loading histories can be well predicted using the unified constitutive model approach with all necessary material constants derived solely from isothermal test data.

The program has also demonstrated rather conclusively that the unified constitutive model concept is a very powerful tool for predicting material response in hot section components under complex, time-varying, thermomechanical loadings. This confidence is gained from extensive correlations between two existing models and a large base of experimental data covering the range in stress, strain rate, and temperature of interest. The unified constitutive models have also been demonstrated to be computationally efficient when incorporated into a large finite element computer code (MARC).

General Electric Contract. Unified constitutive models were also developed and validated for structural analysis of turbine engine hot section components under NASA/HOST contract NAS3-23927, "Constitutive Modeling for Isotropic Materials" (Ramaswamy, 1986). As part of this effort, several viscoplastic constitutive theories were evaluated against a large uniaxial and multiaxial data base on René 80 material, which is a cast nickel-base alloy used in turbine blade and vane applications. Initially, it was the intent to evaluate only available theories; however, it was found that no available approach was satisfactory in modeling the high-temperature time-dependent behavior of René 80. Additional considerations in model development included the cyclic softening behavior of René 80, rate independence at lower temperatures, and the development of a new model for static recovery. These considerations were incorporated in a new constitutive model, which was implemented into a finite element computer code. The code was developed as a part of the contract specifically for use with unified theories. The code was verified by a reanalysis of the turbine tip durability problem, which was part of the pre-HOST activities at General Electric.

Typical of the many results obtained from this effort are the multiaxial thermomechanical comparisons shown in Figs. 5

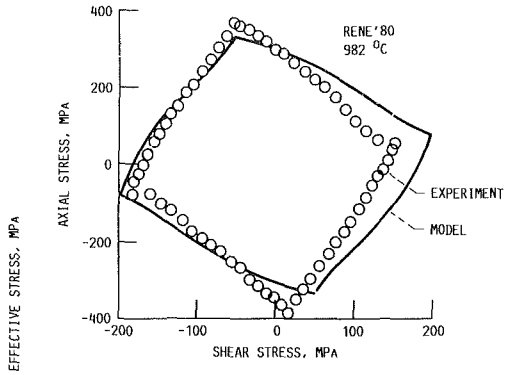

Fig. 5 **René 80 response to 90° out-of-phase tension/torsion cyclic loading**

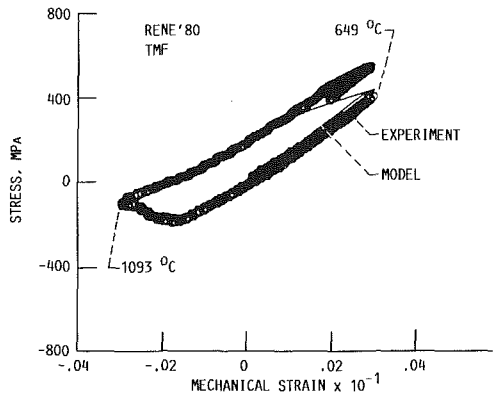

Fig. 6 **René 80 TMF response (649-1093°C out-of-phase)**

and 6. Figure 5 shows that the new theory can predict 90 deg out-of-phase tension/torsion experimental results at elevated temperature with good accuracy. Figure 6 shows a comparison of prediction with experimental data from combined temperature and strain cycling tests. There is reasonably good agreement between predictions and experiment considering the predictions are based only on isothermal data.

The theory was implemented into a new three-dimensional finite element code that uses a 20-noded brick element. The program uses a dynamic time incrementing procedure to minimize cost while guaranteeing an accurate solution. The inelastic rate equations and state variable evolution equations are integrated using a second-order Adams–Moulton predictor corrector technique. Piecewise linear load histories are modeled in order to simplify input. Further economics have been achieved by improving the stability of the initial strain method and further reducing the number of equilibrium iterations.

In summary, a new multiaxial constitutive model that can represent the complex nonlinear high-temperature behavior of René 80 was developed. The model was extensively verified based on data at several temperatures. The thermomechanical proportional and nonproportional cyclic modeling capabilities of the model were demonstrated. The model was implemented in a three-dimensional structural analysis finite element code and a turbine blade was analyzed.

University of Akron Grant. Many viscoplastic constitutive models for high-temperature structural alloys are based exclusively on uniaxial test data, as previously discussed. Generalization to multiaxial states of stress is made by assuming the stress dependence to be on the second principal invariant (J_2) of the deviatoric stress, frequently called the "effective" stress. Testing other than uniaxial, e.g., shear, biaxial, etc., is generally done in the spirit of verification testing, not as part of the data base of the model. If such a J_2 theory, based on uniaxial testing, is called upon to predict behavior

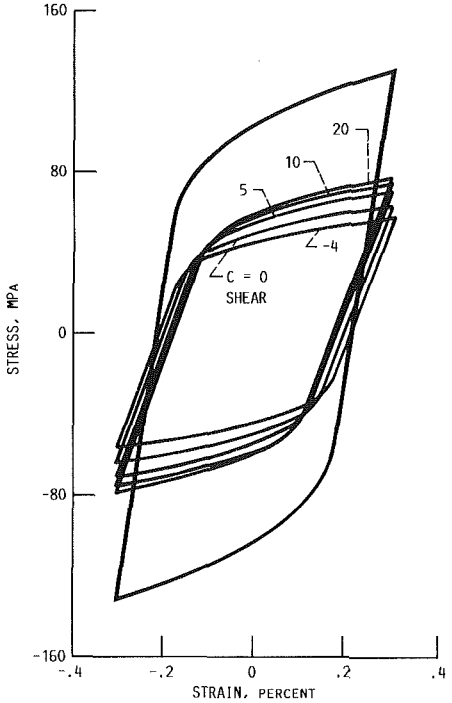

Fig. 7 Saturated hysteresis loops for $\Delta\epsilon = 0.6$ percent and $\dot{\epsilon} = 0.001$/M. Shown are uniaxial response and shear responses for several values of C.

under conditions other than uniaxial, say pure shear, and it does so poorly, nothing is left to adjust in the theory. The exclusive dependence on J_2 must be questioned. For a fully isotropic material whose inelastic deformation behavior is relatively independent of hydrostatic stress, the most general stress dependence is on the two (nonzero) principal invariants of the deviatoric stress, J_2 and J_3. These invariants constitute what is known as an integrity basis for the material.

Under NASA Grant NAG3-379, "A Multiaxial Theory of Viscoplasticity for Isotropic Materials" (Robinson, 1984), a time-dependent description potential function based on constitutive theory with stress dependence on J_2 and J_3 that reduces to a known J_2 theory as a special case was developed. The characterization of viscoplasticity can be made largely on uniaxial testing, but the "strength" of the J_3 dependence must be determined by testing other than uniaxial, e.g., pure shear.

Several calculations have been made using forms of the functions in the model and assoicated material parameters that are typical of ferritic chrome-based and austenitic stainless-steel alloys. Qualitatively similar results can be expected for nickel-based alloys. Figure 7 shows predicted hysteresis loops over a constant strain range ($\Delta\epsilon = 0.6$ percent) and strain rate ($\dot{\epsilon} = 0.001$/m). The curve labeled "uniaxial" can be thought of as having been carefully fit on the basis of uniaxial data. Predictions of pure shear response are also shown, corresponding to different values of C. A J_2, J_3 theory reduces to a J_2 theory for $C = 0$. Even after tedious fitting of uniaxial cyclic data, if the shear prediction does not correlate well with shear data, nothing can be done in a J_2 theory short of compromising the uniaxial correlations. The present J_2, J_3 theory allows some flexibility in accurately predicting response other than uniaxial through the parameter C. Note that the hysteresis loop labeled $C = 10$ indicates a cyclic response that is about 20 percent stronger than the J_2 response ($C = 0$)

Figure 8 shows predictions of creep response, i.e., behavior under constant stress. Here, the strain-time curve labeled "uniaxial and shear $C = 0$" represents both the uniaxial response (using the strain scale on the left) and the shear response for a J_2 material (using the strain scale on the right). Each shear response corresponding to a particular value of C

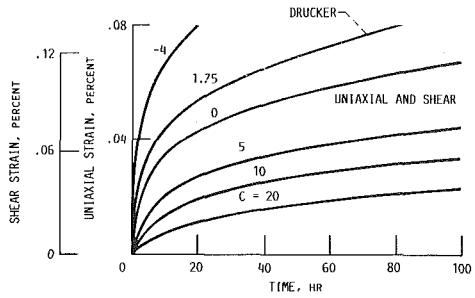

Fig. 8 Creep response in uniaxial tension and shear for several values of C

is to be measured using the right-hand shear strain scale. In creep, the effect of the J_3 dependence appears to be more pronounced than for strain cycling. Here, for $C = 10$, the creep strain after 100 h differs by a factor of 2 from that for the J_2 response ($C = 0$).

Anisotropic Material Modeling

University of Connecticut Grant. Nickel-base monocrystal superalloys have been under development by turbine manufacturers for a number of years. Successful attempts have now been made under grant NAG3-512, "Constitutive Modeling of Single Crystal and Directionally Solidified Superalloys" (Walker and Jordan, 1987) to model the deformation behavior of these materials based on both a macroscopic constitutive model and a micromechanical formulation based on crystallographic slip theory. These models have been programmed as FORTRAN subroutines under contract NAS3-23939 to Pratt and Whitney and included in the MARC nonlinear finite element program. They are currently being used to simulate thermal/mechanical loading conditions expected at the "fatigue critical" locations on a single crystal (PWA 1480) turbine blade. Such analyses form a natural precursor to the application of life prediction methods to gas turbine airfoils.

The difficulty in analyzing the deformation behavior of single-crystal materials lies in their anisotropic behavior. Two separate unified viscoplastic constitutive models for monocrystal PWA 1480 have been completely formulated. In one model, the directional properties of the inelastic deformation behavior are achieved by resolving the summed crystallographic slip system stresses and strains onto the global coordinate system. In the other model, the required directional properties are achieved by operating on the global stresses and strains directly with fourth-rank anisotropy tensors. The crystallographic slip based model is more accurate and has more physical significance than the macroscopic model, but is more computationally intensive than its macroscopic counterpart.

The material constants in both models can be obtained from uniaxial tests on ⟨001⟩ and ⟨111⟩ oriented uniaxial specimens, or from uniaxial and torsion tests on ⟨001⟩ oriented tubular specimens. Both models achieve good correlation with the experimental data in the ⟨001⟩ and ⟨111⟩ corners of the stereographic triangle, and both models correctly predict the deformation behavior of specimens orientated in the ⟨011⟩ direction. The tension-torsion tests on tubular specimens orientated in the ⟨001⟩ direction were carried out at a temperature of 870°C (1600°F) at the University of Connecticut. Further tests at temperatures ranging from room temperature to 1149°C (2100°F) have been carried out at Pratt and Whitney under contract NAS3-23939. Good correlations and predictions are uniformly achieved at temperatures above 649°C (1200°F), but further work appears to be necessary to model the deformation behavior of PWA 1480 monocrystal material below 649°C (1200°F) correctly.

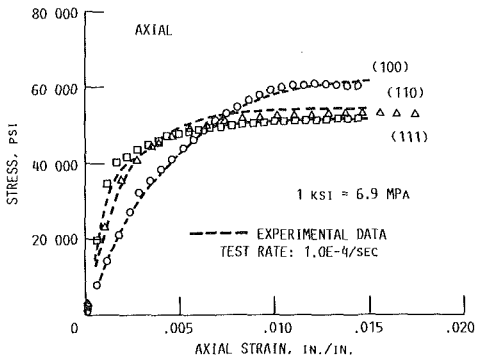

Fig. 9 René N4 predicted tensile response and experimental data for specimen orientations of [100], [110], and [111] at 982°C (1800°F)

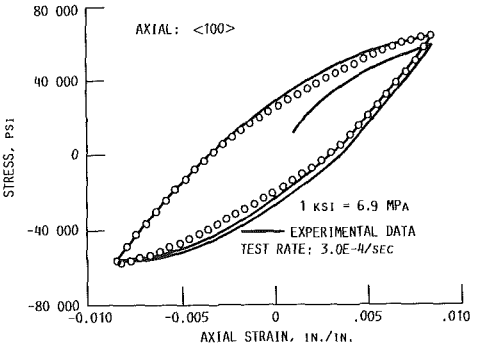

Fig. 10 René N4 predicted cyclic response and experimental data for specimen orientation of [100] at 982°C (1800°F)

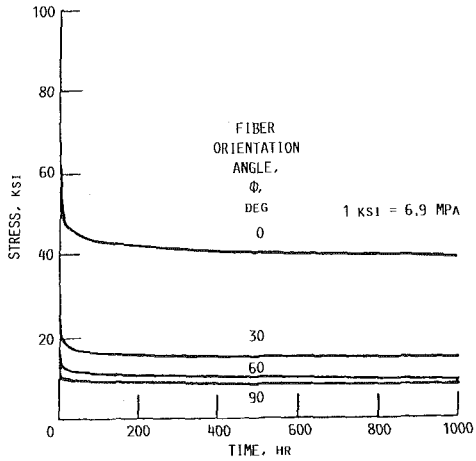

Fig. 11 Relaxation curves for different fiber orientation angles

University of Cincinnati Grant. Nickel-base single-crystal superalloys have attracted considerable interest for use in gas turbine jet engines because of their superior high-temperature properties. In polycrystalline turbine parts, rupture is usually due to crack propagation originating at the grain boundaries. Since single-crystal alloys have no grain boundaries, use of the alloy has significant advantages for increased strength and longer life.

Under grant NAG3-511, "Anisotropic Constitutive Modeling for Nickel-Base Single Crystal Alloy René N4," an anisotropic constitutive model was developed based on a crystallographic approach. The current equations modified a previous model proposed by Dame and Stouffer (1986) where a Bodner–Partom equation with only the drag stress was used to model the local inelastic response in each slip system. Their model was considered successful for predicting both the orientation dependence and tension/compression asymmetry for tensile and creep histories for single crystal alloy René N4 at 760°C (1400°F). However, certain properties including fatigue were not satisfactorily modeled. A back stress state variable was incorporated into the local slip flow equation based on the observed experimental observations. Model predictability was improved especially for mechanical properties such as inelasticity and fatigue loops.

Figures 9 and 10 are typical of the numerous results obtained from this effort. Experimental data and predicted responses of tensile and cyclic conditions for different specimen orientations are compared. Shown in Fig. 9 are the experimental data in [100] and [111] orientations that were used to determine material constants. The response in [110] orientation is the predicted result. The model predicted very well the elastic moduli, hardening characteristics (the knee of the curves), and the saturated values. In Fig. 10, comparisons show the model predicts very well the cyclic tension/compression asymmetry, hardening characteristics, and rate effect for the [100] orientation. The prediction of the hysteresis loop was based solely on saturated constants determined from tensile tests.

University of Akron Grant. Structural alloys used in high-temperature applications exhibit complex thermomechanical behavior that is time-dependent and hereditary. Recent attention is being focused on metal-matrix composite materials for aerospace applications that, at high temperature, exhibit all the complexities of conventional alloys (e.g., creep, relaxation, recovery, rate sensitivity) and, in addition, exhibit further complexities because of their strong anisotropy.

Under grant NAG3-379, "A Continuum Deformation Theory for Metal-Matrix Composites at High Temperature" (Robinson et al., 1986), a continuum theory was developed for representing the high-temperature, time-dependent, hereditary deformation behavior of metallic composites that can be idealized as pseudohomogeneous continua with locally definable directional characteristics. Homogenization of textured materials (molecular, granular, fibrous) and applicability of continuum mechanics in structural applications depends on characteristic body dimensions, the severity of gradients (stress, temperature, etc.) in the structure, and on the relative size of the internal structure (cell size) of the material. Examination reveals that the appropriate conditions are met in a significantly large class of anticipated aerospace applications of metallic composites to justify research into the formulation of continuum-based theories.

The starting point for the theoretical development is the assumed existence of a dissipation potential function Ω for a composite material; that is a two-constituent (fiber/matrix), pseudohomogeneous material.

The potential function is of the form

$$\Omega = \Omega(\sigma_{ij}, \alpha_{ij}, d_i d_j, T) \tag{1}$$

in which σ_{ij} denotes the components of (Cauchy) stress, α_{ij} the components of a tensorial internal state variable (internal stress), $d_i d_j$ the components of a directional tensor, and T the temperature. The symmetric tensor $d_i d_j$ is formed by a self product of the unit vector d_i denoting the local fiber direction. Account can be taken of more than a single family of fibers inherent to the continuum element.

The present theory has been implemented into the commercial finite element code MARC. Several trial calculations have been made under uniaxial conditions using material functions and parameters that approximate a tungsten/copper composite material. A transversely isotropic continuum elasticity theory has been used in conjunction with the present viscoplastic theory. The results of the calculations show the expected responses of rate-dependent plasticity, creep, and relaxation as well as appropriate anisotropic features. Predictions of relaxation and hysteresis loops for different fiber

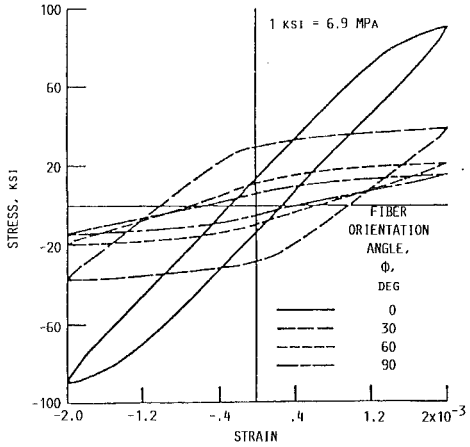

Fig. 12 Hysteresis loops for different fiber orientation angles; strain rate = 0.001/min

orientation angles on a tungsten/copper-like material are shown in Figs. 11 and 12.

Computational Methods and Code Development

General Electric Contract. It has become apparent in recent years that there is a serious problem of interfacing the output temperatures and temperature gradients from either the heat transfer codes or engine tests with the input to the stress analysis codes. With the growth in computer postprocessors, the analysis of hot section components using hundreds and even thousands of nodes in the heat transfer and stress models has become economical and routine. This has exacerbated the problem of manual transfer of output three-dimensional temperatures from heat transfer codes to stress analysis input to where the engineering effort required is comparable to that required for the remainder of the analysis. Furthermore, a considerable amount of approximation has been introduced in an effort to accelerate the process. This tends to introduce errors into the temperature data, which negates the improved accuracy in the temperature distribution achieved through use of a fine mesh. There is, then, a strong need for an automatic thermal interface module. A module was developed under contract NAS3-23272, "Burner Liner Thermal/Structural Load Modeling" (Maffeo, 1984).

The overall objectives of this thermal/structural transfer module were that it handle independent mesh configurations, finite difference and finite element heat transfer codes, perform the transfer in an accurate and efficient fashion, and the total system be flexible for future applications. Key features of the code developed include: independent heat transfer and stress model meshes, accurate transfer of thermal data, computationally efficient transfer, user friendly program, flexible system, internal coordinate transformations, automated exterior surfacing techniques, and geometrical and temporal windowing capability.

A schematic of the TRansfer ANalysis Code (TRANCITS) is shown in Fig. 13. The module can process heat transfer results directly from the MARC (finite element) and SINDA (finite difference) programs and will output temperature information in the forms required for MARC and NASTRAN. The input and output routines in the module are very flexible and could easily be modified through a neutral file to accept data from other heat transfer codes and format data to other stress analysis codes.

This thermal load transfer module has been shown to transfer thermal data efficiently and accurately from dissimilar heat transfer meshes to stress meshes. The fundamental part of the code, the three-dimensional search, interpolation, and surfacing routines, have much more potential.

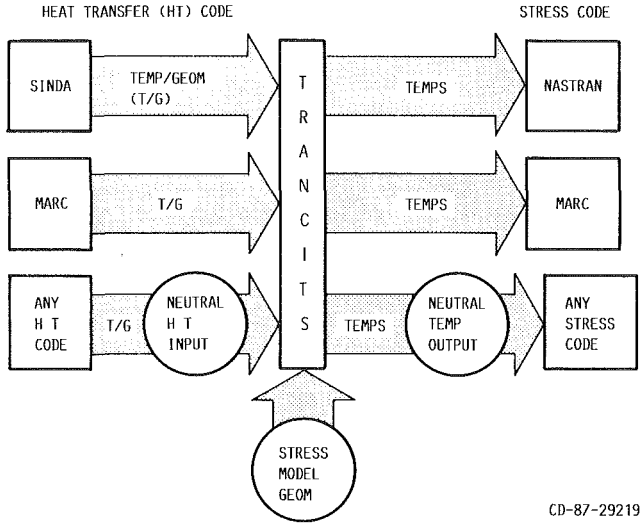

Fig. 13 Schematic for three-dimensional trancits computer program

They form an outstanding foundation for automatic construction of embedded meshes, local element mesh refinement, and the transfer of other mechanical type loading.

General Electric Contract. The overall objective of this program was to develop and verify a series of interdisciplinary modeling and analysis techniques specialized to address hot section components. These techniques incorporate data as well as theoretical methods from many diverse areas including cycle and performance analysis, heat transfer analysis, linear and nonlinear stress analysis, and mission analysis. Building on the proven techniques already available in these fields, the new methods developed through this contract were integrated into a system that provides an accurate, efficient, and unified approach to analyzing hot section structures. The methods and codes developed under this contract, NAS3-23687, "Component-Specific Modeling" (McKnight, 1985) predict temperatures, deformation, stress, and strain histories throughout a complete flight mission.

Five basic modules were developed and then linked together with an executive module. They are:

1 The Thermodynamic Engine Model (TDEM), which is the subsystem of computer software. It translates a list of mission flight points and delta times into time profiles of major engine performance parameters. Its present data base contains CF6-50C2 engine performance data. Adapting this system to a different engine requires only the restocking of this data base with the appropriate engine performance data.

2 The Thermodynamic Loads Model (TDLM), which is the subsystem of computer software that works with the output of the TDEM to produce the mission cycle loading on the individual hot section components. There are separate segments for the combustor, the turbine blade, and the turbine vane. These segments translate the major engine performance parameter profiles from the TDEM into profiles of the local thermodynamic loads (pressures, temperatures, rpm) for each component. The formulas that perform this mapping in the TDLM models were developed for the specific engine components. Adapting these models to a different engine would require evaluating these formulas for their simulation capability and making any necessary changes.

3 Component Specific Structural Modeling, which is the heart of the geometric modeling and mesh generation using the recipe concept. A generic geometry pattern is determined for each component. A recipe is developed for this basic geometry in terms of point coordinates, lengths, thicknesses, angles, and radii. These recipe parameters are encoded in computer software as variable input parameters. A set of default

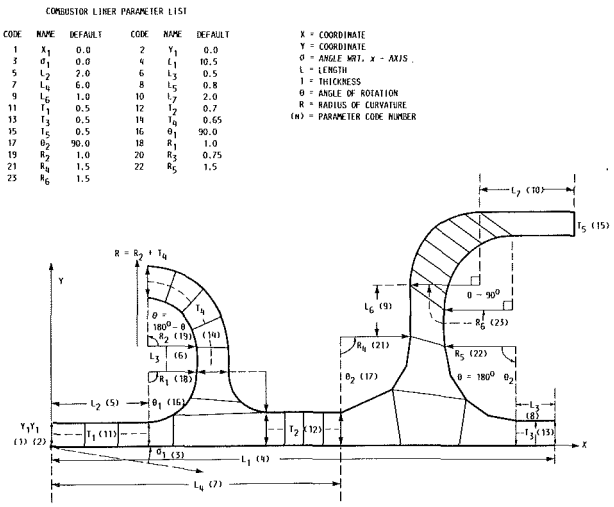

Fig. 14 Combustor liner parameters

numerical values is stored for these parameters. The user need only input values for those parameters that are to have different values. These recipe parameters then uniquely define a generic component with the defined dimensions. The software logic then works with these parameters to develop a finite element model of this geometry consisting of 20-noded isoparametric elements. The user specifies the number and distribution of these elements through input control parameters. Figure 14 shows the generic geometry and recipe for a combustor liner panel.

4 The subsystem that performs the three-dimensional nonlinear finite element analysis of the hot section component model and was developed under the NASA HOST contract NAS3-23698, "Three-dimensional Inelastic Analysis Methods for Hot Section Structures." This software performs incremental nonlinear finite element analysis of complex three-dimensional structures under cyclic thermomechanical loading with temperature-dependent material properties and material response behavior. The nonlinear analysis considers both time-independent and time-dependent material behavior. Among the constitutive models available is the Haisler–Allen classical model, which performs plasticity analysis with isotropic material response, kinematic material response, or a combination of isotropic and kinematic material response. This is combined with a classical creep analysis formulation. A major advance in the ability to perform time-dependent analyses is a dynamic time incrementing strategy incorporated in this software.

5 The COSMO system, which consists of an executive module that controls the TDEM, TDLM, the geometric modeler, the structural analysis code, the file structure/data base, and certain ancillary modules. The ancillary modules consist of a band width optimizer module, a deck generation module, a remeshing/mesh refinement module and a postprocessing module. The executive directs the running of each module, controls the flow of data among modules, and contains the selfadaptive control logic. Figure 15 is a flow chart of the COSMO system showing data flow and the action positions of the adaptive controls. The modular design of the system allows each subsystem to be viewed as a plug-in module. They can be abstracted and run alone or replaced with alternate systems.

The ideas, techniques, and computer software developed in the Component Specific Modeling program have proven to be extremely valuable in advancing the productivity and design-analysis capability for hot section structures.

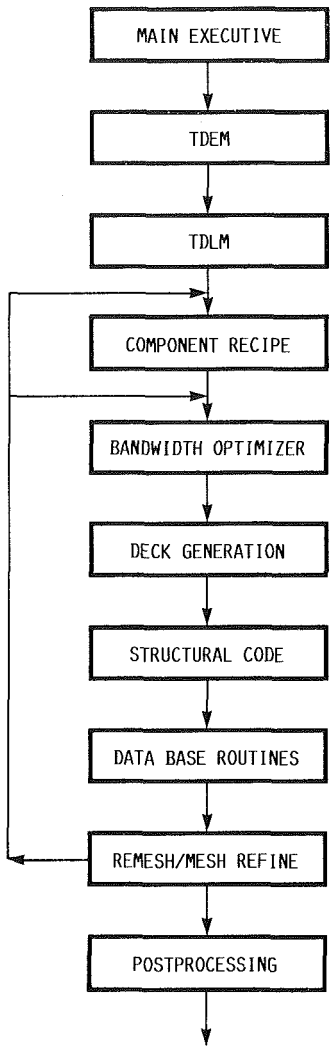

Fig. 15 System flow chart for COSMO

General Electric Contract. Under NASA contract NAS3-23698, "Three-Dimensional Inelastic Analysis Methods for Hot Section Components" (McKnight et al., 1986), a series of three-dimensional inelastic structural analysis computer codes was developed and delivered to NASA Lewis. The objective of this program was to develop analytical methods capable of evaluating the cyclic time-dependent inelasticity that occurs in hot section engine components. Because of the large excursions in temperature associated with hot section engine components, the techniques developed must be able to accommodate large variations in material behavior including plasticity and creep. To meet this objective, General Electric developed a matrix consisting of three constitutive models and three element formulations. A separate program for each combination of constitutive model-element model was written, making a total of nine programs. Each program was given a stand alone capability of performing cyclic nonlinear analysis.

The three constitutive models are in three distinct forms: a simplified theory (simple model), a classical theory, and a unified theory. In an inelastic analysis, the simplified theory uses a bilinear stress-strain curve to determine the plastic strain and a power law equation to obtain the creep strain. The second model is the classical theory of Haisler and Allen. The third model is the unified model of Bodner and Partom. All of the models were programmed for a linear variation of loads and temperatures with the material properties being temperature dependent.

The three element formulations used are an 8-node isoparametric shell element, a 9-node shell element, and a 20-node isoparametric solid element. The 8-node element uses serendipity shape functions for interpolation and Gaussian quadrature for numerical integration. Lagrange shape functions are used in the 9-node element. For numerical integration, the 9-node element uses Simpson's rule. The 20-node solid element uses Gaussian quadrature for integration.

For the linear analysis of structures, the nine codes use a blocked-column skyline, out-of-core equation solver. To analyze structures with nonlinear material behavior, the codes use an initial stress iterative scheme. Aitken's acceleration scheme was incorporated into the codes to increase the convergence rate of the iteration scheme.

The ability to model piecewise linear load histories was written into the codes. Since the inelastic strain rate can change dramatically during a linear load history, a dynamic time-incrementing procedure was included. The maximum inelastic strain increment, maximum stress increment, and the maximum rate of change of the inelastic strain rate are the criteria that control the size of the time step. The minimum time step calculated from the three criteria is the value that is used.

In dynamic analysis, the eigenvectors and eigenvalues can be extracted using either the determinant search technique or the subspace iteration method. These methods are only included with those finite-element codes containing the 8-node shell element.

Pratt and Whitney Aircraft Contract. The objective of the work done under contract NAS3-23697, "Three-Dimensional Inelastic Analysis Methods for Hot Section Components" (Nakazawa, 1987; Wilson and Banerjee, 1986), was to produce three new computer codes to permit accurate and efficient three-dimensional inelastic analysis of combustor liners, turbine blades, and turbine vanes. The three codes developed are called MOMM (Mechanics of Materials Model), MHOST (MARC-HOST), and BEST (Boundary Element Stress Technology). These codes embody a progression of mathematical models for increasingly comprehensive representation of the geometric features, loading conditions, and forms of nonlinear material response that distinguish the three groups of hot section components.

Software in the form of stand-alone codes was developed by Pratt and Whitney Aircraft (PWA) with assistance from three subcontractors: MARC Analysis Research Corporation (MARC), United Technology Research Center (UTRC), and the State University of New York at Buffalo (SUNY-B).

Three increasingly sophisticated constitutive models were implemented in MOMM, MHOST, and BEST to account for inelastic material behavior (plasticity, creep) in the elevated temperature regime. The simplified model assumes a bilinear approximation of stress-strain response and glosses over the complications associated with strain rate effects, etc. The state-of-the-art model partitions time-independent plasticity and time-dependent creep in the conventional way, invoking the von Mises yield criterion and standard (isotropic, kinematic, combined) hardening rules for the former, and a power law for the latter. Walker's viscoplasticity theory, which accounts for the interaction between creep/relaxation and plasticity that occurs under cyclic loading conditions, has been adopted as the advanced constitutive model.

MOMM. This is a stiffness method finite element code that utilizes one-, two-, and three-dimensional arrays of beam elements to simulate hot section component behavior. Despite limitations of such beam model representations, the code will be useful during early phases of component design as a fast, easy-to-use, computationally efficient tool. All of the structural analysis types (static, buckling, vibration, dynamics), as well as the three constitutive models mentioned above, are provided by MOMM. Capabilities of the code have been tested for a variety of simple problem discretizations.

MHOST. This code employs both shell and solid (brick) elements in a mixed method framework to provide comprehensive capabilities for investigating local (sress/strain) and global (vibration, buckling) behavior of hot section components. Attention was given to the development of solution algorithms, integration algorithms for stiffness, strain recovery and residual terms, and modeling methods that permit accurate representations of thermal effects on structural loading and material properties, as well as geometric discontinuities.

The three constitutive models implemented are the secant elasticity model, von Mise's plasticity model, and Walker's creep plasticity model. Temperature dependency and anisotropy can be obtained through user subroutines in MHOST. Nonlinear transient analysis and eigenvalue extraction for buckling and modal analyses are some of the other important features in the program. The improved algorithm models and finite elements implemented in the code significantly reduced CPU (Central Processing Units) time requirements for three-dimensional analyses.

To test the validity of the MHOST finite-element code, considerable efforts were made in applyhing the code in different cases with results compared to theoretical predictions or numerical values generated by other codes. For example, the code was used in-house to analyze a General Electric CF/6-50 engine blade and rotor model with data generated by a computational structural mechanics simulator system. The simulator system provided data, such as pressure and temperature distribution, centrifugal force, and time duration, at various stages of flight. Figure 16 shows the variation of the radical displacement of the leading edge tip in the static condition during the entire flight without consideration of the centrifugal force effect.

BEST3D. This is a general purpose three-dimensional structural analysis program utilizing the boundary element method. The method has been implemented for very general three-dimensional geometries, and for elastic, inelastic and dynamic stress analysis. Although the feasibility of many of the capabilities provided has been demonstrated in a number of individual prior research efforts, the present code is the first in which they have been made available for large-scale problems in a single code. In addition, important basic advances have been made in a number of areas, including the development and implementation of a variable stiffness plasticity algorithm, the incorporation of an embedded time algorithm for elastodynamics, and the extensive application of particular solutions within the boundary element method. Major features presently available in the BEST3D code include: very general geometry definition, including the use of double curved isoparametric surface elements and volume cells, with

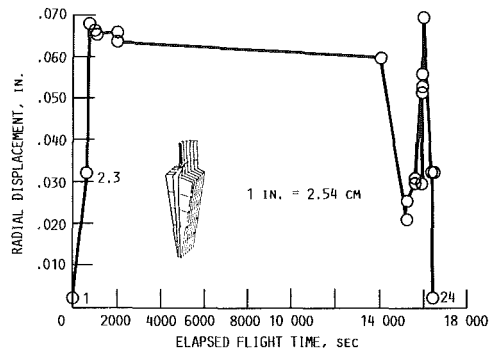

Fig. 16 Radial displacement of leading edge tip, static

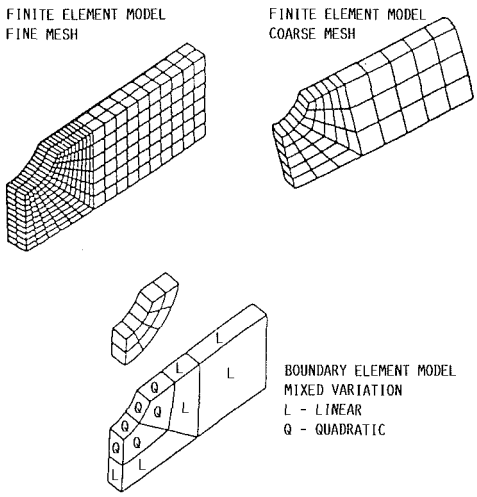

Fig. 17 Meshes used in benchmark notch analysis

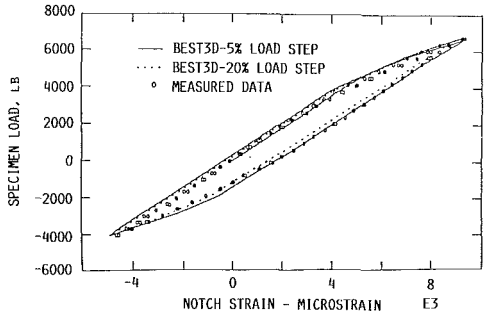

Fig. 18 Cyclic behavior at root of specimen notch

provision of full substructuring capability; general capability for the definition of complex, time-dependent boundary conditions; capability for nonlinear analysis using a variety of algorithms, solution procedures, and constitutive models; and a very complete elastodynamic capability including provision for free vibration, forced response, and transient analysis.

The BEST3D code was validated by comparing predictions from BEST3D with those from theoretical and/or numerical predictions and some experimental data. For example, results from a benchmark notch test program were used. Finite element and boundary element meshes for one-quarter of a specimen gage section are shown in Fig. 17. Measurements of notch root stress-strain behavior for initial uploadings were compared with predictions (Fig. 18). Simulation of first-cycle notch root behavior with BEST3D was proven to be quite accurate.

Experimental Facilities and Data

Oak Ridge National Laboratory Interagency Agreement. An experimental effort was undertaken under Interagency Agreement Number 40-1447-84 and U.S. Department of Energy contract DE-AC05-840R 21400 with Martin Marietta Energy Systems Inc., "Determination of Surface of Constant Inelastic Strain Rate at Elevated Temperature" (Battiste and Ball, 1986). Special exploratory multiaxial deformation tests on tubular specimens of type 316 stainless steel at 649°C (1200°F) were conducted to investigate time-dependent material behavior.

In classical plasticity the concept of yield surfaces in multiaxial stress space plays a central role, not only in the definition of initial yielding but in determining subsequent plastic flow. At high temperatures the deformation behavior of structural alloys is strongly time dependent. Consequently,

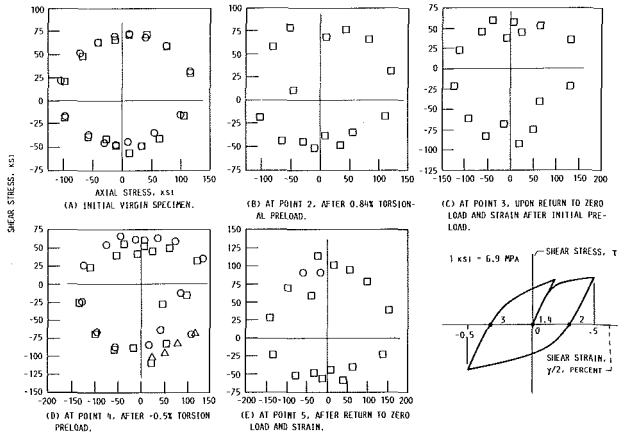

Fig. 19 Measured 650°C surfaces of constant inelastic strain rate for reference SCISRs test program

the significance of yield surfaces breaks down, and it has been proposed that in their place the concept of surfaces of constant inelastic strain rate (SCISR) might be utilized. Such surfaces, called SCISRs, can be shown to have a potential nature and thus constitute the basis of a rational multiaxial viscoplastic constitutive theory.

A surface of constant inelastic strain rate was determined by loading the specimen at a constant effective stress rate in the two-dimensional axial/torsional stress state in various directions until a predetermined inelastic effective strain rate was reached. After each probe, the stress was returned to the initial starting point; thus a locus of points (surface of constant inelastic strain rate) was established.

Two types of test were were conducted. One test specimen was subjected to a time-independent torsional shear strain test history, and SCISRs in an axial/torsional stress space were measured at various predetermined points during the test. A second specimen was subjected to a 14-week time-dependent (creep-recovery-creep periods) torsional shear stress histogram. SCISR determinations were made at 17 points during the test. The tests were conducted in a high-temperature, computer-controlled axial/torsional test facility using an Oak Ridge National Laboratory developed high-temperature multiaxial extensometer.

A key result of this testing effort was that surfaces of constant inelastic strain rate exist and can be determined or measured at an elevated temperature, 650°C. This is shown in Fig. 19. The conclusion is validated or deduced by the execution of the test programs and by the consistency of the surface results, especially the repeated surfaces. To our knowledge, this is the first successful determination of high-temperature surfaces of constant inelastic strain rate.

Although conclusions regarding the effect of these SCISR data on different theories will be left to the constitutive equation developers, several results can be stated. First, the surfaces did not move or change shape in the axial/torsional stress state by any significant amount. Second, a deduction that plastic deformations have a larger effect than creep deformations can be stated. Third, SCISRs determined immediately after large plastic deformation show more inconsistent results than SCISRs that have not undergone immediate prior plastic deformations. Last, the extensometer system and software control system performed extremely well in a difficult application.

In-House Lewis Research Center Experimental Facilities and Data

Uniaxial Test Systems. Under HOST, recent expansion of the uniaxial testing capability of the fatigue and structures laboratory included the addition of four new test systems

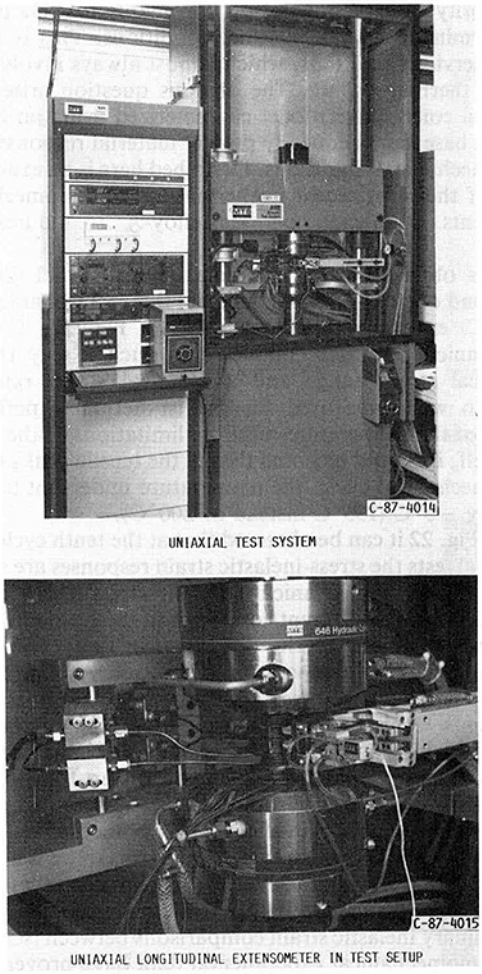

Fig. 20 Uniaxial test system

(Bartolotta and McGaw, 1987). One of these systems is shown in Fig. 20. The load rating for two of the new systems is ±9072 kg (±20 000 lb), and the other two at ±22 680 kg (±50 000 lb). Each system is equipped with a state-of-the-art digital controller. The digital controllers have the ability to complete a smooth control mode transfer, which is accomplished either manually or electronically. This feature will make it possible to conduct some of the more complex tests that have been defined by the constitutive model developers at NASA Lewis and elsewhere. Specimen heat is provided by 5 kW radio frequency induction heaters. Axial strains are measured using an axial extensometer. To study the effects of the environment on creep-fatigue behavior, the two smaller load capacity test systems are equipped with environmental chambers capable to providing a vacuum and/or an inert environment. The environmental chamber is able to sustain a vacuum of 2.67×10^{-4} Pa(2×10^{-6} torr) with a specimen temperature of 1093°C (2000°F). All systems include water-cooled hydraulic grips for simple specimen installation. By exchanging two collets these grips can be adapted to handle flat bar, smooth shank, or threaded-end specimens. Each uniaxial system has its own minicomputer for experimental control and data acquisition. Preliminary software has been developed by the experimentalists to conduct tests as simple as a low cycle fatigue test, and as complicated as thermomechanical tests.

Biaxial Test Systems. In many life and material behavior models, multiaxial representations are formulated by modifying uniaxial criteria. Unfortunately, this method does not always achieve the accuracy needed to meet design goals of hot section components. In response to this need for better life and material behavior predictions under complex states of stress and strain, a multiaxial testing capability is being developed. As an evolutionary step from a uniaxial test capability, a decision was made to begin with biaxial (axial-torsion) test systems (Fig. 21) and eventually progress to triaxial systems through the use of internal pressure. Under HOST, three new biaxial test systems were added to the laboratory (Bartolotta and McGaw, 1987).

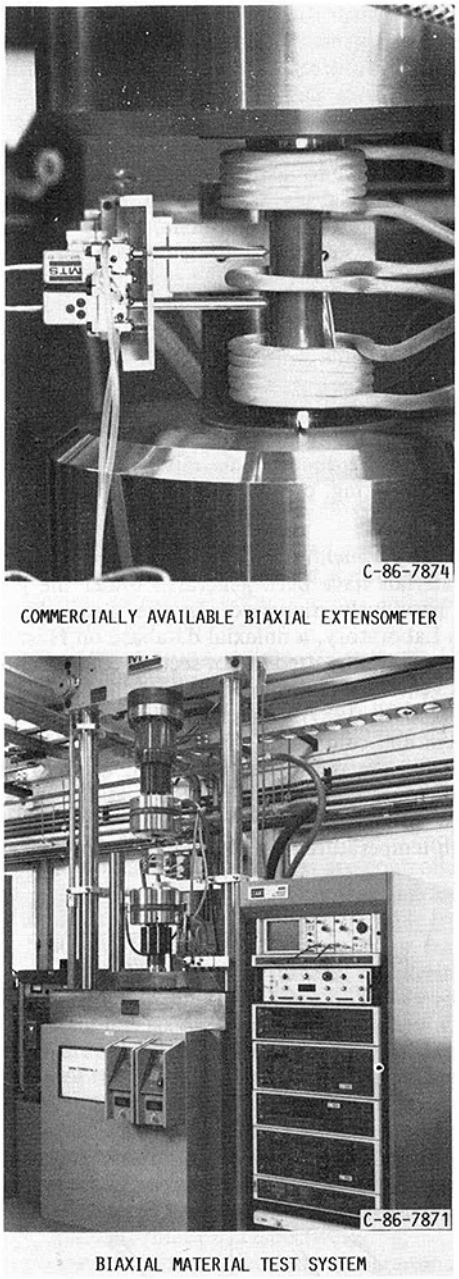

Fig. 21 Biaxial material test system

The load frames for each test system are rated for loads of ±22 948 kg (±50 000 lb) axial and ±2824 N-m (±25 000 in.-lb) torsional. Electronics for these systems consist of two servocontrollers, two data display units, function generators, and an oscilloscope. The two servocontrollers allow for both independent and combined control of axial and torsional loading. Each servocontroller can control specimen loading in one of three modes: load, strain or stroke for axial loading and torque, torsional strain or angular displacement for torsional loading. Data display units are used to monitor analog data signals, and provide an important interface between the test system and the computer system. These units can be programmed to perform a variety of signal processing operations.

The heating system for each biaxial test system consists of an audio frequency induction generator, an induction coil fixture, and a PID controller for closed-loop temperature control. Each generator has a power output of 50 kW at an operating frequency of 9.6 kHz. Audio frequency generators were chosen because of their ability to operate with minimal electrical interference to instrumentation signals.

Each axial-torsional test system is interfaced with its own minicomputer. These minicomputers, along with the data display units, are used for experimental control and data acquisition. Preliminary software is being used to conduct simple tests, while more complicated test programs are still in their developmental stages.

A thin-walled tube was chosen as the basic specimen geometry. This type of geometry has the following advantages: (*a*) easy decomposition of axial-torsional components of stress and strain, (*b*) at high temperatures thermal gradients across the diameter are minimal, and (*c*) for thermomechanical testing, cooling rates are higher.

Uniaxial Experimental Results. Extensive data-bases for several materials have been generated under the grants and contracts previously discussed. In the Lewis Fatigue and Structures Laboratory, a uniaxial database on Hastelloy-X, a nickel-base superalloy used in hot section component applications, was generated (Bartolotta, 1985; Ellis et al., 1986; Bartolotta and Ellis, 1987). These data are being used in the development and calibration of constitutive models. In addition, some of the data generated were used to address a number of questions regarding the validity of methods adopted in characterizing the constitutive models for particular high-temperature materials. One area of concern is that

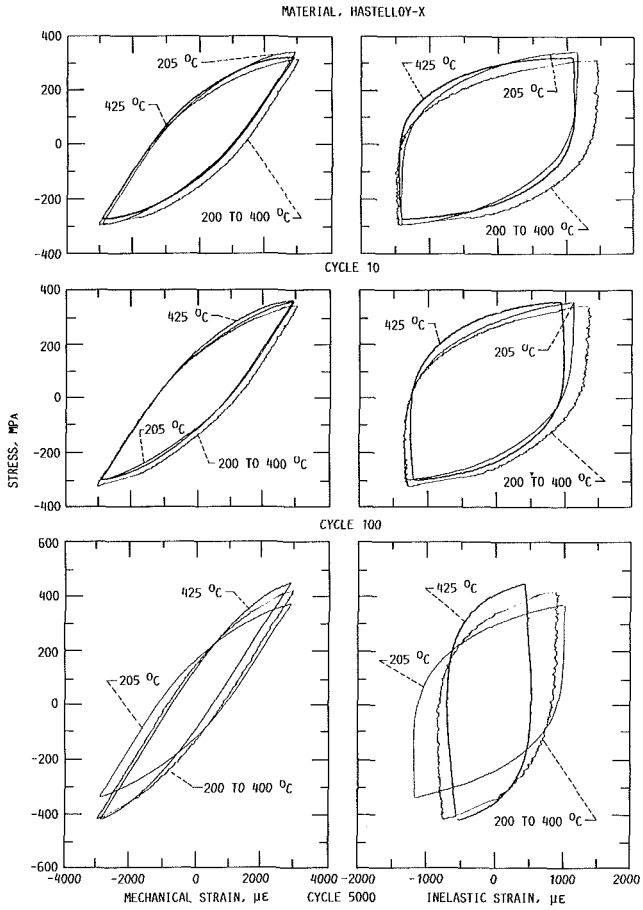

Fig. 22 Comparison of material response determined under isothermal and thermomechanical cyclic loading

the majority of experimental data available for this purpose are determined under isothermal conditions. This is in contrast to service conditions, which almost always involve some form of thermal cycling. The obvious question arises as to whether a constitutive model characterized using an isothermal data base can adequately predict material response under thermomechanical conditions. Described here is an example of results of the most recent isothermal and thermomechanical experiments conducted on Hastelloy-X to address this concern.

Results obtained from two uniaxial isothermal (205 and 425°C) and one out-of-phase uniaxial thermomechanical (200 to 400°C) experiments are presented in Fig. 22. The thermomechanical test was conducted in such a way that the mechanical strain range and mechanical strain rate were similar to what was used for the isothermal experiments. Because of the temperature response limitations of the experiment itself, it should be noted that at the tensile peaks of each thermomechanical cycle, the temperature undershot its lower bound by −5°C (195°C instead of 200°C).

From Fig. 22 it can be observed that at the tenth cycle of the isothermal tests the stress-inelastic strain responses are similar. As for the thermomechanical test, the stress-inelastic strain response is slightly different compared to the isothermal data. This is probably due to the difference in mechanical strain range caused by the temperature overshoot. As can be seen, the stress-inelastic strain response for the thermomechanical experiments seems to follow more closely that of the lower temperature isothermal test. As cycling continues, the thermomechanical material response seems to start following that of the higher temperature isothermal experiment. This observation was also observed in another thermomechanical experiment (400 to 600°C), which suggests that this trend is a general material hardening characteristic, but further investigation will have to be conducted before this can be confirmed.

Preliminary inelastic strain comparisons between isothermal and thermomechanical experimental data have proven useful in developing a better understanding of thermomechanical material response for Hastelloy-X. From these types of comparison it appears that general thermomechanical material behavior can be extracted from isothermal experimental data, but information concerning changes in material strain hardening behavior must come from thermomechanical test data.

Tests on Haynes 188, a cobalt-based superalloy used in hot section component applications were also conducted in the laboratory (Ellis et al., 1987). An example of the test results obtained is presented. In this example we are concerned with determining the stress levels or "thresholds" at which creep deformations first become significant in Haynes 188 over a temperature range of interest. A second series of experiments was conducted to establish whether the thresholds determined under monotonic conditions also apply in the case of thermomechanical loading.

As shown in Table 2, the threshold experiments showed the expected result that early creep response is strongly temperature dependent. It can be seen that at 649°C, stress levels must exceed 207 MPa (30 ksi) before creep strains

Table 2 Creep thresholds determined for Haynes 188 at temperatures in the range 649 to 871°C

Temperature, °C	Creep thresold,[a] ksi
649	30
760	11
871	4

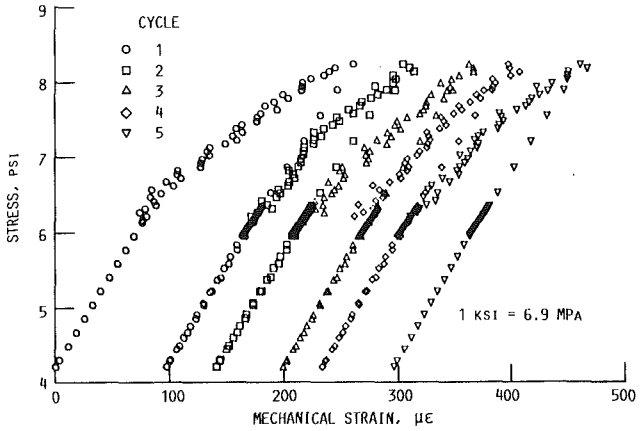

Fig. 23 Creep ratchetting resulting from thermomechanical cycling for 6.17 ksi mean stress

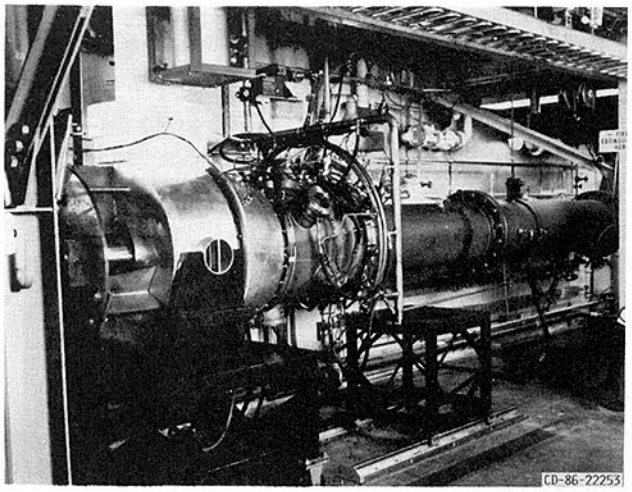

Fig. 24 Structural component response rig

become significant during the 1.5-h hold periods. At temperatures of 760 and 871°C, the corresponding values of stress are 75.9 MPa (11 ksi) and 27.6 MPa (4 ksi), respectively. One important point to be noted about this result is that it would not have been predicted by inspection of handbook data. This is because material handbooks provide little or no information regarding the early stages of creep. It follows that problems can arise if decisions regarding the need for inelastic analysis are based on casual inspection of handbook data. The present study clearly indicated that some form of inelastic analysis is necessary for components operating at temperatures as high as 871°C if stress levels are expected to exceed 27.6 MPa (4 ksi).

Turning to the results of the thermomechanical experiments on Haynes 188, ratchetting behavior can be observed in the data shown in Fig. 23 for a mean stress of 42.5 MPa (6.17 ksi). In this case, the creep strain accumulated during cycle (1) was about 100 $\mu\epsilon$. On subsequent cycles, the creep occurring per cycle was 50 $\mu\epsilon$ or less and the data exhibited considerable scatter. The reason for the scatter is the electrical noise, which complicated interpretation of the 42.5 MPa (6.17 ksi) mean stress data.

The material exhibited creep ratchetting during simulated service cycles. This result was not predicted by analysis using current constitutive models for Haynes 188.

Lewis Annular Combustor Liner Test Facility Structural Component Response Rig. Segments or cylindrical sections of gas turbine engine combustor liners were radiantly heated in the Structural Component Response rig shown in Fig. 24. Quartz lamps were used cyclically to heat the 20-in (0.5 m) diameter test liners. This resulted in axial and circumferential temperature variations as well as through-the-thickness temperature gradients in the test liner similar to those of in-service liners, and thus similar thermally induced stresses and strains. A typical engine mission cycle (take-off, cruise, landing, and taxi) of 3 to 4 h was simulated in 2 to 3 min. The simulated cyclic temperatures and temperature gradients were felt to be adequate to capture the time-independent and time-dependent interactions resulting in deformation as well as the low-cycle thermal fatigue phenomena of in-service liners. The primary purpose of the rig was to generate large quality thermomechanical databases on combustor liners (Thompson and Tong, 1986).

The test program was a cooperative effort with Pratt and Whitney Aircraft (PWA), a division of United Technologies Research, East Hartford, CT. PWA supplied the test rig, which included the quartz lamp heating system and several test liners. Lewis provided the test facility and had the responsibilities from integrating the test rig into the test facility up to and including conducting the tests and acquiring the data. Lewis and PWA personnel developed automated computer control strategies, data acquisition systems, and methods for efficient data reduction and analysis.

The quartz lamp heating system consists of 112-6-kVA lamps configured circumferentially in 16 sectors, each having 7 lamps. This system, in addition to drawing up to 672 kVA of 480-V power, requires 3.5 lb/sec of ambient temperature air at 5 psig, 1.5 lb/sec ambient temperature air at 1 psig, and 80 gal/min of specially treated water for cooling the rig.

A natural-gas and air mixture is burned in a combustor can upstream of the test section to provide preheated cooling air to the test liner. Cooling air temperatures are controllable from 205 to 316°C (400 to 600°F) by varying the fuel/air mixture ratio. The test liner cooling airflow rate is variable from about 4.0 to 7.5 lb/sec at 35 psig. Both the cooling-air temperature and flow rate can be varied to obtain the desired cyclic temperatures on the test liner.

The annular rig has six 5-in.-dia quartz window viewports, three of which are spaced at 120 deg apart, are used to view the middle section of the test liner. The other three, also spaced at 120 deg apart, are used to view the upstream portion of the liner and its attachment piece. These windows are rotated 45 deg from the liner windows. The quartz windows are air and water cooled. Through these windows television, infrared, and high resolution cameras are used to monitor liner condition, temperature, and deformation, respectively.

A microprocessor with a dual-loop programmable controller is used to control the power to the lamps. A specified power-time history is programmed into the microprocessor, and the cooling air temperature and flow rate are appropriately set so that when combined, the desired thermal cycle is imposed on a test liner.

Thermocouples and an infrared thermovision system are used to obtain surface temperatures on the test liner. There are provisions for having a total of 140 thermocouples on the test liner. Both thermocouple and thermal image data are obtained on the cool side of the test specimen. Only thermocouple data are obtained on the hot side (facing the quartz lamps) of the test liner. The thermocouple data provide temperatures at discrete points, while the infrared system provides detailed maps of cool-side thermal information.

The thermal images obtained from the infrared camera are stored on a VHS tape recorder, with the clock time superimposed on each image. Images of the test specimen of from about 4 to about 1 in. in diameter (for finer resolution of temperatures) can be obtained with the zooming capability of the infrared system. Thirty thermal images are captured on tape every second. A computer system is then used to process,

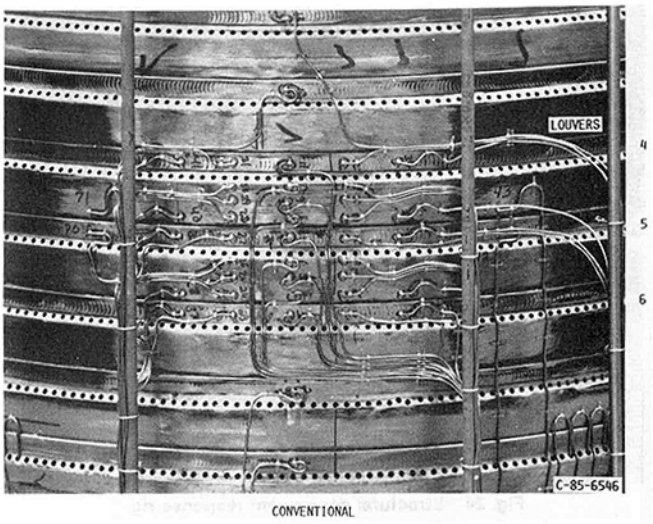

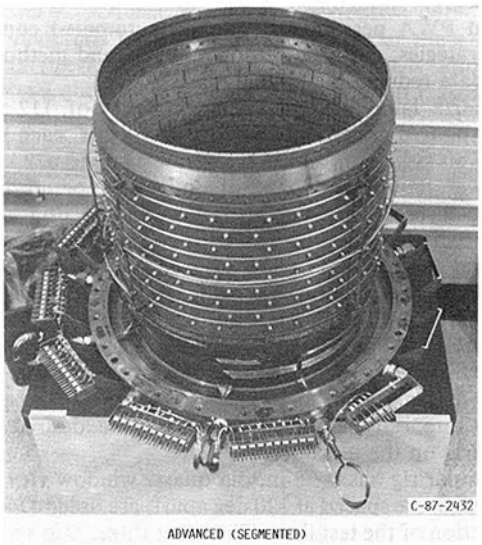

Fig. 25 Conventional and segmented combustor liners instrumented for testing

reduce, enhance, and analyze the transient temperature information. These data are also compared with the thermocouple data. Thermocouple data are used in the calibration of the infrared system.

During a test run both the facilities data (pressure flows, power, etc.) and the research data (primarily temperature) are acquired for each thermal cycle using the ESCORT II data acquisition system at Lewis. These data are stored automatically once every second on a mainframe computer for later reduction and analysis.

Liner Tests and Results. Two combustor liner segments were tested in the Structural Component Response Rig. First, a conventional liner of sheet metal seam-welded louver construction from Hastelloy-X material (Fig. 25) was tested. Second, an advanced paneled liner (Fig. 25) was tested.

A large, quality (thermocouple (96 TCs) and IR) temperature database was obtained on the conventional liner. Some typical thermocouple data are shown in Fig. 26. The corresponding power history for the thermal cycle is shown in Fig. 27. Figure 26 shows the transient temperature response at three locations on louver 5. The temperature measurements are used in the heat transfer/structural analysis of the liner.

The liner was thermally cycled for almost 1800 cycles. Between 1500 and 1600 cycles an axial crack about 0.2 in. in length developed in the liner. This crack occurred at a hot spot

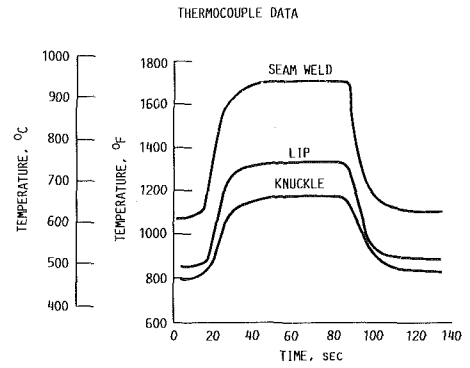

Fig. 26 Cyclic surface liner temperatures at three locations on louver 5

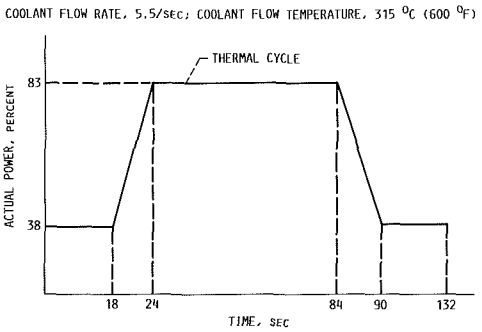

Fig. 27 Power history for thermal cycle

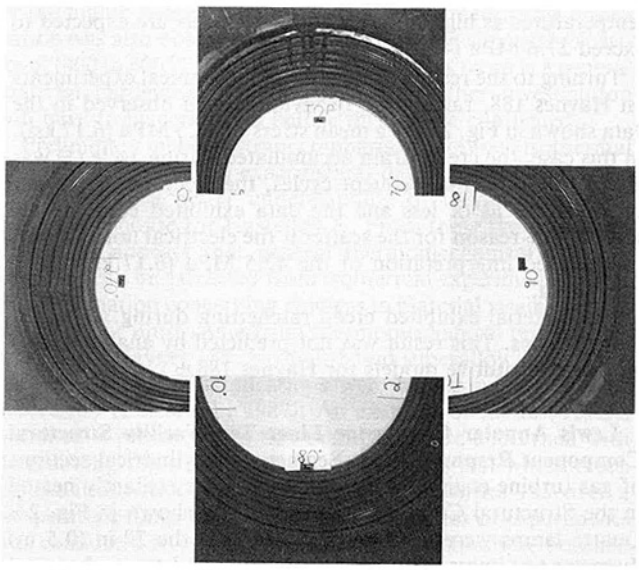

Fig. 28 Composite photograph of hot side conventional liner distortion after 1782 thermal cycles

that developed because of closure of several cooling holes. There was no thermocouple right at the hot spot, but surrounding TCs indicated the maximum temperature was at least 937°C (1720°F) and could have been over 976°C (1890°F).

A composite photograph of the liner after 1782 cycles is shown in Fig. 28. This shows that most of the distortion occurred in louvers 4 to 7, particularly in the bottom (180 deg) and left (270 deg) views. The top (0 deg) and right (90 deg) views show less distortion.

The test program was terminated after 1782 cycles because the distortion of the louvers became severe enough to contact the frame of one of the quartz lamp banks. Measurements of the crack from the initial observation at 1600 to 1728 cycles indicated 2 percent increase in length.

The distortion of the louvers is typical of liners run in ser-

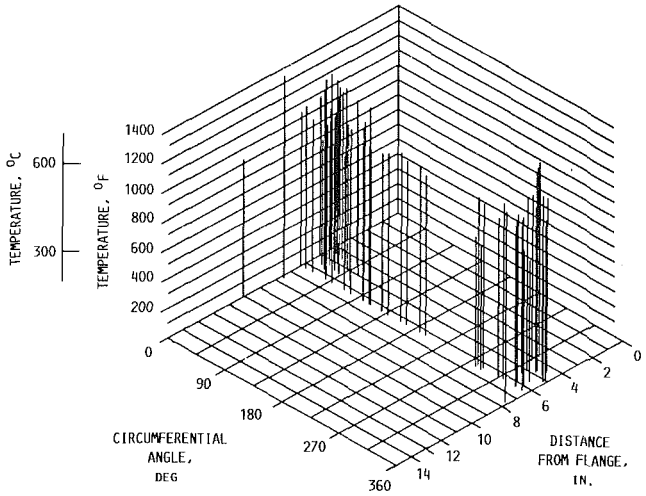

Fig. 29 Isometric plot of temperature on inside of segmented combustor liner

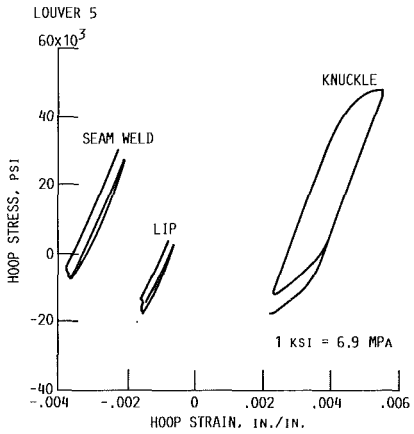

Fig. 30 Representative stress-strain predictions at three locations on the conventional liner

vice. The distortion shows some symmetry to the heat pattern of the lamps in that the peaks of distortion are at the longitudinal center of a lamp bank where the maximum heat flux occurred. It should be noted that a distortion peak was not formed at every bank of lamps.

Similarly, a large quality data base on the advanced combustor liner is being obtained. This liner, consisting of small panels and an outer support shell to which the panels are attached, is instrumented with 125 thermocouples, 73 on the hot side of the panels and 52 on the support shell. A grid system of lines of temperature-sensitive paints was applied to over half of the panels in the liner to increase the area in which we could observe temperature changes. An infrared camera system is being used to obtain temperature maps of a portion of the outer shell of the liner through a quartz viewing window. Over the same field of view, high-resolution photographs of the outer shell are also being taken to determine the total strain during cycling.

Figure 29 is representative of the data obtained on the advanced liner. It is an isometric plot of the thermocouple temperature measurements of the hot side of the liner panels (which shows the cylindrical liner as if it were cut open and flattened out) and shows a maximum temperature of 760°C (1400°F) at the maximum quartz lamp power (cruise condition). A similar plot of the outer shell shows the maximum temperature to be about 316°C (600°F). These temperatures were obtained for a heat flux equivalent to that applied to the conventional liner. Transient data are also being obtained.

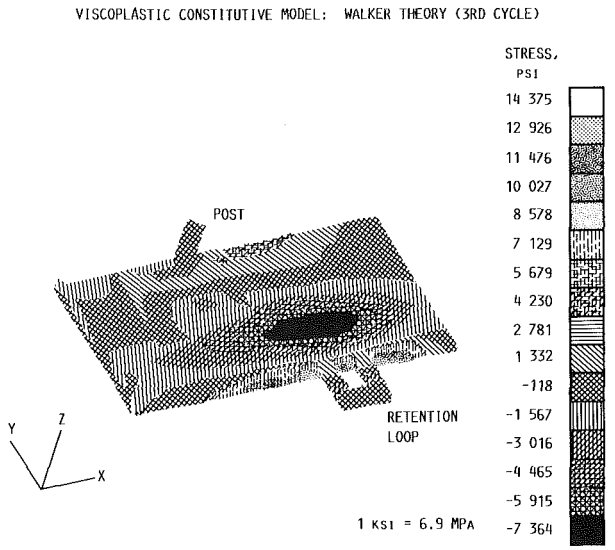

Fig. 31 Advanced combustor liner stress distribution on symmetric panel at an 83 percent power level (X direction)

The thermal paint did not indicate a maximum temperature of more than about 649°C (1200°F). The infrared data and the high-resolution photographs are being reduced and analyzed.

After 1500 thermal cycles the advanced liner is operating at much lower temperatures than the conventional liner (about 205°C (400°F) lower) for the same heat flux. At the lower temperature and low thermal gradients, little distortion to the panels has been observed. Based on the test results and analyses, the operating conditions are not severe enough to distort or damage the advanced liner.

Thermal/Structural/Life Analyses of the Test Liners. The liner surface temperature measurements obtained from the thermocouples and the infrared thermovision system were used to obtain the film coefficients on the cool and hot surfaces. Based on these coefficients, a heat transfer analysis of each liner was performed using MARC, a general purpose nonlinear finite-element heat transfer and structural-analysis program.

Eight-node three-dimensional solid elements were used to construct the liner heat transfer models. The conventional liner model had 546 elements and 1274 nodes, and the advanced liner model had 536 elements and 1117 nodes. Comparisons between predicted and measured transient temperatures showed good agreement.

The temperatures (or thermal loads) are input to the structural analysis program. The MARC program was used to perform the structural analysis. The stress models were identical to the heat transfer models.

The Walker and Bodner viscoplastic models, which were described earlier, were used in the structural analysis. Representative results are the hysteresis loops shown in Fig. 30 for three locations on the conventional liner. Similarly, Fig. 31 is representative of a stress plot of a symmetrically heated panel.

Based on the nonlinear structural analyses of the two liners, it was determined that the critical stress-strain location in the advanced liner was at the retention loop. For the conventional liner, the critical location was at the seam weld.

Based on the stress-strain and temperature at the critical locations, cyclic life of the two liners was assessed. The results are summarized and compared in Table 2. The estimated life of the conventional liner (400 to 1000 cycles) is based on limited cyclic life data. Tests showed liner cracking at the seam weld after 1500 cycles. The advanced liner will have a much longer life than the conventional liner because it has a lower

Table 3 Summary of structural-life analyses of combustor liners at a critical location

(a) Conventional liner

Analytical method	Temperature range, °F	Strain range, με		Mean stress, psi	Predicted life, cycles
		Mechanical	Inelastic		
Unified (Walker)	950 to 1630	5870	3150	-35 000	400 to 1000
Unified (Bodner)	950 to 1630	5800	2700	-28 000	400 to 1000

(b) Segmented liner

Analytical method	Temperature range, °F	Strain range, με		Mean stress, psi	Predicted life, cycles
		Mechanical	Inelastic		
Unified (Walker)	755 to 1180	810	10^{-1}	10 000	$>10^6$
Unified (Bodner)	755 to 1180	820	10^{-1}	15 000	$>10^6$

average temperature (about 215°C (440°F)) and no structural constraint in the circumferential direction. After 1500 cycles the advanced liner shows little distortion and no cracking. The predicted life is greater than 10^6 cycles. These comparisons show there is good agreement between predicted life and measured life.

Conclusions

The broad scope of structural analysis activities carried out under the HOST project, by the combined efforts of industry, government, and universities has resulted in numerous significant accomplishments and, in some cases, major breakthroughs in the nonlinear three-dimensional structural analyses of turbine engine hot section components. The major accomplishments in the three areas of technology addressed synergistically, namely, inelastic constitutive model development, nonlinear three-dimensional structural analysis methods and code development, and experimentation to calibrate and validate the codes are summarized below:

1 New types of multiaxial viscoplastic constitutive models for high-temperature isotropic and anisotropic (single crystal) superalloys, and metal matrix composites have been developed, calibrated, and validated.

2 New and improved nonlinear structural analysis methods and codes, in which the viscoplastic constitutive models were incorporated have been developed and, to some extent, validated.

3 Extensive quality databases, including uniaxial and multiaxial thermomechanical data, were generated for René N4, René 80, Hastelloy-X, MAR M247, B-1900+Hf, PWA1480, and Haynes 188 materials for the purpose of calibrating and validating the constitutive models.

4 Extensive quality databases have been generated for conventional and advanced combustor liner segments and compared with detailed thermal/structural analyses of these liners using many of the analytical tools developed under HOST.

5 Advanced instrumentation to measure temperature, displacement, and strain has been evaluated.

6 High-temperature laboratories and facilities at universities, other governmental agencies, and industry have been modified and upgraded, and at NASA Lewis, a unique high-temperature fatigue and structures research laboratory has been implemented.

7 At NASA Lewis, a high-temperature structural component response research facility for testing large-diameter combustor liner segments has been implemented.

While the structural analysis capabilities and accomplishments described in this paper are a good beginning, there is much room for improvement. It is expected that these capabilities and future improvements will grow rapidly in their engineering applications and have a major impact and payoff in the analysis and design of the next generation aeronautic and aerospace propulsion systems.

References

Bartolotta, P. A., 1985, "Thermomechanical Cyclic Hardening Behavior of Hastelloy-X," NASA CR-174999.

Bartolotta, P. A., 1987, "Use of Inelastic Strain as a Basis for Analyzing Thermomechanical Test Data," *Turbine Engine Hot Section Technology 1987*, NASA CP-2493, pp. 303–315.

Bartolotta, P. A., and McGaw, M. A., 1987, "A High Temperature Fatigue and Structures Testing Facility," NASA TM-100151.

Battiste, R. L., and Ball, S. J., 1986, "Determination of Surfaces of Constant Inelastic Strain Rate at Elevated Temperature," *Turbine Engine Hot Section Technology 1986*, NASA CP-2444, pp. 307–325.

Bodner, S. R., and Partom, Y., 1975, "Constitutive Equations for Elastic-Viscoplastic Strain-Hardening Materials," ASME *Journal of Applied Mechanics*, Vol. 42, No. 2, pp. 385–389.

Chan, K. S., Lindholm, U. S., Bodner, S. R., Hill, J. T., Weber, R. M., and Meyer, T. G., 1986, NASA CR-17922.

Dame, L. T., and Stouffer, D. C., 1986, "Anisotropic Constitutive Model for Nickel Base Single Crystal Alloys: Development and Finite Element Implementation," NASA CR-175015.

Ellis, J. R., Bartolotta, P. A., Allen, G. P., and Robinson, D. N., 1986, "Thermomechanical Characterization of Hastelloy-X Under Uniaxial Cyclic Loading," *Turbine Engine Hot Section Technology 1986*, NASA CP-2444, pp. 293–305.

Ellis, J. R., Bartolotta, P. A., and Mladsi, S. W., 1987, "Preliminary Study of Creep Thresholds and Thermomechanical Response in Haynes 188 at Temperatures in the Range 649 to 871°C," *Turbine Engine Hot Section Technology 1987*, NASA CP-2493, pp. 317–334.

Maffeo, R., 1984, "Burner Liner Thermal-Structural Load Modeling," NASA CR-174892.

McKnight, R. L., 1985, "Component-Specific Modeling," NASA CR-174925.

McKnight, R. L., Chen, P. C., Dame, L. T., Holt, R. V., Hugny, H., Hartle, M., Gellin, S., Allen, D. H., and Haisler, W. E., 1986, "On 3D Inelastic Analysis Methods for Hot Section Components," *Turbine Engine Hot Section Technology 1986*, NASA CP-2444, pp. 257–268.

Nakazawa, S., 1987, "On 3D Inelastic Analysis Methods for Hot Section Components, Vol. I—Special Finite Element Models," NASA CR-179494.

Ramaswamy, V. G., 1986, "A Constitutive Model for the Inelastic Multiaxial Cyclic Response of a Nickel Base Superalloy RENE 80," NASA CR-3998.

Robinson, D. N., 1984, "Constitutive Relationships for Anisotropic High-Temperature Alloys," *Nuclear Engineering and Design*, Vol. 83, No. 3, pp. 389–396.

Robinson, D. N., Duffy, S. F., and Ellis, J. R., 1986, "A Viscoplastic Constitutive Theory for Metal Matrix Composites at High Temperature," NASA CR-179530.

Thompson, R. L., and Tong, M. T., 1986, "Unified Constitutive Materials Model Development and Evaluation for High-Temperature Structural Analysis Applications," *15th Congress of the International Council of the Aeronautical Sciences*, Vol. 2, AIAA, New York, pp. 1505a–1505s.

Walker, K. P., 1981, "Research and Development Program for Non-linear Structural Modeling With Advanced Time-Temperature Dependent Constitutive Relationships," NASA CR-165533.

Walker, K. P., and Jordan, E. H., 1987, "Constitutive Modelling of Single Crystal and Directionally Solidified Superalloys," *Turbine Engine Hot Section Technology 1987*, NASA CP-2493, pp. 299–301.

Wilson, R. B., and Banerjee, P, K., 1986, "On 3D Inelastic Analysis Methods for Hot Section Components, Vol. 2—Advance Special Function Models," NASA CR-179517.

Life Modeling of Thermal Barrier Coatings for Aircraft Gas Turbine Engines

R. A. Miller
NASA Lewis Research Center,
Cleveland, OH 44135

Thermal barrier coating life models developed under the NASA Lewis Research Center's Hot Section Technology (HOST) program are summarized. An initial laboratory model and three design-capable models are discussed. Current understanding of coating failure mechanisms is also summarized.

Introduction

Thermal barrier coatings are being developed for protecting air-cooled turbine blades and vanes in aircraft gas turbine engines. The current state-of-the-art coating system consists of about 0.25 mm of a zirconia-yttria ceramic over 0.13 mm of an MCrAlY alloy bond coat. Both layers are applied by plasma spraying. The benefits arise from the insulation provided by the ceramic layer. This insulation allows higher gas temperatures, lower component temperatures, reduced cooling air requirements, moderation of thermal transients, and/or a decrease in the severity of hot spots. This yields improvements in performance, efficiency, and component durability. Future engine designs are expected to rely heavily on thermal barrier coatings. Thus life models are required to assess the risks associated with any given design and to insure that these coatings can be exploited fully. Further details may be found in Miller (1987), DeMasi et al. (1989), Strangman et al. (1987), and Hillery (1987).

The NASA thermal barrier coating life model development program consisted initially of an in-house program designed to improve understanding and to develop a model suitable for treating laboratory life data (Miller, 1987). This work was then extended via three contracts under the HOST program to the development of design-capable models (DeMasi et al., 1989; Strangman et al., 1987; Hillery et al., 1987). These contracts were devised to determine thermomechanical properties, to analyze coating stresses and strains, and to develop life models. Phase I of each contract has now been successfully completed, and the results will be summarized in this paper.

Coating Failure Mechanisms

A basic understanding of coating failure mechanisms is a prerequisite to the development of life prediction models. Failure mechanisms in gas turbine engines and in laboratory simulations have been discussed in detail elsewhere (e.g., Miller, 1987; DeMasi et al., 1989; Strangman et al., 1987, Hillery et al., 1987). There is now general agreement that these coatings fail primarily as a result of stresses induced by the thermal expansion mismatch between the ceramic and metallic layers, and that these stresses are greatly influenced by time-at-temperature processes such as oxidation and possibly sintering. The stress state in the ceramic layer that leads to crack propagation and eventual spalling is one of biaxial compression in the plane of the coating and radial tension. These stresses are further complicated by the wavy and irregular interface between the ceramic and metallic layers. In fact, HOST-sponsored calculations indicate that the radial stresses above a wavy interface may actually alternate between regions of compression and tension as illustrated in Fig. 1 (Chang et al., 1987). Figure 2 illustrates that the behavior of plasma-sprayed zirconia-based thermal barrier coatings differs significantly from the behavior of conventional ceramics. This behavior, which is believed to result from the splat structure, includes very low thermal conductivity and very high compressive strain tolerance. In-plane tensile strain tolerance of the coating system is also very high because such loading may lead to segmentation cracking in the ceramic with no degradation to the attachment strength. Plasma sprayed zirconia-yttria also exhibits creeplike behavior, presumably as a result of sliding at the splat boundaries, and fatiguelike behavior, presumably as a result of slow crack growth. Experimental evidence of slow crack growth (or microcrack linkup), creep, and fatigue are presented in DeMasi et al. (1989).

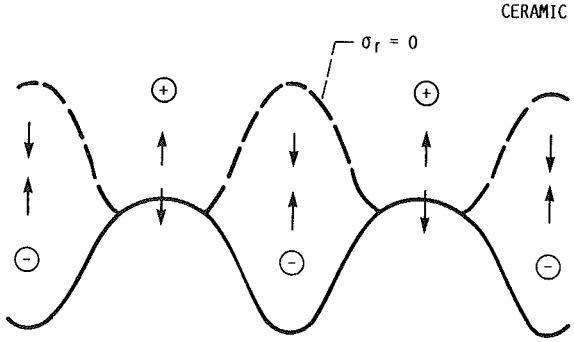

Fig. 1 Schematic representation of calculated radial thermal expansion mismatch stress above a wavy interface

Contributed by the International Gas Turbine Institute and presented at the 33rd International Gas Turbine and Aeroengine Congress and Exhibition, Amsterdam, The Netherlands, June 5-9, 1988. Manuscript received by the International Gas Turbine Institute November 17, 1987.

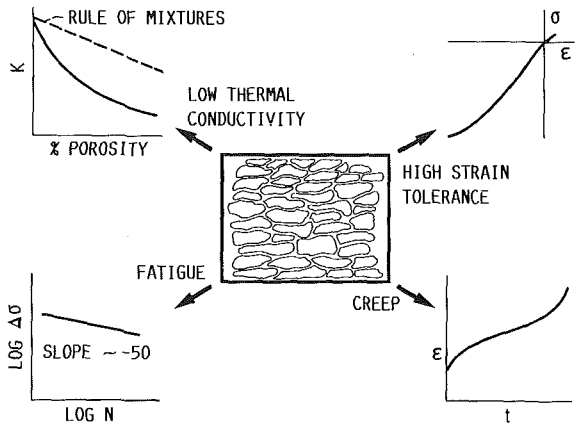

Fig. 2 Schematic representation of thermal mechanical properties resulting from coating splat structure

Initial Laboratory Model Development

A preliminary life prediction model has been described (Miller, 1984, 1987; Miller et al., 1984). This model assumed that the complex state of stress and strain imposed on the coating system by the thermal loads could be expressed in terms of a single parameter. This parameter was labeled ϵ_r, which was taken to be the radial component of the thermal expansion mismatch strain. Next it was assumed that the time-at-temperature effects could be treated in terms of oxidation alone and that oxidation could be characterized by the weight gain at the conclusion of each cycle w_N. Then, weight gain and strain were related using either of two alternative approaches. In the first case, depicted in Fig. 3(*a*), an oxidized coating is assumed to behave as if an effective strain ϵ_e is increasing. At zero weight gain this effective strain equals the radial strain ϵ_r. At a critical weight gain w_c—defined as the weight gain required to fail the coating in a single cycle—the effective strain equals a failure strain ϵ_f. This leads to the expression

$$\epsilon_e = \epsilon_f - \epsilon_r \left(\frac{w_N}{w_c}\right)^m + \epsilon_r \tag{1}$$

where the exponent m has been added to allow the curve in Fig. 3(*a*) to be nonlinear. The alternative assumption (Miller, 1987) is to assume that the failure strain degrades from an initial value ϵ_{f0} to a final value equal to ϵ_r. This case, illustrated in Fig. 3(*b*), leads to the expression

$$\frac{\epsilon_f}{\epsilon_r} = \left(1 - \frac{\epsilon_{f0}}{\epsilon_r}\right)\left(\frac{w_N}{w_c}\right)^m + \frac{\epsilon_{f0}}{\epsilon_r} \tag{2}$$

Cracks in the ceramic layer may be assumed to grow according to a crack growth law of the form

$$\frac{dA}{dN} = A\epsilon_e^b a^c \tag{3}$$

where da/dN is the incremental crack growth per cycle, A is a constant, b and c are exponents related to the subcritical crack growth exponent, and a is the crack length. The model resulting from expression (1) is

$$\sum_{N=1}^{N_f} \left[\left(1 - \frac{\epsilon_r}{\epsilon_f}\right)\left(\frac{w_N}{w_c}\right)^m + \frac{\epsilon_r}{\epsilon_f}\right]^b = 1 \tag{4}$$

and the alternative model resulting from expression (2) is

$$\sum_{N=1}^{N_f} \left[\left(1 - \frac{\epsilon_{f0}}{\epsilon_r}\right)\left(\frac{w_N}{w_c}\right)^m + \frac{\epsilon_{f0}}{\epsilon_r}\right]^{-b} = 1 \tag{5}$$

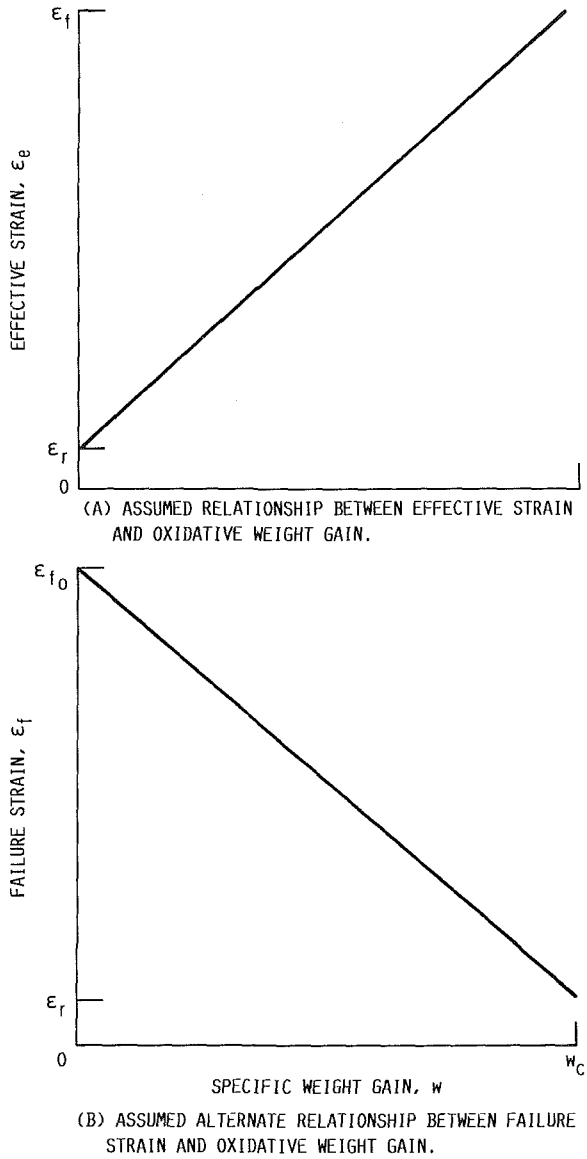

Fig. 3 Assumed weight gain/strain relationships

These models may also be derived from the familiar fatigue expression (Miller et al., 1984; Manson, 1966)

$$N_f = \left(\frac{\epsilon_e}{\epsilon_f}\right)^{-b} \tag{6}$$

and Miner's Law

$$\sum_{N=1}^{N_f} \left(\frac{1}{N_{fN}}\right) = 1 \tag{7}$$

where N_{fN} is the apparent number of cycles remaining after cycle N and weight gain w_N.

Figure 4 illustrates the fits obtained using expression (4) and applying it to life data collected at 1100°C for three different cycle lengths. It should be mentioned that the parameters given in the figure are not unique. Numerous other sets provide equally good fits. For example, raising the assumed value of b while lowering the strain ratio produces an equally good fit. Also, the life data can be fit equally well using expressions (4) or (5).

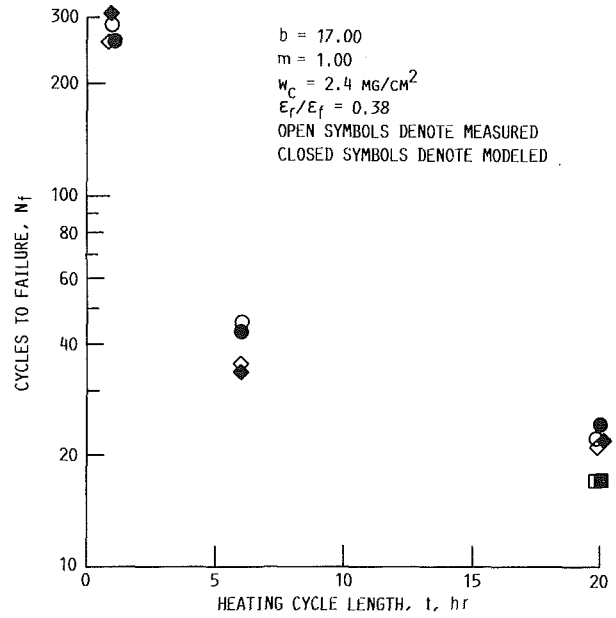

Fig. 4 Comparison of calculated and modeled life as a function of heating cycle duration according to NASA laboratory model

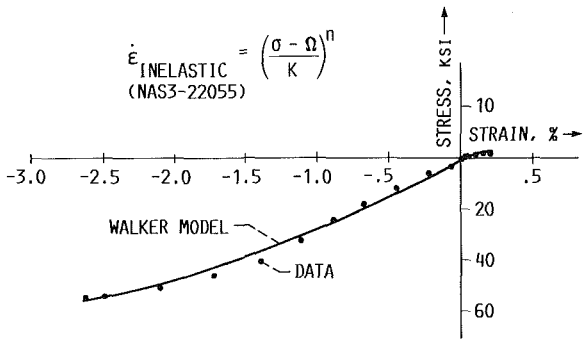

Fig. 5 Ceramic behavior modeled with Walker equation according to the Pratt & Whitney model

Design-Capable Life Modeling

While the above model represented a first step, it was not in a form that would be of use to an engine designer. Therefore three contracts were instituted under the HOST program that were aimed at the development of design-capable models.

Pratt & Whitney Aircraft (DeMasi et al., 1989), along with subcontractor Southwest Research Institute, developed a fatigue-based coating life model that uses Miner's Law (expression (7)) along with expression (6) rewritten as

$$N_f = \left(\frac{\Delta\epsilon_i}{\Delta\epsilon_f}\right)^{-b} \tag{8}$$

where $\Delta\epsilon_i$ is the inelastic strain range defined by

$$\Delta\epsilon_i = \Delta(\alpha\Delta T) + \Delta\epsilon_h + \Delta\epsilon_c - \frac{2\sigma_{ys}}{E} \tag{9}$$

The term $\Delta(\alpha\Delta T)$ in the above expression is the thermal expansion mismatch strain (which was expressed in terms of ϵ_r in the previous section), $\Delta\epsilon_h$ is the strain resulting from the heating transient, $\Delta\epsilon_c$ is the strain resulting from the cooling transient, and σ_{ys}/E is the elastic strain at yielding. The assumed relationship between oxidation and strain, analogous to expression (2), was

$$\Delta\epsilon_f = \Delta\epsilon_{f0}\left(\frac{1-\delta}{\delta_c}\right)^c + \Delta\epsilon_i\left(\frac{\delta}{\delta_c}\right)^d \tag{10}$$

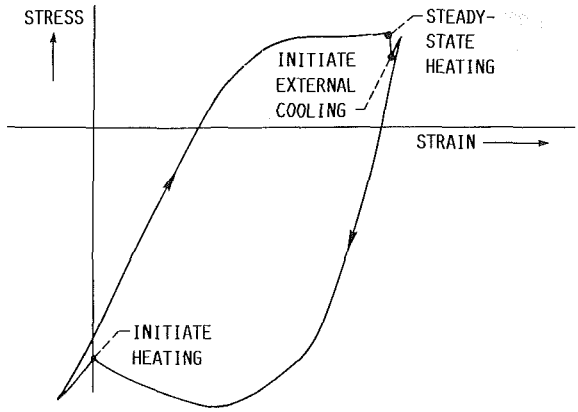

Fig. 6 Schematic of strains calculated for a typical cycle according to the Pratt & Whitney model

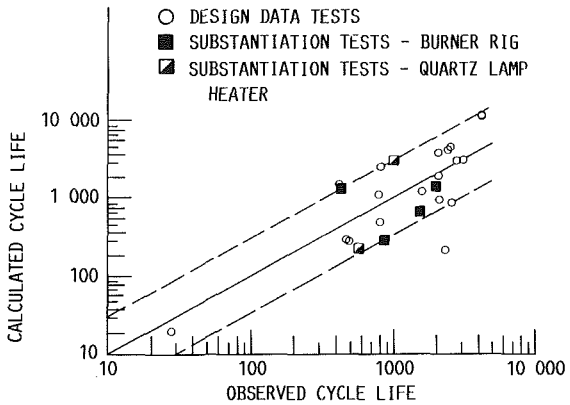

Fig. 7 Comparison of calculated and modeled lives according to the Pratt & Whitney model

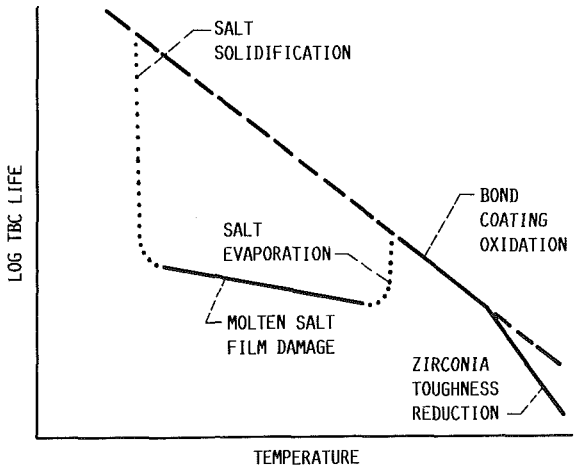

Fig. 8 Schematic of processes considered in the Garrett model

where oxidation has been expressed in terms of the oxide layer thickness δ rather than the specific weight gain w. The inelastic strain range was calculated using finite element techniques, which employed a time-dependent inelastic model developed by Walker (1983). Figure 5 shows an example of the use of this model to calculate compressive and tensile strains which may be compared with experimental data. In Fig. 6 the ceramic stress-strain behavior is calculated for a single cycle. This figure displays the large amount of reversed inelastic strain produced by thermal cycling. Figure 7 shows a plot of observed versus calculated lives for a wide range of test condi-

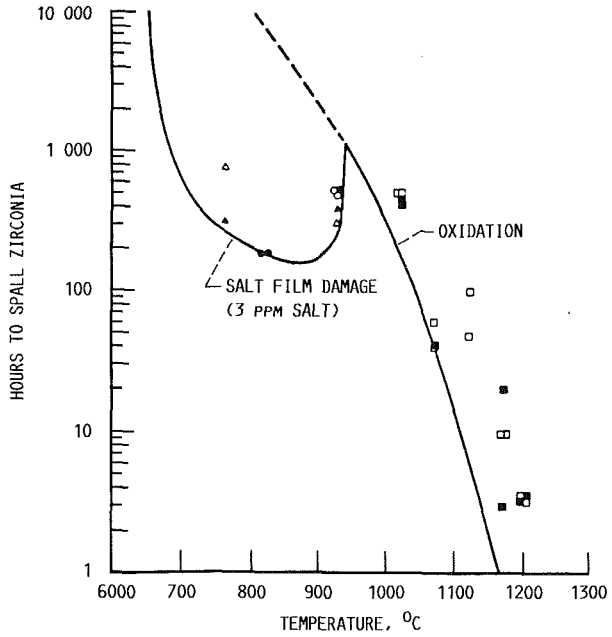

Fig. 9 Conservative fit of laboratory life data to the Garrett model

TBC SYSTEM	BUSINESS JET, HR	MARITIME SURVEILLANCE, HR
PLASMA SPRAY		
CHROMALLOY	16 517	9 843
UNION CARBIDE	6 656	5 207
KLOCK	49 644	29 973
EB-PVD		
TEMESCAL	55 607	2 106

Fig. 10 Mission analysis predictions by the Garrett model

tions. As shown in the figure the model is accurate to plus or minus a factor of 3, which is considered adequate.

The model developed by the Garrett Turbine Engine Company (Strangman et al., (1987) may be expressed as

$$\text{TBC Life} = \frac{1}{\left[\dfrac{\text{Heating cycle length factor}}{(\text{Oxidation life})^{-1} + \dfrac{\text{Zirconia densification}}{\text{plus oxidation life}^{-1}}}\right]^{-1} + \left[\dfrac{\text{Salt film}}{\text{damage life}}\right]^{-1}} \tag{11}$$

Equation (11) is expressed schematically in Fig. 8, which shows that the model considers bond coat oxidation, zirconia toughness reduction, and damage due to molten salt deposits. The model is driven by the thermal analysis of the component of interest for its anticipated mission. The left side of the denominator in expression (11) as determined from test data calibrations is

$$\frac{(t^{0.25}+0.181)\text{MTBREF}}{\{\exp[-0.015(T+273)+C_1]\}^{-1}+\{\exp[-0.041(+273)+C_2]\}^{-1}} \tag{12}$$

where MTBREF is a multitemperature burner rig experience factor that forces predictions and experiment into agreement. The right side of the denominator in expression (11) is calculated using a Garrett-developed model (Strangman, 1984; Strangman et al., 1987). In practice, the model is driven by thermal analysis of the component of interest. An example of the application of the thermal barrier coating life model to

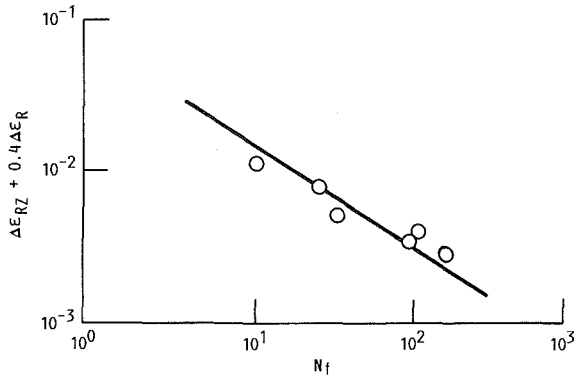

Fig. 11 Correlation between calculated strain relationship and experimental cycles to failure according to the General Electric model

laboratory test data is shown in Fig. 9, and mission analysis predictions are shown in Fig. 10.

The approach used by the General Electric Company (Hillery et al., 1987) employed time-dependent, nonlinear finite element modeling of the stresses and strains present in the thermal barrier coating system, followed by the correlation of these stresses and strains with test lives. The life model developed using this approach may be expressed as

$$\Delta\epsilon_{RZ} + 0.4\Delta\epsilon_R = 0.121N_f^{-0.486} \tag{13}$$

where $\Delta\epsilon_{RZ}$ is the shear strain range, $\Delta\epsilon_R$ is the normal strain range, and N_f is the number of cycles to failure. The above model is the only one to consider failure induced by edges and hence is the only one to consider shear strain. Expression (13) is illustrated graphically in Fig. (11).

Concluding Remarks

In conclusion, the materials and structural aspects of thermal barrier coatings have been successfully integrated under the NASA HOST program to produce models that may now or in the near future be used in design. Efforts on this program continue at Pratt & Whitney Aircraft where their model is being extended to the life prediction of physical vapor deposited thermal barrier coatings.

While the HOST program has been quite successful, it should also be noted that many new and unanswered questions have been raised by this work. For example, the effects of creep and inelasticity in both the ceramic and bond coat layers are poorly understood. The role of shearing stresses, including the role that shearing at an edge may play in reducing the fatigue exponent, is not well understood. The detailed mechanism by which oxidation controls coating system life is not well understood either. Also, it is not known whether the assumption of a smooth interface, commonly employed to simplify finite element analyses can lead to inaccurate or even misleading results. Other areas of uncertainty involve the importance of sintering at high temperatures and hot corrosion at relatively low temperatures.

References

Chang, G. C., Phucharoen, W., and Miller, R. A., 1987, "Behavior of Thermal Barrier Coatings for Advanced Gas Turbine Blades," *Surface and Coatings Technology*, Vol. 30, pp. 13–28.

DeMasi, J. T., Ortiz, M., and Sheffler, K. D., 1989, "Thermal Barrier Coating Life Prediction Model Development," NASA Contractor Report, to be published (Pratt & Whitney Aircraft).

Hillery, R. V., Pilsner, B. H., McKnight, R. L., Cook, T. S., and Hartle, M. S., 1987, "Thermal Barrier Coating Life Prediction Model, Final Report," NASA CR-180807.

Manson, S. S., 1966, *Thermal Stress and Low Cycle Fatigue*, McGraw-Hill, New York, 1966.

Miller, R. A., 1984, "Oxidation-Based Thermal Barrier Coating Life Prediction Model," *Journal of the American Ceramic Science*, Vol. 67, No. 8, pp. 517–521.

Miller, R. A., Agarwal, P., and Duderstadt, E. C., 1984, "Life Modeling of Atmospheric and Low Pressure Plasma Sprayed Thermal Barrier Coating," *Ceramic Engineering Science Proceedings*, Vol. 5, No. 7–8, pp. 470–478.

Miller, R. A., 1987, "Current Status of Thermal Barrier Coatings—An Overview," *Surface and Coatings Technology*, Vol. 30, No. 1, pp. 1–11.

Strangman, T. E., 1984, "Life Prediction and Development of Coatings for Turbine Airfoils," Workshop on Gas Turbine Materials in a Marine Environment, Bath, United Kingdom.

Strangman, T. E., Neumann, J., and Liu, A., 1987, "Thermal Barrier Coating Life Prediction Model Development, Final Report," NASA CR-179648.

Walker, K. P., 1983, "Research and Development Program for Non-linear Structural Modeling With Advanced Time-Temperature Dependent Constitutive Relationships," NASA CR-165533.

P. J. Murphy

D. W. Jones

A. E. Lennert[1]

R. R. Jones, III

Sverdrup Technology, Inc.,
AEDC Group MS 900,
Arnold Air Force Base, TN 37389

Fiber Optics Based Jet Engine Augmenter Viewing System

An augmenter viewing system employing a coherent fiber-optic array was developed for use in jet engine testing applications at AEDC. Real-time viewing of the test article afterburner was obtained in a severe environment under high temperature and vibration levels. The optical system consisted of a conventional front-end lens assembly coupled with the fiber-optic array, and a solid-state color video camera mounted inside the test cell. The advantages and problems associated with a fiber-optics-based viewing system will be discussed in comparison with more conventional viewing techniques for this application.

Introduction

Jet engines must undergo an extensive series of ground and flight tests before being certified for commercial or military use. Much of this ground testing is conducted in facilities at the Arnold Engineering Development Center (AEDC). A wide variety of instrumentation, including video viewing systems, is employed to monitor engine performance. The objective of an augmenter viewing system (AVS) is to monitor the operation of the afterburner of a turbojet engine, including the flameholder, igniters, and nozzle surface, during full-scale altitude testing to verify uniform ignition and flame pattern. Typically, the viewing system is located at distances ranging from 20 to 10 m from the afterburner. The environment in this region is extremely harsh, because of the high temperature exhaust impinging on the optics, and the high vibration levels generated by the engine.

Augmenter viewing has routinely been used at AEDC in various test cells having constant area ejector (CAE) diffusers. In these applications, a video camera is mounted in a water-cooled environmental housing in a fixed positon downstream from the engine. Recently, the introduction of a variable area ejector (VAE) diffuser with a movable centerbody required the development of a new type of viewing system. The VAE centerbody, shown in Fig. 1, is a conical obstruction located within the diffuser, which can be moved axially along the cell. It is used to reduce the velocity of exhaust gases from the engine so that compressors in the exhaust duct can remove the gases and release them into the atmosphere with minimum power consumption. The presence of the obstruction precluded the use of a downstream camera, and any camera located on the centerbody would require either focusing capability or large depth of field.

Design constraints associated with the movable VAE centerbody led to the implementation of a fiber-optic-based augmenter viewing system (AVS). While the use of fiber optics for engine imaging is not novel (Morey, 1984), this application presented some interesting design challenges.

Several alternatives to the present fiber-optics-based system were investigated, including placing a camera directly in the nose of the VAE centerbody, placing off-axis cameras in the diffuser, and installing a boroscope system, but none had any distinct advantages over the present system. In fact, each of these techniques had some type of major technical limitation or uncertainty. The nose camera concept suffered from problems with vibration and restriction of cooling water flow within the centerbody, while the off-axis cameras could not provide desired target coverage because of the camera locations. The boroscope system, while offering some potential improvements in image quality over the fiber-optic cable, had potential vibration and cooling problems, in addition to flow blockage effects on the performance of the VAE.

System Description

The fiber-optic augmenter viewing system transmits an image of a jet engine augmenter from a small aperture located in the forward section of the VAE to a color television camera

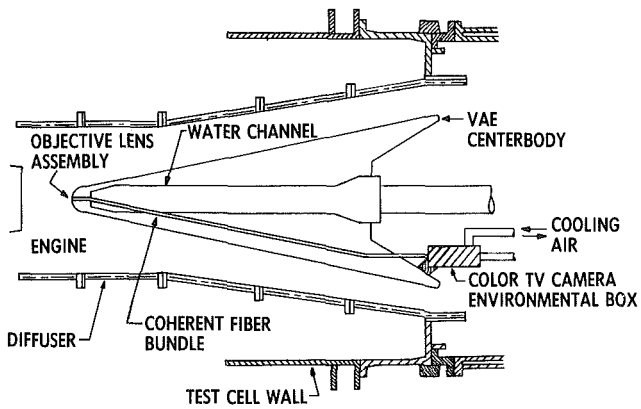

Fig. 1 Schematic of augmentor viewing system

[1]Retired.

Contributed by the International Gas Turbine Institute and presented at the 33rd International Gas Turbine and Aeroengine Congress and Exhibition, Amsterdam, The Netherlands, June 5-9, 1988. Manuscript received by the International Gas Turbine Institute March 1, 1988. Paper No. 88-GT-320.

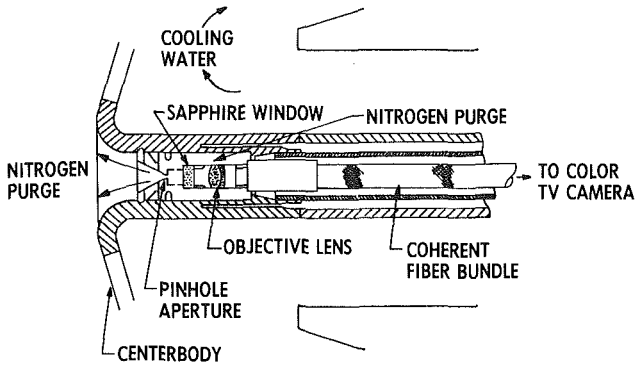

Fig. 2 Objective lens assembly

located aft of the centerbody. The augmenter is imaged by a fixed focal length lens system onto the front surface of a flexible fiber-optic image guide. The image is then transmitted by the image guide to a telephoto lens and the camera. The electrical signal from the camera is transmitted outside the test cell through approximately 6 m of coaxial cable. The entire viewing system is located inside the test cell diffuser as depicted in Fig. 1. Four basic subsystems comprise the fiber-optic AVS: the objective lens assembly, the fiber-optic image cable, the image relay lens system, and the video camera. Each of these subsystems performs a special function and, accordingly, has a unique set of operational and environmental limitations.

The objective lens assembly, shown in Fig. 2, includes a pinhole aperture, a protective sapphire window, and a set of lenses. The pinhole aperture protects the viewing window by reducing the particle impact cross section, and increases the depth of field of the optical system. The latter is necessary because, during testing, the VAE centerbody can traverse a distance of approximately 1 m along the test cell axis. Calculations indicate that under extreme conditions, the water-cooled lens assembly could experience temperatures of up to 180°C. Of the optical elements in the assembly, the sapphire window has the highest probability of attaining this maximum temperautre. To keep the operating temperature of the window to a minimum and to reduce further the number of particles impacting the window, a nitrogen gas purge was used during testing.

The optical system for the VAE application was designed to view a 1-m-dia object at distances ranging from 3.5 to 4.5 m. The objective lens was a short focal length achromatic doublet with a visible antireflective coating. The magnification of the system was chosen so that at the closest point the augmenter image filled the fiber-optic array, thus providing maximum resolution. For this system, a 1-m target size yielded a 3.8-mm-dia image on the fiber array, resulting in a magnification of 0.0038.

The fiber-optic image guide consisted of a coherent array of 80 × 80 minibundles of fibers, 4 m long. A coherent array is one in which there is a one-to-one correspondence between the position of an individual fiber at the input and output faces of the bundles. Each minibundle consisted of a 5 × 5 array of individual 10-μm-dia glass fibers, which are fused into a square matrix, resulting in a 400 × 400 fiber imaging array. Transmission losses in the cable were measured at 8.3 dB in the visible.

The image guide was required to withstand continued use in an adverse environment including water, dust, oil, and temperatures up to 180°C. In this application, only the front end connector had any probability of reaching this maximum temperature. Mechanical protection of the image guide was provided by a corrugated Teflon® sheathing housed in a water-cooled conduit. The fiber-optic cable sheathing was approximately 12.5 mm in diameter and was terminated on each end with a threaded stainless steel ferrule, which mated to the objective lens assembly and to the camera lens attachment.

Images from the exit plane of the fiber-optic bundle were transferred to the sensor array of the video camera by means of a relay system, including a macrolens and a telephoto lens. The telephoto lens provided remote-controlled variable magnification capability. The ability to vary image size was needed to optimize image size and brightness. This function was remotely controlled from the control room.

The jet engine augmenter was a relatively high intensity object that could vary from zero to maximum intensity in less than 5 s. An automatic iris on the telephoto lens controlled light intensity levels and prevented overexposure from changes in light levels on the target. If the auto-iris ceased to function during a test, the system could be adjusted with a remote manual iris adjustment.

A small color TV camera transmitted the augmenter image to an external video monitor and video tape recorder during testing. The image sensor was a solid state MOS array containing 380 × 480 pixels in a 2/3-in. format for an image resolution of 190 × 240 lines. The camera sensitivity was 100 lux. The camera was approximately 10 × 6 × 16 cm long and mounted in a special environmental housing. The cylindrical camera housing was clamped at one end to the centerbody and at the other end to a hollow shaft, which relayed the wiring outside the test cell. The maximum operating temperature of the camera was 50°C, and maximum allowed sinusoidal vibrations were approximately 3g peak at 50 Hz and above. This vibration specification is fairly standard for commercially available color video cameras.

Problem Evaluation

The AVS system design had to account for temperature limitations, the vibration effects, and the dependency of image quality on the optical system resolution and sensitivity.

High temperatures from the engine exhaust required careful cooling of the optical system, which was required to withstand 180°C temperatures. However, the primary lenses were achromatic doublets, which are bonded with an optical epoxy limited in temperature to approximately 90°C. The fact that the lenses survived with no degradation indicates that the temperatures in this region did not exceed the epoxy breakdown temperature. Camera and fiber-optic cable temperatures were adequately controlled using water cooling.

Excessive camera vibration can produce image degradation either by causing the image to move around in the field of view or by mechanically induced electrical noise on the video monitor. Test results indicated that image motion was not a problem for the system, indicating that centerbody displacements were small. Mechanically induced electrical noise, however, was a major factor in reducing image quality. During the test program, the severe vibration levels encountered by the camera caused the video quality to be degraded by the appearance of horizontal noise bars. After operating under these conditions for a period of time, camera failure occurred before an improved isolation system was installed.

Typical solid-state cameras are capable of operating with vibration levels of up to approximately 3g. Figure 3 shows a typical vibration spectrum of an accelerometer mounted on the downstream side of the VAE centerbody. Two major resonances occurred with vibration amplitudes on the order of 7g peak. The camera housing was subjected to even larger accelerations, which were probably due to a combination of acoustic and flow-related phenomena. Figure 4 shows a typical vibration spectrum for the camera housing. Three major resonances occurred with vibration amplitudes of 6.5, 12, and 10g peak, respectively. These vibrations directly affected the performance and longevity of the camera.

Vibration testing of two cameras was conducted at fre-

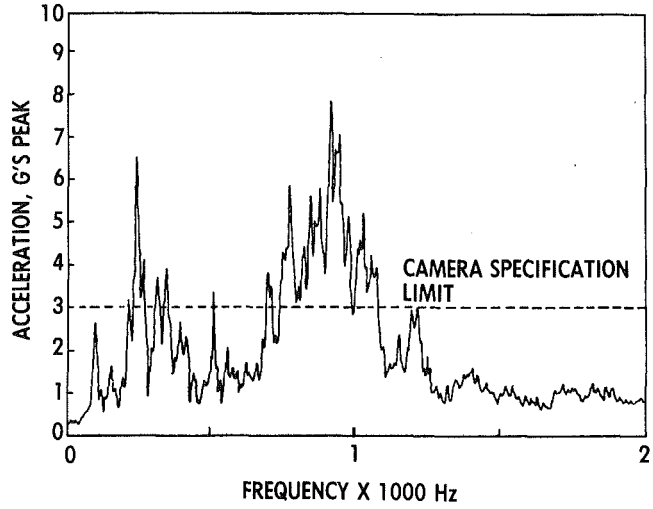

Fig. 3 Centerbody vibration spectrum

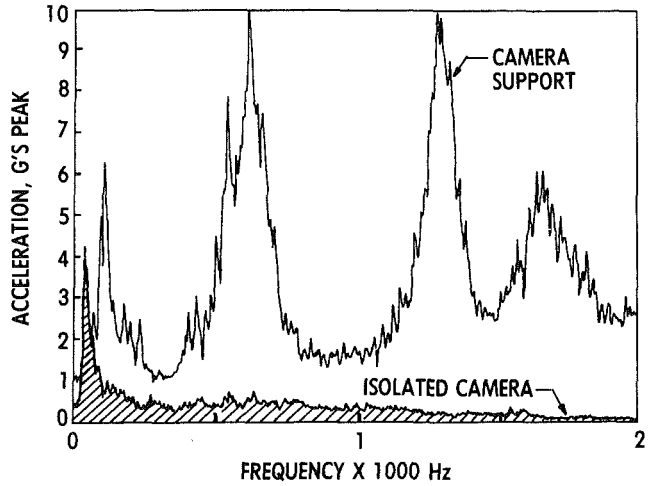

Fig. 4 Vibration spectra for camera and support

quencies ranging from a few cycles per second to 2000 cycles per second, in order to determine safe operating limits. The testing was initially conducted with the cameras in their original condition as shipped by the manufacturerer. Both cameras behaved well at vibration levels of 3*g* peak at 20 Hz and above. At higher vibration levels, the cameras exhibited vibration-induced noise on the video monitor, and at 7*g* peak the cameras ceased to function until the vibration was stopped. The cameras were then modified by installing vibration damping material inside the camera, and retested. The vibration-hardened cameras were then able to function at levels of 10*g*, although noise remained present above 3*g* peak.

To protect the camera further against vibration damage and to minimize signal loss from vibration-induced noise, a vibration isolation system was installed between the camera and the camera housing. The isolation system consisted of four commercially available vibration isolators, which were installed vertically. The isolators were constructed of a highly damping silicone compound having a transmissibility of approximately 3.5. The resulting vibration of the video camera, after being isolated from the camera box vibration, is also shown in Fig. 4. The modified camera system resonated at a frequency of approximately 40 Hz. Although high-frequency vibrations were effectively eliminated, additional vibration damping will be required to bring the resonant amplitude to below the 3*g* limit specified by the manufacturer. This could be accomplished in principle by using a more highly damped vibration isolator. One manufacturer indicated that a special isolator could be supplied with a transmissibility of between 2 to 2.5, which would provide approximately an additional 40 percent reduction in camera vibration levels.

A major factor contributing to the overall quality of the image displayed on the video monitor was the amount of light transmitted through the optical system, and the sensitivity of the camera sensor.

The amount of radiant flux originating from a typical augmenter entering the pinhole aperture at a distance of 4.5 m was estimated to be 200 mW. Of this amount approximately 0.7 percent was estimated to be visible radiation. In photometric units, the amount of light entering the aperture was approximately 0.350 lumens. With a light attenuation of 85 percent attributable to losses in the fiberoptic cable, 0.053 lumens were transmitted to the camera sensor. The average photometric intensity, or illuminance, on the camera sensor was then approximately 180 lux (where lux = lumens/sq meter).

These calculations indicate that the system can detect the afterburner flame, but other details of the engine, including the igniter spark and the outer nozzle surface, will be only marginally visible during normal operation of the augmenter viewing system. This has been verified by observations taken during actual engine tests.

Camera sensitivity can affect image quality by not allowing subtle features of the intensity distribution to be detected. For a clear picture, it is desirable to have the entire intensity distribution above the noise floor of the camera and below the saturation point of the sensors. Because of the high losses in the fiber-optic system, some of the engine features were below the noise floor of the camera, and were therefore not discernable under normal test conditions. By opening up the pinhole aperture, more light entered the system and a brighter overall picture resulted. However, this increased the probability of contaminating the sapphire window from exhaust particles. The addition of in-cell illumination of outer nozzle surfaces would also improve image brightness considerably. Brightness determines the signal to noise of the optical system; with reduced illumination, the signal to noise of the system decreases, although the resolution of the optical system remains the same.

Resolution is a fixed parameter of the optical system and provides a measure of the spatial detail observable in the image. Several factors influenced the image resolution of the augmenter viewing system. These included the imaging lens resolution, the number of fibers in the image guide, the number of detecting elements in the camera sensor, the alignment and separation of the fibers in the image guide, and optical path disturbances resulting from the nitrogen purge flow (as well as from exhaust gases).

Other factors may further reduce image resolution. In the AVS, the target was first imaged onto a fiber-optic array with 400 × 400 individual imaging elements. Mapping the fiber-optic array onto the object resulted in a line width resolution of approximately 2.5 mm. When the image is relayed through the telephoto lens and onto the camera sensor, the 400 image fibers (in one dimension) are focused onto 380 sensor elements. A statistical mismatch occurs between the alignment and size of the source and sensor elements, resulting in a system resolution given by

$$R_{\text{system}} = [R^2_{\text{fiber}} + R^2_{\text{camera}}]^{1/2}$$

where R_{fiber} and R_{camera} represent the image guide and camera sensor resolutions, respectively. For an estimated camera resolution of 2.7 mm, the AVS system resolution is 3.7 mm. To improve this resolution, it would be necessary to increase the total number of fibers in the array, or the number of pixels in the camera sensor. Note that the video camera, if used alone, would provide much better resolution than the camera/fiber-optic combination.

The system resolution quoted above is attainable only when the image totally fills the fiber-optic array. If this is not the case, a loss of resolution occurs because of the unused fibers.

Because the VAE centerbody (along with the AVS) can be located anywhere over a distance of 1 m depending on the specific test configuration, the image can only fill the fiber-optic array at the closest position. Some underfilling will occur at the full-back position of the centerbody. In the present test configuration the resolution will vary between 78 and 100 percent of the maximum resolution as the imaging system moves from 4.5 to 3.5 m from the target, respectively.

A consequence of increasing the image resolution is that the effects of the high-pressure nitrogen purge through the pinhole aperture on the front of the viewing system become more noticeable. The result is a blurring or defocusing of the image, which is probably attributable to a lensing effect caused by pressure gradients across the pinhole aperture. Calculations indicate the strong possibility of the occurrence of a Mach disk, due to the nitrogen purge, in front of the aperture. This defocusing effect has also been noticed in other viewing systems at AEDC employing high-pressure nitrogen purges.

Another factor contributing to reduced image quality is the appearance of lines arising from the minibundles composing the fiber-optic cable. The lines probably are due to the thickness of the epoxy binding the minibundles together. One way to reduce the distraction caused by these lines is to enlarge the area of the fiber-optic bundle to increase the image size, so that the camera focuses on a larger number of fibers. This will reduce the width of the lines relative to the overall image sizes.

Future Improvements

In view of the environmental considerations discussed, it would be advantageous to locate the camera and relay lens system outside the test cell walls using a fiber-optic cable. An externally located camera could be mounted directly to the test cell floor, virtually eliminating mechanical vibration effects. Another advantage of removing the camera from the test cell includes reducing the cooling requirements on the camera. In addition, camera access would be greatly improved, increasing the reliability of the augmenter viewing system.

An added incentive, from the standpoint of future technology requirements, of having an external camera system is the possibility of using an ultraviolet imaging camera for combustion specific viewing. There is an interest on the part of engine manufacturers to observe engine combustion directly, by looking at ultraviolet fluorescence caused by excitation of specific molecules during the burning process. This is not practical with the present AVS configuration because of the excessive losses in the fiber-optic cable. Locating the camera external to the cell also opens up the possibility of adding accessories such as image intensifiers for observing low light level phenomena. However, these advantages must be weighed against any changes in image quality that may occur for the external system.

Current estimates indicate that a fiber-optic image cable length of approximately 10 m will be required to allow the camera to be located outside of the test cell. This would require a different type of fiber-optic image guide consisting of a low-loss fused quartz array. This commercially available array has an active diameter of up to 2 mm and contains approximately 20,000 individual 20-μm-dia fibers. These fibers are fused together to form a solid light-guiding structure, which is available in lengths of up to 50 m. The fact that the quartz bundle can take temperatures of up to 300°C and transmit ultraviolet light makes it very attractive for use in the VAE.

The lower resolution of the quartz cable would, however, be partially offset by a resulting gain in image brightness. Typically, the glass used in the existing type of fiber bundle has an attenuation of approximately 2 dB per meter, or about 85-percent attenuation over the length of the 4-m cable. The quartz fiber is made of a much higher quality material, which may have losses as low as a few dB per kilometer. The quartz fiber bundle that could be purchased for the augmenter viewer is expected to have less than 3 dB loss through the length required for this application.

The quartz fiber bundle contains fibers that have been fused together during the manufacturing process, and if any fiber breakage occurs, one could probably expect the entire bundle to fail simultaneously. An advantage of the existing glass bundle in this case is that although individual fibers may be more susceptible to breakage, the bundle can still be used if it is partially damaged.

An alternative to using a long fused quartz fiber bundle would be to employ two glass fiber bundles similar to those currently in use. In the preferred embodiment, two 15-ft fiber cables would be connected with a one-to-one image relay lens. This type of splice would reduce image resolution of the fiber cables by over 40 percent, bringing the fiber optic resolution to 3.6 mm and the overall system resolution to 5.3 mm, as compared to 2.5 and 3.7 mm resolution, respectively, for the existing system. By comparison, the resolution of the quartz fiber cable is expected to be approximately 10 mm. This number is approximately four times worse than in the existing system, and twice as bad as could be achieved by splicing two glass fiber bundles together. The choice of which type of cable to use will ultimately depend on the sensitivity and resolution required for a given application.

Summary

A review of the fiber-optic augmenter viewer has been presented, including advantages and problems associated with placing the camera inside the test cell with the moving VAE centerbody. Several nontrivial technical challenges in the design of a reliable augmenter viewer were discussed. Any efforts to move the camera outside the test cell with currently available hardware will result in further degradation of image resolution and brightness, unless improvements are made to the state of the art in manufacturing fiber-optic image guides.

Additional improvements for providing an even higher quality, more reliable system have been identified and could be implemented. Installing low-transmissibility vibration isolators in a redesigned camera housing will effectively reduce vibration levels to within the manufacturer's maximum specification. Increasing the diameter of the pinhole aperture will allow more light to traverse the optical system and provide a brighter image. A shorter length fiber-optic image guide with a larger format would provide more light and improved resolution. And finally, by reducing the gas purge pressure somewhat, the defocusing effect currently observed could be eliminated or reduced. These improvements could produce an increase in image brightness by a factor of from 2–10 times, with a slight increase in image resolution.

Acknowledgments

The research reported herein was performed by the Arnold Engineering Development Center (AEDC), Air Force Systems Command. Work and analysis for this research were done by personnel of Sverdrup Technology, Inc./AEDC Group, operating contractor of the AEDC propulsion test facilities. Further reproduction is authorized to satisfy needs of the U. S. Government.

References

Morey, W. W., 1984, "Hot Section Viewing System," NASA CR-174773.

Investigation of Swirler/Dilution Jet Flow Split on Primary Zone Flow Patterns in a Water Model Can-Type Combustor

P. Koutmos

J. J. McGuirk

Imperial College of Science and Technology,
Department of Mechanical Engineering,
Fluids Section,
London SW7 2BX United Kingdom

LDA measurements of the three mean velocity components and the corresponding turbulence intensities have been made to provide qualitative and quantitative information on the flow field in a water model of a can-type gas turbine combustion chamber. The combustor geometry comprised a swirl-driven primary zone, annulus-fed rows of primary and secondary jets, and an exit contraction. The effect of variation of the flow split between the swirler and the dilution holes on the flow pattern in the primary zone has been investigated in detail. Flow visualization studies revealed that significant changes occur in this region due to the interaction between the swirling flow and the radially directed primary jets. A large toroidal recirculation was formed and high levels of turbulence energy were generated in the core of the combustor at low levels of swirler flow rate. As the swirl level increases, the strength of this recirculation was observed to weaken. Beyond a critical level, the primary recirculation was pushed off center and the undesirable feature of a forward velocity on the combustor axis in the primary zone was observed. Despite the dramatic changes brought about in the primary zone, the flow pattern downstream of the secondary jets was practically the same for all flow splits due to the strong mixing caused by the two rows of jets.

Introduction

Modern trends in the design of gas turbine combustion chambers require that the combustor must burn fuel completely, cause little pressure drop, produce an acceptable exit temperature traverse, maintain stable operation over a wide range of conditions, and achieve low pollutant emissions: a set of demands that is most difficult to satisfy simultaneously. The introduction of air passing into the primary zone through swirl vanes in the dome of the can and interacting with a row of impinging jets entering via the can periphery helps to create a flow pattern that is a first step in achieving many of the above requirements. The resulting flow pattern is extremely complex and knowledge of the aerodynamic behavior of the primary zone is incomplete.

At the present time, designers are aided by experimentation on full-scale or subscale models, which mainly correlate a few global flow and performance parameters. Most of the experimental investigations that have provided detailed information on internal combustor flow fields have used axisymmetric geometries and have focused attention on single parameters of the flow. For example, restricting attention to the primary zone and concentrating on the measurement of changes in the flow structure due to introduction and variation of swirl in idealized combustor models without dilution jets was the aim of the experiments of Altgeld et al. (1983), Vu et al. (1982), and Rhode et al. (1983). These works provided useful information on the kind of swirling flow fields to be expected in combustor systems, but neglected any influences due to the interaction between swirler and primary jet flows. The existence of a vortex breakdown phenomenon and its subsequent development in the presence of a downstream contraction was investigated by Escudier and Keller (1985), but again only for an axisymmetric geometry. Following a similar route of isolating a certain feature of combustor flows, Khan et al. (1981) examined only the downstream dilution zone region and the behavior of rows of jets in a crossflow. Green and Whitelaw (1983) included both primary and dilution regions in their experimental arrangement but the upstream and downstream geometry were simplified and no swirl was introduced. Measurements in a realistic can-type geometry have been reported by Jones and Toral (1982) for combusting flow, but only details on the temperature and gas concentration field were obtained.

The present effort stems from a desire to extend the measurements of Green and Whitelaw to a geometry representative of current combustors and, at the same time, provide information on the influence of swirl on the internal flow field. Although the reacting flow field will differ in some respects from the isothermal flow, the dominance of the swirl-

Contributed by the International Gas Turbine Institute for publication in the JOURNAL OF ENGINEERING FOR GAS TURBINES AND POWER. Manuscript received at ASME Headquarters January 17, 1989.

ing motion and its interaction with the dilution jets in controlling the flow pattern (at least in the primary zone, Clarke et al., 1963) encourages the retention of the isothermal water flow type of experiment as conducted by Green and Whitelaw, substituting a perspex model that is geometrically similar to that of Jones and Toral. The optical access problems are thereby alleviated to the extent that laser velocimeter measurements were possible over practically the whole internal volume of the combustor. In the present work, attention is focused on the influence of the variation of the flow split between swirler, primary, and dilution jets on the primary zone and the different modes of interaction between the swirl and the primary jet flows. The aim of the investigation was to provide a sufficiently detailed mapping of the internal velocity field over the range of observed flow patterns so that those significant features of combustor performance that depend strongly on the local turbulent flow structure may be better understood. At the same time, useful information about the primary zone recirculation ratio, a parameter of engineering interest for the design of primary zone configurations, was obtained.

Table 1 Characteristics of the optical arrangement

5 mW He-Ne laser	λ = 632.8 nm
Focal length of lenses (mm) L_1 L_2 L_3	f_1 = 110 nominal f_2 = 300 nominal f_3 = 300 nominal
Beam diameter of $1/e^2$ intensity (mm)	0.8
Half-angle of intersection, in air (degrees)	5.98
Fringe separation (μm)	3.037
Intersection volume diameter at $1/e^2$ intensity (mm) (in water)	0.111
Intersection volume length at $1/e^2$ intensity (mm) (in water)	1.416
Calculated number of fringes within $1/e^2$ intensity band with no frequency shift	37
Velocimeter transfer constant (MHz/ms^{-1}) with no frequency shift	0.329

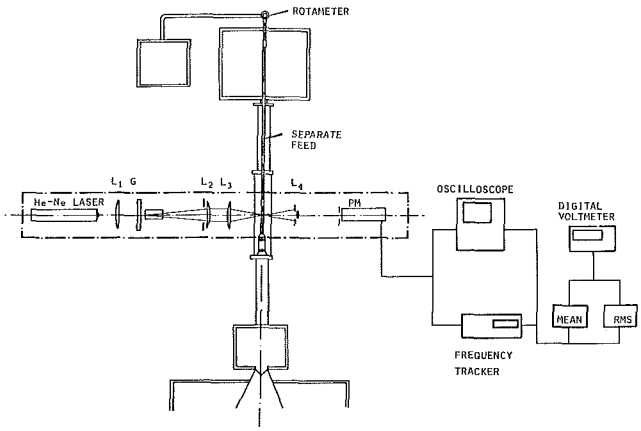

Fig. 1 Experimental arrangement

Flow Configuration

A diagram of the laser velocimeter and details of the model combustor geometry are presented in Fig. 1 and 2, respectively. The model can-type combustor was manufactured from cast acrylic and consisted of a hemispherical "head" section attached to a cylindrical central barrel of 74 mm i.d., which terminated in a circular to rectangular contraction nozzle. The combustor was located concentrically in a larger diameter tube so that an evenly spaced surrounding annular passage was formed. The aerodynamic swirler in the head consisted of eighteen 45 deg vanes and was fed separately from a constant head tank via a rotameter to allow control and regulation of the flow rate of the swirler fluid. The geometry of the vanes corresponded to a swirl number of 0.75, but a more accurate value obtained from measurements close to the swirler exit is 0.87. Primary holes (six in number) 10 mm in diameter, equispaced around the combustor, were located 46 mm downstream of the swirler. A second row of 12 equispaced 10-mm-dia holes was placed a further 80 mm downstream. A single constant head tank supplied water to the larger containing tube to feed both hole rows via the annulus, which was blocked off at the retaining flange at the furthest downstream end. The outflow from the combustor entered (via a free overflow) a large sump tank from where it was recycled to the two constant head tanks. Measurements were carried out for a variety of swirler flow rates, ranging from 10 to 35 percent of the total volume flow rate passing through the combustor. The overall Reynolds number in all experiments was of order 6×10^4 based on the bulk mean velocity and the internal combustor diameter.

Measurement Techniques

A qualitative picture of the flow was obtained using flow visualization via hydrogen bubbles produced from a 1-mm stainless steel wire inserted through tappings in the larger containing tube and entering the combustor through the holes. In addition, flow patterns were investigated with dye injected through the hub of the swirler, which had been blocked off using a perspex plug. Detailed measurements of the three mean velocity components and the corresponding turbulent

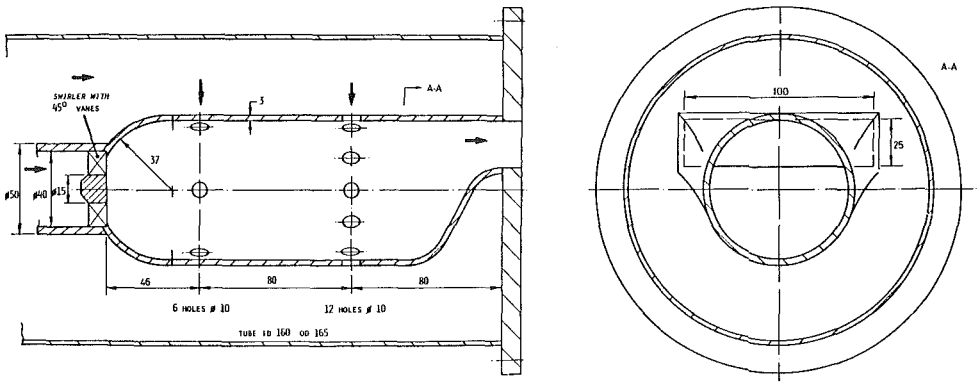

Fig. 2 Model combustor geometry

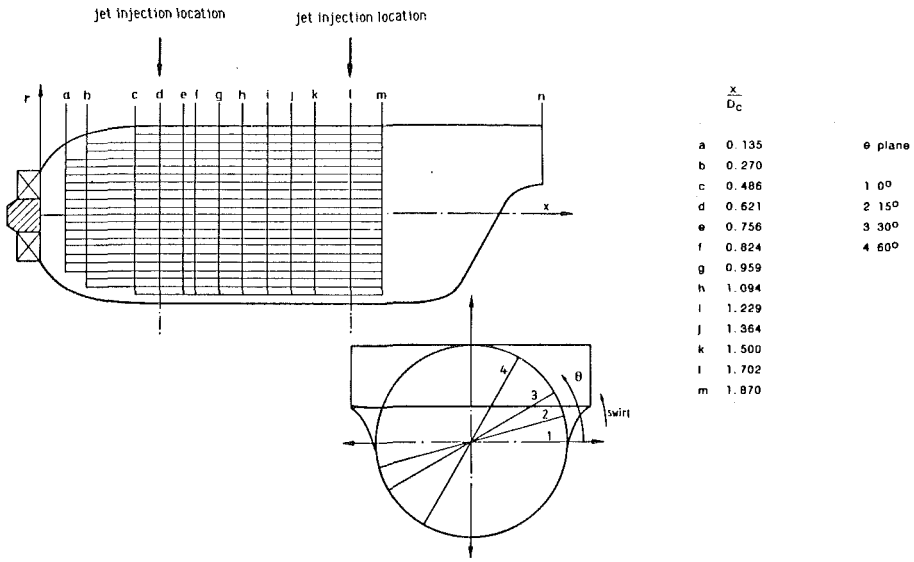

Fig. 3 Coordinate system and network of measurement points

Table 2 Combustor operating conditions in terms of flow splits ($\dot{Q}_{annulus} = \dot{Q}_{prim} + \dot{Q}_{sec}$ held constant at 2.8×10^{-3} m^3/s, except for 35 percent case when $\dot{Q}_{annulus} = 2.405 \times 10^{-3}$ m^3/s)

$\dot{Q}_{sw}$ ($m^3/s \times 10^{-4}$)	$\dot{Q}_{sw}/\dot{Q}_{tot}$ (%)	$\dot{Q}_{prim}/\dot{Q}_{sw}$	$\dot{Q}_{sec}/\dot{Q}_{prim}$
3.1	10	3.5	1.58
4.9	15	2.2	1.58
7.0	20	1.52	1.64
9.3	25	1.14	1.64
10.8	28	0.98	1.64
12.9	35	0.703	1.64

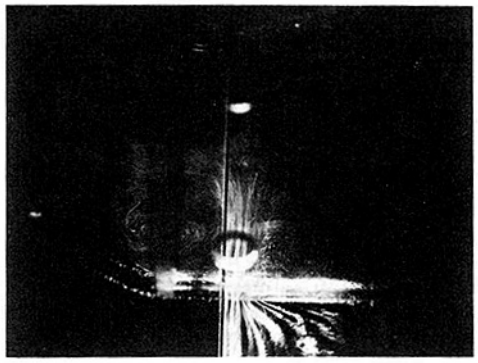

Fig. 4(*a*) Hydrogen bubble flow visualization, 15 percent swirler flow

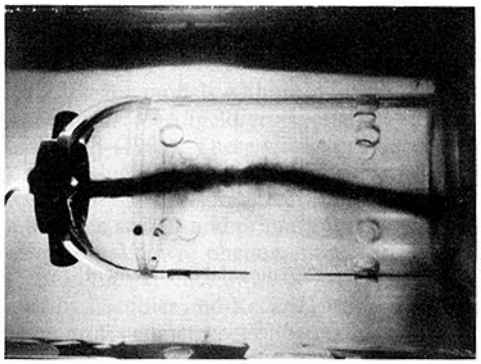

Fig. 4(*b*) Dye flow visualization, 35 percent swirler flow

normal stresses were obtained with a laser-Doppler anemometer operating in the dual beam forward scatter mode. The model and the containing tube were immersed in a plane-walled trough filled with distilled water to minimize the effects of the different refractive indices between air, perspex, and water on the beam passage through the curved tube wall.

The optical arrangement of the velocimeter is shown in Fig. 1 and comprised a 5 mW He-Ne laser, a focusing lens, a rotating diffraction grating (to split the incident beam and provide frequency shifts up to 2 MHz), a light collection system, and a photomultiplier (RCA 4836). Table 1 summarizes the principal characteristics of the system. The Doppler signals were demodulated by a frequency tracker (Cambridge Consultants (CC01)) and the analog output was processed through a true time integrator and an rms meter. A detailed analysis of instrumentation of this type has been provided, for example, by Durst et al. (1981). For a preselected swirl level, measurements of the mean axial azimuthal and radial velocities and their normal stresses have been obtained (Koutmos and McGuirk, 1984) at 14 axial locations and at azimuthal planes corresponding to $\theta = 0$, 15, 30 and 60 deg. The measurement points and the system of coordinates are shown in Fig. 3 (note that the mesh of measurement points has been rotated to lie in the vertical plane in this figure). In what follows, for each set of experimental conditions, measurements are shown for stations *b*, *d*, and *m* on the 0 deg plane, which passes through the centerline of a hole in both primary and secondary rows (rotation of the beams and of the whole internal model via the downstream retaining flange was necessary to obtain these measurements).

Errors associated with the measurements of the mean velocity and rms fluctuation levels include the influence of mean velocity gradients across the measuring volume, finite transit time broadening, instrument noise, and short-term fluctuations in the rotation of the grating. In addition, the error due to the offset in the calibration curve of the tracker output contributed to the error for the mean velocity. Errors in the mean velocities are estimated to be 4 percent of the bulk velocity. Errors in the measurement of the rms level are expected to be about 3 percent. The random error associated with the instability of the grating speed is estimated to be 0.3 percent of the measured velocity values.

Results

Flow visualization studies were carried out for swirler flow rates ranging from 10 to 35 percent of the total flow. It should be emphasized that the swirl number, quoted above and defined as the ratio of angular momentum to axial momentum times effective swirler diameter, remained constant during these variations, and it is the relative flow split between different entry routes into the combustor that is being altered. Table 2 above shows the actual flow rates used and the corresponding flow splits between swirler, primary, and secondary flows. Hydrogen bubbles generated from a wire passing through the primary holes enabled the flow pattern in the primary zone to be studied, at least for the lower swirl levels, and Fig. 4(*a*) shows a typical result at the 15 percent swirl flow level. The presence of a strong recirculation in the primary zone can be clearly identified; dye injected at low forward velocity via a small hole on the combustor centerline through the swirler hub confirmed the strong backflow by being rapidly dispersed and mixed throughout the primary zone. At the highest swirler flow rate of 35 percent, the dominance of this primary vortex system was reduced, and it was replaced by a flow pattern that included a forward velocity on the can centerline all the way through to the nozzle. This is illustrated most clearly by the dye picture in Fig. 4(*b*) and confirms that very different flow patterns could be created in the combustor over this range of conditions. At the highest swirler flow rate, it is clear that a filament of fluid exists in the vicinity of the centerline that hardly mixes with the surrounding fluid, a feature that should clearly be avoided in any combustor design. This filament is obviously related to the existence of a precessing vortex core on the can centerline. Such a feature has been observed previously (e.g., Rhode et al., 1983); the present flow seems to be slightly different, however, in that the vortex core appears without the flow first undergoing large-scale vortex breakdown, as was the case, for instance, in the measurements of Rhode et al. A recirculation region does exist in the primary zone under these conditions in the current measurements, but this seems more to come from the backflow of the primary jets impinging on the central vortex core. Apparently, the introduction of the possibility of interaction between swirler fluid and primary jet fluid influences the nature of the vortex breakdown considerably. The above descriptions will now be quantified using the measured velocity data; this is presented first in the form of radial profiles at three selected stations for each of the flow splits investigated. It is believed that this clarifies the individual features of the flow behavior at a given flow split, which then facilitates comparison between flow splits to convey the changing flow structure.

Figure 5 shows radial profiles of the axial (*a*), azimuthal (*b*), and radial (*c*) velocities and the corresponding intensities for the 10 percent case. It should be noted that the radial coordinate in this and all subsequent figures has been nondimensionalized using the inside diameter of the large containing tube ($D = 160$ mm) and the velocity used for nondimensionalization is the bulk velocity for the particular case under consideration; the velocity scale used in all figures is included on Fig. 5. At both stations *b* and *d*, the axial velocity profiles show a backflow region formed by the combined action of the primary jets and the swirl. The toroidal vortex is confined within the primary zone by the primary jets and was stable and symmetric about the centerline. In this region, the swirl levels are low compared to those found further downstream; the maximum W location changes position from the middle of the can radius at station *b* toward the centerline at station *d* as the inflowing jet fluid carries some swirling fluid toward the centerline. The dominance of the primary jets in the formation of the recirculation region is evident from the presence of strong inward V velocities over the whole diameter at station *d*, decreasing from a maximum in the jet inlet. Because of the double curvature of the hemispherical head and the associated beam refraction, it did not prove possible to make V velocity measurements at plane *b*. The shallower trajectory of the secondary jets may be identified in the axial velocity profile at station *m*. The presence of appreciable V velocities at off-centerline locations, even though this station is somewhat downstream of injection, confirms the lack of penetration. The double **S** shape of the profile in the axial component has been measured in previous studies of jets in crossflow (Khan et al., 1981). The two measured components of the turbulence intensities are of comparable magnitude at station *b*, while at station *d* the magnitudes of the $\overline{w^2}$ and $\overline{v^2}$ intensities are twice $\overline{u^2}$, implying strong anisotropy of the turbulence field in this region, as also found by Green and Whitelaw (1983), and this is related to the strong primary jet impingement (Koutmos and McGuirk, 1984). At station *m*, the off-centerline peaks of the turbulence levels are found in regions where lack of penetration of the secondary jets has caused large velocity gradients at off-centerline locations, implying considerable local shear generation of turbulence.

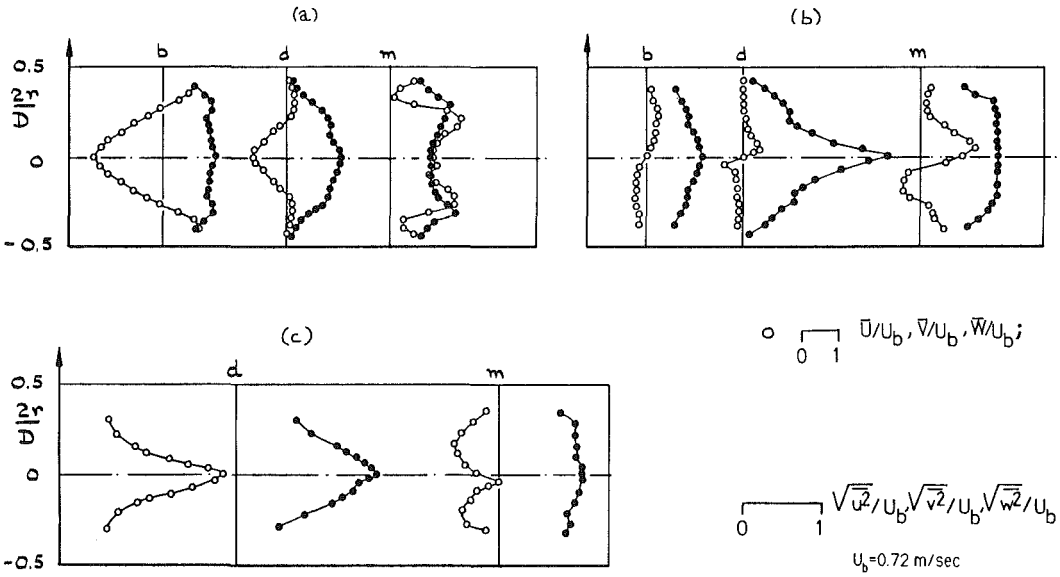

Fig. 5 Velocity field, 10 percent swirler flow: (*a*) axial, (*b*) azimuthal, (*c*) radial

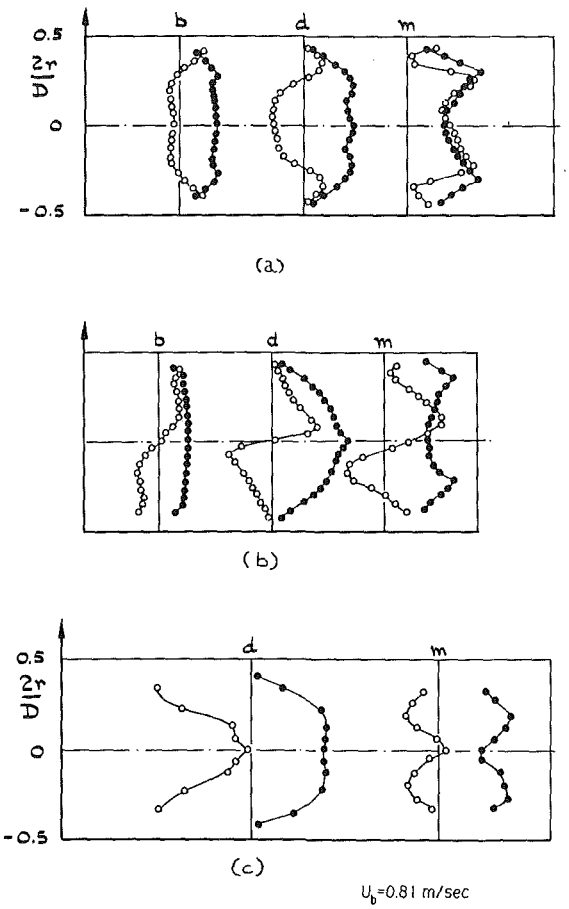

Fig. 6 Velocity field, 20 percent swirler flow: (*a*) axial, (*b*) azimuthal, (c) radial

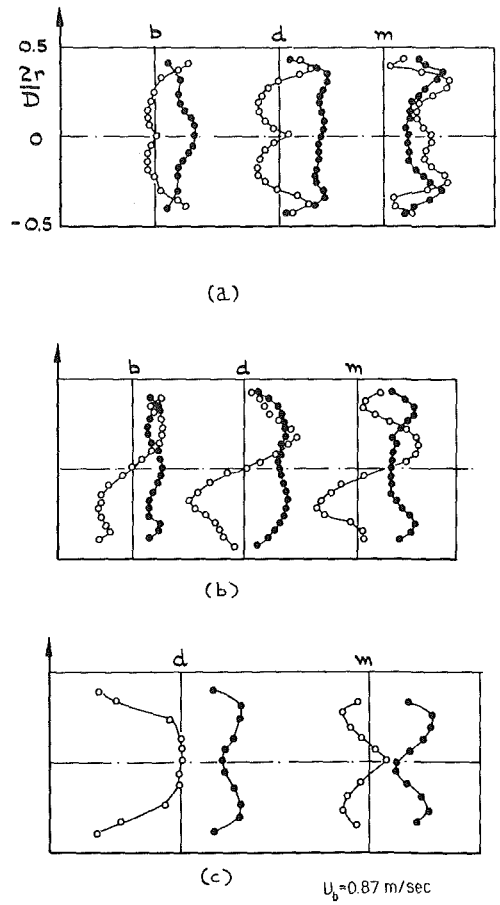

Fig. 7 Velocity field, 25 percent swirler flow: (*a*) axial, (*b*) azimuthal, (c) radial

Radial profiles of the three velocity components and their turbulence intensities for 20 percent swirler flow rate are shown in Fig. 6. Significant changes have started to appear as the flow split changes. The maximum negative axial velocity at station *b* occurs now near the middle of the radius, while on the centerline there is almost zero axial velocity. Similar profile shapes have been presented by Rhode et al. (1983). At station *d*, however, the magnitude of the negative axial velocity is comparable with that of the previous swirl level. If it is assumed that increasing the swirler flow rate tends to make the velocity positive on the centerline (this is confirmed in the measurements that follow), then this backflow arises because at this condition the jets are still just able to impinge upon each other. The swirl velocity has increased from the previous figure and at station *b* the maximum lies near the wall, while at station *d* it moves near the centerline, again due to the inflow effect of the primary jets. A less steep trajectory of the primary jets is evident from the presence of low V velocity fluid near the centerline at station *d*. $\overline{w^2}$ and $\overline{v^2}$ still have their maximum values near the centerline but are significantly lower than the previous case; this is consistent with the interpretation that the primary jets no longer impinge so dramatically. Profiles of all three components and their normal stresses at station *m* seem to have been very little affected by the changes in the primary region.

In Fig. 7, the flow development for the case of 25 percent swirler flow rate is shown. Although little change has incurred in the profile shape at station *b*, the axial velocity on the centerline of station *d* has now also become positive, confirming the trend identified above. The radial profiles of the V component clearly show the very mild trajectory of the primary jets, which do not meet on the centerline. Zero V velocity fluid fills the central core up to 30 percent of the radius and the solid body like nature of the rotation of this central core shows this clearly to be swirler fluid. The swirl velocity profile at station *b* still has its maximum near the wall,

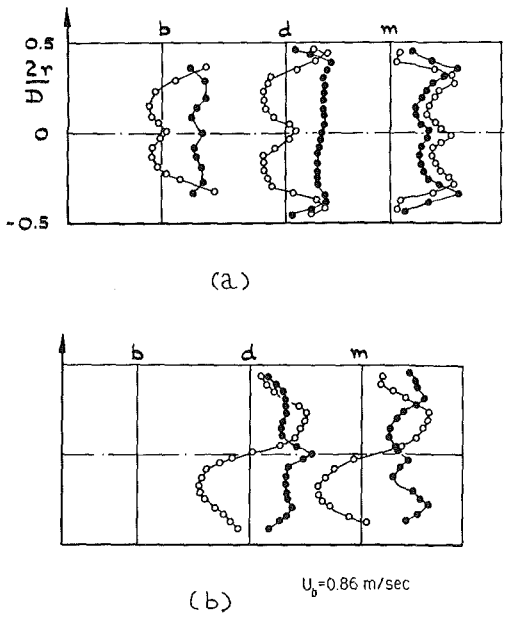

Fig. 8 Velocity field, 35 percent swirler flow: (*a*) axial, (*b*) azimuthal

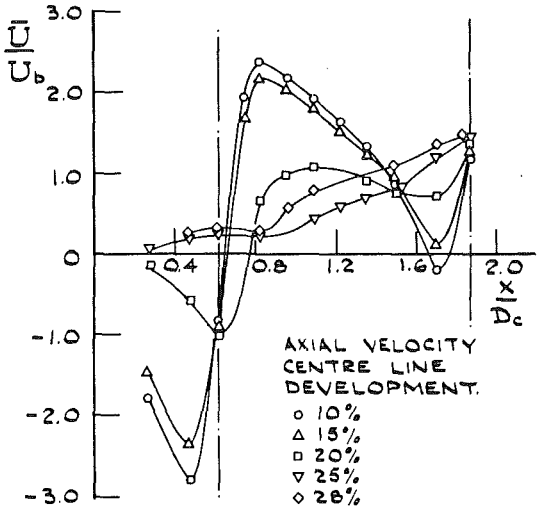

Fig. 9(*a*) Centerline axial velocity development, various swirler flow levels

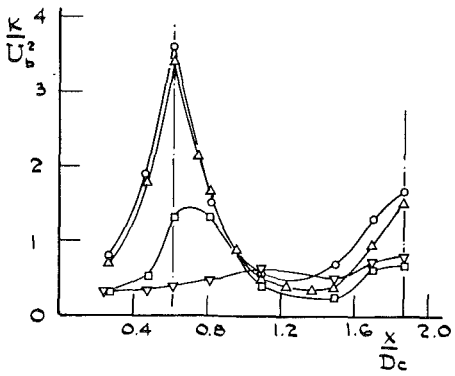

Fig. 9(*b*) Centerline turbulence kinetic energy development, various swirler flow levels

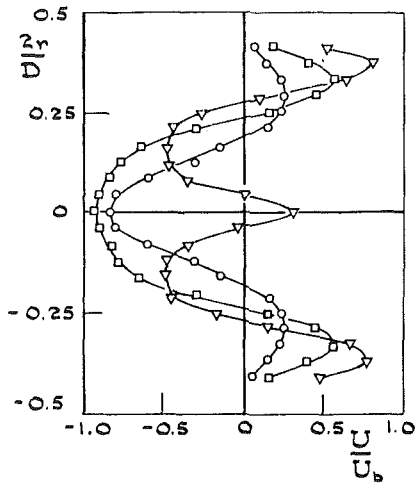

Fig. 10(*a*) Radial profiles of axial velocity at station *d* for three swirler flows

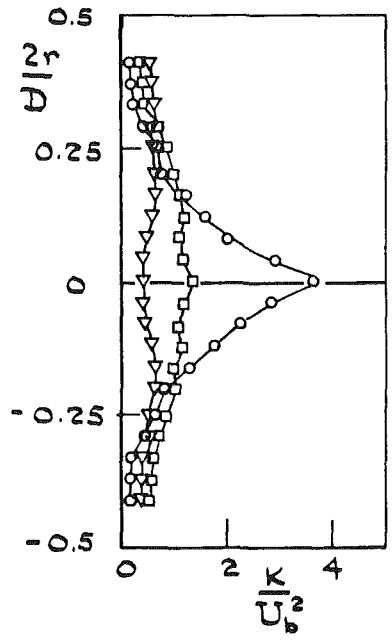

Fig. 10(*b*) Radial profiles of turbulence kinetic energy at station *d* for three swirler flows

while the transfer of the maximum toward the centerline is again evident at station *d* but not as strongly as in the previous figure. Levels of all three intensities are now of comparable magnitude in the primary region.

At 35 percent (Fig. 8), the negative axial velocities at station *b* have increased. Despite this, the positive axial velocity near the centerline has also increased; generally, however, the shape of the profile is similar to the 25 percent case. It is these forward velocities on the centerline that carry the filament of dye unbroken through to the downstream end, as described above and shown in Fig. 4(*b*). In order to obtain repeatability of the measurements in this position, a significantly larger integration time had to be used. The probable cause of this is that this central filament is precessing about the axis with a long time scale; due to this precession, a significant peak in $\overline{w^2}$ is found near the centerline, which grows in magnitude as swirl increases. Fewer measurements have been made at the 35 percent level since this considerably exceeds swirler flow levels likely to be found in practice.

Figures 9 and 10 show the flow development for a range of swirler flow rates; the former collects together the centerline development of axial velocity and turbulence energy and the latter enables comparison of profile shapes of U and k at the primary jet entry plane. The large toroidal vortex shows little change between 10 and 15 percent swirler flows. This is due to the fact that for both of these cases, the jets impinge strongly on the centerline, as evidenced by the high turbulence levels in this region. In the downstream dilution region, however, at 10 percent swirler flow, a small negative velocity appears due to the fact that the bulk flow acting as a crossflow does not have the necessary momentum to prevent the secondary jets impinging on each other. At 15 percent, the through flow is just able to prevent backflow. At 20 percent, the cross-flow fluid entering through the swirler has increased its momentum to the stage where it begins to influence primary jet impingement. The results indicate that these jets still do impinge, but no longer near their geometric axis but further downstream (the maximum and minimum axial velocity locations have shifted downstream). Despite this, the jets are still able to contribute to the primary recirculation region and maximum forward and backflow velocities are still about equal. The weaker impingement has a dramatic effect on the level of turbulence in the primary zone; see Fig. 10(*b*). At 25 percent, the trend is totally different; no negative velocities are measured on the centerline and the presence of a central core of forward flow mixing little with its surroundings has been established. The shape of the axial velocity profile at plane *d* has changed com-

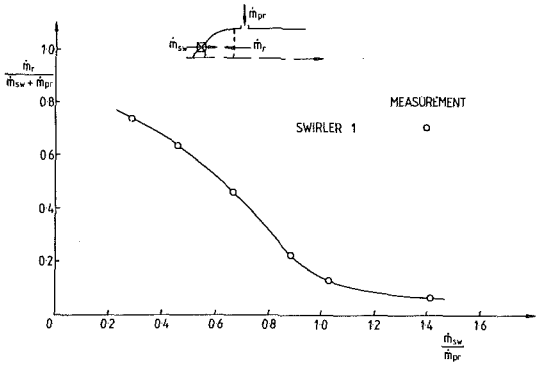

Fig. 11 Recirculation ratio versus primary zone flow split

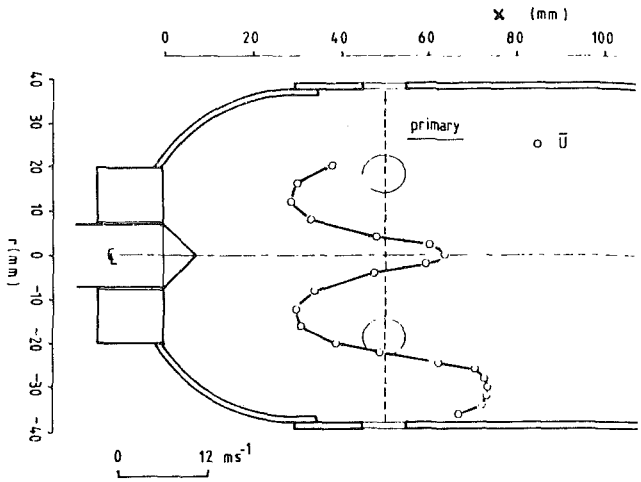

Fig. 12 Axial velocity profile on primary hole axis for a geometrically similar combustor operating under combusting conditions (Bicen and Jones, 1985)

pletely, as discussed earlier, and this flow structure in the primary zone now remains for all higher swirler flow rates investigated. The faster development of the centerline velocity at 28 percent is merely an enhancement of the volume of fluid belonging to the central processing core. As mentioned previously, the changes that occur in the primary zone are effectively swamped by the mixing of the dilution jets so that in all cases the centerline velocity measured at plane *m* is amazingly constant. The acceleration produced by the contraction will make the exit profiles even less aware of the primary zone conditions.

The large changes within the primary zone discussed above are expected to influence the primary zone recirculation, a parameter important in describing the performance of primary zone configurations (Lefebvre, 1983). The magnitude of this parameter for recirculation induced solely by an opposed jet system may be estimated from empirical formulae proposed by Way (1956), Rosenthal (1959), and Verduzio and Campanaro (1971). However, accurate information is lacking on recirculation ratios for primary zones that utilize a combination of swirler and opposed jets (Lefebvre, 1983). In the present investigation, this quantity has been determined by integration of the negative part of the axial velocity profile measured at plane *c* (see Fig. 3):

$$\dot{m}_r = \int_0^{r_{u=0}} \rho U dA$$

This station was chosen because of its proximity to the eye of the primary vortex (deduced from the flow visualization) so that the above integration yields a maximum estimate of the recirculating fluid within the vortex. Figure 11 shows the variation in the recirculation ratio $\dot{m}_r/(\dot{m}_{sw}+\dot{m}_{pr})$ with increase in the swirler mass flow ratio $\dot{m}_{sw}/\dot{m}_{pr}$ for the range of flow splits. The curve indicates an almost linear decrease with increasing $\dot{m}_{sw}/\dot{m}_{pr}$ in the region $0.2<\dot{m}_{sw}/\dot{m}_{pr}<1.0$. At low levels of swirler flow ($\dot{m}_{sw}/\dot{m}_{pr}\approx 0.3$), up to 74 percent of the total ($\dot{m}_{sw}+\dot{m}_{pr}$) participates in the toroidal vortex. Assuming that all of the swirler fluid in this case contributes to the recirculation, then the contribution of the primary jets amounts to about 64 percent. For this case (with jet trajectory near 90 deg), empirical formulae would yield a value of 50 percent (Rosenthal, 1959). Consequently, one can estimate that the extra 15 percent is due to the influence of the swirler. At higher swirler flow ratios ($\dot{m}_{sw}/\dot{m}_{pr}>1.0$), $\dot{m}_r/(\dot{m}_{sw}+\dot{m}_{pr})$ can be severely reduced to less than 10 percent.

The primary zone flow patterns discussed above have also been found by Bicen and Jones (1985) in their investigation of a geometrically similar chamber under combusting conditions. They provided LDA measurements of the axial and tangential mean velocities and turbulence intensities at planes through the ports. Their results with the combustor operating at flow splits similar to those of the 25 percent swirler flow level exhibited good qualitative and quantitative similarity with the results of the present work in the primary zone. This can be seen in Fig. 12 taken from Bicen and Jones (1985), which depicts the axial velocity distribution along the primary jet axis under combusting conditions with gaseous propane fuel and an air-fuel ratio of 70. It clearly shows that all qualitative features found in the similar profiles of the present study (see, for example, Fig. 7(*a*), plane *d*) are also identified under combusting conditions. It is likely then that the variations in the primary zone flow patterns observed here would influence combustor performance, since under reacting conditions parameters such as mean residence times, blowout velocity, and heat release rates are directly related to the mean flow velocity and recirculation ratio (Lefebvre, 1983).

Summary

1 The different flow patterns in the primary zone of a model combustor obtained through variation of the inlet swirler flow rate have been presented for 10, 20, 25, and 35 percent of the total mass flow rate passing through the combustor. The total flow rate through the combustor was varied at the same time in these tests, but this produces merely a change in the overall Reynolds number of the flow and this was always sufficiently high ($5\text{-}7\times10^4$) to lie in a Reynolds number independent flow regime (Bicen and Jones, 1985). The results have, therefore, been analyzed as being brought about by a variation of the flow split in the combustor between swirler, primary, and dilution hole entries.

2 The primary zone flow distribution was found to be strongly dependent on the flow split between swirler and primary ports. The increase in swirler/primary jet mass flow ratio weakened the primary zone vortex and resulted in a sharp reduction in the primary zone recirculation ratio. Highest turbulence levels were generated in the primary zone under conditions of strong impingement of the primary jets (for low swirl flows) and were three times the maximum levels found in the higher swirler flows. Although the changes in flow pattern were significant within the primary zone, they had a smaller effect on the profiles at the exit from the combustor.

3 As demonstrated above, the flow fields obtained in the present investigations are representative of the reacting flow in similar geometries, at least in the primary zone. Consequently, under combusting conditions, the observed primary zone flow variations would influence combustor performance by modifying the local air-fuel ratio. Although, in general, these

changes were not readily apparent in the dilution zone and exit flow patterns, it should be noted that certain features, such as emission of pollutants, are related to the history of the flow at exit from the primary zone (Lefebvre, 1983).

4 The apparently different nature of the precessing core at the higher swirler flow levels in these experiments to that previously reported in axisymmetric studies highlights the presence of a strong interaction in combustor systems between swirler and radial jet flows, and emphasizes the importance of retaining the complete flow system in further studies rather than the separate approach favored to date.

5 Since the flow splits used in this investigation are typical of those encountered in traditional and current combustor designs, and many features of the flow behavior obtained are similar to those observed in rig testing of full-scale production chambers, the flow patterns obtained in the water model are representative of the aerodynamic behavior of practical combustion systems. Nevertheless, the absolute levels of swirler/primary jet mass flow ratio at which the observed phenomena occur and the relative effect of the swirler flow rate on the flow pattern are also determined by the geometric configuration and may vary from one arrangement to the other. The comprehensive measurements presented here are perhaps most suitable as data against which the results of numerical calculation schemes may be tested. The ability to predict this isothermal flow accurately would represent a significant step in the appraisal of combustor prediction methods.

Acknowledgments

The work reported here has been supported by the Ministry of Defence. The authors would like to acknowledge their gratitude for this support and the many useful discussions with staff at RAE (Pyestock) and Rolls-Royce Limited. We would also like to thank Steve Bedley for his assistance in taking the photographs and Elizabeth Hall for typing the manuscript.

References

Altgeld, H., Jones, W. P., and Wilhelmi, J., 1983, "Velocity Measurements in a Confined Swirl Driven Recirculating Flow," *Exp. in Fluids*, Vol. 1, No. 2 pp. 73–78.

Bicen, A. F., and Jones, W. P., 1985, "Velocity Characteristics of Isothermal and Combusting Flows in a Can-Type Combustor," Imperial College, Mechanical Engineering Dept. Report FS/85/04.

Clarke, A. E., Gerrard, A. J., and Holliday, L. A., 1963, "Some Experiences in Gas Turbine Combustion Chamber Practice Using Water Flow Visualisation Techniques," *8th International Symposium on Combustion*, New York Press.

Durst, F., Melling, A., and Whitelaw, J. H., 1981, *Principles and Practice of Laser-Doppler Anemometry*, 2nd ed., Academic Press, New York.

Escudier, M. P., and Keller, J. J., 1985, "Recirculation in Swirling Flow: a Manifestation of Vortex Breakdown," *AIAA Journal*, Vol. 23, No. 1, p. 111.

Green, A. S., and Whitelaw, J. H., 1983, "Isothermal Models of Gas Turbine Combustors," *J. Fluid Mechanics*, Vol. 126, pp. 399–412.

Jones, W. P., and Toral, H., 1983, "Temperature and Composition Measurements in a Research Gas Turbine Combustion Chamber," *Combustion Science and Technology*, Vol. 31, pp. 249–275.

Khan, Z. A., McGuirk, J. J., and Whitelaw, J. H., 1981, "A Row of Jets in a Crossflow," AGARD CP 308, Paper No. 10.

Koutmos, P., and McGuirk, J. J., 1984, "Isothermal Measurements of the Internal Flow Field in a Water Model Can-Type Gas Turbine Combustor," Imperial College Mechanical Engineering Dept. Report FS/84/14.

Lefebvre, A. H., 1983, *Gas Turbine Combustion*, Hemisphere, Washington, DC.

Rhode, D. L., Lilley, D. G., and McLaughlin, D. K., 1983, "Mean Flow Fields in Axisymmetric Combustor Geometries With Swirl," *AIAA Journal*, Vol. 21, No. 4, pp. 593–600.

Rosenthal, J., 1959, "Exploring Methods for the Determination of Gas Flow and Temperature Pattern in Gas Turbine Combustors, ARL/HE Note 235, Aeronautical Research Laboratory, Australia.

Verduzio, L., and Campanaro, P., 1971, "The Air Recirculation Ratio in Can-Type Gas Turbine Combustion Chambers," *Proceedings of the International Propulsion Symposium*, Cranfield, United Kingdom.

Vu, B. T., and Gouldin, F. C., 1982, "Flow Measurements in a Model Swirl Combustor," *AIAA Journal*, Vol. 20, No. 5, pp. 642–651.

Way, S., 1956, "Combustion in the Turbojet Engine," *AGARD Combustion Colloquium*, Butterworth Press, London.

Fluid-Induced Rotordynamic Instability in Rotary Atomizers

J. Colding-Jorgensen
Department of Machine Elements,
The Technical University of Denmark,
DK-2800 Lyngby, Denmark

A theory is presented for the calculation of rotordynamic coefficients for the fluid-rotor interaction in rotary atomizers, based on calculation of the fluid flow through a whirling atomizer wheel. The theory predicts potentially unstable rotor whirl in high-speed rotary atomizers. The whirl frequency can be that of the first critical forward or the first critical backward precession of the rotor, depending on atomizer wheel geometry, speed, fluid properties, and flow rate. The predicted whirl phenomena have been produced in an atomizer test stand. Both forward and backward precession have been observed to become unstable. The observed whirl directions and amplitudes are consistent with the calculated coefficients. Some design parameters are identified that can help control and suppress the whirl.

Introduction

A rotary atomizer is a machine that very much resembles a centrifugal pump, running at high speed and very low flow rate. Liquid is pumped through a distributor, which it leaves through a circular ring gap, with a relatively low velocity. The distributor delivers the liquid into a wheel with radial or curved channels, very much like a centrifugal pump impeller. Once the liquid is caught in the channels, it is pressed against the channel wall by the Coriolis force, forming a thin film. The qualitative nature of this flow has been studied, using a wheel with transparent top plate and stroboscopic light, synchronized to the rotation of the wheel (Fig. 1). At the exit from the wheel, the liquid film meets the air around the wheel with high velocity and is split up into drops.

Atomizers are used for spray drying, in dry scrubbers and other processes.

Often, the rotary atomizer is designed for speeds well beyond the first critical, and it is common to use antifriction bearings. Therefore, the possibility of rotordynamic instability problems is present, and such problems have in fact occurred when new wheel designs have been tested, or when known designs have been used with different fluid properties, flow rates, and other flow-related parameters.

In the following, a calculation of the fluid forces on a whirling atomizer wheel is presented. A whirling motion of the wheel center with respect to the liquid distributor is imposed, resulting in an uneven distribution of liquid into different parts of the wheel, and the fluid force on the wheel is calculated as a function of position and velocity of the wheel center. The stiffness and damping coefficients required for the traditional rotordynamic analysis are found by differentiation of this fluid force function. The results are compared with whirl amplitudes and directions (forward and backward whirl) measured directly on the shaft of a rotary atomizer with variable water flow rate and different wheel geometries.

Contributed by the International Gas Turbine Institute and presented at the 33rd International Gas Turbine and Aeroengine Congress and Exhibition, Amsterdam, The Netherlands, June 5–9, 1988. Manuscript received by the International Gas Turbine Institute June 20, 1987. Paper No. 88-GT-200.

Background

It has been known for decades that internal rotor damping and hydrodynamic bearings can cause rotordynamic instability problems in high-speed rotors. In recent years, much work has been devoted to investigating similar problems caused by the seals in turbomachinery.

Finally, it has been discovered that the fluid forces in high performance turbomachinery can create self-exciting rotor whirl. For axial compressors and turbines, this has been shown theoretically by Alford (1965) and experimentally by Vance and Laudadio (1984). For radial pumps and compressors, the possibility of destabilizing forces created by impeller/volute interaction has been shown theoretically by Colding-Jorgensen (1980), and found experimentally by Chamieh et al. through a program at the California Institute of Technology (1982). An improved correlation between theoretical and experimental results has been obtained by Adkins (1986), through a more detailed calculation of the fluid flow from the impeller to the volute. An overview of the different instability mechanisms is given by Childs and Erich (1984).

So far, a similar analysis on a rotary atomizer has not been reported.

It is possible that the results obtained from the present analysis and experiments can have some relevance also for radial pumps and compressors, since it shows that fluid-induced unstable rotor whirl can occur in a machine with an impeller, even in the absence of a volute or diffuser.

Physical Model

The fluid is assumed to be Newtonian and incompressible. The fluid leaves the distributor and enters the wheel through a circular ring gap with constant width. It is assumed that the flow out of the distributor is uniform. When the wheel center is eccentric with respect to the distributor, the fluid will be distributed unevenly in the wheel.

Looking at Fig. 2, it is seen that the distance r_w from the wheel segment $d\theta_w$ ot the wheel center is given by the equation

$$r_d^2 = (e_x + r_w \cos \theta_w)^2 + (e_y + r_w \sin \theta_w)^2$$

Elimination of second-order contributions in e_x and e_y and

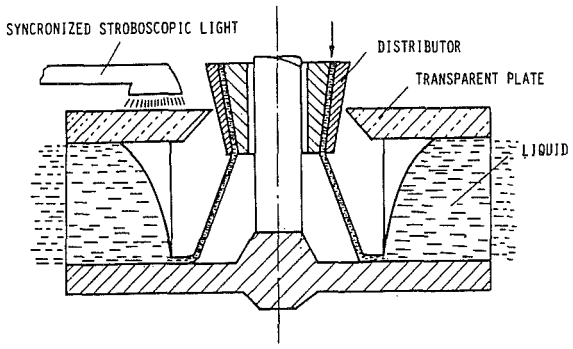

FIG. 1A

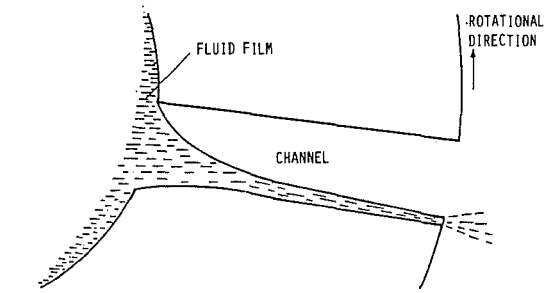

OBSERVED FILM FLOW IN CHANNEL

FIG. 1B

Fig. 1 Observed flow in atomizer wheel

a first-order Taylor expansion in e_x and e_y gives the linearized equation

$$\frac{r_w}{r_d} = 1 - \frac{e_x}{r_d}\cos\theta_w - \frac{e_y}{r_d}\sin\theta_w$$

Consequently, the liquid distributor outlet area delivering into the angular section $d\theta_w$ of the wheel is

$$dA = r_w(\theta_w) \cdot s \cdot d\theta_w$$

where s is the width of the distributor ring gap.

Since the flow from the distributor is uniform, the local flow rate delivered into the wheel angular section $d\theta_w$ must be

$$dV(\theta_w) = \frac{V}{2\pi r_d}\left(1 - \frac{e_x}{r_d}\cos\theta_w - \frac{e_y}{r_d}\sin\theta_w\right) \cdot d\theta_w \qquad (1)$$

It is assumed that the distribution given by equation (1.1) is valid also when the fluid enters the channels in the wheel.

In the channel, the liquid is assumed to have no velocity normal to the channel wall. A free film surface develops from the start (see Fig. 1*b*). From the wall, a boundary layer is assumed to grow. When the film surface meets the boundary layer, we have the fully developed film flow (Fig. 3).

Calculation of Flow in the Channels

The flow in the channels is calculated using an integral boundary layer formulation, where the pressure increase along the channel is assumed to be zero, since the atomizer delivers the fluid into a chamber with atmospheric pressure. ν is the coordinate along the channel wall; ξ is the coordinate perpendicular to the channel wall.

In a rotating coordinate system, the centrifugal force will act as a volume force on the fluid, and the conservation of momentum gives, for nearly parallel, stationary incompressible flow (Arpachi and Scheel Larsen, 1984)

$$\frac{d}{d\nu}\int_0^\delta u^2 d\xi - U\frac{d}{d\nu}\int_0^\delta d\xi = \delta\Omega^2 r\cos\lambda - \delta\frac{\tau_0}{\rho} \qquad (2)$$

Conservation of mass gives

$$\int_0^\delta u d\xi - U_1 \cdot w = 0 \qquad (3)$$

In the free stream, inviscid flow is assumed, and the Euler equation gives

Nomenclature

d = logarithmic decrement
$\mathbf{e} = \begin{pmatrix} e_x \\ e_y \end{pmatrix}$ = vectorial eccentricity of rotor center
$\dot{\mathbf{e}} = \begin{pmatrix} \dot{e}_x \\ \dot{e}_y \end{pmatrix}$ = whirl velocity vector
h = channel height
m = wheel mass
n = number of channels
r_2 = outlet radius
r_1 = inlet radius
s = liquid distributor gap width
r = radial position with respect to wheel center
r_d = liquid distributor ring gap mean radius
t = time
$\mathbf{u}$ = absolute vectorial fluid velocity in rotating, eccentric wheel
u_t = tangential component of $\mathbf{u}$
u_r = radial component of $\mathbf{u}$
u = fluid velocity in channel direction for centered wheel
$\bar{u}$ = mean fluid velocity in channel direction for centered wheel
u_{t2} = u_t at outlet
u_{r2} = mean radial velocity in film at outlet
u_{r20} = mean radial velocity in film at outlet for centered wheel
$u_{\max}$ = surface velocity
$u_{r2\max}$ = film surface radial velocity at outlet
dv = volume element
w = channel inlet width
$d\mathbf{A}$ = vector normal to C.S., pointing outward; length of $d\mathbf{A}$ is equal to surface area element dA
B = damping coefficient
$\underline{\underline{\mathbf{B}}} = \begin{Bmatrix} B_{xx} & B_{xy} \\ B_{yx} & B_{yy} \end{Bmatrix}$ = damping matrix
$\underline{\underline{\mathbf{K}}} = \begin{Bmatrix} K_{xx} & K_{xy} \\ B_{yx} & K_{yy} \end{Bmatrix}$ = stiffness matrix
$\mathbf{F} = \begin{pmatrix} F_x \\ F_y \end{pmatrix}$ = fluid force on wheel
U = free-stream velocity
U_1 = free-stream velocity at inlet
V_d = velocity of disturbance
V_{dr} = radial velocity of disturbance
V = volumetric flow
δ = film thickness
ϵ = boundary layer thickness
θ = angular position in (x, y) system
θ_w = angular position of fluid entering wheel
λ = angle between channel direction and radial direction
μ = viscosity
ν = coordinate in channel direction
ξ = coordinate normal to channel
ρ = density
τ_0 = shearing stress at the channel wall
ϕ = phase angle
ϕ_2 = phase angle at outlet
ω = whirl angular frequency
Ω = rotational angular frequency

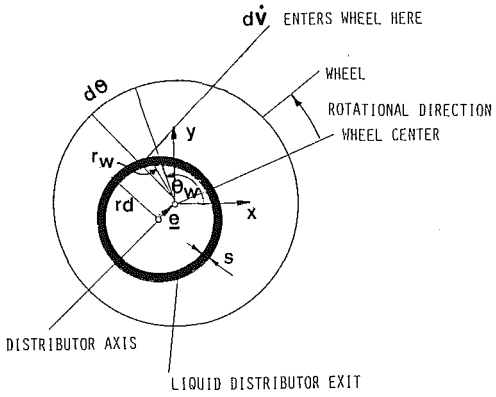

Fig. 2 Wheel—distributor configuration

$$U\frac{dU}{dv} = \Omega^2 \cdot r \cdot \cos\lambda$$

giving

$$U = \sqrt{U_1^2 + \Omega^2(r^2(r^2 - r_1^2)} \tag{3a}$$

For a laminar boundary layer

$$\tau_0 = \mu\left(\frac{\partial u}{\partial \xi}\right)_{\xi=0} \tag{4}$$

We assume a parabolic velocity profile

$$\frac{u}{U} = \begin{cases} 2\xi/\epsilon - (\xi/\epsilon)^2 & 0 \le \xi < \epsilon \\ 1 & \epsilon \le \xi \le \delta \end{cases} \tag{5}$$

Inserting equations (3*a*), (4), and (5) into equations (2) and (3), and rearranging, we get for the laminar boundary layer

$$\frac{d\epsilon}{dv} = -\frac{9}{2}\frac{\Omega^2 \cdot r \cdot \cos\lambda}{U_1^2 + \Omega^2(r^2 - r_1^2)}\epsilon + \frac{\mu}{\rho}\frac{15}{\sqrt{U_1^2 + \Omega^2(r^2 - r_1^2)}}\frac{1}{\epsilon} \tag{6}$$

and

$$\delta = \frac{1}{3}\epsilon + \frac{w}{\sqrt{1 + \dfrac{\Omega^2 \cdot r^2}{U_1^2}(1 - (r_1/r)^2)}} \tag{7}$$

For the turbulent boundary layer, we assumed

$$\tau_0 = \rho U^2 \cdot 0.0225\left(\frac{\mu/\rho}{U \cdot \epsilon}\right)^{1/4} \tag{8}$$

and a 1/7 order velocity profile (Schlicting, 1968)

$$\frac{u}{U} = \begin{cases} \left(\dfrac{\xi}{\epsilon}\right)^{1/7} & 0 \le \xi < \epsilon \\ 1 & \epsilon \le \xi \le \delta \end{cases} \tag{9}$$

Inserting equations (8) and (9) into equations (2) and (3), we get for the turbulent boundary layer

$$\frac{d\epsilon}{dv} = -3.29\frac{\Omega^2 \cdot \cos\lambda}{(U_1^2 + \Omega^2(r^2 - r_1^2))}\epsilon + 0.23\left(\frac{\mu/\rho}{\sqrt{U_1^2 + \Omega^2 - r_1^2)}} \cdot \frac{1}{\epsilon}\right)^{1/4} \tag{10}$$

and

$$\delta = \frac{1}{8}\epsilon + \frac{w}{\sqrt{1 + \dfrac{\Omega^2 \cdot r^2}{U_1^2}(1 - (r_1/r)^2)}} \tag{11}$$

The tangential velocity is assumed to be constant across the film: $u_t = \Omega r + \sin\lambda \cdot V/(nh\delta)$.

Following Fulford (1964) the transition from laminar to turbulent flow is assumed to take place when $R_{e_\epsilon} u \cdot \epsilon \cdot \rho/\mu = 400$.

When $\delta = \epsilon$, we have the fully developed film. In this region, the shear forces must equal the centrifugal force, giving

$$\delta\Omega^2 \cdot r\cos\lambda = \frac{\mu}{\rho}\left(\frac{\partial u}{\partial \xi}\right)_{\xi=0} \quad \text{(laminar)}$$

$$\delta\Omega^2 \cdot r\cos\lambda = u_{\max}^2 \cdot 0.0225\left(\frac{\mu/\rho}{u_{\max} \cdot \epsilon}\right)^{1/4} \quad \text{(turbulent)} \tag{12}$$

Then, using the same velocity distributions as in the boundary layer, we get for the laminar case

$$\delta^3 = \frac{3V\mu}{\rho nh\Omega^2 r\cos\lambda} \tag{13}$$

and for the turbulent film

$$\delta^3 = 0.028\left(\frac{\mu \cdot V^7}{\rho \cdot n^7 \cdot h^7 \cdot \Omega^8 \cdot r^4}\right)^{1/4} \cdot \frac{1}{\cos\lambda} \tag{14}$$

Once the flow is determined, the mean velocity and maximum velocity in the film are given by the velocity distributions (5) and (9).

Calculation of Fluid Force and Rotordynamic Coefficient

The force from the fluid on the wheel is given by

$$\mathbf{F} = -\left(\frac{\partial}{\partial t}\int_{\text{C.V.}} \mathbf{u}\rho dv + \int_{\text{C.S.}} \mathbf{u}\rho u d\mathbf{A}\right) \tag{15}$$

where C.V. is a stationary control volume that at the given time contains the fluid, from the inlet to the outlet channels. C.S. is the surface of C.V. We disregard the forces in the inner part of the wheel, since these are probably very small compared to those in the channels.

Following the calculations in Appendix A, we get

$$\mathbf{F} = \frac{\rho \cdot V}{r_d}\left[\left(\frac{17}{24}u_{r20} \cdot \sin\phi_2 - \tfrac{1}{2}u_{t2} \cdot \cos\phi_2\right)\begin{pmatrix} -e_y \\ e_x \end{pmatrix} + \left(\frac{17}{24}u_{r20} \cdot \cos\phi_2 - \tfrac{1}{2}u_{t2}\sin\phi_2\right)\begin{pmatrix} e_x \\ e_y \end{pmatrix} + \tfrac{1}{2}\int_{r_1}^{r_2}\cos\phi dr \cdot \begin{pmatrix} \dot{e}_x \\ \dot{e}_y \end{pmatrix} + \tfrac{1}{2}\int_{r_1}^{r_2}\sin\phi dr\begin{pmatrix} -\dot{e}_x \\ \dot{e}_y \end{pmatrix}\right] \tag{16}$$

The phase angle

$$\phi_2 = \int_{r_1}^{r_2}\left(\frac{u_t}{r} - \omega\right)\frac{1}{V_{dr}}dr$$

is given by the path followed by a disturbance in the flow rate (see Appendix A).

The rotordynamic coefficients are defined by

$$K_{xx} = -\frac{\partial}{\partial e_x}(F_x)$$

$$K_{yy} = -\frac{\partial}{\partial e_y}(F_y)$$

$$K_{xy} = -\frac{\partial}{\partial e_y}(F_x)$$

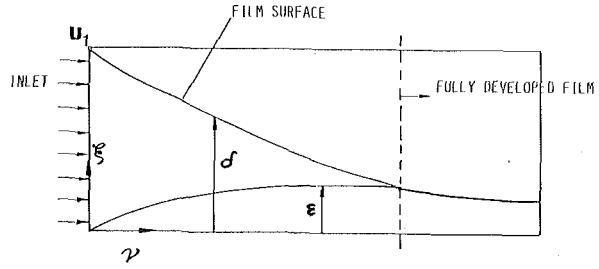

Fig. 3 Film flow in rotating channel

$$K_{yx} = -\frac{\partial}{\partial e_x}(F_y)$$

$$B_{xx} = -\frac{\partial}{\partial e_x}(F_x)$$

$$B_{yy} = -\frac{\partial}{\partial e_y}(F_y)$$

$$B_{xy} = -\frac{\partial}{\partial e_y}(F_x)$$

$$B_{yx} = -\frac{\partial}{\partial e_x}(F_y)$$

Consequently

$$K_{xx} = K_{yy} = \frac{-\rho \cdot V}{r_d}\left(\frac{17}{24}u_{r20}\cos\phi_2 - \frac{1}{2}u_{t2}\sin\phi_2\right)$$

$$K_{xy} = -K_{yx} = \frac{\rho \cdot V}{r_d}\left(\frac{17}{24}u_{r20}\sin\phi_2 + \frac{1}{2}u_{t2}\cos\phi_2\right)$$

$$B_{xx} = B_{yy} = \frac{-\rho \cdot V}{2r_d}\int_{r_1}^{r_2}\cos\phi dr \qquad (17)$$

$$B_{yx} = -B_{xy} = \frac{\rho \cdot V}{2r_d}\int_{r_1}^{r_2}\sin\phi dr$$

In the rotordynamic analysis, these coefficients will add to the stiffness and damping matrices of the rotor system, along with terms from the shaft sections and bearings. The cross-coupling stiffness term $K_{xy} = -K_{yx}$ will have a destabilizing effect on the rotor. The direct damping term $B_{xx} = B_{yy}$ will, when negative, have a destabilizing effect on the same order of magnitude as a cross-coupling stiffness of $\omega \cdot B_{xx}$.

Evaluating the expressions for K_{xy} and B_{xx} in equation (17), it is seen that the order of magnitude of the destabilizing effect of B_{xx} is

$$\omega B_{xx} \sim \frac{\omega}{\Omega}K_{xy}$$

In this particular study, the whirl frequency is approximately one tenth of the rotational frequency, so the influence of the direct damping terms is one order of magnitude less than that of the cross-coupling stiffness.

Therefore, in this case, the destabilizing influence of the fluid force can be evaluated, simply by looking at the value of K_{xy}. When K_{xy} is positive, it will destabilize forward whirl. When negative, it will destabilize backward whirl.

Numerical Procedure

1 First, the flow through the channels of a centered, rotating wheel is calculated. At the inlet, the velocity in the direction of the channel is

$$U_1 = \frac{V\cos\lambda}{wnh}$$

2 After the first small step, $\Delta\nu$, along the channel wall, the boundary layer thickness is found from equation (6). By approximation, we get for small $\Delta\nu$ and ϵ

$$\epsilon = \sqrt{30\frac{\mu}{\rho}\frac{\Delta\nu}{U_1}}$$

The film thickness and mean velocity in the boundary layer are calculated, using equations (5) and (7).

3 The film thickness, boundary layer thickness, and mean velocity are calculated stepwise along the channel, solving equations (6) or (10), depending on whether the flow is laminar or turbulent. The transition from laminar to turbulent flow is assumed to occur when $Re_\epsilon = u \cdot \epsilon \cdot \rho/\mu$ exceeds 400, following Fulford (1964). The numerical method used is a simple pre-

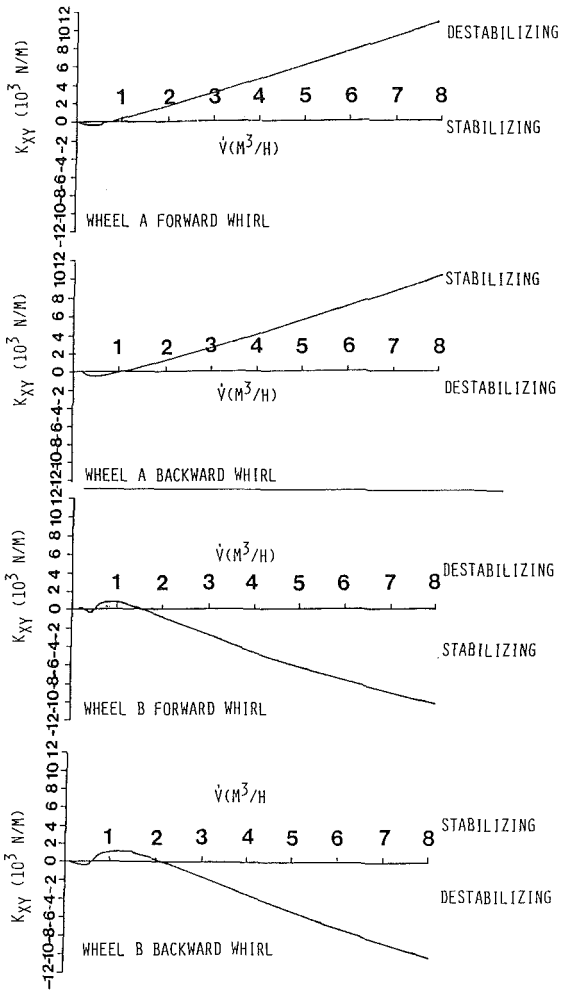

Fig. 4 Calculated cross-coupling stiffness coefficients

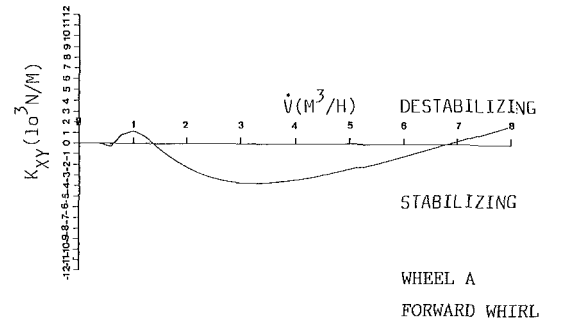

Fig. 5 Calculated cross-coupling stiffness for high-viscosity fluid

dictor-corrector method (the trapezoidal method) with variable steplength based on an error estimate (Lambert, 1977).

4 After a number of steps, the boundary layer meets the free surface, and the fully developed film flow is calculated according to equation (13) or (14), depending on whether the flow is laminar or turbulent at this point.

5 The phase function ϕ_2 is now calculated, using the data obtained in the previous steps. The velocity of a disturbance in the flow rate is assumed to propagate with the speed $V_d = (1 + \epsilon/\delta) \cdot u$, where u is the mean velocity in the boundary layer of the fully developed film (see Appendix A).

6 The cross-coupling term K_{xy} is calculated from the data obtained in the previous steps.

Calculation Results

Calculations were carried out on two wheels, one with straight radial channels (wheel A), and one with forward-curved channels (wheel B). Both wheels had a diameter of 210 mm. Calculations were made for $\Omega = 1900$ rad/s and flow rates between 0 and 8 m³/h (water). Since the whirl frequency ω affects the calculated cross-coupling terms, calculations of K_{xy} were made separately for the two types of whirl. The whirl frequencies used in the calculations are the observed frequencies for forward and backward whirl of the two wheels.

Figure 4 shows the calculated stiffness cross-coupling terms K_{xy}, with the stability effect indicated for each type of whirl. An example is also shown with a viscosity 100 times that of water (see Fig. 5).

It is seen that for the water calculations at higher flow rates, the straight channel wheel should whirl in the forward direction, and the wheel with forward-curved channels should whirl in the backward direction, according to the theory. The destabilizing force generally increases with flow rate.

For intermediate flow rates, changes in the sign of K_{xy} are seen, which indicate that the same wheel could show different whirls, depending on the flow rate, even with water.

With the high viscosity, several changes in sign are seen, indicating a very variable behavior, depending on the flow rate.

Stability Considerations

In order to evaluate the order of magnitude of the calculated cross-coupling coefficient, an estimate of the damping in the rotor is necessary.

By a simple impact test on the rotor standing still in its bearings, a logarithmic decrement of the first critical of $d = 0.07$ was found. The first rotor natural frequency at no rotation was found to be 123 rad/s.

Looking at a simple one-degree-of-freedom model of the rotor, this is equivalent to a damping coefficient of

$$B = \frac{d \cdot m \cdot |\omega|}{\pi}$$

if we assume all the damping to be external. In this simplified model, the calculated cross-coupling term K_{xy} is equivalent to a negative damping term $|K_{xy}/\omega|$. So in order to create unstable whirl, the cross-coupling term must be

$$|K_{xy}| > B \cdot |\omega|$$

The mass of wheel B is 12.8 kg, so $B = (0.07 \cdot 12.8 \text{ kg} \cdot 123 \text{ rad/s})/\pi = 35$ Ns/m.

The observed whirl frequencies are:

Wheel A: 217 rad/s for forward whirl and 116 rad/s for backward whirl.

Wheel B: 167 rad/s for forward whirl and 78.5 rad/s for backward whirl.

Consequently, the cross-coupling stiffness necessary to create unstable whirl is:

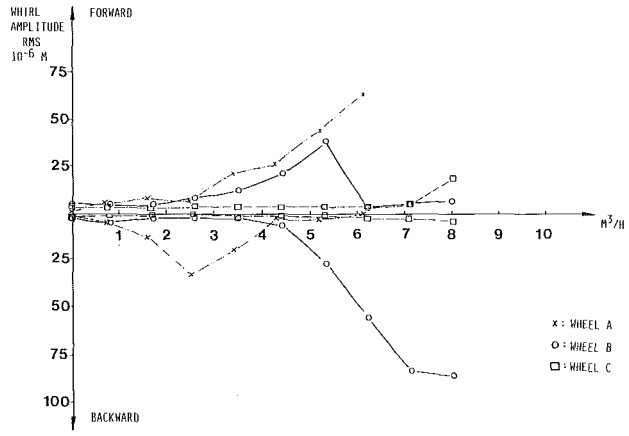

Fig. 6 Measured whirl amplitude

Wheel A

Forward whirl: $K_{xy} > 35$ Ns/m • 217 rad/s = 7595 N/m

Backward whirl: $K_{xy} < -35$ Ns/m • 116 rad/s = −4060 N/m

Wheel B

Forward whirl: $K_{xy} > 35$ Ns/m • 167 rad/s = 5845 N/m

Backward whirl: $K_{xy} < -35$ Ns/m • 78.5 rad/s = −2748 N/m

Looking at Fig. 4, it is seen that the calculated cross-coupling terms should be large enough to create unstable forward whirl for wheel A for a flow rate higher than 5.5 m³/h and unstable backward whirl for wheel B for flow rates higher than 5 m³/h.

Even at lower flow rates, moderate whirl amplitudes should be expected, since the rotor is subject to random excitation while running with fluid. The forward component of this whirl will be amplified when K_{xy} is positive, and the backward component will be amplified when K_{xy} is negative, even when the stability limit is not exceeded.

Whirl Measurements

Measurements were made on an atomizer with a vertical, overhung shaft in rolling element bearings, running at 1900 rad/s, which is roughly 10 times the first critical speed and well below the second critical.

Two proximity probes were used, measuring radial displacement of the shaft relative to the casing at approximately right angles. The probes were placed between the lower bearing and the wheel.

The signals were displayed on an X-Y oscilloscope and a two-channel FFT analyzer, allowing frequency spectra of the individual channel and the cross spectrum to be produced, displayed, and stored digitally. Direction of the whirl was determined, using the phase cross spectrum. The phase of the forward whirl component has the same sign as the synchronous component in the spectrum, and the phase of the backward component has the opposite sign.

Also, the forward whirl has a higher frequency, and the backward whirl a lower frequency, than the first rotor resonance at no rotation, due to the gyroscopic moment (Den Hartog, 1956).

Measurements were made with water pumped through the liquid distributor at flow rates up to 8 m³/h, requiring a power of 100 kW. Normally, this type of atomizer is used up to 4 m³/h or 55 kW.

The measurements were made on wheels with the same geometries as used in the calculations, and on a wheel with the same geometry as wheel B, except for a shape of the inlet to the channels, which has been observed to create extensive backflow from the inlet to the inner wheel (wheel C). The results are shown in Fig. 6.

Comparison of Measurements and Calculations

1 With wheel A, the measured whirl shows high amplitudes in forward direction for flow rates higher than 5 m^3/h. The amplitudes increase as the flow rate is increased. This is exactly what should be expected according to the theory, which predicts unstable whirl in forward direction for flow rates higher than 5.5 m^3/h, with destabilizing force increasing with flow rate.

Wheel B should exhibit unstable whirl in the backward direction, according to the theory. Very high backward whirl amplitudes are in fact measured, at flowrates higher than 5 m^3/h. The backward whirl amplitude increases as the flow rate increases further, as predicted by the theory.

Generally, it is concluded that the agreement between theory and measurements is very good for high flow rates.

2 For intermediate flow rates, moderate whirl amplitudes in the opposite direction are seen, as predicted by the theory, that is, backward whirl for wheel A and forward whirl for wheel B.

The dependency of whirl on flow rate is, however, not exactly as calculated. The change in whirl direction takes place at a higher flow rate than predicted.

3 Measurements on wheel C with the high inlet backflow show almost complete disappearence of the whirl, indicating that the mechanism behind the destabilization can be broken by building up a sufficiently large liquid buffer zone in the inner part of the wheel. This would act to weaken the direct coupling between instant liquid distribution between the channels and instant position of the rotor centre, given by equation (1).

Conclusion

For high flow rates, the agreement between theory and measurements is very good, for both wheels A and B. For intermediate flow rates, the agreement is only qualitatively correct. This is due to changes in the phase function ϕ_2, and this is especially the case for wheels with curved channels, where the traveling time of a disturbance from inlet to outlet of the channel is longer than in a straight channel wheel.

Therefore, a more accurate prediction of the whirl behavior at intermediate and low flow rates, expecially for wheels with curved channels, should probably be based on a better calculation of the velocity of disturbances propagating in the channels. This would have to include the effect of the air flow in the wheel, since an adjoining air stream will affect the velocity of waves on the film significantly (Fulford, 1964).

Further experimental work should include the effect of viscosity and other fluid properties.

The measurements on wheel C show that the shape of the inlet to the channels is decisive for suppressing the instability. A model of the flow in the inner part of the wheel, including backflow from the channel inlet, is necessary to predict the effect of different inlet geometries on the destabilizing force.

Acknowledgments

The experimental part of this work was carried out using the test facilities of Niro Atomizer A/S.

References

Adkins, D. R., 1986, "Analyses of Hydrodynamic Forces on Centrifugal Pump Impellers," Report on NASA Contract NAS 8-33108, California Institute of Technology.

Alford, J., 1965, "Protecting Turbomachinery From Self-Excited Rotor Whirl," ASME JOURNAL OF ENGINEERING FOR POWER, Vol. 87, pp. 333–334.

Arpachi, V. D., and Scheel Larsen, P., 1984, Vol. 87, *Convection and Heat Transfer*, Prentice-Hall, Chap. 8.

Chamieh, D. S., Acosta, A. J., Brennen, C. E., Caughey, T. K., and Franz, R., 1982, "Experimental Measurements of Hydrodynamic Stiffness Matrices for a Centrifugal Pump Impeller," NASA CP 2250, proceedings of a workshop held at Texas A&M University, pp. 382–398.

Colding-Jorgensen, J., 1980, "Effect of Fluid Forces on Rotor Stability of Centrifugal Compressors and Pumps," NASA CP 2133, proceedings of a workshop held at Texas A&M University, May 12–14, pp. 249–265.

Den Hartog, J. P., 1956, *Mechanical Vibrations*, McGraw-Hill, pp. 253–265.

Erich, F., and Childs, D., 1984, "Self-Excited Vibration in High-Performance Turbomachinery," *Mechanical Engineering*, May.

Fulford, G. D., 1964, "The Flow of Liquids in Thin Films," *Advances in Chemical Engineering*, Vol. 5, Academic Press.

Lambert, J. D., 1977, *Computational Methods in Ordinary Differential Equations*, Wiley, pp. 85–114.

Schlichting, H., 1968, *Boundary Layer Theory*, McGraw-Hill, pp. 596–601.

Vance, J. M., and Laudadio, F. J., 1984, "Experimental Measurement of Alfords Force in Axial Flow Turbomachinery," ASME JOURNAL OF ENGINEERING FOR GAS TURBINES AND POWER, Vol. 106, July, pp. 585–590.

APPENDIX A

Calculations of Fluid Force

For simplicity, the integrals in equation (15) are calculated as if the channels were distributed continuously over the circumference of the wheel with a "channel density" of $n/2\pi$. Also, when the wheel is whirling, it is assumed that only the whirl velocity component normal to the channel will add to the fluid velocity. The tangential component of $\mathbf{u}$ is assumed to be constant in θ.

Then:

$$\frac{\partial}{\partial t}\int_{CV}\rho\mathbf{u}dv = \rho\frac{\partial}{\partial t}\int_{r_1}^{r_2}\int_0^{2\pi}\frac{dV}{d\theta}\begin{pmatrix}\cos\theta\\ \sin\theta\end{pmatrix}d\theta dr \qquad \text{(A1)}$$

Using $\dfrac{dV}{d\theta} = h\dfrac{n}{2\pi}\displaystyle\int_0^{\delta} u_r\, d\xi/\cos\lambda.$

The disturbances in the volume flow at the inlet will propagate with a speed V_{dr} in radial direction, so the volume flow distribution $dV/d\theta$ (r, θ) is given by

$$\frac{\mathrm{dV}}{\mathrm{d}\theta}(\mathrm{r},\theta) = \frac{\mathrm{dV}}{\mathrm{d}\theta_w}(\theta_w - \phi)$$

where

$$\phi = \int_{r_1}^{r}\left(\frac{u_t}{r^*} - \omega\right)\cdot\frac{1}{V_{dr}}\cdot\frac{1}{V_{dr}}\,\mathrm{dr}^*$$

Inserting this and the volume flow distribution at the inlet, given by equation (1) into equation (A1) gives, after integration and reduction

$$\frac{\partial}{\partial t}\int_{CV}\rho\mathbf{u}dv = \frac{-\rho\dot{V}}{2r_d}\begin{Bmatrix}\displaystyle\int_{r_1}^{r_2}\cos\phi dr\cdot\dot{e}_x - \int_{r_1}^{r_2}\sin\phi dr\cdot\dot{e}_y\\ \displaystyle\int_{r_1}^{r_2}\sin\phi dr\cdot\dot{e}_x + \int_{r_1}^{r_2}\cos\phi dr\cdot\dot{e}_y\end{Bmatrix} \qquad \text{(A2)}$$

In the calculations of the surface integral in equation (15), it is assumed that the momentum transport into the channel inlet is negligible, since the fluid velocity in the distributor is much smaller than in the channels. Then the integral becomes

$$\int_{CS}\mathbf{u}\rho\mathbf{u}d\mathbf{A} = h\rho\int_0^{2\pi}\frac{n}{2\pi}\int_0^{\delta}\left(u_{r_2}\begin{pmatrix}\cos\theta\\ \sin\theta\end{pmatrix} + u_{t_2}\begin{pmatrix}-\sin\theta\\ \cos\theta\end{pmatrix}\right.$$

$$\left. + \begin{pmatrix}\dot{e}_x\cdot\cos^2(\theta+90\text{ deg}-\lambda)\\ \dot{e}_y\cdot\sin^2(\theta+90\text{ deg}-\lambda)\end{pmatrix}\right)\cdot\Big(u_{r_2} + \dot{e}_x\cos(\theta$$

$$+90\text{ deg}-\lambda)\cos\theta + \dot{e}_y\sin(\theta+90\text{ deg}$$

$$-\lambda)\sin\theta\Big)\frac{d\xi d\theta}{\cos\lambda}$$

Second-order contributions in **e** and **e** are neglected, and u_t is assumed to be constant in θ. Then the integral can be reduced to

$$\int_{CS} \mathbf{u}\rho\mathbf{u}d\mathbf{A} = \rho \cdot \int_0^{2\pi} h \frac{n}{2\pi} \int_0^{\delta} u_{r2}^2 \begin{pmatrix} \cos\theta \\ \sin\theta \end{pmatrix} + u_{t2}u_{r2} \begin{pmatrix} -\sin\theta \\ \cos\theta \end{pmatrix} \frac{d\xi d\theta}{\cos\lambda} \tag{A3}$$

At the outlet, the flow will be a fully developed film for the flow rates considered here, and turbulent, even for extremely small flow rates, so we use the velocity distribution (9) to obtain

$$\int_0^{\delta} u_{r2}^2 \frac{d\xi}{\cos\lambda} = \int_0^{\delta} u_{r2\max}^2 \left(\frac{\xi}{\delta}\right)^{2/7} \frac{d\xi}{\cos\lambda} = \frac{7}{9} u_{r2\max}^2 \cdot \frac{\delta}{\cos\lambda}$$

$$= \frac{\delta}{\cos\lambda} = \frac{7}{9} \cdot \left(\frac{8}{7}\right)^2 u_{r2}^2 \cdot \frac{\delta}{\cos\lambda} \simeq u_{r2}^2 \cdot \frac{\delta}{\cos\lambda}$$

$$= u_{r2} \cdot \frac{dV}{d\theta} \cdot \frac{2\pi}{nh}$$

Looking at the turbulent film as calculated by equation (14), it can be shown that the mean radial velocity is proportional to $V5/12$.

Consequently, using equation (1), u_{r2} can be written

$$u_{r2} = u_{r20} \left(1 - \frac{e_x}{r_d} \cos(\theta - \phi_2) - \frac{e_y}{r_d} \sin(\theta - \phi)\right)^{5/12}$$

and

$$u_{r2} \simeq u_{r20} - u_{r20} \cdot \frac{5}{12} \left(\frac{e_x}{r_d} \cos(\theta - \phi_2) + \frac{e_y}{r_d} \sin(\theta - \phi_2)\right)$$

Using these results, and the same procedure as with the volume integral, the result becomes

$$\int_{CS} \mathbf{u}\rho\mathbf{u}d\mathbf{A} = -\frac{17}{24} \cdot \frac{\rho \cdot V}{r_d} \cdot \mathbf{u}_{r20} \begin{pmatrix} e_x \cos\phi_2 - e_y \sin\phi_2 \\ e_y \cos\phi_2 + e_x \sin\phi_2 \end{pmatrix} - \frac{1}{2} \cdot \frac{\rho \cdot V \cdot u_{t2}}{r_d} \begin{pmatrix} -e_x \sin\phi_2 - e_y \cos\phi_2 \\ -e_y \sin\phi_2 + e_x \cos\phi_2 \end{pmatrix} \tag{A4}$$

In order to calculate the phase function ϕ, it is necessary to estimate the speed V_{dr} with which disturbances propagate in the radial direction.

Following Fulford (1964), the velocity of small disturbances in the flow in a laminar film will propagate along the film surface with a velocity of $3 \cdot u$, where u is the mean velocity in the film.

However, most of the experimental work reviewed by Fulford (1964) indicates a somewhat lower velocity, dependent on the Reynolds number, both for laminar and turbulent films. In this study, a value of $2 \cdot u$ will be used in the fully developed film.

In a free stream with a free surface, it is reasonable to assume that the disturbances will propagate with the free-stream velocity.

Therefore, in the inlet, a mean disturbance velocity of $V_{dr} = u_r(1 + \epsilon/\rho)$ is assumed.

Calculations of the destabilizing force have been carried out with an assumed disturbance velocity in the fully developed film from one to three times the mean film velocity.

The influence of this parameter is very small for high flow rates of water, but considerable for low flow rates or with high-viscosity fluids.

Second-order contributions in **e** and **e** are neglected, and u_t is assumed to be constant in θ. Then the integral can be reduced to

$$\int_{CS} \mathbf{u}\rho\mathbf{u}d\mathbf{A} = \rho \cdot \int_0^{2\pi} h \frac{n}{2\pi} \int_0^{\delta} u_{r2}^2 \begin{pmatrix} \cos\theta \\ \sin\theta \end{pmatrix} + u_{t2}u_{r2} \begin{pmatrix} -\sin\theta \\ \cos\theta \end{pmatrix} \frac{d\xi d\theta}{\cos\lambda} \quad \text{(A3)}$$

At the outlet, the flow will be a fully developed film for the flow rates considered here, and turbulent, even for extremely small flow rates, so we use the velocity distribution (9) to obtain

$$\int_0^{\delta} u_{r2}^2 \frac{d\xi}{\cos\lambda} = \int_0^{\delta} u_{r2\max}^2 \left(\frac{\xi}{\delta}\right)^{2/7} \frac{d\xi}{\cos\lambda} = \frac{7}{9} u_{r2\max}^2 \cdot \frac{\delta}{\cos\lambda}$$

$$= \frac{\delta}{\cos\lambda} = \frac{7}{9} \cdot \left(\frac{8}{7}\right)^2 u_{r2}^2 \cdot \frac{\delta}{\cos\lambda} \simeq u_{r2}^2 \cdot \frac{\delta}{\cos\lambda}$$

$$= u_{r2} \cdot \frac{dV}{d\theta} \cdot \frac{2\pi}{nh}$$

Looking at the turbulent film as calculated by equation (14), it can be shown that the mean radial velocity is proportional to $V5/12$.

Consequently, using equation (1), u_{r2} can be written

$$u_{r2} = u_{r20} \left(1 - \frac{e_x}{r_d} \cos(\theta - \phi_2) - \frac{e_y}{r_d} \sin(\theta - \phi)\right)^{5/12}$$

and

$$u_{r2} \simeq u_{r20} - u_{r20} \cdot \frac{5}{12} \left(\frac{e_x}{r_d} \cos(\theta - \phi_2) + \frac{e_y}{r_d} \sin(\theta - \phi_2)\right)$$

Using these results, and the same procedure as with the volume integral, the result becomes

$$\int_{CS} \mathbf{u}\rho\mathbf{u}d\mathbf{A} = -\frac{17}{24} \cdot \frac{\rho \cdot V}{r_d} \cdot \mathbf{u}_{r20} \begin{pmatrix} e_x \cos\phi_2 - e_y \sin\phi_2 \\ e_y \cos\phi_2 + e_x \sin\phi_2 \end{pmatrix} - \frac{1}{2} \cdot \frac{\rho \cdot V \cdot u_{t2}}{r_d} \begin{pmatrix} -e_x \sin\phi_2 - e_y \cos\phi_2 \\ -e_y \sin\phi_2 + e_x \cos\phi_2 \end{pmatrix} \quad \text{(A4)}$$

In order to calculate the phase function ϕ, it is necessary to estimate the speed V_{dr} with which disturbances propagate in the radial direction.

Following Fulford (1964), the velocity of small disturbances in the flow in a laminar film will propagate along the film surface with a velocity of $3 \cdot u$, where u is the mean velocity in the film.

However, most of the experimental work reviewed by Fulford (1964) indicates a somewhat lower velocity, dependent on the Reynolds number, both for laminar and turbulent films. In this study, a value of $2 \cdot u$ will be used in the fully developed film.

In a free stream with a free surface, it is reasonable to assume that the disturbances will propagate with the free-stream velocity.

Therefore, in the inlet, a mean disturbance velocity of $V_{dr} = u_r(1 + \epsilon/\rho)$ is assumed.

Calculations of the destabilizing force have been carried out with an assumed disturbance velocity in the fully developed film from one to three times the mean film velocity.

The influence of this parameter is very small for high flow rates of water, but considerable for low flow rates or with high-viscosity fluids.

DISCUSSION

William E. Thompson[1]

The author's paper, including some rare experimental results, is a welcome addition to the literature on working fluid-induced effects that may lead to rotordynamic instability. It possesses two attributes that I would like to emphasize.

(*a*) Unsteady flow in a centrifugal impeller alone (without volute or vaned or vaneless diffuser) *can* induce both stiffness and damping effects, which may have a destabilizing influence on the impeller/rotor/bearing system. Perhaps this idea was first introduced by Thompson (1978). Investigation on the topic has been widened by Ohashi et al. (Shoji and Ohashi, 1987, and previous work) by including both vaned and vaneless diffusers. Bolleter et al. (1987) give major results from the EPRI-Sulzer project, in which measurements from a pump with a vaned diffuser were made. The author cites the work on volute pumps (Chamieh et al., 1982; Adkins, 1986). As distinct from the results of Shoji and Ohashi (1987) and Bolleter et al. (1987) as well as those of Chamieh et al. (1982) and Adkins (1986), however, the present paper strongly reinforces Thompson's contention that a destabilizing influence can arise from impeller passage flow. This is suggested to occur at design point operating conditions in the absence of volute or diffuser but when slight circumferential asymmetries are induced from impeller passage to impeller passage.

(*b*) The rotary atomizer is a simple apparatus and gives experimentalists an alternative test bed for observing the influence of asymmetric impeller passage flow. The control over the flow through the distributor yields significant control over the asymmetric passage flow, which is not as directly available to the experimenter using a pump or compressor.

Notwithstanding these features, as well as the interesting computational model for simulating the fluid force on the atomizer wheel, the paper has many frustrations for the reader. I suggest the following topics where further explanation and clarity are desirable.

(*c*) The author emphasizes much too strongly the occurrence of whirl (or lack of it) due to the destabilizing or stabilizing effect of the asymmetric passage flow. Since the atomizer rotor was supported in anti-friction bearings, which may provide little damping to the system, significant whirl may readily follow from small excitation effects. However, consider excitation of rotor vibration due to asymmetric impeller flow, as well as some bearing and seal influences to follow from energy input to the rotor. Further consider attenuation of rotor vibration to result from energy dissipation from the rotor largely in the bearings. Then whirl, as shown by the orbital displacements, is a function of the energy balance between excitation and dissipation. When associating the results of the paper with the more common pump and compressor rotor systems, ascribing whirl solely to the impeller passage flow effects may be misleading.

(*d*) The most important clarification needed is in distinguishing the stationary distributor from the rotating atomizer wheel in Fig. 1. Until that is done, it is not possible to understand satisfactorily the author's physical situation where

[1]Consultant, Rotating Fluid Machinery, 306 W. Victoria Lane, Arlington Heights, IL 60005.

a circumferentially uniform flow leaves the narrow circular ring gap of constant width but an unevenly distributed flow enters the various passages of the wheel. By what means is the flow partially reduced into some of the wheel channels and increased into others?

The uneven flow provides a *forced* asymmetry to the wheel passage flow conditions and is under control of the experimenter. Thus, the results in the paper are all reported as a function of the volumetric distributor flow. In drawing a comparison to a pump or compressor impeller, however, it must be remembered that such impellers are supplied with fluid through an upstream pipe or duct roughly the size of the impeller eye. Whirl of the impeller will not noticeably throttle the inlet cross-sectional area. Rather, asymmetric passage flow may follow from effects *induced* at the impeller blade leading edge. One such mechanism is postulated by Thompson (1978).

(*e*) In comparison to the detail of the first five steps in the Numerical Procedure, the description for calculating K_{xy} and other rotor-dynamic coefficients is inadequate. While the explicit formulas are given, it is the description of the disturbance phenomena, meant to be formulated by the phase function φ, which is so incomplete. Clearly φ is a function of ω, the rotor whirl frequency (and the angular frequency at which the fluctuations occur in the flow entering the atomizer passages). However, it is also a function of r. Hence, its influence is to take into account the differing flow rates entering a channel as the rotor orbit is traversed, as well as the passage flow rate at a radius r, which was initiated at an earlier ϑ_w. Thus, a model for the unsteady passage flow is presumably constructed as a function of rotor orbital position and velocity. The author needs to amplify his conception to a considerable extent in order to be understood on this important point. It does not help that r^* is undefined in the paper and that V_{dr} is given incorrectly in step 5 of the Numerical Procedure.

(*f*) The reader will be aware that the curves of K_{xy} in Fig. 4 are at constant atomizer wheel speed (1900 rad/s = 18,143 rpm). At least an indication of *all* the rotor-dynamic coefficients throughout the speed range would expand the reader's perception of the phenomena.

(*g*) The legend in Fig. 6 is inadequate. In the figure, two curves are drawn through experimental data for each wheel, but there is no clear description of the difference between the curves in each pair either on the figure or in the text. The figure should be completely self-explanatory.

In this paper we have a "rough-cut gem." It is to be regretted that the reviewers did not more effectively assist in polishing the gem for the greater value of the paper and the understanding and appreciation of the reader.

References

Bolleter, U., Wyss, A., Welte, I., and Sturchler, R., 1987, "Measurement of Hydrodynamic Interaction Matrices of Boiler Feed Pump Impellers," ASME *Journal of Vibration, Acoustics, Stress, and Reliability in Design*, Vol. 109, No. 2, pp. 144–151.

Shoji, H., and Ohashi, H., 1987, "Lateral Forces on Whirling Centrifugal Impeller: 1st Report, Theory; 2nd Report, Experiment in Vaneless Diffuser," ASME *Journal of Fluids Engineering*, Vol. 109, No. 2, pp. 94–106.

Thompson, W. E., 1978, "Fluid Dynamic Excitation of Centrifugal Compressor Rotor Vibrations," ASME *Journal of Fluids Engineering*, Vol. 100, No. 1, pp. 73–78.

Author's Closure

The author is grateful to Dr. Thompson for pointing out topics in the paper where more clarity is needed. The reviewers should not be blamed, however, for the lack of clarity, since they have already pointed out several weak points in the explanations. It is the author's responsibility if he has not been successful in trying to incorporate their advice in the final text. It is hoped that the following answers to Dr. Thompson's comments and questions will help in reducing the frustrations of the readers:

(*a*) The author is aware of Dr. Thompson's paper (1978). However, since the most basic physical and computational features of the model presented there could not be disclosed, as they were part of a proprietary development, it was found very difficult to benefit from the analysis.

(*b*) The liquid distributor does *not* control the asymmetric flow. It controls the total flow $\dot{V}$ to the rotating wheel, like a valve in a feedpipe to a pump. Also, it spreads the liquid out into a cone-shaped film, which is symmetric with respect to the distributor axis, but obviously not symmetric with respect to the eccentric rotor axis.

(*c*) The paper only claims to explain the main destabilizing mechanism in a rotary atomizer, not in any type of fluid-handling machinery. However, an adaptation of the analysis to a pump impeller has been submitted as a paper to the next ASME Vibrations conference to be held in Sept. 1989. It is hoped that the relative importance of the mechanism analyzed can be discussed on the basis of that future paper.

(*d*) Figure 1(A) attempts to show the distributor-rotor configuration. The stationary distributor is marked "distributor," and this also includes the inner part, forming the inner boundary for the liquid, which is pumped through in the direction of the arrow, leaving through the ring gap just below the transparent wheel top plate. The rotating parts are the shaft, the wheel bottom with the channels, and the transparent top plate.

The flow is reduced in the channels that move away from the distributor, and increased in the channels that approach the distributor, as the wheel becomes eccentric with respect to the distributor axis. It is postulated that the thin film sticks to the wheel without slip in the tangential direction in the inner wheel and the channel inlet. Extensive slip and backflow will destroy this mechanism, and this is in fact utilized when curing the instability, redesigning the channel inlet to create precisely this type of secondary flow. The uneven flow in the wheel is *not* a forced asymmetry controlled by the experimenter, but is caused by the eccentricity of the rotor, when the rotor whirls freely. This is precisely what creates the self-exciting nature of the resulting vibrations.

(*e*) The symbol r^* was introduced to avoid the appearance of r, both in the boundaries and under the integral sign in the expression for ϕ in Appendix A. V_{dr} is not incorrectly given in step 5 in the numerical procedure. What is given is the disturbance velocity V_d in the direction of the channel. This should have been explained in the list of symbols.

The phase function ϕ describes the asymmetric flow through the wheel in terms of the inlet distribution, given by equation (1), and the radial velocity V_{dr}, of a disturbance that travels as a surface wave on the film in the channel. In an incompressible fluid, completely filling the channel, ϕ would be equal to the angle traversed by the curved channel from the inlet to the outlet. However, free surfaces and compressibility effects will cause the disturbances to move with a finite velocity, introducing a further phase difference between the inlet asymmetry and the asymmetry felt by the channels at some given radius. For the atomizer, this is given as an explicit formula in the paper; for other machines, without the film-type flow in the channels, it would obviously be different.

(*f*) The influence of rotor speed relative to whirl speed has not been investigated, since the experimental program did not allow for this. It has been shown in the paper that for the atomizers, which run at ten times the first critical, the dominating term is the cross-coupling stiffness. Consequently there is no experimental verification of the damping terms in the model, and since these will look quite different in other

machines, we propose postponing discussion of the damping terms until after the publication of the mentioned analysis of a pump impeller.

(*g*) In Fig. 6, curves with positive ordinates are the amplitudes of the forward whirl component, and curves with negative ordinates are the backward component amplitudes, as indicated on the ordinate axis.

Clearly, the above only partially answers the comments and questions raised. Since most of the unclarity is obviously connected to the fact that a rotary atomizer is not a very well-known device outside the community of its designers and users in spray-drying, dry scrubbers, and mineral concentration, a further discussion of the relevance of the analysis for turbomachines should perhaps await the publication of the earlier mentioned adaptation of the model to a centrifugal pump impeller.

It is hoped that the constructive criticism of the reviewers and Dr. Thompson has also added to the author's limited experience in technical presentation, so that this next paper will be less frustrating to the readers.

The Theory and Operation of Evaporative Coolers for Industrial Gas Turbine Installations

R. S. Johnson, Sr.
Principal Engineer,
Solar Turbines Incorporated,
San Diego, CA 92131
Mem. ASME

This paper discusses the theory of evaporative cooling and describes the application of wetted rigid media evaporative coolers to gas turbines. Calculations of parameters used to predict evaporative cooler performance are included. Also included are discussions of evaporative cooler design, installation, operation, feedwater quality, and the causes and prevention of water carry-over.

Introduction

Evaporative coolers are used with gas turbines to increase the density of the combustion air, thereby increasing power output. The air density increase is accomplished by evaporating water into the inlet air, which decreases its temperature and correspondingly increases its density. The water vapor passes through the turbine, causing a negligible increase in fuel consumption.

Water used with evaporative coolers often contains dissolved solids such as sodium and potassium, which, in combination with sulfur in the fuel, are principal ingredients in hot gas path corrosion. For this reason, water quality and the prevention of water carry-over are important considerations in the use of evaporative coolers. The prevention of water carry-over is accomplished by correct design of the evaporative cooler, and proper installation and operation. Water quality requirements depend on the amount of water carry-over expected (or allowed) and can vary from the use of deionized water to water with significant concentrations (as much as several hundred ppm by weight, in water) of sodium and potassium.

Theory

Evaporative cooling involves heat and mass transfer, which occurs when water and the unsaturated air–water mixture of the incoming air are in contact. This transfer is a function of the differences in temperatures and vapor pressures between the air and water. Heat and mass transfer are both operative in the evaporative cooler because heat transfer from the air to the water evaporates water, and the water evaporating into the air constitutes mass transfer.

Heat inflow can be described as either latent or sensible heat. Which term is used depends on the effect. If the effect is only to raise or lower temperature, it is sensible heat. Latent heat, on the other hand, produces a change of state, e.g., freezing, melting, condensing, or vaporizing.

In evaporative cooling, sensible heat from the air is transferred to the water, becoming latent heat as the water evaporates. The water vapor becomes part of the air and carries the latent heat with it. The air dry-bulb temperature is decreased because it gives up sensible heat. The air wet-bulb temperature is not affected by the absorption of latent heat in the water vapor because the water vapor enters the air at the air wet-bulb temperature.

Theoretically, the incoming air and the water in the evaporative cooler may be considered an isolated system. Because no heat is added to or removed from the system, the process of exchanging the sensible heat of the air for latent heat of evaporation from the water is adiabatic. Evaporative cooler performance, therefore, is based on the concept of an adiabatic process.

Rigid Media Evaporative Coolers

Evaporative coolers used in gas turbine applications today are the wetted rigid media type (Fig. 1). In this type of evaporative cooler, the evaporating medium is a saturated porous pad. Water is introduced through a header at the top of the media, sprays into the top of an inverted half-pipe, and is deflected downward onto a distribution pad on top of the media. Water drains through the distribution pad into the media, by gravity action downward through it, and wets enormous areas of media surface contacted by air passing through the cooler.

An evaporative cooler can be either recirculating or nonrecirculating. A recirculating evaporative cooler holds water in a reservoir and uses a pump to supply water to the header pipe. Water drains through the media into the reservoir below. Make-up water replacing evaporated water and water lost through blowdown (which is explained later) flows into the reservoir. For a nonrecirculating cooler, new water is continuously introduced directly into the header from the water supply outside the cooler, passes once through the media, and is

Contributed by the International Gas Turbine Institute and presented at the 33rd International Gas Turbine and Aeroengine Congress and Exhibition, Amsterdam, The Netherlands, June 5–9, 1988. Manuscript received by the International Gas Turbine Institute September 15, 1987. Paper No. 88-GT-41.

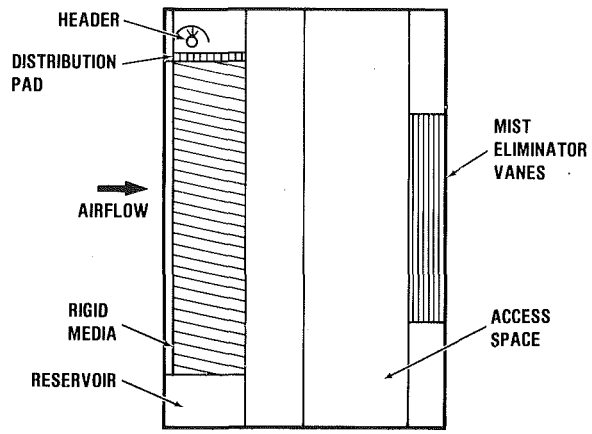

Fig. 1 Rigid medium evaporative cooler

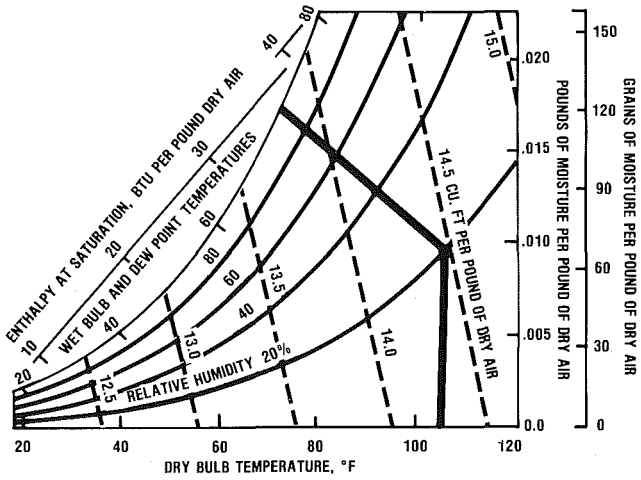

Fig. 2 Psychrometric chart A (barometric pressure 29.92 in. of mercury)

discarded. The water flow rate to the header should be the same for both types of cooler.

Operating Parameters

In determining the effect of the evaporative cooler on turbine performance, the dry-bulb temperature (T_{DB1}) of the air leaving the evaporative cooler must be known. This is calculated using

$$T_{DB2} = T_{DB1} - \frac{N}{100 \text{ percent}} (T_{DB1} - T_{WB}) \quad (1)$$

In most applications, the relative humidity (RH) of the incoming air is known rather than the wet-bulb temperature. The wet-bulb temperature can be found from the psychrometric chart in Fig. 2. For example, assume that it is desired to consider the effect of an evaporative cooler on turbine performance with the following conditions:

- RH = 20 percent
- Ambient temperature (T_{DB1}) = 105°F
- Evaporative cooler effectiveness (N/100 percent) = 0.90

Enter the bottom of the chart at 105°F and proceed upward to intersect the 20 percent RH line. Then follow the diagonal line to the wet-bulb and dew-point temperature lines, and read 72.3°F for T_{WB}. Using equation (1), calculate T_{DB2}:

$$T_{DB2} = 105 - 0.90\ (105 - 72.3) = 75.6°F$$

This is the temperature of the turbine combustion inlet air under the conditions described.

If the evaporative cooler being used is nonrecirculating, this is the only calculation needed. If the cooler is a recirculating type, it is necessary to determine the blowdown and make-up water flow rates. Blowdown is a continuous wastage or bleed-off of water from the reservoir to carry away accumulating minerals. This controls the concentration level of dissolved solids in, and/or hardness of, the water in the reservoir. The rate of blowdown is determined by the initial condition of the water, the rate of evaporation, and the degree of concentration to be allowed. Make-up water is the water added to the reservoir to make up for water lost from blowdown and evaporation.

In order to calculate the blowdown rate (B), it is necessary

Nomenclature

$\dot{A}$ = feedwater rate, gpm
B = blowdown rate, gpm
D = weight of water, lb/gal
E = water evaporation rate, gpm
H = water hardness in reservoir, as $CaCO_3$
N = evaporative cooler effectiveness, percent
$\dot{Q}$ = thermal energy flow rate from water to air, Btu/hr
T = contaminant concentration as Total Fuel Equivalent, ppm by weight
$\dot{V}$ = gas turbine air volume flow rate, ft^3/min
X = feedwater hardness as $CaCO_3$, ppm
AFR = air/fuel mass flow ratio
CFR = water carry-over/fuel mass flow ratio
LHV = lower heating value of fuel, Btu/lb
SFR = steam/flow mass flow ratio
WFR = water/fuel mass flow ratio
A_i = concentration of the ith contaminant in air, ppm by weight
C_i = concentration of the contaminant in carry-over water, ppm by weight
F_i = concentration of the ith contaminant in fuel, ppm by weight
$\dot{m}_a$ = air mass flow rate, lb/hr
$\dot{m}_w$ = water mass flow rate, lb/hr
m_1 = moisture in incoming air, lb moisture/lb dry air
m_2 = moisture in leaving air, lb moisture/lb dry air
p_a = density of air at ambient temperature, lb/ft^3
S_i = concentration of the ith contaminant in steam, ppm by weight
T_{DB1} = dry-bulb temperature of air entering the evaporative cooler, °F
T_{DB2} = dry-bulb temperature of air leaving the evaporative cooler, adiabatic condition, °F
T_{DB2}' = dry-bulb temperature of air leaving the evaporative cooler, nonadiabatic condition, °F
T_{WB} = ambient wet-bulb temperature, °F
W_i = concentration of ith contaminant in water, ppm by weight

Conversion Factors

°C = (°F − 32)/1.8
kg/L = 8.33 lb/U.S. gal.
kg/m^3 = 6.25 E−02 lb/ft^3
kg/s = 7.937 E+03 lb/hr
kJ/kg = 4.292 E−01 Btu/lb
kJ/kg = °C = 2.387 E−01 Btu/lb = °F
L/s = 1.585 E+01 U.S. gal/min
m^3/s = 2.120 E+03 cfm
m = 3.28 ft
W = 3.413 Btu/hr

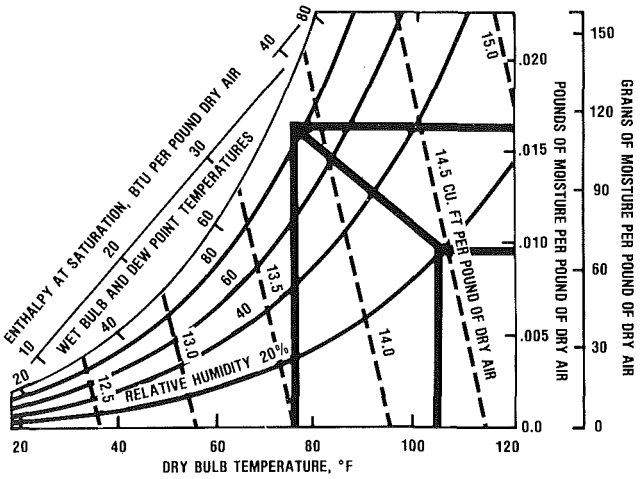

Fig. 3 Psychrometric chart B (barometric pressure 29.92 in. of mercury)

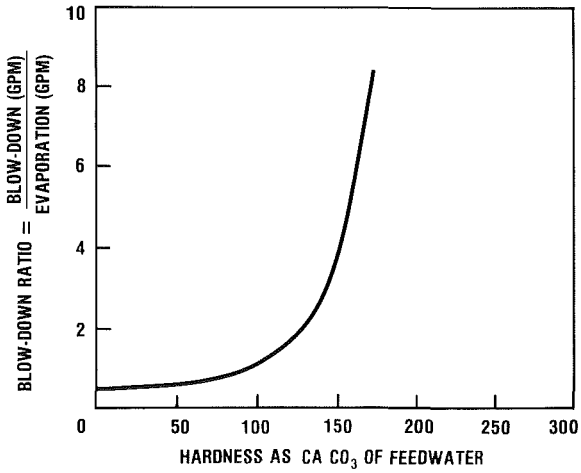

Fig. 4 Hardness as $CaCO_3$ of feedwater

first to calculate the rate of water evaporating ($\dot{E}$). Using the conditions given above and the calculated exiting air dry-bulb temperature (T_{DB2}), equation (2) is employed:

$$\dot{E} = \frac{\dot{V}[m_2 - m_1]P_a}{D} \text{ gpm} \tag{2}$$

To determine the values for m_2 and m_1, enter Fig. 3 at 105°F (T_{DB1}) and proceed upward to the 20 percent RH line. Move perpendicularly to the right and read 0.0094 lb moisture/lb of dry air (m_1). Return to the 20 percent RH line and move diagonally left to intersect the 75.6°F (T_{DB2}) line. Now move perpendicularly to the right and read 0.0162 lb moisture/lb of dry air (m_2). From the psychrometric chart (Fig. 3), the specific volume of air at 105°F and 20 percent relative humidity is 14.442 ft³/lb. Therefore, P_a = 0.0692 lb/ft³.

Assume that the gas turbine combustion airflow rate ($\dot{V}$) is 30,000 cfm. Take D = 8.33 lb/gal and return to equation (2)

$\dot{E}$ = [30,000 cfm (0.0162 lb/lb dry air
− 0.0094 lb/lb dry air) 0.0692 lb/ft³]
÷ 8.33 lb/gal

Therefore

$\dot{E}$ = 1.7 gal/min (the rate at which water evaporates into the inlet air)

The feedwater and blowdown rates can now be determined if the hardness of the feedwater is known. If the feedwater has been tested and found to have, for example, a hardness of 150 ppm as $CaCO_3$, the blowdown rate can be determined. From the curve in Fig. 4, which is widely used in the evaporative cooler industry to estimate blowdown ratio, the blowdown rate ($\dot{B}$) should equal four times the rate of evaporation (E):

$$\dot{B} = 4\ (\dot{E} \text{ gpm}) = 4\ (1.7) = 6.8 \text{ gpm} \tag{3}$$

The feedwater rate is found from

$$\dot{A} = \dot{B} + \dot{E} \text{ gpm} = 6.8 + 1.7 = 8.5 \text{ gpm} \tag{4}$$

The water hardness in the reservoir, measured as $CaCO_3$, can be calculated from

$$H = \frac{\dot{A}X}{\dot{B}} \text{ ppm} = \frac{(8.5 \text{ gpm})(150 \text{ ppm})}{6.8 \text{ gpm}} = 187.5 \text{ ppm} \tag{5}$$

The same procedure can be used to calculate the concentrations of dissolved solids in the reservoir from known concentrations in the feedwater.

A question frequently asked about evaporative coolers involves the use of make-up water from discarded warm water from a manufacturing or industrial process. If the water has satisfactorily low levels of hardness, or dissolved solids, the question then becomes one of whether the water can be used despite its elevated temperature. The following discussion of adiabatic and nonadiabatic cooling attempts to answer this question.

The temperature of the water used with the evaporative cooler is also limited by the type of media. If a cellulose-based rigid media is used, which is the type typically installed in evaporative coolers used with gas turbines, water temperatures above 130°F may damage it.

Adiabatic Cooling

Adiabatic cooling occurs when the temperature of water delivered to the header of the evaporative cooler is equal to the incoming air wet-bulb temperature (T_{WB}), and no external heat enters the process. Because the ambient wet-bulb temperature is constantly changing, this condition only rarely occurs when a nonrecirculating evaporative cooler is being used. In most cases in hot weather, however, it is sufficiently accurate to assume that the water supply temperature approximates the air wet-bulb temperature. This is because the temperature of many water sources is naturally close to, or slightly lower than, the wet-bulb temperature. However, the temperature of water in long runs of sun-struck pipes can be significantly increased.

In a recirculating evaporative cooler, the water temperature will approach the wet-bulb temperature so closely that for all practical purposes, the two temperatures can be taken as equal. This is true even if the water used is significantly above the wet-bulb temperature when it is delivered to the reservoir.

In all cases, some external heat enters the process from the sun shining on the cooler. However, because the air's mass flow rate is so large, its effect is minimal.

The adiabatic process is explained in Fig. 5. The incoming air dry-bulb temperature enters at position 1 and moves at constant enthalpy toward the entering air wet-bulb temperature at position 2. The air does not reach position 2, however, because the evaporative cooler is not 100 percent efficient; the process stops at position 3. Position 3 is the dry-bulb temperature of the air leaving the evaporative cooler.

Nonadiabatic Cooling

Two conditions describe nonadiabatic cooling. The first condition occurs when the evaporative cooler water is delivered to the header at a temperature above the wet-bulb temperature of the air, but below the entering air dry-bulb temperature. In

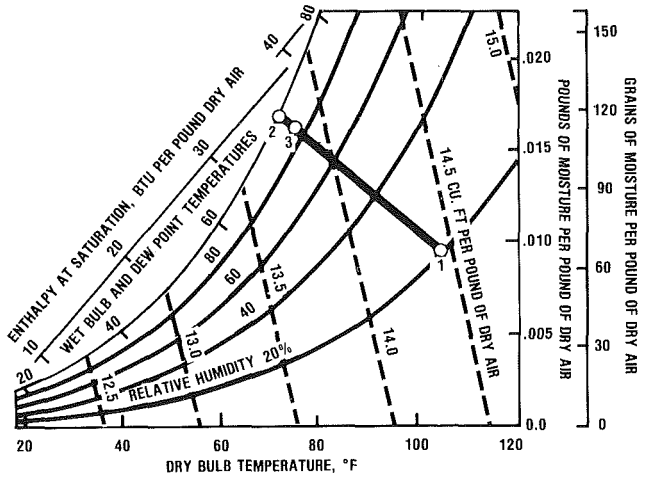

Fig. 5 Psychrometric chart C (barometric pressure 29.92 in. of mercury)

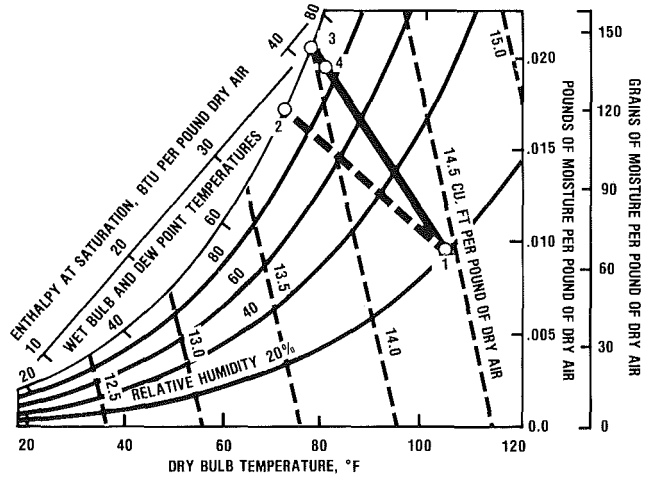

Fig. 6 Psychrometric chart D (barometric pressure 29.92 in. of mercury)

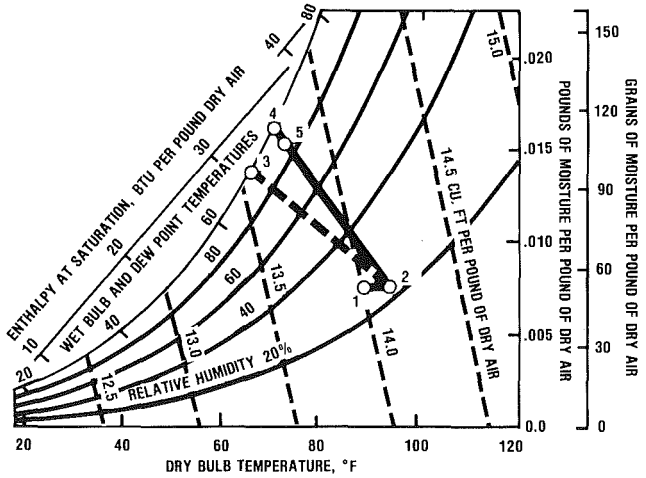

Fig. 7 Psychrometric chart E (barometric pressure 29.92 in. of mercury)

this case, the incoming air dry-bulb temperature enters at position 1 (Fig. 6) and moves toward position 3 at increasing enthalpy and wet-bulb temperature, as the air absorbs the extra heat from the water. Again, position 2 is the air wet-bulb temperature and line 1–2 represents the direction of adiabatic cooling, which does not occur. Position 3 cannot be determined theoretically because the final condition of the air after it has been cooled is indeterminate. Position 4 is the final temperature of the air, which, as in the adiabatic process, is above the saturation temperature because the evaporative cooler is less than 100 percent efficient. Position 4 is the dry-bulb temperature of the air leaving the evaporative cooler.

The second nonadiabatic cooling condition occurs when the water delivered to the header is above the entering air dry-bulb temperature, as well as above the wet-bulb temperature. The incoming air dry-bulb temperature (Fig. 7) enters at position 1 and moves to position 2 as the sensible heat transfer from the water to the air increases the air dry-bulb temperature. The air then moves toward position 4 with increasing enthalpy and wet-bulb temperature, as noted earlier. Position 3 is the air wet-bulb temperature, and line 2–3 is the path of adiabatic cooling, which does not occur. Position 5 is the final, dry-bulb temperature of the air leaving the evaporative cooler.

Calculating the evaporative cooler's exiting dry bulb temperature cannot be done solely by means of equation (1) in a nonadiabatic condition. This is because the process of cooling the air has not been done at constant enthalpy. Some of the enthalpy of the incoming water has produced sensible heat gain in the air. Although the effect of this sensible heat gain cannot be evaluated theoretically, it is possible to estimate its effect. This procedure assumes that the temperature difference between the incoming water and the air wet-bulb temperature represents the available thermal energy given up by the water to the air, as sensible heat, as the water is cooled to the air wet-bulb temperature. However, this is not strictly true because some water will be evaporated and will pass latent heat into the air, which slightly raises the air wet-bulb temperature. But, as with the final dry-bulb temperature, the final wet-bulb temperature is also indeterminate. Therefore, the procedure predicts a dry-bulb temperature (T_{DB2}) that is slightly higher than the actual temperature, if other heat does not enter the cooler. This procedure is slightly conservative and prevents overestimating the effect of the evaporative cooler. The procedure is detailed in the following example

Example

Assumptions:

1 T_W = 100°F, incoming water temperature
2 T_{DB1} = 105°F, incoming air dry-bulb temperature
3 T_{WB} = 72°F, air wet-bulb temperature
4 $\dot{m}_a$ = 126,558 lb/hr, air mass flow rate
5 $\dot{m}_w$ = 5010 lb/hr, water mass flow rate

First, using equation (1), calculate the exiting air dry-bulb temperature from the evaporative cooler, assuming adiabatic conditions

$$T_{DB2} = 105°F - 0.9(105°F - 72°F) = 75°F$$

Now, using equation (6), calculate the available heat from the water

$$\dot{Q} = \dot{m}\, c_p \Delta T$$
$$= (5010 \text{ lb/hr})(1 \text{ Btu/lb} = °F)(100°F - 72°F) \quad (6)$$
$$= 140{,}280 \text{ Btu/hr}$$

Finally, calculate the final dry-bulb temperature of the air using

$$T_{DB2}' = T_{DB2} + \frac{\dot{Q}}{\dot{m}_a c_p}$$
$$= 75°F + \frac{140{,}280 \text{ Btu/hr}}{(126{,}558 \text{ lb/hr})(0.24 \text{ Btu/lb} = °F)} = 80°F \quad (7)$$

This is the air temperature used to predict the gas turbine's theoretical performance. Remember, the correction shown in this example is used only for nonrecirculating evaporative coolers. For equivalent recirculating evaporative coolers adiabatic

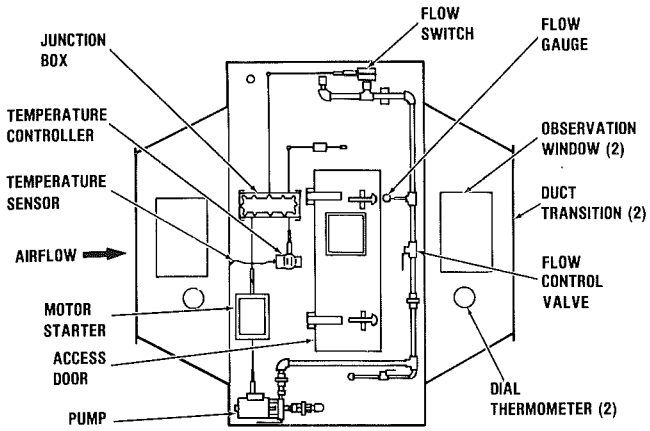

Fig. 8 Typical evaporative cooler

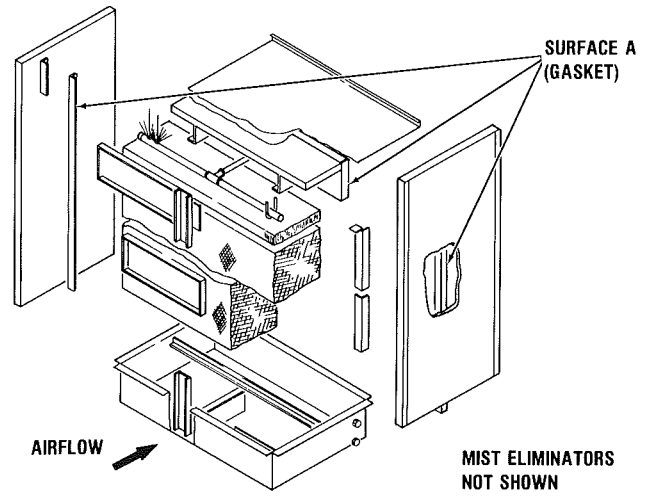

Fig. 10 Vane-type mist eliminator

conditions can be assumed, even when using make-up water at temperatures above the incoming air wet-bulb temperature.

This 5°F temperature difference can have a significant impact on turbine performance. With a recirculating cooler and the conditions used for the example, the available shaft horsepower (neglecting inlet and exhaust losses) at sea level from a 3481-hp compressor set (80°F matched engine) without evaporative cooling is 4052 hp with a recirculating cooler and 4007 hp with a nonrecirculating cooler, which represents gains of 16.4 and 15.1 percent, respectively. Obviously, the recirculating evaporative cooler is recommended for installations using water at elevated temperatures. However, for best results, the water temperature should be close to, or below, the ambient air wet bulb temperature.

Design

Basically, evaporative cooler design involves the packaging of the media in an appropriate housing and the incorporation of several common features that prevent (or minimize) water carry-over in the air leaving the cooler, and reduce maintenance. A typical evaporative cooler is shown in Fig. 8.

Common Features

1 Header. Delivers the water to the distribution pad at the top of the cooler. Should be located toward the front (air-entering side) of the cooler (Fig. 1), which delivers more water to the front of the cooler than a header located at the center of the pad.

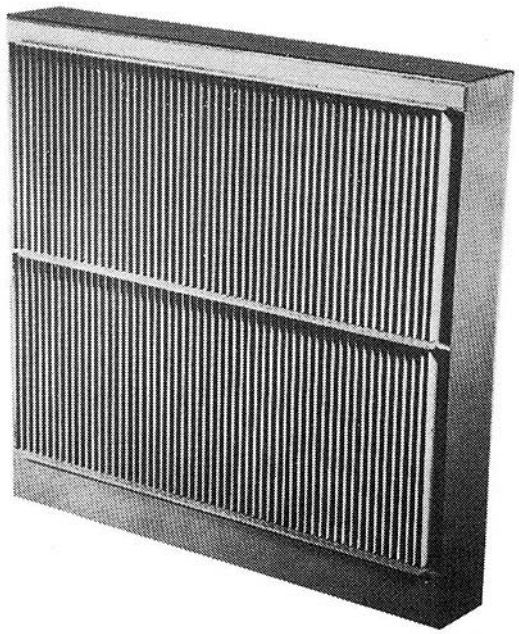

Fig. 9 Evaporative cooler—exploded view

2 Media Retainers. Must be gasketed. These are surfaces on the downstream side of the media that secure the media pack in the housing, shown as surfaces "A" in Fig. 9. A closed-cell, neoprene material, 1/16-in. thick, is recommended for the gaskets. The media must be in contact with the gaskets. This prevents water carry-over in the leaving air caused by water leaking between the media and the retaining surfaces.

3 Vane-Type Mist Eliminator (Fig. 10). Used on the cooler's downstream side. This is intended to remove air-entrained water droplets, if necessary. The mist eliminators should have a minimum droplet cut-off size of 100 μm, which means the mist eliminator has a removal efficiency of 99.9 percent on droplets of 100 μm and larger.

4 Observation Window. Installed in the cooler housing sidewall between the media and the mist eliminators, to allow observation of the air-leaving side of the media. Large amounts of water leaving the media indicate an upset condition, which should be investigated.

Duct sections immediately upstream and downstream of the cooler should have observation windows. This allows examination of the upstream side for dry spots and heavy scale formation on the media.

5 Thermometers. Placed in the ductwork upstream and downstream of the cooler to monitor the effectiveness of the cooler.

6 Temperature Sensor. Measures incoming dry-bulb temperature. Should be in the airstream on the air inlet side of the cooler. Recommended setting is 55°F, below which temperature the cooler is shut off.

7 Water Flow Gage and Valve. Used to monitor and adjust water flow to the header.

8 Movable Wall in the Cooler Housing. Considerably reduces the difficulty of installing or removing the media. This feature is highly beneficial. Without it, installing media in the field is difficult and often leads to damaged media. The wall is backed off the media for media removal and pushes against the media after the media has been reinstalled, compressing the media strips tightly together. Such compression is necessary to prevent water leakage between the strips, which would lead to water entrainment.

9 Water Flow Monitor. Should produce an alarm signal to notify the operator if water flow to the cooler is interrupted.

10 Recirculating Pump. Installed outside the cooler. This

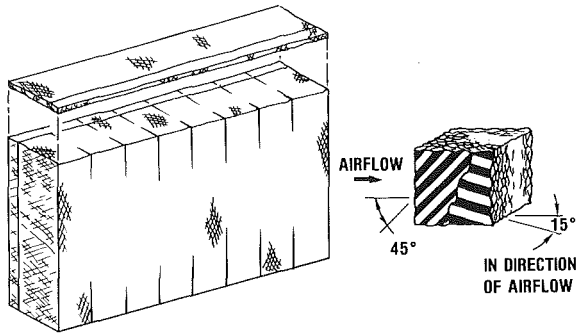

Fig. 11 Media polarity

makes it easier to service the pump and motor while the turbine is operating.

11 Media Face Velocity. 500 ft/min. Higher face velocities of up to about 625 ft/min can be used, but lower face velocities greatly reduce the risk of water entrainment from the media.

These features, except for the thermometers, are standard with the evaporative coolers used by the author's company. Thermometers are a convenience preferred by many operators and are supplied when specified by the user. Media retainer gaskets are not included sometimes, if it is determined the cooler will function satisfactorily without them. However, the vertical retainers on the side wall of the cooler housing are mandatory.

Water Flow Rates

Evaporative cooler manufacturers recommend water flow rates to the evaporative cooler header ranging from 1 to 2 gal/min for each square foot of surface area of the distribution pad (Fig. 1) for coolers up to 6 ft high, and 1-1/4 to 3 gal/min for coolers up to 12 ft high. A flow rate of 1 gal/min/ft^2 of distribution pad surface area for evaporative coolers up to 6 ft high has been shown to work satisfactorily. Accordingly, for evaporative coolers 7 to 12 ft high, 1-1/4 gal/min/ft^2 of distribution pad surface area is recommended. Higher flow rates have the advantage of minimizing the rate of scale formation on the media surface, but lower flow rates minimize the potential for water carry-over. (Water carry-over is discussed in the next section.) These recommended flow rates are considered a practical result of the consideration of these two effects.

According to a major manufacturerer of the media used in rigid medium evaporative coolers, these flow rates could be reduced as much as 20 percent and still retain the full effectiveness of the evaporative cooler. However, lower flow rates are not recommended because the 20 percent margin is a useful safety factor.

A water flow rate that is too low will be indicated by dry spots on the media's upstream surface. If dry spots occur, the water flow rate to the header should be gradually increased. If the dry spots do not disappear after 15 to 20 min, the water flow rate should be increased further. This procedure should be followed until the dry spots are gone.

Although scale will form on any evaporative cooler media over time, heavy scale formation on the front of the media after several weeks or a few months of operation may also indicate a water flow rate that is too low. As with dry spots, the water flow rate should be increased. In both cases, observe the downstream side of the media to look for water carry-over. The mist eliminators will remove entrained water, but water blowing from the media should be minimized, nevertheless. At the first opportunity, the media should be removed from the cooler and washed down or cleaned to remove the scale.

The water flow rate to the header should be set at the time the evaporative cooler becomes operational. If the flow rate is initially set correctly, it should not be necessary to adjust it later. The water flow rate should not be adjusted because of changes in the ambient temperature. Unnecessary water flow rate adjustments, especially those made because of ambient temperature changes, are a primary cause of evaporative cooler problems associated with too much—or too little—water.

Water Carry-Over

Water carry-over is the presence of water droplets in the air leaving the evaporative cooler. Water carry-over will be negligible if the cooler is properly designed, sized, installed, operated, and maintained. However, water carry-over seems to be affected by a large number of parameters and, because these conditions can (and seem to) appear in most evaporative cooler installations, it seems prudent to accept the inevitability of water carry-over in evaporative coolers that do not use vane-type mist eliminators.

Accordingly, in order to eliminate water carry-over, the author's company requires the use of vane-type mist eliminators for all evaporative coolers supplied with its gas turbines. The mist eliminator is installed on the downstream side of the media. Even though a mist eliminator is installed after the media, spray leaving the media should still be investigated and reduced as much as possible because the mist eliminator efficiency is less than 100 percent. This means that some water will pass through the mist eliminator. The greater the water volume impinging on the mist eliminator, the greater the water volume entrained in the turbine's inlet air. The vane-type mist eliminator is extremely effective in removing water droplets, but reducing airborne water droplets to the maximum extent possible upstream of the mist eliminator is advisable and will ensure that water carry-over does not occur.

The ten causes of water carry-over discussed below apply to water carried over from the air-leaving side of the media. These causes are based on field investigation of water carry-over from the evaporative cooler media:

1 Incorrect Media Polarity (Fig. 11). Media may be installed incorrectly by the manufacturer or removed at some point before the evaporative cooler's installation and then replaced incorrectly.

2 Damaged Media. Damage may occur when the media is being reinserted into the evaporative cooler after it has been removed in the field. Damage usually occurs at the edges of the media when the media strips are being forced into position. This can prevent proper alignment of the media strips and can be the cause of open cracks between the media (see item 3). Damage also occurs when the media strips are placed on the ground and then stepped upon. This crushes the media, and water carry-over often occurs at the point of damage.

3 Media Strips Improperly Aligned. The vertically installed media strips may not be flush with each other on the air-leaving side. Excessive misalignment, 3/4 in. or more, can allow water carry-over. In addition, there should be no open cracks between the media strips.

4 Media Not Sealed Against Retainers. Media must be firmly sealed against the media retainers which hold the top and sides of the media on the downstream side of the cooler.

5 Excessive Water Flow. Too much water delivered to the header will flood the media and cause water carry-over. The water flow rate should be no more than needed to wet all media internal surfaces without flooding them.

6 Uneven Water Distribution From the Header. Holes in the water header can become clogged, causing uneven water distribution to the media pad, which means one side of the cooler receives too much water.

7 **Incorrectly Installed Baffle Sheet.** If the evaporative cooler uses a rubber baffle sheet, this sheet should be installed on top of the media pad.

8 **Uneven Airflow Through the Media.** Most likely the result of improper ducting design. The inlet ducting must be designed so that the airflow distribution through the media is as even as possible.

9 **Scale Deposits on the Media.** If the evaporative cooler has been in service for a long time, it may have scale deposits on the media surface, causing water entrainment and necessitating media replacement.

10 **Unsaturated Media.** Some water entrainment may be caused by starting the turbine before the evaporative cooler media is saturated. Normally, the water carry-over will be insignificant because the period required to saturate the media lasts for only a few minutes.

Water Treatment

Field experience from the author's company has demonstrated the necessity of setting a quality specification for water used with evaporative coolers. This specification has established limits for turbidity, pH, hardness as $CaCO_3$, and the concentration of sodium (Na) plus potassium (K).

The specification imposes the following limits:

1	Turbidity	—5000 turbidity units
2	pH	—6–9
3	Hardness as $CaCO_3$	—160 ppm
4	Na + K	—(see below)

The Na + K concentration limit is based on the assumption that water carry-over from the evaporative cooler without the mist eliminator is not more than 10 percent of the water flow rate delivered to the header. Concentrations of several hundred ppm (up to about 1000 ppm) Na + K can be tolerated if mist eliminators having a removal efficiency of at least 99.9 percent on water droplets larger than 100 μm are used.

The 160 ppm for hardness as $CaCO_3$ is a recommended maximum, generally used as a rule of thumb. Water having higher concentrations can be used. However, when the water is saturated with $CaCO_3$, scaling occurs on the evaporative cooler media. In addition to calcium hardness, scaling is also a function of the total dissolved solids, pH, and water temperature. A more accurate determination of the $CaCO_3$ saturation point can be found using the Langelier Saturation Index, Ryznar Stability Index, or the Puckorius Scaling Index.

Typically, water treatment recommendations should be obtained from a water treatment company or a water treatment consultant doing business in the area of the gas turbine installation.

At the author's company, engineering personnel review each evaporative cooler installation, calculating the maximum anticipated carry-over of elemental contaminants in terms of a Total Fuel Equivalent using equation (8). (For the derivation and application of this equation, see Hsu, 1988.)

$$T = (18{,}380/\mathrm{LHV})\,[F_i + (\mathrm{AFR})A_i + (\mathrm{WFR})W_i + (\mathrm{SFR})S_i + (\mathrm{CFR})C_i] \quad (8)$$

where

i = Na, K, V, Pb, etc.

The calculated total fuel equivalent cannot exceed the allowable limit for the gas turbine.

Proper control and treatment of feedwater is necessary to maintain good evaporative cooler performance. If a recirculating evaporative cooler is used, this introduces the added requirement for setting an appropriate blowdown rate and selecting suitable feedwater treatment to prevent scale formation on the media and pH changes of the water.

Scale forms from the precipitation and deposition of dissolved solids, thereby decreasing media performance and shortening its life. Scale formation in the holes of the header reduces water flow and also decreases performance. If the hardness of untreated feedwater exceeds 160 ppm of $CaCO_3$, treatment is recommended because blowdown alone will not prevent scale formation. The ratio of blowdown to evaporation is 5.7 to 1 at 160 ppm, but this ratio becomes excessively high above 160 ppm. Below 135 ppm, feedwater can be used without treatment. Between 135 and 160 ppm, feedwater is usually not treated, but water availability, water costs, and cost of treatment are factors in deciding whether to treat the water.

Even though feedwater treatment due to hardness may be unnecessary, treatment may still be required because of pH changes caused by evaporation and aeration of the water in the reservoir of a recirculating evaporative cooler. Aeration, for example, removes dissolved CO_2 and, thereby, increases the alkalinity, which aids the precipitation of $CaCO_3$.

Deionized water can be used with the evaporative cooler, but it reacts with the stiffening agents in the media, softening the media to the point of collapse. It is also very corrosive to unprotected metal parts of the cooler. If deionized water is used, galvanized materials should not be used. The cooler housing and water piping should be constructed of 304 stainless steel, and the media should be specially constructed with increased stiffening agents.

Installation

Generally, in a gas turbine inlet air system, it is recommended that the evaporative cooler be placed after the inlet air cleaner, not before it. This arrangement will protect the media from the dust and other airborne contaminants that would otherwise impinge upon it. Rigid media evaporative coolers have not been tested for filtration efficiency, but it is known that they can remove substantial amounts of airborne particulate. The effect this particulate removal has on the evaporative cooler's operation will depend on a number of factors, including the average airborne dust concentration, the maximum anticipated airborne dust concentration, and whether the evaporative cooler is recirculating or nonrecirculating.

Recirculating Evaporative Coolers. Light dust concentrations (less than about 1 ppm in air) will not create operational problems for the evaporative cooler. As a rule of thumb, though, the evaporative cooler should follow an air cleaner, if the average dust concentration exceeds 1 ppm. Higher concentrations, especially in dust and sandstorms where concentrations can easily exceed 500–600 ppm, can cause heavy silt in the reservoir and result in damage to pumps and in reduced recirculating water flow.

Water flow rates higher than those recommended for normal operation are needed to wash the dirt from the evaporative cooler media. These higher flow rates greatly increase the risk of water entrainment from the media and of greater water loading on the mist eliminator, which, in turn, increases the risk of water carry-over from the evaporative cooler.

Organic growths also become a problem for recirculating evaporative coolers exposed to sunlight. Growths form on the media and in the reservoir, necessitating chemical treatments to control them.

Nonrecirculating Evaporative Coolers. The nonrecirculating evaporative cooler does not have the silt problems of the recirculating cooler, but it is subject to the same dust loading problems. The higher water flow rates and subsequent risk of water carry-over that apply to the recirculating cooler also apply to the nonrecirculating cooler. Organic growth can also occur on the media.

Acknowledgments

The author wishes to acknowledge John W. Adler, The

Munters Corporation; Harvey von E. Doering, Consultant; Francis R. Story, P.E., Pneumafil Corporation; and Dr. John R. Watt, P.E., Consultant, for their valuable contributions to the quality and accuracy of this paper.

References

Additional Source Material

American Society of Heating, Refrigerating and Air-Conditioning Engineers, 1980, *ASHRAE Handbook*, New York, 1980 Systems Volume, Chap. 36.

Gonzales, D. J., and Short, D. T., 1964, "Some Environmental Control Techniques Affecting Gas-Turbine Performance," ASME Paper No. 64-WA/GTP-10.

Hsu, L. L., 1988, "Total Corrosion Control for Industrial Gas Turbines: Airborne Contaminants and Their Impact on Air/Fuel/Water Management," presented at the 33rd International Gas Turbine and Aeroengine Congress and Exhibition, Amsterdam, The Netherlands, June 5–9.

Puckorius, P., 1983, "Get a Better Reading on Scaling Tendency of Cooling Water," *Power*, Sept., pp. 79–81.

Watt, J. R., P.E., 1986, *Evaporative Air Conditioning Handbook*, 2nd ed., Chapman & Hall, New York.

Nonintrusive Investigations Into Life-Size Labyrinth Seal Flow Fields

J. B. Brownell
Senior Research Officer,
Optical Metrology Group,
Advanced Research Laboratories

J. A. Millward
Manager, Mechanical Research,
Air & Oil Systems

R. J. Parker
Group Leader, Optical Metrology Group,
Advanced Research Laboratories

Rolls-Royce plc,
Derby, United Kingdom

Investigations into the thermodynamic processes in labyrinth seal flow fields have been carried out using the nonintrusive optical technique of holographic interferometry. Labyrinth seals in the form of two-dimensional actual size models were used. The types of seal geometry tested reflected those in current use in aerogas turbines, their sizes being typically 10 mm × 20 mm in section with sealing constrictions as small as 0.25 mm. The tests provided a great deal of information that had not previously been available and confirmed several experimental and theoretical results that were not fully understood. The data were obtained in the form of isodensity contour maps. These full field density measurements of the test section flow were analyzed in several ways to provide an insight into the processes occurring within the labyrinth seal. The effects of kinetic energy carry-over upon seal stage performance were dramatically demonstrated in both straight-through and stepped seals. Useful qualitative, as well as quantitative, information regarding the flow field structure could be obtained from the isodensity maps. An indication of particular flow features was obtained at a glance. The optical technique was found to be ideally suited to the investigations and the expected difficulties associated with working in the very small test sections did not arise. The configuration of the optical system ensured that image aberrations were minimized and temporal flow instabilities did not adversely affect the isodensity contour maps. The paper reviews the optical technique and presents a selection of the holographic results along with their interpretation.

Introduction

In recent years the search for improved efficiencies from gas turbine systems has intensified, nowhere so much as in the civil aviation field where fractions of a percent improvement in fuel efficiency can mean important savings to an airline and greater market strength for engine producers. Improvements in efficiency have been sought in all areas and every last detail examined. In high bypass gas turbine power plants the internal air flow away from the core gas stream represents a major source of loss. Some of this flow is undesirable leakage due to an inability to affect the total closure between adjacent pressure zones. The other portion leaving the internal flow is used purposefully to cool engine components, prevent hot gas ingestion into the disk spaces in the turbine, and to prevent oil leakage from bearing chambers. In all these cases the flow levels need to be kept as low as possible. In controlling these flows labyrinth seals play a major role. They enable sealing to be affected between rotating and static components without mechanical contact or wear. This is achieved by having a series of small, annular constrictions formed by fins adjacent to a lining material. The flow-induced dynamic pressure losses through these small passages produce the blockage.

Early investigations into labyrinth seal performance concentrated on obtaining empirical relationships between pressure difference and flow level (Stodala, 1927). This was reasonable for the seals in steam turbine plants, which consisted of 20 or more stages. Their size and weight was no problem in these large power units. The advent of the aerogas turbine meant lighter, more compact and efficient sealing was required. Notable among works to try and improve the understanding of labyrinth seal operation was Jerie (1948). In his formulations on straight-through labyrinths, he took into consideration the effects of discharge factor, diffusion angle of the stream, turbulent mixing, and vorticity in between seal constrictions. Yet he took no account of compressibility and examined the flow only on a macroscopic scale, keeping many factors constant throughout the seal length. Jerie's work was wholly concerned with straight-through labyrinths and so would not be applicable to seal designs that were generically different. Even though work has been carried out to try to determine both analytically and experimentally the values of important flow parameters, e.g., Vermes (1961), it is thought that this approach holds limited promise in producing global solutions to labyrinth seal flow characteristics.

Contributed by the International Gas Turbine Institute and presented at the 33rd International Gas Turbine and Aeroengine Congress and Exhibition, Amsterdam, The Netherlands, June 5-9, 1988. Manuscript received by the International Gas Turbine Institute September 15, 1987. Paper No. 88-GT-45.

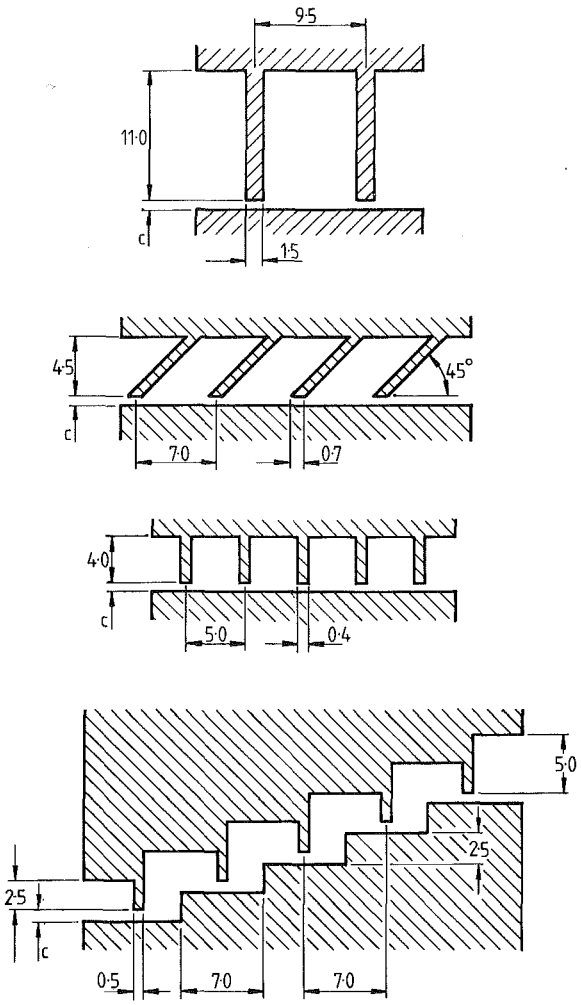

Fig. 1 Seal types tested, two-stage straight-through, four-stage inclined fin, five-stage straight-through, and five-stage stepped

A technique is needed that can account for changes in the flow on a microscopic scale and thus follow accurately alterations in the flow caused by variations in the seal geometry or configuration. Numerical techniques now in use and programmed on computers make available methods of predicting flow conditions within complex regimes on a point-by-point basis (Wittig et al., 1987). But, because almost all seal flows contain some recirculatory elements and numerical techniques find some difficulty in computing such cases, it is essential to have a means of validating the numerical solution. Such validation by experimental means ought to cover the whole field and be readily carried out. The method of holographic interferometry used during the tests presented here is one means of achieving this. The technique of laser anemometry has been used to obtain data from labyrinth flow fields (Stoff, 1980), but it is only a point-by-point measurement and suffers from problems of access to the test volume.

Experimental Arrangement

The tests were conducted upon two-dimensional models of actual size (Fig. 1). These fitted into a small flow rig across which could be set various flow conditions. Uniform inlet velocity was ensured by a long diffusing section, with the outlet side exhausting to ambient pressure and temperature. Optical access to the test section was via two acrylic end windows (50 mm × 50 mm). These were manufactured with sufficient thickness so that internal pressurization of the test section would not cause an increase in physical pathlength for light passing through the seal of greater than $\lambda/8$ and thus produce error fringes in the interferograms.

Four seal types were investigated during the study. These were a two-stage straight-through seal, a five-stage straight-through seal, a four-stage straight-through seal with fins inclined against the flow, and a five-stage stepped seal that could pass flow in both directions (Fig. 1). These seals were all representative of actual size seals from engine configurations. The five-stage straight-through seal was tested with both a plain facing material and an open honeycomb material having a cell size of 2 mm across corners. All the other seal types were tested against plain facings.

For each seal type and configuration the flow characteristic of Q versus P_0/P_n was measured (Figs. 2 and 3). These allowed comparisons to be made between different seal types and individual clearance settings while interpreting the changes with regard to the experimental isodensity contour maps. For each test build, isodensity contour maps were obtained for a range of clearance settings and pressure ratios across the seal.

The validity of carrying out flow tests on two-dimensional seals as opposed to rotating three-dimensional components has long been accepted. As well as being more economical, the nondimensional flow characteristics are comparable with those obtained in three-dimensional rig test situations. It is also much easier to measure accurately the flow and seal conditions in static, two-dimensional models than it is on rotating, three-dimensional seals. This means that comparisons can be made with a much better certainty and small variations in seal performance monitored. Experimental verification of this is provided by Stocker (1978), where for stepped seals, variations of on average only 1.7 percent are observed between static tests and tests on seals rotating with tangential velocities of 239 m/s. It is only in regimes of low Reynolds number and high Taylor number that rotational effects become important (Stoff, 1980), yet in most aerogas turbine applications we have the reverse situation.

Holographic Technique

Holographic interferometry has been applied to the visualization and measurement of fluid flow with great success for at least 15 years. A double exposure hologram of the changing flow produces an interference pattern of dark and bright fringes. These fringes contour changes in the refractive index within the flow. The contours of refractive index in turn map out changes in the density of the fluid as isodensity contours. The technique and its many subtle variations are well documented in the literature (e.g., Vest, 1979; Jones and Wykes, 1983).

Nomenclature

A = geometric flow area, m^2
c = seal constriction height, m
C = Gladstone–Dale constant, m^3/kg
i = seal well number
L = width of test section, m
m = mass flow rate, kg/s
n = total number of seal constrictions
N = fringe number
p = static pressure, N/m^2
P = total pressure, N/m^2
Q = mass flow function = $m \cdot T^{1/2}/A \cdot P_0$, $s \cdot K^{1/2}/m$
R = specific gas constant, $J/kg \cdot K$
T = total temperature, K
γ = adiabatic index
λ = wavelength of light, m
ρ = gas density, kg/m^3
i = seal well number
n = total number of constrictions
0 = inlet condition

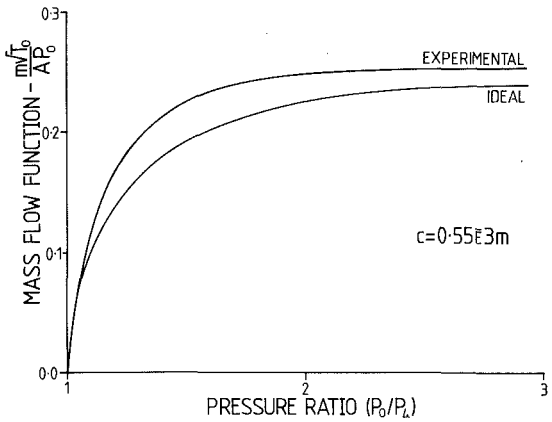

Fig. 2 Flow characteristics for four-stage inclined fin straight-through seal

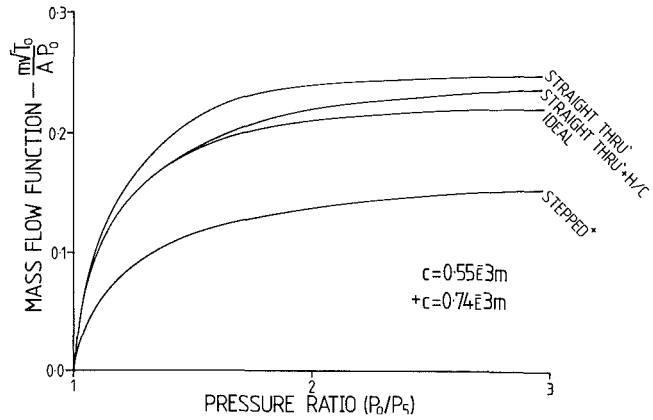

Fig. 3 Flow characteristics for five-stage seals

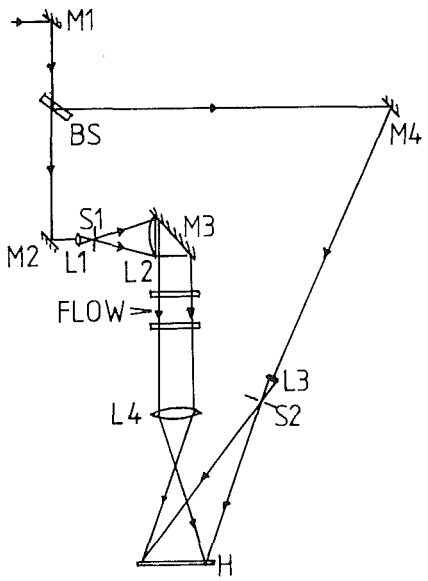

Fig. 4 Holographic recording system (M = mirror, L = lens, BS = beam splitter, S = spatial filter, H = hologram)

The specific technique used in this study was image-plane holographic interferometry. This is particularly suited to the examination of two-dimensional flows in which changes in density are constant along any particular ray passing perpendicularly through the flow. Previously, image-plane holographic interferometery has been successfully applied to flow in two-dimensional turbine cascade profiles (Bryanston-Cross et al., 1981). The test section in the study presented here was

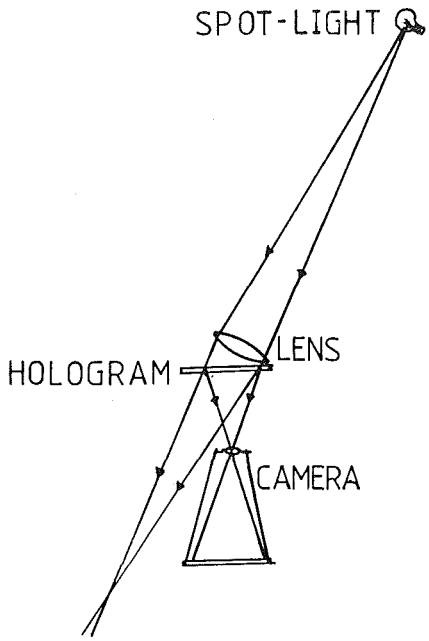

Fig. 5 Holographic reconstruction system

particularly small, 40 mm × 20 mm, with seal constrictions as small as 0.25 mm × 0.50 mm. The expected problems of diffraction obscuring the fringe patterns did not materialize due to careful collimation and alignment of the laser beam traversing the test section.

The optical system shown in Fig. 4 (Parker and Brownell, 1986) for recording the holograms used an argon ion laser giving up to 600 mW of light at a wavelength of 514.5 nm. Holograms of the test section could have been recorded using a laser having an output power two orders of magnitude less than that used, but the high power of the argon ion laser allowed exposure times to be kept very short (≃ 1/25th s). This minimized the effect of temporal instabilities in the flow. Part of the laser output was directed into the reference beam. This was expanded and spatially filtered into a cone of light to fall directly onto the hologram plate. The remainder of the laser output formed the object beam. This was expanded, spatially filtered, and collimated to pass perpendicularly through the test section. The flow field was imaged by a single element lens with a magnification of ×4 onto the 100 mm × 120 mm holographic plate. The coherent recombination of the object and reference beams at the photographic plate forms a complex microscopic interference pattern, this being the hologram. It is a property of holographic recording that two or more holograms may be recorded on a single piece of film; this fact allows easy recording of double exposure holographic interferograms, without the need to go to complex real-time holographic or conventional interferometry. The first exposure records the no-flow state of the seal and the second exposure records the altered density field with flow passing through the seal.

Following development and bleaching of the doubly exposed photographic plate in a conventional manner, the phase hologram, as it had now become, was reconstructed using a simple white-light source (Fig. 5). White-light reconstruction, made possible by the image-plane technique, has several advantages, the principal one being the removal of the characteristic laser speckle seen in coherent reconstructions. The isodensity contour patterns were photographed for ease of reference and the glass holographic plates archived for future use.

Figure 8 shows a reconstruction of a typical double exposure hologram. The first exposure was recorded with zero pressure difference across the seal and thus no air flowing. The second exposure was recorded immediately afterward on the same

Table 1 Thermodynamic values for holographic fringes

PROCESS	Δρ (kg/m³)	ΔP (kPa.)	ΔT (K.)
P1=100 kPa. T1=290 K.			
ISOTHERMAL (Ambient)	0.0223	1.84	0.00
ISOBARIC (Ambient)	0.0223	0.00	−5.21
ISENTROPIC (Ambient)	0.0223	2.59	2.10
P1=200 kPa. T1=290 K.			
ISOTHERMAL (High Pressure)	0.0223	1.84	0.00
ISOBARIC (High Pressure)	0.0223	0.00	−2.62
ISENTROPIC (High Pressure)	0.0223	2.59	1.06

holographic plate with a pressure difference across the seal. The fringes depict isodensity contours. Close spacing indicates rapid changes in density perpendicular to the fringes. It must be kept in mind that the fringes are not streamlines, flow patterns, isobars, or isotherms. Interpretation of particular fringe patterns is presented later in this paper and an analysis of fringe formation and therodynamic relationships is given in the following sections.

Thermodynamic Interpretation

It has been shown previously (Parker and Brownell, 1986) for the image plane hologram used in our tests that the fringe order $N(x, y)$ at any point in the image (x, y) can be expressed directly as a function of the density change $\Delta\rho\ (x, y)$ between the two exposures as

$$N(x, y) = \Delta\rho(x, y) \cdot C \cdot L/\lambda \tag{1}$$

For our test arrangement the wavelength λ was 514.5 nm. The test section length L was 101.6 mm and the Gladstone–Dale constant C for air at 288 K with the above wavelength of light is 0.2273 × 10E-3 m³/kg. This gives a density interval from one fringe to the next of $\Delta\rho$ = 0.0223 kg/m³. This is approximately 1.8 percent of the ambient density and demonstrates the sensitivity of the technique.

Assuming that air obeys the perfect gas equation

$$P/\rho = R \cdot T \tag{2}$$

then the fringe patterns can be used to derive other thermodynamic parameters. Before this is possible and in the absence of a second measured parameter, a decision has to be taken as to the processes taking place within the gas flow. These, for simplicity and to tie in with the "ideal" labyrinth seal flow, are taken to be the isobaric, isothermal, and isentropic processes.

Considering two arbitrary points in the flow, at a particular instant the changes in thermodynamic properties, ΔP, ΔT, $\Delta\rho$, will give rise to

$$P2 = P1 + \Delta P; \quad T2 = T1 + \Delta T; \quad \rho1 = \rho2 + \Delta\rho \tag{3}$$

Equations (2) and (3) give

for an isobaric process

$$\Delta T/T1 = -\Delta\rho/(\rho1 + \Delta\rho) \tag{4}$$

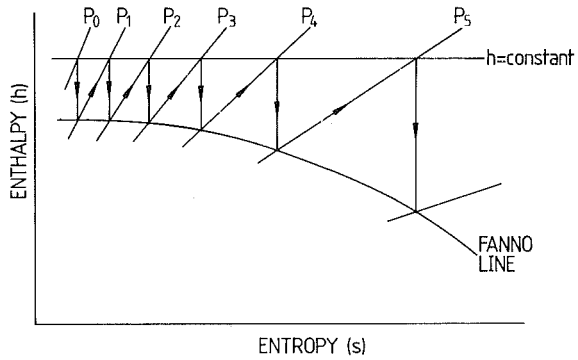

Fig. 6 Fanno curve

for an isothermal process

$$\Delta P/P1 = \Delta\rho/\rho1 \tag{5}$$

for an isentropic process

$$\Delta P/P1 = ((1 + \Delta\rho/\rho1)^{\gamma}) - 1 \tag{6}$$

$$\Delta T/T1 = ((1 + \Delta\rho/\rho1)^{(\gamma-1)}) - 1 \tag{7}$$

These relationships apply between any two points in the flow rather than between adjacent fringes as for the analysis presented previously by Parker and Brownell (1986). For each process the contour interval represented by one fringe order may be calculated. Typical examples are shown in Table 1 for $P1$ = 100 kPa, $T1$ = 290 K and also $P1$ = 200 kPa, $T1$ = 290 K.

"Ideal" Seal Flow

The concept of an "ideal" labyrinth seal is one that proves to be useful in understanding the behavior of actual labyrinth seals and may be taken as a suitable yardstick against which to judge different seal types. The purpose of a labyrinth seal is chiefly to provide the lowest possible mass flow through it, this being balanced against operating parameters of pressure difference, seal running clearance, and the space available to affect sealing. Where room to accommodate the seal is limited more complex seal designs become necessary. Depending upon the geometry, the actual seal flow may be greater than or less than that of an equivalent ideal seal. The ideal seal comprises a series of constrictions and expansion chambers, through which the flow successively accelerates and expands. The following assumptions are made:

(*a*) the flow in each constriction is isentropic
(*b*) the kinetic energy generated at each constriction is recovered as heat during an isobaric process in the downstream expansion chamber
(*c*) the inlet velocity to each constriction is zero
(*d*) the flow is adiabatic
(*e*) the gas flowing through the seal obeys the perfect gas law

These considerations give rise to the well known Fanno curve (Fig. 6) (Kearton, 1952). Here the gas undergoes a series of isentropic accelerations and isobaric diffusions back to its initial enthalpy line.

The conditions listed above are also used in deriving the St. Venant–Wantzel equation of mass flow function, $Q = (m \cdot T^{1/2})/(A \cdot P)$, for a single restriction. Continuity allows this to be extended to the determination of pressure distribution through a seal of n stages; see Appendix I. These relationships involve the thermodynamic flow parameters, the geometric flow area, and number of sealing stages. No account is made of seal geometry from which arise the differences in actual flow levels and pressure distributions. The "ideal" seal flow characteristics and seal well pressure distributions for the tests on four and five-stage seals are shown in Figs. 2, 3, and 7,

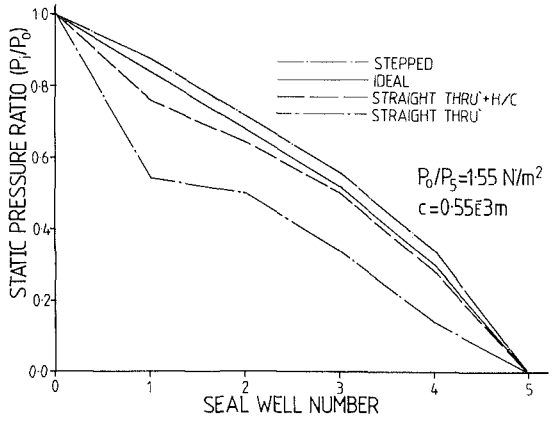

Fig. 7 Pressure distributions for five-stage seal

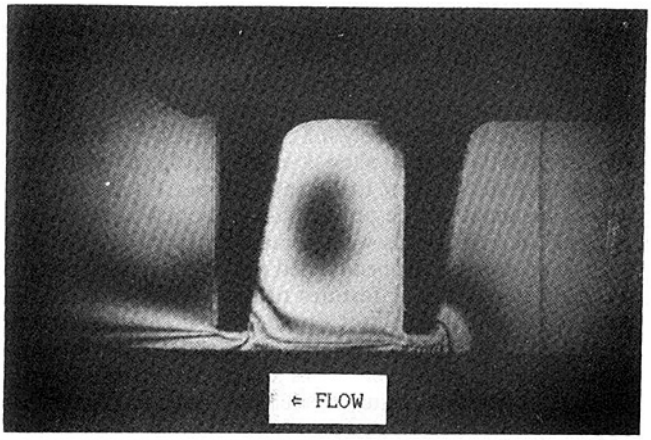

Fig. 8 Two-stage straight-through seal, static versus flowing; P_0/P_1 = 1.27, c = 0.8 mm

along with experimentally derived results for several actual seals. The experimental pressure distributions are based on isothermal fringe counting between adjacent seal wells. The deviation from "ideal" behavior is caused by the opposing effects of discharge coefficient and velocity carry-over factor. Discharge coefficient advantageously reduces the geometric flow area, while the velocity carry-over factor adversely indicates a nonzero inlet velocity to the sealing restriction.

In examining labyrinth seal isodensity maps obtained from our tests, it was hoped to find out why the flow levels and pressure distributions do not match those expected from predictions based on the above thermodynamic grounds. Understanding what causes an actual labyrinth seal to pass more or less flow ought to aid in better design, use, and optimization of these components.

Experimental Results

In the past when conducting experiments on two-dimensional turbine cascades, it has been possible to make the valid assumption of isentropic flow across the whole region. However, it is the nature of labyrinth seals to be loss-inducing components. As such no one single process can be uniquely assigned to the flow through the seal. Fringe audits of the seal flow interferograms (Parker and Brownell, 1986) support the assumption made from the Fanno curve (Fig. 6) that the flow as a whole, when considered between inlet and outlet, is indeed isothermal. However, the Fanno curve also indicates that the flow through the seal constrictions should be isentropic, followed by an isobaric expansion into the seal wells. Thus the problem arises that with only a single parameter defined by the interferograms and with no knowledge of where, if at all, the exact transitions between flow types occurs, it is necessary

Table 2 Pressure distribution through a two-stage seal

	PRESSURE DROP (kPa)	
CONSTRICTION	#1	#2
EXPERIMENTAL FRINGE AUDIT	18.4	9.2
ST. VENANT-WANTZEL PREDICTION	12.7	14.6

to make some assumption as to the positions of these boundaries. The flow regimes assumed in various parts of a labyrinth seal are highlighted in the descriptions of the test results.

Two-Stage Straight-Through Seal. A good appreciation of the conditions pertaining within a labyrinth seal can be gained by studying the density distribution across a two-stage straight-through seal. A typical test case is shown in Fig. 8 where the flow is from right to left, with a pressure difference between inlet and outlet of 27.2 kPa. For a quick and easy analysis it is convenient to make the assumption that the flow is isothermal overall. By doing this we can ascribe to the fringe orders a pressure level and in so doing gain some insight into the overall pressure distribution. Indeed the isothermal assumption is seen to provide a good approximation with which to carry out initial analysis of the flow fields. A total of 15 fringes occurs between inlet and outlet, giving a calculated pressure drop of 27.6 kPa. The 1.5 percent error is well within the expected error level associated with manual fringe analysis.

At the first seal constriction a large fall in density is evident, the calculated Mach number at the exit from this first constriction being approximately 0.45. It is within this region that isentropic flow conditions are taken to exist. Within the expansion chamber downstream of the first constriction are several fringes parallel to the flow direction. These occur as the flow diffuses isobarically into the chamber and increases in static temperature. In the main body of the expansion chamber is a closed circular region of low density. This is evidently an area of recirculation driven by the main flow path along the seal wall. A further density fall is observed across the second constriction along with another region of expansion in the exiting jet downstream of this constriction.

The most interesting point to arise from this test is the imbalance of density/pressure drop between the two constrictions. This is attributed to the detrimental effect of velocity carry-over at the inlet plane of the second constriction. The extent to which carry-over alters the pressure distribution can be seen by comparing the experimental pressure drops with those predicted by the St. Venant–Wantzel equation (Table 2).

Four-Stage Inclined Fin Straight-Through Seal. The inclination of the sealing fins against the flow direction is known to give a reduction in flow relative to that of a seal with fins in an upright position. It is commonly held that attachment of the flow to the downstream face of the seal fin encourages the flow to diffuse more completely into the seal expansion chamber. The improved diffusion in turn leads to a lower carry-over velocity at the next constriction. This, coupled with a decrease in discharge coefficient, acts to lower the flow characteristic of this type of seal. The seal investigated during our testing had four seal fins that were inclined at 45 deg to the flow direction and had an included angle of 10 deg. During the testing some unexpected conditions were found to exist. Whereas all previous tests on other seal types had shown no evidence of temporal instability in the flow, the inclined fin seal exhibited harsh and rapid fluctuations in the flow. This situation was originally seen as a blurring of fringes in the

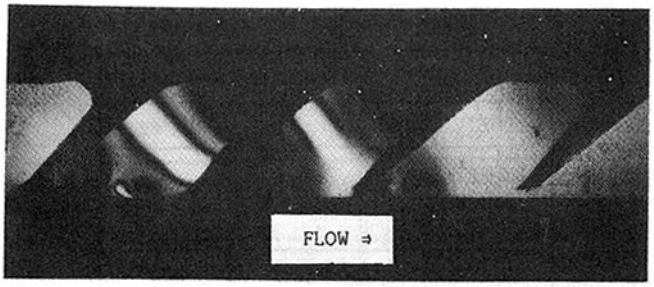

Fig. 9 Four-stage inclined fin seal, double exposure flowing; P_0/P_1 = 1.54, c = 0.55 mm

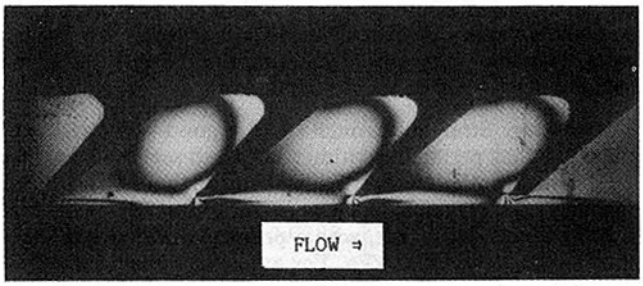

Fig. 10 Four-stage inclined fin seal, static versus flowing; P_0/P_1 = 1.27, c = 0.55 mm

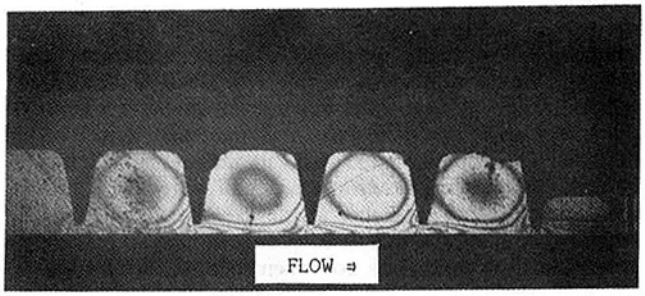

Fig. 11 Five-stage straight-through seal, plain facing static versus flowing; P_0/P_1 = 1.50, c = 0.55 mm

double exposure static versus flowing interferograms. The recording period in these original tests was too long to freeze the changes in flow. A double exposure of the flowing condition, separated by a short time interval (typically 0.5 s) shows the nature of the flow variation (Fig. 9). The change in flow within the seal wells is ordered and its magnitude varies from well to well. In this instance it is greatest in the first well, as shown by the fringes lying perpendicular to the fin inclination. This pattern of fringes suggests a change in vortex strength within the wells, centered about their midpoints.

By shortening the exposure time for recording the hologram by a factor of eight, it was possible to record an interferogram showing the static versus flowing density changes (Fig. 10). The degree of flow attachment to the downstream face of the fins is only small and it could well be that it is the flow instability that is responsible for the favorable flow characteristic of the inclined fin seal as the pressure ratio across it is increased. The pressure distribution through this seal, determined again by isothermal fringe counting, appears unbalanced in a manner similar to the five-stage straight-through seal (Fig. 7). The carry-over factor is seen to affect the second constriction adversely and so produce a large pressure drop across the first constriction.

Further understanding of the flow structure within the inclined fin labyrinth seal was obtained by a real-time holographic technique (Parker and Gates, 1979). This used thermoplastic hologram recording materials to allow in-situ formation of a reference hologram, and when coupled to a high-speed video system having a maximum framing rate of 12,000 Hz the dynamic fringe patterns could be frozen. The slowed down video images showed a clearly defined vortex in each seal well that was fluctuating in strength in a periodic fashion. The temporal changes in vortex strength in each seal well occurred out of phase with each other, suggesting some form of coupling betwen these variations. It is suggested that the reason for the cyclic nature of the flow variation might be the attachment and breakdown of flow along the downstream face of the seal fins. Breakdown of flow attachment from one downstream face leads to a change in flow conditions at the inlet to the next constriction and so to breakdown of attachment to that fin downstream face.

The consequences of such a high-frequency flow instability could be serious in an engine, not only in terms of high noise levels, but also for mechanical integrity at a resonant condition. Further investigation is necessary into this phenomenon so that it can be fully understood and its possibly harmful effects avoided.

Five-Stage Straight-Through Seal—Plain Facing. Testing of the five-stage straight-through labyrinth seal, with the geometry shown in Fig. 1, was carried out. Typically the clearance was 0.58 mm with an operating pressure drop of 54.4 kPa, across the whole seal. Fringe patterns within the seal constrictions, an area approximately 0.6 mm high and 0.5 mm long, were sufficiently clear to allow a quantitative examination of the pressure distribution to be carried out. Taking the isothermal assumption, the pressure distributions from the holographic interferograms were comapred to the St. Venant–Wantzel predictions, Appendix and Fig. 7. The fringe pattern in Fig. 11 shows similar features to the two-fin seal, i.e., isentropic pressure drop across the fins, isobaric diffusion into the seal well, a vortex in the seal well, and a point of flow stagnation on the upstream face of all seal fins except the first. The most interesting feature of this five-stage seal is the distribution of pressure drop. This is plotted in Fig. 7 compared to the St. Venant–Wantzel prediction. The affect of carry-over is seen to reduce the effectiveness of the second sealing gap greatly and to place a disproportionate reliance upon the first constriction's performance. Sealing gaps downstream of the second are uniformly effective as the carry-over becomes more or less constant. Our observations confirm those made by Komotori (1961) showing them to be valid, having removed his uncertainties concerning instrumentation of the flow.They also show good correlation to the predictions of Wittig et al. (1987).

The flow characteristic of the five-stage straight-through seal does not compare favorably with that of the "ideal" seal (Fig. 3). This shows again the detrimental effect that the carry-over has upon the seal's performance and flow characteristics, even in the presence of the opposing discharge coefficient.

Five-Stage Straight-Through Seal With Honeycomb Facing. It has been known for some time that the facing material up against which the seal fins are placed can affect the flow characteristics of a particular seal type. One such material is an open-celled honeycomb. This has two advantages over the normal smooth metal facings. Firstly, growths in radial dimensions during engine operation can be tolerated to a greater extent, allowing tighter build clearances. Secondly the flow through the seal is substantially reduced, at all but very small clearances, with such honeycomb materials (Fig. 3). However it has never been ascertained why the flow in a honeycomb faced seal should be so affected. Our testing with a fine-celled honeycomb (2 mm across corners) shows a significant change in density distribution (Fig. 12), compared to that of a plain walled seal as described in the previous section.

Degradation in the rig windows has obscured the final constriction, but knowing the pressure differential set and isothermal fringe interval it is possible to determine that seven fringes are obscured. Firstly it is observed that the pressure

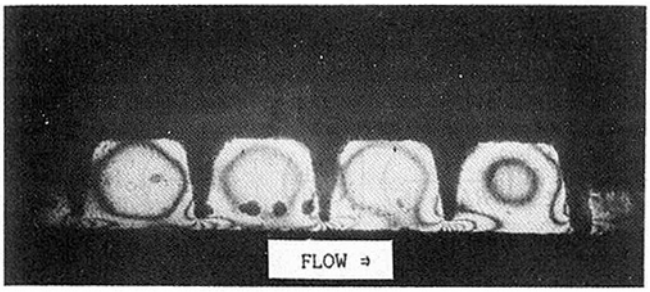

Fig. 12 Five-stage straight-through seal, honeycomb facing, static versus flowing; $P_0/P_1 = 1.55$, $c = 0.55$ mm

distribution through the seal has been affected (Fig. 7), especially in the region of the first two constrictions. This change can be attributed to a major reduction in the carry-over velocity seen at the second constriction. Evidence of this reduction in carry-over is seen in the density pattern of the jets emanating from the constrictions. The density contours have taken on a rounded form and do not extend as far into the seal well as in the case of the plain facing (cf. Fig. 11). Also, the stagnation fringes on the upstream faces of the fins are not so pronounced. These factors would suggest a faster diffusion of the flow caused by the action of the honeycomb structure upon the constriction and wall flows.

As a result of modifying the pressure distribution in the seal the honeycomb gives a reduced flow level (Fig. 3). The closer correlation to the "ideal" characteristic is taken to be a direct result of the improved pressure distribution; each sealing constriction operates closer to the "ideal" in terms of pressure drop.

Five-Stage Stepped Seal. In the majority of labyrinth seal designs the most detrimental factor as regards flow levels is the degree of kinetic energy carry-over seen at the constriction inlets. The stepped seal design aims to prevent carry-over by placing a blocking feature downstream of each constriction. This prevents direct impingement of the diffusing jet upon the next sealing constriction. The beneficial effect of this is illustrated in Fig. 3 where flow characteristics for the stepped seal are compared to those for the straight-through seal type.

The interferograms obtained for the five-stage stepped seal show much more complex fringe patterns than for the straight-through seals. A typical density map is shown in Fig. 13. This was tested at a pressure differential of 81.6 kPa across the seal and a clearance of 0.7 mm. The fringe pattern is well defined and other tests verify that the flow is temporally stable. Within each seal well is a similar fringe pattern that varies only in strength from well to well. Beneath the seal fin a set of closely packed fringes indicates rapid acceleration of the flow in a presumably isentropic manner. Issuing from the seal constrictions are several fringes running parallel to the flow direction. These are associated with an isobaric rise in temperature as the flow diffuses into the seal well. These fringes are seen to turn up into the seal well, as the flow continues to diffuse and is turned by the front of the step. Within the main body of the seal well there are two points of flow stagnation/division and two areas of recirculation. The larger and weaker recirculation lies on the downstream face of the seal fins and the smaller but stronger recirculation is positioned on the front part of the step. The first stagnation point occurs at the top of the seal well where the flow, deviated by the front face of the step, divides. The second point of stagnation is positioned immediately upstream of the seal constriction. This is particularly important as it portrays the nature of the flow at a critical point in the seal. For such a significant stagnation to be present the flow must be running substantially parallel to the upstream face of the fin. Thus, there will be negligible axial velocity to the flow at the inlet to the seal constriction

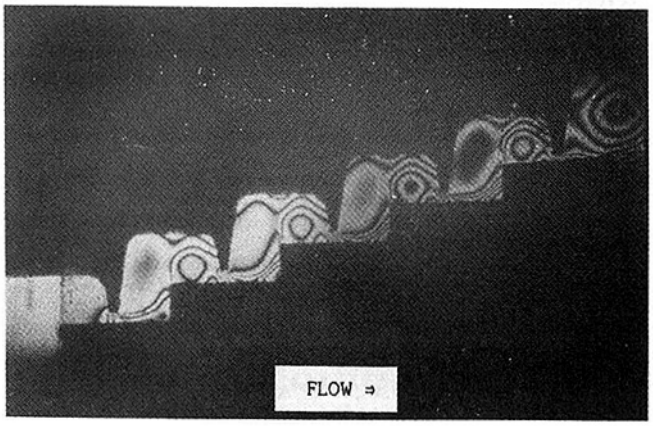

Fig. 13 Five-stage stepped seal static versus flowing; $P_0/P_1 = 1.82$, $c = 0.74$ mm

and to a major extent the effect of carry-over has been overcome. An additional point of stagnation, which is of little interest, is present in the step corner.

The pressure distribution through the stepped seal is markedly different from that for a straight-through seal type having the same number of stages. The fall in pressure through the seal is shown in Fig. 7 compared to that for the "ideal" seal and straight-through seal. It is seen that the effect of carry-over on the pressure distribution is minimized by the stepped configuration.

The introduction of the step into the seal design does introduce an additional parameter to be considered. This is the axial position of the seal fin in relation to the edge of the step. In particular areas of an engine this can be a crucial factor due to differential axial growth of shafts. Tests indicate that the changes in flow level with axial clearance are due to the way in which the step causes the flow emanating from the downstream constriction to deviate. Results show that as the distance between the plane of the sealing constriction and the upstream step edge decreases the flow passed by the seal also decreases. The interferograms show that at these positions the flow has to turn more rapidly around the upstream step edge vortex and so presents itself less favorably to the following seal constriction. However, at positions very close to the step edge the seal geometry again approaches the straight-through case and an increase in flow is observed.

Conclusions

The objective of the work presented here was to begin building a data base for the validation and extension of current and future analysis of labyrinth seal performance. The technique of holographic interferometry is seen to be widely applicable to all types of seals with great success. Even though quantitative analysis of the fringe patterns was not exhaustive, it has been shown that the results thus obtained were of considerable importance and gave a new, more confident insight into the functioning of labyrinth seals.

The technique is not only applicable to labyrinth seal flow fields, but it could be readily used in other, similar investigations, e.g., wall cooling of combustion systems using actual size two-dimensional models.

Acknowledgments

The authors would like to thank the U.K. Ministry of Defence Procurement Executive who provided the funding for this research into labyrinth seal flow fields and would also like to express their gratitude to Rolls-Royce plc for allowing publication of this work.

References

Bryanston-Cross, P. J., Lang, T., Oldfield, M. L. G., and Norton, R. J., 1981, "Interferometric Measurements in a Turbine Cascade Using Image-Plane Holography," ASME JOURNAL OF ENGINEERING FOR POWER, Vol. 103, pp. 124–130.

Jerie, J., 1948, "Flow Through Straight-Through Labyrinth Seals," *Proceedings of the 7th International Congress of Applied Mechanics*, Vol. 2, pp. 70–82.

Jones, R., and Wykes, C., 1983, *Holographic and Speckle Interferometry*, Cambridge University Press, Cambridge, United Kingdom.

Kearton, W. J., 1952, "Leakage of Air Through Labyrinth Glands of Staggered Types," *Proc. IMechE.*

Komotori, K., 1961, "Probleme bei Labyrinth-Stopfpuchsén," *Proc. of the Fujihara Memorial Faculty of Engineering*, Keio University, Vol. 14, No. 54, pp. 1–48.

Parker, R. J., and Brownell, J. B., 1986, "Holographic Flow Visualization Applied to Very Small Flow Sections in Turbomachinery Research," *Society of Photo-Optic Instrumentation Engineers (SPIE)*, Vol. 599.

Parker, R. J., and Gates, J. W. C., 1979, "An Investigation of the Instabilities in Photometric Standard Lamps by Holographic Interferometry," *Journal of Physics E*, Vol. 12, p. 18.

Stocker, H. L., 1978, "Determining and Improving Labyrinth Seal Performance in Current and Advanced High Performance Gas Turbines," AGARD-CP-237 Conference Proceedings, pp. 13/1–13/22.

Stodala, A., 1927, *Steam and Gas Turbines*, McGraw-Hill, New York.

Stoff, H., 1980, "Incompressible Flow in a Labyrinth Seal," *Journal of Fluid Mechanics*, Vol. 100, Part 4, pp. 817–829.

Vermes, G., 1961, "A Fluid Mechanics Approach to the Labyrinth Seal Leakage Problem," ASME JOURNAL OF ENGINEERING FOR POWER, pp. 161/169.

Vest, C. M., 1979, *Holographic Interferometry*, Wiley, New York.

Wittig, S., Schelling, U., Kim, S., and Jacobsen, K., 1987, "Numerical Predictions and Measurements of Discharge Coefficients in Labyrinth Seals," ASME Paper No.87-GT-188.

APPENDIX

St. Venant–Wantzel Equation for a Single Orifice

Using the assumptions made for defining the "ideal" labyrinth seal, the St. Venant–Wantzel equation for the mass flow function of a single orifice can be derived as

$$\frac{m \cdot T_0^{1/2}}{p_0 \cdot A} = \left(\frac{2 \cdot \gamma}{R(\gamma - 1)}\right)\left[\left(\frac{p_1}{p_0}\right)^{2/\gamma} - \left(\frac{p_1}{p_0}\right)^{(\gamma+1)/\gamma}\right]^{1/2}$$

where

T_0 = total temperature at inlet
p_0 = inlet static pressure
p_1 = outlet static pressure

For a series of single constrictions, considering continuity of mass flow and taking T_0, A, R, γ to have constant values throughout, then

$$\left(\frac{m}{A}\right)\left(\frac{R \cdot T_0(\gamma - 1)}{2 \cdot \gamma}\right)^{1/2} = p_i\left[\left(\frac{p_i}{p_j}\right)^{2/\gamma} - \left(\frac{p_i}{p_j}\right)^{(\gamma+1)/\gamma}\right]^{1/2}$$

where $i = j + 1$.

Predicting Gas Turbine Performance Degradation Due to Compressor Fouling Using Computer Simulation Techniques

G. F. Aker[1]
Research Assistant.

H. I. H. Saravanamuttoo
Professor,
Mem. ASME

Department of Mechanical and Aeronautical Engineering,
Carleton University,
Ottawa, Ontario

As part of an ongoing investigation into the effects of compressor fouling on gas turbine performance, the stage stacking technique was used in conjunction with generalized turbine characteristics to simulate the performance of two common pipeline engines, the G. E. LM2500 and the Solar Centaur. A linear fouling model was introduced that simulates the progressive buildup of contaminants in the compressor by modifying the appropriate stage flow and efficiency characteristics in a stepwise fashion. This simulation of the onset and progressive nature of compressor fouling allows quantitative analysis of performance deterioration to be performed on the basis of trends noted in monitored parameters. A preliminary study into how severely a given level of fouling will affect engines of different size indicated that stage loading may be the more critical parameter.

Introduction

Background. The fouling of gas turbine compressors is recognized as one of the most common causes of engine performance deterioration facing users today (Upton, 1974). It is now apparent that even units operating in the benign atmosphere of rural or nonindustrial settings can still become fouled. Typically, dust, insects and pollen are the culprits, which when mixed with engine exhaust and oil vapors from both internal and external leaks, form a sticky mass that readily adheres to the blading and annulus areas of the compressor. The principal effects of compressor fouling are reduced power output and increased heat rate. More insidious effects include an increase in the turbine inlet temperature at a given power setting and a decrease in the compressor surge margin.

However, because the principal effect of compressor fouling is a reduction in power output and an increase in heat rate, neither of which is usually measured, many engines operate for significant periods of time in a fouled and thus uneconomic condition. Initially, this was not a significant problem in that fuel was relatively inexpensive and regularly scheduled maintenance took care of the problem before it reached the critical point. Presently, oil and gas prices are such that previously insignificant inefficiencies have been translated into considerable additional operating costs.

The solution to this problem was to perform regularly scheduled compressor washes. If, however, regularly scheduled washes are performed too frequently, they can lead to unnecessary expense in terms of down time, increased maintenance costs, and the premature erosion of compressor blade surfaces. Similarly, if the period between compressor washes is too long, the washing procedure may not be sufficient to obtain a complete performance recovery. It is also worth noting that the level of fouling experienced by any particular engine is very much a factor of the "local" or site conditions. Although some users still operate on a system of regularly scheduled compressor washes, usually based on previous operating experience, others have gone to the potentially better system of "on-condition" maintenance (Williams, 1981a).

Engine Performance Monitoring. On-condition maintenance involves monitoring engine operating parameters closely to determine when an engine is operating inefficiently. From this, performance monitoring practices were developed where operating parameters, typically compressor delivery pressure (CDP) and interturbine temperature (ITT), were monitored for deviations from a manufacturer's specified baseline. The deviations from these baselines are then plotted as a function of time to form "trendplots." Significant deviation from a reference line on these trendplots is used as a trigger for maintenance action (Matthee and Saravanamuttoo, 1982; Karanjia and Saravanamuttoo, 1980). In order to be effective, this sort of trend analysis system must be accurate enough to indicate trends in engine parameters in the short term. This does not necessarily require the use of expensive automated equipment, as indicated by Karanjia and Saravanamuttoo (1980); however, in some cases improved instrumentation or readouts may be required because many OEM gages are designed for use as warning systems and not for accurate measurements.

Trend analysis was not the total answer as far as maintenance scheduling was concerned because of difficulties in determining

[1]Presently with TransCanada PipeLines Limited.

Contributed by the International Gas Turbine Institute and presented at the 33rd International Gas Turbine and Aeroengine Congress and Exhibition, Amsterdam, The Netherlands, June 5-9, 1988. Manuscript received by the International Gas Turbine Institute August 1, 1987. Paper No. 88-GT-206.

what the abovementioned deviations in operating parameters meant in terms of actual engine duress (Scott, 1977). Without this knowledge, engines could be removed from service when a compressor wash was the appropriate action. Similarly, because gas turbine maintenance can include expensive down time, the question of how long an engine should operate in an uneconomical condition in order to justify the maintenance costs arises. The key to this problem lies in being able to predict not only *when* engine performance is suffering from compressor fouling, but to what degree the performance deterioration has occurred.

Diagnostics. An important step in developing an on-condition maintenance program is to improve the diagnostic capability of trend analysis. Once the operator knows what trends to look for and what they mean, he can correctly deduce the cause of the problem and initiate the appropriate maintenance action. Several authors have attempted to provide a correlation between changes in monitored parameters and various engine problems with some success (Saravanamuttoo and MacIsaac, 1983; Scott, 1979; Agrawal et al., 1978).

A lot of information in the area of diagnostics has come directly from user experience. However, while experience is valuable in evaluating the possible causes of a problem, it is not as proficient at providing an accurate assessment of the degree of performance degradation being experienced. One method of providing a correlation between deviations in monitored parameters and the level of performance deterioration is by computer simulation. However, because gas turbines can vary so greatly in performance, in order to be meaningful, computer simulations of performance deterioration should be performed on actual engines. In this study, the General Electric LM2500-30 and the Solar Centaur engines were selected for evaluation.

Objectives. This paper presents the results of a study into compressor fouling performed at Carleton University using simulation techniques to:

1 predict the effect of increasing levels of fouling on engine operating parameters,
2 provide a correlation between changes in monitored parameters and changes in power output and heat rate resulting from fouling,
3 determine whether engine size has an effect on how severely an engine will be affected by a given level of fouling.

A Systematic Method for Predicting the Effects of Compressor Fouling

Compressor Performance Simulation Using the Stage Stacking Technique. This paper represents another step in Carleton University's investigation into gas turbine compressor fouling. Previous work by Saravanamuttoo and Lakshminarasimha (1985) outlined the benefits of using the stage stacking technique to evaluate the performance of fouled axial compressors. The most significant advantage offered by the stage stacking technique is that the performance of individual stages can be modified to model various forms of deterioration. By restacking the compressor with the modified stages, the corresponding effect on the entire compressor can be observed. This is particularly important when one is investigating compressor fouling where each stage in the compressor can be affected to a different degree. The stage stacking technique therefore provides a systematic and logical approach to simulating compressor fouling and its effect on engine performance.

The theory behind the stage stacking technique has been well documented and so only a brief outline will be presented here. The reader is referred to papers by Stone (1958), Howell (1978), and Southwick (1974) for further detailed information.

The stage stacking technique employs predetermined stage characteristics, consisting of pressure and temperature rise coefficients as functions of a flow coefficient, to define the performance of a rotor-stator pair or stage. The flow coefficient is defined by the axial velocity and blade speed at any given stage. The value of this flow function defines a stage pressure ratio and temperature rise from the pressure and temperature characteristics and the local flow properties. The stage inlet pressure is then multiplied by this stage pressure ratio to provide the stage exit pressure. In a similar manner, the stage temperature rise is added to the stage inlet temperature to provide the stage exit temperature. These exit conditions are then assumed to be the inlet conditions to the next stage where the process is repeated. This process continues until the final stage in the compressor where exit conditions determine the compressor delivery pressure and temperature.

The selection of stage characteristics is an important aspect of any stage stacking procedure. Obviously, the engine manufacturer's stage performance evaluations would be welcomed; however such information is highly proprietary and is usually unavailable. It is therefore necessary to obtain whatever information is required from data reported in the open literature. From this information a generalized stage characteristic can be derived by normalizing the coefficients to their values at the maximum efficiency point and plotting them on a single graph. The characteristics tend to collapse into a relatively similar curve. The stage performance of any given compressor can then be obtained from this generalized characteristic by multiplying through by the appropriate coefficient values of desired stage.

The performance of the clean compressor was obtained by modifying the stator angles and blockage factors and restacking the compressor until the design speed line intersected the mass flow rate and design pressure ratio specified by the manufacturer. A plot of the compressor maps generated by the stage stacking model for the GE LM2500-30 and the Solar Centaur are presented in Figs. 1 and 2, respectively.

Simulation of Compressor Fouling. In continuing their investigation into compressor fouling, Lakshminarasimha and Saravanamuttoo (1985, 1986) simulated the fouling of individual compressor stages in the NACA five-stage compressor described by Sandercock et al. (1954). This was done by adjusting the stage flow and efficiency characteristics to reflect the loss in performance associated with fouling. While the level of adjustment was somewhat arbitrary, this proved to be a valid method of modeling compressor fouling.

While several authors have investigated the effects of fouling on compressor and engine performance (Saravanamuttoo and MacIsaac, 1983; Saravanamuttoo and Lakshminarasimha, 1985; Lakshminarasimha and Saravanamuttoo, 1986), most of these investigations have dealt with the situation as a present entity. Little work has been done in investigating the onset and progression of fouling to the point where it severely affects engine performance. Discussions with engine users revealed that fouling can progress into 40 to 50 percent of the compressor stages. It therefore becomes necessary to develop a model that can simulate this progression of deterioration.

In order to meet this requirement a linear progressive fouling model was developed. In this model, fouling is assumed to progress in steps, where each step increases the number of stages affected by one and the level of flow reduction by one percent. Therefore extremely light fouling is simulated by a one percent decrease in the flow characteristic on the first stage only. Similarly, the next progressive step in the fouling simulation would involve a two percent reduction in the flow characteristic for the first stage with the one percent reduction in flow being transferred to the second stage. This stepwise progression is repeated until all of the stages in the compressor have been affected.

It was reasoned that the level of the efficiency drop expe-

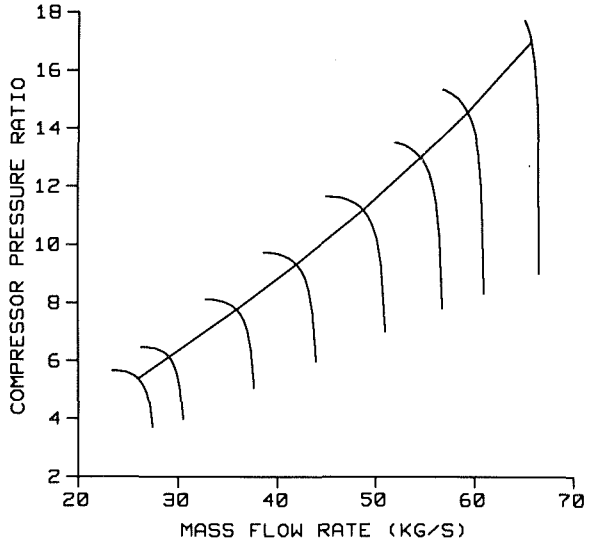

Fig. 1 Predicted LM2500 compressor map

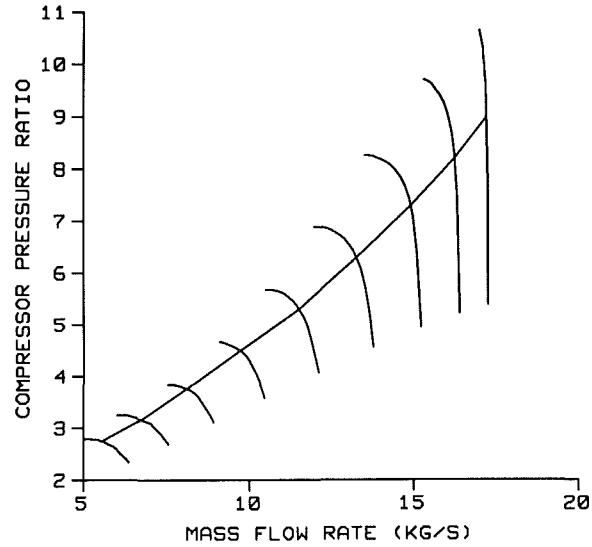

Fig. 2 Predicted Centaur compressor map

rienced by the compressor as a result of fouling would probably be a function of the time since overhaul, the time between washes, and the severity of blade erosion or wear. In order to cover the various combinations of stage flow and efficiency drop in a comprehensive manner, the reduction in stage efficiency was estimated as a function of the percentage of flow characteristic modification. In other words, modeling compressor fouling using only a reduction in the flow characteristic represents the least severe case. The next level of severity was simulated by employing a 0.25 percent drop in the stage efficiency characteristic for every 1 percent drop in the flow characteristic. This progression was repeated at 0.25 percent intervals until both the efficiency and the flow characteristics were modified by one percent per step. It is believed that this fouling model represents the fouling phenomenon reasonably well up to halfway through the compressor. After this point it is likely that the fouling increases more on the first stages than on the later stages as the progression continues through the compressor.

Engine Performance Simulation. Once a compressor map for the engine being simulated had been generated, the performance of the entire engine was modeled by matching the map to generalized turbine characteristics. The matching procedure operated as described by Cohen et al. (1972) with the maximum flow and maximum efficiency of the turbine characteristics being modified until design point specifications for the engines were obtained. This comparison is presented in Tables 1 and 2 for the LM2500 and the Solar Centaur engines, respectively. While it would have been preferable to match the simulation results to an engine operating line, the design points were the only published values available. However, because industrial gas turbines, and in particular those in pipeline use, operate in the 90–105 percent gas generator speed range most of the time, it was felt that the discrepancy induced by this design point matching procedure would be minimal and not affect the trends predicted from this work to any appreciable degree.

Table 1 LM2500 design point specification match

Parameter	Units	Literature	Simulation	Difference
Mass Flow	Kg/s	65.8	65.8	0%
CDP	KPa	1722	1723	0.07%
Power	KW	20134	20163	0.14%
Heat Rate	$\frac{MJ}{KW-HR}$	9.9	10.1	2.43%
EGT	$°C$	504	539	35 $°C$

Table 2 Centaur design point specification match

Parameter	Units	Literature	Simulation	Difference
Mass Flow	Kg/s	17.2	17.2	0%
CDP	KPa	911.7	911.7	0%
Power	KW	2856	2857	0.05%
Heat Rate	$\frac{MJ}{KW-HR}$	13.6	13.3	2.06%
EGT	$°C$	427	428	1 $°C$

The software developed also has the ability to model engines with a variable stator schedule and intake and exhaust losses to allow direct comparison of simulation results to field data.

Model Verification. The performance simulation results were verified using baseline test results provided by NOVA, an Alberta Corporation. This data included output power, SFC, compressor delivery pressure (CDP), and interturbine temperature (ITT) measurements from a "zero time" test of their Solar Centaur located at Meikle River.

The Centaur simulation proved to match the Meikle River data very well as can be seen from Figs. 3 through 7. The ITT data presented in Figs. 5 and 6 do illustrate some variation; however, given their direct dependence on the turbine efficiency characteristics used in the simulation, the results are still quite good.

Results

Effect of Fouling on Engine Operating Parameters Using Various Fouling Schedules. The results of the computer simulation of compressor fouling on various operating parameters are presented in Figs. 8 to 12. These figures relate the changes in various operating parameters, resulting from the fouling schedule applied, to the "clean" simulation values. The effect of increasing the stage efficiency drop per fouling step is also presented in these figures. The stage efficiency drop is represented by the designation (1:x) where "x" is the drop in stage efficiency per fouling step in percent. The "1" refers to the one percent drop in the flow characteristic assigned to each progressive fouling step. All results are shown for operation at a fixed value of compressor "nondimensional" speed.

It is apparent from these results that the stage efficiency has a significant effect on all of the monitored parameters with the exception of the mass flow rate. Thus a reduction in mass flow rate is an accurate indicator of compressor fouling regardless of the effect fouling has on stage efficiency. Unfortunately, mass flow rate is not usually measured and so in order to be used as an indicator, it must be calculated using gas path analysis. The use of inlet depression as suggested by

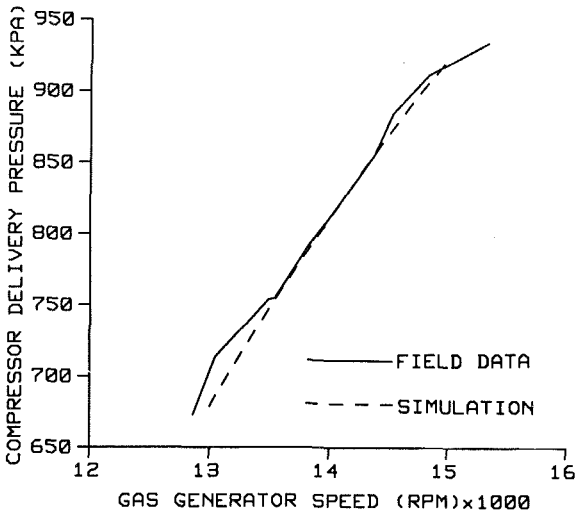

Fig. 3 Solar Centaur Meikle River comparison

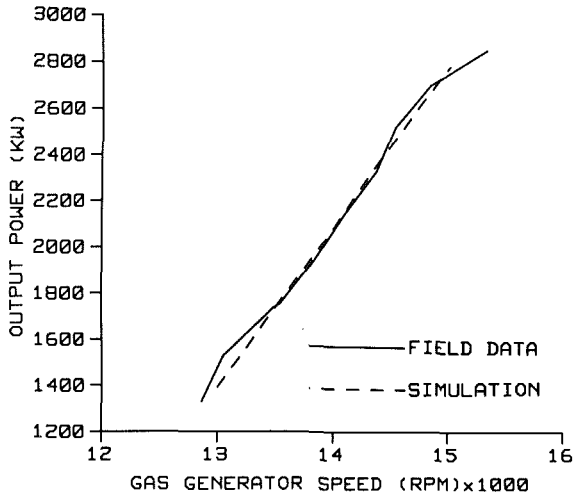

Fig. 4 Solar Centaur Meikle River comparison

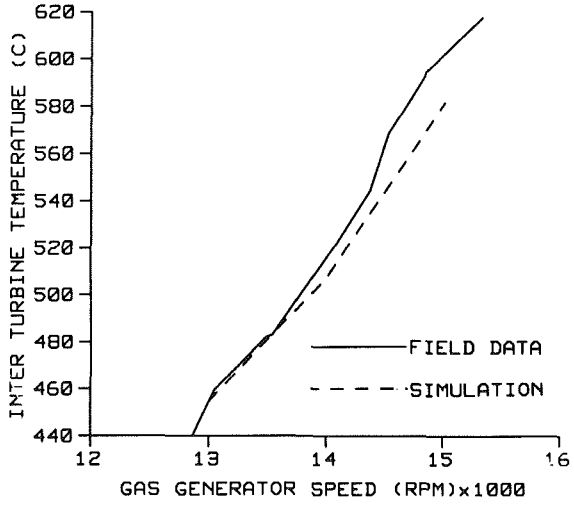

Fig. 5 Solar Centaur Meikle River comparison

Scott (1979) does provide a simple qualitative indication of loss of mass flow.

The compressor delivery pressure is a much more commonly measured parameter and, from the results presented in Fig. 9, appears to be a good indicator of compressor fouling. There is a significant drop in the CDP at all the levels of fouling

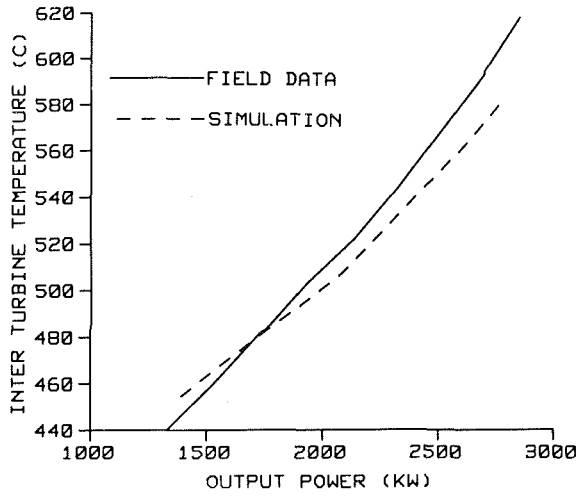

Fig. 6 Solar Centaur Meikle River comparison

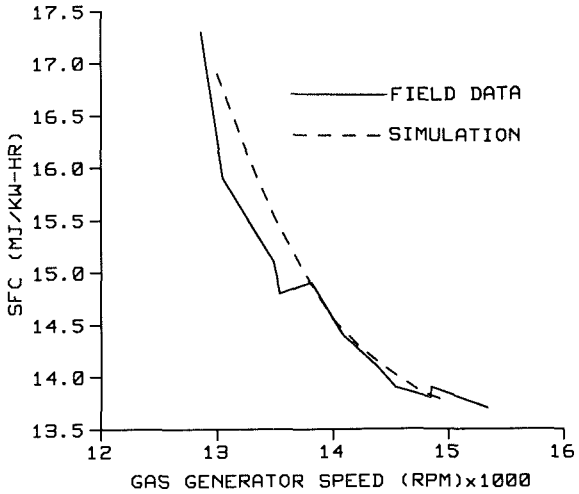

Fig. 7 Solar Centaur Meikle River comparison

simulated regardless of the reduction in stage efficiency, the reduction being basically due to rematching of the compressor characteristic.

The ITT appears to be a less reliable indicator of compressor fouling because it can either increase or decrease as the fouling progresses depending on how the stage efficiency is affected. Under three of the fouling schedules employed, the ITT illustrates a tendency either to decrease slightly or to remain virtually constant. Only when the stage efficiency is significantly reduced is a definite trend of increasing ITT noticeable. This dependency on stage efficiency indicates that the ITT is probably a very good indicator of possible foreign object damage or other faults, which directly affect compressor stage efficiency.

The most significant result of compressor fouling noted in this study was the drop in power output. While the increased temperatures associated with a reduction in compressor stage efficiency tend to reduce the drop in power output at higher levels of fouling, there remains a large drop in power at all levels. Perhaps even more significant is the rate at which this reduction in power occurs. From Fig. 11 it can be seen that even at the first level of fouling, the power has decreased by one percent. By the fourth level this reduction has increased to between 3.5 and 5 percent depending on the reduction in stage efficiency. Since these simulations were run at constant gas generator speed, it has been assumed that the increase in TIT has not exceeded its limit, thus necessitating a reduction

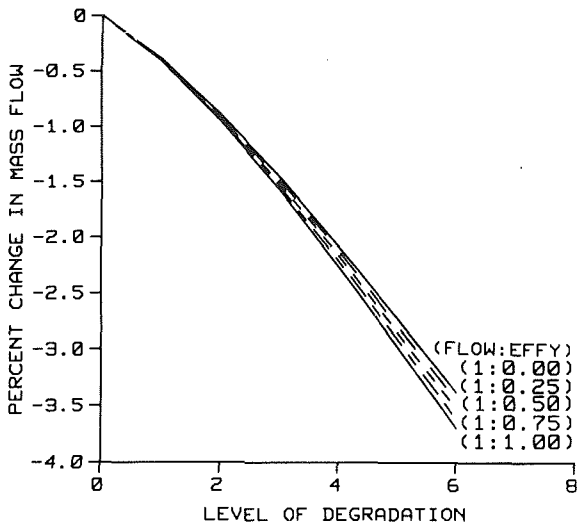

Fig. 8 Centaur simulation mass flow results

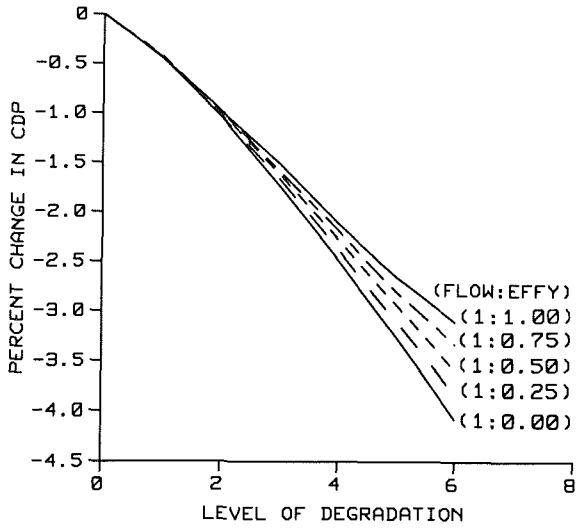

Fig. 9 Centaur simulation CDP results

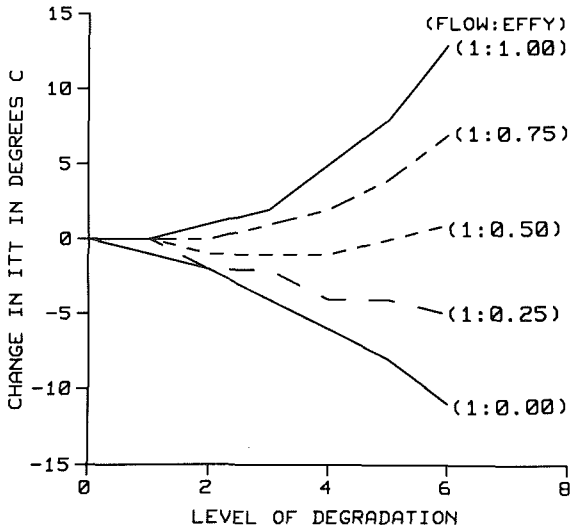

Fig. 10 Centaur simulation ITT results

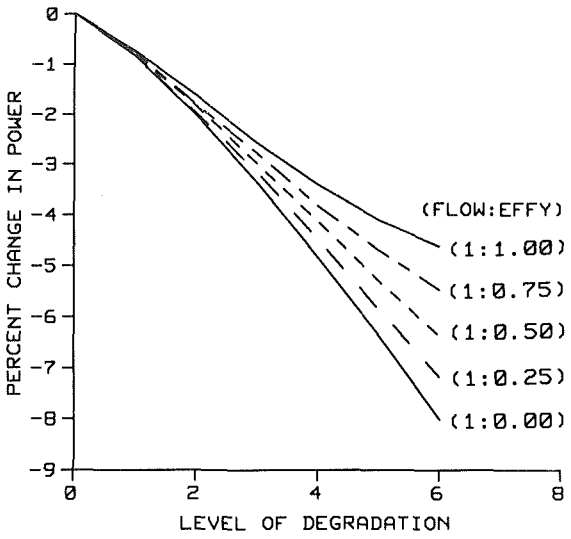

Fig. 11 Centaur simulation power results

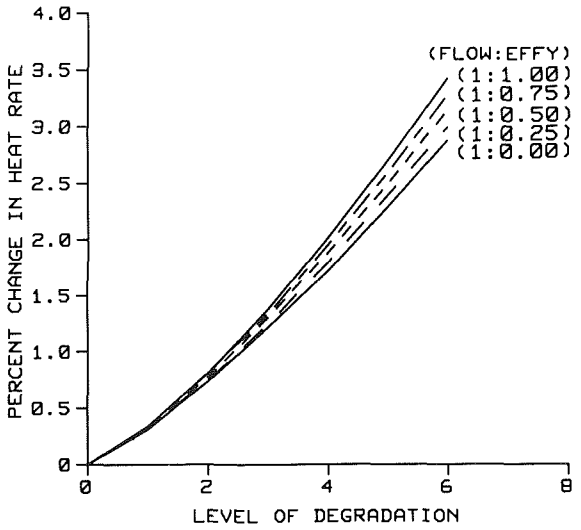

Fig. 12 Centaur simulation heat rate results

in speed; exceeding the TIT limit would lead to a further drop in available power.

Users who run their gas turbines for long hours at high power settings are probably most concerned with the changes in engine heat rate associated with compressor fouling. These results are presented in Fig. 12. Not surprisingly the heat rate is seen to increase at all levels of fouling and becomes worse as the stage efficiency is reduced. It is interesting to note that even assuming the least severe fouling schedule, the heat rate has increased a full percent by the third level of fouling and two percent by the fifth level. What is encouraging however, is that by the fifth level of fouling there are significant changes in the mass flow rate, CDP, power output and in some cases fuel flow and ITT, which can be used to indicate this level of deterioration. As mentioned previously, once the level of deterioration is known, then a cost benefit analysis such as the one described by Williams (1981b) can be performed to determine the most economical time to take the appropriate maintenance action.

In many industrial applications, power output is the critical engine parameter, while in pipeline duty, engine efficiency is typically of paramount importance. Both of these parameters are significantly affected by compressor fouling, as determined in this study. For the user who requires full power from their engines on a continuous basis, even the smallest amount of

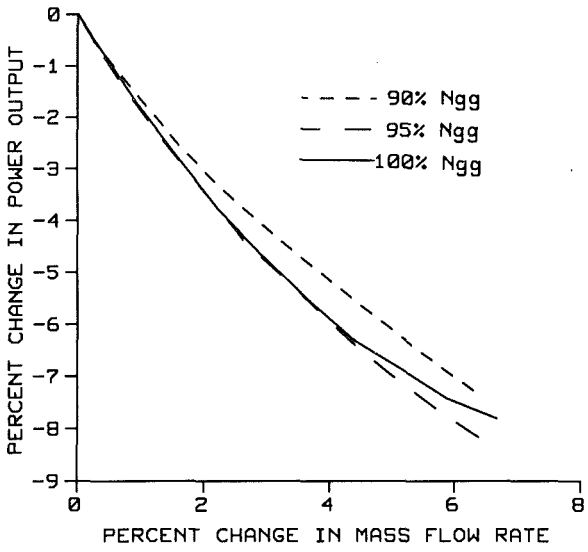

Fig. 13 Mass flow rate diagnostic plot (1:0.75)

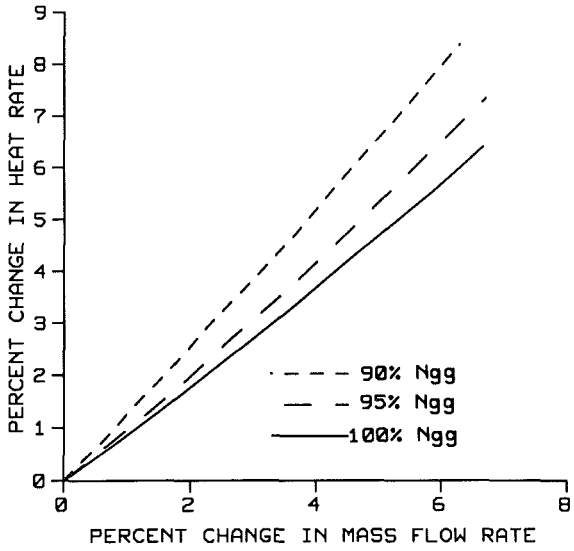

Fig. 14 Mass flow rate diagnostic plot (1:0.75)

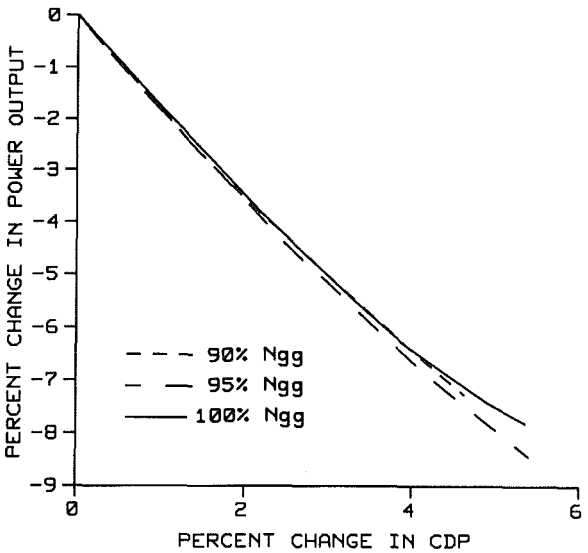

Fig. 15 Mass flow rate diagnostic plot (1:0.75)

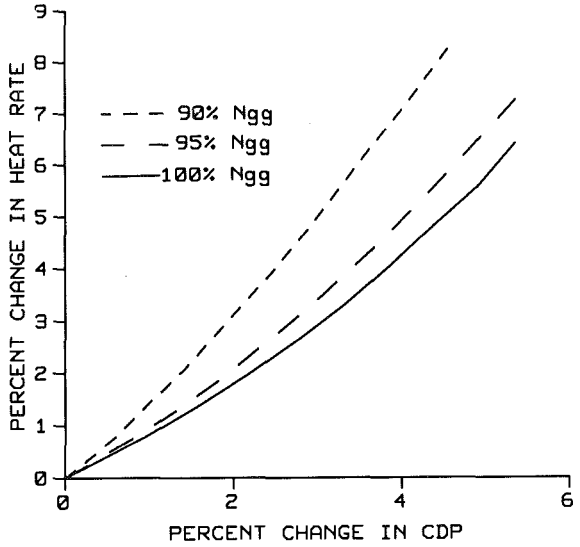

Fig. 16 Mass flow rate diagnostic plot (1:0.75)

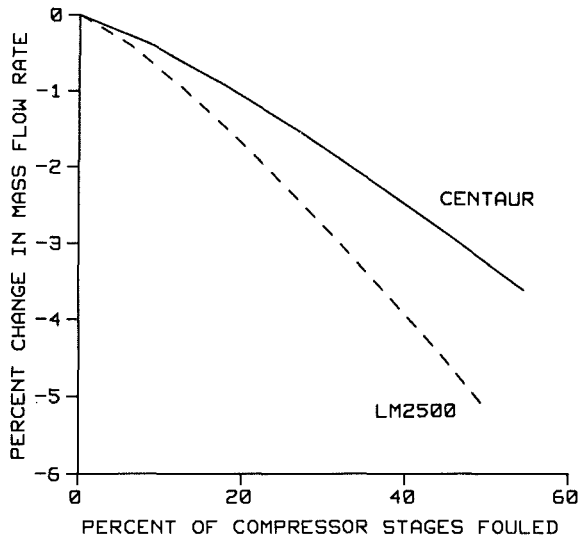

Fig. 17 Engine size comparison: model (1:0.75)

fouling can pose significant problems. In such cases, performing compressor washes using "on-condition" maintenance procedures would appear to offer little advantage over regularly scheduled washing. For the user who requires maximum efficiency from his units at all times, on-condition maintenance does appear to offer several advantages over regularly scheduled compressor washes. These advantages include a reduction in unnecessary compressor washes and/or limiting the amount of time spent operating in an uneconomical condition.

Formation of Diagnostic Plots. In order to facilitate the use of the information obtained in this study, diagnostic plots of the change in power and heat rate in percent, as a function of changes in mass flow rate and CDP, have been developed. The graphs presented in Figs. 13 to 16 are the results obtained from a Solar Centaur engine simulation with a (1:0.75) fouling schedule. The effect of gas generator speed on these parameters was also investigated. Using the identical fouling schedule, the compressor was simulated at speeds of 90, 95, and 100 percent of design speed.

By presenting the changes in power and heat rate as functions of typically monitored parameters, the diagnostic procedures that enable an operator to determine whether an engine is operating in a fouled condition have been simplified. Similarly, these simulation exercises can provide a quantitative estimate

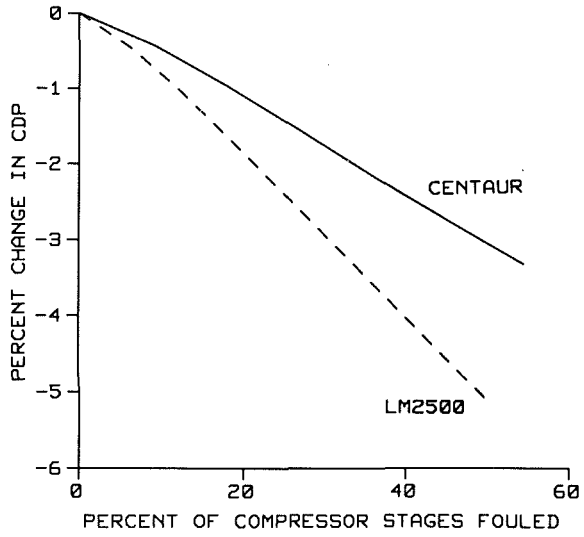

Fig. 18 Engine size comparison: model (1:0.75)

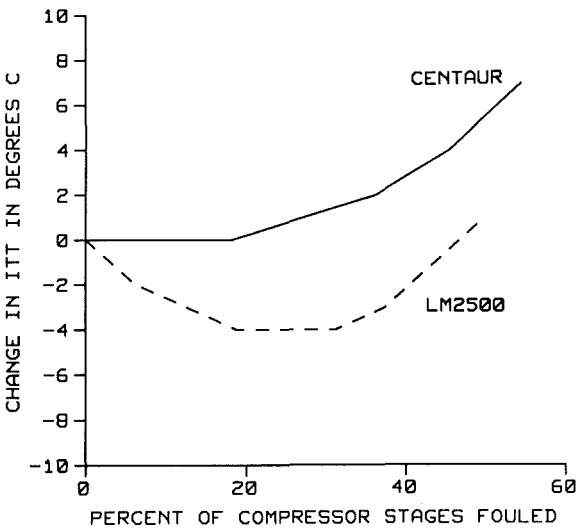

Fig. 19 Engine size comparison: model (1:0.75)

of how severely an engine's performance has suffered as a result of fouling. This information can then be used to evaluate the most economical interval between compressor washes. One of the most significant benefits offered by this type of simulation procedure is that individual engines and installations can be simulated if test baselines of engine performance are available to set up the appropriate input files. Thus, with initial baseline test results and the simulation software outlined in this paper, diagnostic plots for each individual engine could be developed. This not only would improve the accuracy of an "on-condition" maintenance procedure but would also limit the number of false alarms resulting from erroneous data acquisition.

Effect of Engine Size on Fouling Severity. By comparing the changes in operating parameters resulting from the same level of fouling on two engines of different size, an indication of whether fouling affects smaller or larger engines more severely was obtained. Figure 17 illustrates the percent change in mass flow rate through the engine as a function of the percent of the number of compressor stages that are fouled. The fouling was once again simulated using the linear fouling model (1:0.75). There is a dramatic difference between the drop in mass flow rate experienced by the GE LM2500-30 and that experienced by the Solar Centaur. The LM2500-30 was far more affected by compressor fouling than the Centaur, even

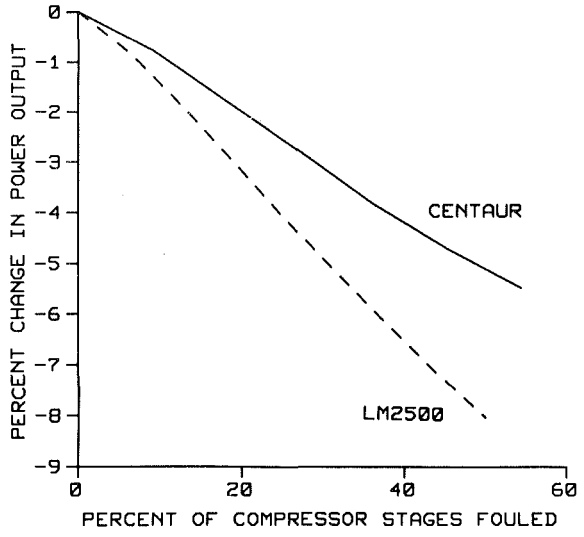

Fig. 20 Engine size comparison: model (1:0.75)

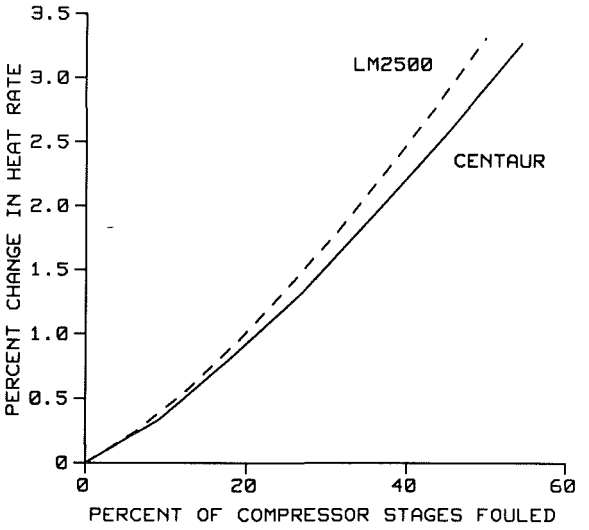

Fig. 21 Engine size comparison: model (1:0.75)

though it is the larger of the two engines. This finding is similarly true for all of the parameters tested, including the drop in power output and the increase in heat rate as presented in Figs. 18 to 21.

This may at first seem somewhat odd in that one would expect the passages of the Centaur to be more severely affected by the buildup of contaminants than the larger annulus areas of LM2500 as suggested by Saravanamuttoo (1985). However, previous investigations of this type by Lakshminarasimha and Saravanamuttoo (1986) have determined that the effect of fouling on a stage is proportional to the stage loading. This would certainly appear to be the case in this instance given that the stage loading of the LM2500-30 is almost twice that of the Centaur. In order to test this hypothesis fully, however, it would be necessary to perform a fouling simulation test on a compressor larger than the Centaur's but with the same stage loading.

As a result of this investigtion, it is possible that high performance aeroderivative gas turbines may be more susceptible to fouling than their industrial counterparts. Further work is needed to evaluate the effect of fouling on highly loaded compressors.

Conclusions

A computer program was developed that predicts gas turbine

performance by matching generalized turbine characteristics to a compressor characteristic generated using the stage stacking technique. The capability of this software to model gas turbine performance accurately was verified by baseline test results from actual field installations.

This study has investigated the effects of compressor fouling on gas turbine performance using a linear fouling model. The linear fouling model appears to be a reasonably accurate representation of the fouling process up to approximately halfway through the compressor.

The effects of progressive compressor fouling on parameters such as mass flow rate, compressor delivery pressure, interturbine temperature, fuel flow rate, power output, and heat rate were evaluated. From this information, diagnostic plots of changes in various typically monitored parameters versus changes in power output and heat rate resulting from compressor fouling were created.

The relative effects of engine size on compressor fouling were the subject of a preliminary investigation and it appears that stage loading may be more critical. It was predicted that a large but highly loaded compressor was more severely affected than a smaller compressor of lower stage loading.

Acknowledgments

The authors would like to acknowledge the financial support of the Natural Sciences and Engineering Research Council of Canada through a Strategic Grant. They would also like to thank Mr. D. Cornies of NOVA for providing data.

References

Agrawal, R. K., MacIsaac, B. D., and Saravanamuttoo, H. I. H., 1974, "An Analysis Procedure for the Validation of On-Site Performance Measurements of Gas Turbines," ASME JOURNAL OF ENGINEERING FOR POWER, Vol. 101, pp. 405–414.

Cohen, H., Rogers, G. F. C., and Saravanamuttoo, H. I. H., 1987, *Gas Turbine Theory*, 3rd ed., Longmans.

Howell, A. R., and Calvert, W. J., 1978, "A New Stage Stacking Technique for Axial-Flow Compressor Performance Prediction," ASME JOURNAL OF ENGINEERING FOR POWER, Vol. 100, pp. 698–703.

Karanjia, D. J., and Saravanamuttoo, H. I. H., 1980, "A Cost Effective Engine Health Monitoring System for On-Board use on Hovercraft," ASME Paper No. 80-GT-185.

Lakshminarasimha, A. N., and Saravanamuttoo, H. I. H., 1986, "Prediction of Fouled Compressor Performance Using Stage Stacking Techniques," *ASME Symposium on Turbomachinery Performance Deterioration*, FED-Vol. 37.

Matthee, F. A. H., and Saravanamuttoo, H. I. H., 1982, "Development of a Low Cost Performance Monitoring System for Use on Board Naval Vessels," ASME Paper No. 82-GT-297.

Sandercock, D. M., Kovach, K., and Lieblein, S., 1954, "Experimental Investigation of a Five Stage Axial Flow Compressor With Transonic Rotors in All Stages; Part I: Compressor Design, NACA RM E54F24," Sept. 1954 "Part II: Compressor Overall Performance," NACA RM E54901, July 1954, "Part III: Interstage Data and Individual Stage Performance Characteristics," NACA RM E56924, July 1956.

Saravanamuttoo, H. I. H., and MacIsaac, B. D., 1983, "Thermodynamic Models for Pipeline Gas Turbine Diagnostics," ASME JOURNAL OF ENGINEERING FOR POWER, Vol. 105, pp. 875–884.

Saravanamuttoo, H. I. H., and Lakshminarasimha, A. N., 1985, "A Preliminary Assessment of Compressor Fouling," ASME Paper No. 85-GT-153.

Scott, J. N., 1977, "Improving Turbo Compressor Efficiency via Performance Analysis Techniques," ASME Paper No. 77-GT-53.

Scott, J. N., 1979, "Axial Compressor Monitoring by Measuring Air Intake Depression," Third Symposium on Gas Turbine Operations and Maintenance, National Research Council of Canada.

Southwick, R. D., 1974, "A Stage Stacking Technique for Axial-Flow Compressors With Variable Geometry," ASD WPAFB, ASD-TR-74-38.

Stone, A., 1958, "Effects of Stage Characteristics and Matching on Axial Flow Compressor Performance," *Trans. ASME*, Vol. 80, pp. 1273–1293.

Upton, A. W. J., 1974, "Axial Flow Compressors and Turbine Blade Fouling: Some Causes, Effects and Cleaning Methods," First Symposium on Gas Turbine Operations and Maintenance, National Research Council of Canada.

Williams, L. J., 1981a, "The Use of Mathematical Modeling in the Analysis of Gas Turbine Compression Unit Test Data," ASME Paper No. 81-GT-217.

Williams, L. J., 1981b, "The Optimisation of Time Between Overhauls for Gas Turbine Compressor Units," *Proc. Fourth Symposium on Gas Turbine Operations and Maintenance*, National Research Council of Canada, Toronto, Canada.

Journal of Engineering for Gas Turbines and Power

Technical Briefs

High Operation Flexibility and Reliability by Multiunit Compressor Arrangement for Gas Storage Applications

H. Neuburg[1] and K. D. Schmidt[1]

OMV in the European Natural Gas Network

Based on OMV's experience in importing gas from the Soviet Union and on Austria's central geographic position in the European natural gas network, other European countries decided to join Austria in importing Soviet natural gas at the existing off-take station at Baumgarten: the Italian company SNAM in 1974, Gaz de France in 1976, and Yugoslavian Petrol Ljubiliana and Ina Naphtaplin in 1978.

To fulfill the contractual obligation to supply natural gas to Austrian consumers, OMV has to take into account an increase in the shares of imported gas. The gas in the storage operation guarantees a reliable supply regardless of any seasonal or peak-demand fluctuations.

For this purpose it was possible to use depleted natural gas reservoirs, which completely fulfilled the requirements for a gas storage facility, e.g., reservoir capacity, storage pressure, hourly flow rate, and proximity to the transit pipelines and customers. Because these are all natural storage reservoirs, their integrity in the appropriate pressure ranges is guaranteed.

A dispatching center is installed in Auersthal (north of Vienna) that controls and supervises the storage facilities and the entire OMV gas pipeline system. Operating in close coordination with the international and national partners, this center performs comprehensive optimization programs and regulates the gas flows to fit the needs of the customers and individual situation immediately.

Today the storage facility at Schoenkirchen contains an available working gas volume of approximately 1500 million nm^3 and a maximum injection and withdrawal rate of nearly 530,000 m^3/h.

The storage plant at Schoenkirchen has three natural, nearly depleted gas reservoirs with partial water drive in various reservoirs at different depths.

The storage plant is located in Neogene in the Vienna basin and is divided into the Sarmatian and Badenian formations. The fifth Sarmat reservoir and the fifth and sixth Torton reservoirs are used.

The Schoenkirchen storage facility was extended in separate phases, which were carried out not only to fit the contractual requirements but also to reach the most economical project size.

In addition to the necessary well structure, special attention was paid to the selection of the most appropriate natural gas compressor with regard to its size and characteristics.

Description of Station

The injection and withdrawal of storage gas are performed via 78 wells with eight distribution collectors. The well distribution system covers the three storage reservoirs, for which three different pressure levels may be used: a maximum pressure of 78 bar for the Sarmat reservoir, and a maximum of 130 bar for each Torton reservoir. The distributor collectors extend radially from the centrally located storage station.

The station is connected to three supply lines with different pressure levels. This allows great flexibility in the selection of the most favorable pressure level.

The following criteria were decisive in the selection of the compressor units:

- Fully automatic, unmanned operation from the dispatching center at Auersthal.
- Fully automatic switching of the compressor units in series and/or in parallel operation modes.
- The most suitable machine size for the gradual extension of the station.
- Reliable and continuous operation during the summer storage period in order to meet the contractual requirements.
- High start-up reliability, especially with regard to the emergency supply.
- Flexible compressor operating characteristics to adapt to reservoir pressure.
- Different compressors for the various pressure levels.
- Rapid change of machine components in case of failure; modular design.
- Fulfilling environmental requirements with regard to exhaust emissions, noise limits, etc.

Compressor Units

Consideration of the key criteria for the station extension led to a general machine concept for the final extension phase. This concept offered a high level of flexibility and was adapted step by step to meet the contractual requirements (Fig. 1).

Currently, six Centaur and two Mars turbine-driven compressor units are installed with different types of centrifugal gas compressors. The piping makes it possible to carry out a series and/or parallel operation of the Centaur units and a parallel operation with the Mars units at the same time (Fig. 2).

The Mars turbine compressor units are now handling constant base load in the storage operation. In the case of peak loads, the smaller Centaur units can be used to meet the additional requirements. The Mars units have a much higher ratio

[1]OMV Gas Division, Auersthal, Austria.

Contributed by the International Gas Turbine Institute and presented at the 33rd International Gas Turbine and Aeroengine Congress and Exhibition, Amsterdam, The Netherlands, June 5–9, 1988. Manuscript received by the International Gas Turbine Institute June 8, 1987. Paper No. 88-GT-230.

of operating hours/starts, and the Centaur units cover the immediate demands of gas dispatching when balancing the differences between the incoming and outgoing natural gas quantities.

In some cases it is necessary to use the Centaur turbine compressor units for withdrawal in order to increase the withdrawal rate. This mode of operation is carried out in spring, toward the end of the withdrawal period, when high withdrawal rates are required at a time of low storage pressures.

Figure 3 shows a clear overview of the optimal, overlapping performance envelopes of each of the C 1685, C 1655, and C 3044X compressors. From this we can see all the requirements of a flexible storage operation together with sharp changes in operating pressure depending on the storage capacity.

Station Control

The station control is of great importance for the unmanned operation of the storage plant and it consists of three major processors:

(A) Logic Processor. Binary tasks include all logical decisions to be performed on the basis of contact inputs from the station, the telecommunications system, the auxiliary units in the control room, the microprocessor-based engine control, the control desk, and from the threshold values deduced from the analog signals.

- Mode control: this function is used to define all gas paths.
- Valve control: operates all functions in connection with the open and close positions.
- Alarm systems: recording, summarizing, and communicating to the telecommunications system, as well as data logging and registering alarms.
- Emergency shutdown systems: all technical aspects required for the safety and security of an emergency shutdown. These are taken into account in the hardware.
- Start–stop logic: this automatic system serves to carry out the starts and stops of the turbocompressor in series operation.
- Auxiliary pump control.
- Cooler control.

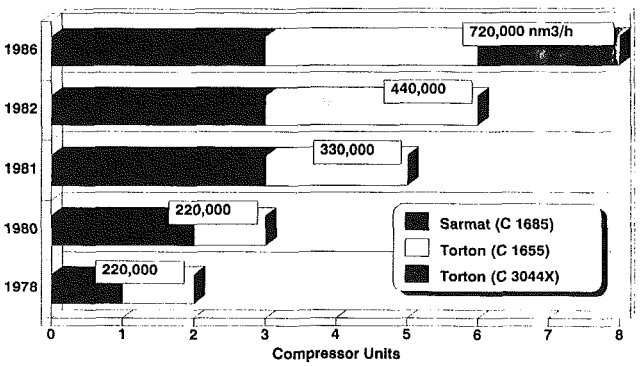

Fig. 1 Extension phases of Schoenkirchen

(B) Mathematic Processor. This area comprises all that has to do with analog values and calculation results from mathematical combinations with analog values and the control systems.

- Recording of analog values: The following rough data are recorded in the Schoenkirchen station: differential pressure, pressure, temperature, level, speed, standard density, and environmental data. Most analog values have to be measured in an area with an explosion hazard. The Exi code (intrinsically safe) is used for explosion protection.
- Control functions: All 32 control circuits that are operated from the metering station are worked out in the computer processor. This also includes the surge control system for both Mars turbine compressor units.
- Decision aid for the dispatcher: This function serves to calculate the flow rates and the corresponding operating modes in advance.
- Data logging: This function processes all analog values that can be recorded in a freely programmable documentation form, such as daily reports, meter readings, etc.
- Event logging: This function records the documentation forms of the binary statuses of status changes, e.g., alarms and their recordings or summaries, etc.
- Trend system: This system can record, store, and even print out all measurement values in a freely programmable and highly accurate sampling system.
- Operator support: In addition to the normal working screen, the operator is supported by a menu screen, on which he can call up modes and related descriptions at any time. Furthermore, all stored data can be shown in either a graphic or list form and can also be used for comparison and calculation purposes when dealing with actual data.

(C) Analog Processor. This computer handles all analog inputs and outputs from and to the field, respectively from and to the telecommunication system.

Vibration Recording

This area is completely separate from the station control,

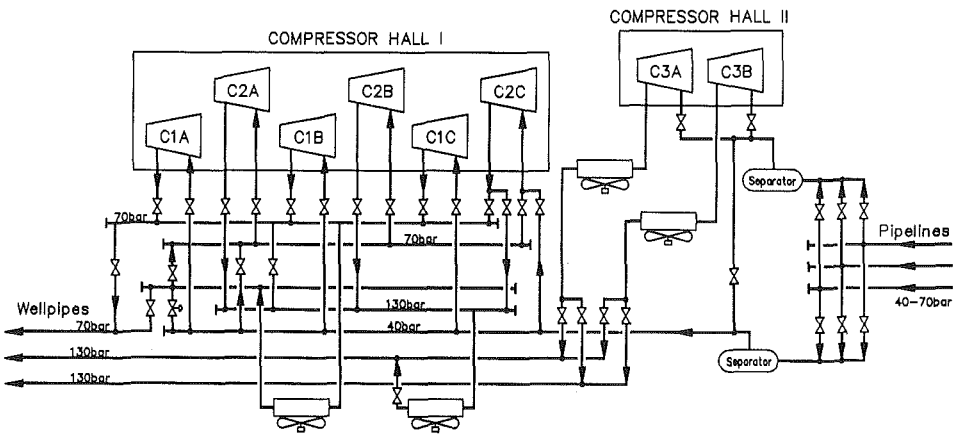

Fig. 2 Principal piping of the compressor station

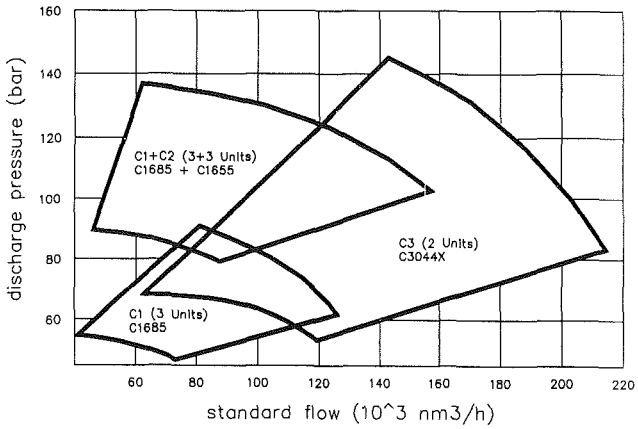

Fig. 3 Compressor performance graphs

since the task involves a very high data acquisition rate. In this unit approximately 42,500 measurements are recorded per second for each machine, in a cyclical way. A further description is in the section on "Maintenance."

Maintenance

To avoid failures during the running period, it is necessary to inspect all storage units after the storage season. Moreover, it is useful to perform an additional inspection in springtime, just before the storage season, in order to detect any corrosion resulting during the extended shutdown. Experience has shown that malfunctions in the instrumentation and control equipment also may result during the extended shutdown. Therefore those systems also must be tested and recalibrated in the spring.

Summary

The findings and experience gained from ten years of storage operation at Schoenkirchen have shown that the decision gradually to develop such a large storage facility in accordance with OMV's delivery contract agreements has proved to be highly successful and effective.

The step-by-step extension of the storage station using small compressor units turned out to be a most economical and suitable solution.

On-condition maintenance has contributed greatly toward ensuring the availability and reliability of the engines during the storage period.

The modular design of the modern gas turbine turbocompressor units has made it possible to replace faulty components quickly, thus minimizing downtime to the lowest level possible.